

**The sensitivity of the photostationary state of NO_x
and its implication for the oxidation capacity in a
semi-rural and boreal forest region**

Dissertation

zur Erlangung des Grades
“Doktor der Naturwissenschaften”
im Promotionsfach Physik

Am Fachbereich Physik, Mathematik und Informatik
der Johannes Gutenberg-Universität Mainz,
ausgeführt am
Max-Planck-Institut für Chemie, Mainz

vorgelegt von
Muhammad Umar Javed
geboren in Rawalpindi, Pakistan

Mainz, 2014

Dekan:

1. Gutachter:

2. Gutachter:

Tag der mündlichen Prüfung: 28. April 2015

Abstract

The roles of nitric oxide (NO) and nitrogen dioxide (NO₂) are strongly coupled with the cleansing capacity of the atmosphere by controlling the photochemical production of ozone (O₃) and affecting the abundance of the hydroxyl (OH) radical and nitrate radical (NO₃). During daytime, when conditions of sufficient radiation and O₃ prevail, NO and NO₂ are in a fast photochemical equilibrium, often labelled as being in a ‘photostationary state’. Therefore the sum of NO and NO₂ is referred to as NO_x. The photostationary state of NO_x has been previously studied at various locations ranging from cities (highly polluted) to remote regions (less polluted). The photochemical cycling between NO and NO₂ is understood reasonably well under high NO_x conditions (typically in urban areas). In contrast, significant gaps in understanding the cycling between NO and NO₂ have been revealed in semi-rural to remote regions under low NO_x conditions. These gaps could be related to potential interferences in NO₂ measurements, especially in case of indirect methods that might suffer from artefacts. If NO₂ interferences can be excluded, it is often concluded that these gaps are related to the presence of an ‘unknown oxidant’ converting NO to NO₂, especially at very low NO_x concentrations. In this study, the photostationary state of NO_x is analysed to evaluate whether unknown processes are present.

A newly developed gas analyser (GANDALF) based on laser induced fluorescence (LIF) for measuring NO₂ directly was deployed for the first time during the 2011 PARADE field study. PARADE took place in a semi-rural area of central Germany in summer 2011. Comprehensive measurements of NO₂ using different techniques (DOAS, CRD, and CLD) facilitated a detailed and successful comparison of GANDALF with other NO₂ measurement techniques. In order to analyse the photostationary state of NO_x based on the NO₂ measurements by GANDALF in this environment, measurements of different relevant trace gas species and meteorological parameters have been carried out. Moderate NO_x levels 10² to 10⁴ parts per trillion were observed during PARADE at the location, while biogenic volatile organic compounds (BVOCs) from surrounding forest, mainly coniferous trees, were of the order of 10² parts per trillion.

The characteristics of the NO_x photostationary state have been studied under low NO_x conditions (10¹ to 10³ parts per trillion) for a different location in a boreal forest region during HUMPPA-COPEC-2010. The field study HUMPPA-COPEC was conducted at the ‘SMEAR II’ field station in Hyttiälä in southern Finland in summer 2010.

The characteristics of the photostationary state of NO_x are compared in this study for the two environments. Furthermore, the comprehensive data set including measurements of trace gases relevant for the radical chemistry [OH and hydroperoxy (HO_2) radicals], as well as measurements of the total OH reactivity, provide the opportunity to test and improve our current understanding of NO_x -related photochemistry using a box model constrained to observations.

Although NO_x levels in HUMPPA-COPEC are lower compared to PARADE, while the BVOCs levels, are higher, the cycling process from NO to NO_2 is understood reasonably well in both cases. The analysis of photostationary state reveals that potential unknown processes are not present at either of the largely different locations. The current representation of NO_x chemistry mechanisms is simulated for HUMPPA-COPEC by using the MIM3* mechanism and found to be consistent with results obtained from the photostationary state of NO_x .

Zusammenfassung

Für das Vermögen der Atmosphäre sich selbst zu reinigen spielen Stickstoffmonoxid (NO) und Stickstoffdioxid (NO₂) eine bedeutende Rolle. Diese Spurengase bestimmen die photochemische Produktion von Ozon (O₃) und beeinflussen das Vorkommen von Hydroxyl- (OH) und Nitrat-Radikalen (NO₃). Wenn tagsüber ausreichend Solarstrahlung und Ozon vorherrschen, stehen NO und NO₂ in einem schnellen photochemischen Gleichgewicht, dem „Photostationären Gleichgewichtszustand“ (*engl.: photostationary state*). Die Summe von NO und NO₂ wird deshalb als NO_x zusammengefasst. Vorhergehende Studien zum photostationären Gleichgewichtszustand von NO_x umfassen Messungen an unterschiedlichsten Orten, angefangen bei Städten (geprägt von starken Luftverschmutzungen), bis hin zu abgeschiedenen Regionen (geprägt von geringeren Luftverschmutzungen). Während der photochemische Kreislauf von NO und NO₂ unter Bedingungen erhöhter NO_x-Konzentrationen grundlegend verstanden ist, gibt es in ländlicheren und entlegenen Regionen, welche geprägt sind von niedrigeren NO_x-Konzentrationen, signifikante Lücken im Verständnis der zugrundeliegenden Zyklierungsprozesse. Diese Lücken könnten durch messtechnische NO₂-Interferenzen bedingt sein - insbesondere bei indirekten Nachweismethoden, welche von Artefakten beeinflusst sein können. Bei sehr niedrigen NO_x-Konzentrationen und wenn messtechnische NO₂-Interferenzen ausgeschlossen werden können, wird häufig geschlossen, dass diese Verständnislücken mit der Existenz eines „unbekannten Oxidationsmittels“ (*engl.: unknown oxidant*) verknüpft ist. Im Rahmen dieser Arbeit wird der photostationäre Gleichgewichtszustand von NO_x analysiert, mit dem Ziel die potenzielle Existenz bislang unbekannter Prozesse zu untersuchen.

Ein Gasanalysator für die direkte Messung von atmosphärischem NO₂ mittels laserinduzierter Fluoreszenzmesstechnik (*engl. LIF – laser induced fluorescence*), GANDALF, wurde neu entwickelt und während der Messkampagne PARADE 2011 erstmals für Feldmessungen eingesetzt. Die Messungen im Rahmen von PARADE wurden im Sommer 2011 in einem ländlich geprägten Gebiet in Deutschland durchgeführt. Umfangreiche NO₂-Messungen unter Verwendung unterschiedlicher Messtechniken (DOAS, CLD und CRD) ermöglichten einen ausführlichen und erfolgreichen Vergleich von GANDALF mit den übrigen NO₂-Messtechniken. Weitere relevante Spurengase und meteorologische Parameter wurden gemessen, um den photostationären Zustand von NO_x, basierend auf den NO₂-Messungen mit GANDALF in dieser Umgebung zu untersuchen.

Während PARADE wurden moderate NO_x Mischungsverhältnisse an der Messstelle beobachtet ($10^2 - 10^4$ ppt_v). Mischungsverhältnisse biogener flüchtige Kohlenwasserstoffverbindungen (BVOC, engl.: biogenic volatile organic compounds) aus dem umgebenden Wald (hauptsächlich Nadelwald) lagen in der Größenordnung 10^2 ppt_v vor.

Die Charakteristiken des photostationären Gleichgewichtszustandes von NO_x bei niedrigen NO_x -Mischungsverhältnissen ($10 - 10^3$ ppt_v) wurde für eine weitere Messstelle in einem borealen Waldgebiet während der Messkampagne HUMPPA-COPEC 2010 untersucht. HUMPPA-COPEC-2010 wurde im Sommer 2010 in der SMEARII-Station in Hyytiälä, Süd-Finnland, durchgeführt. Die charakteristischen Eigenschaften des photostationären Gleichgewichtszustandes von NO_x in den beiden Waldgebieten werden in dieser Arbeit verglichen.

Des Weiteren ermöglicht der umfangreiche Datensatz - dieser beinhaltet Messungen von relevanten Spurengasen für die Radikalchemie (OH, HO₂), sowie der totalen OH-Reaktivität – das aktuelle Verständnis bezüglich der NO_x -Photochemie unter Verwendung von einem Boxmodell, in welches die gemessenen Daten als Randbedingungen eingehen, zu überprüfen und zu verbessern.

Während NO_x -Konzentrationen in HUMPPA-COPEC 2010 niedriger sind, im Vergleich zu PARADE 2011 und BVOC-Konzentrationen höher, sind die Zyklierungsprozesse von NO und NO₂ in beiden Fällen grundlegend verstanden. Die Analyse des photostationären Gleichgewichtszustandes von NO_x für die beiden stark unterschiedlichen Messstandorte zeigt auf, dass potenziell unbekannte Prozesse in keinem der beiden Fälle vorhanden sind. Die aktuelle Darstellung der NO_x -Chemie wurde für HUMPPA-COPEC 2010 unter Verwendung des chemischen Mechanismus MIM3* simuliert. Die Ergebnisse der Simulation sind konsistent mit den Berechnungen basierend auf dem photostationären Gleichgewichtszustand von NO_x .

Contents

1	Scientific Context and Motivation.....	1
1.1	The Troposphere	2
1.1.1	Role of NO _x in tropospheric chemistry.....	4
1.1.1.1	Sources and sinks.....	5
1.1.2	Related photochemistry	8
1.2	The quasi-equilibrium state	11
1.3	Instantaneous photochemical production and loss rates of O ₃	14
1.3.1	Ozone compensation point (OCP)	15
1.3.2	Catalytic efficiency of NO _x	15
1.4	Motivation and the framework.....	16
2	GANDALF.....	29
2.1	The operational method.....	29
2.1.1	Instrumentation	30
2.1.1.1	Diode laser	32
2.1.1.2	Herriott cell.....	32
2.1.1.3	Photon counting head device.....	33
2.1.1.4	Filters	33
2.1.1.5	Optical reference system	34
2.1.1.6	Accessories	36
2.2	Laser on-off cycle selection	37
2.3	Calibration system.....	39
2.3.1	Gas phase titration.....	39
2.3.2	Model simulations with lab comparison	40
2.3.2.1	O ₃ dependency	42
2.3.2.2	Residence time.....	44
2.3.2.3	Effect of temperature and pressure.....	45

2.3.2.4	Atmospheric H ₂ O vapour dependency	48
2.3.3	Automated calibration setup	49
2.4	Interferences by trace species.....	52
2.5	Precision and limit of detection.....	54
2.6	Overview of different LIF instruments	57
3	Field Experiment: PARADE-2011.....	59
3.1	Overview	59
3.1.1	Site description and meteorological conditions	59
3.1.2	Instrumentation	63
3.1.3	Time series PARADE-2011.....	65
3.2	Measurement setup of GANDALF	70
3.2.1	PARADE NO ₂ comparison	71
3.2.2	NO ₂ measurement ratios distribution.....	75
3.3	Ozone photochemistry in PARADE	80
4	Photostationary State (PSS) Analysis: PARADE-2011	93
4.1	Leighton ratio (Φ)	93
4.2	Modified Leighton Ratio (Φ_{mod}).....	99
4.3	Extended Leighton ratio (Φ_{ext}) including measured RO _x	102
5	HUMPPA-COPEC-2010: NO_x photochemistry.....	109
5.1	Overview HUMPPA-COPEC-2010.....	109
5.2	Leighton ratio (Φ)	113
5.2.1.1	$\Phi_{\text{ext}2}$ (Inclusion of NO + HO ₂ in Φ).....	115
5.2.1.2	Estimation of RO ₂ from $\Phi_{\text{ext}2}$	116
5.3	Box model simulations.....	118
5.3.1	Introduction to the mechanism applied.....	118
5.3.2	Results of simulations	119
5.3.2.1	Discrepancy between simulations and PSS	122

5.3.2.1.1	Rate coefficient for RO ₂ + NO	122
5.3.2.1.2	Halogen oxides	122
5.3.2.1.3	Unknown oxidant	123
5.3.2.2	Tuning of (OHReact) _{CAABA/MECCA}	125
5.4	Trend of instantaneous O ₃ production in NO _x -limited regime.....	132
5.5	Decline in Φ at low NO	135
5.6	Effects of alkyl nitrates on NO _x lifetime and OPE.....	139
6	Conclusions and Outlook	145
6.1	Conclusions	145
6.2	Outlook.....	149
7	APPENDICIES	151
7.1	LISTS	151
7.1.1	Figures in main text	151
7.1.2	Tables	155
7.1.3	Abberviations	156
7.2	Instrumental.....	158
7.2.1.1	Optical filters	158
7.2.1.1.1	Absorption.....	158
7.2.1.1.2	Reflectance	159
7.2.1.1.3	Transmittance	160
7.2.1.2	Laser ON/OFF cycle.....	161
7.2.1.3	Appurtenances	161
7.2.1.4	Reactions for calibration simulations	162
7.2.1.5	NO _{GPT}	163
7.2.1.6	Sensitivity and LOD	163
7.2.1.7	NO Accuracy	164
7.2.1.8	Certified Standards	165
7.2.1.8.1	NIST	165

7.2.1.8.2	Mass flow calibrator (DryCal).....	166
7.3	PARADE-2011.....	169
7.3.1.1	Time Series of NMHC.....	169
7.3.1.2	Air Mass Origin.....	169
7.3.1.3	jO^1D versus HO_x	170
7.3.1.4	NO_2 Ratios Correlations.....	170
7.3.1.5	Diel profile of O_3	177
7.3.1.6	BVOCs and NMHC loss rates.....	178
7.3.1.7	Trends.....	179
7.3.1.7.1	Φ colour coded with relative jNO_2	179
7.3.1.7.2	NO_2 v/s NO	179
7.3.1.7.3	Effective lifetime of PAN.....	180
7.4	HUMPPA-COPEC-2010.....	181
7.4.1.1	Time series of BVOCs, $(OHReact)_{meas}$, and others.....	181
7.4.1.2	Φ colour coded with relative jNO_2	182
7.4.1.3	Leighton Ratio with uncertainty.....	183
7.4.1.4	Trends versus NO	183
7.4.1.5	$P(O_3)_{PSS}$ and $P(O_3)_{CAABA/MECCA}$	184
7.5	Mechanism Chemical Equations.....	185
7.6	BIBLIOGRAPHY.....	217
8	ACKNOWLEDGEMENTS.....	235

1 Scientific Context and Motivation

Researchers have been inspired to study the physical and chemical properties of the atmosphere surrounding the planet Earth ever since the discovery of ozone ([Schönbein, 1840](#)) in the mid-19th century. This encompasses the excitement of understanding the thin envelope of air around the globe from the troposphere (0 - 18 km) to thermosphere (> 85 - 90 km). The atmosphere around Earth is a complex layer of different gas species. The most abundant gases of the atmosphere are nitrogen (78 %), oxygen (21 %), argon (0.93 %), and water vapour, the level of which reaches up to 3 % ([Seinfeld and Pandis, 2006](#)). A number of different trace gases are present in a range of parts per quadrillion (ppq_v) to parts per million by volume (ppm_v). Various trace gases are emitted into the atmosphere by several means such as anthropogenic activities and emissions at the surface (trees, soil etc.). These gases directly or indirectly contribute to the radiative balance of Earth and in the chemical properties of the atmosphere ([Seinfeld and Pandis, 2006](#)). In the last 100 years, the physical and chemical mechanisms of the atmosphere have been disturbed due to the increase in anthropogenic activities, such as growing industry, agriculture, and traffic. Global warming (the greenhouse effect), increases in the tropospheric O₃, and ozone depletion in the stratosphere (< 50 km) are a few examples of changes forced by human activities in the Earth's atmosphere ([Brasseur et al., 1999](#)). The increase in primary pollutants, such as nitrogen oxides, sulphur dioxide, volatile organic compounds, and particulates (e.g. soot) affects the air quality. Some of these pollutants undergo photochemical reactions and give rise to secondary pollutants like ozone, oxygenated organic species, organic and inorganic acids, and particulates. The pollution degradation or the self-cleansing mechanism of the troposphere ([Levy, 1971](#)) is initiated by oxidation processes in first step and later subsequent deposition. Hydroxyl and nitrate radicals initiate the oxidation process during day and night time, respectively and control the atmosphere's self-cleansing mechanism ([Lelieveld, 2010](#); [Rohrer et al., 2014](#)). A better understanding of processes within the atmosphere from polluted to clean regions is of interest due to the direct impacts on life.

1.1 The Troposphere

The troposphere is the lowest part of the atmosphere with a maximum depth of about 18 km in the tropics and a minimum depth of 6 - 8 km at the poles (Brasseur et al., 1999). It contains 80 - 90 % of the atmospheric mass (Brasseur et al., 1999) and nearly all the water vapour and aerosols in the atmosphere are present in this layer. The troposphere is well mixed horizontally and vertically compared to the stratosphere (Brasseur et al., 1999). Generally, temperature in the troposphere decreases with increase in height (Brasseur et al., 1999) at about an average lapse rate¹ of $6.5\text{ }^{\circ}\text{C km}^{-1}$. Atmospheric pressure is highest at sea level (1013.25mbar or hPa) and decreases quasi-exponentially with height (Brasseur et al., 1999). The lowest part of the troposphere is called the planetary boundary layer (PBL). The remaining section of the troposphere above the PBL is considered to be part of the free atmosphere (Fig. 1.1) (Stull, 1988). The PBL is directly influenced by the Earth's surface emissions and the depth of the PBL is variable, depending on local topology and meteorology, from a few hundred meters to 1 - 2 kilometres (Brasseur et al., 1999).

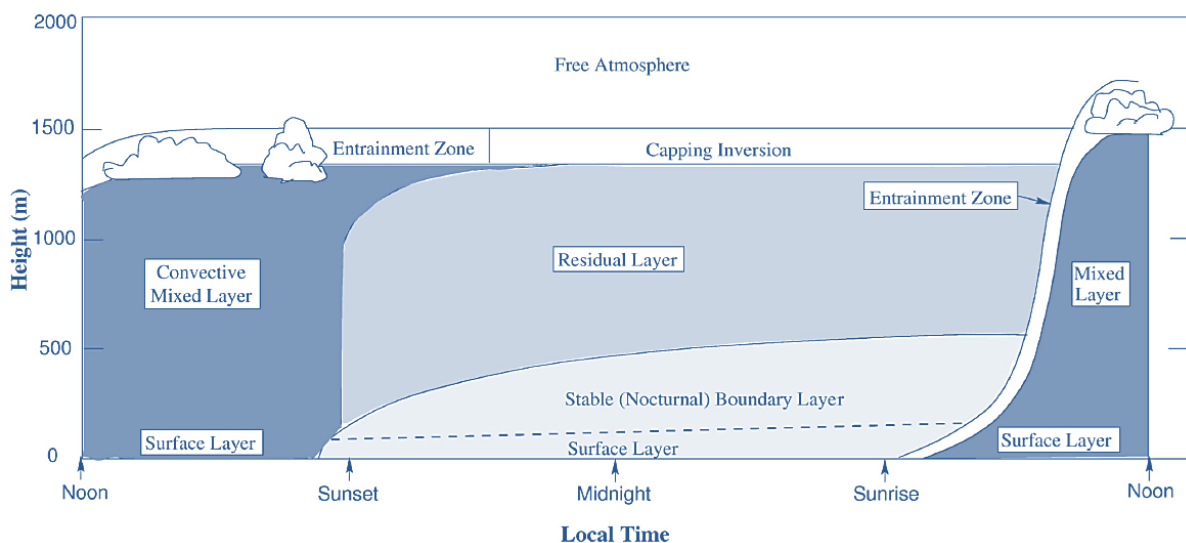


Fig. 1.1: Stratification of planetary boundary layer. [Figure is adapted from (Stull, 1988)]

The PBL evolves with the time of day and contains different sub layers e.g. entrainment zone, convective mixed layer, nocturnal boundary layer, and surface layer (Fig. 1.1). The lower

¹ Negative rate of change in temperature with respect to height.

region of the PBL is called the surface layer and it contains large gradients of pollution concentrations, wind, moisture, and temperature. It is about 10 % of the PBL's depth ([Stull, 1988](#)). The convective mixed layer resides on top of the surface layer; due to convective turbulence during daytime and it has a nearly uniform potential temperature² and humidity ([Stull, 1988](#)). The nocturnal boundary layer is developed due to less turbulence in the absence of surface heating at sunset to sunrise on top of the surface layer. It can be described as a stable boundary layer ([Stull, 1988](#)). On top of this layer, the leftover part of the convective mixed layer resides; this leftover part is called the residual layer ([Stull, 1988](#)). The entrainment zone is the top most part of the PBL and it separates the convective mixed layer and free troposphere. This zone contains statically stable air and has a negative buoyancy flux³ ([Stull, 1988](#)). The entrainment zone limits the exchange of chemical compounds between PBL and free troposphere. The time scale for the exchange is in an order of several hours to days ([Brasseur et al., 1999](#)).

Besides the physical processes, several chemical reactions occur between trace gases in the troposphere. Amongst these chemical reactions, the self-cleansing mechanism is the one which has vast impact on the quality of the Earth's atmosphere. The reactions of radicals with various chemical compounds leading to deprivations of pollutants make up the self-cleansing mechanism. The radical photochemistry also produces secondary pollutants; most prominent is O₃. In the stratosphere, O₃ is primarily responsible for the absorption of harmful ultraviolet (UV - B) radiation from Sun. These UV - B radiation can cause damage to human health (skin cancer) and ecosystems. About 90 % of O₃ in the atmosphere is located in the stratosphere ([Crutzen et al., 1999](#)). Approximately 40 % of the tropospheric O₃ is transported from the stratosphere ([Roelofs and Lelieveld, 1997](#)). The contribution of stratospheric O₃ at the surface ranges from about 10 % in summer to 60 % in winter ([Roelofs and Lelieveld, 1997](#)). The photochemical production of O₃ in the northern and southern hemispheres is 70 % and 50 % ([Roelofs and Lelieveld, 1997](#)), respectively. The increased concentration of O₃ ([Tiao et al., 1986](#); [Logan, 1985](#)) in the troposphere is a major concern. In contrast to the stratosphere, O₃ in the troposphere has several harmful effects e.g. the crop damage ([Wahid, 2006](#); [Avnery et al., 2011a, b](#)), an increase in premature mortality due to an increase of O₃ and particulate matter (PM_{2.5}) ([Lelieveld et al., 2013](#)) etc. NO_x⁴ and RO_x⁵

² The temperature that a parcel [at pressure (P)] would acquire if adiabatically brought to pressure (P₀).

³ The buoyancy associated with the vertical kinematic flux of virtual potential temperature.

⁴ NO_x = [Nitric oxide (NO) + Nitrogen dioxide (NO₂)]

⁵ RO_x = [Hydroperoxyl (HO₂) + sum of organic peroxy radicals (Σ RO₂)]

control the abundances of O_3 in the troposphere. A better understanding of the role of NO_x with RO_x in the O_3 photochemistry is very important.

1.1.1 Role of NO_x in tropospheric chemistry

In presence of O_3 and sunlight, the interconversion between NO and NO_2 is very fast and therefore, the sum of NO and NO_2 is described as $NO_x (= NO + NO_2)$. NO and NO_2 are considered primary pollutants caused by anthropogenic activity, along with carbon monoxide (CO), sulphur dioxide (SO_2), methane (CH_4), and several others. NO_x and volatile organic compounds (VOCs) are responsible for the production of O_3 . The role of NO_x is an important factor in the oxidation capacity of the troposphere because it affects O_3 and contributes to the abundances of OH and NO_3 . The NO_x lifetime is determined by their oxidation capacity and consequently affects their abundance. The transport of NO_x is little because of shorter lifetimes (right panel: Fig. 1.2) compared to other primary pollutants like CO , SO_2 , and CH_4 etc. Due to seasonal variability of OH (Vaughan et al., 2012), the lifetime of NO_x is shorter in the summer compared to the winter (R. 1.7). The tropospheric lifetime of NO_x is in the range of hours to days. Near the Earth's surface it is shorter compared to high altitudes (left side: Fig. 1.2). At higher altitudes NO_x is mostly present in form of NO because of the temperature dependence of the reaction ' $NO + O_3 \rightarrow NO_2$ ' (R. 1.1). The reaction slows at lower temperatures.

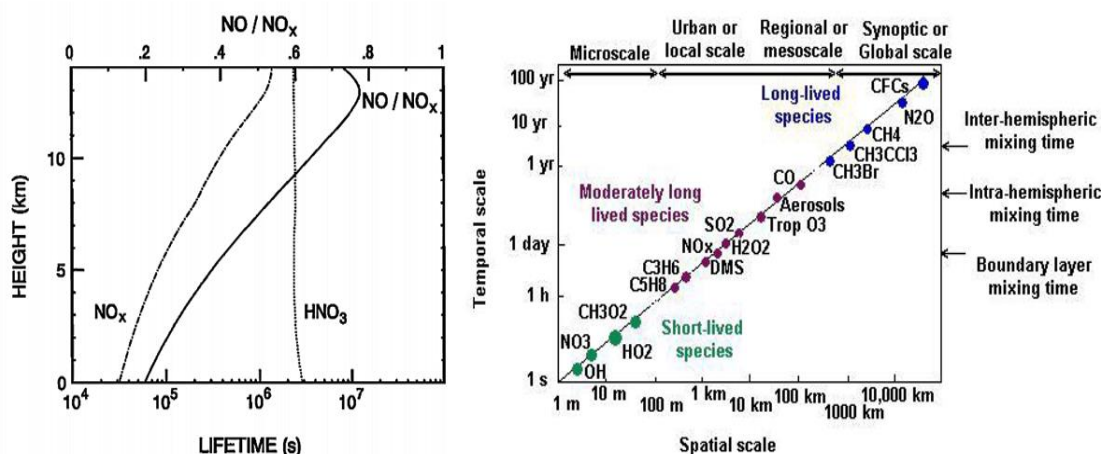


Fig. 1.2: Lifetimes of NO_x as a function of altitude [left panel from (Ehhalt et al., 1992)]. Spatial and temporal scales of variability for atmospheric constituents [right panel from (Seinfeld and Pandis, 2006)].

1.1.1.1 Sources and sinks

The main sources of NO_x (Logan, 1983) are combustion processes, microbial production in soil and lightening. Global NO_x total emissions are about $42.5 - 47.9 \text{ Tg N yr}^{-1}$ [IPCC⁶ (2007), (Solomon et al., 2007)]. About 78.5 % of total emissions of NO_x into the troposphere are due to anthropogenic activities (Solomon et al., 2007). The major contribution of anthropogenic activity comes from the fossil fuel combustion process, which accounts for 80 % of the anthropogenic emissions of NO_x (Solomon et al., 2007). As the major natural sources of NO_x soil emissions and lighting account for a total contribution of up to 29 % (Solomon et al., 2007). The transport from the stratosphere is less than 2 % (Solomon et al., 2007). SCIAMACHY⁷ observations of the average global tropospheric NO_2 column densities (molecule cm^{-2}) between 2002 - 2011 are shown in Fig. 1.3 (Schneider and R. van der A., 2013). The comparatively high values of NO_2 columns (molecules cm^{-2}) can be seen over America, Europe, South Africa, and China.

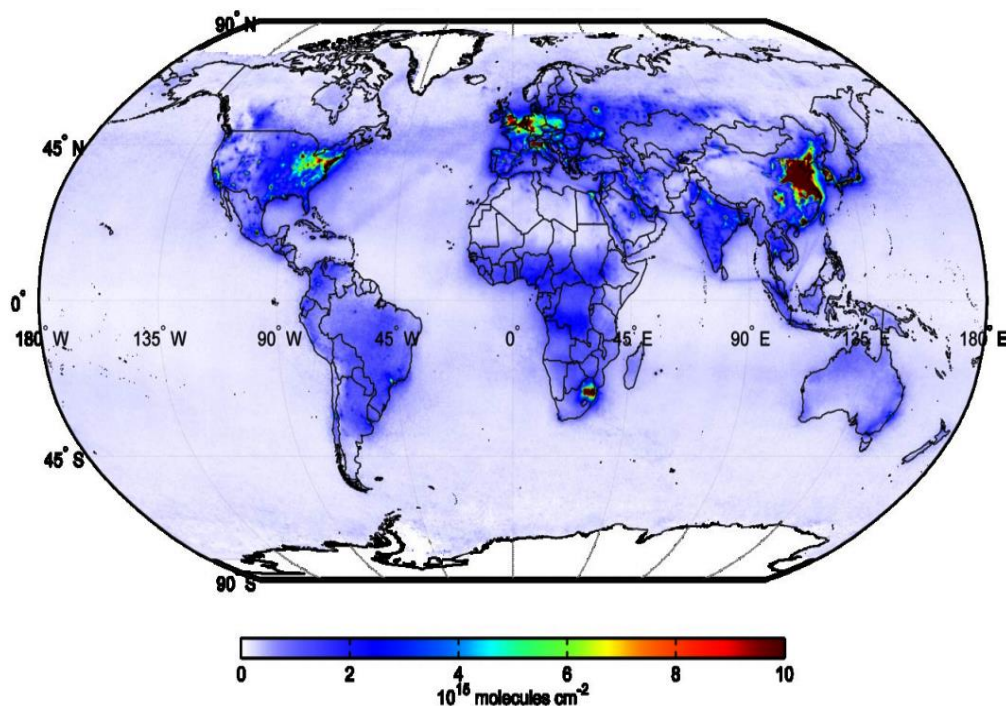
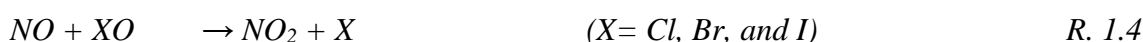


Fig. 1.3: Global average tropospheric NO_2 columns for the period of 2002 to 2011. [figure taken from (Schneider and R. van der A., 2013)].

⁶ Intergovernmental Panel on Climate Change

⁷ SCanning Imaging Absorption spectromETER for Atmospheric CHartographyY (Gottwald et al., 2006) (<http://www.iup.uni-bremen.de/sciamachy/>)

The direct emissions of NO₂ can be variable from 1 % to 30 % ([Lenner, 1987](#); [Kurtenbach et al., 2012](#)). NO_x emissions are mostly in the form of NO ([Harrop, 2002](#)) and later converted to NO₂ by the reaction of NO with O₃, HO₂, RO₂, and other oxidants such as halogen oxides ([R. 1.1](#), [R. 1.2](#), [R. 1.3](#), and [R. 1.4](#)) ([Seinfeld and Pandis, 2006](#)).



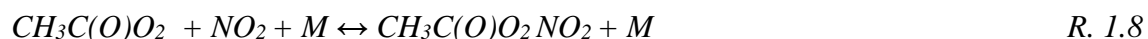
NO_x acts as a key catalyst in the formation of tropospheric ozone ([Crutzen, 1979](#)). The photolysis of NO₂ ([R. 1.5](#)) followed by the reaction [R. 1.6](#) is the main process for the formation of ozone in the troposphere ([Levy, 1972](#); [Chameides and Walker, 1973](#)). NO_x with volatile organic compounds (VOCs)⁸ and sunlight control the photochemical production and loss of O₃ in the troposphere ([Liu et al., 1987](#)). The increase in emissions of NO_x and VOCs leads to photochemical smog by increasing the production of O₃ under hot and sunny conditions. In the presence of sunlight and O₃, the cycle between reactions [R. 1.1](#), [R. 1.5](#), and [R. 1.6](#) is in steady state. The net effect of intercyclng between [R. 1.1](#), [R. 1.5](#) and [R. 1.6](#) is zero in absence of competing reactions. This intercyclng is further discussed in Section 1.2. The reaction [R. 1.5](#) is neither a source nor a sink of NO_x.



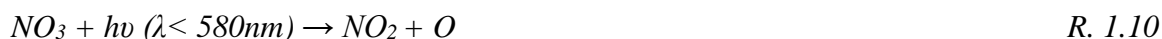
In the troposphere, NO_x leads to the formation of nitric acid (HNO₃), peroxyacetylnitrate (PAN), alkyl nitrates and aerosols. [R. 1.7](#) ([Finlayson-Pitts and Pitts, 2000](#)) is an important reaction in that it provides a daytime sink for NO_x and OH in the troposphere. The HNO₃ deposition (acid rain) contributes to eutrophication with damaging effects on the ecosystem ([Durka et al., 1994](#)). PAN is a dominant nitrate produced

⁸ VOCs = Σ(Anthropogenic + Biogenic)
BVOCs = Σ Biogenic

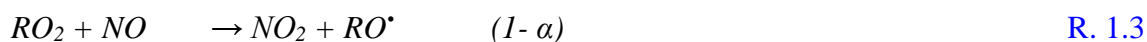
subsequently in the oxidation of acetaldehyde followed by a reaction with NO₂ ([Brasseur et al., 1999](#)) and acts as a reservoir for NO_x ([Singh et al., 1992](#)).



NO₂ reacts with O₃ to form NO₃ and, subsequently, dinitrogen pentoxide (N₂O₅), as shown in [R. 1.9](#) and [R. 1.12](#). In sunlight, [R. 1.12](#) is not significant due to rapid photolysis of NO₃ back to NO₂ or NO. Photolysis rates are typically 0.016 - 0.02 s⁻¹ for the reaction [R. 1.10](#) and 0.17 - 0.19 s⁻¹ for the reaction [R. 1.11](#) at midday ([Orlando et al., 1993](#); [Johnston et al., 1996](#)). During night time, NO₃ takes the role of OH and contributes to the formation of peroxy radicals by oxidation of alkenes. Hydrolysis of N₂O₅ ([R. 1.13](#)) with subsequent deposition is a sink for NO_x during night time.



Alkyl nitrates (ANs) are commonly referred as organic nitrates of form RONO₂ ([Rosen et al., 2004](#)). ANs are formed in a minor branch of reaction [R. 1.3](#), as shown in [R. 1.14](#) ([Rosen et al., 2004](#)) and also with the reaction between alkenes and NO₃ ([Browne and Cohen, 2012](#)). The reaction [R. 1.15](#) is important during night time since in daytime the lifetime of NO₃ is very small. In previous studies, it was concluded that ANs substantially contribute to NO_y (sum of reactive nitrogen oxides) in urban ([Rosen et al., 2004](#); [Perring et al., 2010](#); [Farmer et al., 2011](#)) and rural areas ([Murphy et al., 2006](#); [Day et al., 2009](#); [Beaver et al., 2012](#)). Besides the formation of HNO₃, reaction [R. 1.14](#) and [R. 1.15](#) are important sinks of NO_x at least locally (Section 5.6).



Where α is the yield of the reaction 'RO₂ + NO' that leads to ANs. The variability [1 % to 35 % for ethylperoxy to C₈ peroxy radicals ([Rosen et al., 2004](#); [Thieser, 2013](#))] of α is dependent on the number of carbons in the peroxy radical precursor. It is described as in Eq. 1.1.

$$\alpha := \frac{k_{1.14}}{k_{1.14} + k_{1.3}} \quad \text{Eq. 1.1}$$

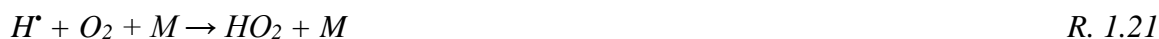
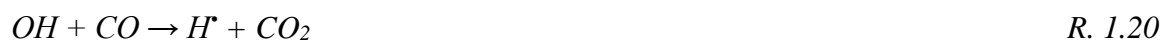
1.1.2 Related photochemistry

The oxidation capacity of the troposphere during daytime is mainly defined by OH and O₃ ([Thompson, 1992](#)). Besides the photolysis of nitrous acid (HONO), photolysis of O₃ is the main process for the primary formation of OH in the troposphere. O(¹D) is formed from the photolysis of O₃ (R. 1.16). In the lower troposphere with H₂O vapour presence (typically 1-2 %), the reaction between O(¹D) and H₂O vapour leads to the OH formation (R. 1.19). The greatest fraction of O(¹D) is subject to quenching process in the presence of a third molecule, mostly with N₂ and O₂ as in R. 1.17. Only about 14 % (at 298 K and 1 % H₂O vapour) of O(¹D) leads to the formation of OH ([Atkinson et al., 2006](#)).



The reaction of OH initiates the breakdown of CO and VOCs, resulting in the formation of RO_x; the simplest of this family is HO₂, which is formed by the oxidation of CO to CO₂. However, CH₄ (most abundant) and other VOCs oxidise to RO_x in the manner shown in R.

1.22 and R. 1.23. The photolysis of HCHO and the reaction ‘HCHO + OH’ also lead to the formation of HO₂ (R. 1.24, R. 1.25, and R. 1.26) ([Seinfeld and Pandis, 2006](#)).



The formation of RO_x also occurs with the oxidation of alkenes by NO₃, but in sunlight, this process is not significant due to the rapid photolysis of NO₃ back to NO or NO₂. In remote areas under very low NO_x concentrations, ‘radical + radical’ reactions (‘OH + HO₂’, ‘HO₂ + HO₂’, and ‘RO₂ + HO₂’) are dominant over ‘HO₂ + NO’ and ‘RO₂ + NO’ reactions, while this dominance disappears with an increase of the NO_x concentration ([Carpenter et al., 1997](#)). RO_x serves as a reservoir for OH and affects the oxidising potential of a region. The reaction R. 1.2 is also very important because it is a secondary source for OH. An overview of NO_x-related chemistry is shown in [Fig. 1.4](#).

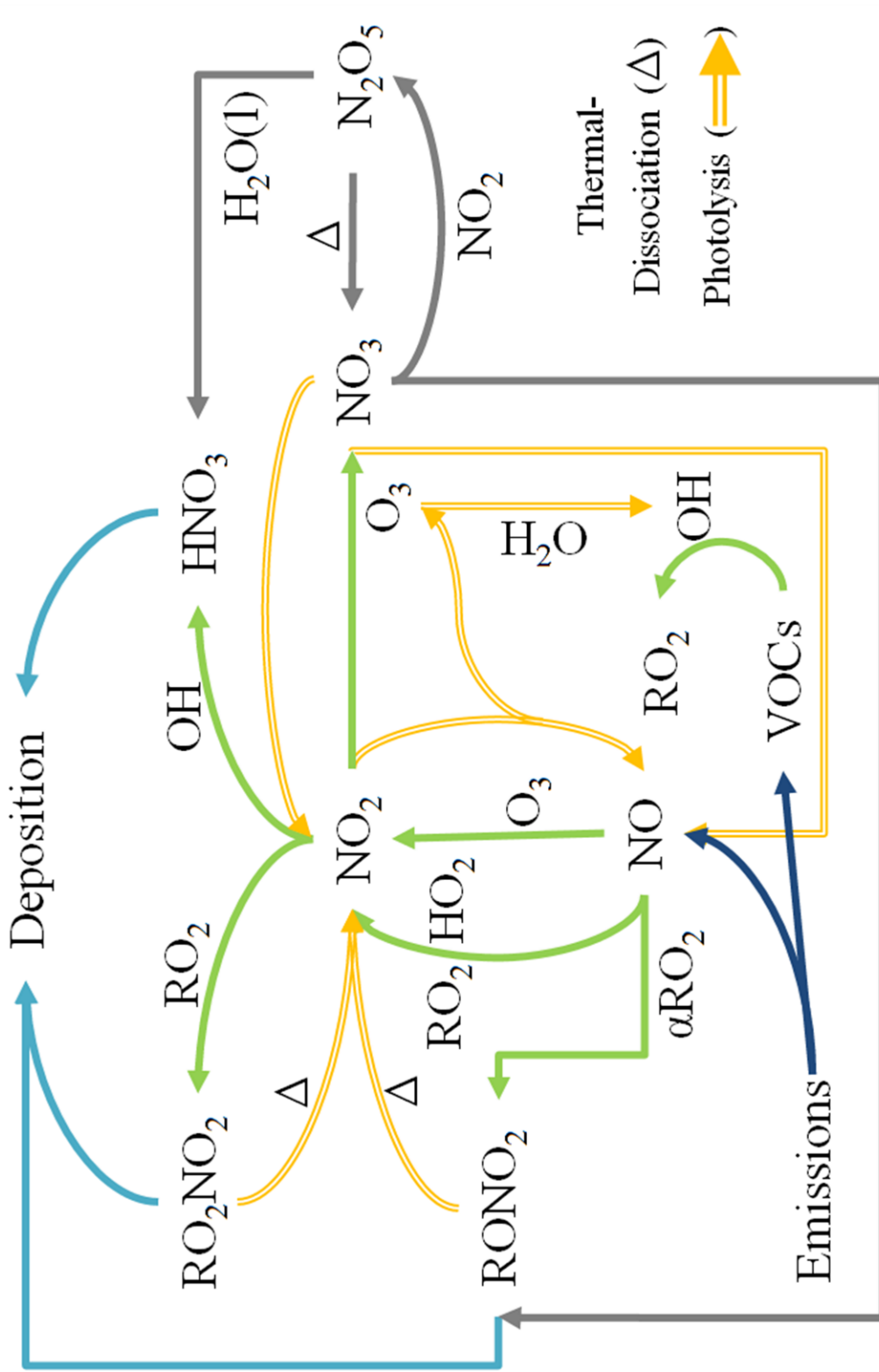
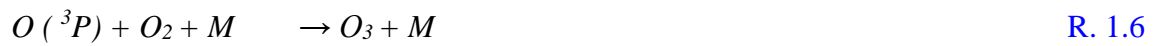


Fig. 1.4: NO_x related tropospheric chemistry.

[Adapted from (Aldener et al., 2006; Thieser, 2013)]

1.2 The quasi-equilibrium state

In the presence of sunlight, a quasi-equilibrium exists between NO and NO₂ due to their rapid conversion to each other that involves multiple oxidants e.g. O₃, HO₂, RO₂ etc. A simple cycling between NO and NO₂ is described by ([Leighton, 1961](#)) involving only O₃. During the cycling between reactions [R. 1.1](#), [R. 1.5](#), and [R. 1.6](#), the production and loss rates of NO, NO₂, and O₃ become equal and there is a null cycle established in the absence of competing reactions. This null cycle is referred as a photostationary state (PSS) ([Cadle and Johnston, 1952](#); [Leighton, 1961](#)) and it can be written as in [Eq. 1.2](#).



$$\frac{[NO_2]}{[NO]} = \frac{k_{1.1} [O_3]}{jNO_2} \quad Eq. 1.2$$

In [Eq. 1.2](#), jNO_2 is the photodissociation frequency (s^{-1}) of NO₂ and $k_{1.1}$ in $cm^3 \text{ molecule}^{-1} s^{-1}$ is the rate coefficient of reaction [R. 1.1](#) ([Atkinson et al., 2004](#); [Sander et al., 2011b](#)). The square bracket in [Eq. 1.2](#) represents concentrations in molecule cm^{-3} . The time constant for the interconversion of NO and NO₂ is in the order of 10^1 to 10^2 s in the presence of sufficient amounts of radiation and O₃. A simple expression [Eq. 1.3](#) can be used to estimate the steady state time constant (τ)_{ss} for the NO_x photostationary state ([Martinez et al., 2003](#); [Trebs et al., 2012](#)).

$$(\tau)_{ss} = (jNO_2 + k_{1.1} [O_3])^{-1} \quad Eq. 1.3$$

Rapid changes in radiation, e.g. passing clouds, and emissions of NO_x in the vicinity of measurements, e.g. mobile emissions, can perturb the balance of the system and lead to scatter in Φ , especially in morning or evening times due to large change in the solar radiation. Under these conditions the assumption of PSS is generally not valid. The possible local sinks of O₃ such as reaction with alkenes can also perturb the PSS. Dissociation or photolysis of

reservoir species such as PAN also forms NO₂. The dissociation can happen in the sampling lines with longer residence time or directly in the atmosphere and leads to a bias in the PSS.

The PSS is often described by a dimensionless parameter, called the Leighton ratio (Φ) as defined in Eq. 1.4 (Leighton, 1961).

$$\Phi := \frac{j\text{NO}_2 [\text{NO}_2]}{k_{1.1} [\text{O}_3][\text{NO}]} \quad \text{Eq. 1.4}$$

At the dynamic equilibrium between NO-NO₂-O₃, Φ should be unity as defined in Eq. 1.4; but these cases are limited to a high NO_x region e.g. (Parrish et al., 1986; Carpenter et al., 1998). In semi-remote areas, it deviates from unity ' $\Phi > 1$ ' e.g. (Volz-Thomas et al., 2003; Mannschreck et al., 2004) and at pristine background conditions [$\text{NO}_x = 5 - 25$ parts per trillion by volume (ppt_v)], deviations from unity are very large ' $\Phi \gg 1$ ' (Hosaynali Beygi et al., 2011). Chemically, O₃ is not the only single oxidant converting NO to NO₂. $\Phi > 1$ can be an indication of other oxidants besides 'NO + O₃' converting NO to NO₂ (Calvert and Stockwell, 1983); HO₂ and RO₂ reactions with NO are well known to form NO₂ (R. 1.2, and R. 1.3). These reactions are mainly responsible for $\Phi > 1$. Under NO_x concentrations in the order of several parts per billion by volume (ppb_v), formation of peroxy radicals is suppressed due to an increase in loss of OH due to reaction R. 1.7, and Φ is often close to unity. These conditions are typically observed in cities and highly polluted regions. While under lower NO_x concentrations in the order of ppt_v, deviations (> 1) in Φ are expected, mainly with a proportional increase of peroxy radical role in NO₂ formation e.g. (Ridley et al., 1992). By taking the contributions from peroxy radicals into account, Eq. 1.2 shows a relative proportioning of NO to NO₂ cycle. The Leighton ratio (Φ) can similarly be extended as Φ_{ext} (Eq. 1.6) with inclusion of peroxy radicals (Calvert and Stockwell, 1983).

$$\frac{[\text{NO}_2]}{[\text{NO}]} = \frac{k_{1.1} [\text{O}_3] + k_{1.2} [\text{HO}_2] + \sum k_{1.3} [\text{RO}_2]}{j\text{NO}_2} \quad \text{Eq. 1.5}$$

$$\Phi_{\text{ext}} := \frac{j\text{NO}_2 [\text{NO}_2]}{(k_{1.1} [\text{O}_3] + k_{1.2} [\text{HO}_2] + \sum k_{1.3} [\text{RO}_2])[\text{NO}]} \quad \text{Eq. 1.6}$$

The deviation $\Phi > 1$ can be used to estimate the concentrations of peroxy radicals ([Cantrell et al., 1997](#); [Mannschreck et al., 2004](#); [Trebs et al., 2012](#)) by rearranging Eq. 1.5 as follows, into Eq. 1.7. In relation Eq. 1.7, k_{eff} is the derived rate coefficient for all RO_x ([Cantrell et al., 1997](#)).

$$(\text{RO}_x)_{\text{PSS}} := \frac{k_{1.1} [\text{O}_3]}{k_{\text{eff}}} (\Phi - 1) \quad \text{Eq. 1.7}$$

$$k_{\text{eff}} \approx \left(\frac{k_{1.2} [\text{HO}_2] + \sum k_{1.3} [\text{RO}_2]}{[\text{HO}_2] + \sum [\text{RO}_2]} \right) \quad \text{Eq. 1.8}$$

Halogen oxides also produce NO_2 by reacting with NO (R. 1.4). The sources of halogen oxides such as sea spray are commonly present close to an ocean. So a contribution to deviations in Φ due to ‘ $\text{XO} + \text{NO}$ ’ reaction (R. 1.4) is expected in these regions ([Harder, 1994](#); [Platt and Janssen, 1995](#)) and should be taken into account. Besides peroxy radicals and halogen oxides, the presence of an unknown oxidant converting NO to NO_2 and lead to deviations in Φ has also been reported ([Volz-Thomas et al., 2003](#); [Mannschreck et al., 2004](#); [Hosaynali Beygi et al., 2011](#)). Besides chemical activity, measurement uncertainty would contribute to deviations in Φ . Interferences in NO_2 measurement could also lead to the deviation in Φ .

1.3 Instantaneous photochemical production and loss rates of O₃

Reactions of RO₂ and HO₂ with NO (R. 1.2 and R. 1.3) drive the production of O₃ in the troposphere. O₃ photochemical production compared to O₃ loss is dominant in the continental boundary layer, while it is smaller in marine regions ([Lelieveld and Dentener, 2000](#); [Lelieveld et al., 2004](#)). In general, VOCs provide the main source, whereas NO_x acts as the catalyst for the production of O₃ in the troposphere. Halogens are commonly present in the marine boundary layer (MBL) ([Cicerone, 1981](#); [Chatfield and Crutzen, 1990](#); [Monks, 2005](#)). In the presence of sunlight, these molecules convert to halogen atoms. Halogen atoms then undergo a chemical reaction with O₃ to form a halogen oxide and follow R. 1.4 to reproduce O₃. There is no net effect on O₃ concentrations in this cycle. But instead of reacting with NO, halogen oxides can also react with HO₂ and lead to net O₃ destruction in the MBL ([Monks, 2005](#)). The instantaneous photochemical production rate of O₃ is described (Eq. 1.9) by the reaction of RO₂ and HO₂ with NO ([Crutzen et al., 1999](#)).

$$P(O_3) \approx (k_{1.2} [HO_2] + \sum k_{1.3} [RO_2])[NO] \quad \text{Eq. 1.9}$$

Since NO₂ photolysis is the main process for O₃ production, the imbalance between reaction R. 1.1, R. 1.5, and R. 1.6 can be used to describe the gross formation rate of O₃ (Eq. 1.10) ([Thornton et al., 2002](#); [Martinez et al., 2003](#)).

$$P(O_3)_{PSS} := (jNO_2 [NO_2]) - (k_{1.1} [O_3][NO]) \quad \text{Eq. 1.10}$$

The photochemical *in-situ* loss of O₃ can be calculated as shown in Eq. 1.11 ([Crutzen et al., 1999](#)).

$$L(O_3) \approx [O_3] (\beta \times jO^1D + k_{OH+O_3} [OH] + k_{HO_2+O_3} [HO_2]) \quad \text{Eq. 1.11}$$

In Eq. 1.11, jO^1D represents the photolysis frequency of O₃ and β the fraction of O(¹D) reacting with H₂O (R. 1.19), while most part of O(¹D) undergoes the process of quenching and produce back O₃ (R. 1.17, R. 1.18). The effective β is defined in Eq. 1.12.

$$\beta := \frac{k_{\text{H}_2\text{O}+\text{O}(^1\text{D})} [\text{H}_2\text{O}]}{k_{\text{H}_2\text{O}+\text{O}(^1\text{D})} [\text{H}_2\text{O}] + k_{\text{N}_2+\text{O}(^1\text{D})} [\text{N}_2] + k_{\text{O}_2+\text{O}(^1\text{D})} [\text{O}_2]} \quad \text{Eq. 1.12}$$

The photochemical production and loss of O_3 depends on an available concentration of NO_x in a region ([Brasseur et al., 1999](#)). The net photochemical tendency of O_3 can be defined by the difference between $P(\text{O}_3)$ and $L(\text{O}_3)$ ([Crutzen et al., 1999](#)).

1.3.1 Ozone compensation point (OCP)

In the troposphere, a point of equilibrium is established between the production and loss of O_3 . This point is called the ozone compensation point (OCP). It is strongly dependent on the NO_x concentration and often referred to by the term “Critical NO ”. A minimum value of “Critical NO ” is suggested to be about 5 ppt_v of NO (about 15 - 20 ppt_v of NO_x) in the troposphere ([Lelieveld and Crutzen, 1990](#)) and it can be calculated from relation in Eq. 1.14 ([Hosaynali Beygi, 2010](#)) by rearranging $P(\text{O}_3)$ and $L(\text{O}_3)$ equations.

$$[\text{NO}]_c = \frac{L(\text{O}_3)}{k_{1.2} [\text{HO}_2] + \sum k_{1.3} [\text{RO}_2]} \quad \text{Eq. 1.13}$$

1.3.2 Catalytic efficiency of NO_x

NO_x plays an important role in the catalytic cycling of O_3 . The instantaneous catalytic efficiency of NO_x in the production of O_3 can be defined as in Eq. 1.14 ([Brasseur et al., 1999](#)). The major loss of NO_x (LNO_x) is the formation of HNO_3 and subsequent deposition. In recent studies, it has been suggested that the formation of ANs can play an important role in reducing the catalytic efficiency of NO_x ([Rosen et al., 2004](#); [Farmer et al., 2011](#); [Browne and Cohen, 2012](#)).

$$\text{Catalytic efficiency of } \text{NO}_x = \frac{P(\text{O}_3)}{\text{LNO}_x} \quad \text{Eq. 1.14}$$

Eq. 1.14 does not include the thermal or photolytic dissociation of reservoir species like HNO_3 , ANs, and PAN etc. Such processes could be important for releasing NO_2 and affecting the catalytic efficiency.

1.4 Motivation and the framework

O₃ is important in the oxidation capacity of the atmosphere and effect on the abundance of the OH radical, the main oxidant of the atmosphere; it is therefore influential in controlling the self-cleansing capability of the atmosphere. It was suggested that even very low concentrations of NO_x can be relevant in the production of O₃ ([Lelieveld and Crutzen, 1990](#); [Carpenter et al., 1997](#)). Hence the self-cleansing mechanism of the atmosphere is indirectly affected by NO_x. The inter-coupling of HO_x and NO_x in the catalytic cycling of O₃ continue until the chain termination reactions take place, like the formation of HNO₃ and ANs. HNO₃ formation and subsequent deposition is generally considered as the main loss process of NO_x in the troposphere but the formation of ANs is also another major instantaneous sink of NO_x in areas with the significant biogenic emission ([Browne and Cohen, 2012](#)). ANs are important in determining the lifetime of NO_x and catalytic efficiency of NO_x in the production of O₃. Recently, a significant impact of the reaction (R. 1.14) has been studied in the urban and rural areas ([Browne and Cohen, 2012](#)). It was concluded that under low NO_x (< 500 ppt_v), the lifetime of NO_x is nonlinear with change in fraction of α ([Browne and Cohen, 2012](#)).

The concept of the PSS of NO_x provides a tool to test our current understanding of the coupling between NO_x, RO_x, and HO_x in the O₃ photochemistry and its implementation in the current atmospheric models. The PSS has been widely applied in the troposphere for the estimation of the O₃ production rates and NO_x, RO_x, and halogen oxides concentrations in the absence of the relevant measurements, and an enormous effort has been made by the scientific community in the past to understand the PSS and its applicability. A summary of the PSS analysis from previous studies is formulated in [Table 1.1](#). A large number of past studies provide evidence about the importance of the concept and need to determine its reliability when applied to field observations. In past studies ([Table 1.1](#)), the PSS was evaluated with some degree of success, but often there had been a bias observed between the PSS estimates and observations ([Table 1.1](#)). The Leighton ratio ([Eq. 1.4](#)) is often used to investigate the PSS. The concept of the Leighton ratio ([Section 1.2](#)) is also used in this study to understand the NO to NO₂ conversion. The main cause of positive deviation from unity of the classical Leighton ratio is that the assumption in the classical Φ that NO₂ only forms from the O₃ and NO reaction. This assumption is erroneous, as HO₂, RO₂, and halogen oxides also contribute considerably, depending on their concentrations and the location ([Table 1.1](#)). The classical Leighton ratio had been found to be a reasonable assumption in urban regions e.g.

([Shetter et al., 1983](#)) but far off from reality in semi-rural regions e.g. ([Volz-Thomas et al., 2003](#)) and remote regions e.g. ([Hosaynali Beygi et al., 2011](#)). Even after taking HO₂ and RO₂ contributions into account (Eq. 1.6), there can be several other reasons for the unexplained positive deviations, for example potential interferences in NO₂ instruments ([Davis et al., 1993](#); [Crawford et al., 1996](#); [Cantrell et al., 1997](#)), errors in the measurements ([Cantrell et al., 1996](#)), or unknown oxidant ([Volz-Thomas et al., 2003](#); [Mannschreck et al., 2004](#); [Hosaynali Beygi et al., 2011](#)), etc. The bias of the PSS is generally attributed due to potential interference in the measurement of NO₂, and to missing information regarding an unknown oxidant for NO to NO₂ conversion (Table 1.1). Accurate measurement of the atmospheric species is obviously important for the understanding of the atmospheric processes and validation of model results. The reliability of the PSS is also quite dependent on the accuracy of NO_x measurements. Accurate measurements of NO_x in the ppt_v range are quite challenging. Chemiluminescence is a reliable and common method for direct *in-situ* detection of NO. In Table 1.1 it is evident of that almost all studies of the PSS were done by using an indirect NO₂ measurement with one exception of ([Matsumoto et al., 2006](#)). The potential role of interference in the indirect measurements of NO₂, which is typically the case in commercial instruments, cannot be ruled out completely. It was concluded in past (Table 1.1) that interference in the NO₂ measurement was a reason for the bias between the PSS and observations ([Davis et al., 1993](#); [Crawford et al., 1996](#); [Cantrell et al., 1997](#)). This has motivated a need for the direct, spectroscopically specific, and sensitive *in-situ* measurement of NO₂.

The tropospheric concentrations of NO₂ can vary from few ppt_v (parts per trillion by volume) to 100ppb_v (parts per billion by volume), depending on the remote ([Hosaynali Beygi et al., 2011](#)) and urban conditions ([Clapp and Jenkin, 2001](#)), respectively. The high variability in NO₂ complicates its measurement. In order to perform NO₂ measurements at the remote areas (e.g. the MBL), in the upper troposphere, and lower stratosphere, a resolution of a few ppt_v is required. This is often not possible with current instruments, especially those available commercially. Techniques like the cavity ring-down absorption spectroscopy' [CRDS; ([Osthoff et al., 2006](#); [Hargrove et al., 2006](#))], tunable diode laser absorption spectroscopy [TDLAS; ([Herndon et al., 2004](#))], cavity enhanced absorption spectroscopy [CEAS; ([Wojtas et al., 2007](#))], and cavity attenuated phase shift spectroscopy [CAPS; ([Ge et al., 2013](#))] provide a direct, *in-situ* measurements of NO₂. However, sensitivities of these direct methods are still not sufficient to measure NO₂ in ranges of a few ppt_v. The laser induced fluorescence

(LIF) technique for NO₂ detection is a promising technique for highly sensitive and selective measurements. It has already been demonstrated in several past studies [e.g. ([Fong and Brune, 1997](#);[Thornton et al., 2000](#);[Matsumi et al., 2001](#);[Cleary et al., 2002](#);[Taketani et al., 2007](#);[Dari-Salisburgo et al., 2009](#))], but most of these systems have large and complex laser systems. In recent times due to the availability of diode lasers, the development of a more compact LIF system with high sensitivity and selectivity has become possible. In this study, an instrument to observe NO₂ by applying the LIF technique is reported, which will also be a part of the OMO (**O**xidation **M**echanism **O**bservation) mission on HALO [**H**igh **A**ltitude and **L**ong Range Research Aircraft; funded by the German Federal Ministry of Education and Research, the Helmholtz-Gemeinschaft and the Max-Planck-Gesellschaft]. The investigation of the NO to NO₂ cycling has been performed by using measurements of LIF-NO₂ during the PARADE (**P**articles and **R**adicals: **D**iel observations of the impact of urban and biogenic **E**missions) field experiment in 2011 in a semi-rural forest area. The investigation and related effects have been studied for a different boreal forest location during HUMPPA-COPEC (**H**yytiälä **U**nited **M**easurements of **P**hotochemistry and **P**articles in **A**ir - **C**omprehensive **O**rganic **P**recursor **E**mission and **C**oncentration study) in 2010.

Table 1.1: An historical overview of studies related to PSS analysis.

Reference	Detection	Platform	Environment
<p>Conclusions</p> <p>(Cadle and Johnston, 1952); (Leighton, 1961)</p> <p>Proposed classical or simple PSS equation Eq. 1.2.</p>	NO ₂		Theoretical
<p>(O'Brien, 1974)</p> <p>A chamber study was done to validate the concept of photostationary state. Equilibrium prevailed in the chamber between NO, NO₂, and O₃ with hydrocarbons of low reactivity. The author also introduced the concept of estimating the concentration of radical species based on the imbalance of the classical PSS.</p>		Smog chamber experiment	
<p>(Kelly et al., 1980)</p> <p>It was concluded that the classical PSS does not hold in clean air.</p>	Indirect	Ground 1 km (ASL ⁹)	Rural, remote (Niwot Ridge, mountains of Colorado, USA)
<p>(Stedman and Jackson, 1975); (Calvert, 1976);(Shetter et al., 1983)</p> <p>Early studies to test the classical PSS (Eq. 1.2) and NO → NO₂ conversion by only O₃ accounted well.</p>		Urban	

⁹ ASL (above sea level)

(Calvert and Stockwell, 1983)	Theoretical		
Inclusion of HO ₂ and RO ₂ is important in Eq. 1.2 for rural regions.			
(Mcfarland et al., 1986)	Indirect	Airborne 20 - 31 km altitude	30° - 50° N
This study was done in the stratosphere. The calculated ratio (NO ₂ / NO, Eq. 1.2) corresponded with the observation within the combined uncertainty of measurements and calculations.			
(Parrish et al., 1986)	Indirect	Ground 3 km (ASL)	Rural (Southeast of Niwot Ridge, rocky mountains of Colorado, USA)
In this study an overestimation of the PSS estimates of oxidants was observed compared to a model and it was concluded that the type of oxidant for the conversion (NO → NO ₂) is a mixture of peroxy radicals and halogen oxides; if exclusively peroxy radicals, enhanced concentrations can only locally contribute to the imbalance between observation and the PSS.			
(Chameides et al., 1990)	Indirect	Airborne (0 - 5 km) altitude	The west coast at Moffett Field, California, USA.
An overall 25 % overestimation of the observed ratio (NO ₂ / NO) was seen when compared to the PSS estimate of NO ₂ / NO (Eq. 1.5). The authors emphasised the requirement of accurate NO ₂ measurements for an accurate test of the PSS.			

<p style="text-align: center;">(Ridley et al., 1992)</p>	<p style="text-align: center;">Indirect</p>	<p style="text-align: center;">Ground</p>	<p style="text-align: center;">Remote (Mauna Loa, Hawaii)</p>
<p>The results of the PSS estimates reasonably agreed with the photochemical model calculations.</p>			
<p style="text-align: center;">(Cantrell et al., 1993)</p>	<p style="text-align: center;">Indirect</p>	<p style="text-align: center;">Ground 91 m (ASL)</p>	<p style="text-align: center;">Rural (Western Alabama, USA)</p>
<p>$(RO_x)_{PSS}$ (Eq. 1.7) in this study agreed with the measured RO_x for most of the time but an overestimation of $(RO_x)_{PSS}$ had been observed for some period of time. A bias was concluded to exist in the measured RO_x or $(RO_x)_{PSS}$.</p>			
<p style="text-align: center;">(Davis et al., 1993)</p>	<p style="text-align: center;">Indirect</p>	<p style="text-align: center;">Airborne (2 - 6 km) altitude</p>	<p style="text-align: center;">North and South Atlantic</p>
<p>Inconsistency was observed between observations and the theory for some data and this bias had been attributed to unidentified interference in the NO_2 measurements.</p>			
<p style="text-align: center;">(Bakwin et al., 1994)</p>	<p style="text-align: center;">Indirect</p>	<p style="text-align: center;">Ground</p>	<p style="text-align: center;">Taiga woodland (Northern Quebec, Canada)</p>
<p>Measurements were made above the forest canopy. High values of Φ (Eq. 1.4) were calculated. The median value for midday conditions was $\Phi = 2.9$. The oxidation of O_3 was not sufficient to explain the observed ratio of NO / NO_2. This study agreed with the results of previous studies e.g. (Parrish et al., 1986).</p>			

<p>(Poulida et al., 1994)</p>	<p>Indirect</p>	<p>Ground</p>	<p>Rural (North Carolina, USA)</p>
<p>The calculated values of Φ (Eq. 1.4) were up to 1.42 for hourly-based data set. The presence of oxidants other than O_3 for $NO \rightarrow NO_2$ conversion was concluded.</p>			
<p>(Harder, 1994); (Platt and Janssen, 1995)</p>	<p>Indirect</p>	<p>Ground</p>	<p>Semi-remote (Coast of Brittany)</p>
	<p>Theoretical</p>		
<p>Generally, it was proposed that an inclusion of halogen oxides is required in equation Eq. 1.5.</p>			
<p>(Kleinman et al., 1995)</p>	<p>Indirect</p>	<p>Ground</p>	<p>Forested (Metter, Georgia, USA)</p>
<p>A reasonably good agreement is observed between $(RO_x)_{PSS}$ (Eq. 1.7) and the calculated RO_x with the budget approach.</p>			
<p>(Crawford et al., 1996)</p>	<p>Indirect</p>	<p>Airborne (0 - 12 km) altitude</p>	<p>Western and central North Pacific</p>
<p>Interference in the NO_2 measurements was concluded to be the reason for a discrepancy between the theory and observations. The authors also emphasised the need for the spectroscopically specific NO_2 detection with a detection limit of a few ppt_v.</p>			

<p>(Cantrell et al., 1996)</p> <p>Inconsistency between the measurements of NO_x and RO_x was concluded to be the reason for a bias in the PSS analysis.</p>	<p>Indirect</p>	<p>Ground</p>	<p>Remote (Mauna Loa, Hawaii)</p>
<p>(Cantrell et al., 1997)</p> <p>Indicated possible positive interference in NO_2 measurements based on an observed 32 % overestimation of the calculated NO / NO_2 ratio from the PSS compared to the measured NO / NO_2 ratio. Also $(\text{RO}_x)_{\text{PSS}}$ was observed to be higher (factor 2.1) than the measured RO_x. Generally, errors in the measurements were attributed to be a cause of difference.</p>	<p>Indirect</p>	<p>Ground 3 km (ASL)</p>	<p>Forested (Idaho Hill, Colorado, USA)</p>
<p>(Hauglustaine et al., 1996)</p> <p>High levels of $(\text{RO}_x)_{\text{PSS}}$ (Eq. 1.7) were observed compared to measured RO_x.</p>	<p>Indirect</p>	<p>Ground</p>	<p>Remote (Mauna Loa, Hawaii)</p>
<p>(Carpenter et al., 1998)</p> <p>The PSS estimates of peroxy radicals were overestimated compared to results of a model. It was stated that the O_3 loss other than NO is non-negligible and the PSS approach is reliable only in high NO_x regions.</p>	<p>Indirect</p>	<p>Ground</p>	<p>North Norfolk coast, UK</p>

(Rohrer et al., 1998)	Indirect	Ground	Rural (Pennewitt, North-eastern Germany)
<p>Positive deviations in Φ (Eq. 1.4) were observed. Maximum value of Φ was 1.85. Effects of NO emissions on Φ were described.</p>			
(Bradshaw et al., 1999)	Indirect	Airborne (0 - 12 km) altitude	Over Pacific (Southern regions)
<p>The NO₂ measurements were performed with a modified NO₂ inlet to avoid interference from the dissociation of NO_y species. Authors showed good agreement between the measured and calculated NO₂, with a median value of 0.93 for the ratio NO_{2meas.} / NO_{2cal.} Also the results were compared with a data set prior to the modification of the NO₂ inlet and a discrepancy [NO_{2meas.} / NO_{2cal.} = 3.36 (Mdn.)] had been observed between the measured and calculated NO₂. It was concluded that the main reason for the bias was interference from NO_y species [mainly PAN and pernitric acid (HO₂NO₂)].</p>			
(Burkert et al., 2001)	Not reported	Ground	Forest (Tábua, Portugal, 70 km east of the Atlantic coast).
<p>In this study the theory and observation did not match and it was concluded that the PSS concept to derive RO₂ is inadequate.</p>			

<p>(Salisbury et al., 2002)</p>	<p>Indirect</p>	<p>Ground 24 m (ASL)</p>	<p>Semi-remote (Mace Head, Atlantic coast of Ireland)</p>
<p>The results are in agreement qualitatively with (Cantrell et al., 1997) and (Carpenter et al., 1998).</p>			
<p>(Volz-Thomas et al., 2003)</p>	<p>Indirect</p>	<p>Ground</p>	<p>Rural (Pabstthum, Germany)</p>
<p>The potential presence of ‘unknown oxidant’ converting NO to NO₂ was concluded because of the overestimation of the PSS based calculations compared to the observations. Authors also pointed out that the PSS approach is not suitable for calculating the production rates of O₃.</p>			
<p>(Cantrell et al., 2003)</p>	<p>Indirect</p>	<p>Airborne (0 - 8 km)</p>	<p>Northern middle and high latitude</p>
<p>The PSS estimates of peroxy radicals and the NO / NO₂ ratio agreed with measurements at a range of NO concentration greater than 20 ppt_v. But over estimation of the PSS estimates was unexplained for the NO concentrations lower than 20 ppt_v.</p>			
<p>(Yang et al., 2004)</p>	<p>Indirect</p>	<p>Ground</p>	<p>Remote (Cape Norman, Newfoundland)</p>
<p>Authors had discussed the potential errors of the measurements (NO_x, jNO₂, and O₃) and their impact on the derived estimates of the PSS. In this study, it was seen that (RO_x)_{PSS} (Eq. 1.7) level was 77 ppt_v, considerably larger than the one observed at remote marine regions.</p>			

(Mannscheck et al., 2004)	Indirect	Ground 985 m (ASL)	Hill, Forest (Bavarian foothill of Alps, Germany)
<p>Generally, an overestimation of the PSS based quantities compared to the field measurements was observed. $(RO_x)_{PSS}$ (Eq. 1.7) were higher by factor of 2 to 3 than the measured RO_x. The potential presence of ‘unknown oxidant’ converting $NO \rightarrow NO_2$ was concluded.</p>			
(Matsumoto et al., 2006)	Direct	Ground 20 m(ASL)	Urban (Southern Osaka, Japan)
<p>Φ_{ext} (Eq. 1.6) was not significantly different from unity and the oxidation of NO by unknown species was not observed.</p>			
(Fleming et al., 2006)	Indirect	Ground	North Norfolk coast, UK
<p>In this study the PSS approach is used to calculate the production of O_3 [$P(O_3)_{PSS}$ (Eq. 1.10)] and is generally in agreement with (Volz-Thomas et al., 2003).</p>			
(Griffin et al., 2007)	Indirect	Ground	15 km inland from Atlantic Ocean (New England, USA)
<p>71% of the observed positive deviations in Φ (Eq. 1.4) were explained by the modelled RO_x. The rest of the positive deviations were assumed to be due to the presence of halogen chemistry most likely due to iodine.</p>			

<p style="text-align: center;">(Shon et al., 2008)</p>	<p style="text-align: center;">Indirect</p>	<p style="text-align: center;">Airborne (0 - 7 km) altitude</p>	<p style="text-align: center;">Over Urban region (Mexico city)</p>
<p>The $\text{NO} \rightarrow \text{NO}_2$ was reasonably well described by Eq. 1.5. The potential role of halogen oxides was observed for the air masses from a marine region.</p>			
<p style="text-align: center;">(Hosaynali Beygi et al., 2011)</p>	<p style="text-align: center;">Indirect</p>	<p style="text-align: center;">Ship</p>	<p style="text-align: center;">MBL (Punta Arenas, Chile to La Réunion Island)</p>
<p>Eq. 1.5 does not justify the cycling from $\text{NO} \rightarrow \text{NO}_2$. A large discrepancy was observed between the PSS estimates and observations. The PSS estimates were overestimated compared to observations at very low NO_x levels. The potential presence of ‘unknown oxidant’ converting NO to NO_2 was concluded.</p>			
<p style="text-align: center;">(Trebs et al., 2012)</p>	<p style="text-align: center;">Indirect</p>	<p style="text-align: center;">Ship</p>	<p style="text-align: center;">Rivers of the city of Manaus (Amazonas State, Brazil)</p>
<p>In some cases levels of $(\text{RO}_x)_{\text{PSS}}$ (Eq. 1.7) are significantly exceed to the modelled RO_x but generally found that the level of $(\text{RO}_x)_{\text{PSS}}$ are within the range of the model result.</p>			

2 GANDALF

This chapter describes a new Gas Analyser for Nitrogen Dioxide Applying Laser induced Fluorescence (GANDALF). GANDALF is designed for accurate [4.5 % (1 σ)], precise [0.5 % + 3ppt_v (1 σ)], *in-situ* observations of NO₂ with a low limit of detection (5 - 10 ppt_v). The instrument's characteristics are described in upcoming sections.

2.1 The operational method

The working principle of GANDALF is Laser-Induced Fluorescence (LIF) at low pressure (<10 hPa). NO₂ is excited with a wavelength well above the photolysis threshold ($\lambda > 420$ nm for NO₂) and the red-shifted fluorescence is detected during laser-off periods. The absorption cross-sections and quantum yield of NO₂ are shown in Fig. 2.1.



The detected fluorescence $h\nu'$ is directly proportional to the amounts of NO₂ in the cell. The artefact signal from wall scatters (laser light) and dark counts (detector) are removed as the background level (i.e. zero level) of the instrument. The background level of GANDALF is determined by using synthetic air¹⁰. The atmospheric mixing ratios of NO₂ are derived by using Eq. 2.1.

$$NO_2 = \left[\frac{\text{Signal} - S_{BG}}{\alpha_c} \right] \quad \text{Eq. 2.1}$$

Where 'Signal' is counts (s⁻¹) and α_c is the calibration factor or sensitivity in counts (s⁻¹ppb⁻¹). ' α_c ' is derived from the slope of counts versus the known amounts of NO₂. 'S_{BG}' is the synthetic air background level in counts (s⁻¹).

¹⁰ "Synthetische Luft KW-frei", Westfalen, Germany

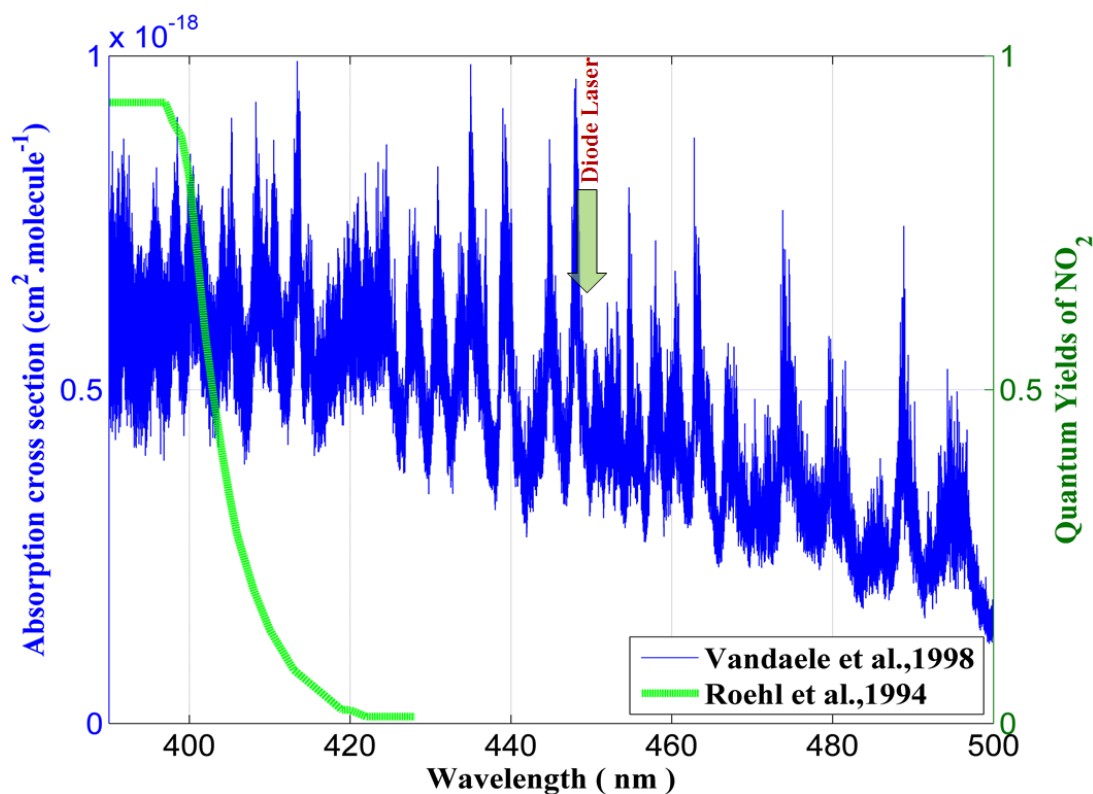


Fig. 2.1: NO₂ absorption cross-sections with quantum yields. Excitation wavelength above the photolysis threshold is shown with an arrow. The absorption cross-sections and quantum yields are plotted from data (Vandaele et al., 1998) and (Roehl et al., 1994), respectively.

2.1.1 Instrumentation

The instrument contains a detection axis connected to a scroll pump and calibrator (Fig. 2.18). The mechanical and optical parts of the detection axis are visible in Fig. 2.2. All mechanical parts inside GANDALF are black anodised and most optical components (Fig. 2.2, no.12 and no.13) are continuously flushed with synthetic air (3×50 sccm) during the period of operation to avoid dead air pockets, dust, fog etc. The inlet for sampling flow is a small orifice with a diameter of 0.7 mm. The distance from point of entrance at the orifice to the centre of the detection cell (laser beams are focused at this spot) is about 150 mm. This orifice and scroll pump combination provides a pressure of 7 hPa inside the detection cell. The current sampling flow is 4100 ± 41 sccm and less than 30 ms time is required for the air molecules to reach the centre of detection cell from the point of entrance.

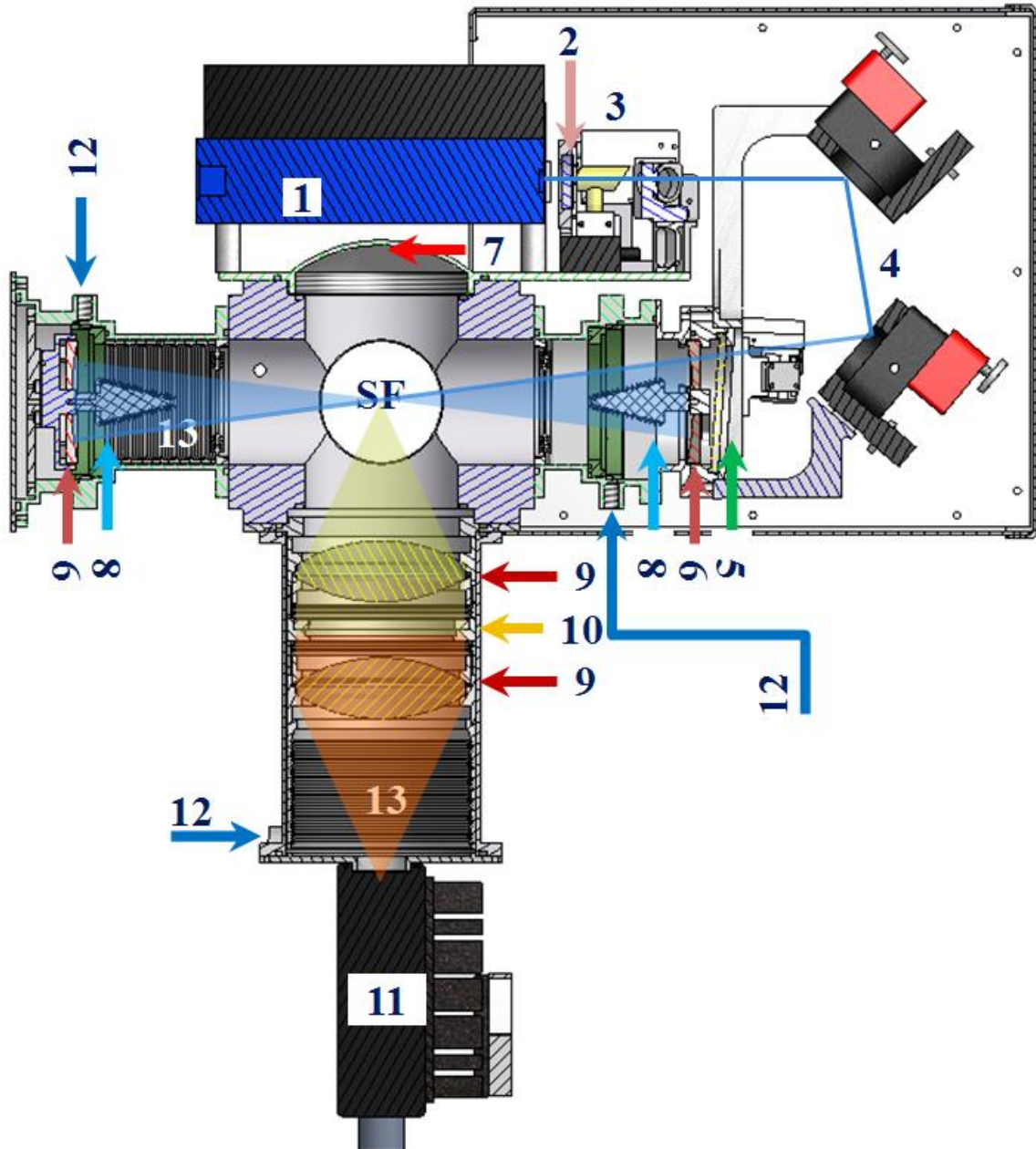


Fig. 2.2: The section view of GANDALF [Inventor-2009: The drawing is created by defining a plane used to cut through assembly. The figure represents the surface area of the cut];

SF: Sampling flow 1: Diode laser 2: Focussing lens 3: Optical Reference System 4: Motorised mirrors 5: Laser entrance window with wedge 6: Herriott cell's mirrors 7: Concave mirror 8: Conical baffles 9: Focusing lens 10: Optical filters 11: PMT 12: The flushing for optics 13: Zigzag surfaces for reduction of the laser scatter. [3D AutoCAD models in Fig. 2.2; the diode laser (no. 1) is by courtesy of Omicron Laserage Laserprodukte GmbH (www.omicron-laser.de), opto-mechanical parts (parts in no. 3 and 4) by courtesy of Newport (www.newport.com)].

2.1.1.1 Diode laser

The diode laser¹¹ in this system has a maximum output power of 250 mW with a modulation frequency of 5 MHz and a wavelength (λ) of 447 - 450 nm. A plot of the measured intensity versus wavelength for the diode laser is shown in Fig. 2.3. The wavelength of the diode laser is measured with a spectrometer¹². The spectrometer is calibrated by using a mercury lamp. The convolution of the laser profile and the NO₂ absorption cross-sections (Vandaele et al., 2002) yields to an effective NO₂ absorption cross-section of $5.3 \times 10^{-19} \text{ cm}^2 \text{ molecule}^{-1}$ for the wavelength of the diode laser.

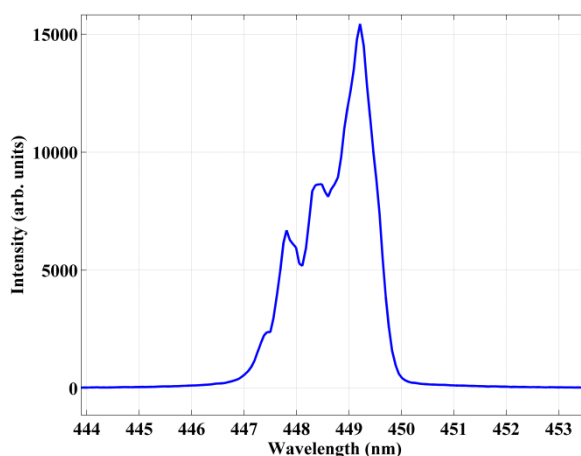


Fig. 2.3: Wavelength plot for the diode laser, operated with repetition rate of 5MHz.

2.1.1.2 Herriott cell

The Herriot cell (Herriott et al., 1964) is used to achieve multiple passes for the enhancement of the laser light at the centre of the detection cell. The detection cell of GANDALF is positioned in between the Herriott cell's mirrors. The Herriott cell's mirrors have 99.99 % reflectivity (IBS coating)¹³ in the spectral range of 445 nm to 455 nm. The absorption of light in the Herriot cell's mirror is very small (< 0.1 %). The distance between the Herriott cell's mirrors is twice to their radius of curvature ($R = 128 \text{ mm}$). The fluorescent contaminants of Herriott cell's mirrors are measured with the background level measurements (zero air). The laser beam is directed (Fig. 2.2, no.4) into the detection cell by using motorised mirrors. These mirrors are coated to achieve high reflectivity (> 99 %) for a light incidence at 45° (angle of incidence) with a wavelength range between 445 and 455 nm. The laser beam makes a conical shape of multiple passes (25 to 30) inside the detection cell as shown in Fig. 2.4 (A). The multiple passes of the laser beam makes a diameter of about 8 mm at the centre of the detection cell as shown in Fig. 2.4 (A). An open system is also shown in Fig. 2.4 (B),

¹¹ Omicron Laserage (CW Diode-Laser), laserprodukte GmbH, Germany
Power stability <1 % hour⁻¹, pointing stability: <10 μ rad
Beam diameter: 2.55 (perpendicular: 0°/mm) & 2.53 (parallel: 90°/mm)

¹² HR4000 High-Resolution Spectrometer, Ocean Optics, USA

¹³ ATFilms (IBS coating), USA

but this is based on an arbitrary setting on optical bench and here distance between Herriott cell's mirrors is not twice to the radius of curvature.

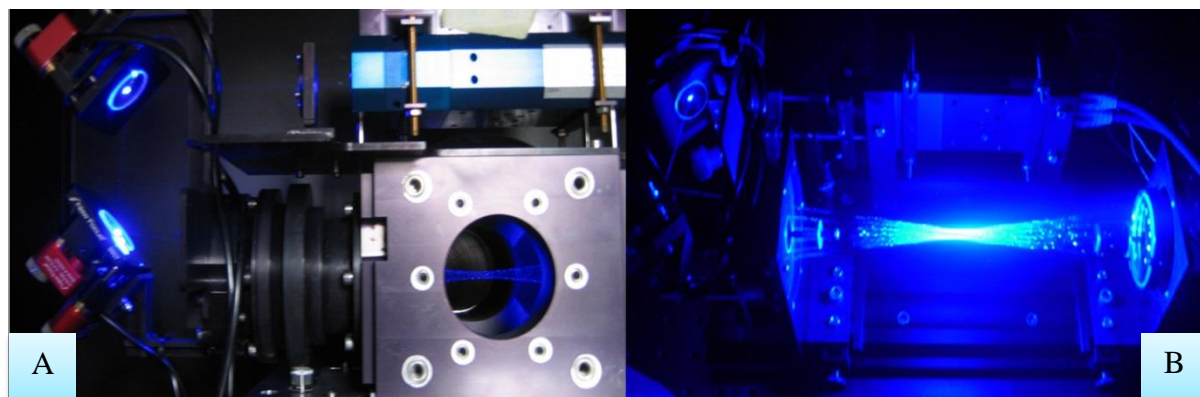


Fig. 2.4: Multiple passes of the laser beam are visible in the detection cell (A) and in between the Herriott cell's mirrors on an optical bench (B).

2.1.1.3 Photon counting head device

A photomultiplier¹⁴ (PMT) is used for the detection of fluorescence. The PMT is located at a perpendicular position from the sampling flow. The effective area of the PMT is 5 mm in diameter and has a GaAsP / GaAs photocathode with a radiant sensitivity of 87.4 mA W^{-1} . The spectral response of the PMT is in wavelengths of between 380 nm and 890 nm. The PMT has peak sensitivity at 800 nm with a quantum efficiency of 12 %. The fluorescence signal is focused on the PMT by using collimating lenses (Fig. 2.2, no.9) and there is an aluminium concave mirror (Fig. 2.2, no.7) located opposite of the PMT, which redirects fluorescent photons towards the detector.

2.1.1.4 Filters

In front of the PMT, interference filters¹⁵ (Fig. 2.2, no.10) are used to get rid of any contributions of photons due to scatter from walls of the sampling chamber, Rayleigh scattering and Raman scattering. The filters have a cut-on wavelength of 470 nm and 550 nm with an average transmission of 98 % in the spectral range from cut-on +3 nm to 900 nm. The reflectivity of filters is higher than 99 % for the spectral ranges below the cut-on

¹⁴ Hamamatsu (H7421-50), Japan
Count sensitivity: $2.1 \times 10^5 \text{ s}^{-1} \text{ pW}^{-1}$ at 550 nm and $3.9 \times 10^5 \text{ s}^{-1} \text{ pW}^{-1}$ at 800 nm

¹⁵ Barr Associates, Inc., USA

wavelengths. The filters have a very small (< 1 %) absorption leading to the fluorescence. The fluorescent contaminant is corrected with the background level measurements.

2.1.1.5 Optical reference system

An optical system is installed to monitor the change in the wavelength and power of the diode laser continuously during a period of operation. The optical system (Fig. 2.2, No.3) consists of photodiodes¹⁶, beam splitters, and a NO₂-filled cuvette before the detection cell as shown in Fig. 2.5. The laser beam splits into a ratio about 9:1 at the beam splitter (Fig. 2.5, 3.1) and ~ 85 - 90 % of the beam goes into the detection cell. The remaining part of the beam (approx. 10 - 15 % i.e. about 25 - 35 mW) splits in to a ratio 1:1 at the beam splitter (Fig. 2.5, 3.2). One half (approx. 5 %) goes to the photodiode (*ref.*) (Fig. 2.5, 3.3) and the other half (approx. 5 %) passes through a NO₂-filled cuvette (Fig. 2.5, 3.4) that is detected by the second photodiode (*CNO₂*) (Fig. 2.5, 3.5). The signal from the photodiode (*ref.*) is used for the continuous diode laser's power monitoring and also as reference for the other photodiode (*CNO₂*). The photodiode (*CNO₂*) is used to monitor the changes in wavelength of the diode laser. The change in wavelength of the diode laser is identified with relative absorption in the cuvette. The signals from these photodiodes are used to account for any relative changes in the power and wavelength of the diode laser.

To suppress stray light, BG12¹⁷ band-pass filters are used in front of the photodiodes. A diode test to check the dependency of absorption in the cuvette (Fig. 2.5, 3.4) with respect to wavelength is shown in Fig. 2.6. During the test, the amount of NO₂ was kept constant inside the detection cell and only the bias current of the diode laser was changed to achieve different wavelength. The signals from the PMT and the photodiode (*CNO₂*) are normalised to the photodiode (*ref.*) to account for change in the power of the diode laser. A correlation plot between [(*CNO₂*) / (*ref.*)] and [PMT / (*ref.*)] is shown in Fig. 2.6. The values of ratio on the y-axis represent the signal from the fluorescence of NO₂, while the ratio on the x-axis is due to the absorption of the laser light. When the wavelength of the diode laser corresponded to the highest absorption of NO₂, at the same time the highest fluorescence signal is detected by the PMT. There is one photodiode (not shown) at the outlet of the detection cell. The signal from this photodiode is used to monitor any changes inside the Herriott cell, such as mirror reflectivity, beam deflection, and for the Herriott cell's alignment.

¹⁶ OSD 50-5T, Centronic, UK

¹⁷ ITOS (transmittance of approximately 80% at 450nm), Germany

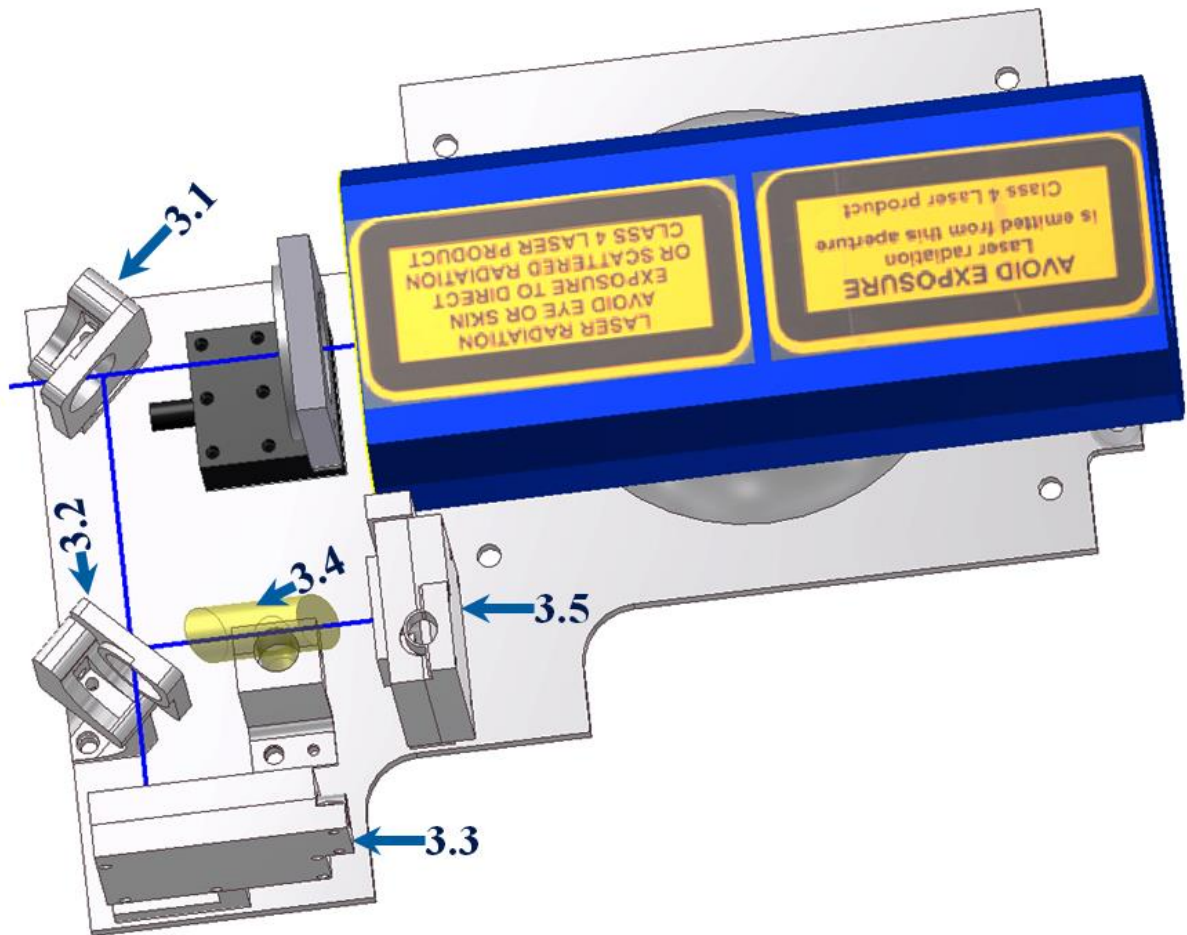


Fig. 2.5: Inventor 2009 assembly of the optical reference system

3.1: Beam splitter (reflectivity 10 % at 45°)

3.2: Beam splitter (reflectivity 50 % at 45°)

3.3: Photodiode (*ref.*)

3.4: NO₂ cuvette

3.5: Photodiode (*CNO₂*)

[3D AutoCAD models in Fig. 2.5; for the diode laser (blue) is by courtesy of Omicron Laserage Laserprodukte GmbH (www.omicron-laser.de) and beam splitter holder (3.1 and 3.2) by courtesy of Newport (www.newport.com)].

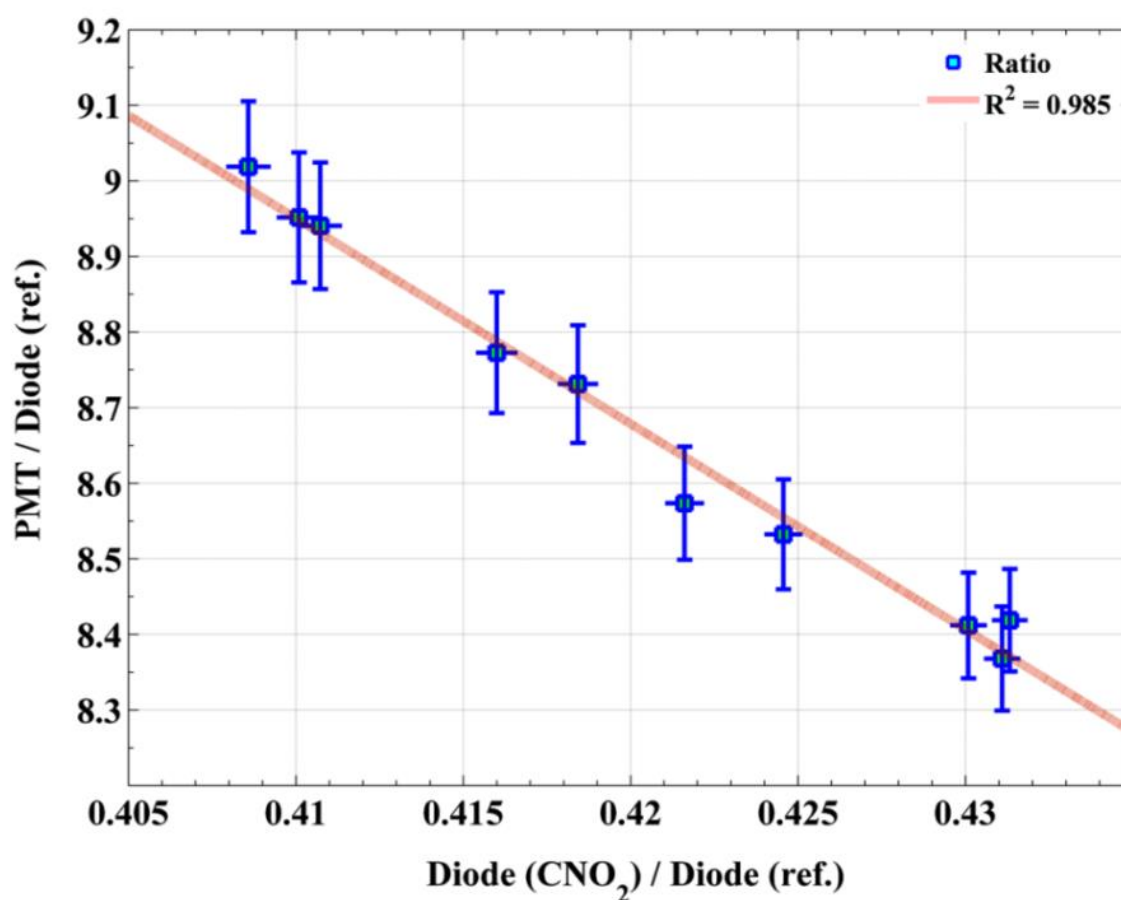


Fig. 2.6: A plot between the PMT and photodiode (CNO_2); both signals are normalised to the photodiode (*ref.*).

2.1.1.6 Accessories

The stray light in the system is reduced to a minimum level by using a combination of baffles. There are different types of baffles (Fig. 2.2, No.11 and 13) used inside the system to reduce scatter from walls or mirrors. The shape of a baffle surface is based on a zigzag pattern with a 30° angle. The sharpened edges of a baffle provide less surface area for the laser light to scatter and have the characteristic of a beam dump (7.2.1.2; A, B, and C). While operating the instrument in the field trial and lab, the diode laser and PMT are continuously kept at a constant temperature (25 ± 2 °C) by using a circulated water chiller. There is a need to keep the PMT and the diode laser system at constant temperature according to the manufacturer's recommendations. An elevated temperature can lead to an increase in the dark counts of the PMT, change in the power or wavelength of the diode laser, and even permanent damage from overheating. Similarly a decrease in temperature can lead to

condensation. So, it is required to avoid such changes by maintaining constant temperature. Based on calculations for ambient conditions, a chiller with a cooling capacity of about 100 W is required to maintain temperature. Copper cooling plates (7.2.1.2, D) are designed to generate turbulent flow for good cooling efficiency.

2.2 Laser on-off cycle selection

The diode laser has a 'Deepstar' mode, which is exploited as an advantage for the system. While operating in this mode, with the fast repetition rate of 5 MHz, there is no laser radiation during the off period. The rise time for the diode laser to transition from on to off is based on a theoretical calculation by taking into account key parameters like NO₂ absorption cross-section, pressure, flow velocity, lifetime NO₂ fluorescence, interference filter's suppression and the power of the diode laser. Fig. 2.7 shows a simulated fluorescence signal from 1 ppbv of NO₂ available during the duty cycles of '100 ns / 100 ns' and '100 ns / 300 ns' as an example for an initial 5000 ns period. The calculated sensitivity for different laser on-off cycles is shown in Fig. 2.8. For a comparison to current operational on-off cycle, three different possibilities have been demonstrated in Fig. 2.8. Relative sensitivity is plotted against the diode laser turn-off duration for a different turn-on time. The best sensitivity of the instrument is achievable by the operating on-off cycle of 200 ns. The diode laser is operated currently with the on-off cycle of 200 ns (1:1). The raw signal is stored in 4 ns bins (4 ns bin = 1 channel) for a specified time of integration (typically 1 s is used). In GANDALF, the laser on-off cycle is 200 ns and the fluorescence from NO₂ is detected during laser off period (channel 15 - 39, appendix 7.2.1.2). The first few channels (channel 15 - 19) of the laser off period are ignored because these channels contain scatters from the laser light and walls of detection cell. The sum of channels (in this case 20 - 38) is considered as a signal for NO₂ for further data acquisition.

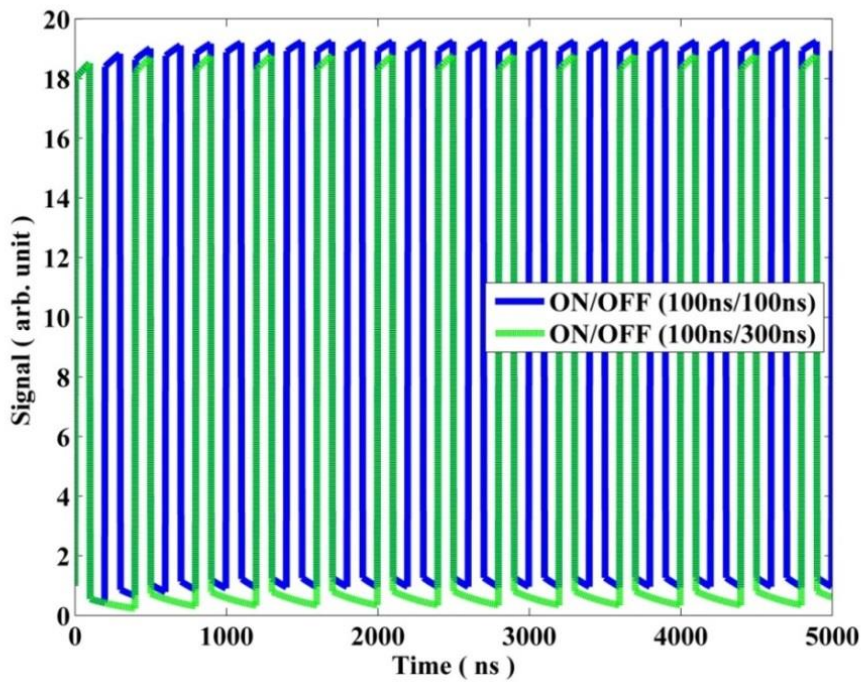


Fig. 2.7: Simulated ON/OFF cycles for operating the diode-laser

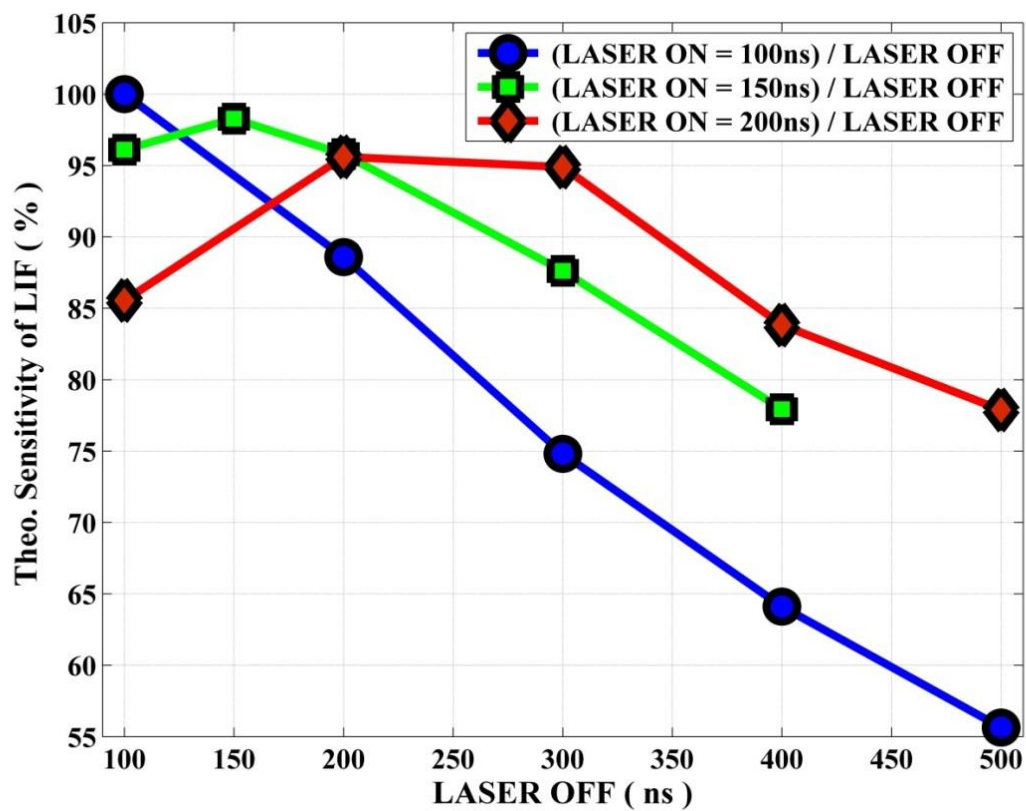


Fig. 2.8: Sensitivity of the instrument based on simulation is demonstrated for three different on/off cycles of diode laser operation.

2.3 Calibration system

The LIF method is not an absolute method and requires calibration. The sensitivity (Eq. 2.1) of GANDALF is determined with known amounts of NO₂ for different conditions such as background noise, laser power or wavelength, temperature, pressure, residence time in sampling line etc. The calibration system is described with its characteristics and uncertainties in the following sections.

2.3.1 Gas phase titration

NO₂ gas is available commercially and it can be used for calibration ([Thornton et al., 2000](#); [Dari-Salisburgo et al., 2009](#)), but there is much concern about the stability of NO₂ in a cylinder. Therefore, the quantitative gas phase titration between NO and O₃ (R. 1.1) is used to produce NO₂ for the calibration of GANDALF. NO standards are available commercially; in this case the NO calibration mixture for the gas phase titration is traceable to a primary NIST¹⁸ standard ($4.91 \pm 0.04 \mu\text{mol mol}^{-1}$). The uncertainty of the primary NIST standard is better than 1 % (level of confidence 95 %). The overall uncertainty of the derived value of NO calibration mixture is 2 %. This includes the uncertainty of the primary NIST standard and the maximum relative standard deviation (1.5 %) of the derived value of NO calibration mixture (appendix 7.2.1.7).

NO concentrations are almost completely consumed during a gas phase titration in the calibrator. This is achieved by using a high concentration of O₃. NO₂ also react with O₃ to form NO₃ (R. 1.9). Although the reaction [$\text{NO}_2 + \text{O}_3$] (R. 1.9) has a slow reaction rate [$3.5 \times 10^{-17} \text{ cm}^3 \text{ molecule}^{-1} \text{ s}^{-1}$ at k_{298} ([Atkinson et al., 2004](#))] compared to the $\text{NO} + \text{O}_3$ reaction [$1.8 \times 10^{-14} \text{ cm}^3 \text{ molecule}^{-1} \text{ s}^{-1}$ at k_{298} ([Atkinson et al., 2004](#))], but with the presence of higher concentrations and longer residence times, the reaction between NO₂ and O₃ can be important and leads to a loss of the NO₂ generated in the calibrator. The reaction (R. 1.9) also leads to a further reaction between NO₂ and NO₃ (R. 1.12). The calibrator for GANDALF has a reaction chamber, which is used for the gas phase titration between NO and O₃ and afterward, the calibration gas is diluted with synthetic air (zero air). A box model is used to assess a best possible scenario for the calibration setup. Several effects have been studied with a model to derive the setup of the calibrator e.g. amounts of concentrations, residence time, and flow rates etc.

¹⁸ National Institute of Standards and Technology [an agency of U.S. Department of Commerce, www.nist.gov]

2.3.2 Model simulations with lab comparison

A best scenario is found for the calibration setup by using Box Model (BM) simulations (appendix 7.2.1.4). These simulations helped to optimise the effect of factors like residence time, pressure, temperature, and reactions (like; R. 1.1, R. 1.9, and R. 1.12). The balance between NO and O₃ concentration varied to achieve maximum conversion efficiency for NO → NO₂ in simulations and compared with lab results. According to the best scenario, a residence time of about 7.5 s with a ratio of O₃ to NO larger than 12 is required inside the reaction chamber. This way, NO can be converted efficiently to NO₂ and the negative effects of different parameters (as described above) will be minimised. This setup was deployed for calibration and results compared with the model. The comparison between lab tests and model simulation is good. A BM simulation based on typical parameters¹⁹ of the calibrator for gas phase titration between NO and O₃ is shown in Fig. 2.9 and Fig. 2.10. The mixing ratios of NO, O₃, and NO₂ are plotted as a function of residence time in Fig. 2.9. This simulation shows that more than 99 % of NO is converted inside the reaction chamber. The major fraction of NO is converted to NO₂ with in the residence time of 7.5 s. Inside the reaction chamber, Fig. 2.10 shows evidence that the formation of NO₃ and N₂O₅ is negligible (< 0.5 ppb_v) compared to NO₂ (> 100 ppb_v). The formation of NO₃ and N₂O₅ can only raise 1 % uncertainty in the generated NO₂ for typical operating conditions of the calibrator.

¹⁹ For this specific simulation, initial parameters;

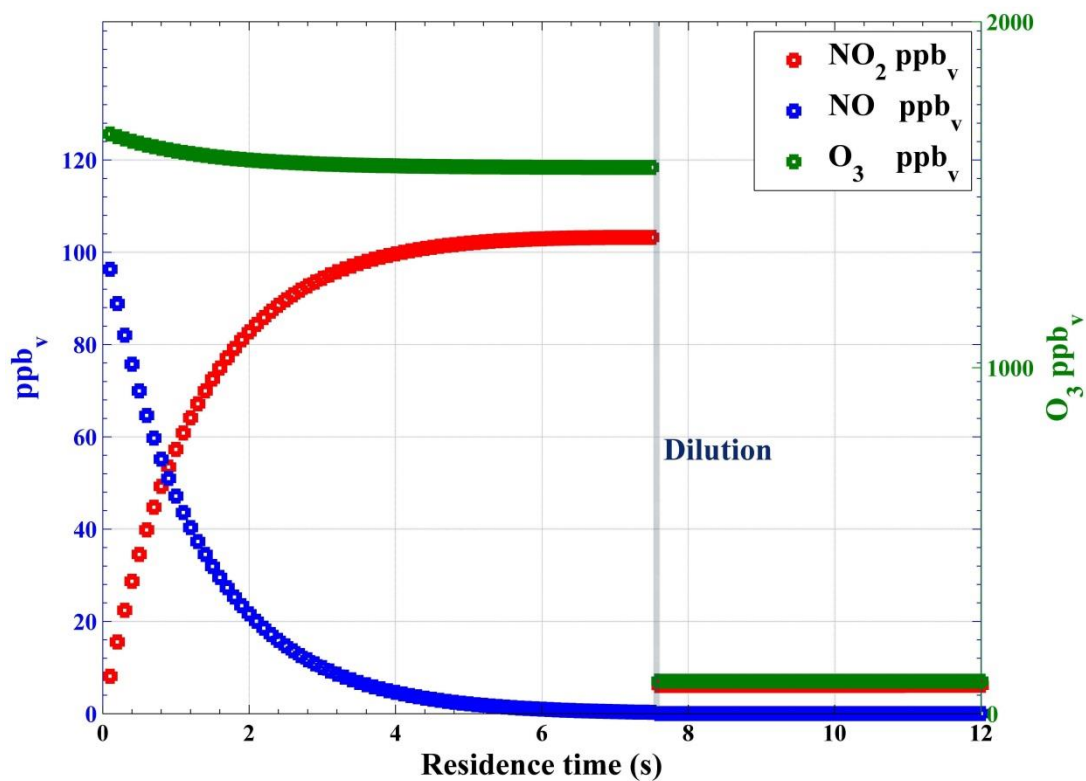
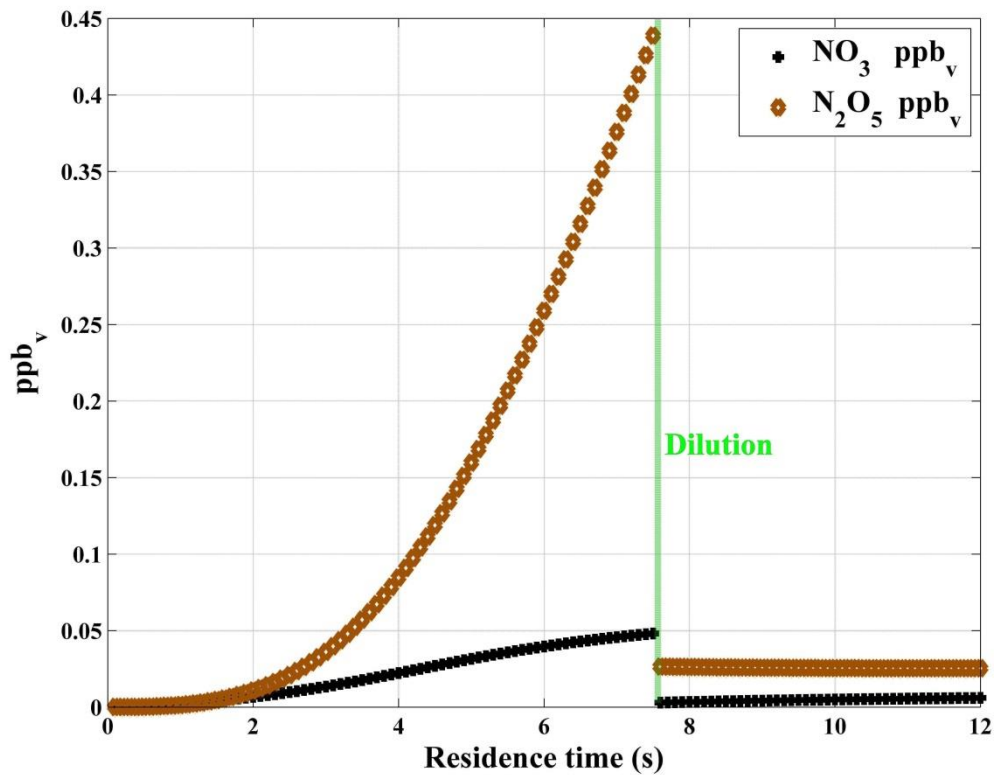
NO = 5 sccm × 10.55 ppm_v,

O₃ = 500 sccm × 1.7 ppm_v,

Residence time = 7.5s,

Flow = 8000 sccm

Temperature and Pressure = 298 K and 1013.25 hPa

Fig. 2.9: Box model simulation of gas phase titration between NO and O₃Fig. 2.10: Formation of NO₃ and N₂O₅, based on simulation shown in Fig. 2.9.

2.3.2.1 O₃ dependency

To check the optimum ranges of O₃ concentrations, for an optimum combination of residence time and conversion efficiency, the calibration system was tested with different concentrations of O₃ in the lab. Fig. 2.11 shows the response of the PMT of GANDALF to a change in the O₃ mixing ratios of the calibrator with a constant NO concentration. The PMT signal is proportional to the amount of NO₂ generated inside the calibrator. At concentrations of O₃ lower than 1 ppm_v in the calibrator, a lower signal of the PMT was observed (Fig. 2.11). This is because not all the NO is utilised within the reaction chamber. The PMT signal started to decrease after achieving a maximum signal at about 1.3 ppm_v of O₃ for a constant concentration of NO. This is also well explained by BM simulations. The peaks are similar in case of the PMT signal and BM simulations. The decrease in PMT signals at high O₃ concentrations (1.3 ppm_v to 5 ppm_v) is also well explained by the derived NO₂ concentrations from the BM. This decrease in PMT signal is mainly due to a loss of NO₂ because of reactions R. 1.9 and R. 1.12 at a high concentrations of NO₂ and O₃.

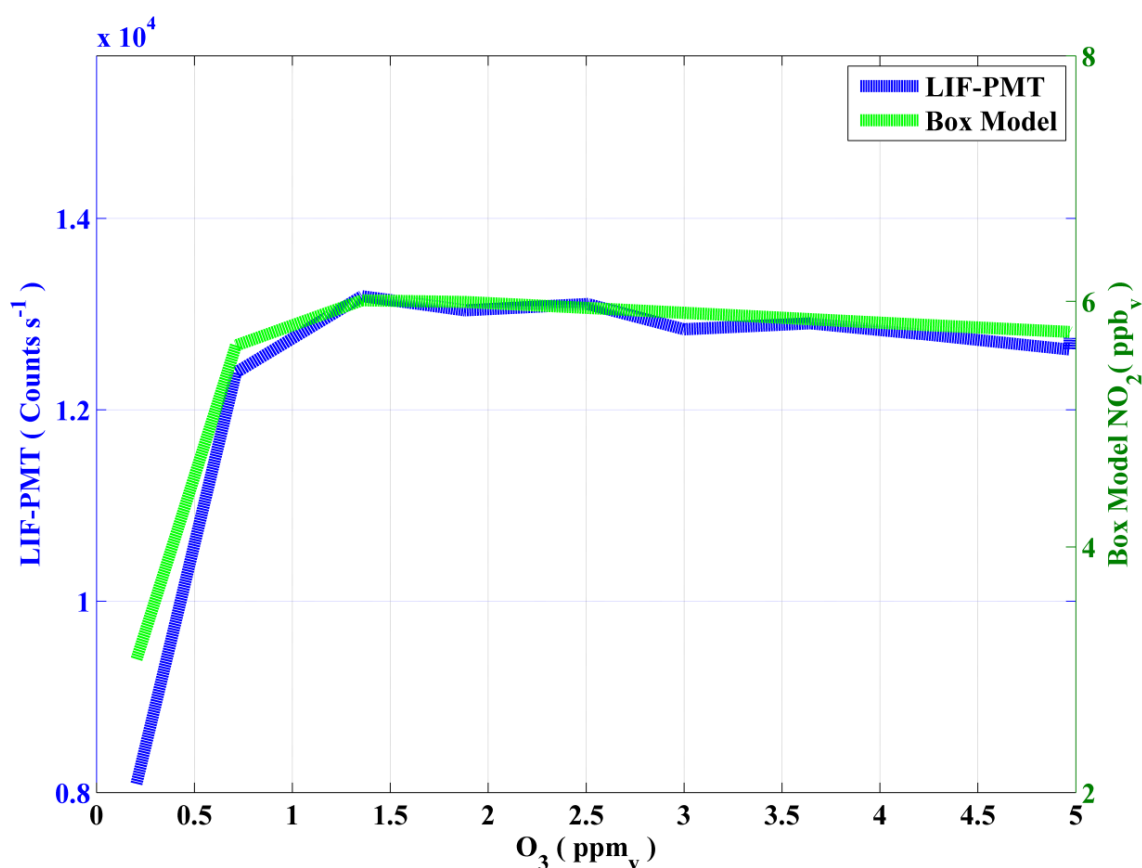


Fig. 2.11: PMT signal with respect to change in O₃ mixing ratios.

The higher O₃ concentration in the calibrator provides a shorter NO lifetime. The uncertainty of the generated NO₂ ('NO + O₃' titration) is much less sensitive to O₃ compared to NO. This uncertainty arises due to an increase in the loss of NO₂ inside the reaction chamber because of the formation of NO₃ and N₂O₅. The reduction in NO₂ is only 1 % (Fig. 2.12) with an increase of 1 ppm_v in O₃ above the maxima at about 1.3 ppm_v of O₃ (Fig. 2.11). The O₃ concentrations are always kept above this threshold limit and the concentrations are measured with an O₃ analyser having a typical precision of 5 %. Above the threshold, a 5 % change in O₃ can only produce an uncertainty in NO₂ of less than 0.5 %.

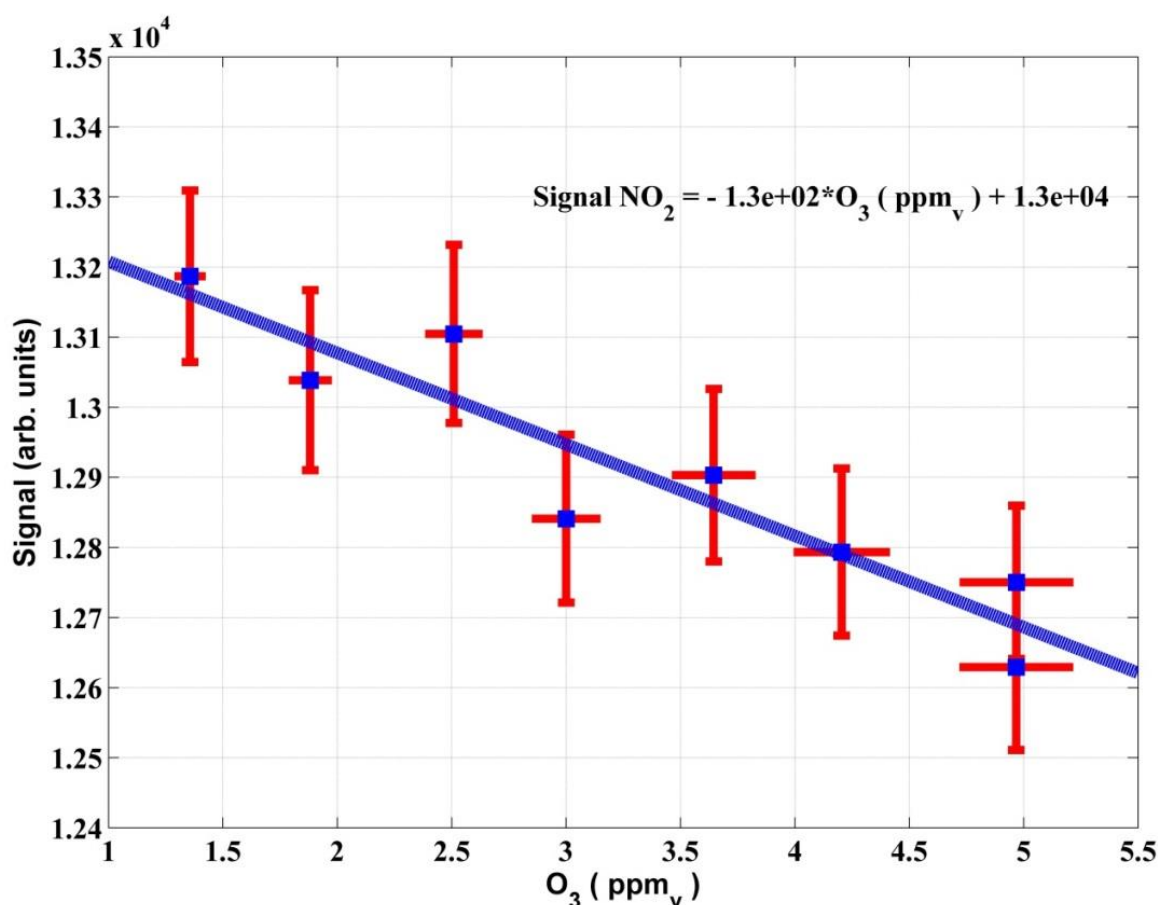


Fig. 2.12: NO₂ loss due to increase in O₃ inside the GANDALF calibrator.

2.3.2.2 Residence time

A NO_x analyser²⁰ is used to determine the remaining concentrations of NO inside the calibrator after the gas phase titration. About 99 % of NO is utilised in the gas phase titration for most of the cases at O₃ > 1.3 ppm_v. Based on NO and O₃ concentrations, there are two different regimes inside the calibration system as a function of flow rate: (1) reaction chamber for the gas phase titration (2) dilution with synthetic air after the reaction chamber. For the calibration system, the total residence time for the synthetic calibration gas is determined by using Eq. 2.3.

$$\text{NO}_{\text{GPT}} = D [\text{NO}_i] \left(e^{-(k_{1,1} [\text{O}_3] t_1)} \right) \left(e^{-(k_{1,1} [D \times \text{O}_3] t_2)} \right) \quad \text{Eq. 2.2}$$

$$\Rightarrow [t_1 + D t_2] = - \left[\frac{\ln \left(\frac{\text{NO}_{\text{GPT}}}{D [\text{NO}_i]} \right)}{k_{1,1} [\text{O}_3]} \right] \quad \text{Eq. 2.3}$$

In Eq. 2.3, ‘NO_{GPT}’ is measured with a NO_x analyser and is defined as ‘the remaining concentration of NO in the calibration gas after the gas phase titration and dilution’. ‘NO_i’ is the initial concentration of NO without the gas phase titration. ‘D’ is the dilution factor and is a ratio between the reaction chamber flows to total flow. ‘t₁’ is the residence time for the reaction chamber and ‘t₂’ is the travel time for gas required after the reaction chamber to the inlet of GANDALF. ‘O₃’ is the concentration inside the reaction chamber and is measured with a commercial UV-photometer²¹. ‘k_{1,1}’ is the temperature dependent rate coefficient for R. 1.1. There are two slightly different values reported in the literature for ‘k_{1,1}’ as follows:

$$k_{1,1} = 3 \times 10^{-12} \times e^{(-1500/T)} \quad (\text{Sander et al., 2011b}) \quad (\text{JPL})$$

$$k_{1,1} = 1.4 \times 10^{-12} \times e^{(-1310/T)} \quad (\text{Atkinson et al., 2004}) \quad (\text{IUPAC})$$

²⁰ Model: ECO PHYSICS CLD 780 TR, Switzerland

²¹ ANSYCO, O3-41M, ‘Analytische Systeme und Komponenten GmbH’, Germany

Based on Eq. 2.3, the average value of total residence time ' $[t_1 + D t_2]$ ' is 7.32 s (JPL) with a variability of 0.25 s and 8.38 s (IUPAC) with a variability of 0.29 s. The estimated accuracy of these two values of the total residence time is 6.5 % (1σ). The calculated total residence time with assumption of plug flow is 7.73 s. The likelihoods for being accurate for $k_{1.1}$ (IUPAC) and $k_{1.1}$ (JPL) are indistinguishable with respect to plug flow assumption as shown in Fig. 2.13, with blue and green shaded areas for $k_{1.1}$ (IUPAC) and $k_{1.1}$ (JPL), respectively.

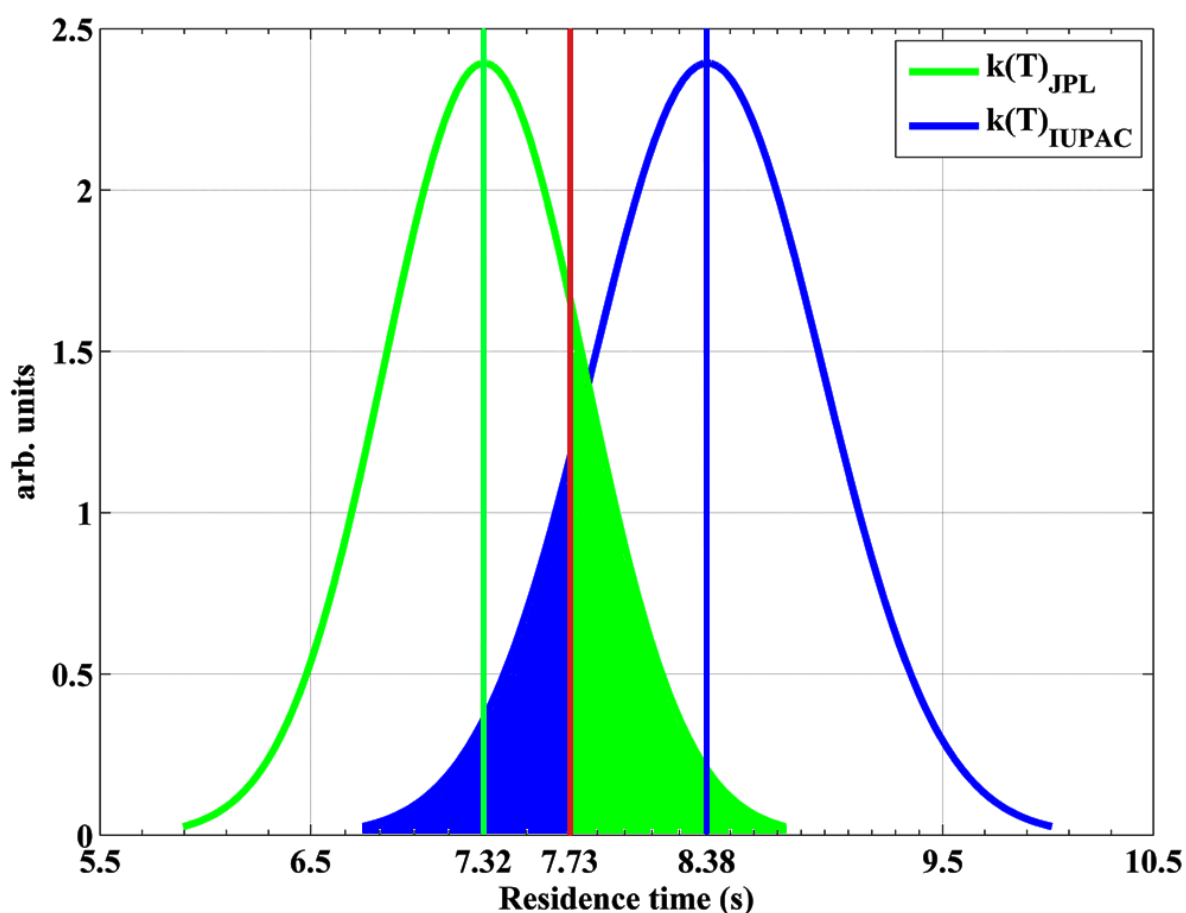


Fig. 2.13: Residence time for NO₂ calibration gas in the calibrator.

2.3.2.3 Effect of temperature and pressure

The temperature and pressure also affect the formation of NO₂ inside the reaction chamber. These effects are tested with the BM. In simulations, all parameters except temperature or pressure are kept constant. The change in temperature always affects the rate of the reactions.

At low temperatures, the reaction between NO and O₃ slows, and the conversion efficiency from NO to NO₂ can be disturbed for a constant residence time. The temperature inside the GANDALF's calibrator is about 30 to 40 °C. The BM simulation suggested that any change in the temperature within an interval of [5, 45 °C] leads to an uncertainty of only 1 % (1 σ). Similarly, the effect on the calibration gas due to a change in the atmospheric pressure is not significant. Based on the BM simulation, the uncertainty in the NO₂ concentration of calibration gas due to a change in the atmospheric pressure over an interval of [800, 1013.25] hPa can be maximally 0.5 % (1 σ). Fig. 2.14 and Fig. 2.15 show the plot (BM) for NO₂ formation versus residence time inside the reaction chamber at different temperatures and pressures, respectively. Notice in the figures of BM simulations that the mixing ratios of formed NO₂ are fairly constant from a residence time of 6 s to 7.5 s.

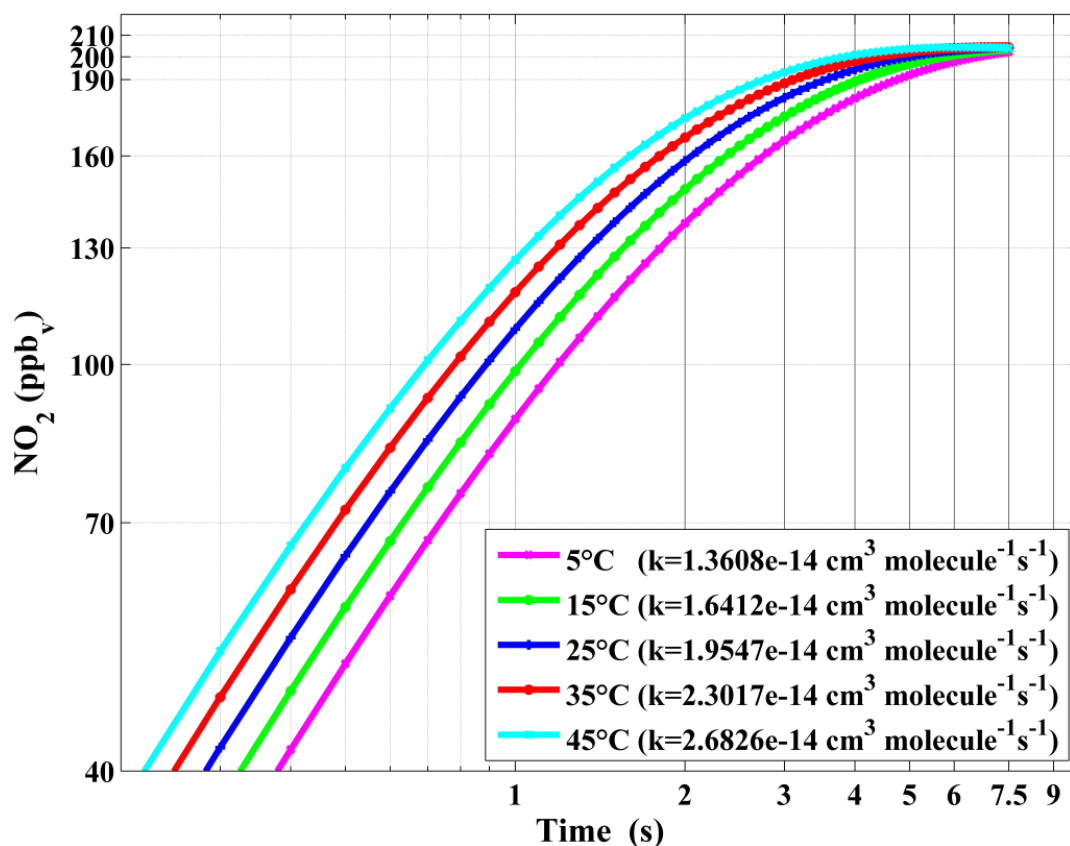


Fig. 2.14: NO₂ concentrations (BM simulation) inside the calibrator as a function of time based on different temperatures.

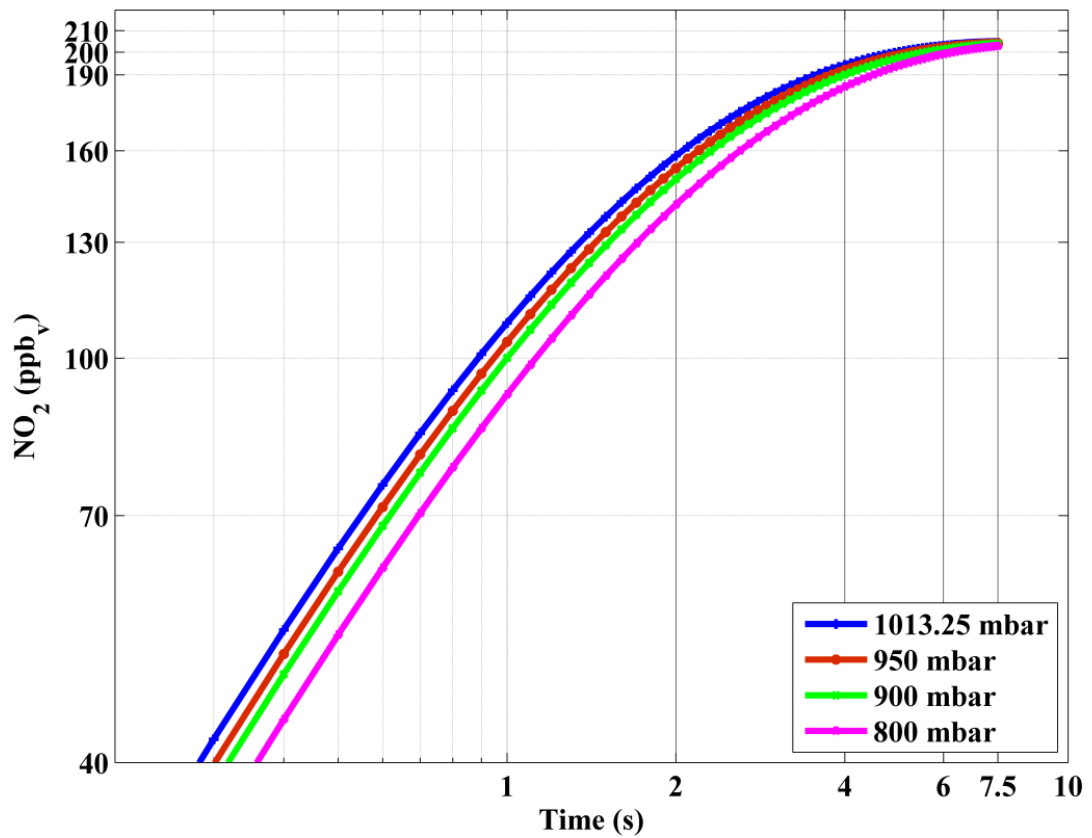


Fig. 2.15: NO₂ concentrations (BM simulation) inside the calibrator as a function of time for different pressures (mbar or hPa).

2.3.2.4 Atmospheric H₂O vapour dependency

The calibration gas for GANDALF primarily contains N₂ (~79.5 %) and O₂ (~20.5 %) with H₂O vapour (< 25 ppm_v). The level of H₂O vapour in the atmosphere reaches up to 3 % (Seinfeld and Pandis, 2006). The sensitivity of the instrument is mainly reduced by rising the atmospheric H₂O vapour because an increase of atmospheric H₂O vapour leads to an increase in the quenching of NO₂ fluorescence. The effect of atmospheric H₂O vapour on sensitivity is corrected for by the simultaneous measurement of H₂O vapour in the atmosphere. The H₂O dependency is checked by diluting the calibration gas with known amounts of water vapour concentrations. The H₂O concentrations are determined with an existing calibration system for the LIF-OH instrument (Martinez et al., 2010).

The effect observed for H₂O vapour is slightly different for channel 20 - 23 and channel 24 - 38. In the data analysis, each of the sections is evaluated for H₂O vapour dependency separately. Fig. 2.16 (L) shows a plot for the LN of intensity with respect to time and based on different H₂O concentrations. The distinguishing slopes in Fig. 2.16 (L) for the two sections present relevant quenching effects. Fig. 2.16 (R) demonstrates the effects of change in the atmospheric H₂O on the sensitivity of GANDALF. The decrease in the sensitivity for channel 20 - 23 and channel 24 - 38 is $4.5 \% \pm 0.3 \% (1\sigma)$ and $5 \% \pm 0.3 \% (1\sigma)$, respectively, at 1 % of atmospheric H₂O vapour.

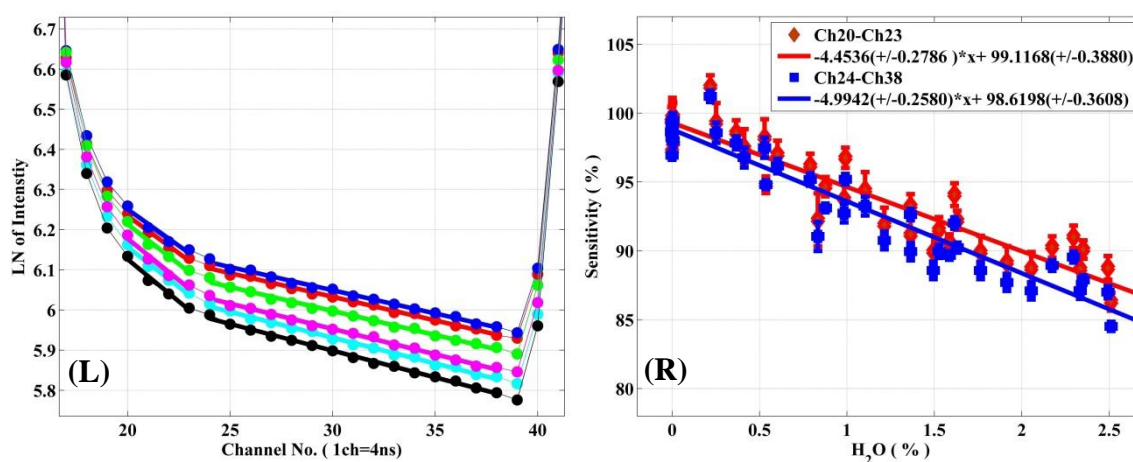


Fig. 2.16: The dependence of NO₂ fluorescence intensity on increasing water vapour concentrations in GANDALF (L). Change in sensitivity (normalised to zero H₂O %) due to change in water vapour (scale equivalent to atmospheric H₂O %) (R).

2.3.3 Automated calibration setup

A robust calibration system has been developed for the automated calibration of the instrument. GANDALF is calibrated 4 - 8 times per day during a field operation to determine changes in the sensitivity and shift in the background level of the instrument. An example for a plot of the instrument signal counts (s^{-1}) versus known amount of NO_2 concentration is shown in Fig. 2.17. The calibration system is controlled by Mass Flow Controllers (MFC)²² and electronic valves²³. All MFC are calibrated using a DryCal²⁴ sensor which is trace able to a NIST standard (NIST traceability is confirmed by Westphal²⁵). The uncertainty in operating range of flow, based on a certified value is 1 % (level of confidence 95 %). O_3 is generated for the calibration using an ozone generator²⁶. The concentrations of O_3 are measured from time to time by using a commercial UV photometer. Different NO_2 mixing ratios are achieved by changing the NO flow (range up to 10 ± 0.1 sccm), whereby the O_3 concentration (> 1.3 ppm_v) and flow (500 ± 5 sccm) are kept constant. Fig. 2.18 shows a schematic of the setup for the automated calibration procedure of GANDALF. A small calibration pump (Cal. pump) is connected to the main sampling line of GANDALF. A three-way electronic valve (EV2) and manual needle valve (MNV) are attached in front of the Cal. pump. To achieve residence time of less than 0.1 s in the sampling line for minimising the line effects (e.g. decomposition of species like PAN, chemical reaction of the ambient NO and O_3 etc.), a flow ≥ 10000 sccm is required during ambient air measurements. GANDALF has a flow of 4100 sccm through the pin hole and the rest of the flow is diverted to a main exhaust by the Cal. pump. The EV2 opens line L1 or L2 for the Cal. Pump at positions P1 or P2, respectively. The amount of total sampling flow can be increased or decreased by adjusting the MNV. During ambient air measurements, EV2 is opened for L1 at position P1 and allows an extra flow of about 8000 - 9000 sccm to pass from the sampling flow to the Cal. Pump, as shown by the L1 line (green) plus arrow (white) in Fig. 2.18. Line L1 is simultaneously used to condition the NO calibration line with a flow of 2 sccm NO gas. Frequent zero-air measurements (once per hour during PARADE-2011 for example) are necessary to monitor changes in the background level of GANDALF. During background level measurements, an excess of zero-air 3900 sccm (aqua colour arrow, Fig. 2.18) is

²² MKS Instruments and Bronkhorst HIGH-TECH B.V, USA

²³ Solenoid Operated Diaphragm, Galtek, USA

²⁴ DC-2, BIOS International Corporation, USA

²⁵ WESTPHAL measurement and control technique GmbH & Co. KG, Germany

²⁶ SOG2, 185nm, UVP - Ultraviolet Products, USA

diverted to the Cal. pump through the line L1 at P1(EV2) along with 5100 sccm flow of ambient air. A three-way electronic valve (EV3) with MFC (Syn.) is used to switch synthetic air background flow (8000 ± 80 sccm) on and off in the line L3 at P2 (EV3) and the dilution of NO_2 calibration gas at P1 (EV3). During calibration of GANDALF, EV2 is open in the line L2 at P2 to take an overflow of 3900 sccm with 5100 sccm from the ambient as shown with the red colour line (L2) in Fig. 2.18. For the gas phase titration, the flow of O_3 is switch on and off with two-way electronic valve EV1 and MFC (O_3). The flow of NO (1 - 10 sccm) is controlled by a MFC (NO) as shown in Fig. 2.18. Since all overflows are diverted to an exhaust, this setup allows frequent checks of the GANDALF's sensitivity and background level without disturbing the ambient conditions for a nearby operating instrument. Based on calibrations during PARADE-2011, the deviation in repeatability of the sensitivity was less than 2.7 % (1σ). The overall uncertainty of the calibration system taking propagation of errors into account is better than 5 % (1σ).

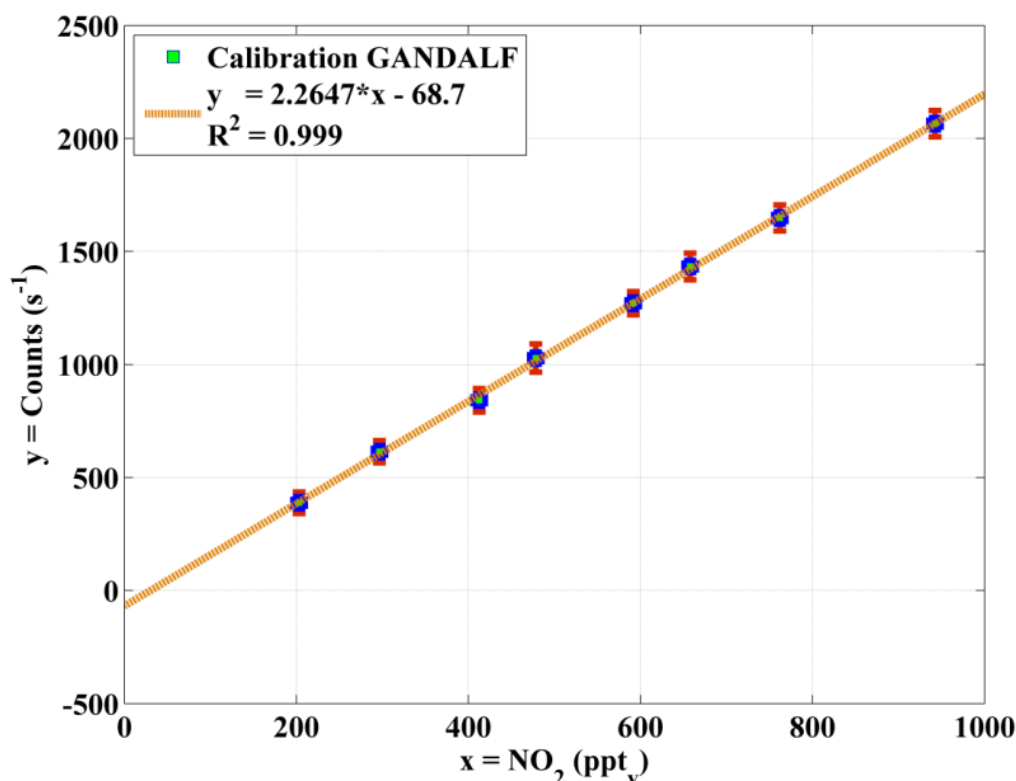


Fig. 2.17: A plot between known amounts of NO_2 versus the fluorescence signal as an example of the calibration of GANDALF. The calibration constant α_c (Eq. 2.1) is determined by the slope of the curve.

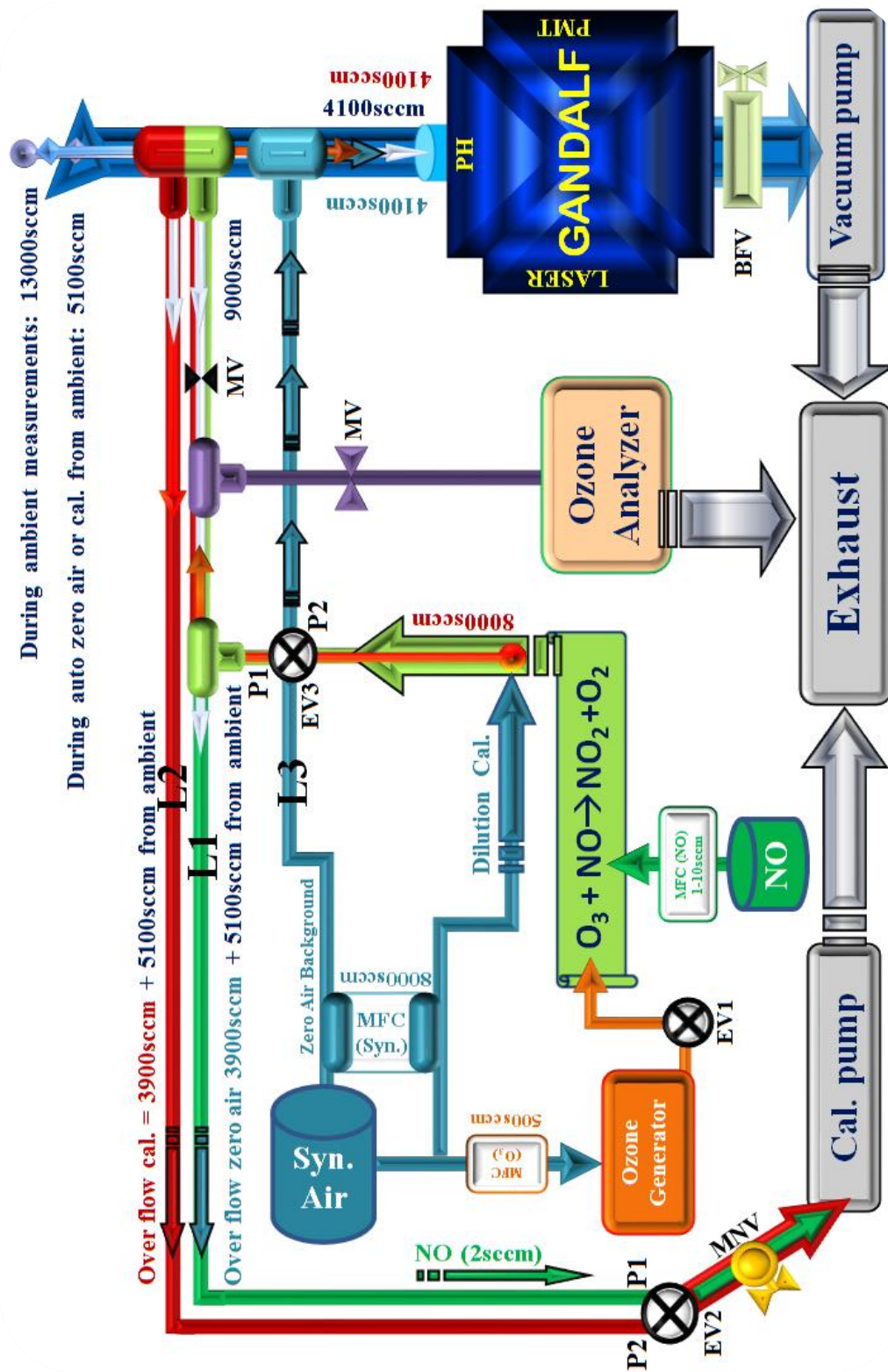


Fig. 2.18: Schematic view of Setup for automated calibrations during out door operation.

2.4 Interferences by trace species

There can be several atmospheric gas species that can absorb the laser light inside the detection cell and undergo a process of photodissociation and fluorescence. These processes can lead to interference for the NO₂ measurements with GANDALF directly (photodissociation process) or indirectly (fluorescence). The absorption cross-section of several abundant gas species is checked at the wavelength of the diode laser. Iodine monoxide (IO) has an absorption cross-section [$3.9 \times 10^{-18} \text{ cm}^2 \text{ molecule}^{-1}$, ([Harwood et al., 1997](#))] factor about 8 times higher than NO₂ at 449 nm and the presence of IO has been reported in the marine areas ([Commane et al., 2011](#)). Even a few ppt_v of IO in the atmosphere can contribute significantly to the fluorescence signal of NO₂, but the fluorescence lifetime of IO is only 1-10 ns [e.g. ([Bekooy et al., 1983](#); [Newman et al., 1998](#))]. The initial 20 ns signal during laser off period is neglected in the GANDALF data evaluation and therefore after 20 ns the IO fluorescence signal is insignificant to interfere with the NO₂ fluorescence signal.

Nitrogen containing inorganic species (NO₃, N₂O₅, HONO₂, HO₂NO₂, PAN, ClONO, ClONO₂, and ClONO₂) can produce NO₂ by photodissociation and this can happen inside the detection cell. The absorption cross-sections at 449 nm has not been reported in literature for these gas species [N₂O₅ ([Harwood et al., 1993](#)), HONO₂ ([Burkholder et al., 1993](#)), HO₂NO₂ ([Singer et al., 1989](#)), PAN ([Talukdar et al., 1995](#)), and ClONO ([Molina and Molina, 1977](#))] and it is not known that these species exhibit any absorption of the laser light resulting in photodissociation. The absorption cross-section for the gas species [ClONO₂ ([Molina and Molina, 1979](#)), and ClONO₂ ([Ghosh et al., 2012](#))] is a factor about 10⁴ smaller than NO₂ at 449 nm and can therefore be neglected.

NO₃ has a larger absorption cross-section ([Wayne et al., 1991](#)) at 449 nm compared to previously described nitrogen containing inorganic species. The effective absorption cross-section [calculated from ([Wayne et al., 1991](#))] is about a factor of 2 smaller compared to that of NO₂ at the wavelength of the diode laser. NO₃ also has a red-shifted fluorescence spectra ([Wood et al., 2003](#)) similar to the case of NO₂. So NO₃ is the species with the most potential to interfere with NO₂ measurements in GANDALF. The recommended quantum yield of NO₃ is about 1 at wavelengths below 585 nm ([Sander et al., 2011b](#)); hence, its fluorescence is not likely to interfere with the NO₂ fluorescence because the photodissociation of NO₃ to NO₂ is by far the most dominant process present inside the detection cell. Interference from photodissociation of NO₃ is a two-photon process for the instrument as below:



The ratio of the atmospheric concentration between NO_2 and NO_3 is very high e.g. during PARADE the median value of the ratio $\text{NO}_2 / \text{NO}_3 = 430$ at $\text{NO}_3 > 0$ with a minimum value 12, so the impact of NO_3 to NO_2 conversion compared to the ambient NO_2 is insignificant inside the detection cell (e.g. Eq. 2.5). A relative contribution $[\text{NO}_3 \rightarrow \text{NO}_2 / \text{NO}_{2(\text{ambient})}]$ of 1% is achievable inside the detection cell only if NO_3 in the atmosphere is a factor about 62 larger than NO_2 , but this scenario is highly unlikely, as NO_3 will always be smaller than NO_2 in the atmosphere. The photodissociation lifetime of NO_3 is about $1.2 \times 10^4 \mu\text{s}$ (Eq. 2.4) while the residence time in the beam of the laser is only about $2 \mu\text{s}$. So the efficiency of the one-photon process ($\text{ambient NO}_2 + h\nu_{\text{DiodeLaser}} \rightarrow \text{NO}_2^* \rightarrow \text{NO}_2 + h\nu'$) will always be greater than the two-photon process as previously described in this paragraph, so it will predominate.

$$\begin{aligned} \tau(\text{NO}_3)_{\text{photodis.}} \approx & \left(\left\{ \text{Eff. abs. cross - section} = 2.7 \times 10^{-19} \frac{\text{cm}^2}{\text{molecule}} \right\} \right. \\ & \times \{ \text{Quantum yield} = 1 \} \\ & \left. \times \left\{ \text{Laser photon flux} = 3 \times 10^{20} \frac{\text{photon}}{\text{cm}^2} \text{ s}^{-1} \right\} \right) \approx 10^4 \mu\text{s} \end{aligned} \quad \text{Eq. 2.4}$$

$$\begin{aligned} \text{NO}_3 \rightarrow \text{NO}_2 \approx & \left(\left\{ \text{Eff. abs. cross - section} = 2.7 \times 10^{-19} \frac{\text{cm}^2}{\text{molecule}} \right\} \right) \\ & \times \{ \text{Quantum yield} = 1 \} \times \{ \text{Residence time} = 2 \mu\text{s} \} \\ & \times \left\{ \text{Laser photon flux} = 3 \times 10^{20} \frac{\text{photon}}{\text{cm}^2} \text{ s}^{-1} \right\} \\ & \times \left\{ \text{Ambient NO}_3 = 2 \times 10^9 \frac{\text{molecule}}{\text{cm}^3} \right\} \approx \frac{10^5 \text{ molecule}}{\text{cm}^3} \end{aligned} \quad \text{Eq. 2.5}$$

Alkenes and aromatics (aldehydes and benzene) are also abundant in the troposphere. The absorption cross-sections of alkenes and aromatics exist in the UV range ($< 300 \text{ nm}$) (Keller-Rudek et al., 2013), well below the visible wavelengths and cannot interfere with GANDALF (contains blue laser light). To minimise the impact of heterogeneous or thermal

conversion of species like, PAN, HO₂NO₂, and N₂O₅ to yield NO₂, a short residence time of < 0.1 s is generally used by keeping the sampling flow high [e.g. PARADE ≈ 12000 sccm in 0.1 m long sampling line, (Section 3.2 and 7.3.1.4)]. The systematic dependency on the several measured atmospheric quantities was checked for differences between GANDALF and other measurements of NO₂ during PARADE-2011. No evidence of systematic correlation for a potential interference is observed for GANDALF (Section 3.2.2).

2.5 Precision and limit of detection

The precision of the instrument is evaluated by taking random individual calibration points into account during the field experiment (PARADE-2011) and the relative precision of GANDALF is shown in Fig. 2.19 for these data points. The relative precision on calibration points was better than 0.5 % ($1 \sigma \text{ min}^{-1}$) for most of the data points despite a few outliers (Fig. 2.19). An absolute value of 3 ppt_v is required to add in the relative precision for overall precision of GANDALF. The absolute value of 3 ppt_v (1σ) is obtained from an offset of a fit between absolute precision of calibration points versus the mixing ratios of NO₂. This absolute value arises from variability in the zero-air signal. The variations in background level signal for GANDALF follows a square root dependency on integration time. These variations around an average value for zero-air mostly control precision of the instrument close to detection limit. The zero-air deviations can be reduced by using a high averaging interval. The precision of the instrument background level was also investigated using a continuous signal of zero-air for about 50 minutes. In order to verify the square root dependency of the signal variability on integration time, an Allan deviation plot is used (Riley, 1995; Land et al., 2007). Fig. 2.20 shows an overlapping (Riley, 2008) Allan deviation plot of variations in a background level with respect to averaging time. The variations in background level with a 60 s integration time is equivalent to an absolute NO₂ value of about 3 ppt_v. This plot (Fig. 2.20) also shows that the random noise of the instrument background level can be reduced by averaging, with square root dependency of time, up to a 500 s period. The background level of GANDALF is frequently checked during a field operation (e.g. during PARADE, 1 background level check per hour). An extra variable uncertainty can also be involved that depends on the time interval between two background level measurements (Section 3.2).

The background level is important for defining the limit of detection (LOD). It can be assessed by the variation of the zero-air signal. Based on an Allan deviation plot (Fig. 2.20), a limit of detection about 3 ppt_v of NO₂ for 1 minute averages is expected and even lower for higher averages of time up to 500 s. In this case the LOD of GANDALF is calculated based on relation (Eq. 2.6) by considering a background level twice to the actual background level.

$$\text{LOD} = \frac{\text{SNR}}{\alpha_c} \sqrt{\frac{2 S_{\text{BG}}}{t}} \quad \text{Eq. 2.6}$$

In Eq. 2.6, α_c is the calibration factor or sensitivity in counts (s⁻¹ ppb⁻¹) and SNR is 2. S_{BG} is synthetic air background in counts (s⁻¹) and 't' is the averaging time in seconds. The LOD for GANDALF, based on sensitivity and background measurements during the field experiment (PARADE-2011), varied between 5 and 10ppt_v.

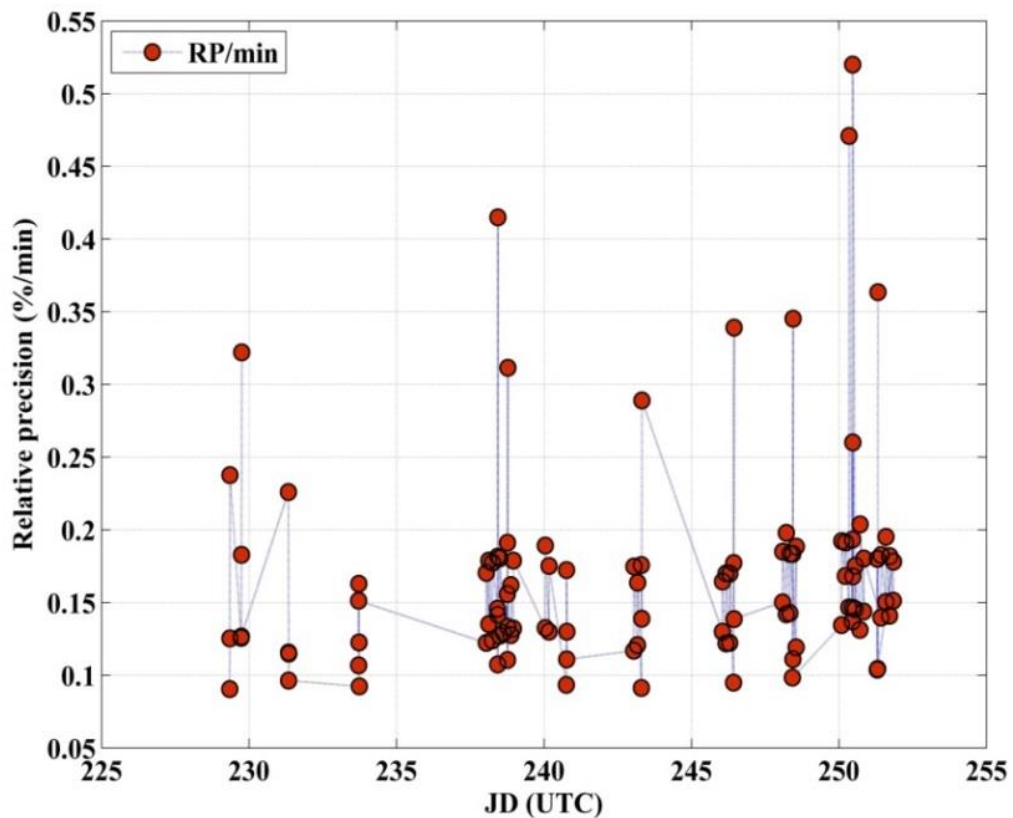


Fig. 2.19: Relative precision check of GANDALF for randomly selected NO₂ calibration points.

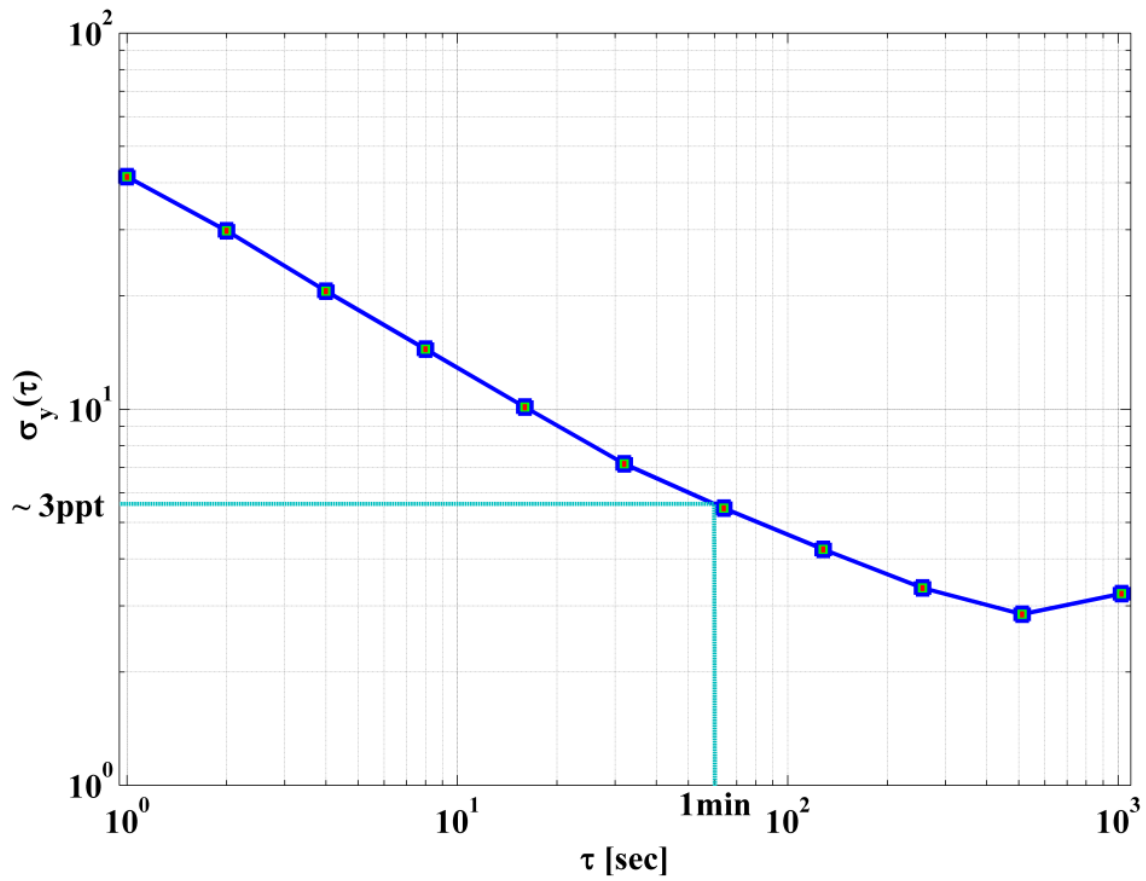


Fig. 2.20: An overlapping Allan deviation plot for the dependence of the 1σ variation in the background level vs. integration time.

2.6 Overview of different LIF instruments

Table 2.1: Overview of different LIF instruments (operating parameters and LOD)

Reference	$\lambda^{\text{laser type}}$ (nm)	Laser power (mW)	Abs. cross-sec. ($\times 10^{-19}$) $\text{cm}^2 \text{ molecule}^{-1}$	Cell pressure (Pa)	LOD [SNR = 2] (ppt, min^{-1})
(George and Obrien, 1991)	532 ²⁷	250	1.5	37	600
(Fong and Brune, 1997)	565 ²⁸	250	0.6	1000	460
(Thornton et al., 2000)	585 ²⁹	100-400	1	467	6
(Matsumi et al., 2001)	440 ³⁰	100	7	35	12
(Matsumoto et al., 2001)	523.5 ³¹	360	1.4	93	125
(Cleary et al., 2002)	640.2 ³²	16	3.9 ^C	27	145
(Matsumoto and Kajii, 2003)	532 ³³	6500	1.5	267	4
(Taketani et al., 2007)	410 ³⁴ , 473 ³⁵	10, 15	6, 3	67	390, 140
(Parra and George, 2009)	406.3 ³⁶	35	6	101325	2000 ^A
(Dari-Salisburgo et al., 2009)	532 ³⁷	8000-12000	1.5	60	12
GANDALF	447- 450 ³⁸	max. 200	5.3 ^E	700	5-10

^E Effective absorption cross-section (Section 2.1.1.1).

^C Cooling enhancement.

^A Ambient pressure in the detection cell.

²⁷ Nd:YAG laser

²⁸ Copper vapour laser-pumped dye laser

²⁹ Pulsed YAG-pumped dye laser

³⁰ Optical parametric oscillator laser

³¹ Nd:YLF laser harmonic

³² External-cavity tunable diode laser

³³ Nd:YVO₄ pulse laser pumped by a solid-state laser

³⁴ GaN-based laser diode

³⁵ Diode-pumped Nd:YAG laser

³⁶ CW GaN semiconductor laser diode

³⁷ YAG Q-switched intra-cavity doubled laser

³⁸ CW diode laser

3 Field Experiment: PARADE-2011

An overview of the conditions is provided in this chapter. The intercomparison of NO₂-measurements and O₃-related photochemistry is discussed in up-coming sections.

3.1 Overview

The PARADE (**P**Articles and **R**Adicals: **D**iel observations of the impact of urban and biogenic **E**missions) field experiment took place at the Taunus Observatory on Kleiner Feldberg (825m ASL; 50° 13' 25'' N, 8° 26' 56'' E), in Germany from the 15th of August (DOY³⁹ = 226) to the 9th of September (DOY = 251) 2011. The general focus of PARADE was to investigate summertime biogenic emissions and photochemistry in a semi-rural environment. A description of conditions from previous observations can be found in ([Crowley et al., 2010](#)). The objective of PARADE was to investigate the photochemistry at the interface between the biosphere and the lower troposphere. This includes the study of nitryl chloride's chemistry ([Phillips et al., 2012](#)), the VOCs emission response of Norway spruce (*Picea abies*) trees with seasonal variations ([Bourtsoukidis et al., 2012;2014](#)) and related effect of the total OH reactivity ([Nölscher et al., 2013](#)), and the impact of radicals on aerosol chemistry ([Bonn et al., 2013](#)). In this chapter, NO₂ measurements with GANDALF are discussed in comparison to other instruments. A budget for the O₃ photochemistry is presented to estimate the O₃ tendency of the region.

3.1.1 Site description and meteorological conditions

The observatory is located in the vicinity of the Taunus region at the hilltop of Kleiner Feldberg ([Fig. 3.1](#)). The measurement site is a semi-rural area with significant biogenic emissions. A total area of 5 km radius around the observatory is dominated by coniferous (40 %), broad-leaved (32.5 %), and mixed forest (9 %). The coniferous forest is a major contributor of biogenic emissions from the northeast side, whereas the southwest side is dominated by broad leaved forest. The measurement platform ([Fig. 3.4](#)) was located at the top of the observatory. The area around the platform (in 50 m radius) has only a few trees and the land is covered with grass and blueberry bushes. The site is often affected by

³⁹ DOY (Day of year 2011)

3.1 Overview

anthropogenic activities of nearby cities such as Frankfurt/Main (30 km SE), Wiesbaden (20 km SW), Mainz (25 km SSW), and some roads within 5 - 10 km, depending on the wind directions. To provide an overview of the area around the observatory (50 km radius), Table 3.1 shows a percentage composition of different land uses.

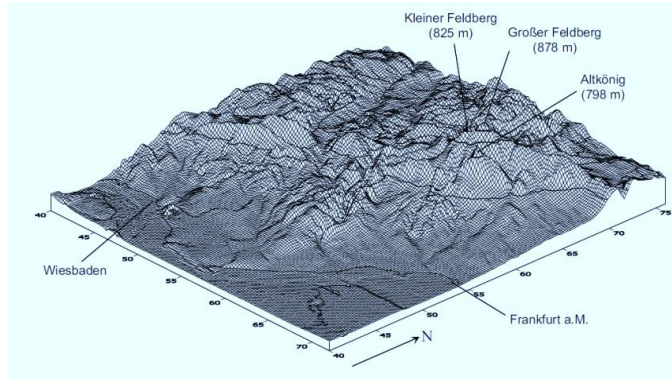


Fig. 3.1: Orography of the Taunus region
[adapted from (Handisides, 2001)]

The temperature during PARADE varied within the range of 5 - 28 °C with an overall average of 14.8°C. The temperature conditions during PARADE can be separated into two phases. The periods of DOY = 226 - 237 and DOY = 243 - 246) for PARADE were slightly warmer and the temperature mostly stayed above 15 °C, whereas in the other periods of DOY = 238 - 242 and DOY = 248 - 252 the temperature was below 15°C. The relative humidity (RH) had an overall average value of 77 % and variations within the interval of [37, 100] %. There were several episodes of rain during PARADE. In the later part of the campaign, consistent fog was persisted in the early morning hours. An overview of several measured meteorological parameters is presented in Fig. 3.2.

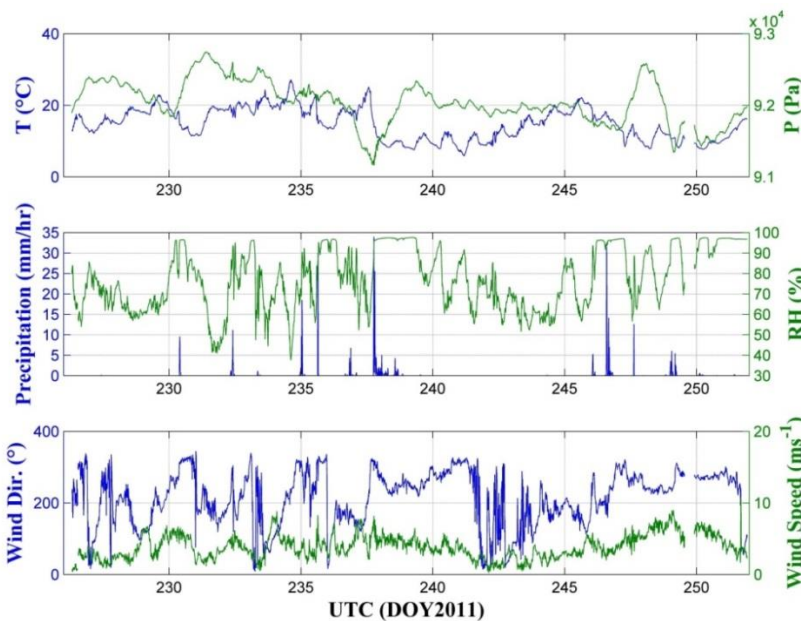


Fig. 3.2: Time series of some meteorological parameters during PARADE-2011.

The dominant air mass at the observatory arrived from the southwest (SW) to the northwest (NW) side of Kleiner Feldberg. Based on HYSPLIT (Hybrid Single-Particle Lagrangian Integrated Trajectory) (Draxler and Hess, 1998) back trajectories for 48h, the air mass originated from five different sectors (Phillips et al., 2012; Thieser, 2013). In the initial period of PARADE (15 - 26 August), its origin was from the south to west wind sectors over the Continental region, with some contributions from the Mediterranean Sea, whereas during the period of 29 - 31 August, contributions from the UK were dominant. In the last phase of PARADE (5 - 10 September), its origin was westerly coming from Atlantic. Fig. 3.3 shows wind rose frequency distributions measured at the observatory over a Google map view. The shaded area in Fig. 3.3 shows an expected high anthropogenic influence.

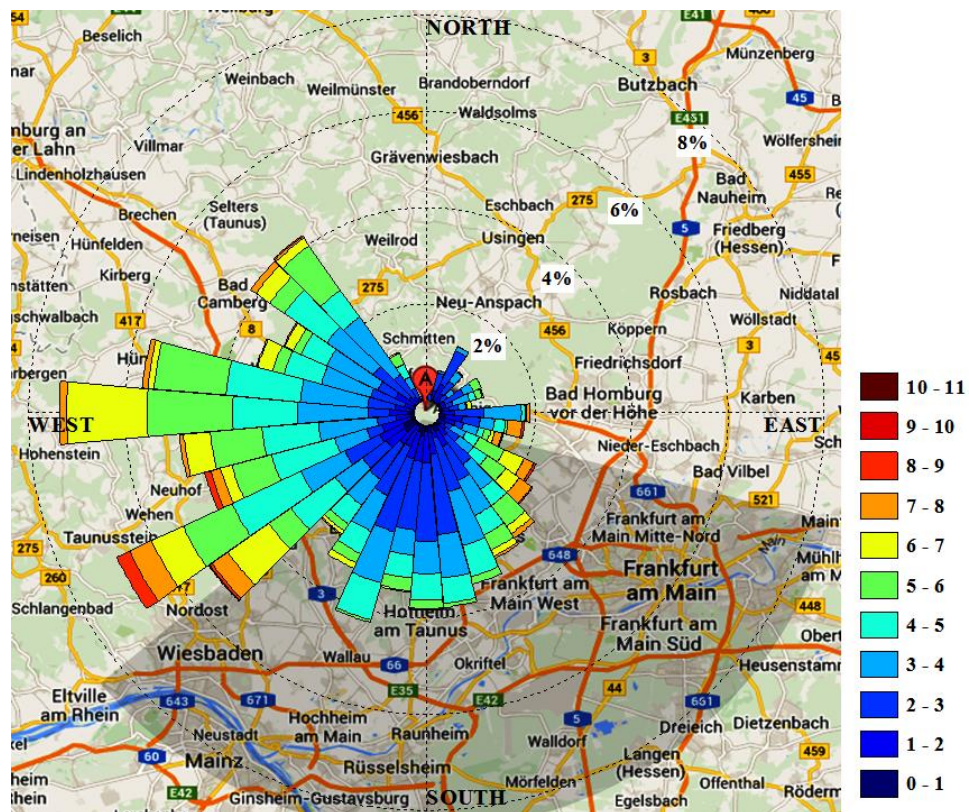


Fig. 3.3: Frequency distributions of wind directions with wind speed (colour-coded: wind speed in ms^{-1}). [Google Map view⁴⁰].

⁴⁰ www.google.com/maps/

Table 3.1: Land use within a radius of 50 km.

Land use	50 km radius %	NW %	NE %	SW %	SE %
URBAN FABRIC (continuous)	0.10	0.01	0.02	0.12	0.24
URBAN FABRIC (discontinuous)	10.91	6.33	9.41	10.15	17.76
INDUSTRIAL & COMERCIAL UNITS	1.78	0.36	0.86	1.58	4.35
ROAD AND RAIL NETWORKS	0.12	0.04	0.07	0.05	0.32
PORT AREAS	0.06	-	-	0.09	0.13
AIRPORTS	0.30	-	-	0.18	1.03
MINERAL EXTRACTION SITES	0.23	0.32	0.18	0.11	0.31
DUMP SITES	0.09	0.04	0.02	0.22	0.09
CONSTRUCTION SITES	0.01	-	-	-	0.04
GREEN URBAN AREAS	0.41	0.01	0.16	0.35	1.13
SPORT FACILITES	0.54	0.17	0.23	0.40	1.34
NON IRRIGATED ARABLE LAND	32.52	29.56	40.33	31.37	28.80
VINEYARDS	2.35	-	-	9.36	0.03
FRUIT TREES & BERRY PLANTATIONS	1.06	-	1.03	2.35	0.87
PASTURES	7.91	14.90	9.18	3.01	4.54
COMPLEX CULTIVATION PATTERNS	4.40	4.95	4.36	4.44	3.85
AGRICULTURE AND NATURAL VEG.	1.34	2.01	1.19	1.52	0.66
BROAD-LEAVED FOREST	19.77	26.94	19.91	20.07	12.14
CONIFEROUS FOREST	5.46	2.56	4.30	3.70	11.30
MIXED FOREST	9.38	11.57	8.24	8.06	9.64
NATURAL GRASSLANDS	0.31	0.05	0.24	0.53	0.41
TRANSITIONAL WOODLAND-SHRUB	0.18	0.15	0.08	0.30	0.18
SPARSELY VEGETATED AREAS	0.01	-	0.04	-	-
INLAND MARSHES	0.04	-	0.02	0.13	-
WATER COURSES	0.59	-	-	1.86	0.49
WATER BODIES	0.15	0.03	0.14	0.08	0.36

Table 3.1 is adapted from the analysis of land uses⁴¹.

⁴¹ Analysis of land uses

Prepared by: Pablo J. Hidalgo (University of Huelva)

Digital cartographic database: Corine Land Cover'2006

(<http://www.eea.europa.eu/publications/COR0-landcover>)

- Corine Land Cover 2006 raster data - version 13 (02/2010)

- 100 meters resolution raster data on land cover for the CLC2006 inventory.

- Data file: g100_06.tif, available at <http://www.eea.europa.eu/data-and-maps/data/corine-land-cover-2006-raster/>

3.1.2 Instrumentation

Sampling lines for most of the trace gas monitoring instruments were located within a 5 m area at the top of the platform (Fig. 3.4). The height of the platform was about 8 m above ground and the top of platform was above the forest canopy. A brief overview of the instrumentation during PARADE and their uncertainties with detection limits is presented in Table 3.2. Note that all data sets for analysis are based on available 10 minute averages.



Fig. 3.4: The platform location at the Taunus Observatory on Kleiner Feldberg

Table 3.2: An overview of instrumental methods deployed during PARADE.

Parameters	Instrument/Technique	Limit of detection	Uncertainties of measurements	Operator
O ₃	UV Photometric An.	1 ppb _v	4 ppb _v ; 1.6 %	MPIC ^I
NO	CLD	4 ppt _v / 2s	21 ppt _v ; 4 %	MPIC
CO	RT-QCLS	3 ppb _v / 1 s	5 %	MPIC
CO ₂	NDIR Abs.		1.5 ppm _v	UM ^{II}
H ₂ O ₂	AL2021	32.9 ppt _v / 3 s	14.2 %	MPIC
HCHO		25.4 ppt _v / 3 s	14.3 %	
NO ₂	See! Table 3.3			
PAN	Iodide CIMS	-	20 % + 2 ppt _v	MPIC
PAA			20 % + 2 ppt _v	
ClNO ₂			25 % + 2 ppt _v	
NO ₃	CRDS	2 - 3 ppt _v	20 % + 2 ppt _v	MPIC
N ₂ O ₅		5 - 6 ppt _v	15 % + 2 ppt _v	
ANs	TD-CRDS	> 50 ppt _v	5 - 6 %	MPIC

3.1 Overview

PANs		> 50 ppt _v	5 - 6 %	
OH, HO ₂	LIF	$4 \times 10^5 \text{ cm}^{-3}$, 0.2 ppt _v	Accu.= 30 %, 30 % Prec.= 30 %, 5 %	MPIC
RO _x = Σ (RO ₂) + HO ₂	PeRCA	1 - 3 ppt _v	50 %	IUP-UB ^{III}
OH reactivity	CRM/PTR-MS	4 s ⁻¹	20 %	MPIC
BVOCs	TD-GC-MS	10 ppt _v	20 - 30 %	MPIC
NMHC(C ₂ - C ₁₂)	GC-FID	-	-	MPIC
Methanol, toluene	PTR-TOF-MS	0.24 ppb _v , 13 ppt _v	5 - 7 %	UW ^{IV}
H ₂ SO ₄	CIMS	$4 \times 10^4 \text{ cm}^{-3}$	-	GUF ^V
Aerosol size distribution	FMPS, APS	-	-	MPIC
Photolysis rates	CCD spectrometer	-	> 10 %	FZ Jülich ^{VI}
HONO	LOPAP	7 ppt _v	10 %	FZ Jülich
Particle size dist.	Nano-SMPS	-	-	GUF
NO ₂ , NO ₃ , O ₃ , SO ₂ , HCHO, HONO	LPDOAS	-	2 %, 2 %, 2 %, 0.1 %, 5 %, 5 %	IUP-HD ^{VII}
Meteo.	-	-	-	GUF, DWD ^{VIII} , HLUG ^{IX}

^I MAX-PLANCK-INSTITUT FÜR CHEMIE

(Department of Air Chemistry, Particle Chemistry, Satellite Research Group and Biogeochemistry)

^{II} JOHANNES GUTENBERG UNIVERSITÄT Mainz (Atmospheric Physics Department)

^{III} UNIVERSITÄT Bremen (Institute of Environmental Physics)

^{IV} BERGISCHE UNIVERSITÄT Wuppertal (Atmospheric Physics Group)

^V GOETHE UNIVERSITÄT Frankfurt (Institute for Atmospheric and Environmental Sciences)

^{VI} FORSCHUNGSZENTRUM Jülich (Institut for Atmospheric Chemistry, Institute for Energy and Climate Research)

^{VII} RUPRECHT-KARLS-UNIVERSITÄT Heidelberg (Institute of Environmental Physics)

^{VIII} Deutscher Wetterdienst

^{IX} Hessisches Landesamt für Umwelt und Geologie

3.1.3 Time series PARADE-2011

Time series of selected atmospheric trace gases measurements and photolysis frequencies during PARADE are shown in [Fig. 3.5](#). The photolysis frequency of NO₂ ($j\text{NO}_2$) was measured using a CCD-array (charge-coupled device) actinic spectroradiometer above the canopy; the details about the instrument and operating principle are described elsewhere ([Bohn et al., 2008](#)). The local time at the location was UTC (Coordinated Universal Time) + 2.

High values of $j\text{NO}_2$ up to 0.01 s^{-1} were observed around 11:00 UTC. The overall median concentration of NO_x (NO + NO₂) was 2.1 ppb_v with variations in the range of [0.44, 21] ppb_v. NO was measured by using a chemoluminescence detector (CLD) at the top of the platform. This method is a direct technique for NO measurements and is based on chemiluminescent gas phase reaction of NO and O₃ to yield excited NO₂ ([Fontijn et al., 1970](#)); the emitted photons from the chemiluminescent reaction are proportional to the ambient levels of NO. The instrument setup for NO was similar to the one described by ([Hosaynali Beygi et al., 2011](#)). NO was higher corresponding to daytime from 4:00 to 19:00 UTC with a maximum concentration of about 5 ppb_v. The median concentration of NO over the entire period during daytime and night time was $0.2 \pm 0.5 (1\sigma)$ ppb_v and $4 \pm 5 (1\sigma)$ ppt_v, respectively. NO₂ was measured with several different techniques ([Table 3.3](#)). Based on the measurements of GANDALF ([Chapter 1](#)) the median concentration of NO₂ for the entire period of PARADE was $2.0 \pm 2.1 (1\sigma)$ ppb_v with minimum and maximum concentrations of 0.41 ppb_v and 20.8 ppb_v, respectively. Higher concentrations of NO₂ were observed during rush hours in the morning and evening times ([Fig. 3.5](#)).

The concentrations of O₃ varied from]9, 90[ppb_v, with an overall median value of 41.3 ppb_v. O₃ was measured based on the UV absorption method with an O₃ analyser (Thermo-Electron, model 49C, USA), that shared the sampling line with the CLD instrument. O₃ concentrations have shown a dip on several occasions with high NO and NO₂ concentrations. This dip can be related to fresh NO emissions at roads close by the observatory. An increase in O₃ was observed under sunny conditions due to photochemical production on several days during the initial part of the campaign. The daily profile of O₃ shows maximum concentrations at afternoon to evening times for the entire period. During night time a decreasing trend was observed in O₃ for PARADE.

CO was measured by using a quantum cascade laser based spectrometer in the mid-infrared (about 2190 cm^{-1}). A description of the instrument can be found in ([Li et al.,](#)

2012). The concentration of CO varied from [71, 180] ppb_v with a median value of 99 ppb_v for the entire period of PARADE. In general, there was a co-existence between the elevated levels of NO_x and CO. This is appeared to be related with a transport of wind from regions with higher concentrations of pollutants.

The biogenic volatile organic compounds (BVOCs) were measured above the canopy by using a Thermal Desorber Gas Chromatograph Mass Spectrometer (TD-GC-MS) and the setup for the instrument was similar to the one described previously for a different location (Song et al., 2011). Measured Σ BVOCs⁴² showed a pronounced diurnal cycle with maximum value of about half a ppb_v at 16:00 UTC. The overall median value of Σ BVOCs concentrations was 137 ppt_v with a standard deviation of 76 ppt_v. Also a set of BVOCs concentrations was measured close to the forest edge within a dynamical plant cuvette (Bourtsoukidis et al., 2012). The concentrations derived from the cuvette measurement are roughly a factor about 10 higher than the concentrations measured at the top of platform (about 60 m away in the open) with TD-GC-MS instrument. A clear decline in levels of BVOCs at the platform is present compared to inside the cuvette and this decline is mainly related to the dilution.

The measurements of total RO_x (HO₂ + RO₂) were also available throughout the intensive period of the campaign. The measurements of RO_x are based on the PeRCA (Peroxy Radical Chemical Amplification) technique. The technique is an indirect method for the detection of RO_x. In the PeRCA instrument, RO_x is chemically converted into NO₂ in a chain reaction and subsequently the resultant NO₂ is detected (Andrés-Hernández et al., 2001). The uncertainty of RO_x measurements were high (overall 50 % level reported) due to potential malfunction in the PeRCA instrument. The RO_x data is averaged over 10 min. intervals by using a Savitzky-Golay filter (Savitzky and Golay, 1964). RO_x averages showed a positive trend with temperature but no trend with the measured BVOCs. The median value of the RO_x concentrations for the entire period was 8 ± 6 (1 σ) ppt_v with a maximum value of 39 ppt_v.

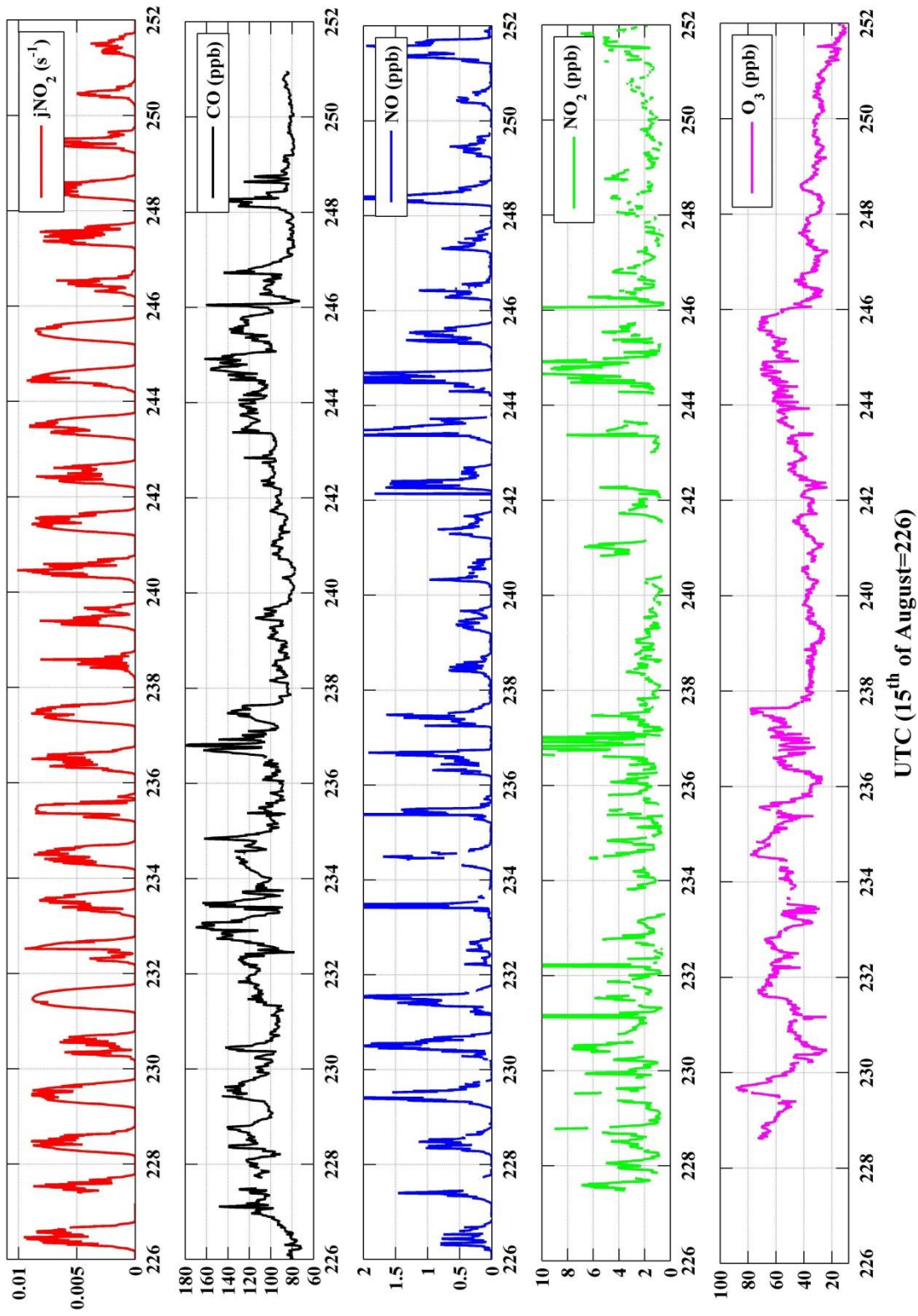
The total OH loss rate (OH reactivity) was also measured using a Comparative Reactivity Method (Nölscher et al., 2012) above the forest canopy. The observed OH reactivity reached up to the value of about 7.7 s⁻¹ with an overall median value of 1.28 s⁻¹ for the entire period. For most of the period of PARADE, the total OH reactivity was low and the measurements were under the detection limit (4 s⁻¹) of the instrument.

⁴² Σ (Isoprene+ α -pinene+myrcene+limonene)

In the later period of PARADE, OH (beginning on DOY = 242) and HO₂ (beginning on DOY = 246) radicals were measured with a LIF instrument above the canopy using a setup similar to the one as described for HUMPPA ([Hens et al., 2013](#)). The median observed concentrations of OH and HO₂ were $9 \pm 3.1 (1\sigma) \times 10^5$ molecule cm⁻³ and $3 \pm 1.53 (1\sigma)$ ppt_v, respectively for the measurement period. A correlation between OH and the photolysis frequency of O₃ (jO¹D) was used to estimate OH concentrations for the entire duration of PARADE. This correlation is described by an empirical power-law function as (Eq. 3.1) ([Rohrer and Berresheim, 2006](#)).

$$[\text{OH}] = a \times (jO^1D)^b + c \quad \text{Eq. 3.1}$$

Where coefficients ‘*a*’, ‘*b*’, and ‘*c*’ describe the average influence of ‘reactants’, ‘light dependent’ and ‘light independent’ processes on OH. A least squares fit (appendix 7.3.1.3) of the function for the measured OH (in molecule cm⁻³) versus jO¹D / 10⁻⁵ (s⁻¹) yields ‘*a*’ (slope) = $5.18 \pm 0.2 (1\sigma) \times 10^5$ and ‘*b*’ = $0.88 \pm 0.07 (1\sigma)$. The parameters are obtained by neglecting night time data of measured OH [*@* jO¹D > 1 × 10⁻⁷ s⁻¹] and the parameter ‘*c*’, in order of -10⁴ molecule cm⁻³, can be neglected compared to the atmospheric OH concentrations (in order of 10⁵ - 10⁶ molecule cm⁻³). The calculated concentrations of OH for PARADE vary over the range of [0.008, 1.3] × 10⁶ molecule cm⁻³. The relative uncertainty (100 %) of the calculated OH based on the function (Eq. 3.1) is estimated from 1σ residuals of the fit. A linear correlation between jO¹D and HO₂ was observed for PARADE and it is used to estimate HO₂ for the total period of the campaign. Based on filtered data for jO¹D > 1 × 10⁻⁷ s⁻¹ (neglecting night data), the correlation between the measured HO₂ (in ppt_v) and jO¹D / 10⁻⁵ (s⁻¹) yields a slope of $2.3 \pm 0.3 (1\sigma)$ with an offset of $2.1 \pm 0.2 (1\sigma)$ ppt_v (appendix 7.3.1.3). The offset corresponds to a non-photolytic source e.g. ozonolysis of alkenes involved in the production of HO₂. The calculated HO₂ has a median value of $3.5 \pm 1.7 (1\sigma)$ ppt_v for the entire period. The relative uncertainty of the calculated HO₂ is < 45 % and is also assessed with 1σ residuals of the fit.



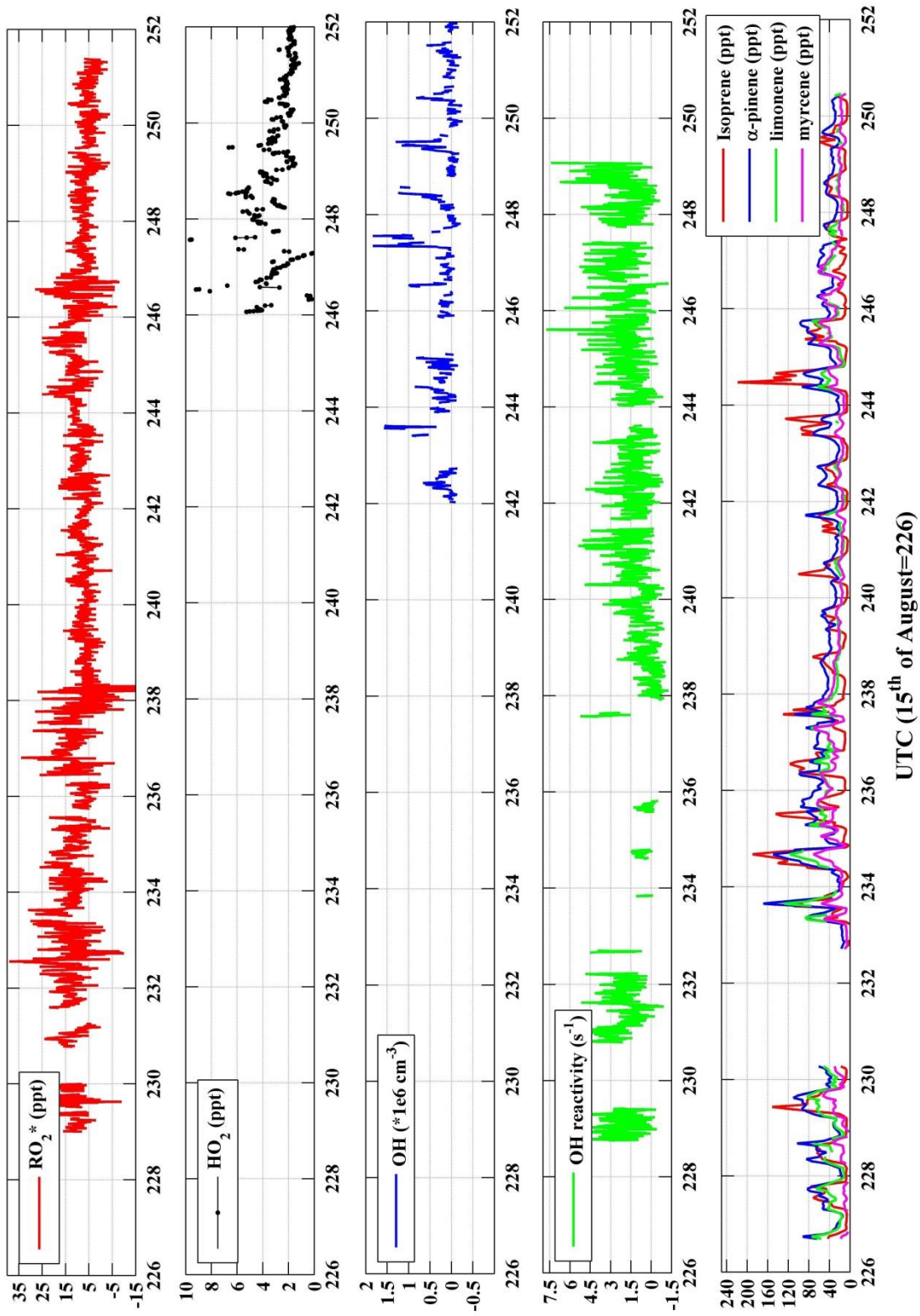


Fig. 3.5: Time series of some relevant atmospheric species during PARADE-2011

3.2 Measurement setup of GANDALF

GANDALF was deployed outside at the platform on top of a container (Fig. 3.4). The flow in the sampling line was 12000 ± 120 sccm. A flow of 4100 ± 41 sccm was required for the detection axis, while the excess flow was diverted to an exhaust line by using a second pump. The sampling flow rate provided a residence time of less than 0.1 s in a 0.1 m sampling line. This was sufficient to suppress the impact of heterogeneous or thermal conversion of PAN, peroxyacetic acid (HO_2NO_2), methyl peroxy nitrate ($\text{CH}_3\text{O}_2\text{NO}_2$) and N_2O_5 to yield NO_2 . The formation of NO_2 in the sampling line was negligible due to the faster reaction between ambient NO and O_3 . The campaign averages of the observed concentrations of NO , O_3 and NO_2 were 0.25 ppb_v, 44 ppb_v and 2.6 ppb_v respectively. Based on average NO and O_3 concentrations, the formation of NO_2 from the reaction ‘ $\text{NO} + \text{O}_3$ ’ in the sampling line was less than 0.01 % with respect to the ambient NO_2 concentrations. Line loss or photolysis of NO_2 was avoided by using PTFE lines (Polytetrafluoroethylene) covered with a black heat-shrink material.

The average pressure inside the detection cell for the entire period of PARADE was 6.95 ± 0.27 (1σ) hPa. Several automated calibrations (2 - 10 per day) and background level measurements (once per hour) were conducted during PARADE to ensure the precision and accuracy of the instrument. Based on the hourly background level measurements, we established that the deviations for 70 % successive background level measurements (no. of measurements > 500) were less than an absolute value of 8 ppt_v of NO_2 . An overall picture of a general setup is presented in Fig. 2.18. A malfunction of the O_3 generator had occurred within the period of 4 to 9 September that disturbed the GANDALF calibration system. A correction of 12 % is introduced for the period of 4 to 9 September, based on the correlation of GANDALF with CRDS prior to 4 September. During the last few days from 4 to 9 September, an extra baffle (7.2.1.2, C) was also installed in GANDALF. The baffle can be inserted easily into the detection block of GANDALF without disturbing the alignment of the laser. The advantage of the baffle is that it reduces the background counts by ~50 % while decreasing sensitivity by less than 5 %.

3.2.1 PARADE NO₂ comparison

NO₂ concentrations were measured with eight different instruments. Two instruments (HLUG and MoLa) were located at ground while six instruments were sampling at the top of the platform. The measurement techniques, uncertainties, time resolutions and LOD are summarised in Table 3.3 for the instruments located on the platform (Fig. 3.4). The average ambient concentrations of NO₂ during PARADE were approx. 2 - 3 ppb_v with a range of approx. 400 ppt_v to 20 ppb_v. NO₂ instruments listed in Table 3.3 represent *in-situ* measurement techniques with the exception the LP-DOAS (Long Path Differential Optical Absorption Spectroscopy), which is detailed below.

LP-DOAS: This instrument is based on traditional Differential Optical Absorption Spectroscopy (DOAS) (Platt et al., 1979;Perner and Platt, 1979). DOAS follows the Beer-Lambert law of absorption to determine total amounts of the atmospheric trace gases (Platt and Stutz, 2008). DOAS allows direct and absolute measurements of multiple trace gases in the atmosphere by using the distinct absorption band structure of the specific molecule. LP-DOAS is based on active remote sensing and requires an artificial light source (Chan et al., 2012). It provides an average concentration of NO₂ or other trace gases through quantitative detection using the absorption over a light path of typically a few kilometres.

CE-DOAS: Cavity-Enhanced DOAS (Platt et al., 2009) measurements of NO₂ were also available during PARADE. This method is based on absorption spectroscopy in a cavity and provides *in-situ* measurements of trace gases (Platt et al., 2009). CE-DOAS requires calibration to quantify the Rayleigh scattering and losses of the cavity.

CRDS: Besides the DOAS instruments, another NO₂ measurement technique using a Cavity Ring-Down Spectrometer (CRDS) was available. CRDS is a cavity-assisted method like CE-DOAS (Platt et al., 2009). It is a direct method for *in-situ* measurements and requires calibration of the Rayleigh scattering and losses of the cavity like in the case of CE-DOAS. In CRDS, reflective mirrors are used across an optical cavity. To obtain the concentration of a trace gas with CRDS, absorption measurements to determine the time constant for exponential decay of the light intensity with and without an absorber are made in an optical cavity (Brown et al., 2001;Schuster et al., 2009;Paul and Osthoff, 2010;Thieser, 2013). The major uncertainty of the above-mentioned methods is due to the error in the absorption cross-section of NO₂.

CLD/Blue-light converter: Along with the absolute methods, the concentrations of NO₂ were determined with a two-channel chemoluminescence detector (CLD). The CLD

instrument of MPIC (Table 3.3) is a modified version (Hosaynali Beygi et al., 2011) of the ECO-Physics CLD 790 SR. CLD is an indirect method of *in-situ* NO₂ measurement. In this technique, NO₂ is detected by conversion via photolysis to NO [$\text{NO}_2 + h\nu (< 420 \text{ nm}) \rightarrow \text{NO}$] with subsequent detection of NO by chemoluminescence.

LIF: This is a direct method for the detection of NO₂ based on laser induced fluorescence. The description of LIF has already been provided in chapter 1.

Table 3.3: NO₂ instruments during PARADE-2011

(located or sampling at the top of platform)

Measurements (Operator)	Technique	Uncertainty of measurements	Limit of detection	Time resolution
GANDALF (MPIC)	Laser-Induced Fluorescence	5 % (1σ) + 11 ppt _v	5 - 10 ppt _v 1 min ⁻¹ (SNR:2)	1 s
CLD (MPIC)	Two-channel Chemoluminescence Detector	105 ppt _v ; 10 %	55 ppt _v 2 s ⁻¹ (1σ)	2 s
CRDS (MPIC)	Cavity Ring-Down Spectrometer	5 - 6 %; 20 ppt _v	50 ppt _v 4s ⁻¹ (2σ)	4 s
CE-DOAS (IUP-HD)	Cavity-Enhanced DOAS	5 - 10 %	300 ppt _v	30 s
LP-DOAS (IUP-HD)	Long Path DOAS	2 %	-	-
CLD (IUP-UB)	Chemoluminescence Detector	Data is not available.		

A median value of the atmospheric NO₂ concentration is derived from the NO₂ measurements of all individual instruments at the platform. For a valid correlation between the derived median NO₂ and individual NO₂ measurements, only those values of the derived median NO₂ were selected when simultaneous data for all NO₂ measurements were available. Fig. 3.6 shows plots of the correlation between individual NO₂ measurements and the derived median NO₂ concentrations. The uncertainty of individual instruments is shown as error bars on the

y-axis while horizontal error bars represents the standard deviation of the derived median NO₂. The regression is done by using a ‘bivariate’ fit according to the method as described in (York et al., 2004; Cantrell, 2008). The York method accounts for the uncertainties in both dimensions (x-axis and y-axis).

The correlation between **GANDALF** and the derived median NO₂ is $R^2 = 0.99$ [panel **B** of Fig. 3.6]. The measurements of GANDALF show an over-estimation of 3 % compared to the derived median values of NO₂. This overestimation from the derived median value is insignificant as it is within the range of the instrument uncertainties. The relative uncertainty of GANDALF is about 5 % and it follows an exponential trend versus the absolute NO₂ concentrations. The slope and offset of fit are 1.03 and 0.027 ppb_v with the absolute error of fit being 0.006 and 0.01 ppb_v, respectively.

The correlation ($R^2 = 0.99$) between **CLD** and the derived median NO₂ values is shown in panel **C** of Fig. 3.6. Overall, the data of the CLD is about 5 % below the median, but this difference is within the uncertainty of the CLD measurement. The reported uncertainty of the CLD for the NO₂ measurements is the larger of 105 ppt_v or 10 %. The slope and offset are 0.95 and -0.1 ppb_v, respectively.

The slope and offset in case of **CRDS** are 1.06 and 0.01 ppb_v with correlation $R^2 = 0.99$ as shown in the panel **D** of Fig. 3.6. The reported upper limit of uncertainty in case of CRDS is larger of 6 % or 20 ppt_v. The differences between CRDS and the derived median NO₂ values are below the limitation of instrument errors in this case as well.

LP-DOAS and **CE-DOAS** instruments showed correlations with the derived median NO₂ values with $R^2 = 0.96$ and $R^2 = 1$ ([E] and [F] Fig. 3.6), respectively. In the case of LP-DOAS, the slope is 1.02 with a negligible offset of -0.002 ppb_v. The slope and offset for CE-DOAS is 0.92 and -0.032 ppb_v, respectively. In the case of both DOAS instruments, the differences from the derived median NO₂ values are well within the measurement uncertainties (Table 3.3).

Generally all instruments for NO₂ showed reasonable agreement with the derived median NO₂. GANDALF (+ 3 %), CRDS (+ 6 %) and LP-DOAS (+ 2 %) showed over-estimation compared to the derived median values while CLD was about -5 % and CE-DOAS about -8 % below the median values. The overall differences are within the range of instrument uncertainties.

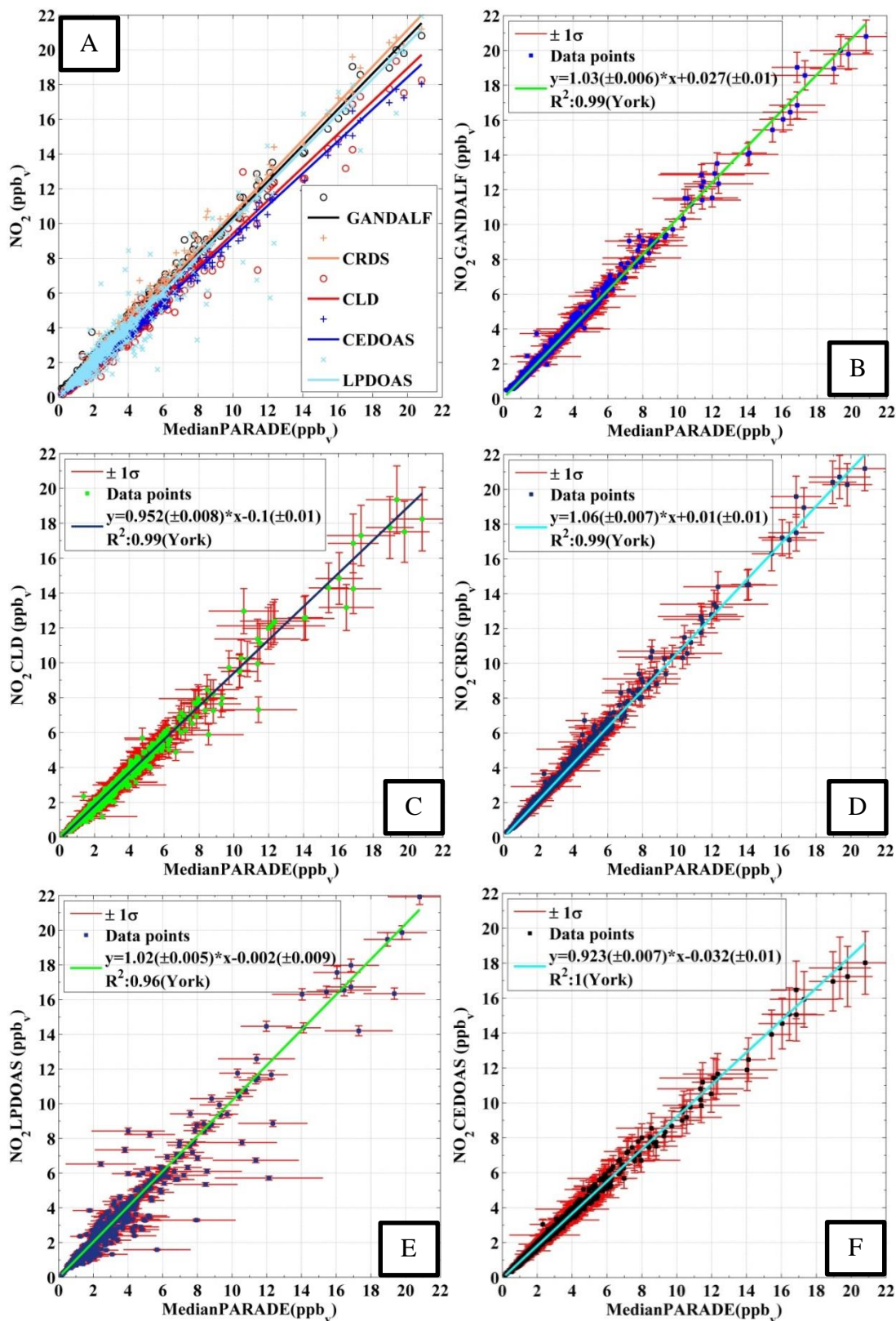


Fig. 3.6: Correlation plots (Overall [A], GANDALF [B], CLD [C], CRDS [D], LPDOAS [E], CE-DOAS [F]) of individual NO_2 measurement versus the derived median values of all NO_2 measurement at platform during PARADE.

3.2.2 NO₂ measurement ratios distribution

Different measurements of trace gases, meteorological parameters, and photolysis frequencies (Table 3.2) during PARADE provided an opportunity to look for any indication of a systematic difference between NO₂ instruments. The inlets of the *in-situ* NO₂ instruments (Table 3.3) were located within a radius of 5 m at the top of platform. Ratios of the individual NO₂ measurements and GANDALF are calculated and compared in respect of different atmospheric parameters, which are referred to as ratios further in this section. The distribution of ratios is shown as a histogram in the upper panel of Fig. 3.7 [A1, A2, A3, and A4]. The histograms show the distribution of ratios with their respective normal distribution fits. The ‘normal probability plot’ for empirical probability versus ratios is shown in the lower panel of Fig. 3.7 [B1, B2, B3, and B4]. This plot is interpreted as a graphical representation of the normal distribution of ratios. The plot stays linear as long as the distributions are normal, and the deviation from the linear fit shows the departure of ratios from normal distribution. The solid line in the lower panel of Fig. 3.7 is between the 25th and 75th interquartile range of a ratio. The gap between probabilities (y-grid lines) is not linear and it is representative of the distance between quantiles of normal distribution.

The average, median, and standard deviation (STD) values of ratios comparing GANDALF with other instruments are given in Table 3.4. The variation in these ratios (CRDS/GANDALF, CE-DOAS/GANDALF, and CLD/GANDALF) is small compared to the one in case of LP-DOAS/GANDALF. This is expected as the LP-DOAS is not an *in-situ* technique and instead determines an average concentration over the light path. The average and median values of ratios are similar in all cases. The ratios CRDS / GANDALF and LP-DOAS/GANDALF are close to unity, whereas in the case of CE-DOAS/GANDALF and CLD/GANDALF, it deviates from unity by 0.15. All ratios generally show a normal distribution Fig. 3.7 [A1, A2, A3, and A4] but the skewness in LP-DOAS / GANDALF (A1 in Fig. 3.7) on both sides of the average value is larger than other cases (A2, A3, and A4 in Fig. 3.7).

Table 3.4: Overall average, median and standard deviation values of ratios with respect to GANDALF and other NO₂ measurements during PARADE.

Ratio	Average	Median	STD (1σ)
LP-DOAS/GANDALF	0.96	0.97	0.19
CRDS/GANDALF	1.01	1.01	0.06
CE-DOAS/GANDALF	0.86	0.86	0.07
CLD/GANDALF	0.85	0.84	0.09

In the lower panel of Fig. 3.7 [B1, B2, B3, and B4], the probabilities show a deviation from normality and a tail on top (towards right) and bottom (towards left) sides can be observed. Tail is an indicator of outliers caused for example by the non-normality of the precision at low values, background level, and potential interferences of NO₂ instruments. Panels ([B1, B2, B3 and B4] of Fig. 3.7) show that a major fraction of the ratios is normally distributed, as it can be observed from the 25th to 75th interquartile range of probability in all cases. The percentile of probability towards normality is slightly greater (about 10th to 90th percentile) in case of CLD/GANDALF compared to others. The percentile is about 15th to 80th and 25th to 90th with (CRD/GANDALF, CE-DOAS/GANDALF) and (LP-DOAS/GANDALF), respectively. A perfect normal distribution should not be expected for ratios as NO₂ instruments are not measuring exactly the same quantity due to differences in length of sampling lines and potential interference.

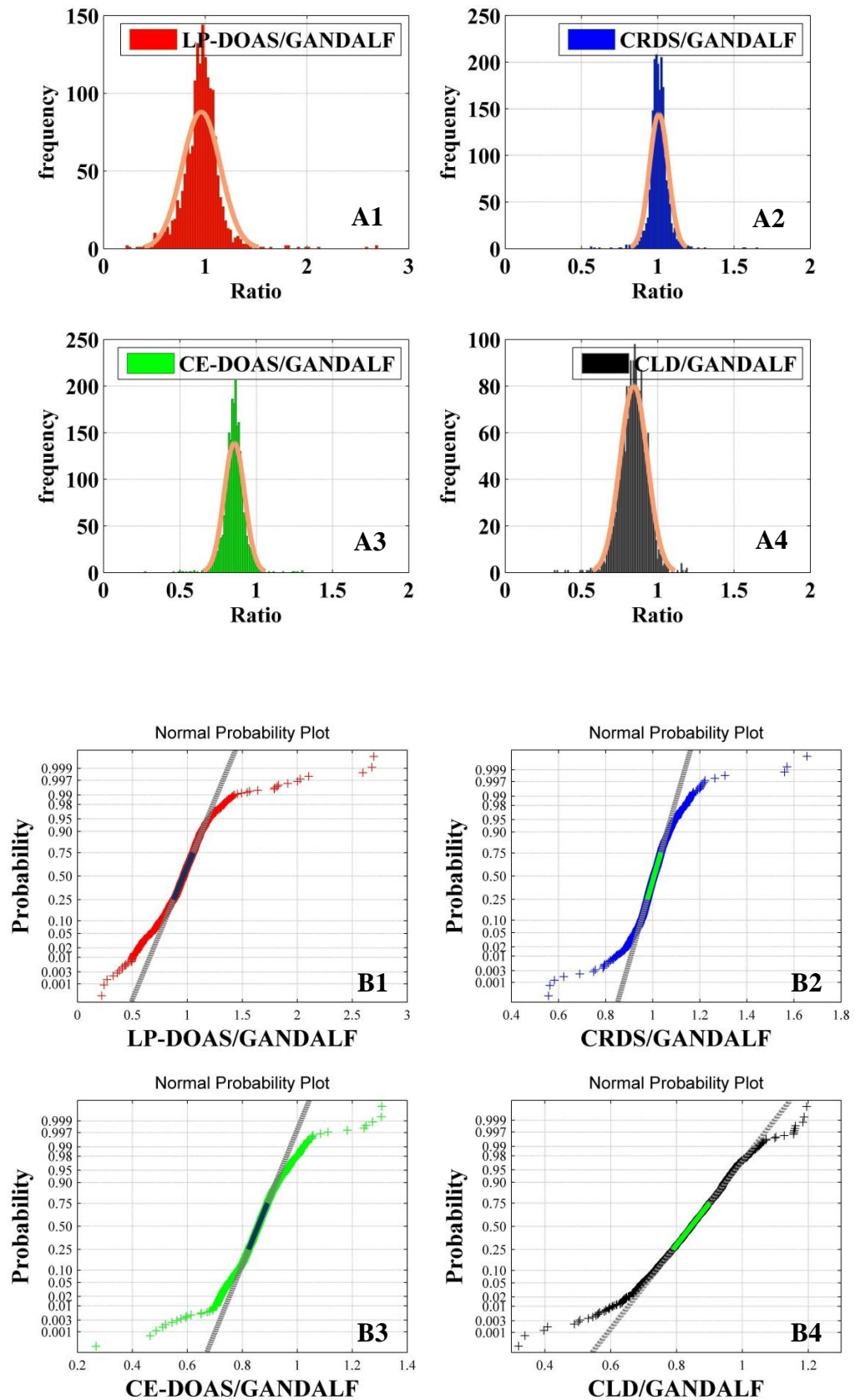


Fig. 3.7: Distribution for comparative instrument ratios is shown in upper panels and a normal probability plot for comparative instrument ratios is shown in lower panels.

To identify systematic deviations based on other trace gases or parameters, ratios are further compared with the observed data of several trace gases, radiation, and metrological parameters. There are only two cases, where a systematic correlation of ratios was observed with the observed quantities during PARADE, as shown in Fig. 3.8 and Fig. 3.9. In **Case 1**, ratios are presented as a function of the observed O_3 concentrations. The ratio between CLD and GANDALF shows a decreasing trend with respect to increase in the O_3 concentrations (subplot C4, Fig. 3.8). This ratio (CLD/GANDALF) averages 0.95 at levels less than 20 ppb_v O_3 . It decreases to an average of 0.86 over the interval of 20 to 42 ppb_v O_3 , while averaging 0.81 at levels above 42 ppb_v of O_3 . There is no trend observed in other ratios (CRDS/GANDALF, LP-DOAS/GANDALF, and CE-DOAS/GANDALF) as shown in Fig. 3.8. The trend for CLD/GANDALF might be attributed to some line loss of NO_2 with respect to the increase in ambient O_3 in the CLD data set. The subplot (C4, Fig. 3.8) is also cross checked by altering the GANDALF data in the denominator to the other three measurements (LP-DOAS, CRDS, and CE-DOAS) and similar results are observed as in the previous case with GANDALF.

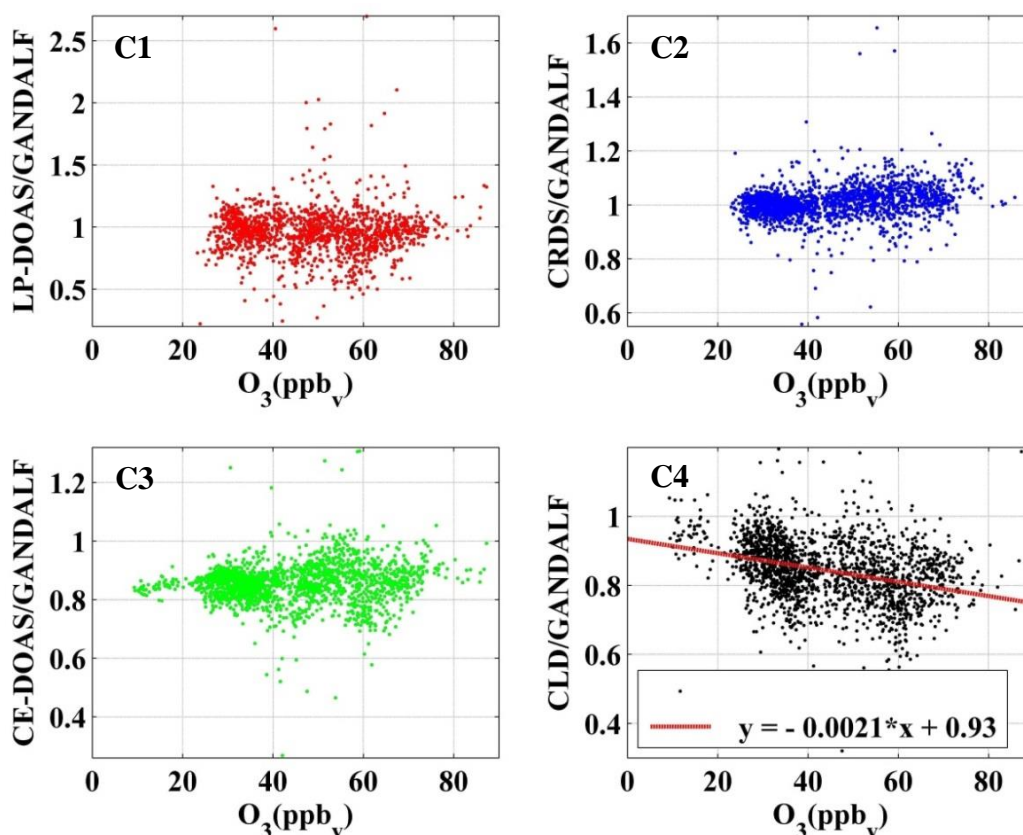


Fig. 3.8: Ratios as a function of the ambient O_3 during PARADE.

In **Case 2** (subplot **D3**, Fig. 3.9), a correlation is observed for the ratio between CE-DOAS/GANDALF as a function of $j\text{NO}_2$. At higher values of $j\text{NO}_2$, the ratio approaches unity. The sampling line for CE-DOAS and CRDS was the same and no correlation for the ratio between CRDS and GANDALF is seen with respect to $j\text{NO}_2$. So, the cause of correlation is not expected to be due to the accumulation of NO_2 in the sampling line of CE-DOAS. The correlation might be related to background level corrections for the Rayleigh scattering in CE-DOAS or potential interference due to some species other than NO_2 in the sampling line at high levels of solar radiation. This correlation is also not observed between other ratios (in case of LP-DOAS and CLD) with respect to GANDALF. Also, a cross check was done for panel D3 (Fig. 3.9) by switching GANDALF in the denominator to three other measurements (LP-DOAS, CRDS, and CLD); similar results were observed as previously. Besides the above-described systematic correlations, no indication of a potential interference is observed for any instrument (appendix 7.3.1.4).

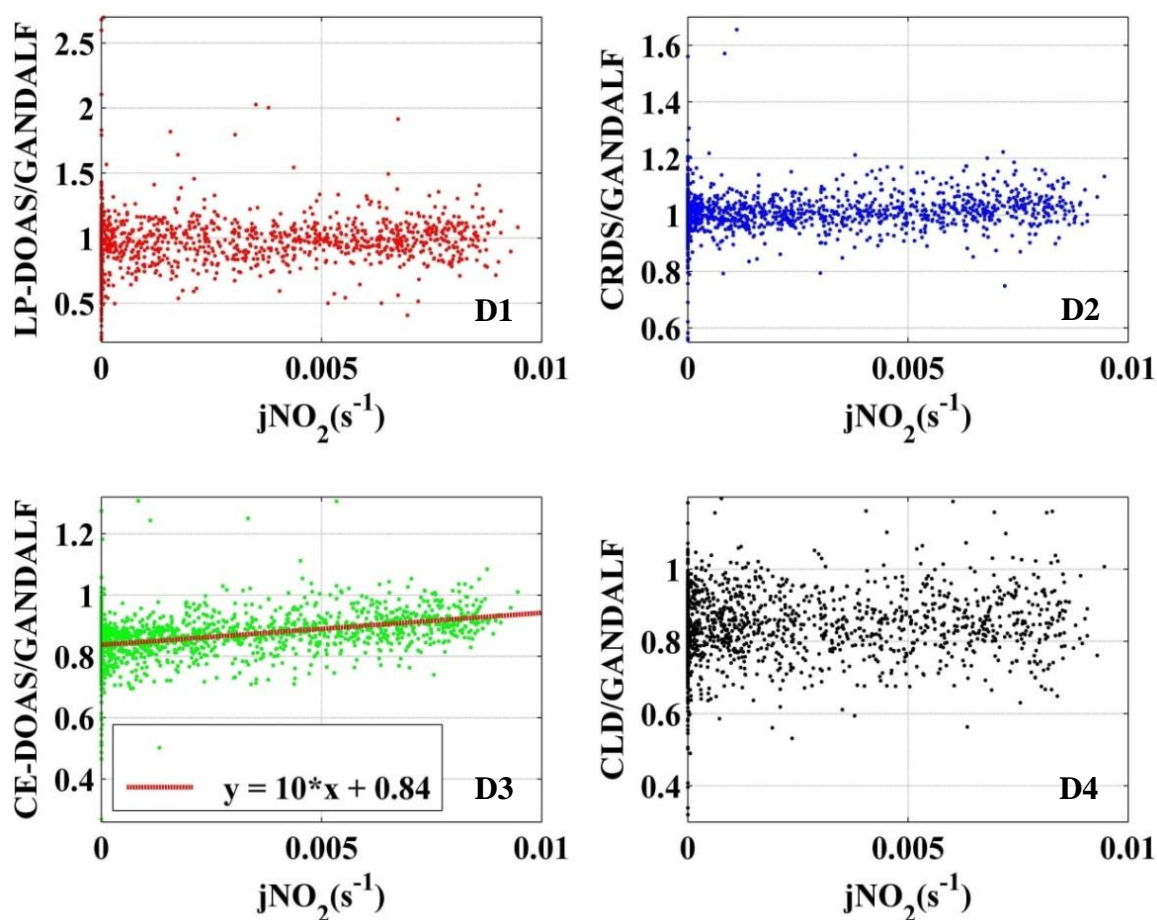


Fig. 3.9: Ratios as a function of the measured $j\text{NO}_2$ during PARADE.

3.3 Ozone photochemistry in PARADE

The role of O₃ is crucial in defining the tropospheric oxidation capacity as it leads to the atmospheric oxidants OH (R. 1.16 followed by R. 1.19) and NO₃ (R. 1.9). The *in-situ* instantaneous O₃ production is a complex function of proportioning between NO_x, HO_x, and RO_x = (HO₂ + RO₂). RO_x radicals are formed by the reaction of VOCs and OH. The reaction between NO and RO_x is responsible for the formation of O₃ via NO₂ photolysis in the troposphere. A null cycle exists between NO-NO₂-O₃ in the absence of competing reactions and under the steady-state conditions (Section 1.2), which leads to no net O₃ production or loss. The null cycle is perturbed by the presence of peroxy radicals. This chemical imbalance of the perturbed null cycle can also be used to estimate the instantaneous net photochemical production rates of O₃ (Eq. 1.10) (Thornton et al., 2002; Volz-Thomas et al., 2003; Martinez et al., 2003). However, this concept is only valid under the photostationary state condition (Section 1.2). The main source for the formation of O₃ is come from VOCs and NO_x act as a catalyst. The instantaneous O₃ production has a positive tendency with an increase in NO_x concentrations under VOC-saturated conditions. The VOC-saturated or NO_x-sensitive regime is referenced to conditions when the loss of odd hydrogen radicals due to ‘radical + radical’ reactions (‘OH + HO₂’, ‘HO₂ + HO₂’, ‘RO₂ + HO₂’) forming peroxides is dominant (Sillman, 1999) compared to ‘radicals+ NO_x’ reactions forming HNO₃ and ANs (R. 1.7 and R. 1.14). While under VOC-limited or NO_x-saturated conditions, the loss of odd hydrogen radicals is mainly controlled by ‘radicals + NO_x’ reactions. A negative trend of the instantaneous O₃ production versus NO_x is expected in the NO_x-saturated or VOC-limited regimes (Thornton et al., 2002).

The O₃ photochemistry is assessed for PARADE by considering several reactions that contribute to the *in-situ* production and loss of O₃. To exclude night time data, a photolysis frequency filter ($jO^1D > 1 \times 10^{-7} s^{-1}$) has been applied. Further, to avoid periods with heavy fog and condensation, only data with specific conditions (visibility > 1 km, relative humidity < 90 % and precipitation = 0 mm hr⁻¹) are selected. A positive trend is reported between O₃ and temperature at several places with biogenic emissions (Duenas et al., 2002; Rasmussen et al., 2012). A positive correlation between the locally measured temperature and O₃ is also observed during PARADE (appendix 7.3.1.5). At elevated temperatures (> 13 °C), higher values of O₃ were observed and the reverse for temperatures ≤ 13 °C. Based on this separation by temperature, the data set for O₃ photochemical production or loss rates was further divided into two different regimes [low (≤ 13 °C) and

high (> 13 °C)] to provide a more detailed analysis. Rate coefficients for O₃ reactions are taken from the literature ([Finlayson-Pitts and Pitts, 2000](#); [Atkinson et al., 2004, 2006](#); [Sander et al., 2011b](#)). Based on filtered data, the available time window for the O₃ budget analysis is from 5:00 UTC to 18:00 UTC.

O₃ is formed in the troposphere via NO₂ photolysis. So any loss of NO₂ other than through photolysis will also contribute in the reduction of O₃ production efficiency under NO_x-limited conditions. The loss processes involving radicals such as formation of nitric acid, ANs, and peroxides lead to the loss of NO₂ and ultimately decrease the O₃ production efficiency. The formation of nitric acid, ANs, and peroxides are referred to here as the indirect loss of O₃. PAN is assumed to be in steady state and it does not lead to a source or sink for radicals ([Spirig et al., 2002](#); [Kleinman, 2005](#)), therefore the production and decomposition of PAN is not considered.

The measurement of total ANs was available during PARADE ([Table 3.2](#)) and in the absence of information regarding separate fractions of ANs, the correlation between ANs and O_x (O₃ + NO₂) can be used to derive the effective branching ratio α_{eff} ([Rosen et al., 2004](#); [Perring et al., 2010](#); [Farmer et al., 2011](#)). According to correlation between ANs and O_x, the effective branching ratio for [R. 1.14](#) can be defined as in [Eq. 3.2](#).

$$\alpha_{\text{eff}} = \frac{2}{\Delta[\text{O}_x] / \Delta[\text{ANs}]} \quad \text{Eq. 3.2}$$

In relation [Eq. 3.2](#), $\Delta[\text{O}_x] / \Delta[\text{ANs}]$ is estimated from slope of correlation between O_x and ANs. For PARADE, α_{eff} varied in the range of [2.2, 4.7] % with an average value of 3.37 ± 0.75 % ([Thieser, 2013](#)). In the reaction (' $\alpha \text{RO}_2 + \text{NO}$ ', [R. 1.14](#)), the average value of α_{eff} is used for the calculation of ANs production. The average value of α_{eff} is based on composite mixture of all VOCs including CO ([Browne and Cohen, 2012](#)) because the measured O_x concentration contains contributions from both HO₂ and RO₂ radicals. Therefore α_{eff} would be smaller than the actual branching ratio for RO₂ species ([Browne and Cohen, 2012](#)).

The photochemical O₃ tendency [T(O₃) = P(O₃) - L(O₃)] is a measure of the net O₃ production due to its production and loss processes ([Crutzen et al., 1999](#)). The O₃ tendency is positive during PARADE for the daytime periods. The net O₃ production described here is the production of O₃ due to peroxy radicals and the direct loss of O₃. RO_x measurement of the PerCA instrument contains the sum of RO₂ and HO₂. Based on reactions ' $\text{RO}_x (\text{PerCA}) + \text{NO}$ ',

the median value of the production rate of O₃ is $[15 \pm 31 (1\sigma)] \times 10^6$ molecule cm⁻³ s⁻¹. A generic rate coefficient (Jenkin et al., 1997;Saunders et al., 2003) is used for the reaction 'RO_x (PeRCA) + NO'. There is no significant difference [Median ratio = $k_{(\text{HO}_2+\text{NO})} / k_{\text{generic}} = 0.98 \pm 0.004 (1\sigma)$] between the generic rate constant and the 'HO₂ + NO' rate constant, so the separation based on $[\text{RO}_2 = \text{RO}_x(\text{PeRCA}) - \text{HO}_2(\text{calculated})]$ does not contribute considerably to the above-described median value of the O₃ production. The variability of the O₃ production is larger due to the scatter in the observed RO_x concentration. The standard error ($1\sigma / \sqrt{n}$) of the O₃ production is $\pm 1.2 \times 10^6$ molecule cm⁻³ s⁻¹. Based on hourly median values of the O₃ production, the maximum value of 37×10^6 molecule cm⁻³ s⁻¹ is calculated to occur at about 12:00 UTC for elevated temperatures.

The *in-situ* O₃ loss rates are described previously in Eq. 1.11. This assumption only represents the major *in-situ* photochemical loss in remote regions. Other reactions also contribute to an O₃ loss like reaction with alkenes in the boundary layer. Several different alkenes were measured during PARADE. Here, alkenes are divided into two different groups for the calculation of the direct O₃ loss. **1**) those emitted by the vegetation are called as BVOCs⁴³ and **2**) the remaining alkenes like NMHC⁴⁴. Besides alkenes, O₃ reactions with aromatics (benzene and toluene) are also considered for the total or fractional loss calculations of O₃. The overall loss of O₃ for PARADE is described in Eq. 3.3.

$$L(\text{O}_3) \approx [\text{O}_3] (\beta \times j\text{O}^1\text{D}) + k_{\text{OH}+\text{O}_3} [\text{OH}] + k_{\text{HO}_2+\text{O}_3} [\text{HO}_2] + k_{\text{BVOCs}+\text{O}_3} [\text{BVOCs}] \\ + k_{\text{NMHC}+\text{O}_3} [\text{NMHC}] + k_{\text{arom}+\text{O}_3} [\text{aromatics}]$$

Eq. 3.3

Where β in Eq. 3.3 is the fraction of O(¹D) reacting with H₂O to produce OH. Reactions leading to photolysable species such as NO₂ and NO₃ are not considered a loss during daytime due to the rapid photolysis and reformation of O₃, as discussed previously (Section 1.1.1.1). The O₃ photochemical loss in Eq. 3.3 is based on measured data, while in case of OH and HO₂ on calculated data. The total loss (Eq. 3.3) of O₃ versus daytime fraction is shown in the subplot [A] of Fig. 3.10. The overall median value of the total O₃ loss is $2.2 \pm 1.5 (1\sigma) \times 10^6$ molecule cm³ s⁻¹ and the standard error is $\pm 0.08 \times 10^6$ molecule cm⁻³ s⁻¹. The O₃ loss increases up to 7×10^6 molecule cm⁻³ s⁻¹ and 2×10^6 molecule cm⁻³ s⁻¹ for the

⁴³ isoprene, α -pinene, myrcene, limonene

⁴⁴ ethene, propene, 1,3-butadiene, cis-2-butene, 1-pentene.

time window of 12:00 UTC to 14:00 UTC with temperature $> 13\text{ }^{\circ}\text{C}$ and $\leq 13\text{ }^{\circ}\text{C}$, respectively. The absolute chemical loss rates of O_3 due to different reactants as a daytime fraction and hourly median values are shown in Fig. 3.10 for two different temperature conditions. Hourly median values of relative fractional contribution to the O_3 loss are also shown in Fig. 3.11 for different reactants.

Photolysis of O_3 described with β is the largest loss during the middle of day, being up to $5 \times 10^6 \text{ molecule cm}^{-3} \text{ s}^{-1}$. β (Eq. 1.12) has varied in the range of [3.5, 13.2] % with average and median values of 8 % and 7 %, respectively. The absolute median value (Fig. 3.10) of the O_3 photolysis loss is $[1 \pm 1.12 (1\sigma)] \times 10^6 \text{ molecule cm}^{-3} \text{ s}^{-1}$ for temperatures higher than $13\text{ }^{\circ}\text{C}$ and $[0.26 \pm 0.3 (1\sigma)] \times 10^6 \text{ molecule cm}^{-3} \text{ s}^{-1}$ at lower temperatures $\leq 13\text{ }^{\circ}\text{C}$. The relative fraction of the photolytic loss of O_3 to total loss is up to 60 % (at temperatures $> 13\text{ }^{\circ}\text{C}$) around 12:00 UTC (Fig. 3.11). This fractional loss of O_3 decreases to $< 30\%$ at morning and evening times. In comparison, the relative fraction of the photolytic O_3 loss in the case of the temperatures $\leq 13\text{ }^{\circ}\text{C}$ has shown similar trend but slightly less compared to the one in the case for temperatures greater than $13\text{ }^{\circ}\text{C}$.

The loss of O_3 with respect to HO_x ($\text{OH} + \text{HO}_2$) is also highest in the middle of the day. The maximum values [up to $0.8 \times 10^6 \text{ molecule cm}^{-3} \text{ s}^{-1}$] are observed around 12:00 UTC. The median value of the O_3 loss due to HO_x is $[0.27 \pm 0.15 (1\sigma)] \times 10^6 \text{ molecule cm}^{-3} \text{ s}^{-1}$ and $[0.13 \pm 0.08 (1\sigma)] \times 10^6 \text{ molecule cm}^{-3} \text{ s}^{-1}$ at elevated ($> 13\text{ }^{\circ}\text{C}$) and lower temperatures ($\leq 13\text{ }^{\circ}\text{C}$), respectively. The O_3 loss due to the reaction with OH is much lower than the reaction with HO_2 . The ratio $[(\text{O}_3 \text{ loss due to OH}) / (\text{O}_3 \text{ loss due to HO}_2)]$ varies in the range of]0.006, 0.25[for PARADE. The fractional variations in the O_3 loss due to HO_x mainly stay in the interval of]7, 13[% and]11, 18[% at higher and lower temperatures, respectively.

The O_3 loss due to overall measured BVOCs is comparable to the one observed in the case of O_3 photolysis but not occurring at the same time. The highest loss due to BVOCs was at 16:00 UTC [up to $2.7 \times 10^6 \text{ molecule cm}^{-3} \text{ s}^{-1}$]. Higher concentrations of myrcene and limonene were observed in morning times during PARADE. So the prominent high loss of O_3 due to BVOCs is present in the morning period of the time around 7:00 UTC [up to $1.6 \times 10^6 \text{ molecule cm}^{-3} \text{ s}^{-1}$]. The median value of the O_3 loss due to BVOCs is $[1 \pm 0.5 (1\sigma)] \times 10^6 \text{ molecule cm}^{-3} \text{ s}^{-1}$ and $[0.33 \pm 0.08 (1\sigma)] \times 10^6 \text{ molecule cm}^{-3} \text{ s}^{-1}$ at higher and lower temperatures, respectively. Amongst the observed BVOCs, the highest loss of O_3 is due to myrcene [up to $0.12 \times 10^6 \text{ molecule cm}^{-3} \text{ s}^{-1}$] while the smallest is due to isoprene

[maximum up to 0.08×10^6 molecule $\text{cm}^{-3} \text{s}^{-1}$]. The lowest relative fractional loss due to BVOCs (about 20 %) is present around 12:00 UTC and it increases up to 55 % and 70 % during morning and evening times for higher temperatures, respectively. The relative fraction of O_3 loss due to BVOCs stays higher at high temperatures and vice versa.

The highest loss of O_3 due to NMHC is present during morning hours (some outliers) and evening times. Over all, an increasing tendency in the O_3 loss due to NMHC is observed with respect to daytime at higher temperatures, while a negative trend is observed for lower temperatures. The median value of O_3 loss due to BVOCs is $[0.33 \pm 0.12 (1\sigma)] \times 10^6$ molecule $\text{cm}^{-3} \text{s}^{-1}$ and $[0.2 \pm 0.04 (1\sigma)] \times 10^6$ molecule $\text{cm}^{-3} \text{s}^{-1}$ at higher and lower temperatures, respectively. The relative fraction of this loss is higher during morning times; for both temperature regimes, it stays in the range of]35, 40[%. It decreases in the range of]5, 13[% at 12:00 UTC and increases again to]22, 25[% at evening times. Despite outliers due to propene, 1-pentene remains the largest contributor among NMHC, while ethene is the smallest contributor to the loss of O_3 .

The relative fractions of the O_3 loss due to aromatics (benzene and toluene) are $\ll 1$ % and negligible compared to others. Therefore absolute or fractional losses of O_3 due to aromatics are not shown in [Fig. 3.10](#) and [Fig. 3.11](#).

Reaction of alkenes with O_3 is a removal process for them, as are the alkenes beside reactions between OH and alkenes. Although the rate coefficients for ' $\text{O}_3 + \text{alkenes}$ ' reactions are very small in magnitude compared to the corresponding ' $\text{OH} + \text{alkenes}$ ' reactions, but high tropospheric O_3 concentrations make this removal process important ([Finlayson-Pitts and Pitts, 2000](#)). The removal of BVOCs due to O_3 was higher than the corresponding removal due to OH during PARADE. The BVOCs loss due to O_3 varies in the range of $[0.12, 0.92] \times 10^6$ molecule $\text{cm}^{-3} \text{s}^{-1}$ with a median value of $0.82 \pm 0.54 (1\sigma) \times 10^6$ molecule $\text{cm}^{-3} \text{s}^{-1}$. The corresponding loss due to OH has a median value of $[0.22 \pm 0.24 (1\sigma)] \times 10^6$ molecule $\text{cm}^{-3} \text{s}^{-1}$ with a variation in the range of $[0.002, 1.01] \times 10^6$ molecule $\text{cm}^{-3} \text{s}^{-1}$. In the case of NMHC however, the loss with respect to OH is larger compared to the corresponding loss with respect to O_3 . The median value of the NMHC loss due to reaction with OH is $[0.5 \pm 0.4 (1\sigma)] \times 10^6$ molecule $\text{cm}^{-3} \text{s}^{-1}$ with variations of $[0.007, 1.77] \times 10^6$ molecule $\text{cm}^{-3} \text{s}^{-1}$. In the case of reaction with O_3 , the median value of NMHC loss is $[0.30 \pm 0.12 (1\sigma)] \times 10^6$ molecule $\text{cm}^{-3} \text{s}^{-1}$ with small variations of $[0.12, 0.92] \times 10^6$ molecule $\text{cm}^{-3} \text{s}^{-1}$ compared to OH ([appendix 7.3.1.6](#)).

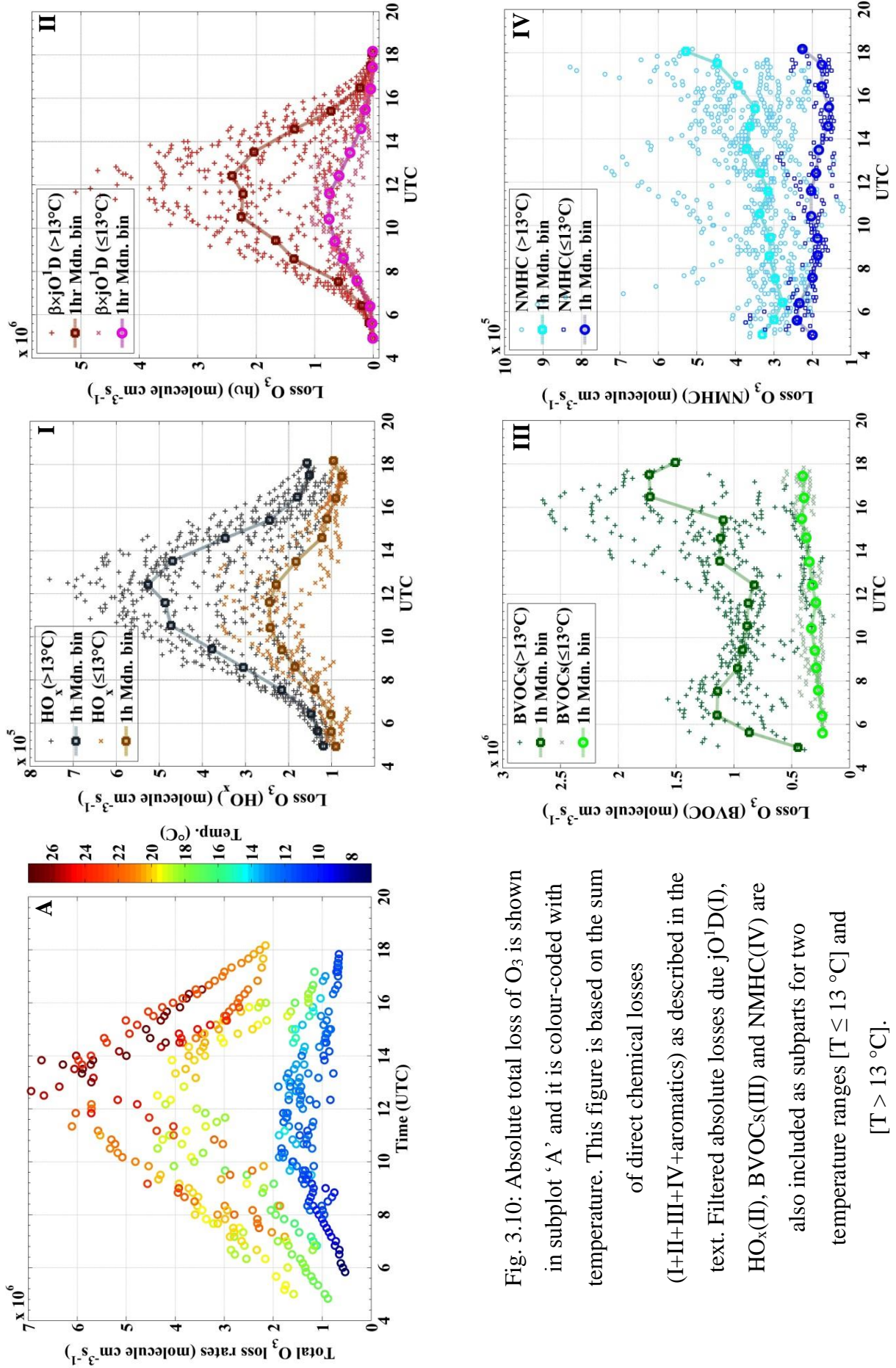


Fig. 3.10: Absolute total loss of O₃ is shown in subplot 'A' and it is colour-coded with temperature. This figure is based on the sum of direct chemical losses (I+II+III+IV+aromatics) as described in the text. Filtered absolute losses due to jO¹D(I), HO_x(II), BVOCs(III) and NMHC(IV) are also included as subparts for two temperature ranges [T ≤ 13 °C] and [T > 13 °C].

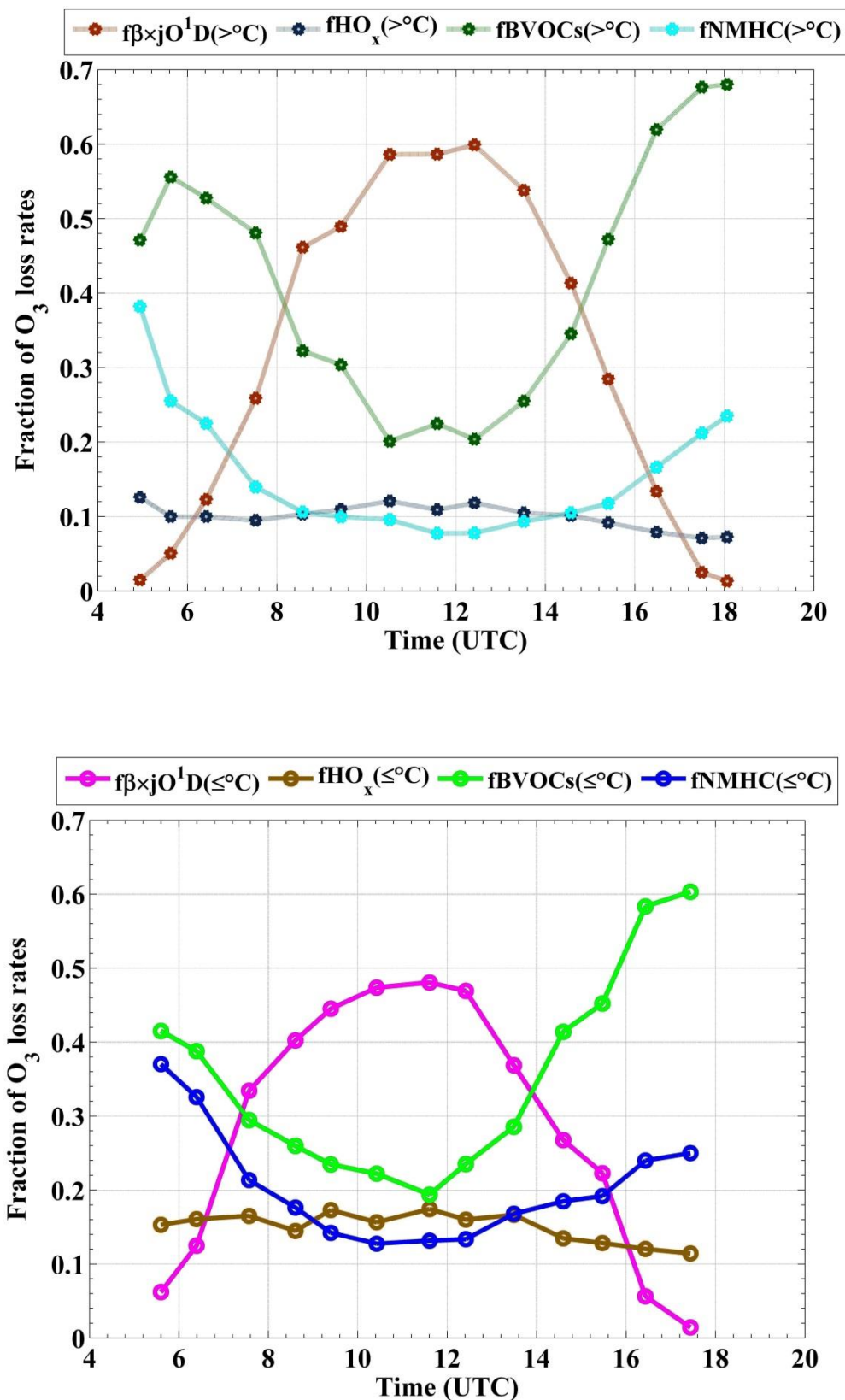


Fig. 3.11: Fractional contribution to total loss of O₃ with several groups of measured species as described in the text for T > 13 °C and T ≤ 13 °C in the upper and lower panels, respectively.

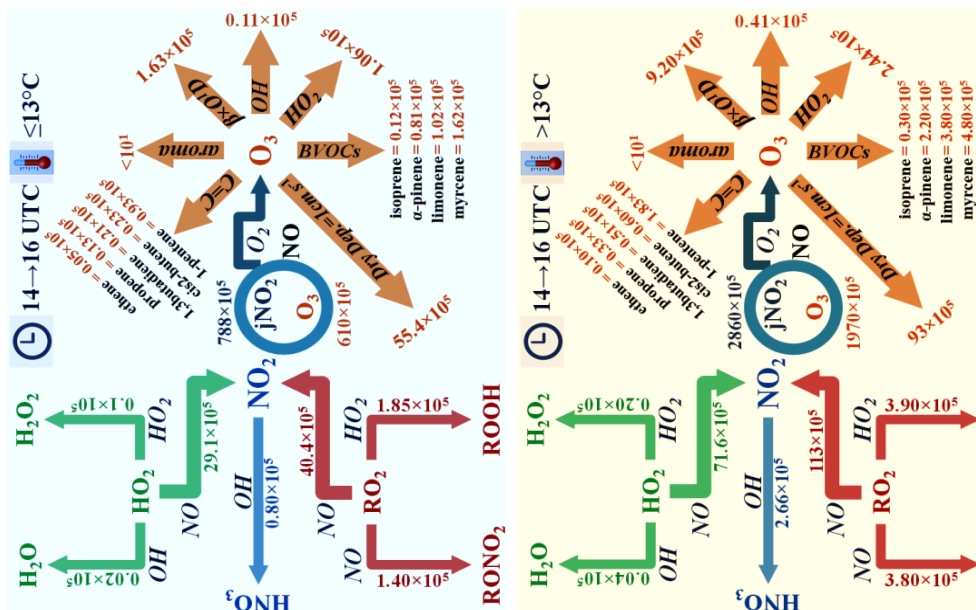
For the contribution of different species to production and loss of O₃, three different time windows of daytime fraction were selected as follows. (1):- [8:00, 10:00] UTC, (2):- [10:00, 14:00] UTC, (3):- [14:00, 16:00] UTC. Overall median values of production and loss rates of O₃ for PARADE during the different time windows, in two different temperature regimes, are shown in Fig. 3.12. The O₃ tendency is positive for the different selected time windows regardless of the temperature filter. The maximum net O₃ production rate (21.7×10^6 molecule cm⁻³s⁻¹) is calculated for time window (2) at higher temperature. This is due to higher radiation and eventually higher OH leading to the higher production of peroxy radicals. The lowest net O₃ production rate (0.62×10^6 molecule cm⁻³ s⁻¹) is found in the time window (3) at lower temperatures.

The production of HNO₃ is similar to the production of ANs in time windows (1) and (2) at lower temperatures. The loss of NO_x to HNO₃ is higher than the corresponding loss to ANs at higher temperatures for time windows (1) and especially (2). But the loss of NO_x to HNO₃ becomes smaller than the corresponding loss to ANs for time window (3) regardless of temperature. This indicates that the role of ANs as a sink for NO_x is important and could not be neglected, as suggested in a previous study ([Browne and Cohen, 2012](#)).

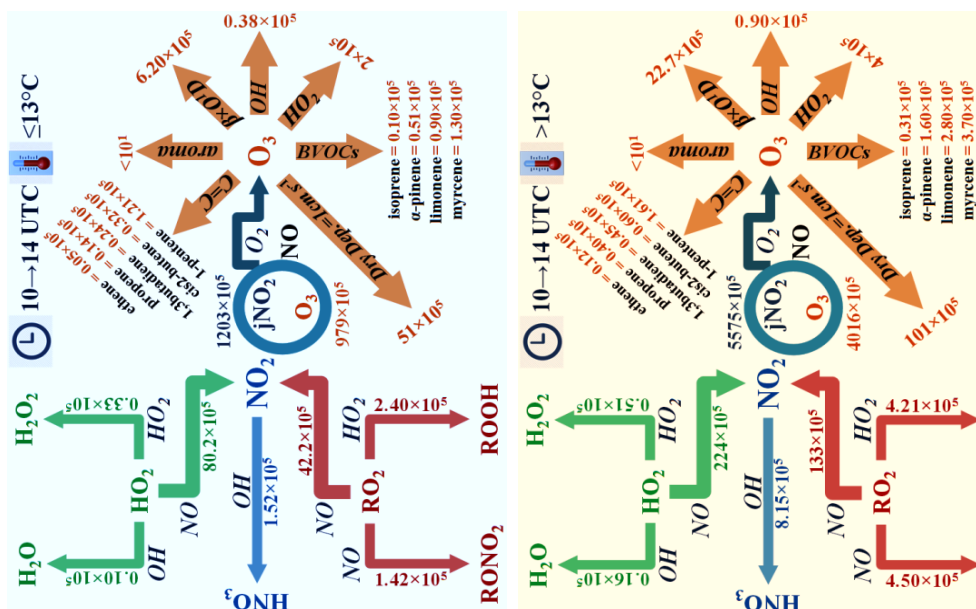
The reaction of 'HO₂ + RO₂' shows dominance over other 'radical + radical' reactions at all times. In addition, rates in [Fig. 3.12](#) for 'radical + radical' reactions are not multiplied by 2. Two radicals are lost in each 'radical + radical' reaction, so the numbers should be considered as (2 × Rates), but only for 'radical + radical' reactions ('HO₂ + OH', 'HO₂ + HO₂' and 'HO₂ + RO₂').

The O₃ loss due to dry deposition is dominant over chemical loss in PARADE during daytime and it is calculated based on the characterisation of the boundary layer height (BLH) by radiosonde (type: GRAW DFM - 06) measurements on several days at different time scales. The median values of O₃ loss rates due to dry deposition are also shown in [Fig. 3.12](#) for different time windows by considering a deposition velocity of 1 cm s⁻¹ for O₃ ([Droppo, 1985](#); [Finlayson-Pitts and Pitts, 2000](#)) based on median values of BLH.

-3-



-2-



-1-

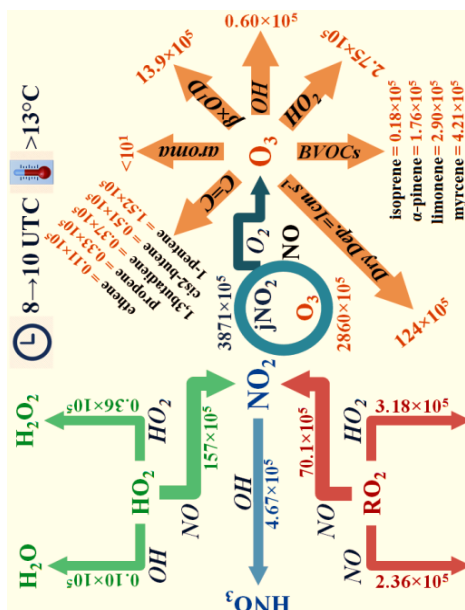
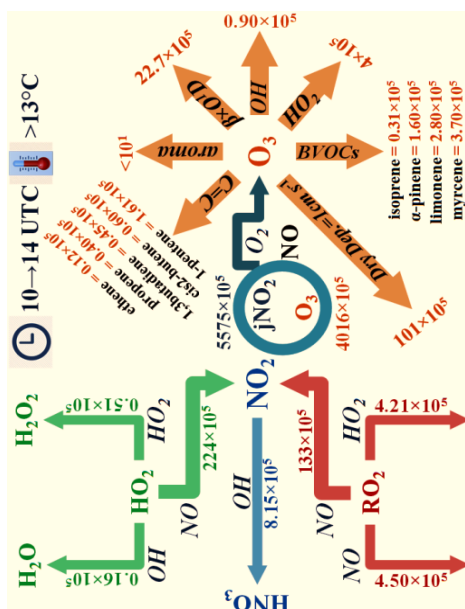
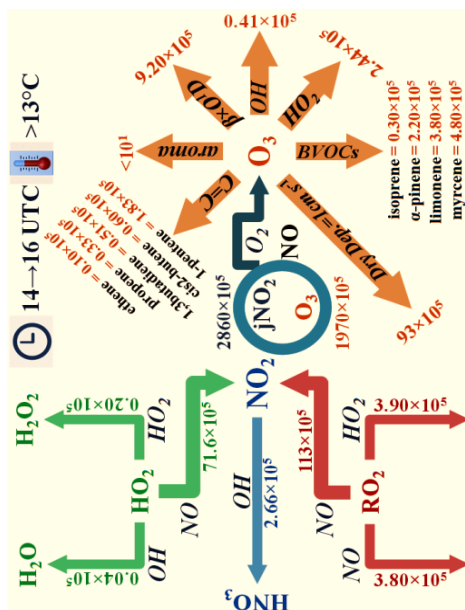
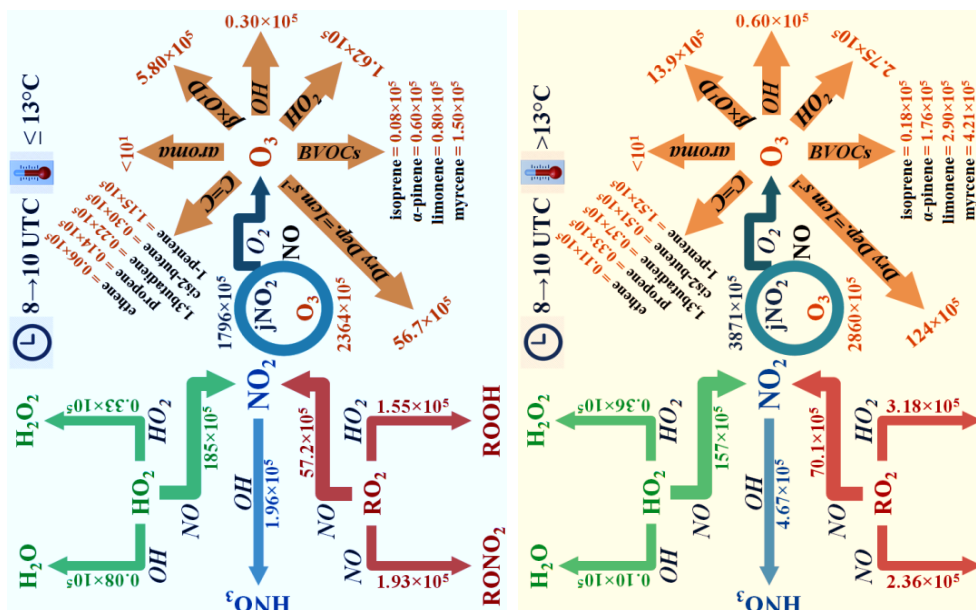


Fig. 3.12: Median values of different indirect and direct loss rates of O₃ in molecule cm⁻³s⁻¹ for three different time windows [8, 10], [10, 14] and [14, 16] UTC and two different temperature ranges (13°C > T ≤ 13°C).

The calculated lifetime of O₃ during PARADE with respect to reaction with different species is summarised in (Table 3.5, Table 3.6 and Table 3.7) for different periods of time of the day. The shortest O₃ lifetime was due to photolysis at middle of day [10:00, 14:00] UTC and at the higher temperature ranges, while it decreases within the morning and afternoon time windows and also with the decrease in temperature. The longest O₃ lifetimes were with respect to aromatics like toluene and benzene. The O₃ lifetimes due to BVOCs (except isoprene) and HO₂ have smaller scales compared to NMHC and OH. The overall photochemical lifetimes of O₃ can be calculated as in $\tau(\text{O}_3)$ (Eq. 3.4).

$$\tau(\text{O}_3) = \frac{1}{k_{\text{X}+\text{O}_3} [\text{X}] + k_{\text{Y}+\text{O}_3} [\text{Y}] + \dots} \quad \text{Eq. 3.4}$$

'X' and 'Y' (Eq. 3.4) represent different species (like; OH, HO₂, alkenes, etc.) with their respective rate coefficients for reaction with O₃. For PARADE, the average and median values of $\tau(\text{O}_3)$ are 7.1 days and 6.6 days, respectively, with variations of]2.6, 18.1[days.

Table 3.5: Lifetimes of O₃ with respect to different species measured at PARADE-2011.

Time window [08:00, 10:00] UTC.

Rate × [conc.] as on Y-axis Fig. 3.10	Lifetime of O ₃ for respective loss (days) @ Temp. > 13 °C					Lifetime of O ₃ for respective loss (days) @ Temp. ≤ 13 °C				
	Avg.	Mdn.	Max.	Min.	STD	Avg.	Mdn.	Max.	Min.	STD
$\beta \times \text{JO}^1\text{D}$	12	9	48	5	7	18	16	39	11	6
$k_{\text{OH}+\text{O}_3}[\text{OH}]$	279	238	974	152	132	334	298	608	196	103
$k_{\text{HO}_2+\text{O}_3}[\text{HO}_2]$	52	48	95	35	12	58	55	81	41	10
$k_{\alpha\text{pin}+\text{O}_3}[\alpha\text{-pin}]$	87	82	199	60	24	181	162	316	93	71
$k_{\text{lm}+\text{O}_3}[\text{limonene}]$	53	51	93	29	14	117	120	151	77	23
$k_{\text{myr}+\text{O}_3}[\text{myrcene}]$	42	35	105	22	17	64	58	99	42	18
$k_{\text{iso}+\text{O}_3}[\text{isoprene}]$	839	720	2277	287	415	1183	1215	1886	727	260
$k_{\text{tol}+\text{O}_3}[\text{toluene}]$	0.5 × 10 ⁷	0.4 × 10 ⁷	1.5 × 10 ⁷	0.1 × 10 ⁷	0.3 × 10 ⁷	1.2 × 10 ⁷	1 × 10 ⁷	3.1 × 10 ⁷	0.2 × 10 ⁷	0.8 × 10 ⁷
$k_{\text{Ben}+\text{O}_3}[\text{benzene}]$	1 × 10 ⁷	0.8 × 10 ⁷	4 × 10 ⁷	0.4 × 10 ⁷	0.6 × 10 ⁷	1.6 × 10 ⁷	1.5 × 10 ⁷	3.7 × 10 ⁷	0.7 × 10 ⁷	0.8 × 10 ⁷
$k_{\text{E}+\text{O}_3}[\text{ethene}]$	1215	1221	2238	532	372	1627	1919	2554	633	668
$k_{1,3\text{BD}+\text{O}_3}[\text{butadiene}]$	377	378	521	245	62	458	449	509	403	29
$k_{\text{P}+\text{O}_3}[\text{propene}]$	370	398	737	76	201	680	775	1358	263	303
$k_{\text{Cis}2\text{B}+\text{O}_3}[\text{cis-2-butene}]$	303	283	654	115	127	345	339	421	285	39
$k_{1\text{P}+\text{O}_3}[\text{1-pentene}]$	87	90	107	71	9	88	82	123	73	15

Table 3.6: Lifetimes of O₃ with respect to different species measured at PARADE-2011.

Time window]10:00, 14:00] UTC.

Rate × [conc.] on Y-axis Fig. 3.10	Lifetime of O ₃ for respective loss (days) @ Temp. > 13 °C					Lifetime of O ₃ for respective loss (days) @ Temp. ≤ 13 °C				
	Avg.	Mdn.	Max.	Min.	STD	Avg.	Mdn.	Max.	Min.	STD
$\beta \times jO^4D$	8	7	29	3	4	20	16	75	8	13
k_{OH+O_3} [OH]	202	179	1994	129	132	353	271	1111	181	205
$k_{HO_2+O_3}$ [HO ₂]	41	40	109	30	9	57	52	99	39	16
$k_{\alpha pin+O_3}$ [α -pin]	104	95	250	46	39	196	212	286	109	61
k_{lm+O_3} [limonene]	67	61	150	29	27	127	128	173	102	15
k_{myr+O_3} [myrcene]	63	45	174	22	39	89	89	141	45	31
k_{iso+O_3} [isoprene]	677	534	2705	183	440	1196	1076	6717	391	880
$k_{tol.+O_3}$ [toluene]	0.6 × 10 ⁷	0.4 × 10 ⁷	3.3 × 10 ⁷	0.12 × 10 ⁷	0.6 × 10 ⁷	1.8 × 10 ⁷	1.6 × 10 ⁷	3.9 × 10 ⁷	0.5 × 10 ⁷	0.9 × 10 ⁷
$k_{Ben.+O_3}$ [benzene]	1.2 × 10 ⁷	0.9 × 10 ⁷	4.8 × 10 ⁷	0.4 × 10 ⁷	0.8 × 10 ⁷	2.1 × 10 ⁷	2 × 10 ⁷	11 × 10 ⁷	0.7 × 10 ⁷	1.6 × 10 ⁷
k_{E+O_3} [ethene]	1334	1255	4118	478	596	2300	2345	4303	942	838
$k_{1,3BD+O_3}$ [butadiene]	343	341	517	170	68	442	459	588	218	76
k_{P+O_3} [propene]	463	477	1348	59	251	835	890	1518	333	338
$k_{Cis2B+O_3}$ [cis-2-butene]	273	249	798	87	122	371	366	585	288	60
k_{1P+O_3} [1-pentene]	91	91	145	74	10	98	98	133	76	18

Table 3.7: Lifetimes of O₃ with respect to different species measured at PARADE-2011.
Time window]14:00, 16:00] UTC.

Rate × [conc.] on Y-axis Fig. 3.10	Lifetime of O ₃ for respective loss (days) @ Temp. > 13 °C					Lifetime of O ₃ for respective loss (days) @ Temp. ≤ 13 °C				
	Avg.	Mdn.	Max.	Min.	STD	Avg.	Mdn.	Max.	Min.	STD
$\beta \times jO^1D$	22	17	72	6	15	72	72	174	17	36
$k_{OH+O_3} [OH]$	492	382	4352	184	398	1064	962	2338	300	486
$k_{HO_2+O_3} [HO_2]$	68	65	119	41	16	93	95	114	55	14
$k_{\alpha pin+O_3} [\alpha-pin]$	83	79	175	33	31	131	126	230	96	29
$k_{lm+O_3} [limonene]$	53	47	125	19	27	97	98	110	61	13
$k_{myr+O_3} [myrcene]$	47	37	122	16	25	68	61	127	43	24
$k_{iso+O_3} [isoprene]$	627	615	1208	221	247	912	856	1334	686	167
$k_{tol.+O_3} [toluene]$	0.7 × 10 ⁷	0.6 × 10 ⁷	4.6 × 10 ⁷	0.1 × 10 ⁷	0.7 × 10 ⁷	1.6 × 10 ⁷	1.7 × 10 ⁷	3.2 × 10 ⁷	0.8 × 10 ⁷	0.5 × 10 ⁷
$k_{Ben.+O_3} [benzene]$	1 × 10 ⁷	0.9 × 10 ⁷	3.1 × 10 ⁷	0.5 × 10 ⁷	0.4 × 10 ⁷	1.9 × 10 ⁷	1.9 × 10 ⁷	2.4 × 10 ⁷	1.1 × 10 ⁷	0.4 × 10 ⁷
$k_{E+O_3} [ethene]$	1706	1721	3329	622	581	2357	2370	2885	2011	192
$k_{1,3BD+O_3} [butadiene]$	358	355	531	154	87	476	482	570	392	44
$k_{P+O_3} [propene]$	524	570	873	61	199	833	905	1255	557	216
$k_{Cis2B+O_3} [cis-2-butene]$	309	289	609	98	136	439	446	554	331	50
$k_{1P+O_3} [1-pentene]$	88	91	118	74	8	107	108	144	78	26

4 Photostationary State (PSS) Analysis: PARADE-2011

The focus of this chapter is to understand the role of different species in the cycling between NO and NO₂ and specifically evaluate the potential role of an ‘unknown’ oxidant for PARADE-2011. The PSS is investigated by using the concept of the Leighton ratio ([Leighton, 1961](#)).

4.1 Leighton ratio (Φ)

The Leighton ratio Φ ([Eq. 1.4](#)) is often used to describe the PSS between NO and NO₂. During periods of sunlight, a null cycle exists between NO-NO₂-O₃ as described by reactions [R. 1.1](#), [R. 1.5](#), and [R. 1.6](#). However, variations in the intensity of solar radiation like passing clouds and the local emissions of NO_x can perturb the PSS.

To avoid scatter in Φ due to rapid changes in solar radiation during early morning and late evening, a filter corresponding to $j\text{NO}_2 \geq 5 \times 10^{-3} \text{ s}^{-1}$ for high photolysis frequency has been applied. Based on this filter, the calculated median time (τ)_{ss} ([Eq. 1.3](#)) for the establishment of PSS is 33 s with a variation in the range of]23, 65[s. The relative change in $j\text{NO}_2$ (10 minute averages) was less than 15 % for most of the filtered data set. No correlation is observed between the variation in $j\text{NO}_2$ and deviations in Φ ([appendix 7.3.1.7.1](#)). The reason for the absence of a correlation is that the data set for the calculation of Φ is based on averages over longer time periods (600 s) while the PSS is established within less than 65 s. Thus the averaging over longer period provides sufficient time for readjustments of the PSS even after an interruption of radiation. Emissions of NO_x in the vicinity of the measurement site can perturb the PSS. The nearby main emissions of NO_x were expected from road traffic. Based on the values of the locally measured wind speed, a distance in the range of]25, 463[m from the sampling point is required to buffer the PSS (@ $j\text{NO}_2 \geq 5 \times 10^{-3} \text{ s}^{-1}$). There were no major roads located within a 300 m radius of the observatory; the nearest main roads were at a distance of 335 m north and > 700 m west of the field site. There was a small road around the observatory within a distance > 150m, but it had only infrequent traffic. So in order to avoid emissions from the nearest road at 335 m north, which can perturb the PSS, an extra filter (Filter_Road) has been applied. Consequently, any data point with conditions ‘Filter_Road = $2 \times (\tau)_{\text{ss}} \text{ (s)} \times \text{wind speed (m s}^{-1}\text{)} > 300 \text{ m}$ ’ is rejected. Thus the application of

'Filter_Road' minimised the possibility for disturbance of the PSS due to local emissions. Moreover, the PSS is expected to settle within 150 m prior to the sampling point for the remaining set of data points. The corresponding time window for the data analysis is between 7:00 to 16:00 UTC. During PARADE, the local time at the observatory was UTC + 2.

The time series for NO, NO₂, O₃, jNO₂ and others have been already shown in Fig. 3.5. Φ (Eq. 1.4) (Leighton, 1961) has been calculated for PARADE by using the measured data of NO, NO₂, O₃ and jNO₂. Fig. 4.1 shows the calculated Φ as a function of NO_x mixing ratios. Φ nearly converged to unity for higher NO_x levels while there are significant deviations from unity ($\Phi > 1$) at NO_x values of less than 4 ppb_v. Since O₃ is not the only oxidant converting NO to NO₂, these deviations ($\Phi > 1$) are probably due to NO₂ being formed by other oxidants which are not accounted in Eq. 1.4.

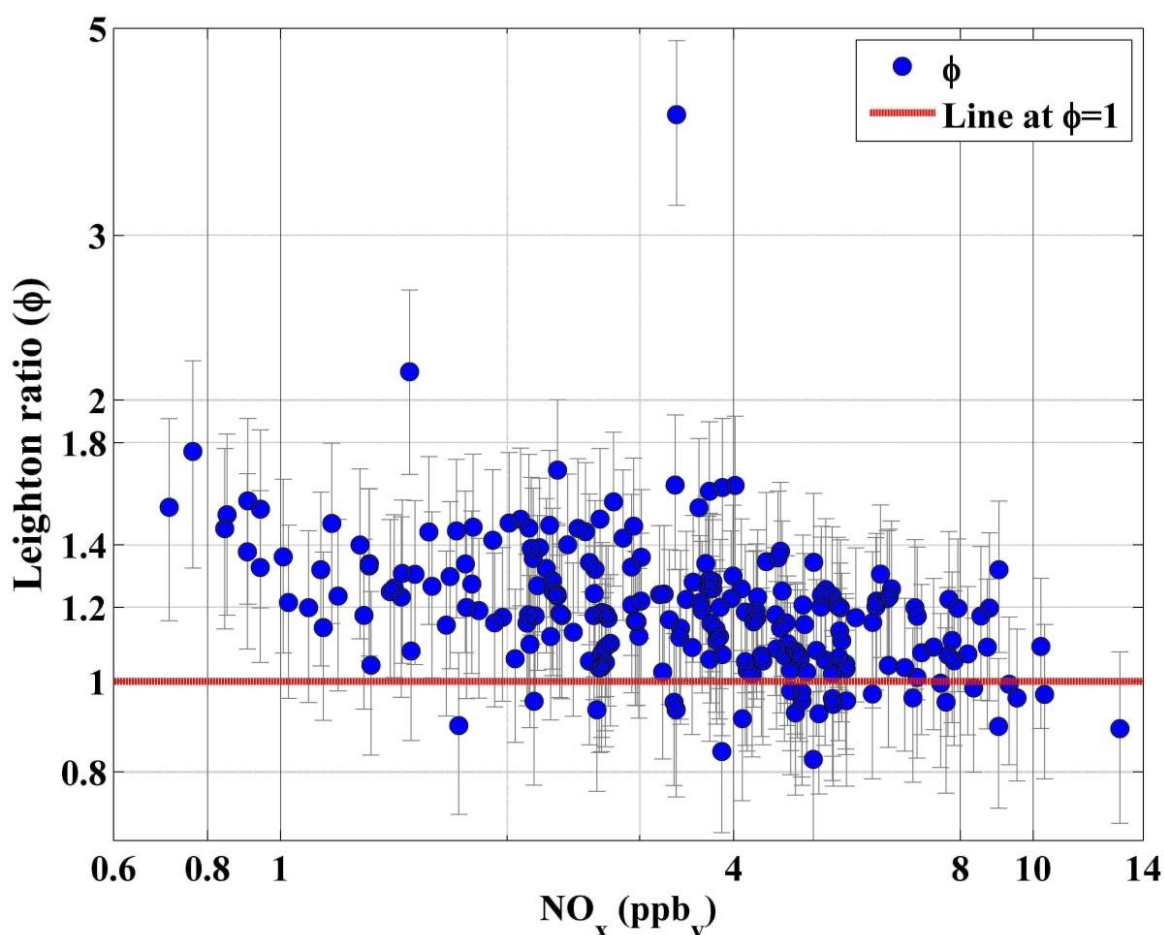


Fig. 4.1: Leighton ratio (Φ) during PARADE with respect to NO_x (log-log scale). Errors in Φ due to measurement uncertainties are indicated by the vertical error bars.

Errors in individual values of Φ are also shown in Fig. 4.1. The overall uncertainties of the measured parameters in Φ were listed in Table 3.2 and Table 3.3. The average and median values of the relative uncertainty in Φ are 19 % and 18.7 %, respectively, with variations in the interval of [18, 25] %. The uncertainty is determined by the propagation of errors based on parameters in Eq. 1.4 by using the following Eq. 4.1.

$$\Delta\Phi^2 = \left(\left(\frac{\partial\Phi}{\partial j\text{NO}_2} \times \Delta j\text{NO}_2 \right)^2 + \left(\frac{\partial\Phi}{\partial \text{NO}_2} \times \Delta \text{NO}_2 \right)^2 \right. \\ \left. + \left(\frac{\partial\Phi}{\partial k_{1.1}} \times \Delta k_{1.1} \right)^2 + \left(\frac{\partial\Phi}{\partial \text{NO}} \times \Delta \text{NO} \right)^2 + \left(\frac{\partial\Phi}{\partial \text{O}_3} \times \Delta \text{O}_3 \right)^2 \right) \quad \text{Eq. 4.1}$$

In Eq. 4.1, ‘ Δ ’ represents the individual uncertainty of parameters in Φ . The uncertainty in Φ is on average 16 % larger at levels of $\text{NO}_x < 4 \text{ ppb}_v$ compared to levels of $\text{NO}_x \geq 4 \text{ ppb}_v$. With respect to different parameters in Φ , a relative fractional contribution (RFC⁴⁵) absolute value of the individual errors to the sum of absolute values of individual errors is shown in Fig. 4.2 as a function of NO_x . The binned averages of the RFC with standard deviations (1σ) for $0.3 \text{ ppb}_v \text{ NO}_x$ intervals are also shown in Fig. 4.2.

From the error of rate coefficient ($k_{1.1}$) of the reaction R. 1.1, The maximum RFC is up to about 42.3 % of the total uncertainty in Φ ; this maximum RFC is observed at around 4 ppb_v of NO_x . It decreases to ~32 % with the decrease in NO_x to less than 2 ppb_v .

The RFC from measurement errors of O_3 is in the range of [17, 25] %. There is no significant trend in the RFC with the variability of NO_x levels.

$$^{45} \text{ RFC} = \frac{\left| \frac{\partial\Phi}{\partial X_i} \times \Delta X_i \right|}{\left| \frac{\partial\Phi}{\partial j\text{NO}_2} \times \Delta j\text{NO}_2 \right| + \left| \frac{\partial\Phi}{\partial \text{NO}_2} \times \Delta \text{NO}_2 \right| + \left| \frac{\partial\Phi}{\partial k_{1.1}} \times \Delta k_{1.1} \right| + \left| \frac{\partial\Phi}{\partial \text{NO}} \times \Delta \text{NO} \right| + \left| \frac{\partial\Phi}{\partial \text{O}_3} \times \Delta \text{O}_3 \right|}$$

where $X_i = j\text{NO}_2, \text{NO}_2, k_{1.1}, \text{NO}, \text{and } \text{O}_3$

The RFC for $j\text{NO}_2$ varies between 13 to 14 % for NO_x above 2 ppb_v . A minor decrease in the RFC of $j\text{NO}_2$ to 10.6 % is observed with respect to a decrease in NO_x below 2 ppb_v .

Measured NO RFC [10.3, 24.6] % increases with decrease in NO_x . For NO_x higher than 3 ppb_v , the RFC of NO is 10.3 to 11.5 %, whereas it increases to ~ 25 % for NO_x values below 0.9 ppb_v .

Maximum contribution (> 14.5 %) in the Φ uncertainty due to NO_2 measurements is observed at around 4 ppb_v of NO_x . The RFC due to NO_2 does not show significant trend with respect to NO_x levels and mainly varies between 13 to 15 %.

The absolute errors in Φ (Eq. 4.1) are greater at low NO_x levels. The error contributed by NO increases about 15 % at lower NO_x ; however, at the same time there is about 10 to 15 % combined decrease is observed in errors due to $k_{1.1}$, $j\text{NO}_2$, and NO_2 . The increasing trend in Φ with the decrease in NO_x levels (Fig. 4.1 or Fig. 4.3) has a chemical explanation and is only partially due to uncertainties of the NO measurement.

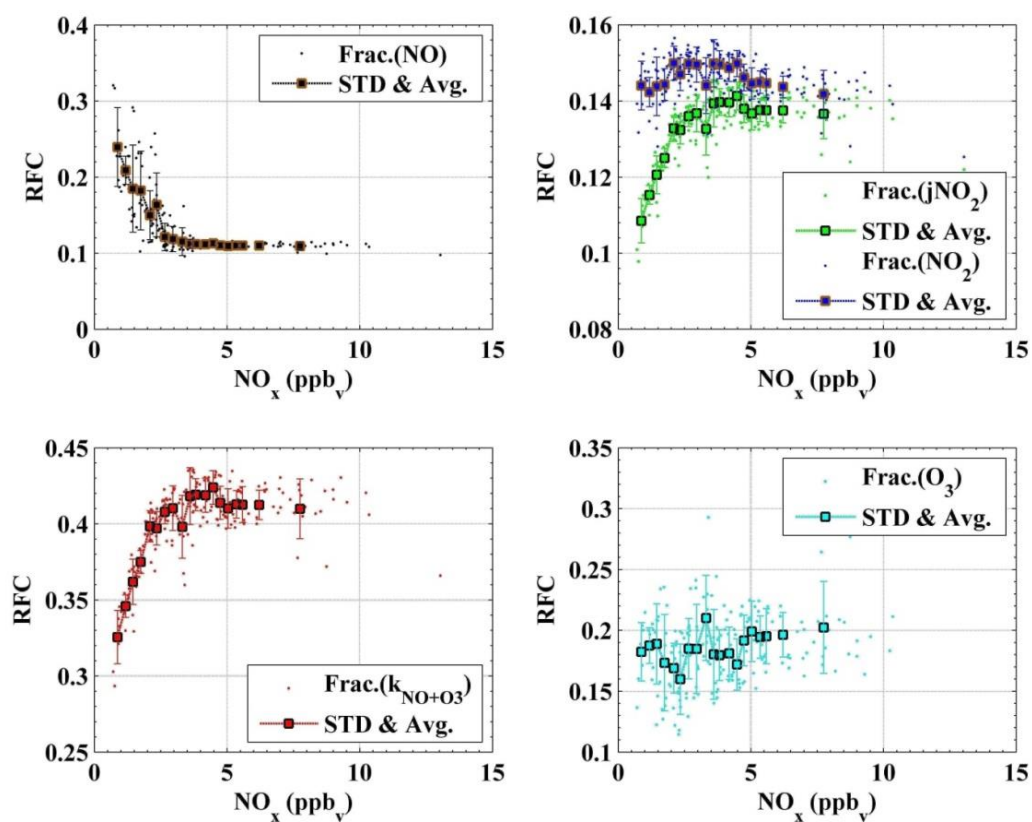


Fig. 4.2: Relative fraction of the uncertainty in Φ due to different parameters as a function of NO_x mixing ratios.

Fig. 4.3 shows an overview of Φ and colour-coded locally measured wind direction for correlations to different air masses. The average values of Φ and the average measurement error are calculated for 0.3 ppb_v NO_x bins and shown in Fig. 4.3 as well. To calculate averages, the minimum limit for a NO_x bin is at least 5 data points. The deviation of Φ increases with decrease in NO_x below to 4 ppb_v. There is no correlation observed for deviations of Φ with respect to the locally measured wind directions.

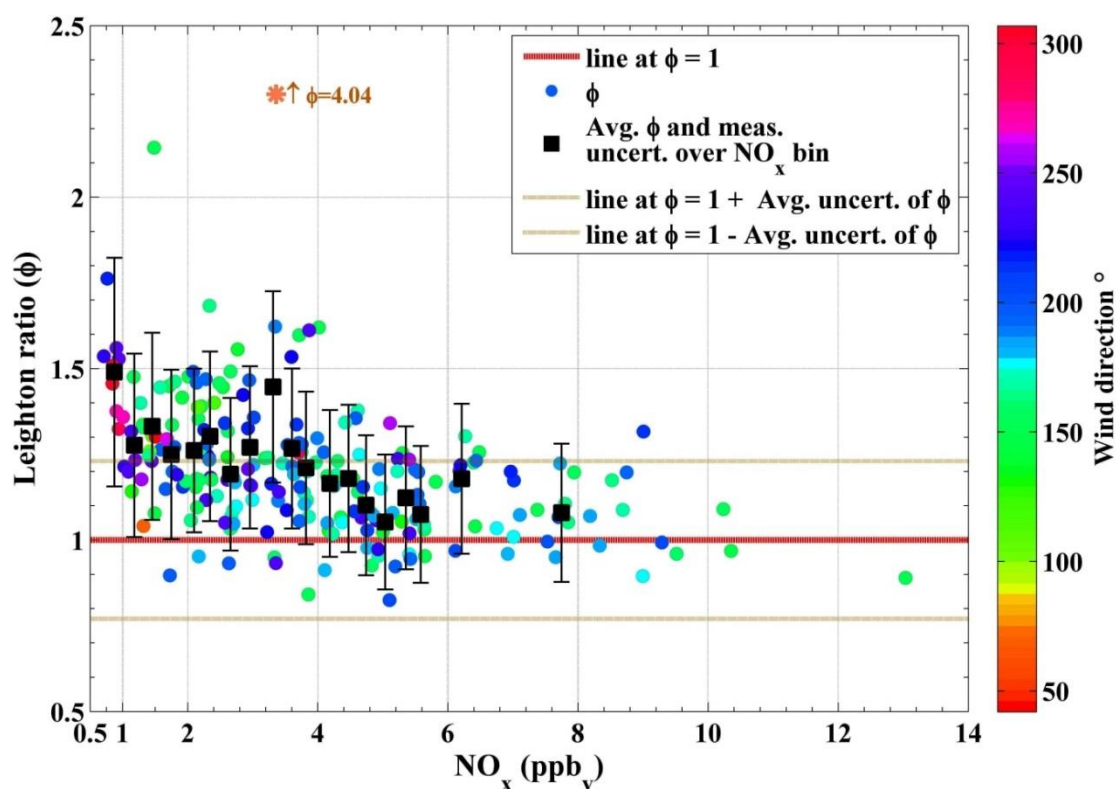


Fig. 4.3: Average Φ as a function 0.3 ppb_v of NO_x bin with measurement uncertainty of over bin averages.

In addition to O₃, RO_x (HO₂ + RO₂) are well known oxidants that react with NO, to produce NO₂. The observed negative trend in the case of RO_x versus NO (Fig. 4.5) during PARADE is similar to the case of Φ versus NO_x (Fig. 4.3). RO_x contributes to deviations ($\Phi > 1$) at least to some extent, even if other oxidants like the halogen oxides are present or there are other reasons such as loss of O₃ due to the ‘O₃ + alkenes’ reaction. To support the notion that RO_x contributes to positive deviation in Φ , the instantaneous production rates of NO₂ have been calculated by taking reactions like ‘NO + O₃’ (R. 1.1), ‘NO + RO_x’ (R. 1.3,

R. 1.2), and PAN decomposition (R. 1.8) into account. Fig. 4.4 shows the relative fraction of the NO_2 production rates (median = $3.2 \pm 2.8 (1\sigma) \times 10^8 \text{ molecule cm}^{-3} \text{ s}^{-1}$) during PARADE for ‘ $\text{NO} + \text{O}_3$ ’, ‘ $\text{NO} + \text{RO}_x$ ’, and decomposition of PAN. The relative fraction of ‘ $\text{NO} + \text{RO}_x$ ’ compared to ‘ $\text{NO} + \text{O}_3$ ’ decreases with elevated NO_2 . Major contribution in NO_2 production rates occurs from the ‘ $\text{NO} + \text{O}_3$ ’ reaction. The relative fraction of ‘ $\text{NO} + \text{O}_3$ ’ remains above 90 % for $\text{NO}_2 > 2 \text{ ppb}_v$. Maximum relative fraction of ‘ $\text{RO}_x + \text{NO}$ ’ was observed for $\text{NO}_2 < 2 \text{ ppb}_v$; it was scattered in the range of [5, 25[%; based on 0.3 $\text{ppb}_v \text{ NO}_x$ bins, it averages up to 12.6 %. During PARADE, a decrease in RO_x with respect to increasing NO was observed (Fig. 4.5). This appears to be due to an increase in RO_x sinks with increasing NO levels, as described by reactions R. 1.2, R. 1.3, and R. 1.14. Similar to RO_x , a decrease in O_3 was also observed with increasing NO concentrations. A positive trend in ANs with respect to NO (Fig. 4.5) indicates increase in the loss of radicals forming organic nitrates at higher NO_x . This shows that positive deviation in Φ at low NO_x levels is most probably caused by the reaction ‘ $\text{NO} + \text{RO}_x \rightarrow \text{NO}_2$ ’.

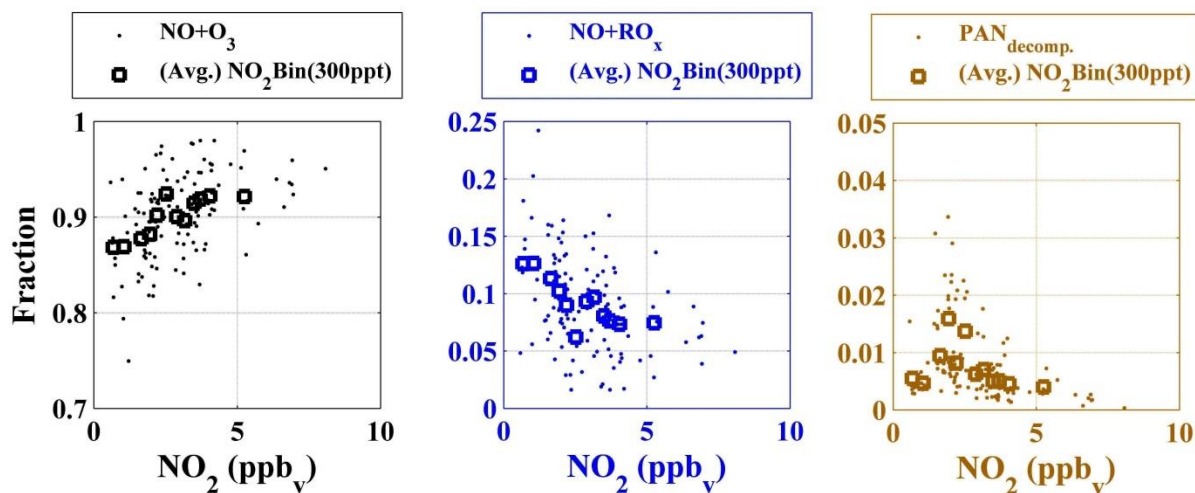


Fig. 4.4: Fraction of NO_2 production rates for different reactions.

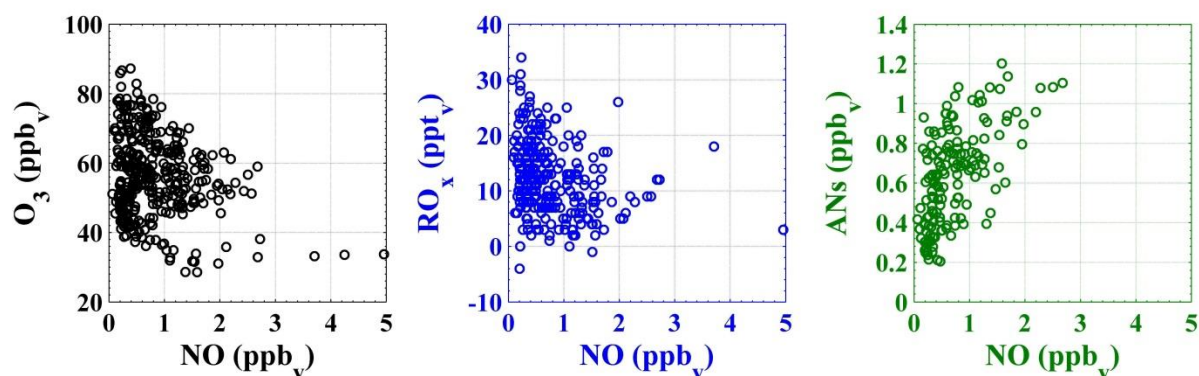


Fig. 4.5: Measured O_3 , RO_x and ANs as a function of NO during PARADE.

4.2 Modified Leighton Ratio (Φ_{mod})

NO , NO_2 and O_3 also react with different trace gases apart from the reactions [R. 1.1](#), [R. 1.5](#) and [R. 1.6](#). The PSS establish in shorter time scales; the impact from other processes such as O_3 deposition, ‘ $NO + OH$ ’, ‘ $NO_2 + OH$ ’, PAN decomposition, O_3 photolysis, and ‘ $O_3 +$ alkenes’ is not great enough to perturb the PSS.

During PARADE, the O_3 lifetime was in order of days, excluding the dry deposition (Section [3.3](#), [Table 3.5](#), [Table 3.6](#) and [Table 3.7](#)). So any loss of O_3 is not sufficient to perturb the PSS for PARADE.

The reaction of NO_2 with OH ([R. 1.7](#)) is a NO_x sink. The lifetime of NO_2 due to reaction with OH during PARADE was in the range of $[6 \times 10^4, 4 \times 10^5]$ s. This reaction ([R. 1.7](#)) cannot perturb NO_2 concentrations enough to affect the PSS.

The decomposition of PAN can increase the concentration of NO_x . The effective lifetime of PAN (τ_{PAN}) is described by [Eq. 4.2](#) ([Finlayson-Pitts and Pitts, 2000](#)) and it was greater than 7×10^3 s ([appendix 7.3.1.7.3](#)) during PARADE.

$$(\tau)_{PAN} = \frac{1}{k_{CH_3C(O)OONO_2 \rightarrow NO_2}} \left(1 + \frac{k_{CH_3C(O)OO + NO_2} [NO_2]}{k_{CH_3C(O)OO + NO} [NO]} \right) \quad \text{Eq. 4.2}$$

The time scale for the PAN decomposition to NO_2 is very large compared to the characteristic time required for establishing the PSS. Therefore, the decomposition of PAN cannot considerably perturb the PSS for PARADE.

The lifetime of NO due to OH was greater than 7.8×10^4 s and is likewise unable to perturb the PSS considerably.

The sensitivity of the deviation in Φ for $\Phi > 1$ was tested based on the time scale required for the PSS establishment. A modified form Φ_{mod} (Eq. 4.3) was calculated to see the absolute effects on deviations and compared with Φ (Eq. 1.4). This estimation (Eq. 4.3) is useful to assess the effect on Φ deviations due to involvement of NO, NO_2 and O_3 in chemical reactions (excluding ' $\text{RO}_x + \text{NO} \rightarrow \text{NO}_2$ ').

$$\Phi_{\text{mod}} = \left(\frac{j\text{NO}_2 [\text{NO}_2 + \text{NO}_{2\text{eff}}]}{k_{1.1} [\text{O}_3 + \text{O}_{3\text{eff}}] [\text{NO} + \text{NO}_{\text{eff}}]} \right) \quad \text{Eq. 4.3}$$

The major production or loss processes of NO, NO_2 , and O_3 are accounted for in Eq. 4.3. The production and loss in NO, NO_2 , and O_3 are described by NO_{eff} , $\text{NO}_{2\text{eff}}$, and $\text{O}_{3\text{eff}}$, respectively, in Eq. 4.4, Eq. 4.5, and Eq. 4.6 for the time window of $(\tau)_{\text{ss}}$ (Eq. 1.3). The basic idea behind Φ_{mod} (Eq. 4.3) is that it will describe actual Φ in an absence of production or loss processes other than NO- NO_2 - O_3 cycle R. 1.1, R. 1.5, and R. 1.6 but excluding ' $\text{RO}_x + \text{NO} \rightarrow \text{NO}_2$ '.

$$\text{NO}_{\text{eff}} \approx (\tau)_{\text{ss}} \times k_{\text{OH} + \text{NO}} [\text{OH}][\text{NO}] \quad \text{Eq. 4.4}$$

$$\text{NO}_{2\text{eff}} \approx (\tau)_{\text{ss}} \times (k_{\text{OH} + \text{NO}} [\text{OH}][\text{NO}_2] - k_{\text{Diss.}} [\text{PAN}]) \quad \text{Eq. 4.5}$$

$$\begin{aligned}
O_{3\text{eff}} \approx (\tau)_{\text{ss}} \times [O_3] \times & \left(\beta \times jO^1D \right. \\
& + k_{\text{NO}_2 + O_3} [\text{NO}_2] + k_{\text{OH} + O_3} [\text{OH}] + k_{\text{HO}_2 + O_3} [\text{HO}_2] \\
& + k_{\text{Iso.} + O_3} [\text{isoprene}] + k_{\alpha\text{-Pin.} + O_3} [\alpha\text{-pinene}] + k_{\text{Myr.} + O_3} [\text{myrcene}] \\
& + k_{\text{lm} + O_3} [\text{limonene}] \\
& + k_{\text{Eth.} + O_3} [\text{ethene}] + k_{\text{Pro.} + O_3} [\text{propene}] + k_{\text{ButD} + O_3} [1,3\text{-butadiene}] \\
& + k_{\text{Cis2B.} + O_3} [\text{cis-2-Butene}] + k_{\text{1-P.} + O_3} [1\text{-pentene}] \\
& + k_{\text{Ben.} + O_3} [\text{benzene}] + k_{\text{tol} + O_3} [\text{toluene}] \\
& \left. + V_d / \text{BLH} \right)
\end{aligned}$$

Eq. 4.6

Based on the information ‘concentration = $(\tau)_{\text{ss}} \times$ loss or production rates’, the loss processes are added and the production processes are subtracted. In NO_{eff} , the loss processes for NO due to P(HONO) is considered over the time scale of $(\tau)_{\text{ss}}$. The loss of NO_2 towards HNO_3 , and production from PAN decomposition is considered in Eq. 4.5, where k_D (Atkinson et al., 2004) is the decomposition rate. In Eq. 4.6, several loss processes are taken into account for O_3 , based on the available measurements of alkenes during PARADE. V_d is the deposition velocity of O_3 and a value of 1cm s^{-1} (Droppo, 1985; Finlayson-Pitts and Pitts, 2000) for upper estimate is used with a boundary layer height (BLH) of 1000 m.

The ratio Φ / Φ_{mod} is shown in Fig. 4.6. The median value of Φ / Φ_{mod} is 1.015 ± 0.005 (1σ) at NO_x lower than 3 ppbv. The maximum value of contribution to the deviation of Φ from the production and loss processes as described in Eq. 4.4, Eq. 4.5, and Eq. 4.6 is less than 3 % and it is insignificant if the uncertainties of the measured quantities in Eq. 4.4, Eq. 4.5, and Eq. 4.6 are considered. The local sinks of O_3 (Eq. 4.6) were not important in accounting for the positive deviations in Φ . Even multiplying BVOCs (isoprene, α -pinene, myrcene and limonene in Eq. 4.6) concentrations by a factor of 20 and allowing a 10 times enhancement in the photolytic loss of O_3 [$\beta = 1$ (Eq. 1.12)] cannot produce considerable difference in the ratio Φ / Φ_{mod} . Hence, it can be concluded that for PARADE, the observed deviations in Φ are not significantly affected by the involvement of NO, NO_2 , and O_3 with other physical or chemical processes, excepting ‘ $\text{RO}_x + \text{NO}$ ’.

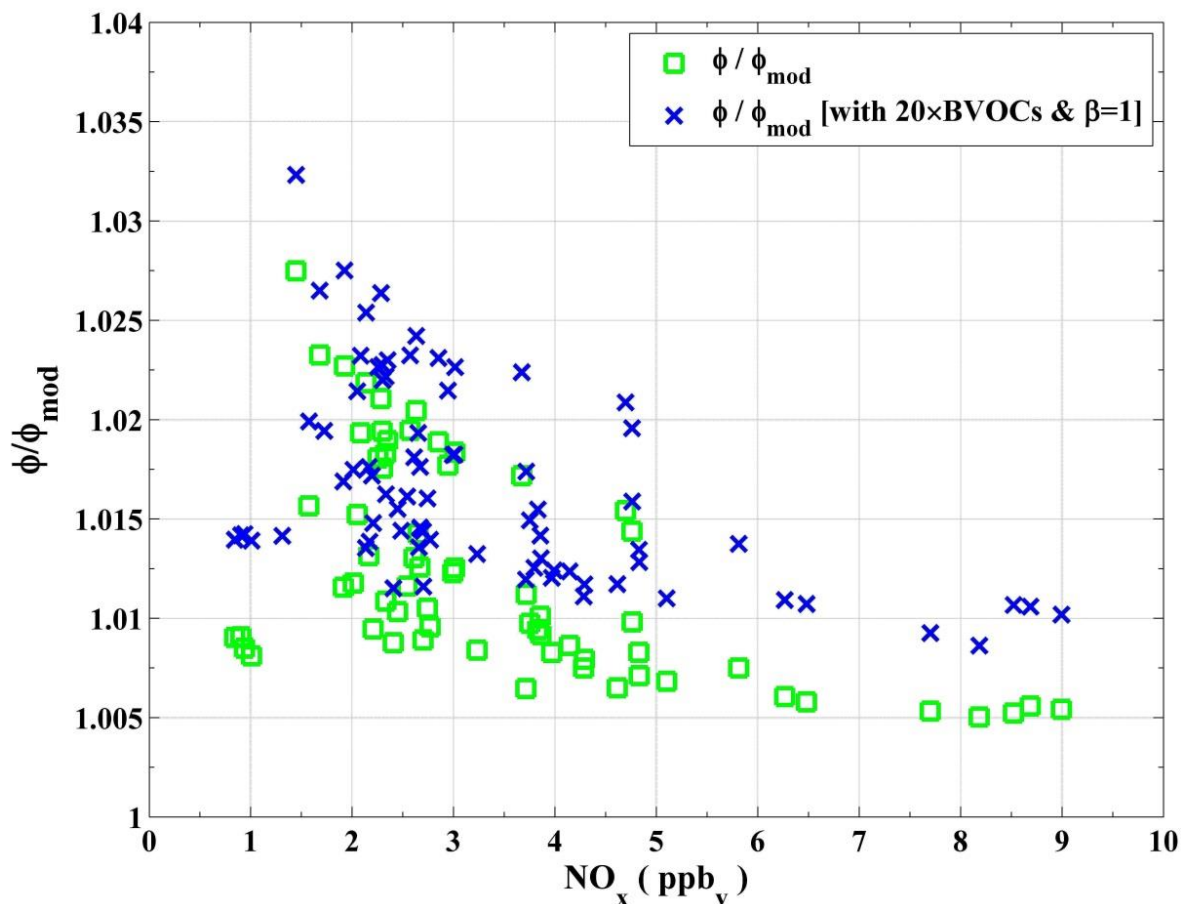


Fig. 4.6: Effect on Φ due to the involvement of NO , NO_2 , and O_3 in other chemical and physical processes.

4.3 Extended Leighton ratio (Φ_{ext}) including measured RO_x

Interconversion of NO and NO_2 in the presence of O_3 is rapid during periods of sunlight (Cadle and Johnston, 1952; Leighton, 1961) and the role of RO_x in the process cannot be ignored (Calvert and Stockwell, 1983; Bradshaw et al., 1999). The classical Leighton ratio Φ has been extended by the contribution of RO_x . The total sum of peroxy radicals ($\text{HO}_2 + \text{RO}_2$) was measured with the **PeRCA** instrument during PARADE and these measurements were used to evaluate the extended Leighton ratio Φ_{ext} (Eq. 1.6). The inclusion of RO_x significantly reduces the deviation in Φ as observed in Φ_{ext} (Fig. 4.7). The resulting reduction in Φ at lower NO_x concentration (< 4 ppb_v) is greater than the reduction in Φ at elevated NO_x values.

This is because of the fact that the larger RO_x concentrations were observed at lower NO_x concentrations (Fig. 4.4). Deviations in $\Phi_{\text{ext}} > \text{or} < 1$ are mostly below the uncertainty of Φ_{ext} , as shown in Fig. 4.8.

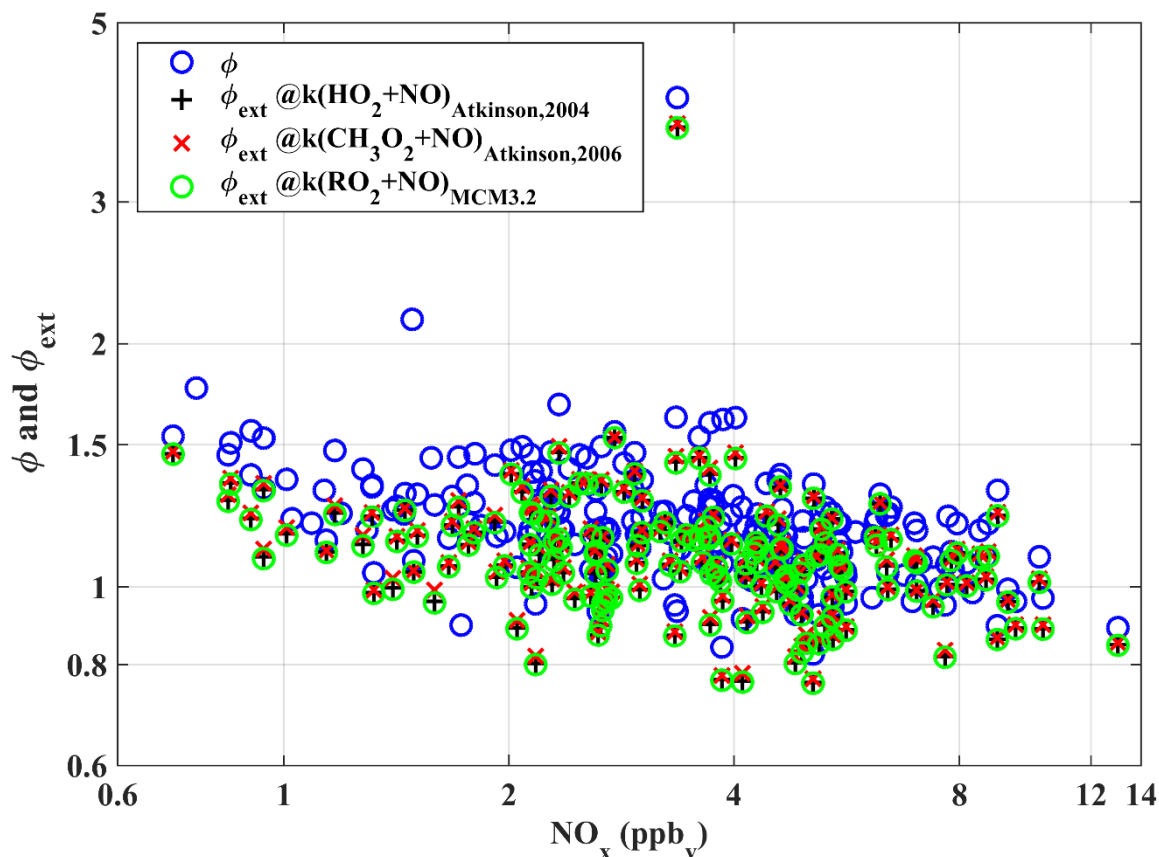


Fig. 4.7: Extended (Φ_{ext}) and classical Leighton ratio (Φ) are plotted versus NO_x mixing ratios for PARADE (log-log scale).

Different types of peroxy radicals present in the atmosphere react with NO at different rates. Φ_{ext} has been calculated (Fig. 4.7) using three different assumptions for the rate coefficient ' $k_{(\text{RO}_x+\text{NO})}$ ' value of the ' $\text{RO}_x + \text{NO}$ ' reaction as follow.

(1) If all the measured RO_x are considered as HO_2 , then ' $k_{(\text{RO}_x+\text{NO})}$ ' = ' $k_{(\text{HO}_2+\text{NO})}$ ' (Atkinson et al., 2004).

(2) If RO_x = methyl peroxy radical (CH_3O_2), then ' $k_{(\text{RO}_x+\text{NO})}$ ' = ' $k_{(\text{CH}_3\text{O}_2+\text{NO})}$ ' (Atkinson et al., 2006).

(3) If a generic rate coefficient is used for ' $k_{(\text{RO}_x+\text{NO})}$ ' from MCM3.2 ([Jenkin et al., 1997](#); [Saunders et al., 2003](#)).

The reduction in deviations is smaller in the case (2) compared to cases (1) and (3), as shown in [Fig. 4.7](#). The average difference of the reduction between cases (1), (2), and (3) is less than 1.4 % and is not significant. An overview of Φ_{ext} for PARADE is presented in [Fig. 4.8](#), with the generic rate coefficient used for the ' $\text{RO}_x + \text{NO}$ ' reaction and an uncertainty of 25 % assigned to it. Φ_{ext} is also shown in [Fig. 4.8](#) with calculated uncertainty due to measurements ([Table 3.2](#)). The deviations in Φ_{ext} are slightly larger than 1 at $\text{NO}_x < 3.6 \text{ ppb}_v$ compared to higher $\text{NO}_x > 3.6 \text{ ppb}_v$. For more than 82 % of data set, the observed deviations in Φ_{ext} are within the range of the uncertainty in Φ_{ext} .

The overall population average of Φ_{ext} is plotted in the lower panel of [Fig. 4.8](#). The standard error of the average is derived from the distribution of Φ_{ext} by using $1\sigma / \sqrt{n}$. Only a single data point with a value $\Phi_{\text{ext}} = 3.70$ at $\text{NO}_x = 3.36 \text{ ppb}_v$ is omitted from the calculation of the average, as it does not seem to be the part of the distribution. The average value of Φ_{ext} is 1.09 with standard error of ± 0.02 . The average uncertainty due to measurement for Φ_{ext} is ± 0.2 (1σ). Due to the uncertainty (± 0.2) of measurements, the average value (1.09) of Φ_{ext} is not significantly different from unity. The sensitivity of the average value of $\Phi_{\text{ext}} = 1.09$ is also tested by varying the values within the uncertainty of some parameters in Φ_{ext} ([Eq. 1.6](#)). The lowest uncertainty in the measured NO is about 0.021 ppb_v . By changing the measured NO to $+0.021 \text{ ppb}_v$, the average value for Φ_{ext} is improved to 1.045 ± 0.13 (1σ) with a standard error of 0.01. If the values for $j\text{NO}_2$ are reduced to 5 %, the average value for Φ_{ext} distribution is 1.035 ± 0.14 (1σ) with standard error of 0.01. Similarly, combining these two variations of NO and $j\text{NO}_2$, the average of Φ_{ext} is 0.99 ± 0.131 (1σ). This suggests that within the uncertainty of the measurements, Φ_{ext} appears to 1 for case-4 (combine change in NO and $j\text{NO}_2$) as shown in [Fig. 4.8](#), it is still noteworthy that in the case-1 (normal) a systematic bias remains as shown in the lower panel of [Fig. 4.8](#).

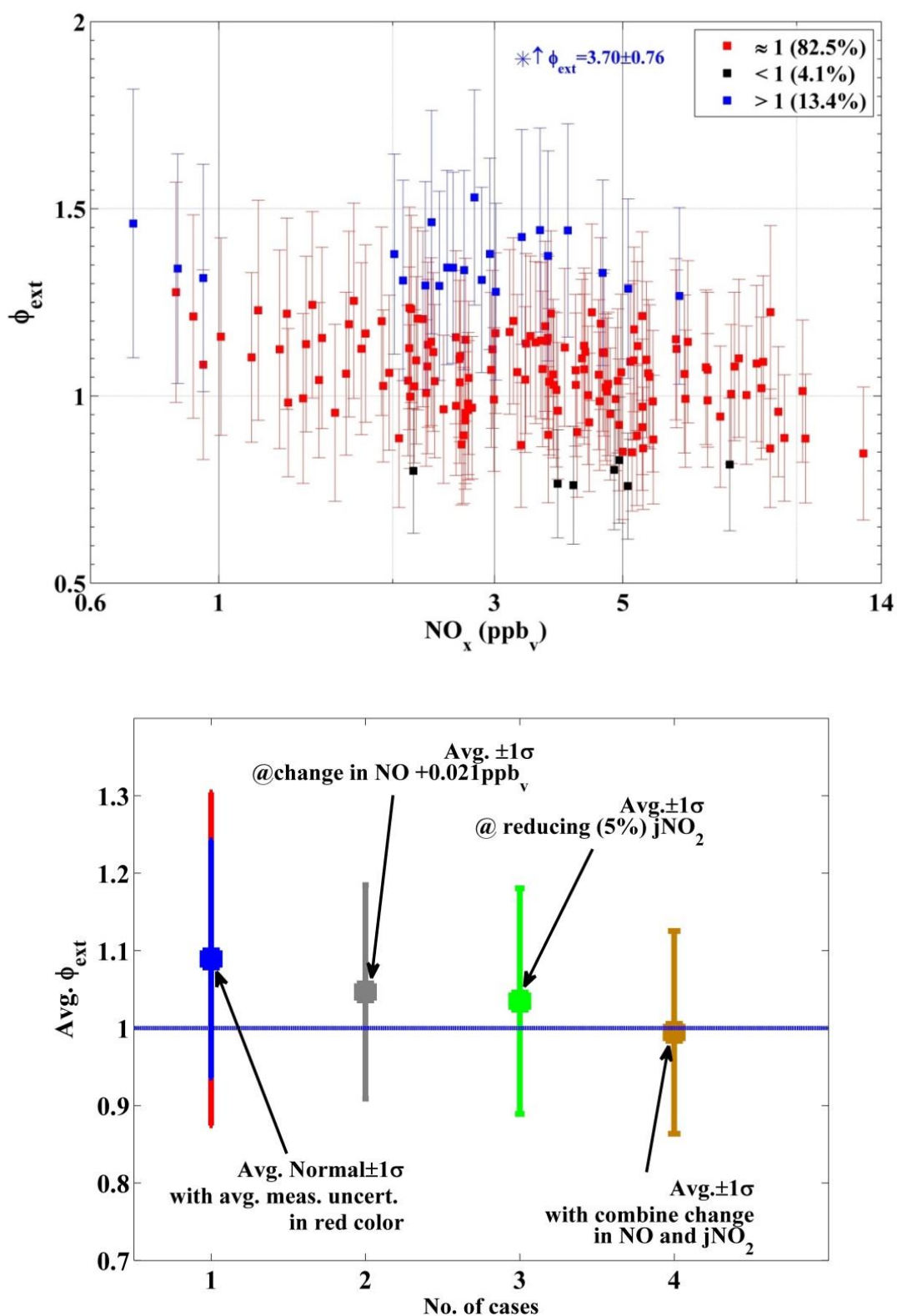


Fig. 4.8: Overview of Φ_{ext} (with measurement uncertainties) as a function of NO_x mixing ratios in the upper panel with x-axis in log scale. The lower panel shows averages with $\pm 1\sigma$ variability. Note that for the lower panel, all avg. Φ_{ext} have less than 1.2 % standard error ($1\sigma / \sqrt{n}$).

The PSS was further tested to verify the significance of deviations with respect to the measured NO_2 during PARADE. NO_2 from the PSS is calculated for two cases: with and without RO_x inclusion as shown in Eq. 4.7 and Eq. 4.8, respectively.

$$(\text{NO}_2)_{\text{PSS}} = \left(\frac{k_{1.1} [\text{O}_3][\text{NO}]}{j\text{NO}_2} \right) \quad \text{Eq. 4.7}$$

$$(\text{NO}_2)_{\text{PSSext}} = \left(\frac{k_{1.1} [\text{O}_3] + k_{\text{MCM3.2}} [\text{RO}_x]_{\text{PeRCA}}}{j\text{NO}_2} \right) [\text{NO}] \quad \text{Eq. 4.8}$$

The absolute errors in the calculated NO_2 were evaluated by using propagation of errors according to the relation in Eq. 4.9. X_i represents the different quantities in Eq. 4.9. The maximum and minimum absolute errors in $(\text{NO}_2)_{\text{PSS}}$ and $(\text{NO}_2)_{\text{PSSext}}$ are given in Table 4.1 for two different NO_x ranges. The relative errors are found to be larger for the lower NO_x values for both $(\text{NO}_2)_{\text{PSS}}$ and $(\text{NO}_2)_{\text{PSSext}}$.

$$\Delta(\text{NO}_2)_{\text{PSSext}} = \sqrt{\sum \left(\Delta X_i \times \frac{\partial (\text{NO}_2)_{\text{PSSext}}}{\partial (X_i)} \right)^2} \quad \text{Eq. 4.9}$$

Table 4.1: Absolute errors in NO_2 calculated from PSS (Eq. 4.7 and Eq. 4.8).

	$\text{NO}_x \leq 3.8 \text{ ppb}_v$			$\text{NO}_x > 3.8 \text{ ppb}_v$		
	Min (ppb _v)	Max (ppb _v)	Mdn (ppb _v)	Min (ppb _v)	Max (ppb _v)	Mdn (ppb _v)
$(\text{NO}_2)_{\text{PSS}}$	0.08	0.46	0.25	0.32	1.48	0.62
$(\text{NO}_2)_{\text{PSSext}}$	0.09	0.52	0.30	0.36	1.5	0.66

Based on the York method (York et al., 2004), which takes both x and y errors into account (Fig. 4.9), a good overall correlation [$R^2 > 0.95$] is observed between the measured NO_2 and calculated NO_2 [$(\text{NO}_2)_{\text{PSS}}$ and $(\text{NO}_2)_{\text{PSSext}}$].

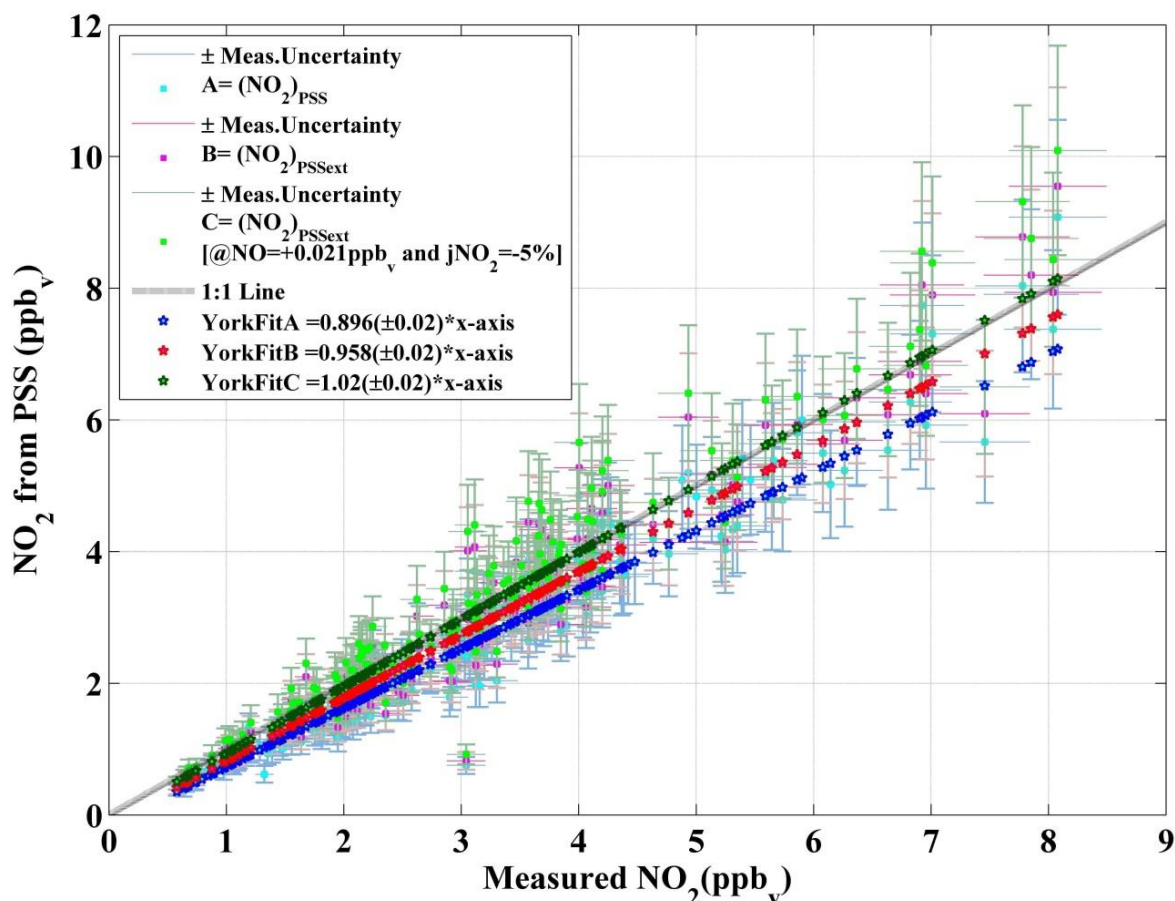


Fig. 4.9: Calculated NO_2 from PSS versus measured NO_2 during PARADE. Three different possibilities are shown $\mathbf{A} = (\text{NO}_2)_{\text{PSS}}$, $\mathbf{B} = (\text{NO}_2)_{\text{PSSext}}$, $\mathbf{C} = (\text{NO}_2)_{\text{PSSext}} [@ \text{NO} = \text{NO} + 0.021 \text{ ppb}_v \text{ and } j\text{NO}_2 = j\text{NO}_2 - (0.05 \times j\text{NO}_2)]$.

$(\text{NO}_2)_{\text{PSS}}$ from Eq. 4.7 is overall 10 % less than the measured NO_2 . In contrast, taking the RO_x measurements into account in the $(\text{NO}_2)_{\text{PSSext}}$ calculation (Eq. 4.8), reduces the difference to 4 % compared to the measured NO_2 . For the combined effect of cases ‘ $\text{NO} = \text{NO} + 0.021 \text{ ppb}_v$ ’ and ‘ $j\text{NO}_2 = j\text{NO}_2 - (0.05 \times j\text{NO}_2)$ ’ as described in this section above, $(\text{NO}_2)_{\text{PSSext}}$ is further improved and overestimated by only 2 % compared to the measured NO_2 .

The remaining deviations (> 1) in Φ_{ext} were smaller than the uncertainty in Φ_{ext} . The sensitivity of Φ_{ext} was tested by varying NO and $j\text{NO}_2$ below the corresponding uncertainty of measurement and further improvements in reducing the remaining deviations were observed. It seems that the Φ_{ext} converged to unity within the uncertainties of measurements (case 4, Fig. 4.8). Similarly, in the second approach, the NO_2 calculations based on Eq. 4.8 agree reasonably well with the measured NO_2 below the uncertainty of the NO_2 measured data

(about 5 %). Therefore, it is concluded that the NO_x -related photochemistry is explained by the PSS model during PARADE and it is consistent with the field measurements of NO_2 though within the uncertainty of the measurements. It is important to mention that a small bias persists in Φ_{ext} or the NO_2 calculations from PSS for normal-cases and this bias could translate up to about 10 ppt_v of ‘equivalent RO_2 ’ concentrations but considering the uncertainties of the measurements it is statistically insignificant. Concluding for PARADE, a statistical evidence to justify the presence of an ‘unknown oxidant’ is insufficient and limited by the measurement uncertainties.

5 HUMPPA-COPEC-2010: NO_x photochemistry

Emissions of reactive organic species from a boreal forest provide sinks for oxidants OH, O₃ and NO₃. The boreal forest makes up one-third of the world's forest and covers about 15 million km² area of the northern latitude ([FAO, 2010](#)); the impact on the oxidation photochemistry over this large area of land is expected to be large. The general objective of the field experiment was to characterise the chemical and physical phenomenon of the atmosphere over a boreal forest ([Williams et al., 2011](#)). This includes the study of the HO_x budget ([Hens et al., 2013](#)), organic aerosol characterisation ([Vogel et al., 2013](#)), a study of PAN and peroxyacetic acid (PAA) with its implications for PAN fluxes ([Phillips et al., 2013](#)), OH reactivity ([Nölscher et al., 2012](#)), emissions rates of terpenes ([Yassaa et al., 2012](#)), and the impact of the boundary layer on the atmospheric chemistry ([Ouwensloot et al., 2012](#)). The objective of the work in this chapter is to investigate the PSS under very low NO_x conditions. A model is also used to test the validity of our current understanding of the cycling between NO_x and the potential role of an 'unknown oxidant'. The role of alkyl nitrates is also discussed in relation to the NO_x lifetime and O₃ production efficiency (OPE) in the boreal forest region.

5.1 Overview HUMPPA-COPEC-2010

HUMPPA-COPEC (**H**yytiälä **U**nited **M**easurements of **P**hotochemistry and **P**articles in **A**ir - **C**omprehensive **O**rganic **P**recursor **E**mission and **C**oncentration study) campaign took place between 12 July and 12 August 2010 at the boreal forest research station SMEAR II (**S**tation for **M**easuring **E**cosystem-**A**tmosphere **R**elation) at Hyytiälä (181 m ASL; 61°51' N, 24°17' E), Southern Finland. The location is a remote area with high biogenic emissions. The dense forest coverage within 5 km the station is composed of coniferous⁴⁶ forest (62 %), mixed⁴⁷ forest (25 %), and shrubs (7.6 %). Coniferous trees are a significant contributor to emissions of monoterpenes and these emissions are a function of temperature ([Guenther et al., 1995](#)). The nearest large city is Tampere (200k pop. in 2012) at a distance of about 60km S-SW direction from the station. SMEAR II ([Hari and Kulmala, 2005](#)) is equipped with towers and

⁴⁶ mainly Scots pine and spruce

⁴⁷ Birch and confers

masts to provide platforms for several instruments to monitor the atmospheric parameters at different altitudes.

The average temperature during the period of measurement was 20 °C with variations of]10, 33[°C. These were remarkably high compared to temperatures recorded in previous years at the location. A comparison of temperatures with previous years can be found in ([Williams et al., 2011](#)). The pressure varied in the range of]979, 1003[hPa with an average value of 992 hPa. Daylight lasted about 18h at the site location during HUMPPA-COPEC. Based on three-day HYSPLIT back trajectories ([Draxler and Hess, 1998](#)), air mass origin can be segregated into the four wind sectors (NW, NE, SW, and SE) ([Williams et al., 2011](#)). Most (53.7 %) of the air masses arrived at site from the SW direction. The contributions to the air mass originating from the SE and NW were 20.7 % and 10.3 %, respectively.

Analytical techniques: For HUMPPA-COPEC, an additional tower was installed at the SMEAR-II site. The height of tower was about 24 m and the top of the tower was about 2 - 3 m above the forest canopy. The inlet lines and sensors for different atmospheric parameters were at top of the tower (24 m). [Table 5.1](#) gives an overview of the measured gas species and photolysis frequencies at the top of tower related to this discussion. The analysis is based on the available 5 min averages of the data set listed in [Table 5.1](#). A vast data set of more than 50 parameters was measured at different heights and within a radius of 200 m. A detailed list of instrumentation can be found in ([Williams et al., 2011](#)). The time series of important quantities regarding the PSS ([Table 5.1](#)) are shown in

[Fig. 5.1](#) and appendix [7.4.1.1](#). Based on results from PARADE, it was observed that HO₂ and RO₂ along with O₃ are important for the PSS analysis, so during HUMPPA-COPEC a period is selected when HO₂ and OH (a precursor for RO₂) measurements above the canopy were available. The period starts on the 1st of August 2010 (JD = 213) and lasts until the 7th of August 2010 (JD = 219). The local time during HUMPPA-COPEC at the observatory was UTC + 3.

Highest values of photolysis frequencies were present at 10:00 UTC. OH and HO₂ radicals were measured with a well-established instrument based on laser-induced fluorescence technique. Details of the measurement setup and procedure for HUMPPA-COPEC are discussed in ([Hens et al., 2013](#); [Novelli et al., 2014](#)). OH followed a pronounced daily profile with peak concentrations at about 10:00 UTC (maximum value of 4.6×10^6 molecule cm⁻³). The variations in HO₂ were in the range of [2.5, 46.7] ppt_v with a median value of 12 ppt_v. NO and NO₂ measurements were conducted with a chemiluminescence detector (CLD) ([Hosaynali Beygi et al., 2011](#)). An increase in the NO

concentrations was observed beginning at sunrise around 2:00 UTC in the morning because of the photolysis of NO₂. From 12:00 UTC onward, NO concentrations were started to decrease until 19:00 UTC (Fig. 5.1). During the night, from about 8:00 UTC to 2:00 UTC, the median value of the observed NO was 1.2 ± 2 (1 σ) ppt_v. Lower NO₂ concentrations had been measured from 6:00 to 18:00 UTC with a median value of 0.25 ± 0.1 (1 σ) ppb_v. For the remaining interval, the median value of NO₂ was 0.45 ± 0.2 (1 σ) ppb_v. The variation in NO₂ for the whole period was [0.09, 2] ppb_v (Fig. 5.1). O₃ was measured by using the UV-absorption technique described in (Gros et al., 1998). The concentration of O₃ showed a positive trend with respect to time from 4:00 to 12:00 UTC and decreased for the later period until 4:00 UTC. The median concentration of O₃ was 41.6 ppb_v with variations of]22, 62[ppb_v.

Table 5.1: A list of instrumentation during HUMPPA-COPEC related to this discussion.

Parameter	Instrument/Technique	LOD	Uncertainty	Institute
O ₃	UV	1 ppb _v	1 %; 4 ppb _v	MPIC
NO	CLD	5 ppt _v	10.3 ppt _v + 5 %	MPIC
NO ₂	CLD (+BLC ⁴⁸)	5 ppt _v	14.2 ppt _v + 6 %	MPIC
OH	IPI-LIF-FAGE ⁴⁹	$9 \times 10^5 \text{cm}^{-3}$	Accu. = 30 % Prec. = $5 \times 10^5 \text{cm}^{-3}$	MPIC
HO ₂	LIF-FAGE	0.4 ppt _v	Accu. = 30 % Prec. < 0.8 ppt _v	MPIC
Photolysis freqs.	Filter-radiometer	-	5 - 15 %	FZ Jülich
Total OH Reactivity	CRM ⁵⁰	3 s ⁻¹	Accu. = 16 % Prec. = 3 - 4 s ⁻¹	MPIC
BVOCs	TD-GC-MS ⁵¹	9 ppt _v	10 - 15 %	MPIC
PAN	CIMS	-	-	MPIC
HCHO	Aerolaser AL4021	17.4 ppt _v	34 %	MPIC
CO	Aerolaser AL5002	1 ppb _v	< 10 %	MPIC
Meteo.	-	-	-	SMEAR II

⁴⁸ Blue light convertor

⁴⁹ InletPreInjector-Laser-Induced Fluorescence-Fast Gas Expansion

⁵⁰ Comparative Reactivity Method (Nölscher et al., 2012)

⁵¹ Thermal Desorber Gas Chromatograph Mass Spectrometer

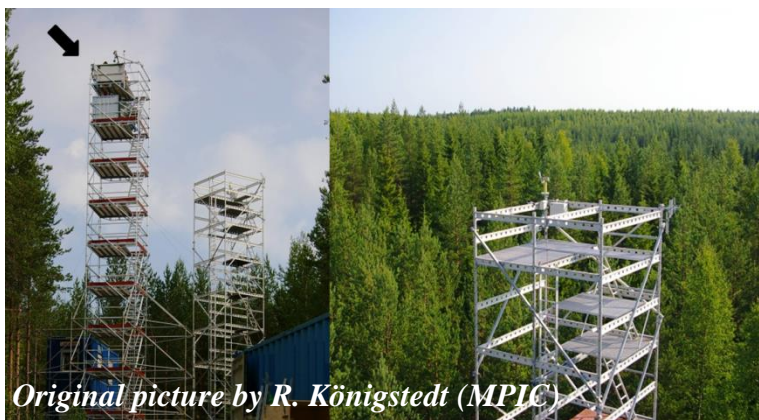
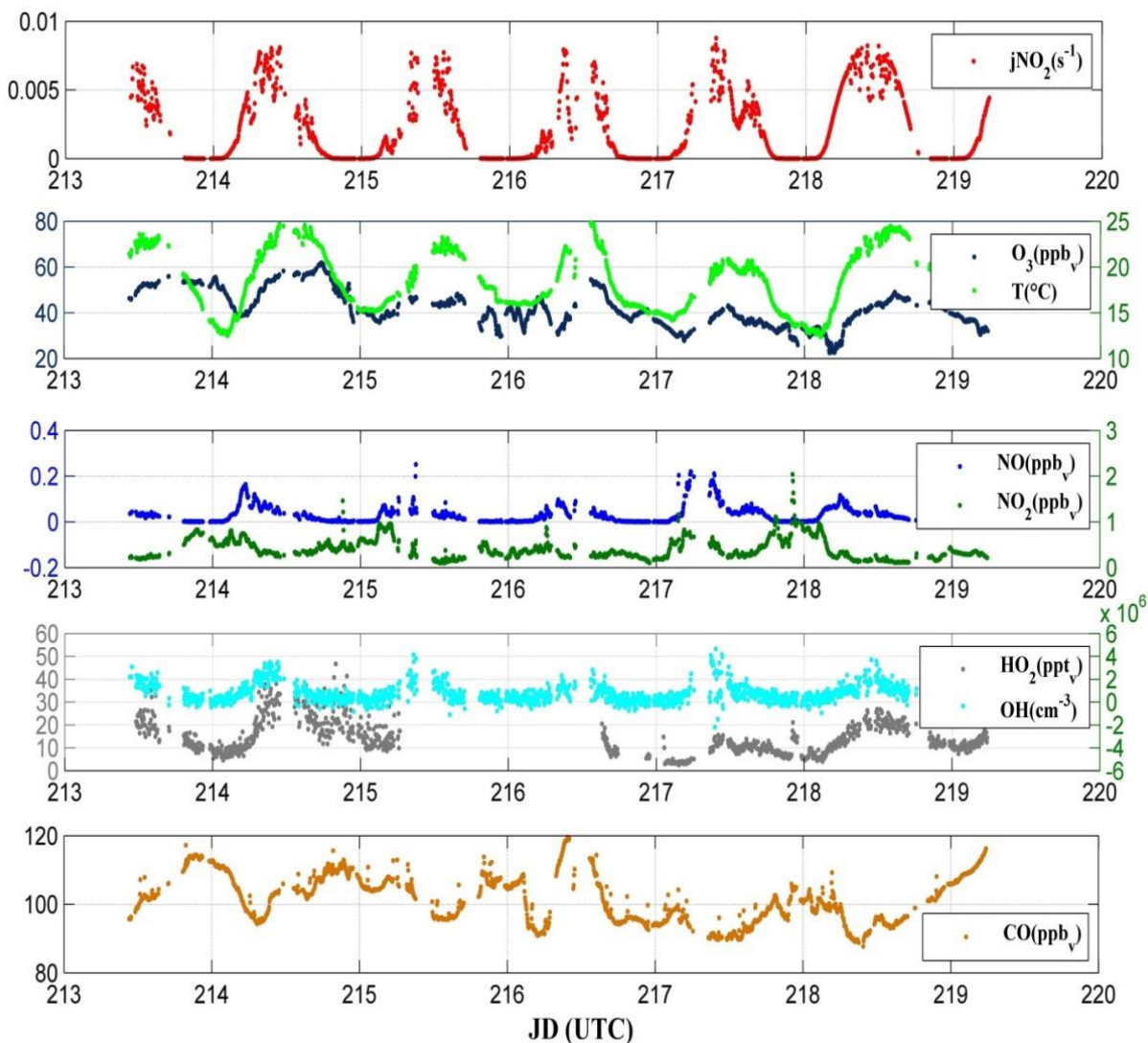


Fig. 5.1: Time series of some important trace gas species, $j\text{NO}_2$, and meteorological parameters during HUMPPA-COPEC-2010 in the upper panel. Lower panel shows an overview of the setup.

5.2 Leighton ratio (Φ)

The conditions during HUMPPA-COPEC were different than PARADE in terms of the NO_x and BVOCs concentrations. The O₃ concentration was similar to the one for PARADE. Generally, the conditions in HUMPPA-COPEC can be regarded as NO_x-limited (Section, 5.4).

A sufficient actinic flux and O₃ concentrations are required to achieve the PSS within a short period of time. To gain access the period where the PSS is expected to become established in a short time interval, the data for Φ (Eq. 1.4) is filtered for jNO₂ (jNO₂ $\geq 5 \times 10^{-3} \text{ s}^{-1}$) as it was in the analysis of the PARADE data set. During HUMPPA-COPEC, the average value of the estimated time to establish NO_x equilibrium was 40 s with a variation of]29, 61[s. Variations in radiation, such as passing clouds can perturb the PSS. In this case, the effect of local variation in the radiation is assessed by calculating point-to-point relative differences in the available 5 minute averages of the measured jNO₂ data. The relative change for most of the data set is less than 20 %. There was no correlation observed between variation in jNO₂ and deviation in Φ (appendix 7.4.1.2). The reason for the lack of correlation is that the data set for the calculation of Φ is based on averages over a longer time period compared to the time required for the PSS to establish. Based on the locally measured wind speeds, NO_x should be in equilibrium within a distance of less than 200 m around the sampling point. The major roads around the observatory are at a distance of 1 km (SW), 1.8 km (W), and 1.9 km (E). Therefore, emissions of NO_x at these roads are unlikely to perturb the local PSS at the sampling site. Note all upcoming discussions are based on the filtered data.

NO_x concentrations⁵² during HUMPPA-COPEC were low compared to PARADE. Φ (Eq. 1.4) is calculated for HUMPPA-COPEC based on measured data of NO, NO₂, O₃, and jNO₂. Φ as a function of NO for both HUMPPA-COPEC and PARADE is shown in Fig. 5.2. Deviations in $\Phi > 1$ are larger in HUMPPA-COPEC compared to PARADE. This indicates that the role of oxidants other than O₃ in converting NO to NO₂ is higher compared to PARADE. The deviation (> 1) in Φ in the case of HUMPPA-COPEC increased with a decrease in NO concentrations up to 44 ppt_v, while a decreasing trend is observed with the further decrease in NO below 44 ppt_v. This decreasing trend is discussed further in Section 5.5. The relative error in Φ in case for HUMPPA-COPEC due to parameters in Eq. 1.4 varied

⁵² HUMPPA-COPEC; NO_x =]0.1, 0.9[ppb_v and NO =]0.019, 0.25[ppb_v
 PARADE; NO_x =]0.7, 13.5[ppb_v and NO =]0.09, 5[ppb_v

from 30 to 65 % at NO values of 100 to 20 ppt_v (appendix 7.4.1.3). The lifetime of O₃ including deposition during HUMPPA-COPEC was within]1 × 10⁵, 3 × 10⁵[s. Lifetimes of NO and NO₂ due to reaction with OH at OH > 0 were within]2 × 10⁴, 8 × 10⁵[s and]1.8 × 10⁴, 7 × 10⁵[s, respectively. These lifetimes are in the order of 10⁴ to 10⁵ s and very high compared to the time required (]29, 61[s) for NO_x to reach equilibrium, so the reactions ‘O₃ + BVOCs’, ‘NO₂ + OH’, and ‘NO + OH’ are unlikely to contribute in $\Phi > 1$ deviations as had been observed in the case of PARADE.

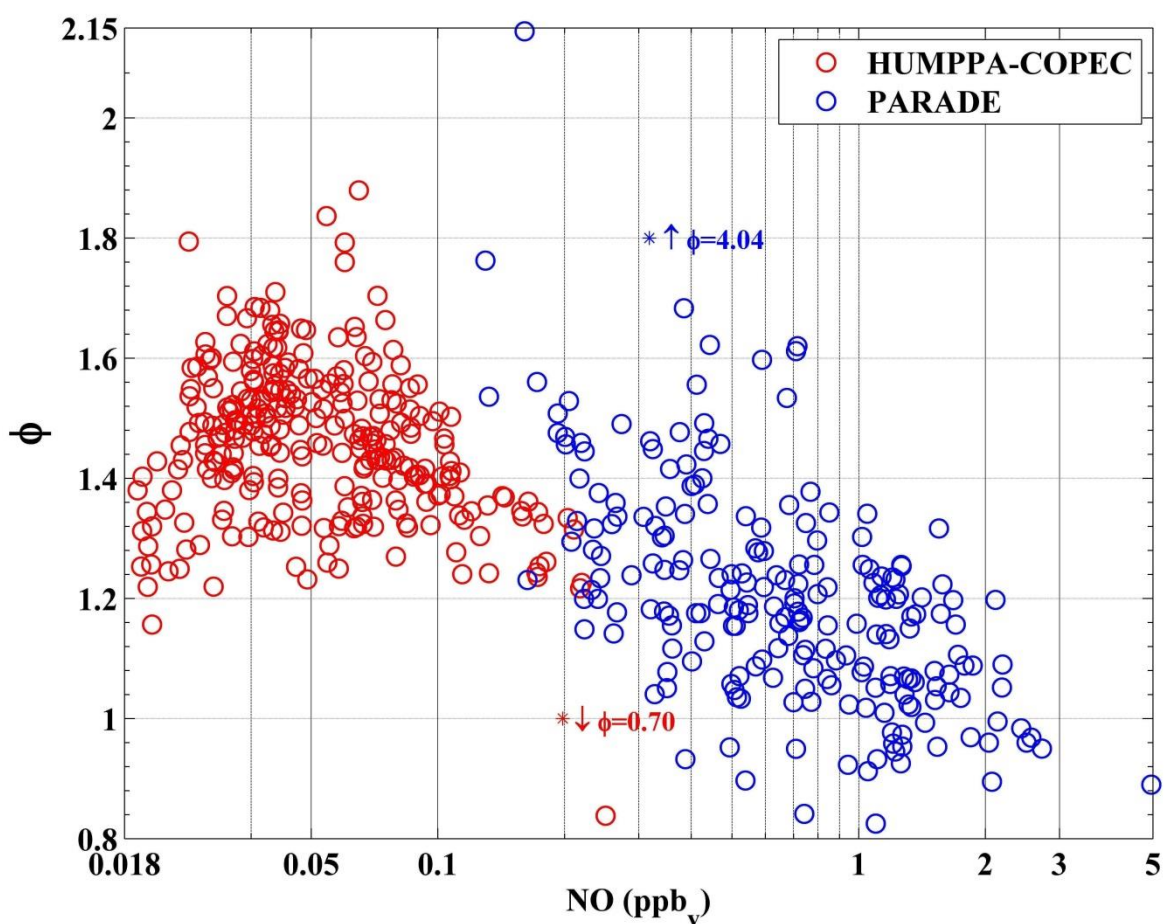


Fig. 5.2: Φ as a function of NO for HUMPPA-COPEC-2010 and PARADE-2011. NO concentrations on x-axis are represented in log scale.

5.2.1.1 Φ_{ext2} (Inclusion of NO + HO₂ in Φ)

BVOCs and OH are precursors for RO_x and larger concentrations of these species were measured (appendix 7.4.1.1) during HUMPPA-COPEC compared to PARADE, so the deviations in Φ (> 1) due to high RO_x are expected to be larger as well. HO₂ measurements were available during HUMPPA-COPEC. Based on these measurements, the contribution of R. 1.2 to Φ is introduced and defined as Φ_{ext2} (Eq. 5.1).

$$\Phi_{\text{ext2}} := \frac{j\text{NO}_2 [\text{NO}_2]}{(k_{1.1} [\text{O}_3] + k_{1.2} [\text{HO}_2]) [\text{NO}]} \quad \text{Eq. 5.1}$$

In (Eq. 5.1), $k_{1.2}$ (Atkinson et al., 2004) is the rate coefficient for the reaction of NO and HO₂ (R. 1.2). Φ and Φ_{ext2} are shown in Fig. 5.3 as a function of NO for HUMPPA-COPEC. The deviations ($\Phi > 1$) are reduced with inclusion of ‘NO + HO₂’ contributions, but Φ_{ext2} is still significantly larger (40%) than unity at levels of NO < 0.1 ppb_v and the remaining deviations (> 1) in Φ_{ext2} are expected to be from ‘NO + RO₂’. The calculated NO₂ from the PSS (Eq. 4.7) was about 17 % less than the measured NO₂ for HUMPPA-COPEC, whereas this difference was only 11 % in case of PARADE. If all deviations in Φ for HUMPPA-COPEC are related to peroxy radicals and no unknown chemistry is involved, then this difference of the calculated NO₂ (Eq. 4.7) tells that the concentrations of peroxyradicals are roughly a factor of about 1.5 higher than during PARADE. The difference decreased 17 % to 9 %, after inclusion of HO₂ in the PSS by using Eq. 5.2 for HUMPPA-COPEC. Eq. 5.2 is slightly different from Eq. 4.8, as this only contains HO₂ measurements, not RO_x (available in case of PARADE).

$$(\text{NO}_2)_{\text{PSSext2}} = \frac{(k_{1.1} [\text{O}_3] + k_{1.2} [\text{HO}_2]) [\text{NO}]}{j\text{NO}_2} \quad \text{Eq. 5.2}$$

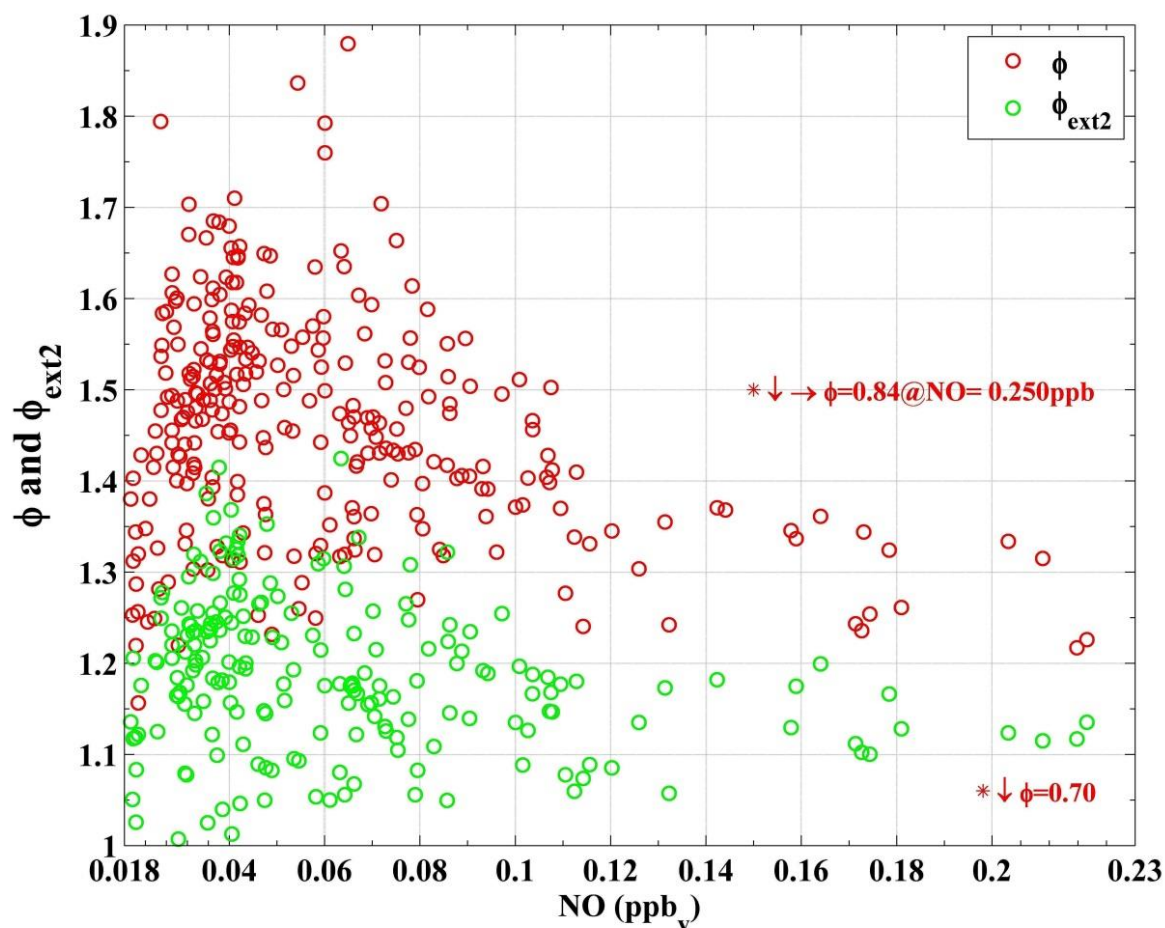


Fig. 5.3: Φ and $\Phi_{\text{ext}2}$ as a function of NO for HUMPPA-COPEC.

5.2.1.2 Estimation of RO_2 from $\Phi_{\text{ext}2}$

If it is assumed that the cause for the deviation in $\Phi_{\text{ext}2}$ (> 1) is RO_2 , then this difference (> 1) can be used to derive RO_2 concentrations for HUMPPA-COPEC according to relation Eq. 5.3.

$$(\text{RO}_2)_{\text{PSS}} \approx \frac{k_{1.1} [\text{O}_3] + k_{1.2} [\text{HO}_2]}{k_{1.3}} (\Phi_{\text{ext}2} - 1) \quad \text{Eq. 5.3}$$

In Eq. 5.3, $k_{1.3}$ is generic rate coefficient for reaction between RO_2 and NO ([Jenkin et al., 1997](#); [Saunders et al., 2003](#)). For HUMPPA-COPEC, the median value of the ratio between $(\text{RO}_2)_{\text{PSS}}$ and HO_2 is 1.04 ± 0.5 (1σ). $(\text{RO}_2)_{\text{PSS}}$ concentrations are shown as a function of NO in Fig. 5.4. A negative trend is observed in $(\text{RO}_2)_{\text{PSS}}$ with respect to increase in NO

concentrations. Concentrations of $(\text{RO}_2)_{\text{PSS}}$ below 20 ppt_v are calculated at NO levels > 100 ppt_v, while the variations in $(\text{RO}_2)_{\text{PSS}}$ at NO levels < 100 ppt_v are in the range of]0, 51[ppt_v.

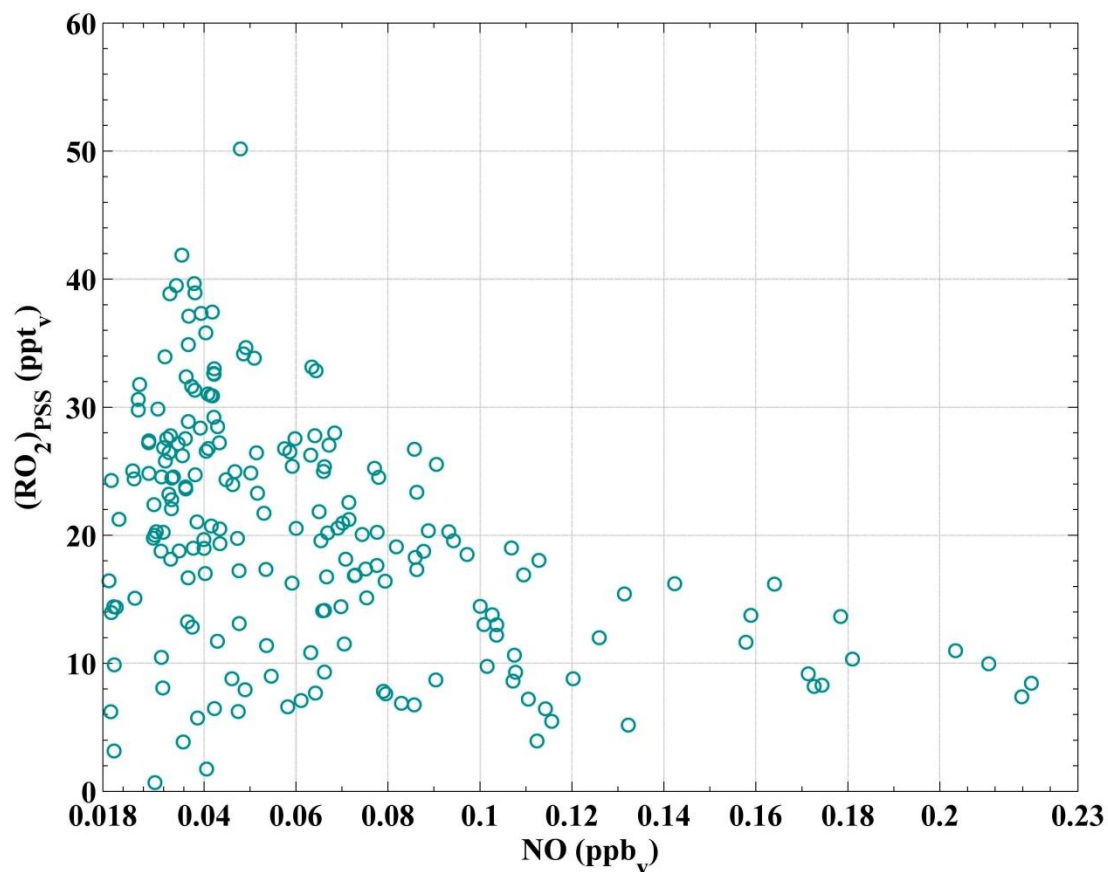


Fig. 5.4: Estimated RO_2 for HUMPPA-COPEC as a function of NO.

5.3 Box model simulations

Deviations (> 1) in Φ are observed as shown previously in [Fig. 5.3](#). These deviations (> 1) decline with the inclusion of the ‘HO₂ + NO’ contribution for the case of $\Phi_{\text{ext}2}$. RO₂ measurements were not available during HUMPPA-COPEC. So to assess the effects of RO₂ on remaining deviations (> 1) in $\Phi_{\text{ext}2}$ ([Fig. 5.3](#)), an alternative method is used to calculate RO₂.

Numerical models are used commonly in the atmospheric studies to simulate the effects of missing species. These models are often combined with chemical and physical processes. In this case, CAABA/MECCA [Chemistry As A Boxmodel Application / Module Efficiently Calculating the Chemistry of the Atmosphere] model is used to estimate the levels of RO₂ for HUMPPA-COPEC.

5.3.1 Introduction to the mechanism applied

CAABA is a box model used with MECCA chemistry and it is referred as CAABA/MECCA ([Sander et al., 2011a](#)). MECCA includes a comprehensive set of atmospheric reactions. In this case the monoterpene mechanism (MTM) is used together with the MIM3* mechanism. MIM3* mechanism is an MIM2 [Mainz Isoprene Mechanism ([Taraborrelli et al., 2009](#))]-like version of MIM3 ([Taraborrelli et al., 2012](#)) with oxidation of the major terpenes (α -pinene, β -pinene, β -myrcene, Δ^2 -carene, Δ^3 -carene and α -farnesene) additionally added ([Hens et al., 2013](#)). The difference between MIM3 and MIM3* is that reactions like ‘RO₂ + HO₂’, hydroperoxy-aldehyde and H-shifts are considered as in MIM2. The oxidation of α - and β -pinene is same as in MCM [Master Chemical Mechanism, MCM3.2 ([Jenkin et al., 1997](#); [Jenkin et al., 2005](#))], while the oxidation of β -myrcene and α -farnesene follows an isoprene like oxidation path with carene assumed to yield products similar to α -pinene. A detailed set of equations in the mechanism can be found in [Section 7.5](#) or in the supplement of ([Hens et al., 2013](#)). The deposition of nitrates, PAN, aldehydes, and peroxides in the mechanism is added from the literature ([Evans et al., 2000](#)). The halogen and sulphur chemistry with heterogeneous and aqueous phase reactions were deactivated in the simulations.

The model is constrained to include quantities like concentrations of NO, O₃, OH, HO₂, H₂O, HCHO, isoprene, α -pinene, β -pinene, Δ^3 -carene, β -myrcene and photolysis frequencies, i.e. the values are fixed to observed concentrations. The simulations terminates

when NO₂ has reached equilibrium. These simulations are only carried out if data of all constrained species is available at a photolysis frequency of $j\text{NO}_2 \geq 5 \times 10^{-3} \text{ s}^{-1}$.

5.3.2 Results of simulations

An estimate of different RO₂ species has been obtained based on CAABA/MECCA simulations. The CAABA/MECCA simulations are referred as simulations for the remainder of the text. The simulated median values of the mixing ratios of RO₂ species from different precursors are given in Table 5.2. From the simulations, about 70 % of relative median fractions are due to α -pinene-related RO₂ and methyl peroxy radical (CH₃O₂). CH₃O₂ is the largest individual contributor to the RO₂ concentration. The relative contributions to total RO₂ from isoprene-related RO₂ are less than 10 % based on median values. Total median contributions from β -pinene and myrcene-related RO₂ are less than 5 %. Less than 17 % of the total RO₂ fraction is from other RO₂ species, mainly with C₃, C₄ and higher carbon numbers. A bar chart is shown in Fig. 5.5 that shows the relative fraction of RO₂ species from different precursors as a function of the measured NO concentrations. In addition to CH₃O₂, monoterpene (pinene and carene)-related RO₂ are considerably large compared to isoprene-related RO₂. This confirms the importance of monoterpenes compared to isoprene-related chemistry in boreal forest condition as concluded in previous studies ([Williams et al., 2007](#); [Nölscher et al., 2012](#)).

Table 5.2: Average, median and standard deviation values of different RO₂(CAABA/MECCA) species.

Type	Average (ppt _v)	Median (ppt _v)	STD (1 σ)
CH ₃ O ₂	2.50	2.37	1.34
α - pinene related RO ₂	2.71	2.40	1.55
β - pinene related RO ₂	0.1	0.1	0.04
Myrcene related RO ₂	0.3	0.2	0.34
Isoprene related RO ₂	0.70	0.54	0.52
RO ₂ with C ₄	0.25	0.22	0.19
Others	1.10	0.86	0.84

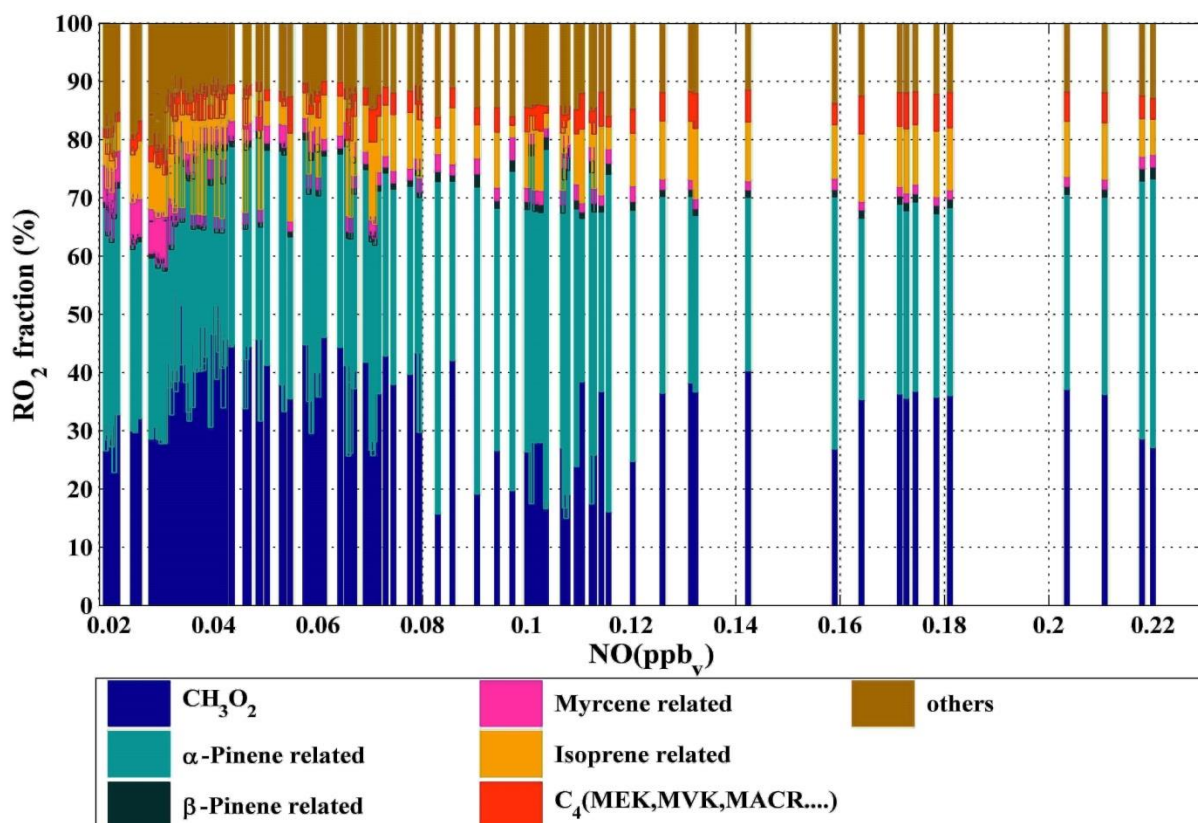


Fig. 5.5: Relative fraction of RO_{2(CAABA/MECCA)} as a function of NO.

The sum of RO₂ based on simulation values [(RO₂)_{CAABA/MECCA}] mostly stayed below 10 ppt_v for NO > 100 ppt_v. At low NO concentrations, the variations in (RO₂)_{CAABA/MECCA} are within the interval of]0, 27[ppt_v. Based on the median values, the derived (RO₂)_{PSS} from the PSS (Eq. 5.3) are higher than the simulated (RO₂)_{CAABA/MECCA} by a factor of 2.72 ± 3.6 for NO < 100 ppt_v and 2.02 ± 1.4 for NO > 100 ppt_v. More than 90 different RO₂ species are present in the applied mechanism and ‘RO₂ + NO’ reactions are differentiated based on yields and some rate coefficients for NO₂ formation. All ‘RO₂ + NO’ reactions from simulations are considered separately and applied individually to investigate the PSS. In Fig. 5.6, Φ , $\Phi_{\text{ext}2}$ and Φ_{ext} are plotted as a function of NO. As a brief reminder for the reader, Φ only contains the contribution of ‘NO + O₃’, while $\Phi_{\text{ext}2}$ only contains contributions from ‘NO + O₃’ and ‘NO + HO₂’. Φ_{ext} contains the contribution of ‘NO + O₃’, ‘HO₂ + NO’ and ‘(RO₂)_{1→n} + NO’. There are significant deviations (> 1) up to about 30 - 40 % remaining for levels of NO (< 80 ppt_v). At higher levels of NO (> 80 ppt_v), Φ_{ext} almost converges to 1.1, but It can be

clearly observed that the simulated (RO₂)_{CAABA/MECCA}, measured HO₂ and O₃ are not sufficient to justify NO to NO₂ conversion occurring especially at NO levels below 80 ppt_v.

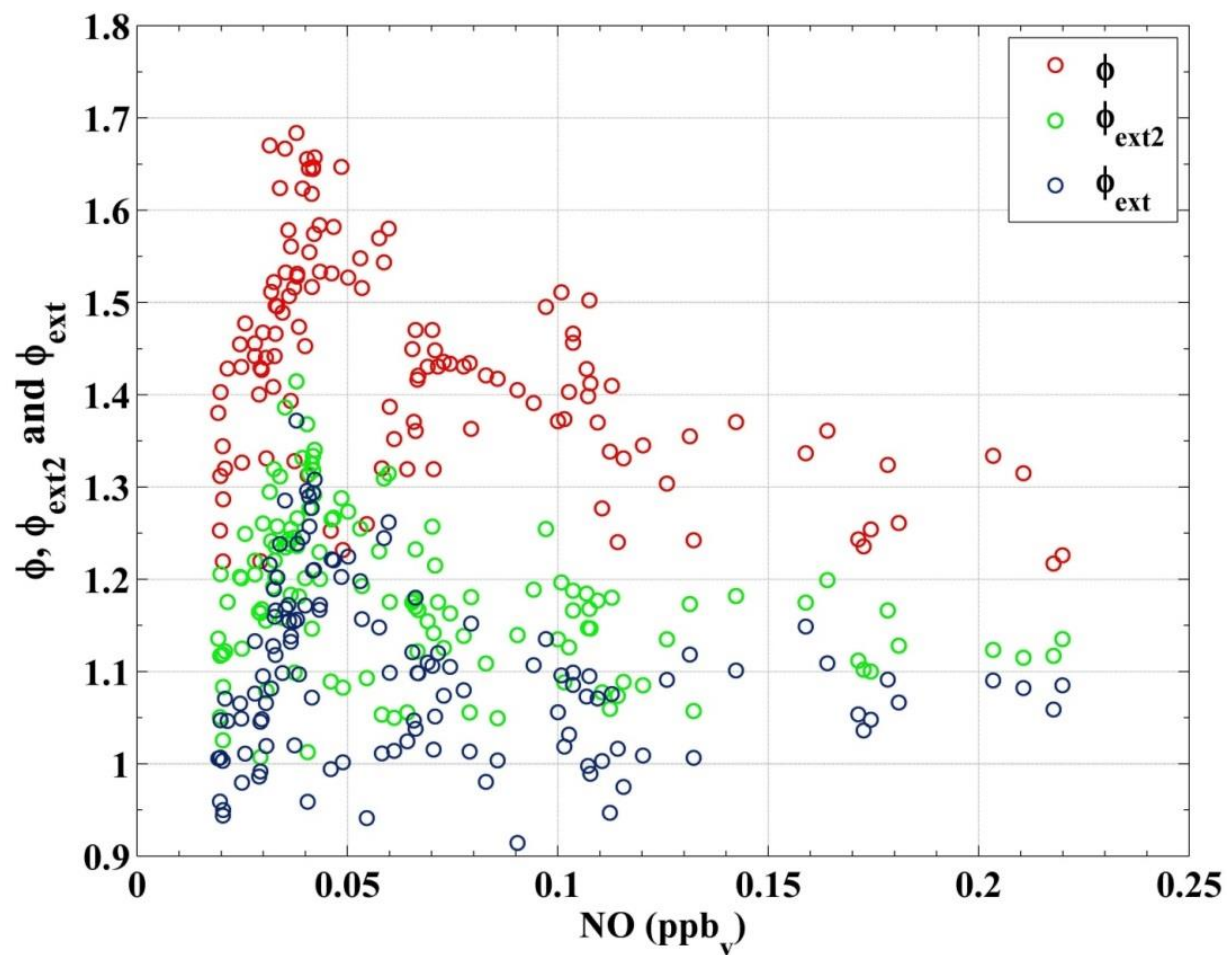


Fig. 5.6: Φ , Φ_{ext2} , and Φ_{ext} are shown as a function of NO.

5.3.2.1 Discrepancy between simulations and PSS

The possible reasons for the discrepancy between simulations and the PSS system are discussed in the following sections.

5.3.2.1.1 Rate coefficient for RO₂ + NO

It had been suggested that the rate coefficient for the calculation of (RO₂)_{PSS} could be critical ([Matsumoto et al., 2006](#)) and lead to a discrepancy. The rate coefficients for an individual ‘RO₂ + NO’ are different from the one used to derive (RO₂)_{PSS} from deviations of Φ_{ext2} ([Eq. 5.3](#)). This difference in the rate coefficients between an individual ‘RO₂ + NO’ and the generic rate coefficient can lead to the discrepancy. The advantage of the MIM3* mechanism is that the rate coefficients for the individual ‘RO₂ + NO’ reactions are differentiated based on yields and some rate coefficients for the formation of NO₂. A weighted rate coefficient ‘k_{1.3W}’ for the reaction ‘RO₂ + NO’ ([R. 1.3](#)) is calculated and compared with the generic rate coefficient ‘k_{1.3}’ applied in the case of (RO₂)_{PSS} ([Eq. 5.3](#)). The relative amounts of various RO₂ species to sum in RO₂ [(RO₂)_{CAABA/MECCA}] is provided by simulations. ‘k_{1.3W}’ is calculated according to relation [Eq. 5.4](#).

$$k_{1.3W} \approx \left[\frac{1}{\sum_{i=1}^N [R_i O_2]} \left(k_{R_1 O_2 + NO} [R_1 O_2] + \dots + k_{R_N O_2 + NO} [R_N O_2] \right) \right] \quad \text{Eq. 5.4}$$

Considering the temperature dependence, the calculated average and median values of weighted rate coefficient ‘k_{1.3W}’ are 9.53×10^{-12} and 9.45×10^{-12} cm³ molecule⁻¹ s⁻¹, respectively, while the generic rate coefficient ‘k_{1.3}’ in [Eq. 5.3](#) has average and median values of 9.15×10^{-12} and 9.14×10^{-12} cm³ molecule⁻¹ s⁻¹, respectively. So the difference between both rate coefficients is less than 5%. The difference between ‘k_{1.3W}’ and ‘k_{1.3}’ is not sufficient to explain a factor > 2 over-estimation of the derived (RO₂)_{PSS} compared to the simulated RO_{2(CAABA/MECCA)}.

5.3.2.1.2 Halogen oxides

Halogen chemistry was deactivated in simulations. Halogen oxides are well known to react with NO and form NO₂ ([R. 1.4](#)) but these reactions are not expected in the absence of halogen

sources like sea salt spray in the middle of a boreal forest region in the case of HUMPPA-COPEC. The required amounts of halogen oxides based on deviation in Φ_{ext} can be estimated as in Eq. 5.5.

$$(\text{XO})_{\text{PSS}} \approx \frac{k_{1.1} [\text{O}_3] + k_{1.2} [\text{HO}_2] + k_{1.3} [\text{RO}_2]_{\text{CAABA/MECCA}}}{k_{1.4}} (\Phi_{\text{ext}} - 1) \quad \text{Eq. 5.5}$$

In Eq. 5.5, $k_{1.4}$ is a rate coefficient for the reaction between halogen oxides and NO (R. 1.4). XO is representative of halogen oxides such as ClO, BrO and IO. The value of rate coefficients for reactions ‘ClO + NO’, ‘BrO + NO’, and ‘IO + NO’ varies in the range of $[1.95, 2.1] \times 10^{-11} \text{ cm}^3 \text{ molecule}^{-1} \text{ s}^{-1}$ at 298 K based on IUPAC data. In Eq. 5.5, an average value of rate coefficient ($1.91 \times 10^{-11} \text{ cm}^3 \text{ molecule}^{-1} \text{ s}^{-1}$) for the reactions ‘ClO + NO’, ‘BrO + NO’, and ‘IO + NO’ is used. Based on Eq. 5.5, the calculated average and median values for XO concentrations are 6.1 ± 5.1 (1σ) ppt_v and 6.0 ± 5.1 (1σ) ppt_v at NO < 100 ppt_v, respectively. The variations in the estimated concentrations of XO are in the range of]–4, 18[ppt_v at NO less than 100 ppt_v. For NO larger than 100ppt_v, the estimated average and median values for XO concentrations are 3.1 ± 2 (1σ) ppt_v and 2.5 ± 2 (1σ) ppt_v, respectively and the variation in the estimated XO are within the interval of]–2, 6[ppt_v. The required concentrations of XO to explain deviations in Φ_{ext} are very large and no measurement has been reported with such a high concentrations of halogen oxides in a boreal forest.

5.3.2.1.3 Unknown oxidant

Levels of RO₂ from deviations in Φ are not explained by the model studies or measurements in the past (Carpenter et al., 1998). It had been concluded that the presence of an unknown oxidant converting NO to NO₂ could lead to unexplained deviations in $\Phi > 1$ (Volz-Thomas et al., 2003;Mannschreck et al., 2004;Hosaynali Beygi et al., 2011). In order to test the hypothesis of unknown oxidant for the location, it is important to check whether the amount of VOCs yielding to RO₂ production is complete in simulations. Almost all VOCs react with OH, so the loss rate of OH in CAABA/MECCA would be a good indicator of completeness of the constrained VOCs.

The total OH reactivity (s^{-1}) [(OHReact)_{meas}] was measured above the forest canopy during HUMPPA-COPEC. (OHReact)_{meas} was detected based on a Comparative Reactivity Method (CRM). In the CRM, the total OH reactivity is determined by the competitive-

reactions of OH to a selected reagent e.g. pyrrole compared to OH by other atmospheric reactive compounds (Nölscher et al., 2012). The model does not provide the OH reactivity directly; therefore it is calculated based on simulation results by summing all loss rates of OH and dividing them by the OH concentration.

The ratio between the measured and simulated OH reactivity $[(\text{OHReact})_{\text{meas}} / (\text{OHReact})_{\text{CAABA/MECCA}}]$ is shown in Fig. 5.7 as a function of NO for HUMPPA-COPEC. The simulation failed to reproduce the values of $(\text{OHReact})_{\text{meas}}$. $(\text{OHReact})_{\text{CAABA/MECCA}}$ mostly under-estimated by a factor in the range of]1.01, 8[compared to the measured $(\text{OHReact})_{\text{meas}}$. Generally, the under-estimation of $(\text{OHReact})_{\text{CAABA/MECCA}}$ is larger at around 50 ppt_v NO and at about the same level of NO, the maximum deviations (> 1) were observed in Φ (Fig. 5.6). Also unexplained deviations in Φ_{ext} [with O₃, HO₂, and $(\text{RO}_2)_{\text{CAABA/MECCA}}$] are higher at similar scales of NO (Fig. 5.6). In simulations, it was observed that the constrained VOCs are not sufficient to explain $(\text{OHReact})_{\text{meas}}$. The reaction between VOCs and OH is a precursor for RO₂, so a missing OH reactivity in simulations is an indication of the missing RO₂ precursors, leading to under-estimation of $(\text{RO}_2)_{\text{CAABA/MECCA}}$ compared to $(\text{RO}_2)_{\text{PSS}}$. This could be a possible reason for the unexplained remaining deviations in Φ_{ext} after using $(\text{RO}_2)_{\text{CAABA/MECCA}}$. This hypothesis of missing VOCs for the input of simulation is tested further and explained in the next section.

5.3.2.2 Tuning of (OHReact)_{CAABA/MECCA}

A series of simulations were performed using an increment of the measured BVOCs concentrations large enough to achieve a match between the measured total OH reactivity [(OHReact)_{meas}] and the OH reactivity from the model [(OHReact)_{CAABA/MECCA}]. An initial guess for how much to increase all constrained BVOCs was provided by the difference in the ratio between (OHReact)_{meas} and (OHReact)_{CAABA/MECCA}. Increasing BVOCs concentrations by some factor, to get a match between (OHReact)_{meas} and (OHReact)_{CAABA/MECCA}, is referred to here as tuning (OHReact)_{CAABA/MECCA}. Tuning is done until (OHReact)_{CAABA/MECCA} and (OHReact)_{meas} agree within a difference of $\pm 5\%$. This procedure is only performed for those data points where the ratio (OHReact)_{meas} / (OHReact)_{CAABA/MECCA} was greater than 1. The ratio between (OHReact)_{meas} and tuned (OHReact)_{CAABA/MECCA} is shown in Fig. 5.7. Also, the plot in Fig. 5.7 is colour-coded to show the additional tuning factor for the measured BVOCs. A factor of 1 means no increase in the measured BVOCs whenever the measured reactivity was smaller than the model reactivity.

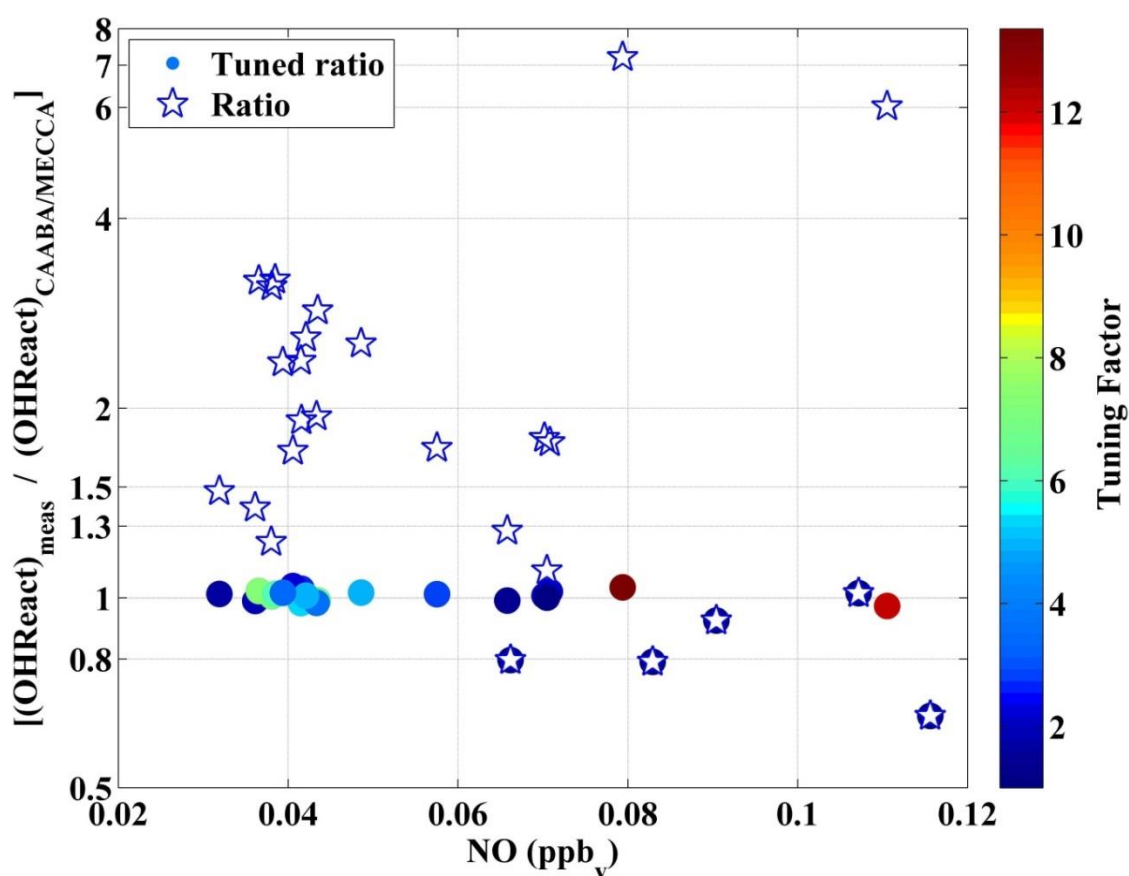


Fig. 5.7: Ratio between the total measured and simulated OH reactivity as a function of NO.

Prior to the tuning, no correlation was observed between the simulated RO_2 [$(\text{RO}_2)_{\text{CAABA/MECCA}}$] and $(\text{OHReact})_{\text{meas}}$ as shown in the left panel of Fig. 5.8. Based on simulations without the tuning, the ratio $(\text{RO}_2)_{\text{PSS}} / (\text{RO}_2)_{\text{CAABA/MECCA}}$ was 2.73 (Mdn.), $3.84 (\text{avg.}) \pm 3.6 (1\sigma)$ at NO concentrations of $\leq 100 \text{ ppt}_v$ and 2.03 (Mdn.), $2.24 (\text{avg.}) \pm 1.4 (1\sigma)$ at NO concentrations $> 100 \text{ ppt}_v$, respectively. $(\text{RO}_2)_{\text{CAABA/MECCA}}$ was lower than $(\text{RO}_2)_{\text{PSS}}$ by a factor 2 to 3.

After the tuning of the OH reactivity, $(\text{RO}_2)_{\text{CAABA/MECCA}}$ from the new simulations correlates with $(\text{OHReact})_{\text{meas}}$ as shown in the right panel of Fig. 5.8. The ratio between $(\text{RO}_2)_{\text{PSS}}$ and $(\text{RO}_2)_{\text{CAABA/MECCA}}$ is improved to 1.11 (Mdn.), $1.24 (\text{avg.}) \pm 0.6 (1\sigma)$ at less than 100 ppt_v of NO for the new simulations with the tuned OH reactivity. Based on this improvement for the ratio between $(\text{RO}_2)_{\text{PSS}}$ and $(\text{RO}_2)_{\text{CAABA/MECCA}}$, it is therefore likely that a lack of VOCs in the previous simulations was the major cause for underestimation of $(\text{RO}_2)_{\text{CAABA/MECCA}}$ compared to $(\text{RO}_2)_{\text{PSS}}$.

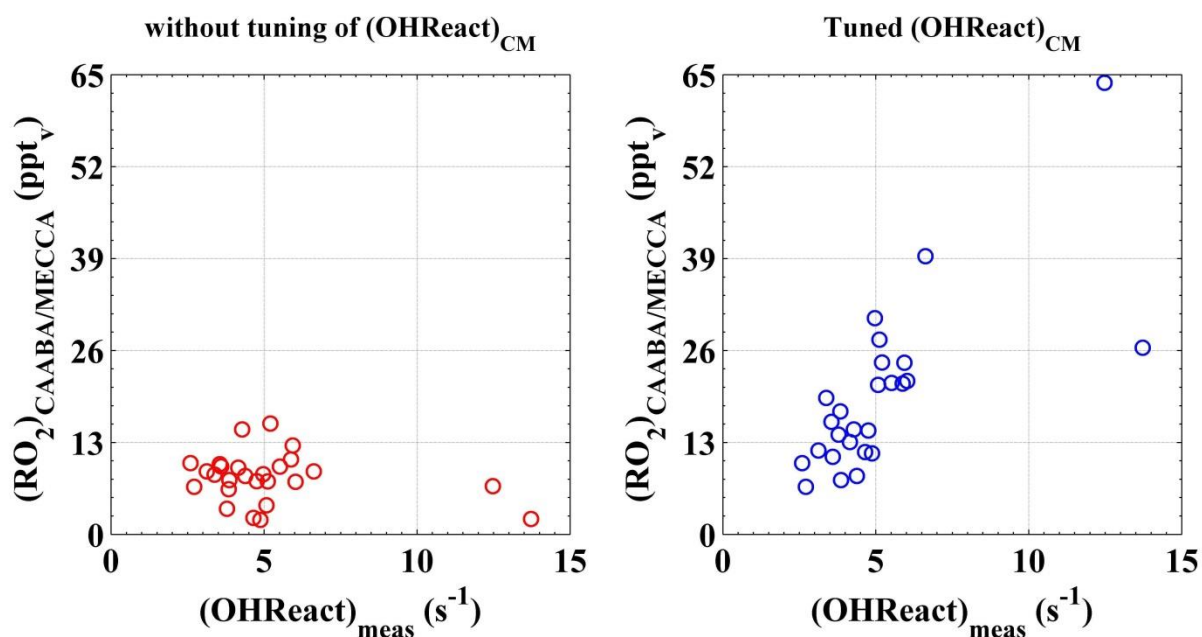


Fig. 5.8: RO_2 based on simulations as a function of the measured OH reactivity. The left hand side in the figure is prior to the tuning while the right hand side is based on tuned $(\text{OHReact})_{\text{CAABA/MECCA}}$.

The remaining deviations in $\Phi_{\text{ext}} (> 1)$ as shown previously in Fig. 5.6 are further investigated based on the new simulations with the tuned (OHReact)_{CAABA/MECCA}. Φ_{ext} is again calculated for the new simulations, and referred to here as $\Phi_{\text{ext(T)}}$, is shown in Fig. 5.9 along with Φ and Φ_{ext} . An improvement in the reduction of the deviation with the tuned (OHReact)_{CAABA/MECCA} for the case of $\Phi_{\text{ext(T)}}$ is clearly visible in Fig. 5.9. The overall median and average values of $\Phi_{\text{ext(T)}}$ are $1.001 \pm 0.105 (1\sigma)$ and $0.996 \pm 0.105 (1\sigma)$, respectively. Neglecting the one outlier in $\Phi_{\text{ext(T)}}$ [$\Phi_{\text{ext(T)}} = 0.63$ at $\text{NO} = 0.11 \text{ ppb}_v$], the median and average values for remaining of $\Phi_{\text{ext(T)}}$ are $1.00 \pm 0.07 (1\sigma)$ and $1.01 \pm 0.07 (1\sigma)$, respectively.

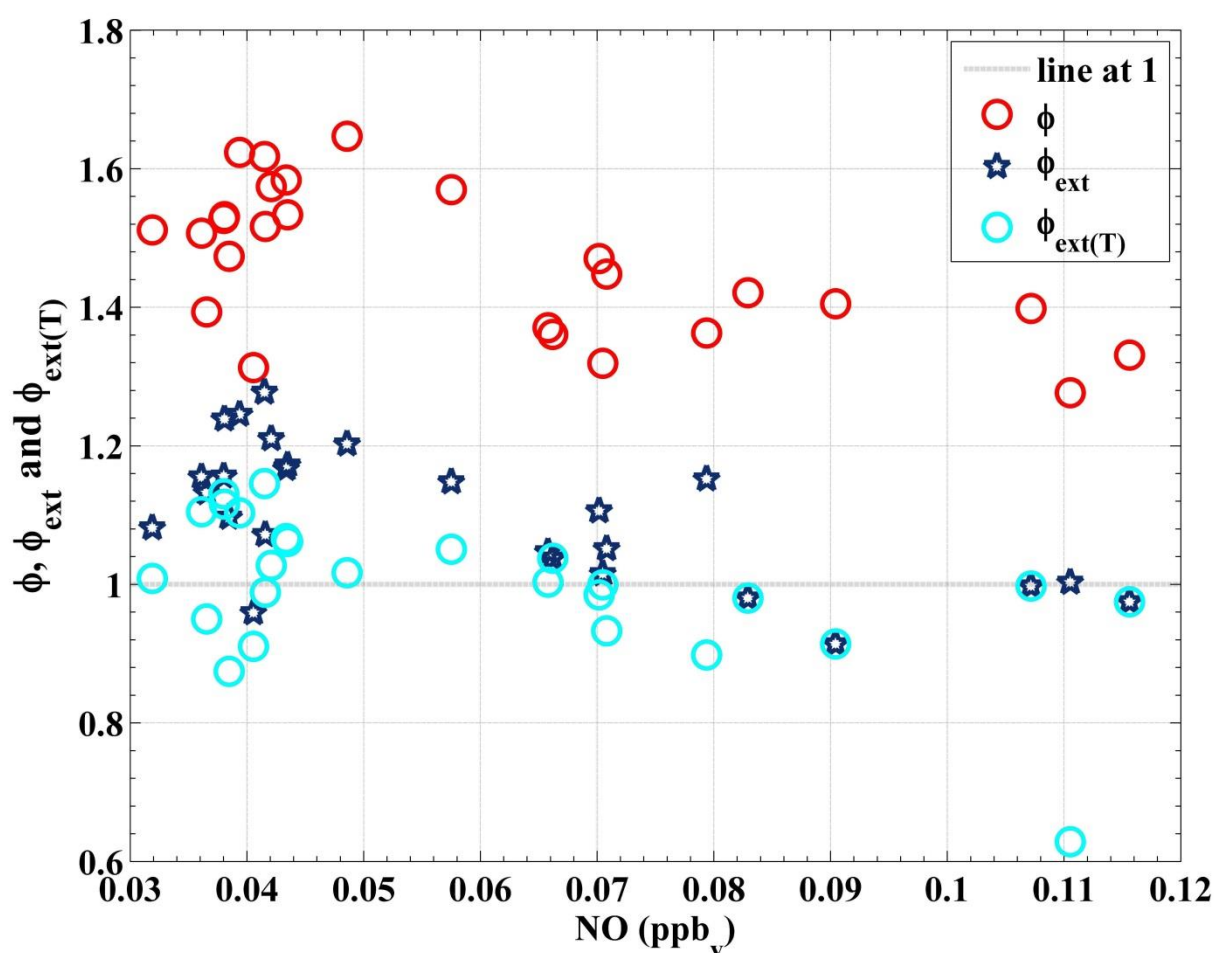


Fig. 5.9: Φ , Φ_{ext} is based on the measured data and simulations at normal BVOCs concentrations. $\Phi_{\text{ext(T)}}$ is based on results from the new simulations with the tuned OH reactivity in the model.

Prior to the tuning of $(\text{OHReact})_{\text{CAABA/MECCA}}$, the ratio between the measured NO_2 [$\text{NO}_{2(\text{meas})}$] and the simulated NO_2 [$\text{NO}_{2(\text{CAABA/MECCA})}$] as a function of NO concentration is shown in (Fig. 5.10, [A]). A considerable difference, larger than the uncertainty (avg. $< 13\%$) of the NO_2 measurement, exists between the measured NO_2 and $\text{NO}_{2(\text{CAABA/MECCA})}$. 41.7 % of $\text{NO}_{2(\text{CAABA/MECCA})}$ data points under-estimated compared to the NO_2 measurement by]10, 40[%. About 45.6 % of $\text{NO}_{2(\text{CAABA/MECCA})}$ data points from simulations under-estimated the measurements $\leq 10\%$. Only 12.6 % of $\text{NO}_{2(\text{CAABA/MECCA})}$ data points over-estimated the measurements up to 10 %.

The ratio between $\text{NO}_{2(\text{meas})}$ and $\text{NO}_{2(\text{CAABA/MECCA})}$ is improved for the simulations with the tuned $(\text{OHReact})_{\text{CAABA/MECCA}}$. For the data set where OH reactivity data was available, except for a single outlying data point with a value of 0.61 at 110 ppt_v of NO , all of the deviations in $\text{NO}_{2(\text{meas})} / \text{NO}_{2(\text{CAABA/MECCA})}$ (tuned) are within $\pm 15\%$ from unity as shown in Fig. 5.10 panel [B]. The corresponding data points without tuned $(\text{OHReact})_{\text{CAABA/MECCA}}$ simulations are plotted in Fig. 5.10 panel [B] for comparison. The error bars are plotted in Fig. 5.10 panel [B] at $1 \pm$ uncertainty of the measured NO_2 . Despite a single point, all of variations in the ratio are below the uncertainty of NO_2 measurements.

The production rates of O_3 are also simulated to compare with $\text{P}(\text{O}_3)_{\text{PSS}}$ (Eq. 1.10). A minor branch of the reaction ‘ $\text{RO}_2 + \text{HO}_2$ ’ that leads to O_3 formation had been reported in literature [e.g. MCM3.2 (Jenkin et al., 1997;Saunders et al., 2003), (Groß, 2013)]. In the simulation results, the ‘ $\text{RO}_2 + \text{HO}_2$ ’ branch leading to the O_3 formation was in order of 10^5 molecule $\text{cm}^{-3} \text{s}^{-1}$ and it is therefore negligible compared to reactions ‘ $\text{RO}_2 + \text{NO}$ ’ and ‘ $\text{HO}_2 + \text{NO}$ ’ in the order of 10^7 molecule $\text{cm}^{-3} \text{s}^{-1}$.

Without the tuned $(\text{OHReact})_{\text{CAABA/MECCA}}$, the production rates of O_3 [$\text{P}(\text{O}_3)_{\text{CAABA/MECCA}}$] based on simulations were under-estimated by about 30 to 50 % compared to the rate derived from the PSS (Eq. 1.10, $\text{P}(\text{O}_3)_{\text{PSS}}$). The average and median values of the ratio $\text{P}(\text{O}_3)_{\text{PSS}} / \text{P}(\text{O}_3)_{\text{CAABA/MECCA}}$ at $\text{NO} < 100$ ppt_v were 1.50 ± 0.5 (1σ) and 1.46 ± 0.5 (1σ), respectively. At $\text{NO} > 100$ ppt_v, the average and median values of the ratio $\text{P}(\text{O}_3)_{\text{PSS}} / \text{P}(\text{O}_3)_{\text{CAABA/MECCA}}$ were 1.30 ± 0.27 (1σ) and 1.31 ± 0.27 (1σ), respectively.

With the tuned $(\text{OHReact})_{\text{CAABA/MECCA}}$, the ratio between $\text{P}(\text{O}_3)_{\text{PSS}}$ and $\text{P}(\text{O}_3)_{\text{CAABA/MECCA}}$ is notably improved for simulations. The new average and median values of this ratio at $\text{NO} < 100$ ppt_v are 1.04 ± 0.24 (1σ) and 1 ± 0.24 (1σ), respectively. This improvement in the ratio shows that the model has explained reasonably well the production of O_3 compared to the PSS approach and the previously found bias is considerably reduced.

The uncertainty of simulated results due to rate coefficients is estimated by using the Monte Carlo method in CAABA/MECCA (Sander et al., 2011a). Typically, a Monte Carlo simulation consists of several hundred runs of the applied mechanism with slightly different rate coefficients in each run and the given model run is terminated at the equilibrium condition like just the actual simulation. The boundary for the variations in rate coefficients for Monte Carlo simulation was kept within the uncertainty of a rate coefficient. In the absence of an uncertainty estimate in the literature, the relative uncertainty of 25 % was used. The result from a Monte Carlo simulation of 9999 runs based on MIM3* mechanism is shown in Fig. 5.11. The binned frequency distribution from the Monte Carlo simulation is shown for various estimated quantities, such as the concentration of (RO₂)_{CAABA/MECCA}, the concentration of NO_{2(CAABA/MECCA)}, the OH reactivity based on the model simulations (OHReact)_{CAABA/MECCA} and the instantaneous production rates of O₃ from simulations [P(O₃)_{CAABA/MECCA}]. The relative uncertainty of different quantities based on Monte Carlo simulations is given in Table 5.3. The values in Table 5.3 describe the largest found uncertainty due to rate coefficients.

Table 5.3: Relative uncertainty based on Monte Carlo simulations

	Relative uncertainty (1σ)
(RO ₂) _{CAABA/MECCA}	14 %
NO _{2(CAABA/MECCA)}	25 %
(OHReact) _{CAABA/MECCA}	10 %
P(O ₃) _{CAABA/MECCA}	12 %

Concluding for HUMPPA-COPEC, it has been observed that the NO to NO₂ conversion is reasonably well explained for the boreal forest and the deviations in Φ during HUMPPA-COPEC are accounted for by known chemistry. The main contributors to deviations in Φ are peroxy radicals. By adding measured HO₂ + modelled RO₂ using the tuned OH reactivity, the overall median and average values of $\Phi_{\text{ext}(T)}$ were 1.001 ± 0.105 (1σ) and 0.996 ± 0.105 (1σ). Therefore, PSS is an effective and realistic approach for assessing

NO to NO₂ conversion. Further, NO_x chemistry in the current chemical mechanism reasonably agrees with the PSS system.

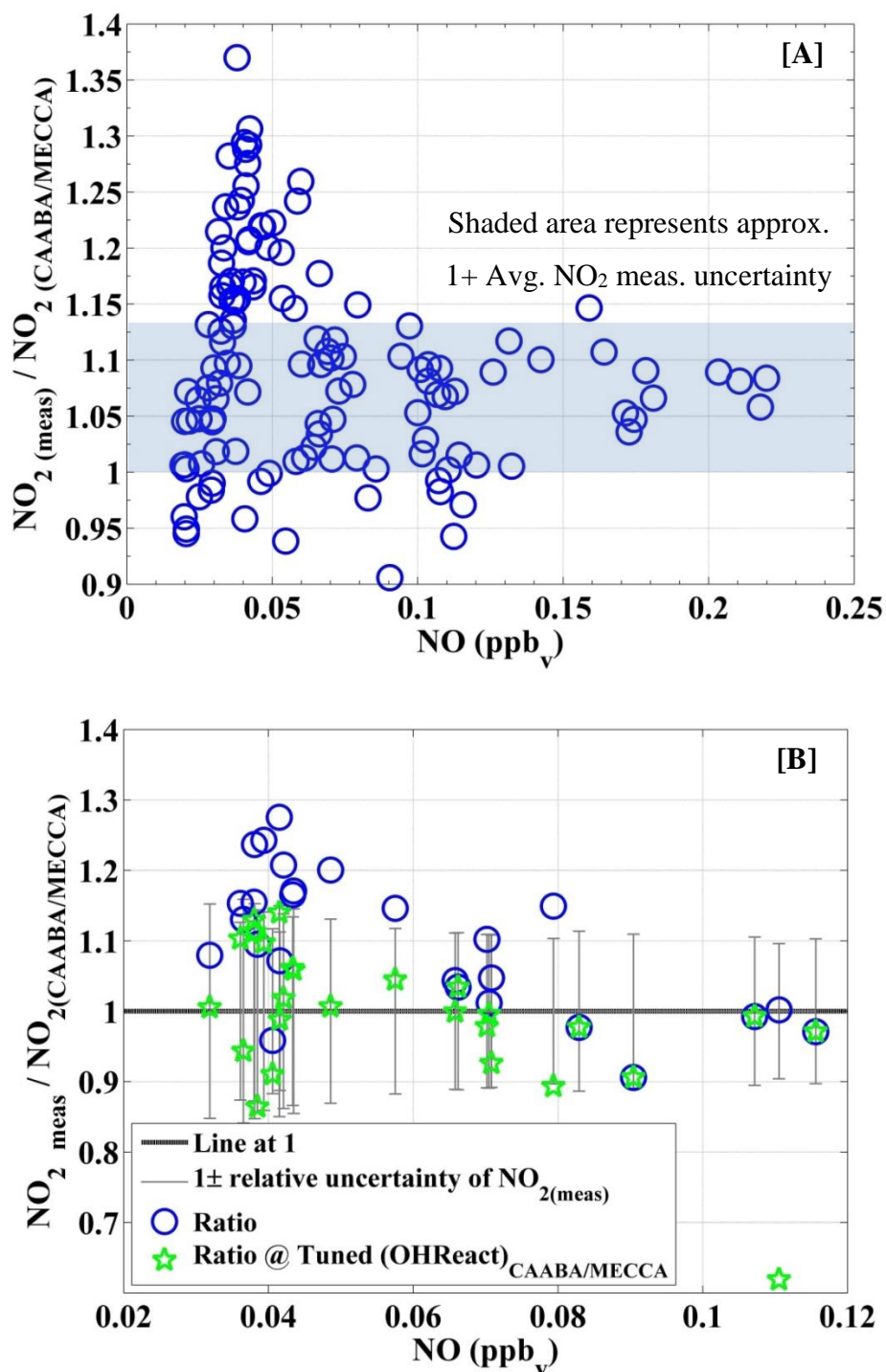


Fig. 5.10: [A] Ratio $[\text{NO}_{2(\text{meas})} / \text{NO}_{2(\text{CAABA/MECCA})}]$ as a function of NO for simulations without tuned OH reactivity. [B] Ratio $[\text{NO}_{2(\text{meas})} / \text{NO}_{2(\text{CAABA/MECCA})}]$ as a function of NO for simulations with tuned $(\text{OHReact})_{\text{CAABA/MECCA}}$.

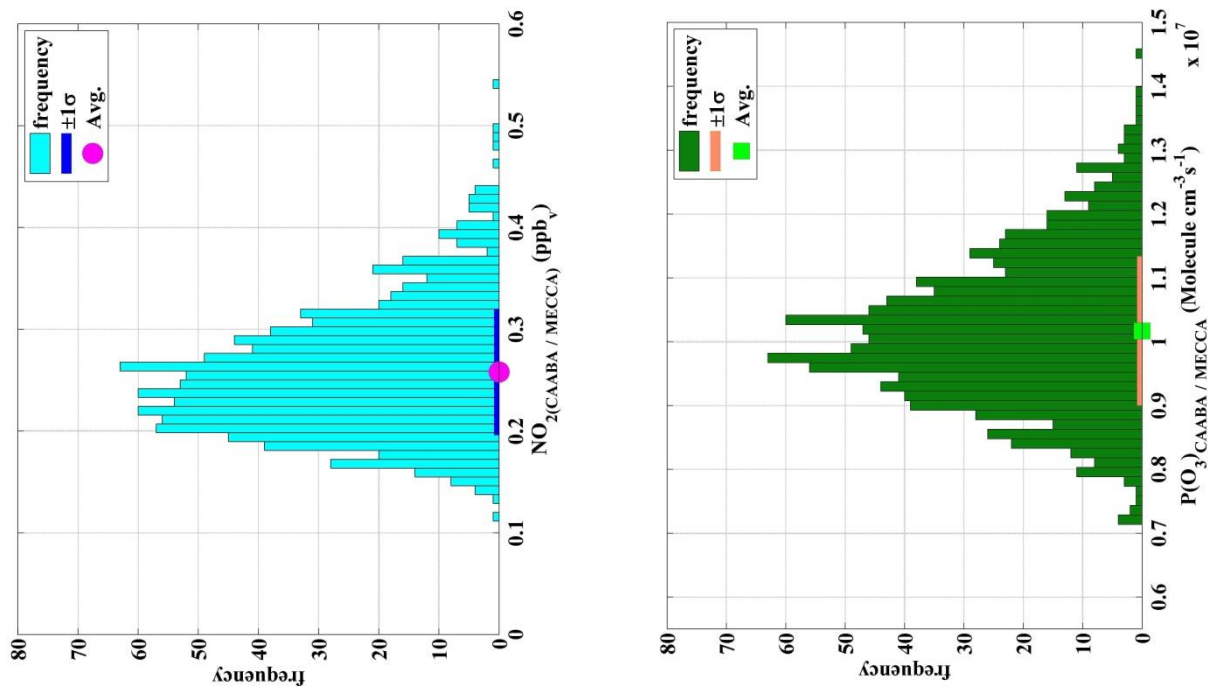
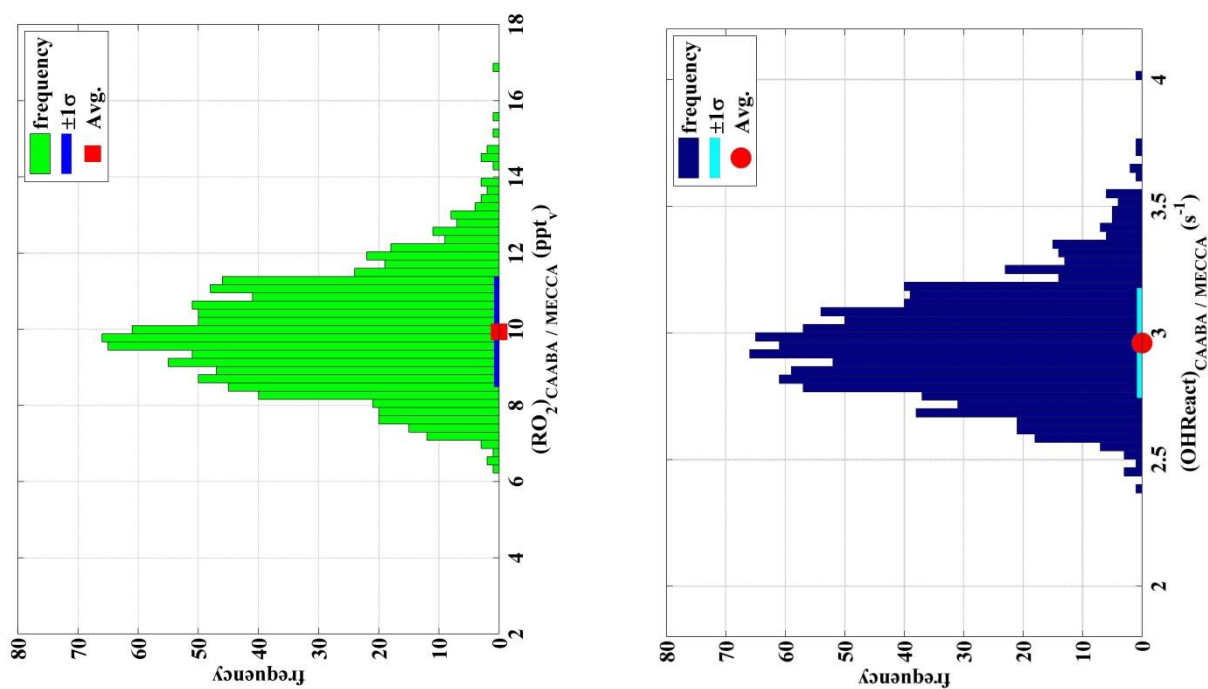


Fig. 5.11: Monte Carlo simulations for the estimation of uncertainties due to rate coefficients in $(\text{RO}_2)_{\text{CAABA/MECCA}}$, $\text{NO}_2(\text{CAABA/MECCA})$, $(\text{OHReact})_{\text{CAABA/MECCA}}$ and $\text{P}(\text{O}_3)_{\text{CAABA/MECCA}}$.



5.4 Trend of instantaneous O₃ production in NO_x-limited regime

The instantaneous photochemical production rate of O₃ [P(O₃)_{PSS}] is calculated by using Eq. 1.10. The median value of P(O₃)_{PSS} for HUMPPA-COPEC is $1.15 \pm 0.60 (1\sigma) \times 10^7$ molecules cm⁻³ s⁻¹. The instantaneous production rates of HUMPPA-COPEC are roughly a factor > 2 smaller than for PARADE at similar conditions of radiations ($j\text{NO}_2 \geq 5 \times 10^{-3} \text{ s}^{-1}$). P(O₃)_{PSS} for HUMPPA-COPEC as a function of NO is shown in Fig. 5.12. The absolute uncertainty in P(O₃)_{PSS} at NO levels ≥ 0.1 ppb_v is in the range of $[0.9, 2.7] \times 10^7$ molecules cm⁻³ s⁻¹. At low NO levels < 0.1 ppb_v, the absolute uncertainty varied within the interval of $[0.6, 1.4] \times 10^7$ molecules cm⁻³ s⁻¹. The absolute average uncertainty of P(O₃)_{PSS} due to measurements is 1×10^7 molecules cm⁻³ s⁻¹ with a 1σ variability of $\pm 0.3 \times 10^7$ molecules cm⁻³ s⁻¹. Generally, the relative uncertainties in P(O₃)_{PSS} decrease with increasing NO. A linear increase in P(O₃)_{PSS} is observed with respect to increasing NO during HUMPPA-COPEC. In Fig. 5.12, P(O₃)_{PSS} shows two distinct gradients in respect to NO. The best separation between the two gradients could be distinguished by temperature $\leq / > 21$ °C but the mechanism for an underlying process related to temperature is not clear. Comparing the slopes, the rise in P(O₃)_{PSS} with respect to NO were about 3 times faster at values below about 50 ppt_v of NO (Fig. 5.12) compared to values at elevated NO levels.

The instantaneous production of O₃ is proportional to the NO_x concentration during HUMPPA-COPEC. This type of trend of the O₃ production versus NO_x is usually expected in VOC-saturated or NO_x-limited conditions (Thornton et al., 2002). In this regime, the main loss of radicals is due to the ‘radical + radical’ chain termination reactions such as ‘HO₂ + OH’, ‘HO₂ + HO₂’, and ‘HO₂ + RO₂’. Note ‘RO₂ + RO₂’ reactions are not loss reactions for the radicals and therefore not considered. The role of ‘radical + NO_x’ reactions leading to chain termination is not expected to be significant. This has been investigated using a similar approach to one in a previous study at a different location (Thornton et al., 2002). The losses of radicals due to chain termination processes are calculated from equations (Eq. 5.6, Eq. 5.7 and Eq. 5.8) as described in (Thornton et al., 2002).

$$L\text{NO}_x \text{HO}_x = L\text{NO}_x + L\text{HO}_x \quad \text{Eq. 5.6}$$

$$L\text{NO}_x = k_{1.7} [\text{NO}_2][\text{OH}] + \alpha_{\text{eff}} \times k_{1.14} [(\text{RO}_2)_{\text{PSS}}][\text{NO}] \quad \text{Eq. 5.7}$$

$$LHO_x = 2k_{HO_2+OH} [HO_2][OH] + 2k_{HO_2+HO_2} [HO_2]^2 + 2k_{HO_2+RO_2} [HO_2][(RO_2)_{PSS}] \quad \text{Eq. 5.8}$$

In Eq. 5.7 and Eq. 5.8, generic rate coefficients are considered for ‘ k_{RO_2+NO} ’ and ‘ $k_{HO_2+RO_2}$ ’ based on MCM3.2 (Jenkin et al., 1997;Saunders et al., 2003). The ANs production is described as in the reaction R. 1.14 by the branching ratio (α_{eff}). The average fraction for the production of organic nitrates with > 2 carbon atoms can be up to 10 % under typical BVOCs emissions like isoprene and monoterpenes from a forest (Browne and Cohen, 2012). However, the fraction for the formation of $CH_3O_2 + NO \rightarrow CH_3ONO_2$ is only $(1 \pm 0.7) \%$ (Butkovskaya et al., 2012). In the case of the tuned (OHReact)_{CAABA/MECCA} (Section 5.3.2.2), the median value of the CH_3O_2 relative contribution to total RO_2 was only 23.7 %. The effective branching ratio (α_{eff}) for ‘ $(RO_2)_{PSS} + NO$ ’ in Eq. 5.7 should be smaller than 10 % as $(RO_2)_{PSS}$ has major contributions from both types of VOCs, i.e. biogenic and CH_4 . By considering a 1 % yield of ANs from CH_3O_2 and 10 % yield of ANs from the rest of RO_2 , a value for $\alpha_{eff} \approx 7$ to 8 % had been determined for the total ANs formation in Eq. 5.7. A more detailed analysis is done in Section 5.6.

Radical + radical reactions (Eq. 5.8) have shown a clear dominance over ‘radicals + NO_x’ reactions (Eq. 5.7) for this area. A median value of $1.24 \pm 0.7 (1\sigma) \times 10^7$ molecules $cm^{-3} s^{-1}$ is calculated for LHO_x (Eq. 5.8), which is much higher than that for LNO_x (Eq. 5.7) with a median value of only $0.06 \pm 0.03 (1\sigma) \times 10^7$ molecules $cm^{-3} s^{-1}$. The ratios [LHO_x / LNO_xHO_x and LNO_x / LNO_xHO_x] are plotted against NO in Fig. 5.13. The relative efficiency (loss / total loss) of both loss processes are clearly separated over the whole range of NO concentrations during HUMPPA-COPEC. The loss of radicals due to ‘radical + radical’ reactions is dominant over the whole range of NO concentrations compared to the loss process due to reaction with NO_x. The efficiency of the loss due to radicals radicals reactions stays above 90 % below 0.1 ppb_v of NO. Generally a crossover in efficiencies is associated with the change of chemical regimes from VOC-saturated to VOC-limited (Thornton et al., 2002). The efficiencies of both loss processes approached at elevated NO level > 0.2 ppb_v but never crossed each other. This supports the hypothesis that the regime during HUMPPA-COPEC was mainly VOC-saturated.

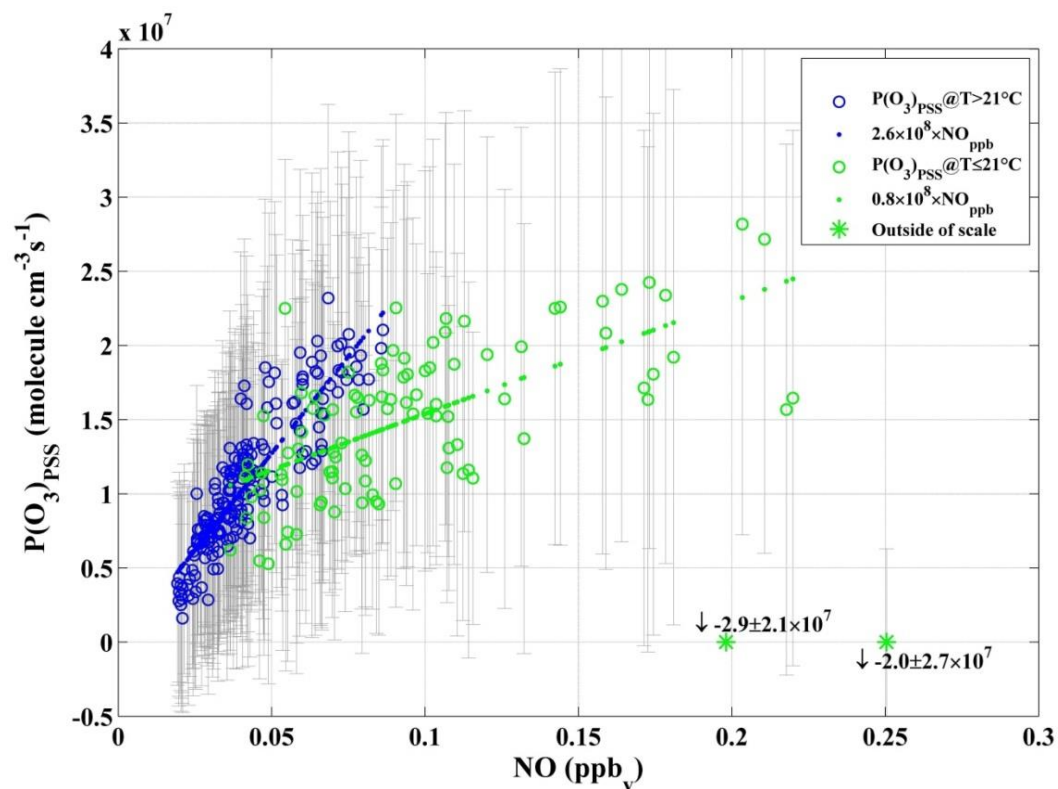


Fig. 5.12: P(O₃)_{PSS} as a function of NO during HUMPPA-COPEC-2010.

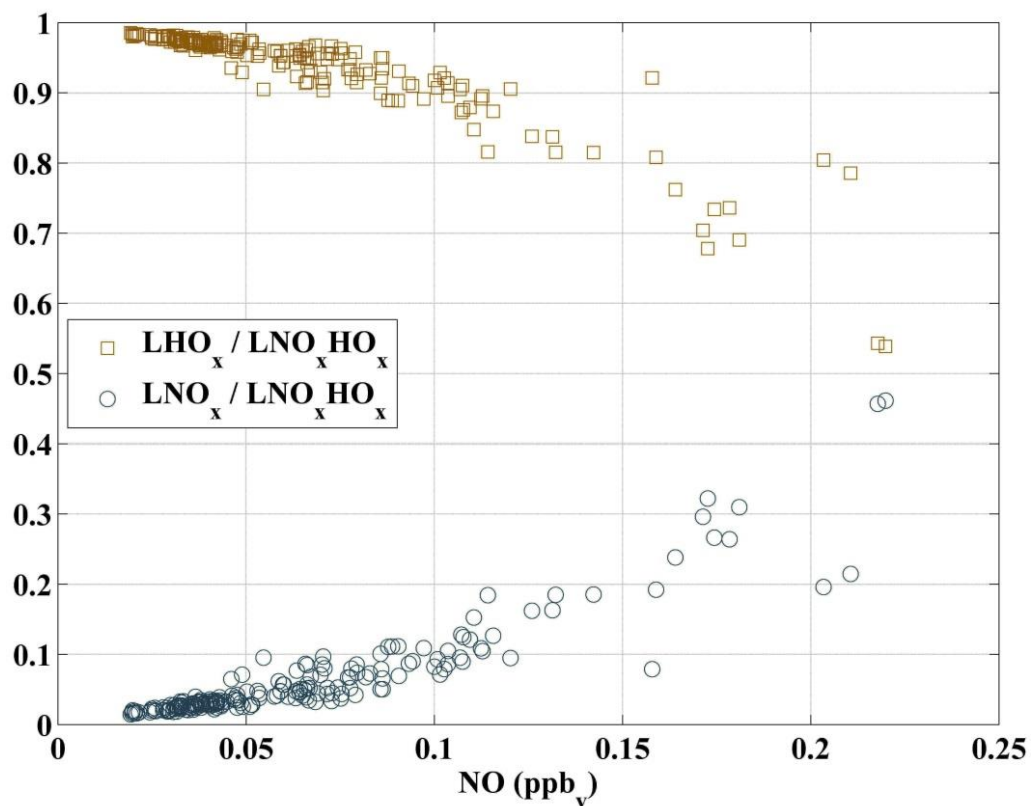
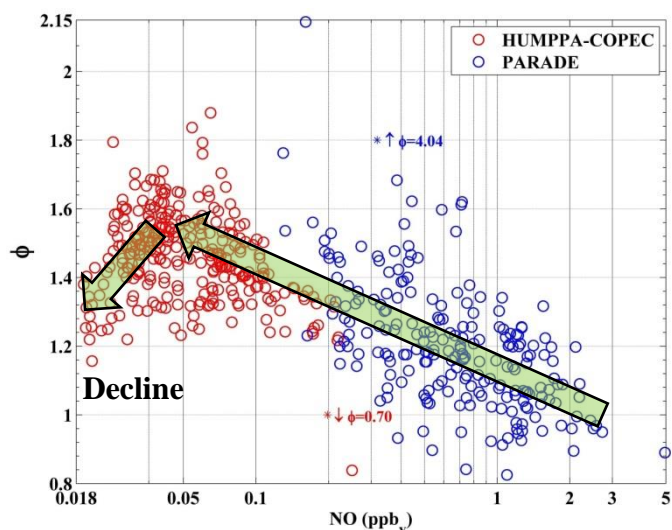


Fig. 5.13: The efficiency of the chain termination processes as a function of NO.

5.5 Decline in Φ at low NO

A negative trend was observed in Φ with decrease in the NO concentrations from about 44 to 20 ppt_v (Fig. 5.2). The peak value of Φ was observed at about 44 ppt_v of NO. The peak value (at 44 ppt_v NO) is determined by taking the average of Φ over NO bins of 10 ppt_v. A decrease was observed in OH and HO₂ with respect to the decrease in NO below 44 ppt_v (Section 7.4.1.4) during HUMPPA-COPEC. This decrease in radicals might be related to the decrease in the production of radicals or an increase in the loss of radicals mainly due to ‘radical + radical’ reactions. OH is the precursor for HO₂ and RO₂, so a decrease in the OH concentrations would also lead to a decrease in HO₂ and RO₂ concentrations. The conditions during HUMPPA-COPEC were mostly NO_x-limited (Fig. 5.13). The point of decline at the peak in Φ is selected for further investigation of the production and loss efficiencies of O₃ under a NO_x-limited regime.



(Fig. 5.2): Φ as a function of NO.

The conditions during HUMPPA-COPEC were mostly NO_x-limited (Fig. 5.13). The point of decline at the peak in Φ is selected for further investigation of the production and loss efficiencies of O₃ under a NO_x-limited regime.

The instantaneous *in-situ* production rate of O₃ [$P(O_3)_{PSS}$ as in Eq. 1.10] was compared with the direct and indirect loss rates of O₃. The direct loss rates of O₃ [$DL(O_3)$] were calculated by considering individual available measurements of OH, HO₂ and BVOCs. ‘Radical + radical’ reactions decrease the *in-situ* production efficiency of O₃. Radicals are formed in the chain of O₃ as O₃→OH→RO_x→O₃; at the end of chain, the initial O₃ is recycled. But ‘radical + radical’ reactions lead to a chain termination and the initial O₃ is not recycled. The radical loss rate due to ‘radical + radical’ reactions is referred as an indirect loss rate of O₃ [$IL(O_3)$]. For HUMPPA-COPEC, $IL(O_3)$ and $DL(O_3)$ are described in Eq. 5.9 and Eq. 5.10, respectively.

$$IL(O_3) = L_{HO_2+OH} + L_{HO_2+HO_2} + L_{HO_2+RO_2} \quad \text{Eq. 5.9}$$

$$DL(O_3) = k_{O_3+OH} [O_3][OH] + k_{O_3+HO_2} [O_3][HO_2] + k_{O_3+BVOCs} [O_3][BVOCs] \quad \text{Eq. 5.10}$$

The balance between the production and loss rates of O_3 is an important factor in the tropospheric O_3 budget. HO_2 and RO_2 reactions with NO (R. 1.2 and R. 1.3) lead to O_3 production whereas ‘ $HO_2 + OH$ ’, ‘ $HO_2 + RO_2$ ’, and ‘ $HO_2 + HO_2$ ’ are indirectly related to O_3 loss with some exceptions, but not a significant one in some ‘ $HO_2 + RO_2$ ’ reactions. In order to examine the efficiency of radical reaction rates as a function of NO_x , the total rate (**TR**) is defined as the sum of *in-situ* reaction rates based on reactions ‘ $HO_2 + NO$ ’ and ‘ $RO_2 + NO$ ’ that collectively lead to O_3 production and ‘radical + radical’ reactions that do not lead to O_3 production. The relative efficiencies in these cases are defined as ratios of $R_{Rad+Rad} / TR$ and R_{Rad+NO} / TR . These ratios of radical reaction efficiencies are shown in the upper panel of Fig. 5.14. A negative trend is seen in the ratio R_{Rad+NO} / TR with declining NO. The ratio R_{Rad+NO} / TR declines from about 0.9 at $NO > 150$ ppt_v to approx. 0.25 at $NO < 20$ ppt_v. The competing ratio $R_{Rad+Rad} / TR$ showed an increase from about 0.15 at $NO > 150$ ppt_v to about 0.75 at $NO < 20$ ppt_v. A crossover point between ratios R_{Rad+NO} / TR and $R_{Rad+Rad} / TR$ can be observed around 50 ppt_v of NO. The role of radicals is defined by the availability of NO_x in context of the O_3 production or loss. Under low NO_x conditions, the competition is shifted in favour of ‘radical + radical’ reactions compared to ‘ $RO_x + NO$ ’ reactions. This shift is suggested by the **decline** in Φ for the condition during HUMPPA-COPEC because deviations (> 1) in Φ are directly related to concentration of RO_x .

The O_3 production and direct loss rates as a function of NO are shown in the lower panel of Fig. 5.14. The measured concentrations of BVOCs (isoprene, α -pinene, β -pinene, β -myrcene and Δ^3 -carene) are used for the calculation of the O_3 loss rates. Due to less frequent data a median value of loss frequency based on methacrolein (MACR) and methyl vinyl ketone (MVK) measurements is added in calculating the loss rates of O_3 . The measurements of the O_3 deposition velocity were also available. The depositional loss rates of O_3 are calculated with BLH of 1000m during HUMPPA-COPEC. Based on radiosonde measurements, the average, median, and geometric-mean values of the BLH for the mixed layer were 1081, 1100, and 956 meters, respectively.

The $P(O_3)_{PSS}$ (Eq. 1.10) remained higher than $DL(O_3)$ (Eq. 5.10) over wide ranges of $NO > 30$ ppt_v concentrations. But including the depositional loss of O_3 (Dep) to $DL(O_3)$, $P(O_3)_{PSS}$ and ‘ $DL(O_3) + Dep$ ’ become similar below NO concentrations of 40 ppt_v (Fig. 5.14). Eq. 5.11 is considered to verify the crossover by using equations as described previously Eq. 5.9, Eq. 5.10, and Eq. 1.10. The crossover points are calculated by using Eq. 5.11 to derive

the value of NO concentration by considering that at crossover ' $P(O_3)_{PSS} \approx IL(O_3)$ ' and ' $P(O_3)_{PSS} \approx DL(O_3)$ '.

$$(NO)_{IC} = \frac{IL(O_3)}{\left(\frac{jNO_2[NO_2]}{[NO]} - k_{1.1}[O_3]\right)} \quad \text{and} \quad (NO)_{DC} = \frac{DL(O_3)}{\left(\frac{jNO_2[NO_2]}{[NO]} - k_{1.1}[O_3]\right)} \quad \text{Eq. 5.11}$$

The derived values of NO concentration $(NO)_{IC}$ and $(NO)_{DC}$ from Eq. 5.11 are presented in Table 5.4. Based on averages in Table 5.4, the value of NO $[(NO)_{IC}]$ for crossover point between $P(O_3)_{PSS}$ and $IL(O_3)$ is about 27 % higher than the value of NO for the peak in Φ (Fig. 5.2) at about $NO = 44 \text{ ppt}_v$. This contrasts with the case of $DL(O_3)$, in which the crossover point is about 74 % lower than the value (44 ppt_v) of NO for the peak in Φ . With the addition of the O_3 depositional loss in Eq. 5.11, the value for the cross over point between $P(O_3)_{PSS}$ and ' $DL(O_3) + Dep$ ' versus NO remains to 20 % lower than the value (44 ppt_v) of NO for the peak in Φ . Due to the missing measurements of some VOCs and secondary species, the loss of O_3 is under-estimated for this case. This missing loss is likely to shift the crossover towards the value of NO concentration where the peak in Φ occurred. The derived values (Eq. 5.11) of NO concentration are based on the measured data, so the errors in these values (Table 5.4) are large (roughly $> 80 \%$). The crossover points in Fig. 5.14 are unique in describing the balance between 'radical + radical' reactions and 'radical + NO' reactions. In low NO_x conditions, the balance is shifted in favour of the chain termination process as described by the 'radical + radical' reactions and leads to decrease in O_3 production efficiency.

Table 5.4: Analytically derived average and median values of $(NO)_{IC}$ and $(NO)_{DC}$ according to Eq. 5.11 for different concentrations of species.

Eq. 5.11	Average (ppt _v)	Median (ppt _v)	1σ variability (ppt _v)
$(NO)_{IC}$	55.7	55.2	16.2
$(NO)_{DC} @ DL(O_3)$	11.5	10.8	3.2
$(NO)_{DC} @ DL(O_3) + Dep$	35.2	31.5	12.9

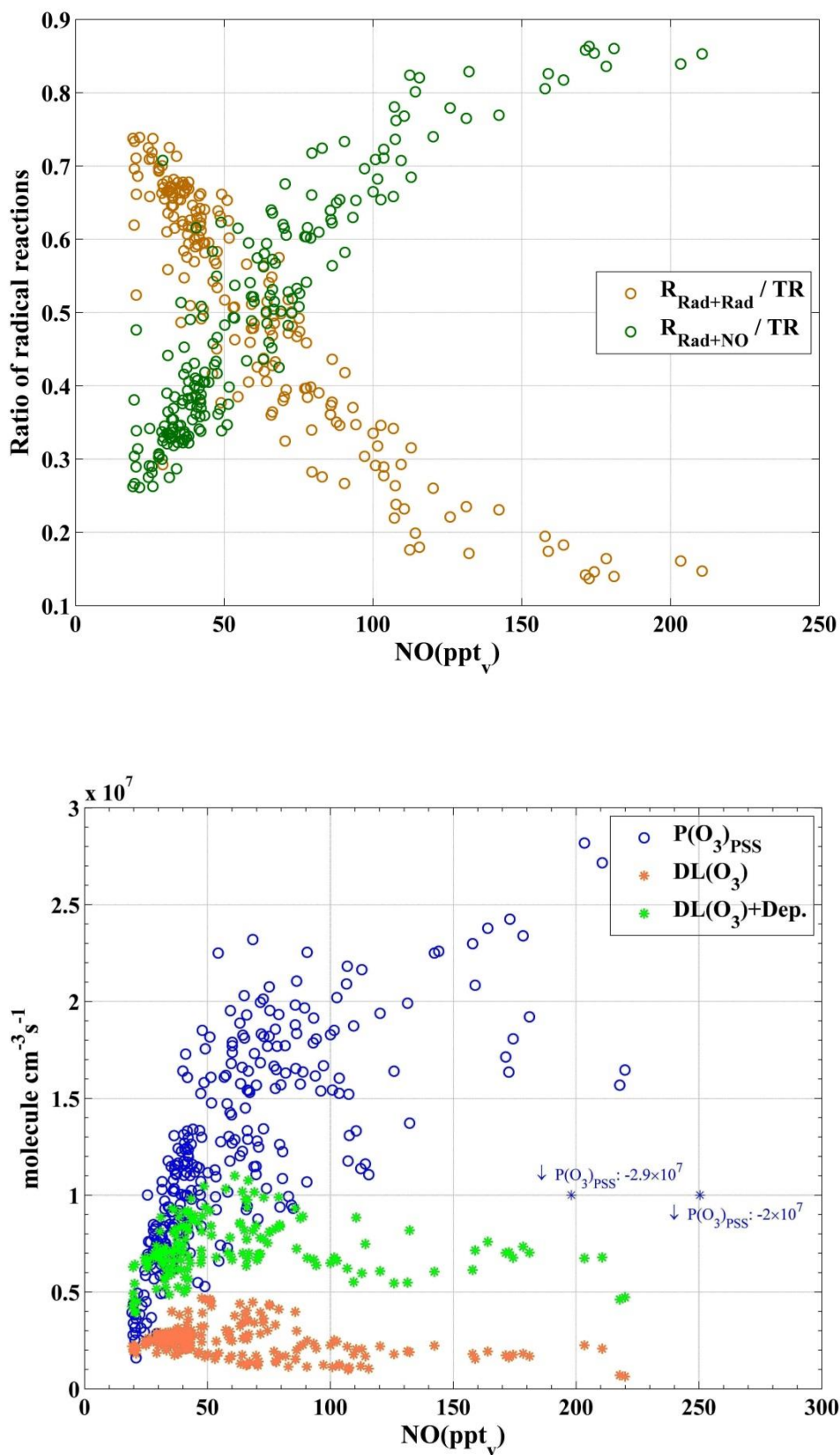


Fig. 5.14: Upper panel shows radical reaction rate efficiency in term of production and indirect loss of O_3 . The lower panel shows the O_3 production and direct loss rates as a function of NO.

5.6 Effects of alkyl nitrates on NO_x lifetime and OPE

Alkyl nitrates (ANs) are regarded as reservoir species for tropospheric reactive nitrogen and the pathway for their photochemical formation is similar to the one for O₃ [[\(Simpson et al., 2006\)](#) and reference there in]. ANs are mainly formed in the troposphere by a minor branch reaction between RO₂ and NO ([R. 1.14](#)). The fraction of this branch ([R. 1.14](#)) compared to [R. 1.3](#) is described by α ([Eq. 1.1](#)). The effective branching ratio α for ANs varies in the atmosphere, depending on the availability of different RO₂ species ([Thieser, 2013](#); [Browne and Cohen, 2012](#)). The direct emission of ANs from anthropogenic activities like industrial activity are also observed ([Simpson et al., 2002](#)). These species represent the substantial fraction of total NO_y species from rural ([Murphy et al., 2006](#); [Day et al., 2009](#); [Beaver et al., 2012](#)) and urban regions ([Rosen et al., 2004](#); [Perring et al., 2010](#); [Farmer et al., 2011](#)).

ANs are regarded as local sinks for NO_x because the typical chemical lifetime of ANs is in order of days to weeks [[\(Nollet, 2006\)](#) and reference there in]. The production of ANs is an important sink of NO_x during day and night in addition to the loss via the production of HNO₃. The nocturnal formation of ANs mainly results from reaction between NO₃ and alkenes. The fractional loss of NO_x to ANs formation is dominant nocturnally compared to HNO₃ formation ([Browne and Cohen, 2012](#)). The importance of ANs increases with high biogenic activity, in context to the loss of NO_x. Photolysis and reaction with OH are important atmospheric loss processes for ANs ([Talukdar et al., 1997](#)) during daytime and the loss of ANs increases with the increase in chain length of alkyl group ([Schneider et al., 1998](#)). In a recent study based on a steady-state box model and WRF-Chem model ([Browne and Cohen, 2012](#)), it has been concluded that ANs play important role in the lifetimes of NO_x and in O₃ production efficiency. The aim of this discussion is to determine the qualitative effects of ANs on the NO_x-related photochemistry in the boreal forest region characterised by significant emission of biospheric VOCs. The effects of varying α ([R. 1.14](#) and [Eq. 1.1](#)) have been assessed for HUMPPA-COPEC on the fate of NO_x in the O₃-related photochemistry. RO₂ concentrations for this discussion are based on $\Phi_{\text{ext}2}$ deviations ([Section 5.2.1.2](#)), so the filter ($j\text{NO}_2 \geq 5 \times 10^{-3} \text{ s}^{-1}$) is used.

The losses to HNO₃ [$\text{LNO}_x(\text{HNO}_3)$] and ANs [$\text{LNO}_x(\text{ANs})$] are considered as the main chain terminating processes for NO_x. The instantaneous loss rate of NO_x to HNO₃ based on reaction 'NO₂ + OH' is lower ([Table 5.5](#)) than the one in case of NO_x to ANs based on reaction 'NO + α RO₂'.

Table 5.5: NO_x loss rate to HNO₃ and ANs based on median concentrations of reactants during HUMPPA-COPEC.

Param.	Median @ ($j\text{NO}_2 \geq 5 \times 10^{-3} \text{ s}^{-1}$)	LNO _x to (HNO ₃) $\times 10^5$ (molecule cm ⁻³ s ⁻¹)	LNO _x to (ANs) $\times 10^5$ (molecule cm ⁻³ s ⁻¹)
NO ₂	5.82×10^9 molecule cm ⁻³	1.21	3.88 (with $\alpha = 0.075$)
NO	1.16×10^9 molecule cm ⁻³		
RO ₂	4.87×10^8 molecule cm ⁻³		
OH	1.78×10^6 molecule cm ⁻³		
$k_{(\text{NO} + \text{RO}_2)}$	9.15×10^{-12} cm ³ molecule ⁻¹ s ⁻¹		
$k_{(\text{NO}_2 + \text{OH})}$	1.17×10^{-11} cm ³ molecule ⁻¹ s ⁻¹		

The sensitivity of the NO_x loss rates changes with the variation in α . The loss of NO_x to formation of HNO₃ and ANs increases with increasing NO_x levels. Also the ratio LNO_x(HNO₃) / LNO_x(ANs) has a positive trend with increase in NO_x. The relative change in LNO_x(HNO₃) to the total loss [LNO_x(HNO₃) + LNO_x(ANs)] rises, while the relative change in LNO_x(ANs) to total loss declines with the increase in NO_x concentrations. The relative fraction of both losses to total loss as a function of NO_x is shown in Fig. 5.15. A negative trend in the ratio (shown in green) due to ANs formation and a positive trend in the ratio (blue) due to HNO₃ formation are described by the trend line. Based on these results, the production of ANs is very important, much higher and dominant under low-NO_x conditions compared to the production of HNO₃.

The sensitivity of ANs formation was tested by varying the value of α and observing the corresponding effects on the effective lifetime of NO_x [$\tau(\text{NO}_x)$] and catalytic efficiency of NO_x for the production of O₃. $\tau(\text{NO}_x)$ is calculated according to relation (Eq. 5.12) (Browne and Cohen, 2012) for HUMPPA-COPEC.

$$\tau(\text{NO}_x) = \frac{[\text{NO}_x]}{\text{LNO}_x} \quad \text{Eq. 5.12}$$

$$\text{LNO}_x = k_{1.7} [\text{NO}_2][\text{OH}] + \alpha \times k_{1.14} [(\text{RO}_2)_{\text{PSS}}][\text{NO}] \quad \text{Eq. 5.7}$$

To investigate the effect of α on the NO_x lifetime, it was varied within the range of [0, 10] % in Eq. 5.7. A negative and nonlinear effect of $\tau(\text{NO}_x)$ with respect to increase in α is

observed. Panels (I to VI) in Fig. 5.16 show the effect of α on $\tau(\text{NO}_x)$ for different ranges of NO_x. The panel 'L' of Fig. 5.16 shows a combined plot of panels (I to VI) and vertical error bars represent the 1 σ variability of the calculated median values. The absolute values of $\tau(\text{NO}_x)$ have changed significantly from $\alpha = 0\%$ to $\alpha = 10\%$. The absolute change in $\tau(\text{NO}_x)$ at the low NO_x concentrations is much larger compared to the change at high NO_x concentrations (Fig. 5.16). For example in panel I of Fig. 5.16 for the NO_x range of ≤ 150 ppt_v, the lifetime of NO_x is about 23 hr at $\alpha = 0\%$ and it changes to 5 hr at $\alpha = 10\%$. In panel VI of Fig. 5.16 for larger than 470 ppt_v of NO_x, the lifetime of NO_x is about 12 hr at $\alpha = 0\%$ and it changes to 3 hr at $\alpha = 10\%$. However, the relative change in $\tau(\text{NO}_x)$ from $\alpha = 0\%$ to $\alpha = 10\%$ was in the range of [75, 87] % for panels I to VI in Fig. 5.16.

ANs reduce the production efficiency of O₃ by providing a sink for NO_x. The effect of α was further investigated in terms of the catalytic efficiency of NO_x in the production of O₃ as described in Section 1.3.2. The total production of O₃ from HO₂ and RO₂ is considered based on chemical imbalance of the PSS as described by Eq. 1.10. The catalytic efficiency of NO_x is calculated according to relation Eq. 1.14 and it is shown as a function of NO_x in Fig. 5.17. The catalytic efficiency of NO_x in production of O₃ can be stated as the O₃ production efficiency (OPE) (Liu et al., 1987; Brasseur et al., 1999). The median values of the OPE are calculated at specific ranges of NO_x bins for HUMPPA-COPEC (Fig. 5.17). The minimum number of data points to calculate a median value for the OPE is 5. More data was present at NO_x concentrations < 470 ppt_v compared to the larger concentrations, so a NO_x bin range of 50 ppt_v is used there, while for higher levels NO_x bin is 100 ppt_v. The OPE is reduced significantly by up to 90 % at the highest value (10 %) of α . Based on the expected values of α [5 - 10] % in a forest region (Browne and Cohen, 2012), OPE is expected to decline in the range of]45, 90[% compared to the case when $\alpha = 0\%$ for HUMPPA-COPEC. The reduction in OPE for $\alpha = 3\%$, 5 %, and 10 % compared to the case $\alpha = 0\%$ is remarkably large at lower NO_x levels (Fig. 5.17). In context of the OPE versus NO_x, the difference in the reduction of OPE at levels of NO_x > 470 ppt_v is smaller compared to the levels of NO_x < 470 ppt_v. This shows that the effect of ANs formation on the OPE is very important, especially at low NO_x levels. A negative trend in the OPE versus NO_x concentrations for HUMPPA-COPEC was observed at NO_x levels ≥ 470 ppt_v in all cases of α . The negative trend versus increase in NO_x is more prominent in the case of $\alpha = 0\%$ and $\alpha = 1\%$ over the whole NO_x range. For cases $\alpha = 3\%$, 5 % and 10 %, no significant trend is present in OPE versus increase in NO_x at NO_x levels < 470 ppt_v. Also, the relative differences between OPE at $\alpha = 3\%$, 5 %, and 10 % are fairly constant at levels of NO_x < 470 ppt_v.

The chain termination processes for NO_x , leading to HNO_3 and ANs, provide an upper estimate for $\tau(\text{NO}_x)$ and OPE as the conversion of HNO_3 and ANs back to NO_x will minimise these effects. The results have shown that $\tau(\text{NO}_x)$ and OPE are very sensitive to α for HUMPPA-COPEC and suggest that the effect of ANs formation for climate models and future strategies regarding O_3 abundances is very important, especially in the forest regions and at low NO_x concentrations.

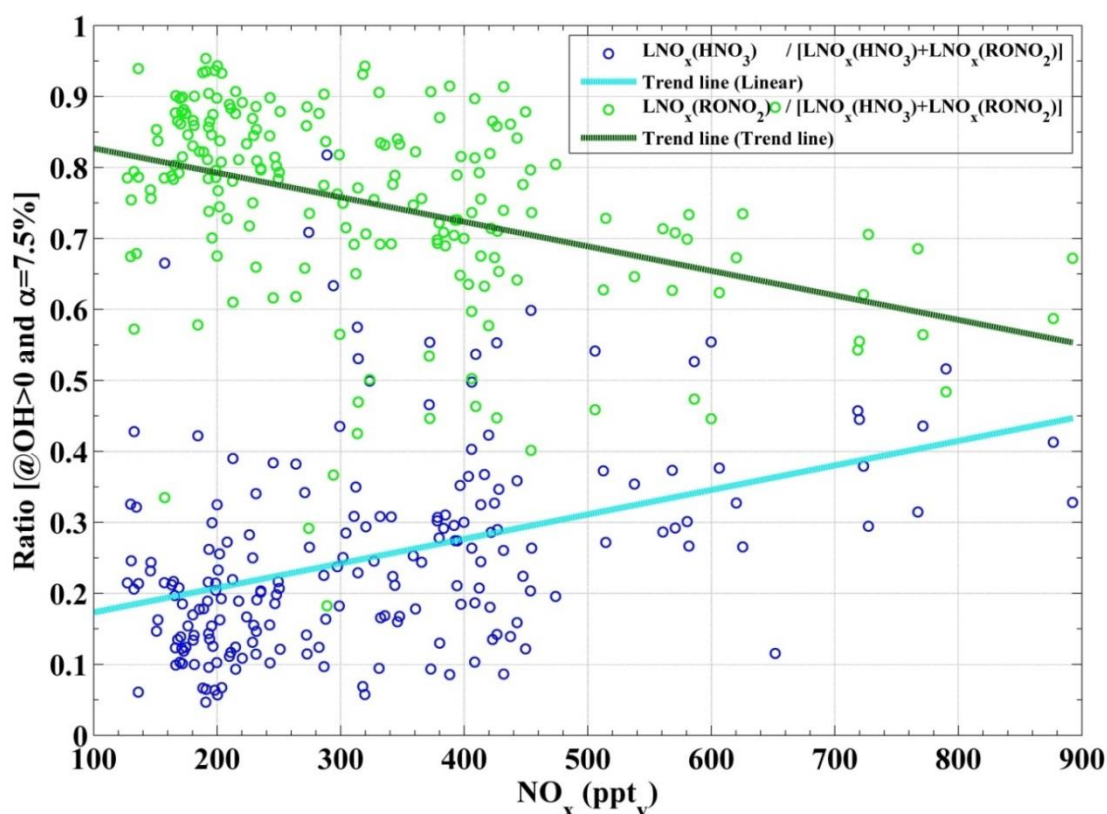


Fig. 5.15: The ratio for the loss of NO_x via formation of HNO_3 [$\text{LNO}_x(\text{HNO}_3)$] to the total loss and the loss of NO_x via formation of ANs [$\text{LNO}_x(\text{ANs})$] to the total loss are shown as a function of NO_x . Trend lines in both cases are shown according to least squares fit.

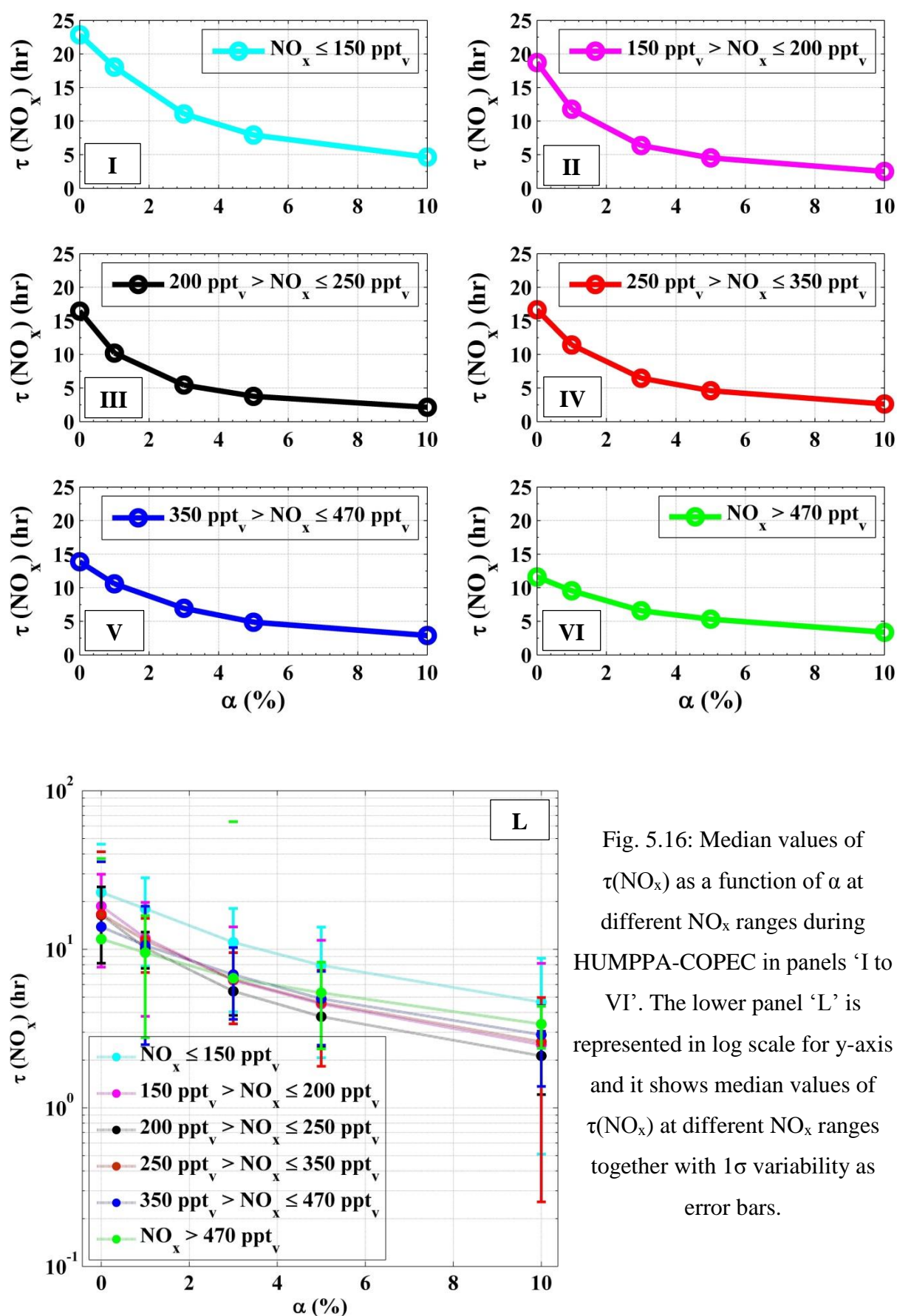
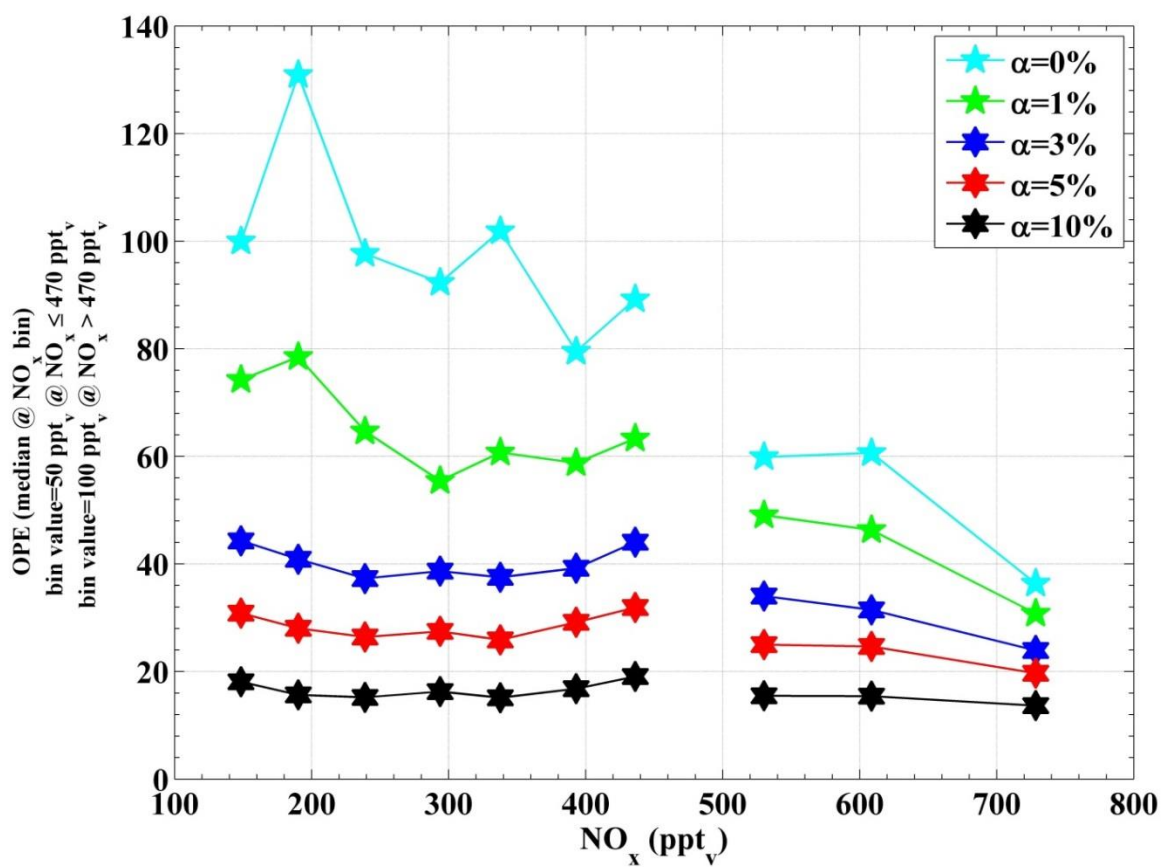


Fig. 5.16: Median values of $\tau(\text{NO}_x)$ as a function of α at different NO_x ranges during HUMPPA-COPEC in panels 'I to VI'. The lower panel 'L' is represented in log scale for y-axis and it shows median values of $\tau(\text{NO}_x)$ at different NO_x ranges together with 1σ variability as error bars.

Fig. 5.17: OPE as a function of NO_x concentrations during HUMPPA-COPEC.

6 Conclusions and Outlook

6.1 Conclusions

A laser-induced fluorescence (LIF)-based instrument (GANDALF) has been developed for the measurement of atmospheric NO₂. LIF instruments have already been deployed in past to measure NO₂ directly and selectively, reaching detection limits down to 5 ppt_v (Table 2.1). This required the use of large and expensive laser systems like Nd:YAG lasers or dye laser systems. Recently, the availability of much smaller and lighter diode lasers makes it possible to build much more compact instruments with comparable sensitivities. First attempts in previous projects to build such systems using diode lasers have compact design but did not achieve detection limits suitable for measurements of NO₂ in remote regions and the upper troposphere (Table 2.1). GANDALF has been tailored towards a compact design [diode laser (mass = < 2 kg and power = max. 250 mW)] with a low detection [5 - 10 ppt_v at 1 minute with signal to noise ratio (SNR) = 2], a high precision of better than 0.5 % + 3 ppt_v for 1 minute time interval and a fast repetition rate of 5 MHz, making it capable of measuring NO₂ throughout the troposphere. The reliability of GANDALF was successfully tested during the PARADE-2011 field campaign and during a successful comparison carried out at the observatory of the Deutscher Wetterdienst (DWD) in Hohenpeissenberg, Germany. The selectivity of NO₂ measurement with GANDALF was assessed during PARADE in ambient air and no potential interference was found.

In past studies, there appeared to be a lack of understanding of the cycling between NO and NO₂. This was often linked to the presence of an ‘unknown oxidant’ converting NO to NO₂. In order to understand the cycling between NO and NO₂, the photostationary state of NO_x (PSS) for a semi-rural area during PARADE was investigated using the concept of the Leighton ratio (Φ Eq. 1.4) by using measurements of NO₂ conducted with the newly developed GANDALF instrument. The Leighton ratio is calculated based on the measured data of NO, NO₂, O₃, and jNO₂. Φ converged towards unity for higher NO_x concentrations but higher positive deviations in Φ were observed under low NO_x conditions (Fig. 4.3). In order to investigate the potential cause of these positive deviations, the role of NO, NO₂, and O₃ in other chemical reactions in addition to the null cycle of NO-NO₂-O₃, excluding the reactions ‘HO₂ + NO’ and ‘RO₂ + NO’, was assessed (Φ_{mod} Eq. 4.3). The effect of these

chemical and physical (O_3 deposition) processes on deviations in Φ was less than 3 % and insignificant as discussed in the Section 4.2.

The total sum of peroxy radicals RO_x ($\text{HO}_2 + \text{RO}_2$) was measured by the PerCA instrument of the University of Bremen during PARADE. This enabled the ‘ $\text{RO}_x + \text{NO}$ ’ contribution to be calculated and included in the Leighton ratio, producing an extended ratio Φ_{ext} (Eq. 1.6), and the aforementioned positive deviations from unity were reduced. The average Φ_{ext} was 1.09, a divergence from unity of 9 %, with an associated measurement error of about 0.2. In order to test the significance of this 9 % difference, the sensitivity of Φ_{ext} to only NO and jNO_2 was further tested by varying them in amount below the corresponding measurement uncertainties. Φ_{ext} converged from 1.09 to 1.045 ± 0.13 (1σ) by introducing + 21 ppt_v in NO, and from 1.09 to 1.035 ± 0.14 (1σ) by reducing jNO_2 only 5 %. These changes of values in NO, and jNO_2 are within the range of measurement accuracy of the respective data. Further, by performing this sensitivity test with a combined change of values in NO and jNO_2 , Φ_{ext} declined further to become 0.99 ± 0.13 (1σ) (case-4, Fig. 4.8). Based on the evidence of the analyses in this study, it is concluded that there is no statistically significant evidence for or suggestion of an ‘unknown oxidant’ in PARADE, and peroxy radicals along O_3 account wholly for the conversion of NO to NO_2 .

A lack of understanding the underlying process of NO to NO_2 conversion is revealed to be most prominent at low NO_x conditions. The measured data set from HUMPPA-COPEC was used to contrast and compare the NO to NO_2 cycling with PARADE. NO_x levels at HUMPPA-COPEC were low, while biogenic volatile organic compounds (BVOCs) were high compared to PARADE. The reactivity of BVOCs and related secondary compounds was expected to be greater compared to PARADE. The observed deviations (>1) in Φ for this location are even larger compared to PARADE (Fig. 5.2). This is expected, as higher levels of HO_2 were measured compared to PARADE. By introducing the contributions from ‘ $\text{HO}_2 + \text{NO}$ ’ in Φ ($\Phi_{\text{ext}2}$, Eq. 5.1) for HUMPPA-COPEC, positive deviations of Φ declined but remained considerably larger than unity (Fig. 5.3). RO_2 levels [$(\text{RO}_2)_{\text{PSS}}$] were inferred from the remaining deviations (> 1) of $\Phi_{\text{ext}2}$ (Eq. 5.1). In the absence of measured RO_2 , a model was deployed to calculate RO_2 concentrations for HUMPPA-COPEC in order to assess the nature of Φ deviations. The model was constrained with several observed quantities like concentrations of NO, O_3 , HO_2 , OH, BVOCs, HCHO, CO, CH_4 , and H_2O vapor with photolysis frequencies. Levels of peroxy radicals (measured HO_2 + simulated RO_2) were not sufficient to explain the deviation (> 1) in Φ (Fig. 5.6). Generally, ‘BVOCs + OH’ reactions

leading to RO₂ formation are important in a forested region. The adequacy of the simulated RO₂ was tested by using a comparison of the total measured OH reactivity and simulated OH reactivity. The simulated OH reactivity was significantly lower than the measured OH reactivity. This suggested there were missing precursors of RO₂ in the simulations. The unexplained higher measured OH reactivity is indirect evidence for unmeasured BVOCs or secondary oxidation products. This hypothesis was tested by tuning the model OH reactivity with increasing concentrations of BVOCs, enough to match the model OH reactivity with the measured OH reactivity (Fig. 5.7). With these matched OH reactivity inputs, the positive deviations in Φ are substantially reduced by the introduction of measured HO₂ and simulated RO₂ in Φ for the case of $\Phi_{\text{ext(T)}}$ (Fig. 5.9). The overall median and average values of $\Phi_{\text{ext(T)}}$ were 1.001 ± 0.105 (1σ) and 0.996 ± 0.105 (1σ), respectively. These aspects suggest the Φ deviations (> 1) during HUMPPA-COPEC can be explained by peroxy radicals. The NO_x-related photochemistry is reasonably well explained within the measurement uncertainty by the PSS model at two different locations and it is consistent with the field measurements of NO₂. Evidence for or suggestion of an unknown oxidant converting NO to NO₂ is statistically insignificant in case of either PARADE or HUMPPA-COPEC. In addition, use of the Leighton ratio is a realistic approach even under low-NO_x conditions.

The O₃ budget was assessed during PARADE for daytime chemistry. The daytime tendency of O₃ was significantly positive for semi-rural conditions. The major loss mechanism of O₃ at this site was due to dry deposition and was significantly higher than photochemical losses (Fig. 3.12). The lifetimes of O₃ were longer due to chemical losses compared to those of depositional loss. The largest photochemical loss rate observed was due to the photolysis of O₃, while the smallest loss rate was due to aromatics like benzene and toluene. During PARADE, the reaction with O₃ was the major removal process of primary BVOCs like isoprene, α -pinene, myrcene, and limonene collectively and it was a factor of about 3.7 higher compared to corresponding removal due to OH. In contrast, the collective removal for anthropogenic alkenes such as ethene, propene, 1, 3-butadiene, cis-2-butene, and 1-pentene due to OH was a factor about 1.66 larger than the removal due to O₃. The production of O₃ during HUMPPA-COPEC was smaller than PARADE by more than a factor of two.

A decrease in the measured HO₂ was observed with respect to decrease in NO levels during HUMPPA-COPEC. The corresponding effect is well described by the decline from the peak in the Leighton ratio with respect to decrease in NO at about 44 ppt_v. A crossover point at about 55 ppt_v of NO was observed between the reaction rates of ‘radical + NO’

reactions and ‘radical + radical’ reactions. The crossover point indicates equal importance and a balance between the ‘radical + NO’ reactions and ‘radical + radical’ reactions. This crossover point was about 20 % higher than the NO level for the peak in Φ . Meanwhile, a crossover between the production and direct loss rates of O₃ (based on measured species and with dry deposition) is observed at NO concentration of 30 to 35 ppt_v. With the assumption of the existence of additional, unmeasured BVOCs, this crossover point between the O₃ production and direct loss would most likely shift towards higher NO levels where the peak in Φ occurred. This unique peak in Φ at the specific level of NO can be a good indication of the balance between the O₃ production and loss (Table 5.4 and Fig. 5.14). This specific level of NO is different to the one described as ‘Critical NO’ in the literature (Lelieveld and Crutzen, 1990), as ‘Critical NO’ is based on the chemical loss of O₃ but not sum of chemical and physical losses as in this case.

The effect of alkyl nitrates (ANs) was tested for the NO_x lifetime and the O₃ production efficiency (OPE). It was observed that the lifetime of NO_x and the OPE are reduced and very sensitive to the formation of ANs as suggested by a previous study (Browne and Cohen, 2012). Based on calculations for HUMPPA-COPEC using the measured data and RO₂ derived from the PSS, it is concluded that the correct estimate for the branching ratio for the ANs formation is necessary, especially under conditions of low NO_x in an area characterised by high BVOCs abundances. The potential role of ANs formation as a sink of NO_x is similar to or might be even more important than HNO₃ formation and should be considered in climate models and forecasts of regional O₃ abundances.

6.2 Outlook

The formation of ANs is an important sink for NO_x and effects the OPE. The accurate measurement of ANs is important for the assessment of local O₃ abundances. LIF systems in combination with the thermal dissociation method ([Day et al., 2002](#)) are also used and very useful for the detection of ANs. Without any substantial modification, GANDALF will be capable of measuring ANs by coupling with the thermal dissociation. This improvement can provide very useful data on ANs for the future to constrain models and further improve the current understanding of regional O₃ concentrations.

It has been observed that the use of the PSS is valid under two different forest ecosystems. But there is still a need to validate the PSS system under different conditions such as the upper troposphere, the marine boundary layer, and the tropical rain forest. The analysis of the PSS in past had been done in several studies at ground level, but only a few of this analyses took airborne measurements from ground to the upper troposphere. Airborne measurements of NO₂ especially in the upper troposphere face the challenge of fast decomposition of nitrates so instruments have difficulties in providing highly selective, precise, and fast measurements as required for NO₂ observations in the upper troposphere. Experienced has been that LIF is a reliable and promising method for the *in-situ* measurement of NO₂. During the OMO⁵³ project, including NO₂ measurements with GANDALF, several other important radical measurements (e.g. OH, HO₂, and RO₂) will be conducted. This will be a future opportunity to analyse the PSS from the surface to the upper troposphere.

A few PSS-related studies in past are done in the marine boundary layer ([Hosaynali Beygi et al., 2011](#); [Trebs et al., 2012](#)). But often the halogen oxides measurements for the analysis of the PSS are missing. With a small modification, GANDALF can fulfil the requirement of iodine monoxide (IO) measurements for the PSS analysis in coastal regions. The current CW diode laser of the instrument will be replaced by a mono-mode dual diode laser [λ (online) = 445 nm and λ (offline) = 442 nm] for on and off resonance measurements of NO₂. The absorption cross-sections of IO are 1.1×10^{-17} cm² molecule⁻¹ (high) and 3.5×10^{-19} cm² molecule⁻¹ (low) at 445 nm and 442.09 nm, respectively ([Bloss et al., 2001](#)). In addition, LIF systems have been used in past for the IO measurement ([Whalley et al., 2007](#)). With the new mono-mode laser, GANDALF can also be used for direct measurements of IO simultaneously with NO₂. This ability of GANDALF to measure the atmospheric IO

⁵³ HALO [High Altitude and LOng Range Research Aircraft] campaign called OMO [Oxidation Mechanism Observation].

simultaneously with NO_2 will improve PSS analysis in coastal regions. Besides investigation of the PSS, the effect of halogen oxide on O_3 loss had been found to be important in coastal regions, e.g. ([Dix et al., 2013](#)). So a measurement of such species is helpful for model studies to quantify the effect of halogen oxides on the O_3 budget.

7 APPENDICES

7.1 LISTS

7.1.1 Figures in main text

Fig. 1.1: Stratification of planetary boundary layer. [Figure is adapted from (Stull, 1988)]....	2
Fig. 1.2: Lifetimes of NO _x as a function of altitude [left panel from (Ehhalt et al., 1992)]. Spatial and temporal scales of variability for atmospheric constituents [right panel from (Seinfeld and Pandis, 2006)].....	4
Fig. 1.3: Global average tropospheric NO ₂ columns for the period of 2002 to 2011. [figure taken from (Schneider and R. van der A., 2013)].....	5
Fig. 1.4: NO _x related tropospheric chemistry.	10
Fig. 2.1: NO ₂ absorption cross-sections with quantum yields. Excitation wavelength above the photolysis threshold is shown with an arrow. The absorption cross-sections and quantum yields are plotted from data (Vandaele et al., 1998) and (Roehl et al., 1994), respectively....	30
Fig. 2.2: The section view of GANDALF [Inventor-2009: The drawing is created by defining a plane used to cut through assembly. The figure represents the surface area of the cut];	31
Fig. 2.3: Wavelength plot for the diode laser, operated with repetition rate of 5MHz.....	32
Fig. 2.4: Multiple passes of the laser beam are visible in the detection cell (A) and in between the Herriott cell's mirrors on an optical bench (B).	33
Fig. 2.5: Inventor 2009 assembly of the optical reference system.....	35
Fig. 2.6: A plot between the PMT and photodiode (<i>CNO₂</i>); both signals are normalised to the photodiode (<i>ref.</i>).	36
Fig. 2.7: Simulated ON/OFF cycles for operating the diode-laser	38
Fig. 2.8: Sensitivity of the instrument based on simulation is demonstrated for three different on/off cycles of diode laser operation.	38
Fig. 2.9: Box model simulation of gas phase titration between NO and O ₃	41
Fig. 2.10: Formation of NO ₃ and N ₂ O ₅ , based on simulation shown in Fig. 2.9.....	41
Fig. 2.11: PMT signal with respect to change in O ₃ mixing ratios.....	42
Fig. 2.12: NO ₂ loss due to increase in O ₃ inside the GANDALF calibrator.....	43
Fig. 2.13: Residence time for NO ₂ calibration gas in the calibrator.	45

Fig. 2.14: NO ₂ concentrations (BM simulation) inside the calibrator as a function of time based on different temperatures.	46
Fig. 2.15: NO ₂ concentrations (BM simulation) inside the calibrator as a function of time for different pressures (mbar or hPa).....	47
Fig. 2.16: The dependence of NO ₂ fluorescence intensity on increasing water vapour concentrations in GANDALF (L). Change in sensitivity (normalised to zero H ₂ O %) due to change in water vapour (scale equivalent to atmospheric H ₂ O %) (R).	48
Fig. 2.17: A plot between known amounts of NO ₂ versus the fluorescence signal as an example of the calibration of GANDALF. The calibration constant α_c (Eq. 2.1) is determined by the slope of the curve.	50
Fig. 2.18: Schematic view of Setup for automated calibrations during out door operation. ...	51
Fig. 2.19: Relative precision check of GANDALF for randomly selected NO ₂ calibration points.....	55
Fig. 2.20: An overlapping Allan deviation plot for the dependence of the 1σ variation in the background level vs. integration time.	56
Fig. 3.1: Orography of the Taunus region [adapted from (Handisides, 2001)]	60
Fig. 3.2: Time series of some meteorological parameters during PARADE-2011.	60
Fig. 3.3: Frequency distributions of wind directions with wind speed (colour-coded: wind speed in ms ⁻¹). [Google Map view].....	61
Fig. 3.4: The platform location at the Taunus Observatory on Kleiner Feldberg.....	63
Fig. 3.5: Time series of some relevant atmospheric species during PARADE-2011	69
Fig. 3.6: Correlation plots (Overall [A], GANDALF [B], CLD [C], CRDS [D], LP-DOAS [E], CE-DOAS [F]) of individual NO ₂ measurement versus the derived median values of all NO ₂ measurement at platform during PARADE.....	74
Fig. 3.7: Distribution for comparative instrument ratios is shown in upper panels and a normal probability plot for comparative instrument ratios is shown in lower panels.	77
Fig. 3.8: Ratios as a function of the ambient O ₃ during PARADE.....	78
Fig. 3.9: Ratios as a function of the measured jNO ₂ during PARADE.	79
Fig. 3.10: Absolute total loss of O ₃ is shown in subplot 'A' and it is colour-coded with temperature. This figure is based on the sum of direct chemical losses (I+II+III+IV+aromatics) as described in the text. Filtered absolute losses due jO ¹ D(I), HO _x (II), BVOCs(III) and NMHC(IV) are also included as subparts for two temperature ranges [T ≤ 13 °C] and [T > 13 °C].	85

Fig. 3.11: Fractional contribution to total loss of O ₃ with several groups of measured species as described in the text for T > 13 °C and T ≤ 13 °C in the upper and lower panels, respectively.	86
Fig. 3.12: Median values of different indirect and direct loss rates of O ₃ in molecule cm ⁻³ s ⁻¹ for three different time windows [8, 10], [10, 14] and [14, 16] UTC and two different temperature ranges (13°C > T ≤ 13°C).	88
Fig. 4.1: Leighton ratio (Φ) during PARADE with respect to NO _x (log-log scale). Errors in Φ due to measurement uncertainties are indicated by the vertical error bars.	94
Fig. 4.2: Relative fraction of the uncertainty in Φ due to different parameters as a function of NO _x mixing ratios.	96
Fig. 4.3: Average Φ as a function 0.3 ppb _v of NO _x bin with measurement uncertainty of over bin averages.	97
Fig. 4.4: Fraction of NO ₂ production rates for different reactions.	98
Fig. 4.5: Measured O ₃ , RO _x and ANs as a function of NO during PARADE.	99
Fig. 4.6: Effect on Φ due to the involvement of NO, NO ₂ , and O ₃ in other chemical and physical processes.	102
Fig. 4.7: Extended (Φ _{ext}) and classical Leighton ratio (Φ) are plotted versus NO _x mixing ratios for PARADE (log-log scale).	103
Fig. 4.8: Overview of Φ _{ext} (with measurement uncertainties) as a function of NO _x mixing ratios in the upper panel with x-axis in log scale. The lower panel shows averages with ± 1σ variability. Note that for the lower panel, all avg. Φ _{ext} have less than 1.2 % standard error (1σ / √n).	105
Fig. 4.9: Calculated NO ₂ from PSS versus measured NO ₂ during PARADE. Three different possibilities are shown A = (NO ₂) _{PSS} , B = (NO ₂) _{PSSext} , C = (NO ₂) _{PSSext} [@ NO = NO + 0.021 ppb _v and jNO ₂ = jNO ₂ - (0.05 × jNO ₂)].	107
Fig. 5.1: Time series of some important trace gas species, jNO ₂ , and meteorological parameters during HUMPPA-COPEC-2010 in the upper panel. Lower panel shows an overview of the setup.	112
Fig. 5.2: Φ as a function of NO for HUMPPA-COPEC-2010 and PARADE-2011. NO concentrations on x-axis are represented in log scale.	114
Fig. 5.3: Φ and Φ _{ext2} as a function of NO for HUMPPA-COPEC.	116
Fig. 5.4: Estimated RO ₂ for HUMPPA-COPEC as a function of NO.	117
Fig. 5.5: Relative fraction of RO _{2(CAABA/MECCA)} as a function of NO.	120
Fig. 5.6: Φ, Φ _{ext2} , and Φ _{ext} are shown as a function of NO.	121

Fig. 5.7: Ratio between the total measured and simulated OH reactivity as a function of NO.	125
Fig. 5.8: RO ₂ based on simulations as a function of the measured OH reactivity. The left hand side in the figure is prior to the tuning while the right hand side is based on tuned (OHReact) _{CAABA/MECCA} .	126
Fig. 5.9: Φ , Φ_{ext} is based on the measured data and simulations at normal BVOCs concentrations. $\Phi_{\text{ext(T)}}$ is based on results from the new simulations with the tuned OH reactivity in the model.	127
Fig. 5.10: [A] Ratio $[\text{NO}_{2(\text{meas})} / \text{NO}_{2(\text{CAABA/MECCA})}]$ as a function of NO for simulations without tuned OH reactivity. [B] Ratio $[\text{NO}_{2(\text{meas})} / \text{NO}_{2(\text{CAABA/MECCA})}]$ as a function of NO for simulations with tuned (OHReact) _{CAABA/MECCA} .	130
Fig. 5.11: Monte Carlo simulations for the estimation of uncertainties due to rate coefficients in	131
Fig. 5.12: P(O ₃) _{PSS} as a function of NO during HUMPPA-COPEC-2010.	134
Fig. 5.13: The efficiency of the chain termination processes as a function of NO.	134
Fig. 5.14: Upper panel shows radical reaction rate efficiency in term of production and indirect loss of O ₃ . The lower panel shows the O ₃ production and direct loss rates as a function of NO.	138
Fig. 5.15: The ratio for the loss of NO _x via formation of HNO ₃ [LNO _x (HNO ₃)] to the total loss and the loss of NO _x via formation of ANs [LNO _x (ANs)] to the total loss are shown as a function of NO _x . Trend lines in both cases are shown according to least squares fit.	142
Fig. 5.16: Median values of $\tau(\text{NO}_x)$ as a function of α at different NO _x ranges during HUMPPA-COPEC in panels ‘I to VI’. The lower panel ‘L’ is represented in log scale for y-axis and it shows median values of $\tau(\text{NO}_x)$ at different NO _x ranges together with 1 σ variability as error bars.	143
Fig. 5.17: OPE as a function of NO _x concentrations during HUMPPA-COPEC.	144

7.1.2 Tables

Table 1.1: An historical overview of studies related to PSS analysis.....	19
Table 2.1: Overview of different LIF instruments (operating parameters and LOD)	57
Table 3.1: Land use within a radius of 50 km.....	62
Table 3.2: An overview of instrumental methods deployed during PARADE.....	63
Table 3.3: NO ₂ instruments during PARADE-2011	72
Table 3.4: Overall average, median and standard deviation values of ratios with respect to GANDALF and other NO ₂ measurements during PARADE.	76
Table 3.5: Lifetimes of O ₃ with respect to different species measured at PARADE-2011. Time window [08:00, 10:00] UTC.	90
Table 3.6: Lifetimes of O ₃ with respect to different species measured at PARADE-2011. Time window]10:00, 14:00] UTC.	91
Table 3.7: Lifetimes of O ₃ with respect to different species measured at PARADE-2011. Time window]14:00, 16:00] UTC.	92
Table 4.1: Absolute errors in NO ₂ calculated from PSS (Eq. 4.7 and Eq. 4.8).	106
Table 5.1: A list of instrumentation during HUMPPA-COPEC related to this discussion. ..	111
Table 5.2: Average, median and standard deviation values of different RO ₂ (CAABA/MECCA) species.....	119
Table 5.3: Relative uncertainty based on Monte Carlo simulations	129
Table 5.4: Analytically derived average and median values of (NO) _{IC} and (NO) _{DC} according to Eq. 5.11 for different concentrations of species.	137
Table 5.5: NO _x loss rate to HNO ₃ and ANs based on median concentrations of reactants during HUMPPA-COPEC.	140

7.1.3 Abbreviations

- (OHReact)_{meas}
total OH reactivity (s⁻¹) measurement, 125
- ANs
Alkyl nitrates, 7
- ASL
above sea level, 19
- BG
Background, 55
- BLH
Boundary layer height, 88
- BM
Box Model, 40
- BVOCs
Biogenic Volatile Organic Compounds, 67
- CAABA
Chemistry As A Boxmodel Application, 120
- CAPS
Cavity Attenuated phase Shift Spectroscopy, 17
- CCD
charge-coupled device, 66
- CEAS
Cavity Enhanced Absorption Spectroscopy, 17
- CE-DOAS
Cavity Enhanced Differential Optical Absorption Spectroscopy, 72
- CLD
Chemoluminescence Detector, 66
- CRDS
Cavity Ring-Down Absorption Spectroscopy, 17
- D
dilution factor, 44
- DL(O₃)
direct loss rates of O₃, 137
- DOY
Day of year, 59
- E
east, 115
- EV
Electronic Valve, 49
- GaAsP/GaAs
Gallium Arsenide Phosphide, 33
- GANDALF
Gas Analyzer for Nitrogen Dioxide Applying Laser induced Fluorescence, 29
- HALO
The High Altitude and LOng Range Research Aircraft, 18, 151
- HR
High Reflectivity, 32
- HUMPPA-COPEC
Hyttiälä United Measurements of Photochemistry and Particles in Air - Comprehensive Organic Precursor Emission and Concentration study, 18
- HYSPLIT
Hybrid Single-Particle Lagrangian Integrated Trajectory, 61
- IL(O₃)
indirect loss rate of O₃, 137
- k_{eff}
effective (derived rate coefficient) for all ROx, 13
- LIF
Laser-Induced Fluorescence, 29
- LN
Natural logarithm (base e), 48
- LOD
limit of detection, 55
- LP-DOAS
Long Path Differential Optical Absorption Spectroscopy, 72
- MBL
marine boundary layer, 14
- MCM
Master Chemical Mechanism, 120
- MECCA
Module Efficiently Calculating the Chemistry of the Atmosphere, 120
- MFC
Mass Flow Controller, 49
- MIM
Mainz Isoprene Mechanism, 120

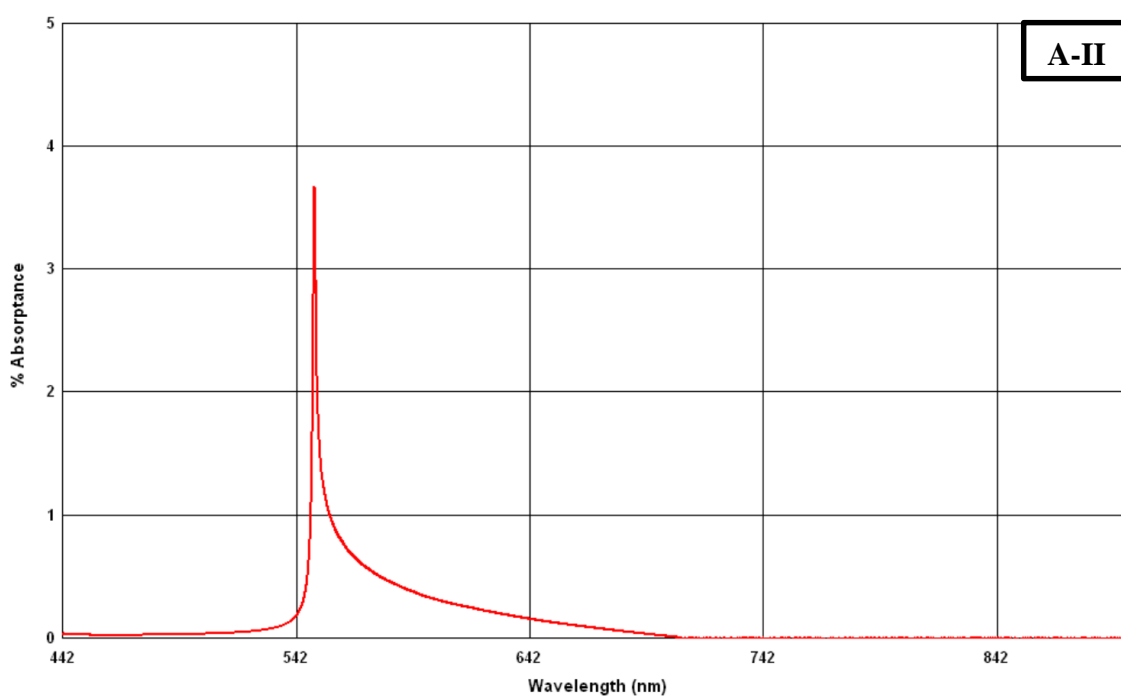
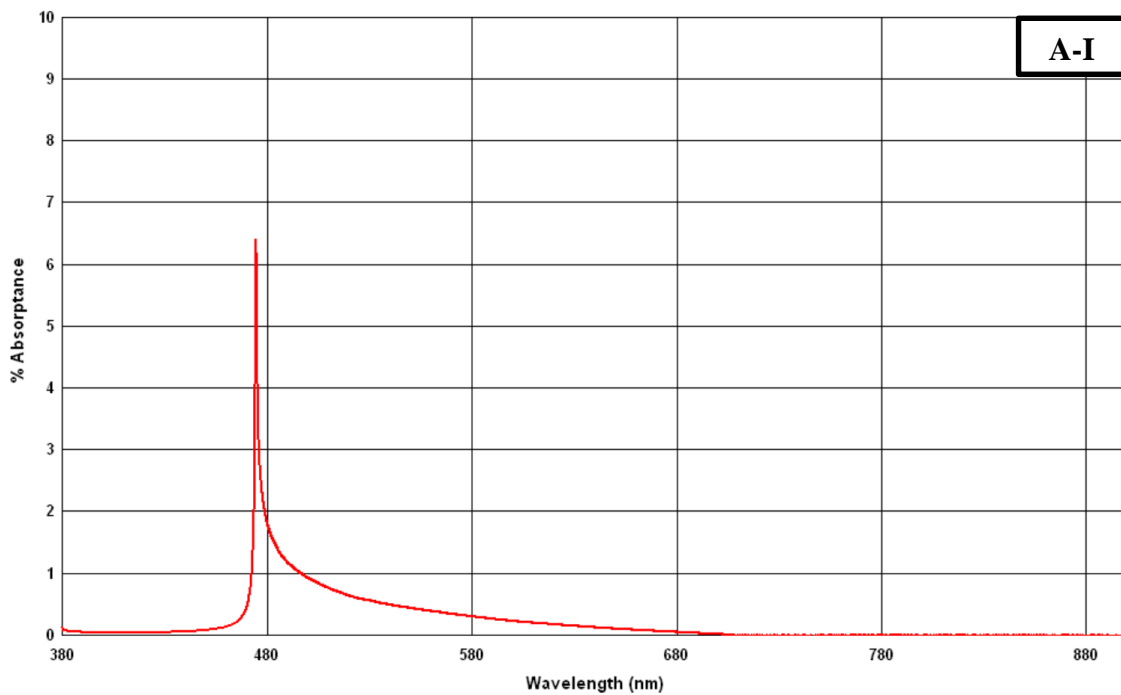
MNV	Manual Needle Valve, 49	photostationary state, 11
NE	northeast, 112	PTFE
NIST	National Institute of Standards and Technology (an agency of US Department of Commerce), 39	Polytetrafluoroethylene, 71
NO ₂ (CAABA/MECCA)	the simulated NO ₂ , 130	RFC
NO _{GPT}	the remaining concentration of NO in the calibration gas after gas phase titration, 44	relative fraction of contribution, 97
NO _x	[Nitric oxide (NO) + Nitrogen dioxide (NO ₂)], 3	RH
NW	northwest, 61	relative humidity, 60
OCP	ozone compensation point, 15	RO _x
OPE	O ₃ production efficiency, 143	[Hydroperoxyl (HO ₂) + sum of organic peroxy radicals (Σ RO ₂)], 3
P(O ₃) _{CAABA/MECCA}	The production rates of O ₃ from simulations, 130	SCIAMACHY
PAN	peroxyacetylnitrate, 6	SCanning Imaging Absorption spectroMeter for Atmospheric CHartography, 5
PARADE	PARTicles and RADicals	SE
	Diel observations of the impact of urban and biogenic Emissions, 18	southeast, 112
PBL	planetary boundary layer, 2	SW
PMT	Photomultiplier (Photon counting head), 33	southwest, 61
ppb _v	parts per billion by volume, 12	T(O ₃)
ppm _v	parts per million by volume, 1	photochemical ozone tendency, 82
ppqv	parts per quadrillion by volume, 1	TD-GC-MS
ppt _v	parts per trillion by volume, 12	Thermal Desorber Gas Chromatograph Mass Spectrometer, 67
PSS		TDLAS
		Tunable Diode Laser Absorption Spectroscopy, 17
		VOCs
		volatile organic compounds, 6
		W
		west, 115
		Φ
		Leighton ratio, 12
		Φ _{ext}
		extended Leighton ratio, 12
		Φ _{ext} (T)
		Φ _{ext} with the tuned OH reactivity for the model, 129
		Φ _{ext2}
		extended Leighton ratio only with O ₃ and HO ₂ contributions, 117
		Φ _{mod}
		modified Leighton ratio with inclusion of several loss or formation processes, 102

7.2 Instrumental

7.2.1.1 Optical filters

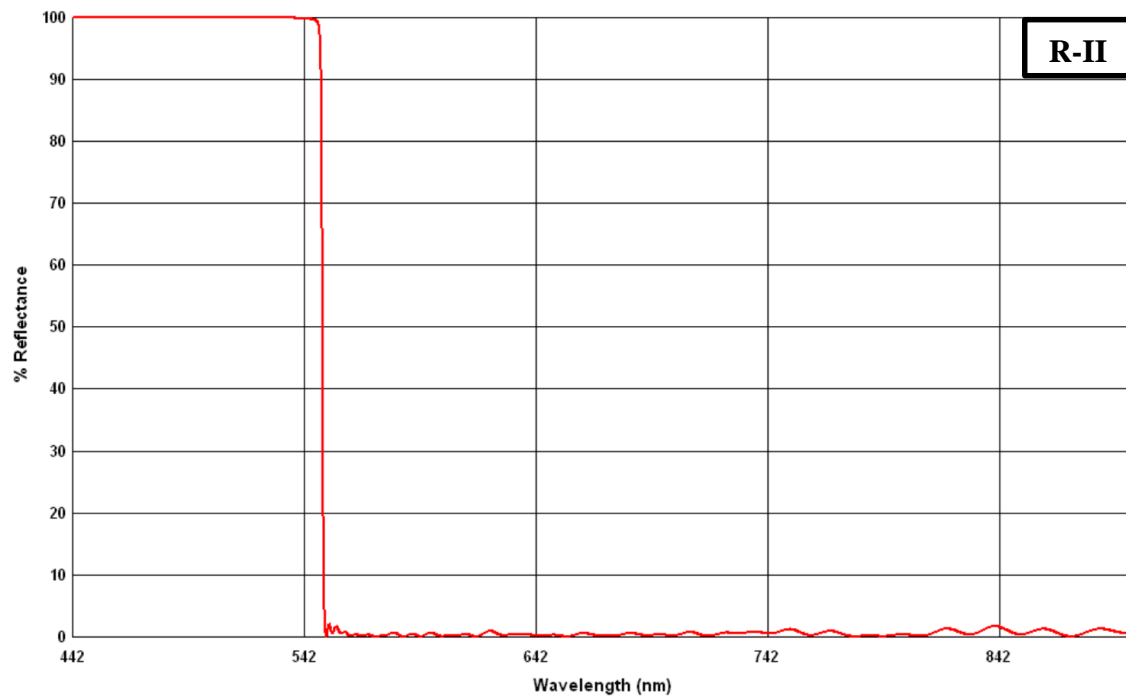
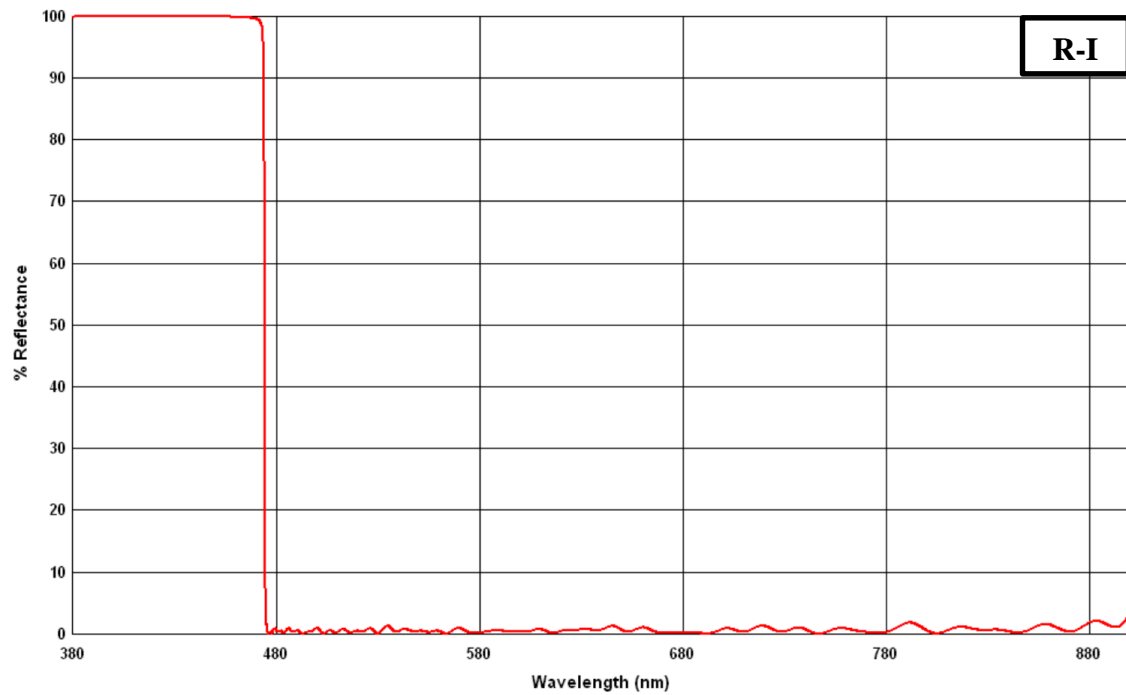
7.2.1.1.1 Absorption

The absorption of two different cut on filters inside the detection optics of GANDALF. (A-I: [x-axis: 380-900nm] cut on at 470nm and A-II: [x-axis: 440-900nm] cut on at 550nm). These figures (A-I and A-II) are provided by Barr Associates, Inc. (www.barrassociates.com).



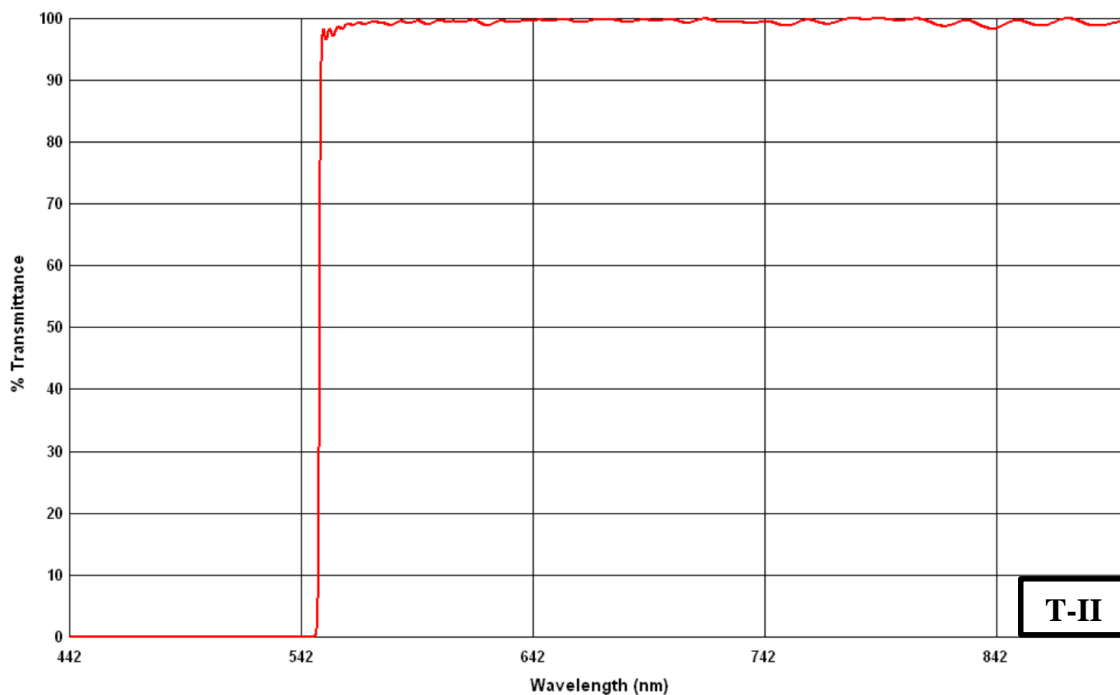
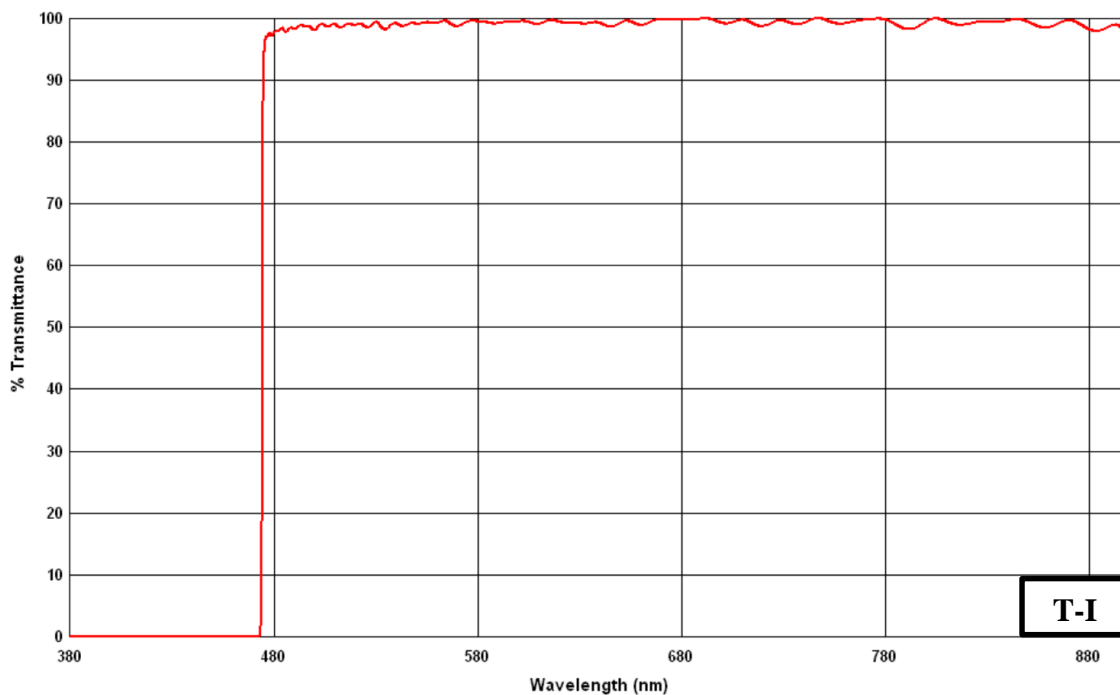
7.2.1.1.2 Reflectance

The reflectance of two different cut on filters inside the detection optics of GANDALF. (R-I: [x-axis: 380-900nm] cut on at 470nm and R-II: [x-axis: 440-900nm] cut on at 550nm). These figures (R-I and R-II) are provided by Barr Associates, Inc. (www.barrassociates.com).



7.2.1.1.3 Transmittance

The transmittance of two different cut on filters inside the detection optics of GANDALF. (T-I: [x-axis: 380-900nm] cut on at 470nm and T-II: [x-axis: 440-900nm] cut on at 550nm). These figures (T-I and T-II) are provided by Barr Associates, Inc. (www.barrassociates.com).



7.2.1.2 Laser ON/OFF cycle

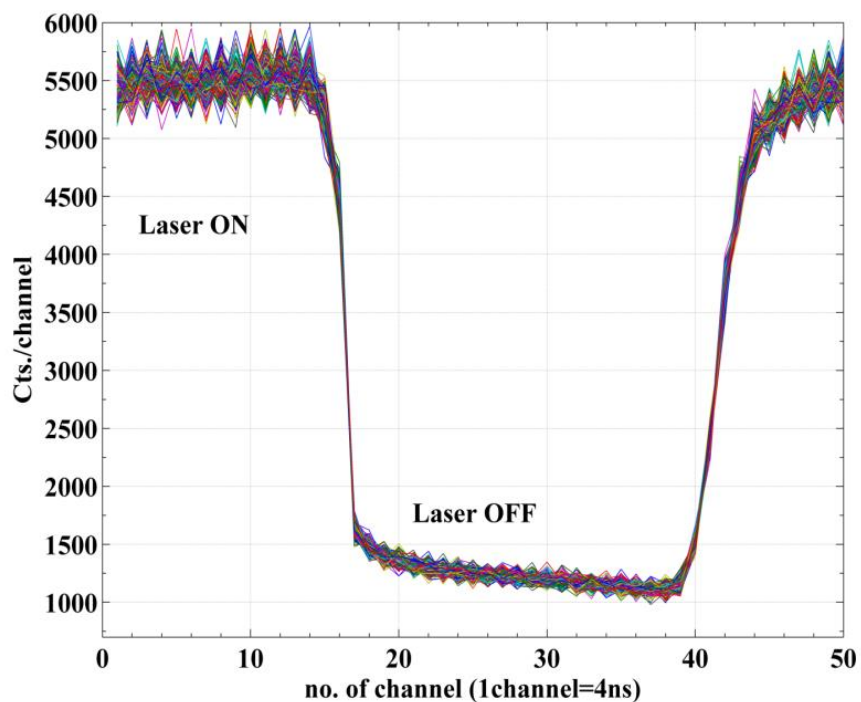


Figure: 200ns on-off cycle of laser for a signal ($\sim 12\text{ppb}_v \text{NO}_2$) [y-axis arb. unit]

7.2.1.3 Appurtenances

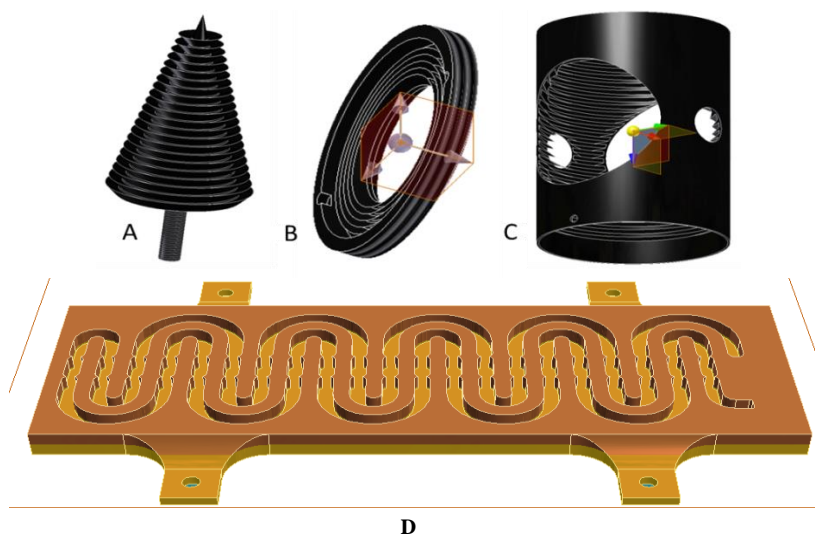
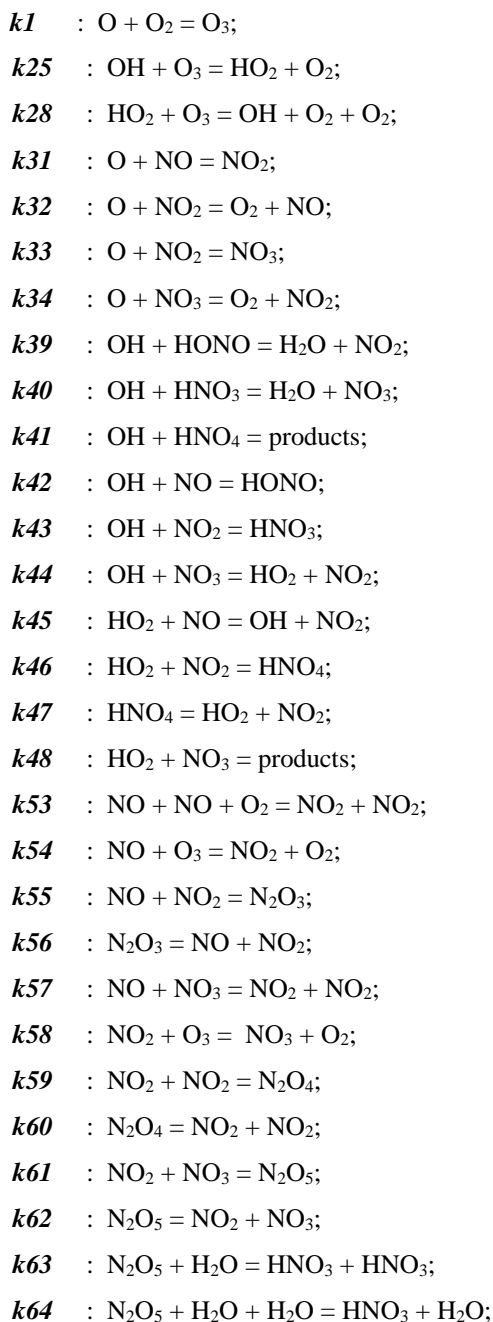


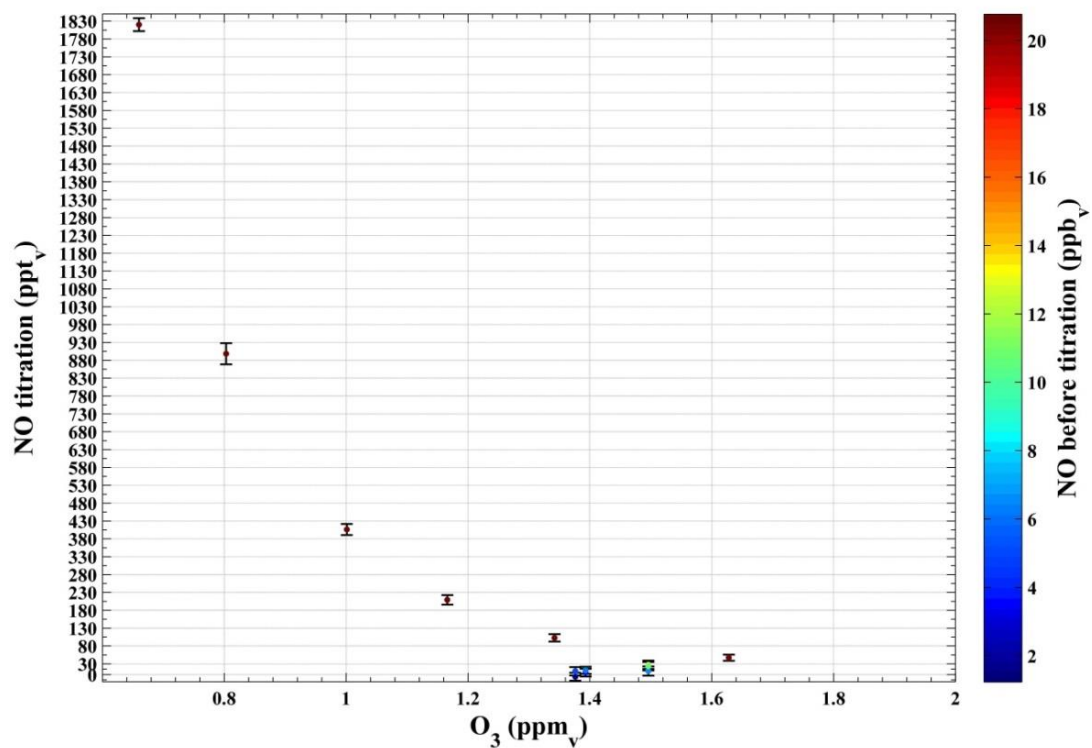
Figure: Baffles (A,B,C) and cooling plate internal structure (D).

7.2.1.4 Reactions for calibration simulations

Note; all rate coefficients from *k1* to *k64* are based on temperature dependence and taken from ([Atkinson et al., 2004](#)).



Atkinson, R., Baulch, D. L., Cox, R. A., Crowley, J. N., Hampson, R. F., Hynes, R. G., Jenkin, M. E., Rossi, M. J., and Troe, J.: *Evaluated kinetic and photochemical data for atmospheric chemistry: Volume I - gas phase reactions of O_x , HO_x , NO_x and SO_x species*, *Atmos Chem Phys*, 4, 1461-1738, 2004.

7.2.1.5 NO_{GPT}Figure: NO_{GPT} (NO after gas phase titration), as measured by a CLD

7.2.1.6 Sensitivity and LOD

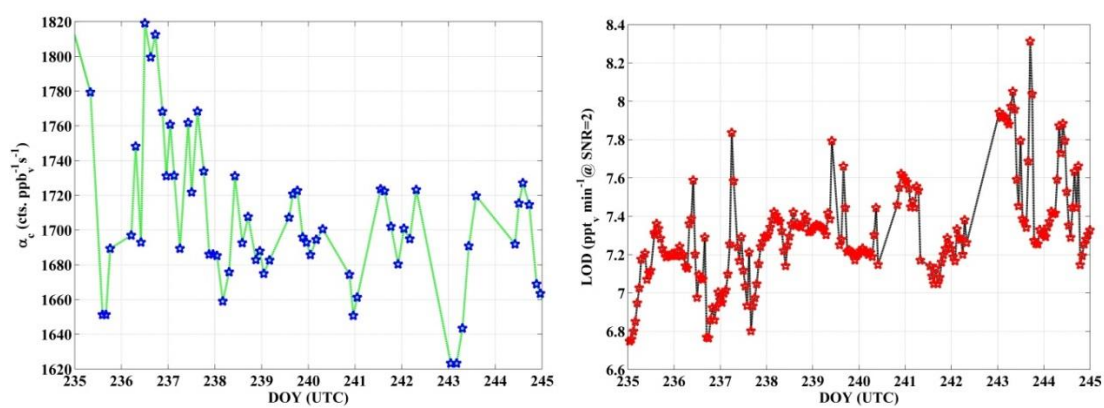


Figure: An example for the sensitivity of GANDALF in left panel, taken from an automated calibrated period of PARADE-2011. LOD for the same period in the right panel.

7.2.1.7 NO Accuracy

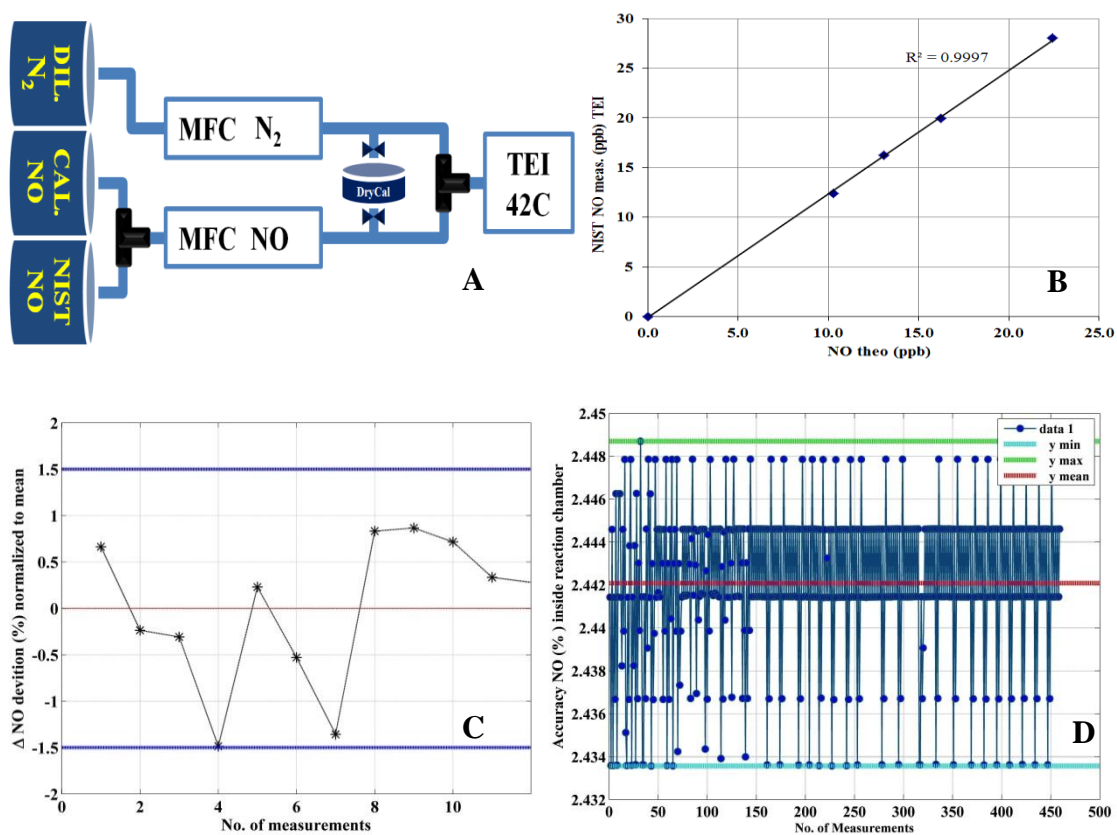



Figure: [A] diagram for NIST setup. [B] An example of NIST measured by TEI⁵⁴ monitor. [C] Deviations (max 1.5 %) around average derived NO mixture value based on NIST. [D] The calculated NO accuracy (max 2.5 %) inside reaction chamber for different flows of NO during PARADE.

⁵⁴ C42, Thermo Environmental Instrument

7.2.1.8 Certified Standards


7.2.1.8.1 NIST

National Institute of Standards & Technology (NIST) standard used to compare NO calibration gas for the calibrator of GANDALF.

	<p>National Institute of Standards & Technology</p> <p>Certificate of Analysis</p> <p>Standard Reference Material® 2627a</p> <p>Nitric Oxide in Nitrogen</p> <p>(Nominal Amount-of-Substance Fraction – 5 µmol/mol)</p> <p><i>This certificate reports the certified values for Lot 48-H-XX.</i></p>
<p>This Standard Reference Material (SRM) is a primary gas mixture for which the amount-of-substance fraction, expressed as concentration [1], may be related to secondary working standards. The SRM is intended for the calibration of instruments used for nitric oxide determinations and for other uses.</p>	
<p>This SRM mixture is supplied in a DOT 3AL specification aluminum (6061 alloy) cylinder with a water volume of 6 L. Mixtures are shipped with a nominal pressure exceeding 12.4 MPa (1800 psig) which provides the user with 0.65 m³ (23.0 ft³) of useable mixture. The cylinder is the property of the purchaser and is equipped with a CGA-660 stainless steel valve, which is the recommended outlet for this nitric oxide mixture.</p>	
<p>Certified Value: This SRM mixture has been certified for the concentrations of nitric oxide (NO) and total oxides of Nitrogen (NO_x) in a nitrogen (N₂) matrix. The certified values, given below, apply to the identified cylinder and NIST sample number.</p>	
Nitric Oxide (NO) Concentration:	4.91 µmol/mol ± 0.04 µmol/mol
Total oxides of Nitrogen (NO _x) Concentration:	5.09 µmol/mol ± 0.04 µmol/mol
Cylinder Number: CAL016555	NIST Sample Number: 48-H-61
<p>The uncertainty of the certified value includes the estimated uncertainties in the NIST standards, the analytical comparisons to the lot standard (LS), and the uncertainty of comparing the LS with each of the mixtures comprising this lot. This uncertainty is expressed as an expanded uncertainty $U = ku_c$ with u_c determined by experiment and a coverage factor $k = 2$. The true value for the nitric oxide and total oxides of nitrogen amount-of-substance fraction is asserted to lie in the interval defined by the certified value $\pm U$ with a level of confidence of approximately 95 % [2].</p>	
<p>Expiration of Certification: This certification is valid from this certificate issue date until 31 December 2011, within the measurement uncertainties specified, provided the SRM is handled and stored in accordance with the instructions given in this certificate.</p>	
Hydrotest Date: May 2005	Blend Date: September 2005
<p>Cylinder and Gas Handling Information: A high-purity, two-stage pressure regulator with a stainless steel diaphragm and CGA-660 outlet should be used to safely reduce the pressure and to deliver this SRM mixture to the instrument. The regulator should be evacuated and purged to prevent accidental contamination of the SRM by repeatedly (minimum five times) opening the valve and pressurizing the regulator, then closing the valve and releasing the pressure safely into a vent line. This SRM should NOT be used after the internal pressure drops below 0.8 MPa (100 psig). This SRM should be stored under normal laboratory conditions within the temperature range of 15 °C and 30 °C.</p>	
<p>The analytical measurements leading to the certification of this current SRM lot were performed by W.J. Thorn III of the NIST Analytical Chemistry Division.</p>	
<p>Stephen A. Wise, Chief Analytical Chemistry Division</p>	
<p>Gaithersburg, MD 20899</p>	
Certificate Issue Date: 02 June 2008	<p>Robert L. Watters, Jr., Chief Measurement Services Division</p>
SRM 2627a	Page 1 of 2

7.2.1.8.2 Mass flow calibrator (DryCal)

NIST standard for DryCal sensors, DC-LC-1 and HC-LC-1, BIOS International.



Neuwegweg 283a Tel. +31 (0)24 379 2120
 6603BN WILDHVEN Fax +31 (0)24 379 1063
 The Netherlands Web: www.tpf-control.nl

Cal Date : 08 June 2010
 Page : 1 of 1

Calibration Certificate

GENERAL DETAILS

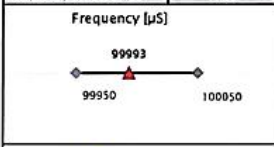
Customer name : Westphal Mess- und Regeltechnik	Manufacturer : Bios International
Customer ref : R10-000379	Product : DC-2 base
Internal ref. : 12875	Serial no. : 104451
	Revision : 1.15

AS RECEIVED TEST DATA

Temperature, pressure and frequency are tested following the Bios procedure PR04-05 Rev.E

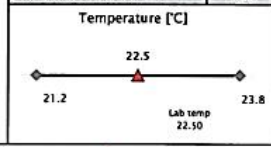
Tool Number	Description	Cal. Date	Due Date	Cert.
DVM001	Frequency counter	10/8/2009	10/8/2010	
T00101	PT100 sensor	9/11/2009	9/11/2010	
P00107	UNI3 pressure ind.	11/27/2009	11/27/2010	409752

▲ Ind. freq. [µS]	99993.10
Frequency in tolerance	Yes



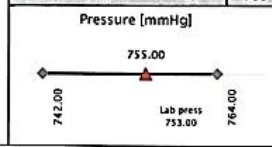
◆ Minimum value / Maximum value ▲ Measured / indicated value

▲ Ind. Temp [°C]	22.50
Temp in tolerance ± 1.3 °C	Yes



◆ Minimum value / Maximum value ▲ Measured / indicated value

▲ Ind. P. [mmHg]	755.00
Pressure in tolerance ± 11 mmHg	Yes



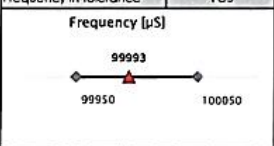
◆ Minimum value / Maximum value ▲ Measured / indicated value

AS SHIPPED TEST DATA

Temperature, pressure and frequency are tested following the Bios procedure PR04-05 Rev.E

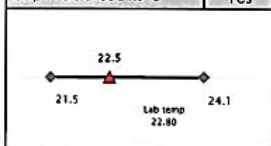
Tool Number	Description	Cal. Date	Due Date	Cert.
DVM001	Frequency counter	10/8/2009	10/8/2010	
T00101	PT100 sensor	9/11/2009	9/11/2010	
P00107	UNI3 pressure ind.	11/27/2009	11/27/2010	409752

▲ Ind. freq. [µS]	99993.10
Frequency in tolerance	Yes



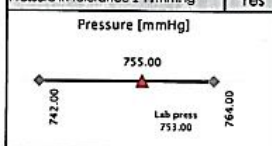
◆ Minimum value / Maximum value ▲ Measured / indicated value

▲ Ind. Temp [°C]	22.50
Temp in tolerance ± 1.3 °C	Yes



◆ Minimum value / Maximum value ▲ Measured / indicated value

▲ Ind. P. [mmHg]	755.00
Pressure in tolerance ± 11 mmHg	Yes




◆ Minimum value / Maximum value ▲ Measured / indicated value


Technician Name : Khalid Harkach

Printed date : 08/06/2010


Certificate no. 12876



This report shall not be reproduced except in full, without the written approval of TPF Control. Results only relate to the items calibrated.
 This report is produced by an electronic data system and is valid without signature.
 Form BMS-41.03 / Rev A dated 11 aug 08



TPF CONTROL



**CALIBRATION
RVA K 149**

CALIBRATION CERTIFICATE

12877

Applicant	Westphal Mess- und Regeltechnik
Customer name	E. Reuveni
Contact	Lourweg 20
Address	85321 - Olching Germany
Order reference applicant	R10-000379
Order reference TPF Control	12875
Instrument information [PUT]	
Instrument	Primary Flow Calibrator
Manufacturer	Bos International
Serial no.	10461
Model	DC-IC-1
Revision	F
Calibration method	The device under test is connected in a parallel setup to the mentioned flow calibrator to compare flow readings. An appropriate warm up time is incorporated. Bios - Dycal products; a flow source is used to generate a flow. This flow is measured in an A-B method (A-reading lab standard, B-reading device under test).
Period of calibration	8 Juni 2010
Calibration result	The results of the calibration are presented on page 2 of 2. The reported uncertainty of measurement is based on the standard uncertainty multiplied by a coverage factor k=2 which provides a confidence level of approximately 95%. The standard uncertainty of measurement has been determined in accordance with EA-402.
Calibration traceability	The measurements have been executed using standards for which the traceability to international standards has been demonstrated towards the RVA.
Remarks	
Certificate issue date	Wijchen, 8 Juni 2010
Calibration technician	Khalid Hartoch
Technical Manager	Rik van de Bovenkamp


TPF Control B.V.
Hilversweg 203a
1441 BT Hilversum (NL)
Tel: +31 24 377 2120
Fax: +31 24 377 1063
Web: www.tpf-control.nl

RVA is member of the European Co-operation for Accreditation (EA) and one of the signatories of the metrology conventions of the calibration and measurement assurance (CMA) for the mutual recognition of the mutual recognition of calibration certificates.


Reproduction of the complete certificate is allowed. Parts of the certificate may only be reproduced with written permission of the calibration provider but neither the total nor appropriate nor TPF CONTROL B.V. name may be used.

Form BMS 41.09 - Rev D dated 1-05-10

Page 1 of 2



TPF CONTROL



**CALIBRATION
RVA K 149**

CALIBRATION CERTIFICATE

12878

Applicant	Westphal Mess- und Regeltechnik
Customer name	E. Reuveni
Contact	Lourweg 20
Address	85321 - Olching Germany
Order reference applicant	R10-000379
Order reference TPF Control	12875
Instrument information [PUT]	
Instrument	Primary Flow Calibrator
Manufacturer	Bos International
Serial no.	10464
Model	DC-IC-1
Revision	E
Calibration method	The device under test is connected in a parallel setup to the mentioned flow calibrator to compare flow readings. An appropriate warm up time is incorporated. Bios - Dycal products; a flow source is used to generate a flow. This flow is measured in an A-B method (A-reading lab standard, B-reading device under test).
Period of calibration	8 Juni 2010
Calibration result	The results of the calibration are presented on page 2 of 2. The reported uncertainty of measurement is based on the standard uncertainty multiplied by a coverage factor k=2 which provides a confidence level of approximately 95%. The standard uncertainty of measurement has been determined in accordance with EA-402.
Calibration traceability	The measurements have been executed using standards for which the traceability to international standards has been demonstrated towards the RVA.
Remarks	
Certificate issue date	Wijchen, 8 Juni 2010
Calibration technician	Khalid Hartoch
Technical Manager	Rik van de Bovenkamp

TPF Control B.V.
Hilversweg 203a
1441 BT Hilversum (NL)
Tel: +31 24 377 2120
Fax: +31 24 377 1063
Web: www.tpf-control.nl

RVA is member of the European Co-operation for Accreditation (EA) and one of the signatories of the metrology conventions of the calibration and measurement assurance (CMA) for the mutual recognition of the mutual recognition of calibration certificates.

Reproduction of the complete certificate is allowed. Parts of the certificate may only be reproduced with written permission of the calibration provider but neither the total nor appropriate nor TPF CONTROL B.V. name may be used.

Form BMS 41.09 - Rev D dated 1-05-10

Page 1 of 2



CALIBRATION CERTIFICATE

12877

AS FOUND RESULTS

Lab. Temperature 20.8 °C

Lab. Pressure 1004.2 mbar

INSTRUMENT READING		LAB STANDARD READING		DEVIATION (ERROR)		UNCERTAINTY	
[ml/min]	[ml/min]	Flow [ml/min]	Tool no.	Of Rate [%]	Flow [ml/min]	Limit [%]	Flow [%]
29.45	29.25	800101		0.70	0.20	1.00	0.32%
101.70	100.51	800101		1.19	1.20	1.00	0.33%
485.45	498.24	800101		-2.57	-12.79	2.00	0.33%

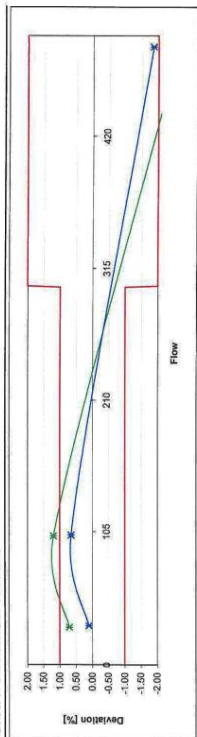
CALIBRATION RESULTS AFTER ADJUSTMENT

Lab. Temperature 20.8 °C

Lab. Pressure 1004.3 mbar

INSTRUMENT READING		LAB STANDARD READING		DEVIATION (ERROR)		UNCERTAINTY	
[ml/min]	[ml/min]	Flow [ml/min]	Tool no.	Of Rate [%]	Flow [ml/min]	Limit [%]	Flow [%]
30.76	30.72	800101		0.10	0.03	1.00	0.33%
102.25	101.59	800101		0.65	0.66	1.00	0.34%
491.15	500.40	800102		-1.85	-9.25	2.00	0.32%

GRAPH DEVIATION vs FLOW



Remarks:
The deviation is determined by: Instrument reading - Lab standard reading
Lab standard reading + 100 %



CALIBRATION CERTIFICATE

12878

AS FOUND RESULTS

Lab. Temperature 21.2 °C

Lab. Pressure 1004.5 mbar

INSTRUMENT READING		LAB STANDARD READING		DEVIATION (ERROR)		UNCERTAINTY	
[ml/min]	[ml/min]	Flow [ml/min]	Tool no.	Of Rate [%]	Flow [ml/min]	Limit [%]	Flow [%]
501.20	495.41	800101		0.56	2.79	1.00	0.32%
5034.00	5023.65	800104		0.21	10.35	1.00	0.37%
50100.00	49602.00	800104		1.00	498.00	1.50	0.38%

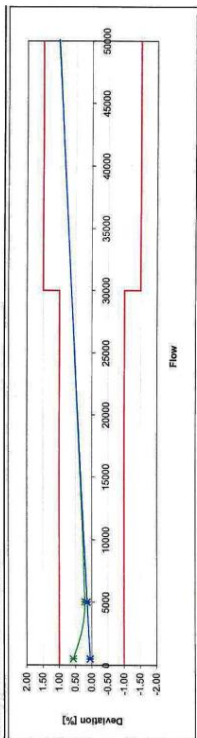
CALIBRATION RESULTS AFTER ADJUSTMENT

Lab. Temperature 20.7 °C

Lab. Pressure 1004.4 mbar

INSTRUMENT READING		LAB STANDARD READING		DEVIATION (ERROR)		UNCERTAINTY	
[ml/min]	[ml/min]	Flow [ml/min]	Tool no.	Of Rate [%]	Flow [ml/min]	Limit [%]	Flow [%]
491.25	491.05	800101		0.04	0.21	1.00	0.32%
5012.00	5005.30	800104		0.13	6.70	1.00	0.37%
50080.00	49573.50	800104		1.02	506.50	1.50	0.37%

GRAPH DEVIATION vs FLOW



Remarks:
The deviation is determined by: Instrument reading - Lab standard reading
Lab standard reading + 100 %

7.3 PARADE-2011

7.3.1.1 Time Series of NMHC

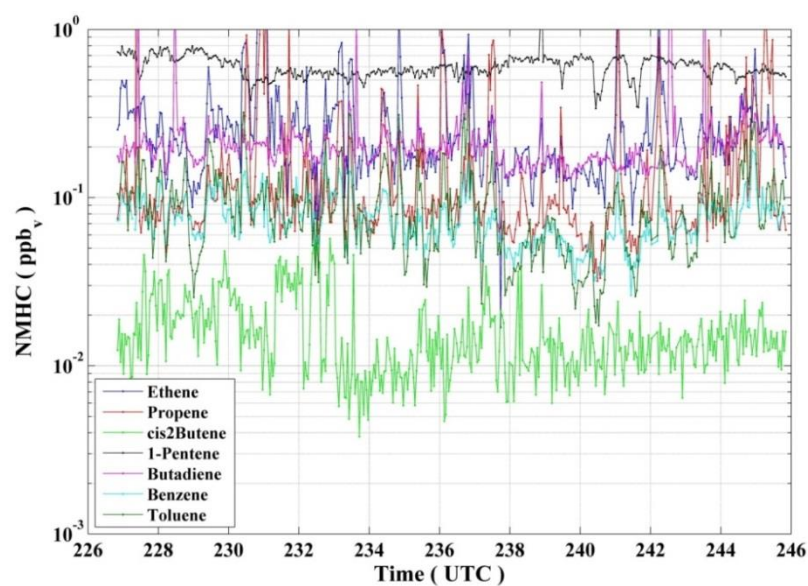


Figure: Time series of different alkenes and aromatics during PARADE-2011.

7.3.1.2 Air Mass Origin

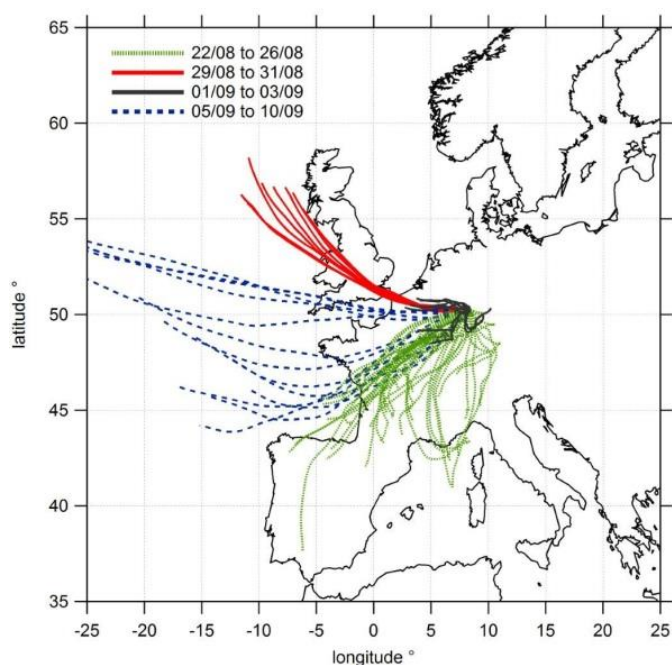
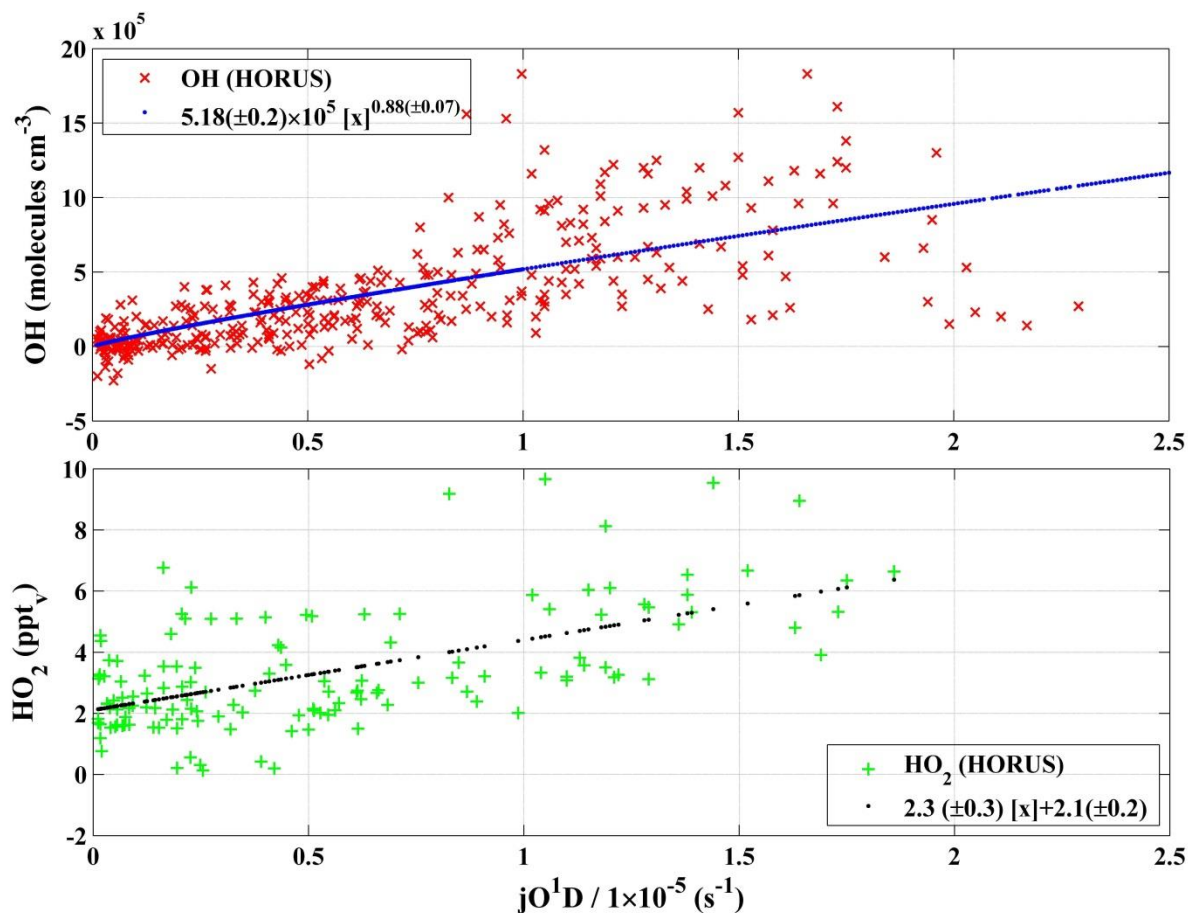


Figure: Origin of air mass for PARADE-2011 [Figure is taken from Crowley, J., 2012 (Presentation at PARADE data meeting Mainz)]

7.3.1.3 jO^1D versus HO_x 

A plot of correlation of the measured OH and HO_2 versus jO^1D in upper and lower panel, respectively, based on filter ($jO^1D > 1 \times 10^{-7} s^{-1}$) during PARADE.

7.3.1.4 NO_2 Ratios Correlations

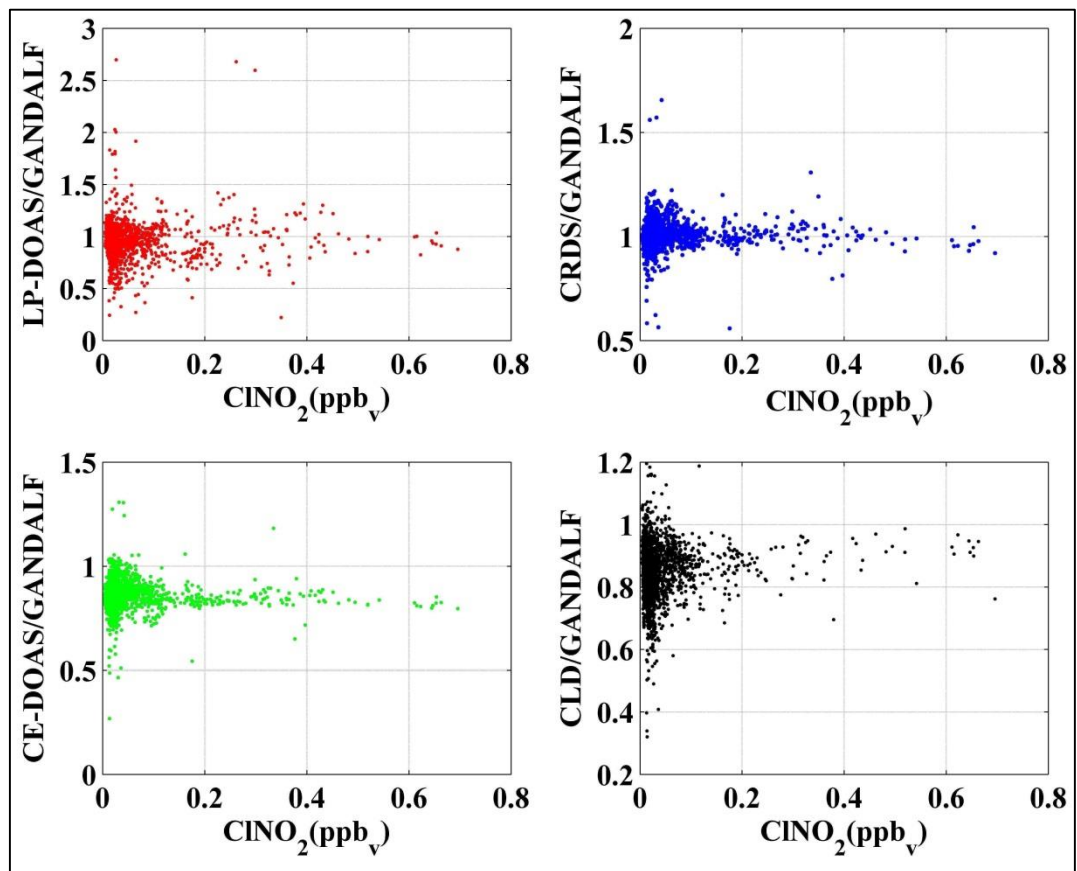
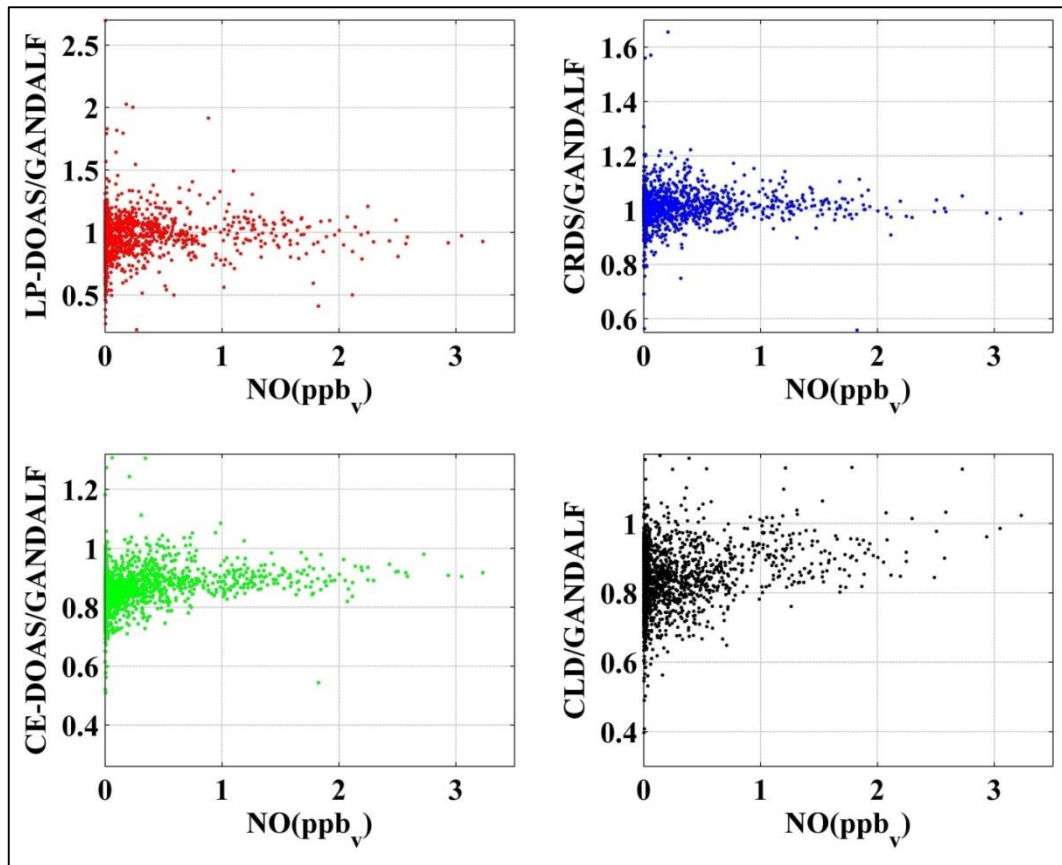
This section is related to NO_2 comparison for PARADE. A series of upcoming figures shows ratio (between all NO_2 measurements and GANDALF) as a function of different observed quantities to see any systematic correlation. Each figure is a set of four subplots according to different instruments. Y-axis of figures below is shown as follow (with data colour to show sequence of upcoming figures for quick go through).

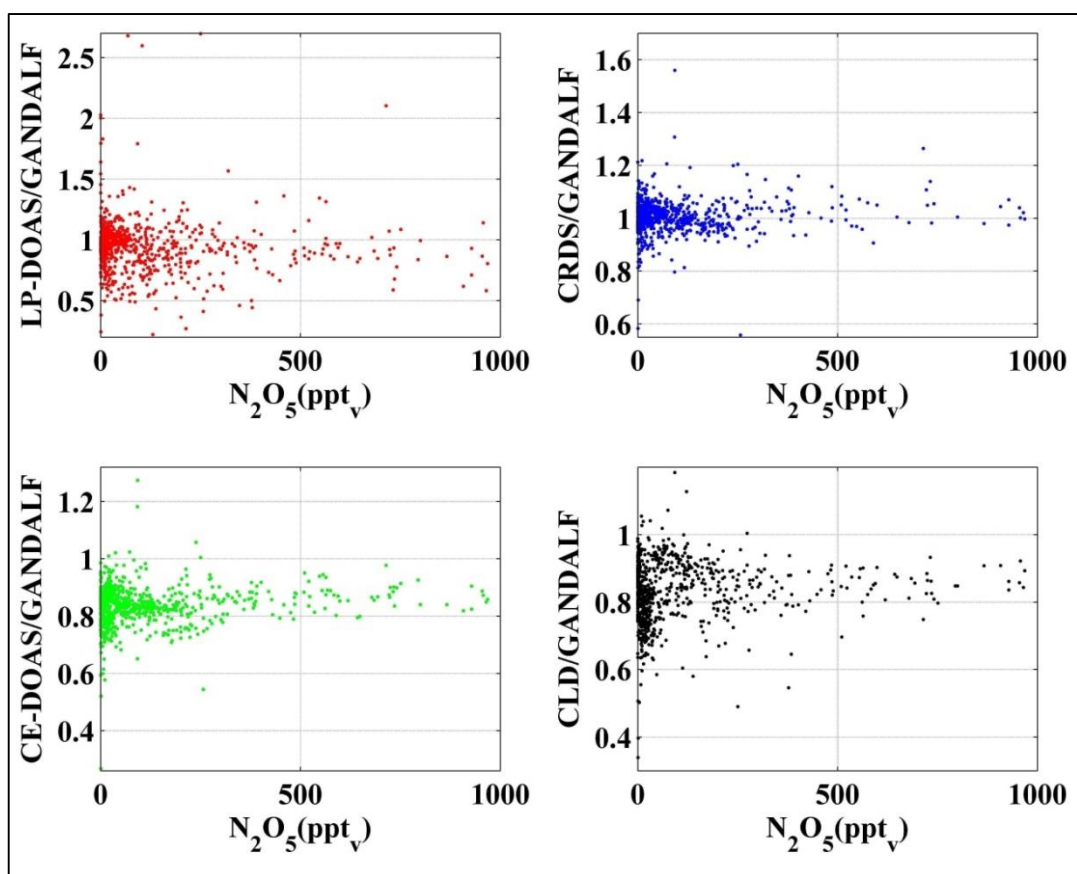
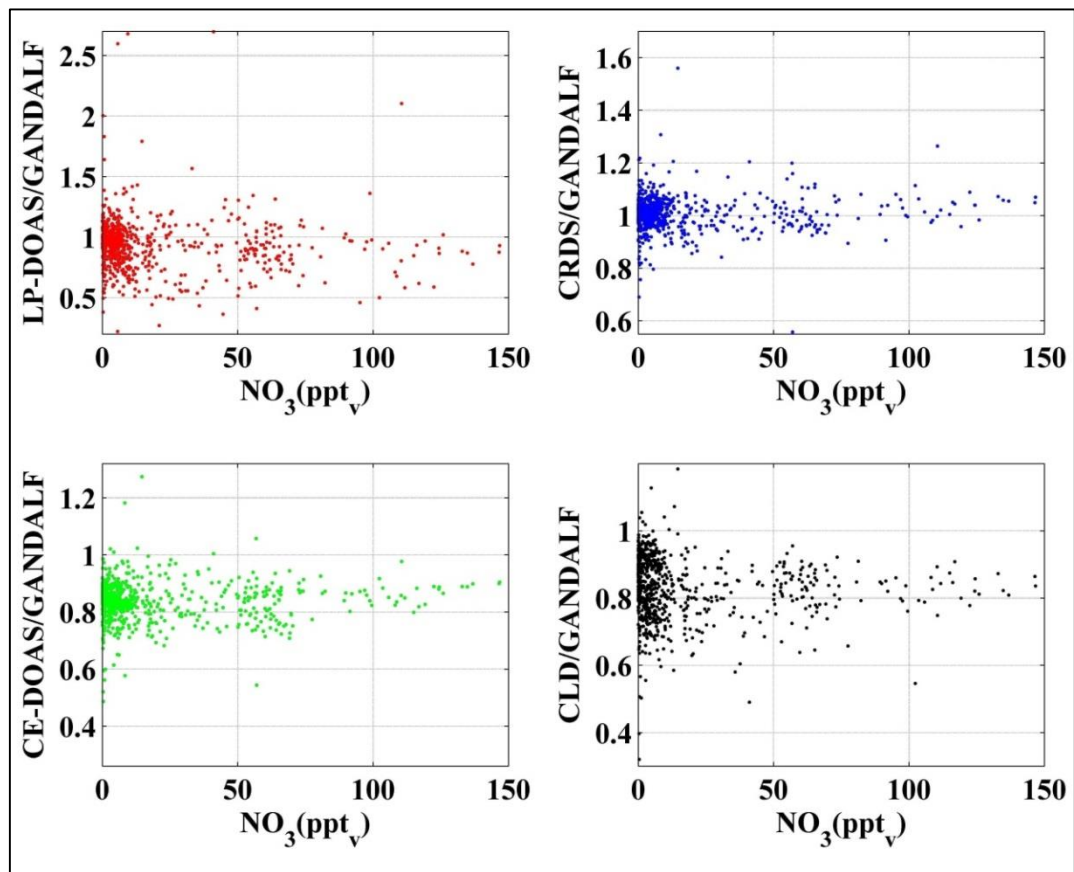
LP-DOAS/GANDALF

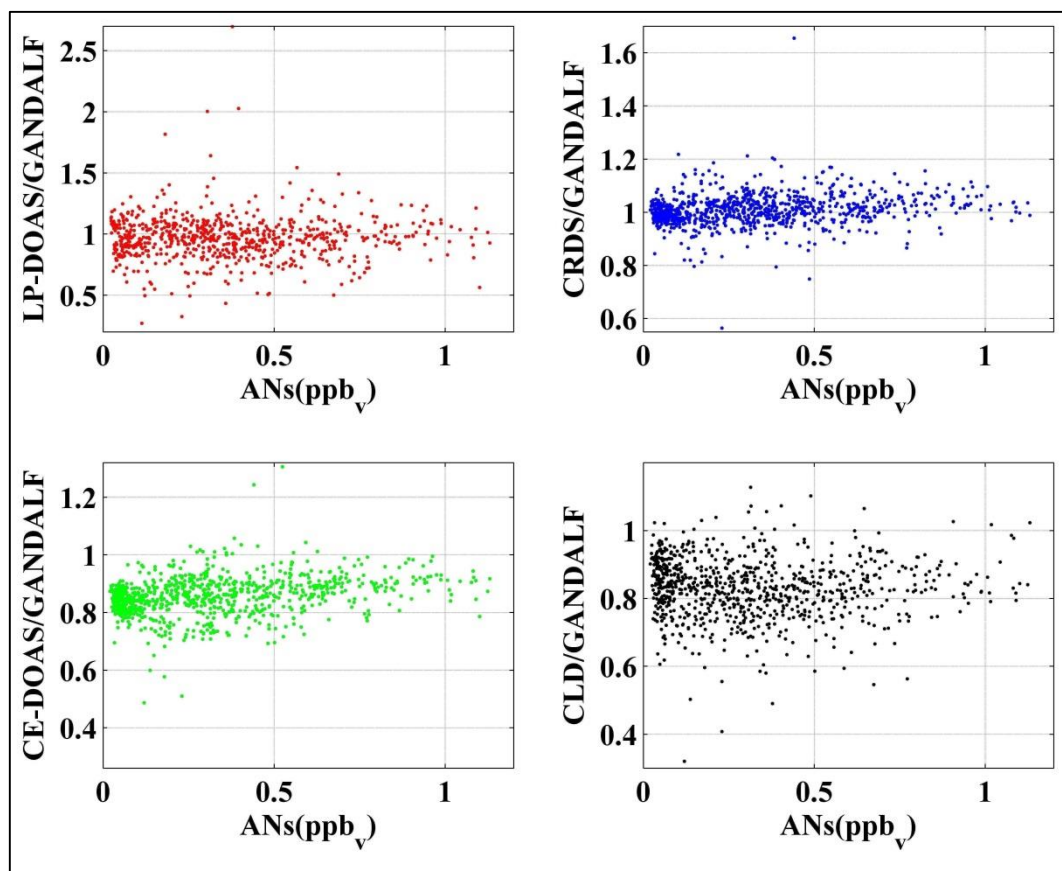
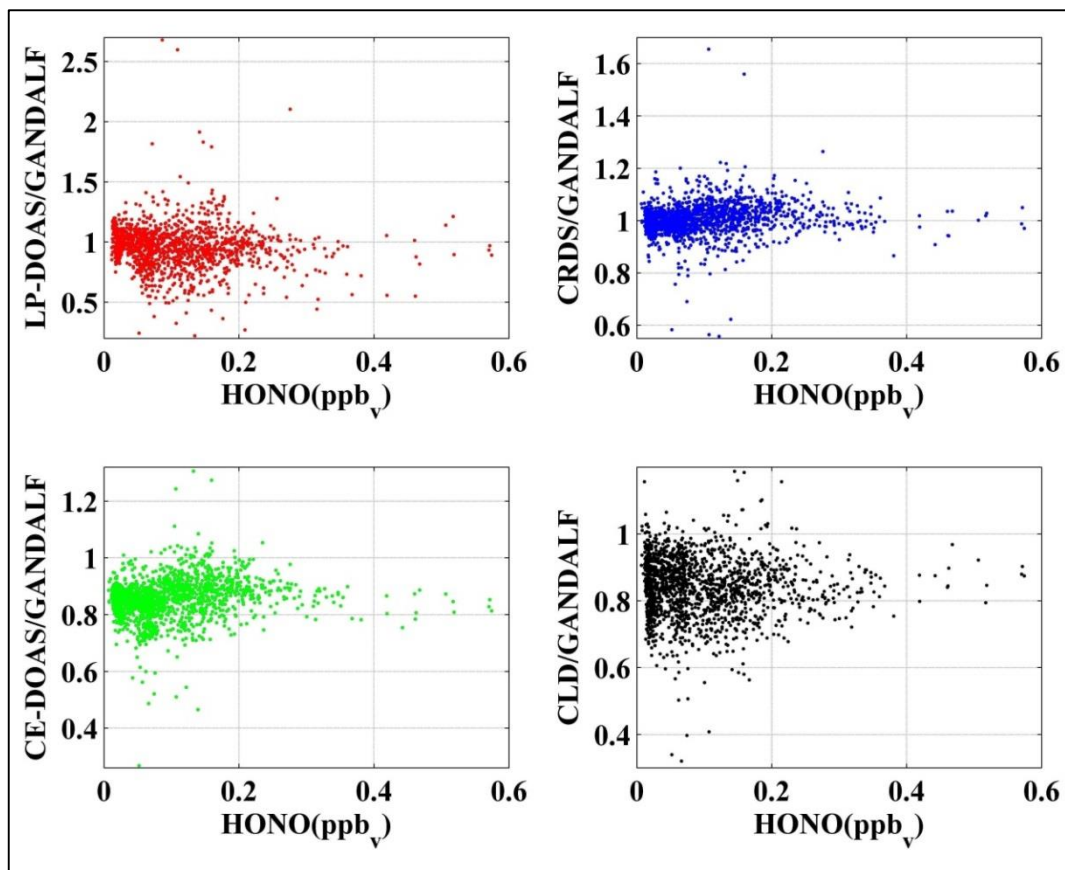
CRDS/GANDALF

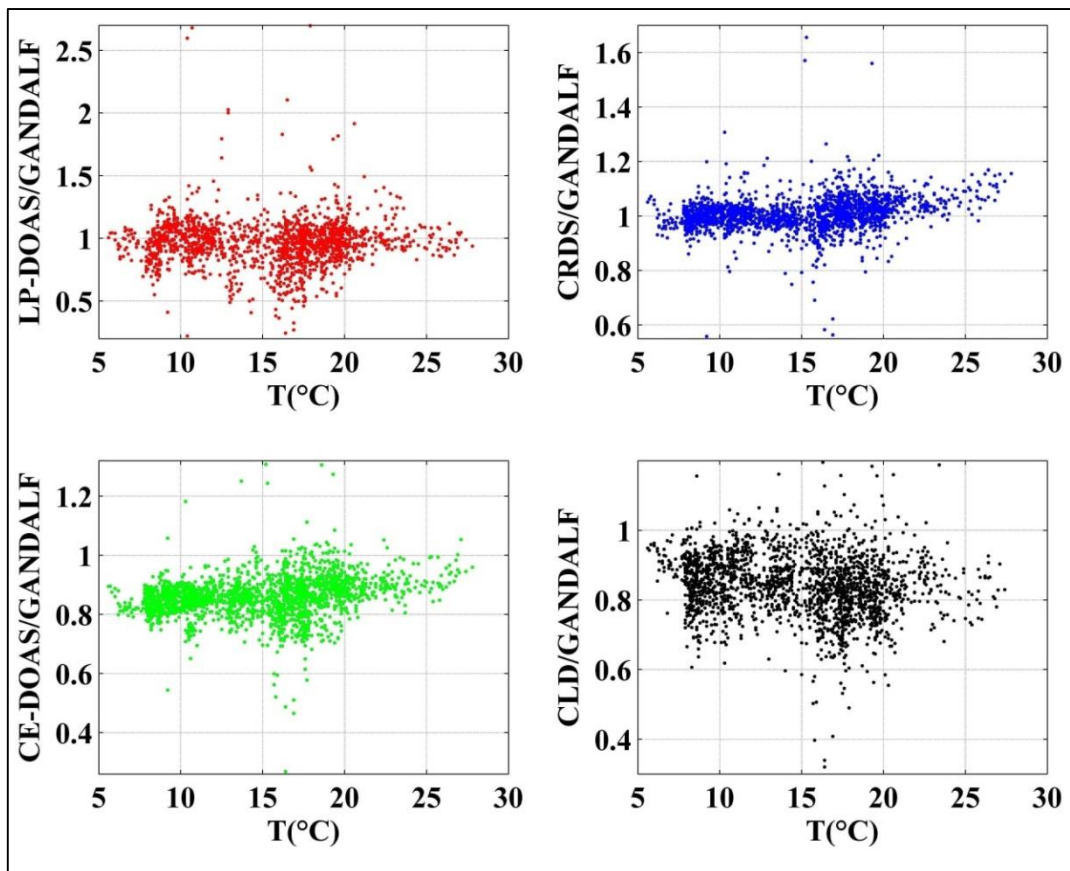
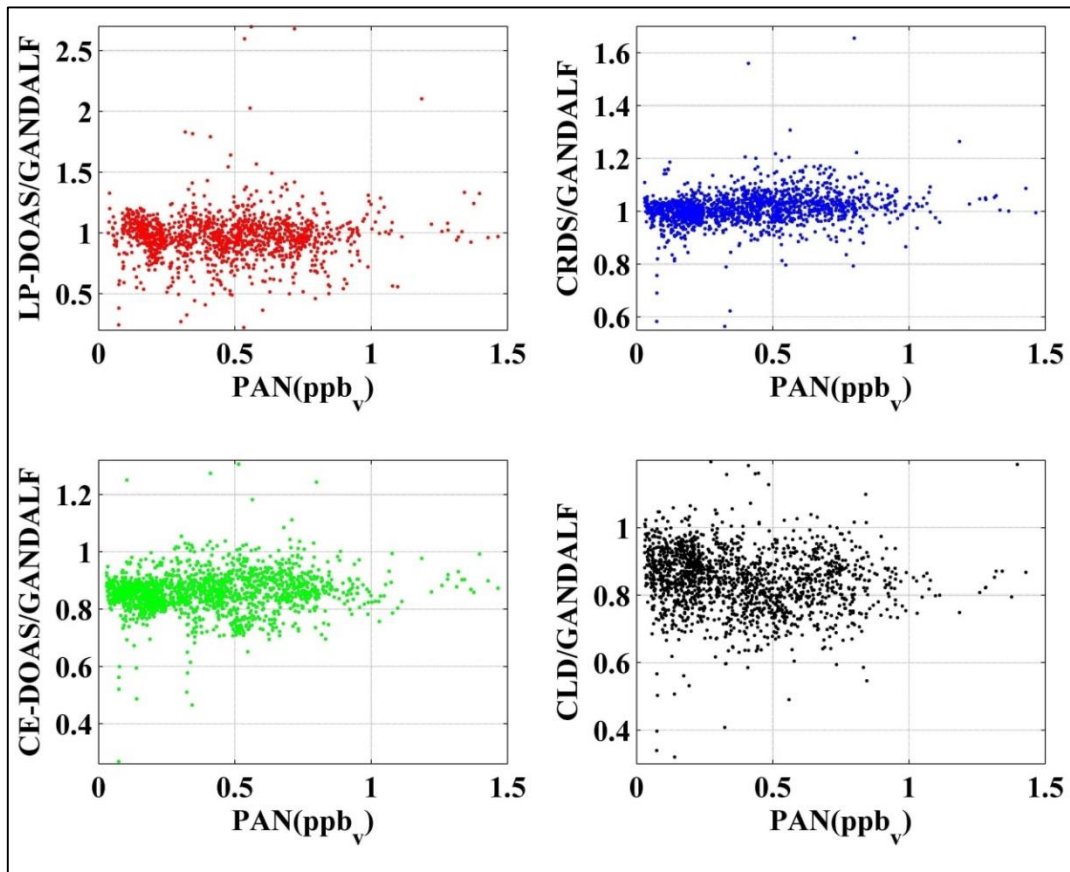
CE-DOAS/GANDALF

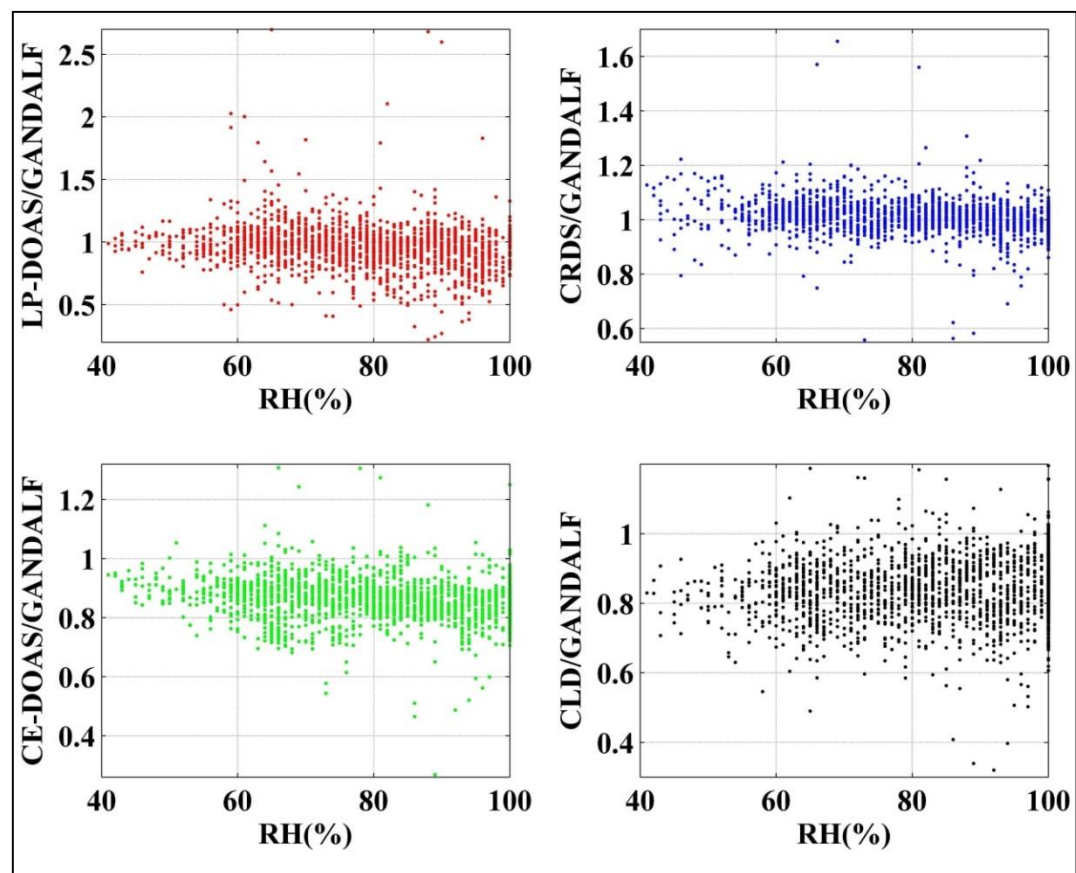
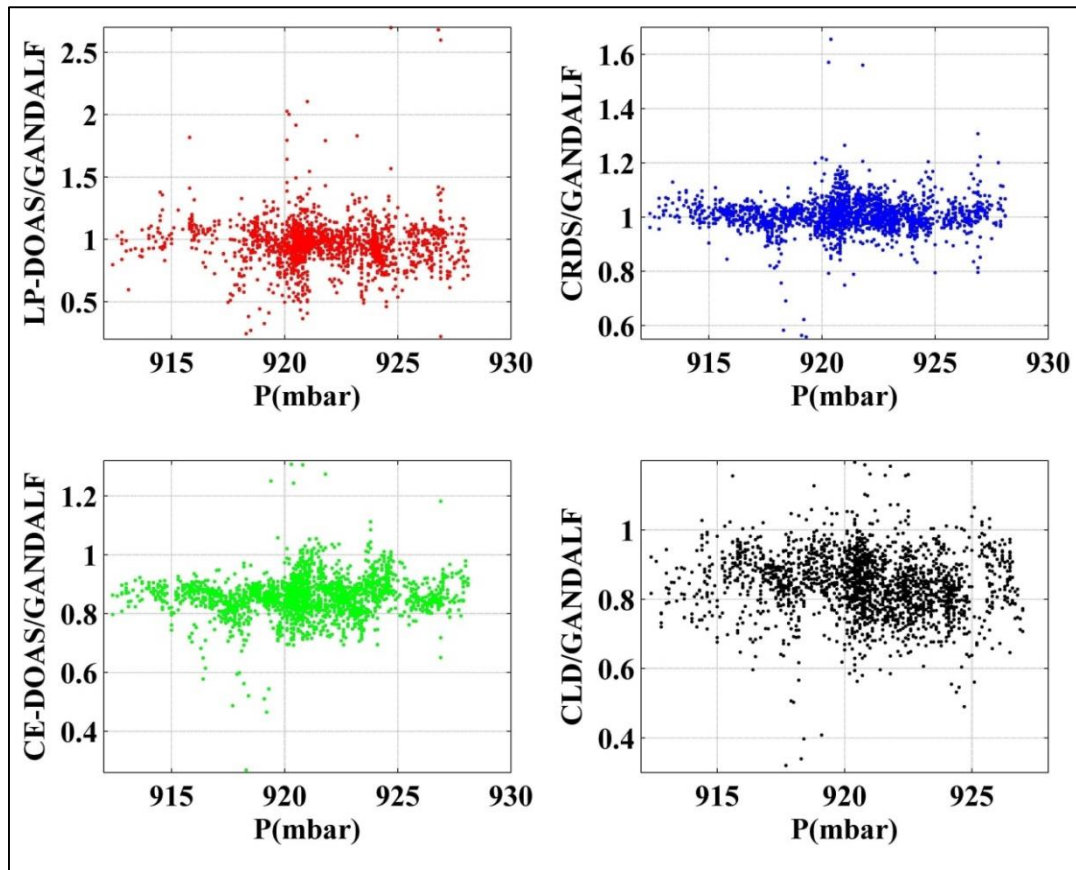
CRD/GANDALF

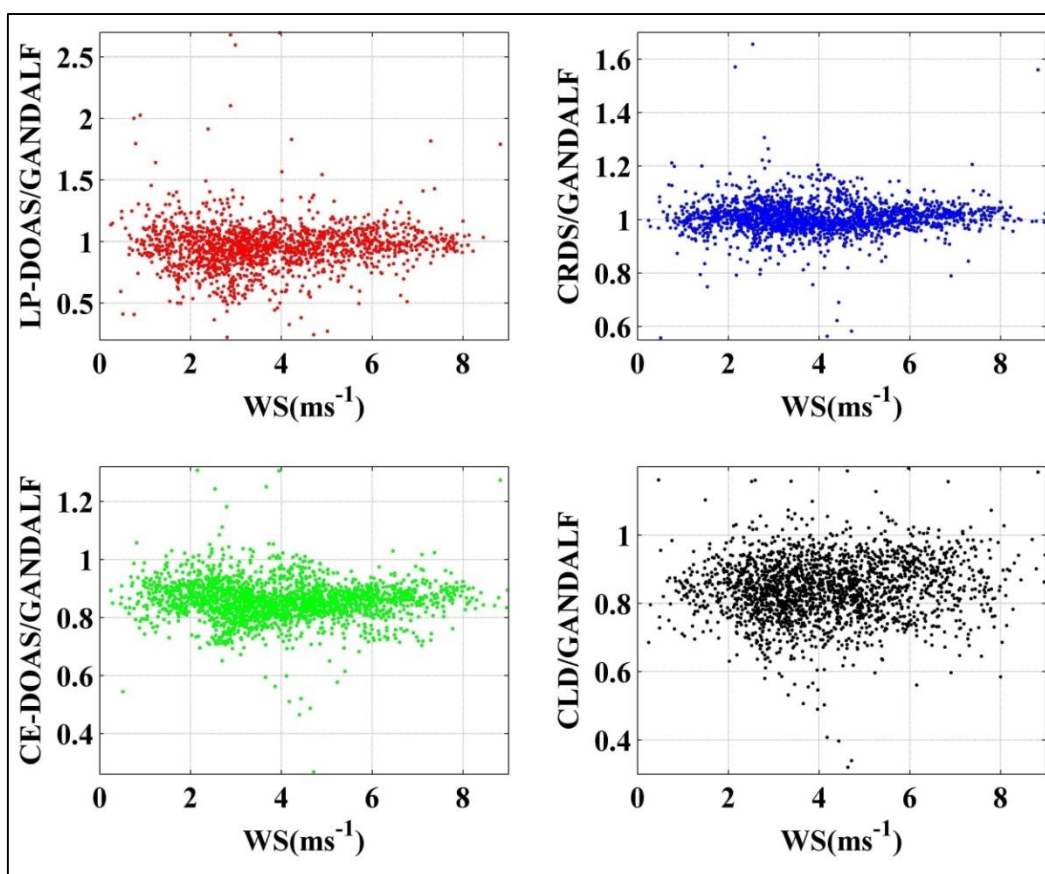
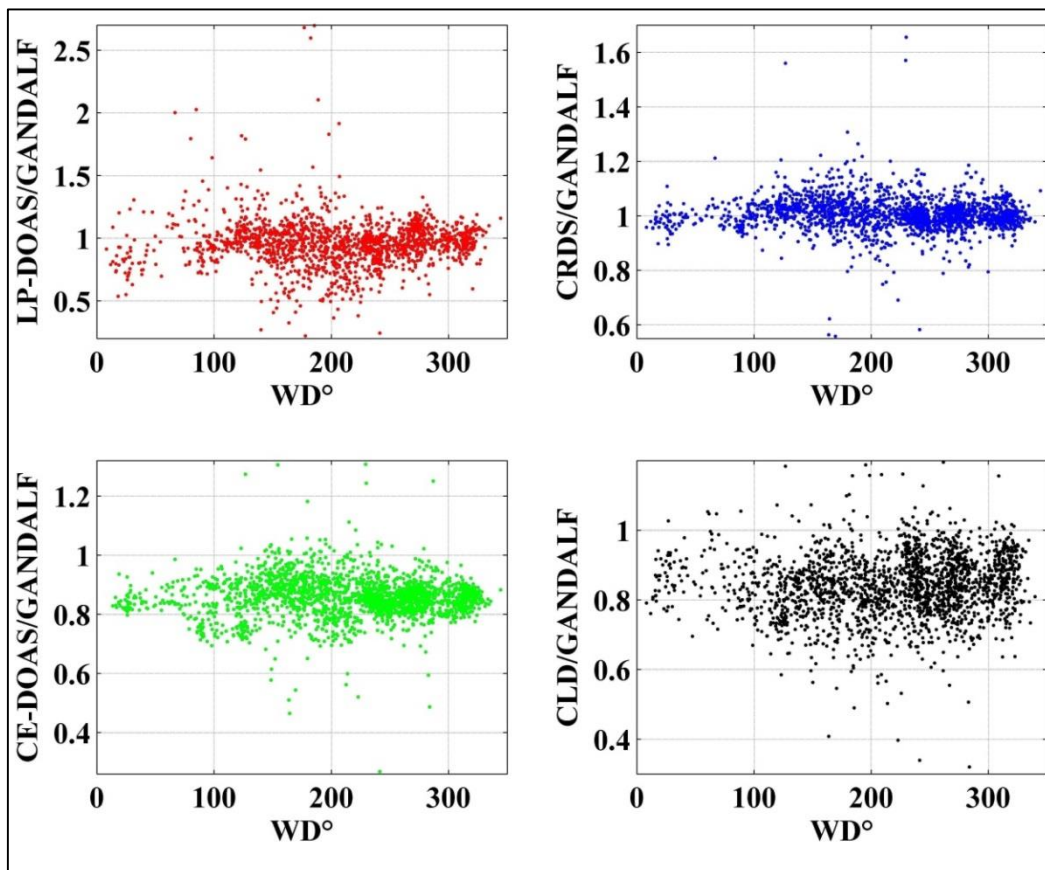












7.3.1.5 Diel profile of O₃

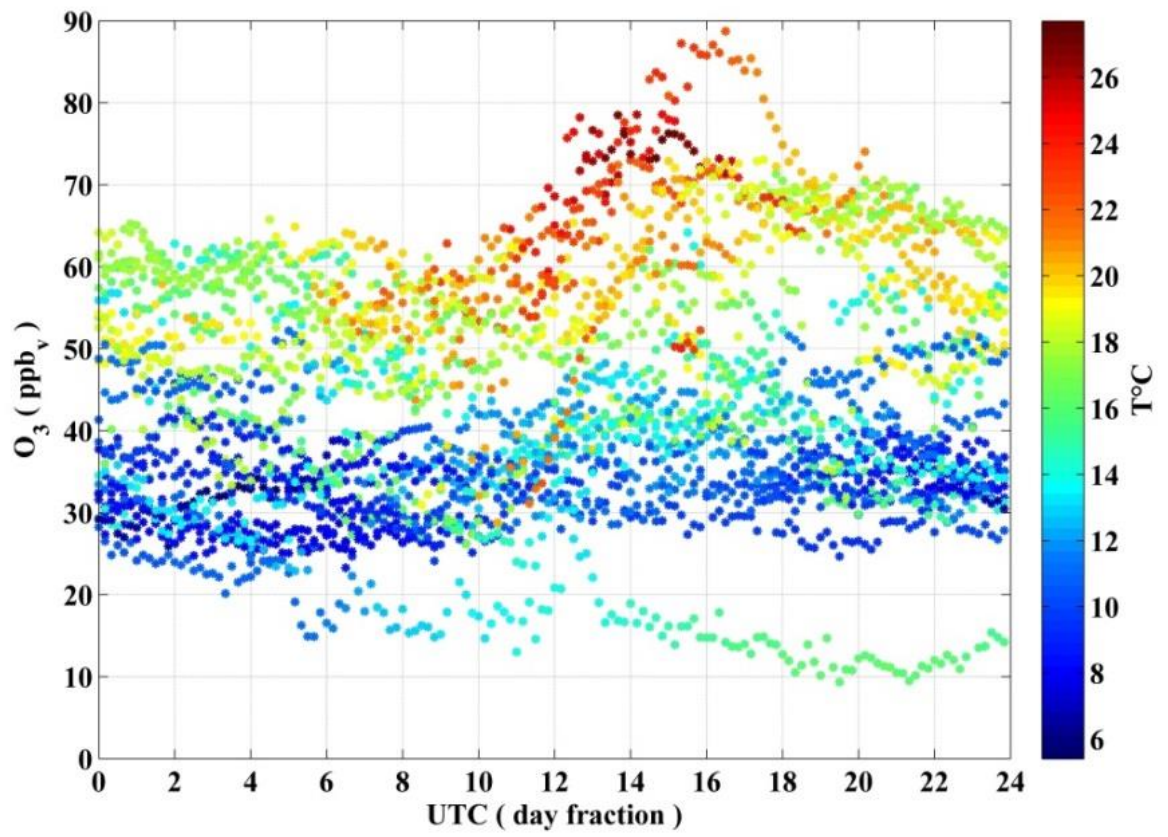
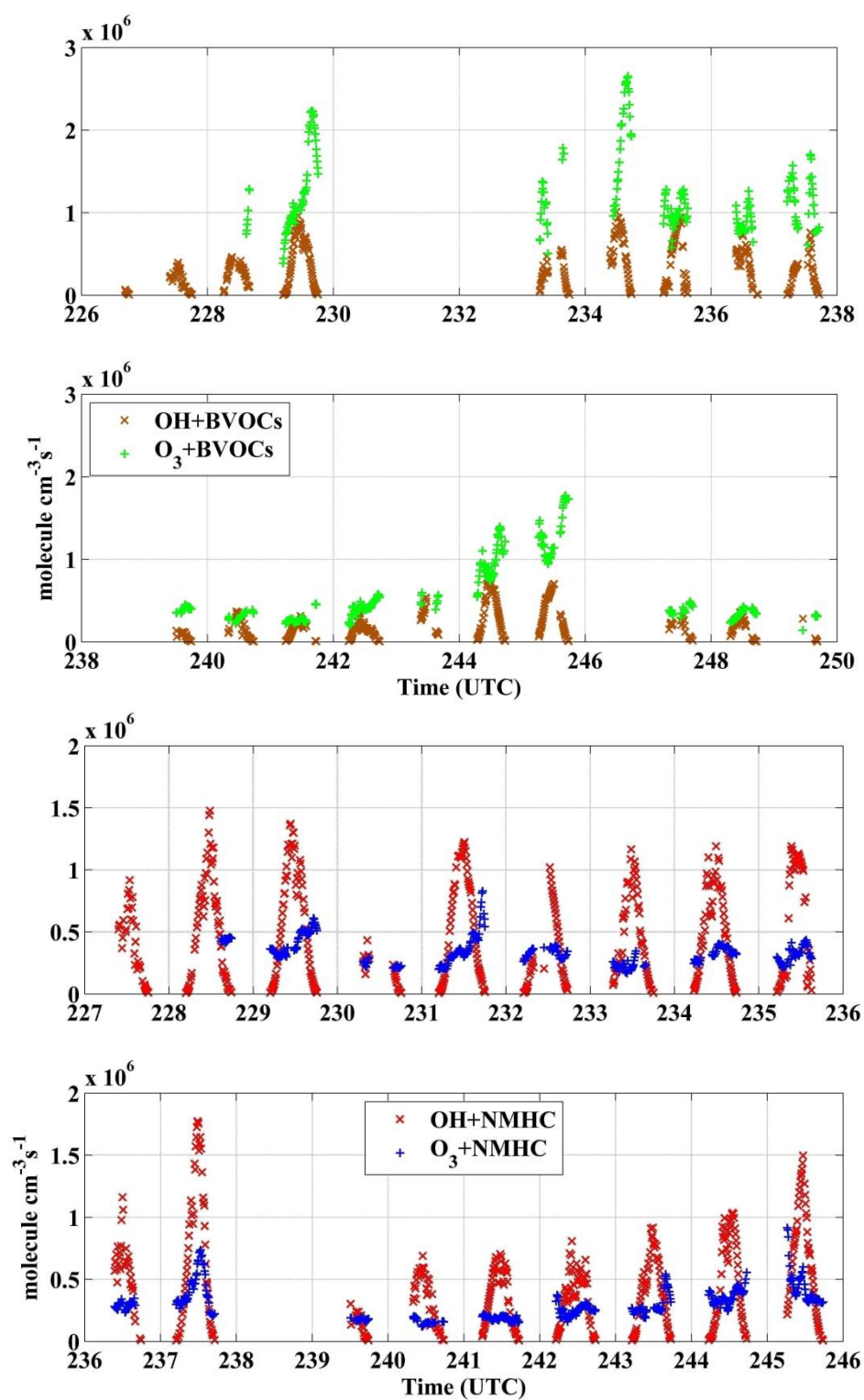


Figure: O₃ v/s day fraction during PARADE-2011 and colour coded with temperature.

7.3.1.6 BVOCs and NMHC loss rates

Figure: Loss rates of alkenes with respect to O₃ and OH during PARADE.

7.3.1.7 Trends

7.3.1.7.1 Φ colour coded with relative $j\text{NO}_2$

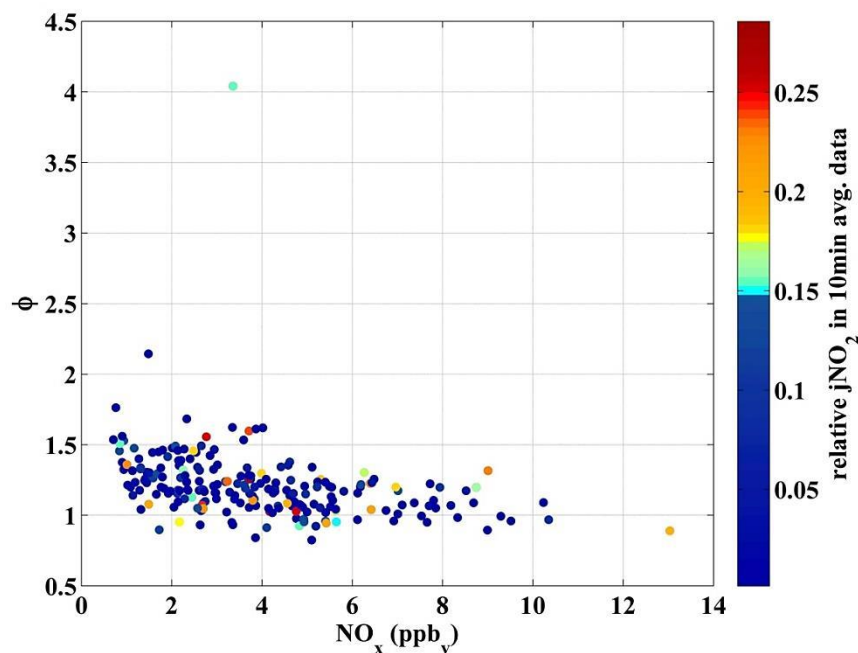


Figure: Φ as a function of NO and colour coded with relative change in $j\text{NO}_2$ during 10minute.

7.3.1.7.2 NO_2 v/s NO

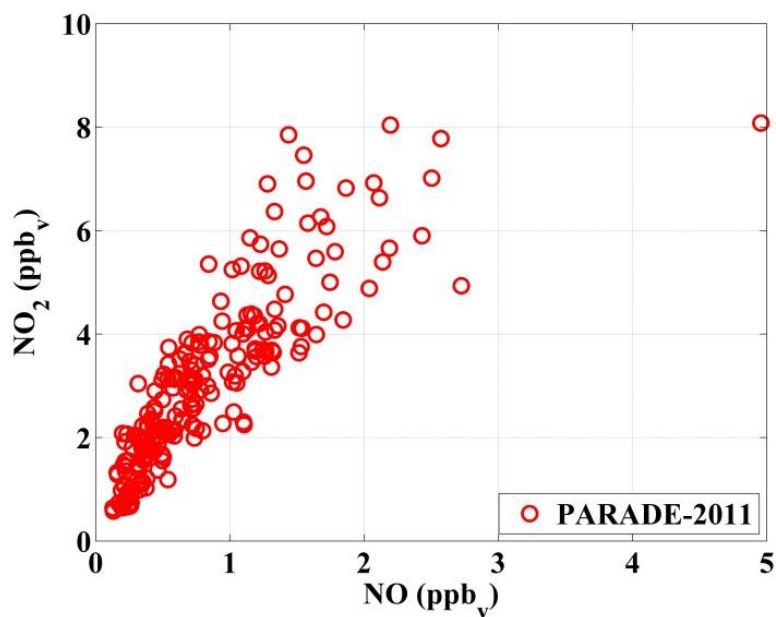


Figure: NO_2 as a function of NO during PARADE-2011 at $j\text{NO}_2 \geq 5 \times 10^{-3} \text{s}^{-1}$ and Filter_Road.

7.3.1.7.3 Effective lifetime of PAN

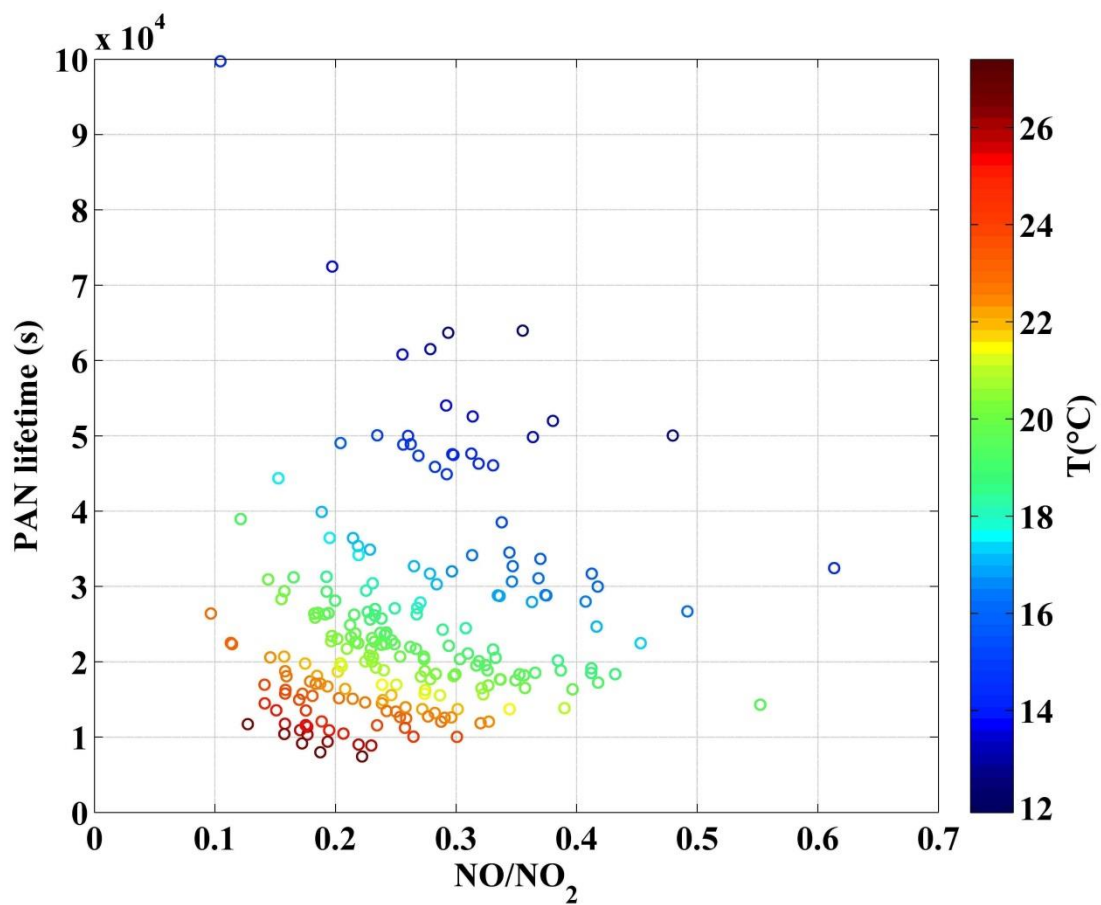
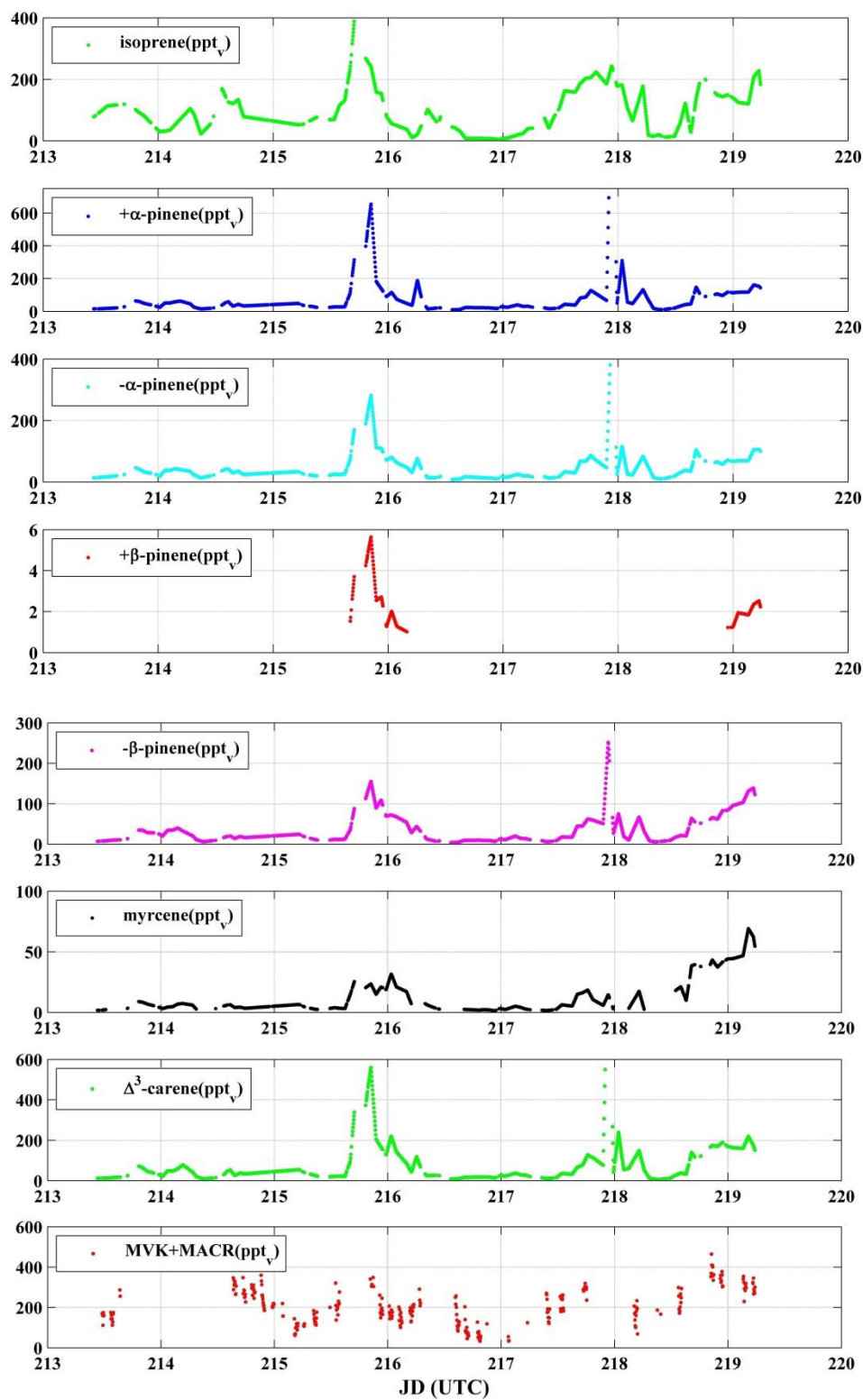
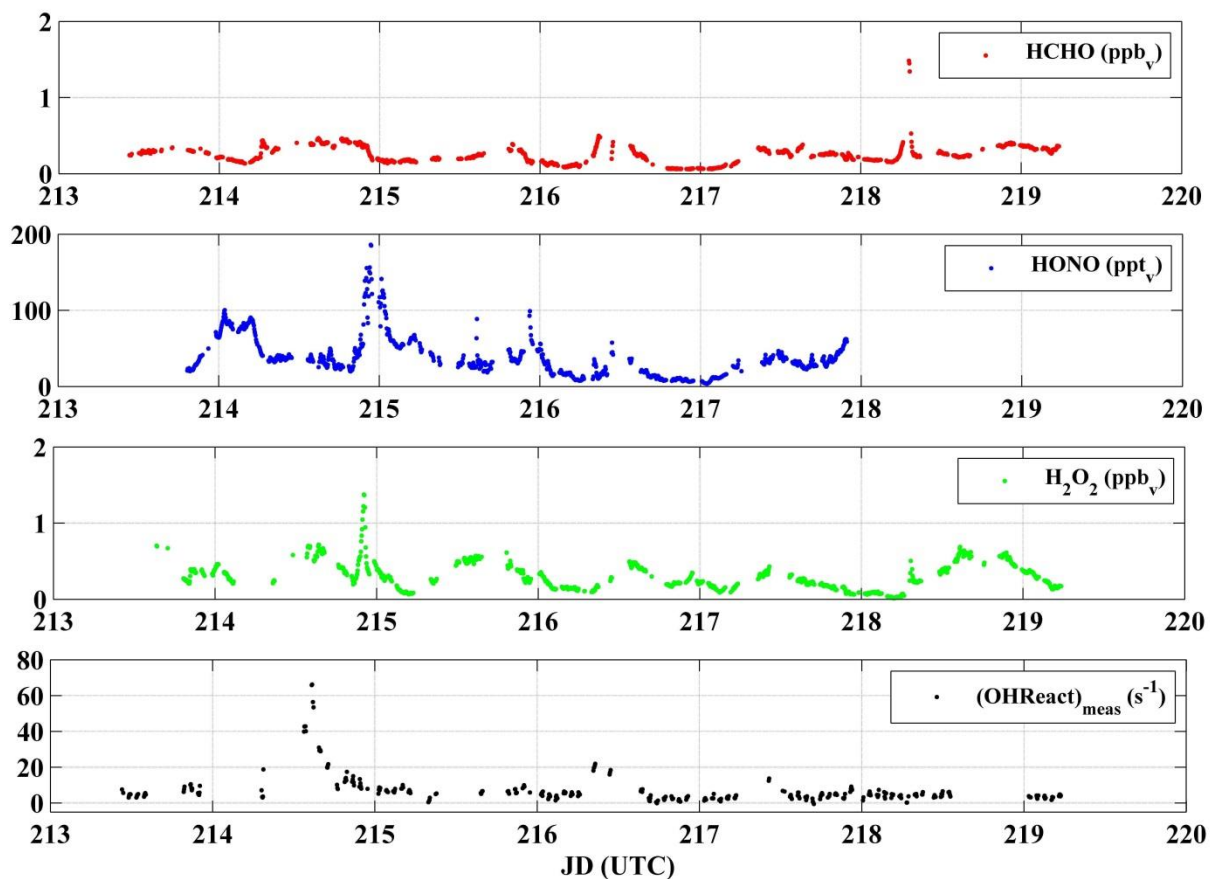


Figure: The effective lifetime of PAN during PARADE as a function of NO/NO₂ ratio for filtered data. The plot is also colour-coded with temperature.

7.4 HUMPPA-COPEC-2010

7.4.1.1 Time series of BVOCs, (OHReact)_{meas}, and others





7.4.1.2 Φ colour coded with relative $j\text{NO}_2$

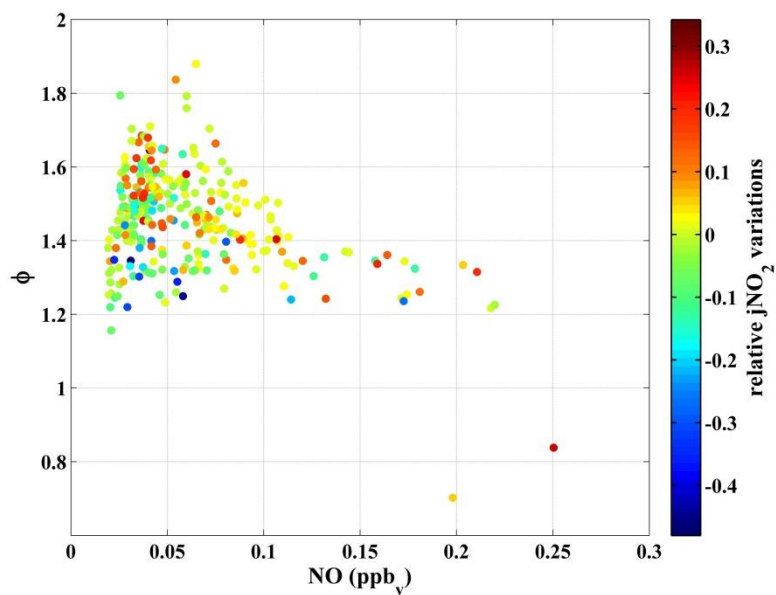


Figure: Φ as a function of NO and colour coded with relative change in $j\text{NO}_2$.

7.4.1.3 Leighton Ratio with uncertainty

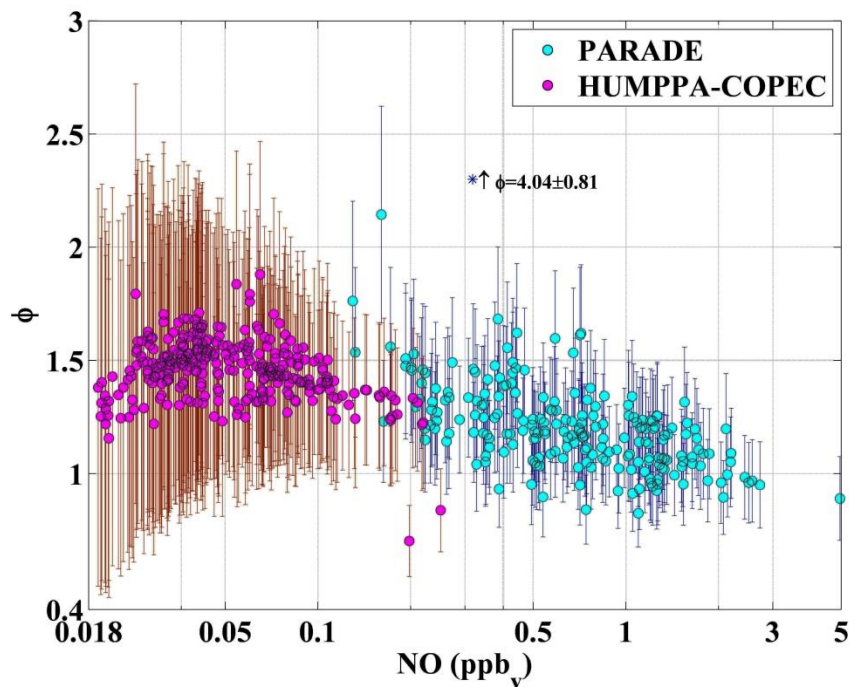


Figure: Φ with measurement uncertainty is shown as a function of NO for PARADE and HUMPPA-COPEC.

7.4.1.4 Trends versus NO

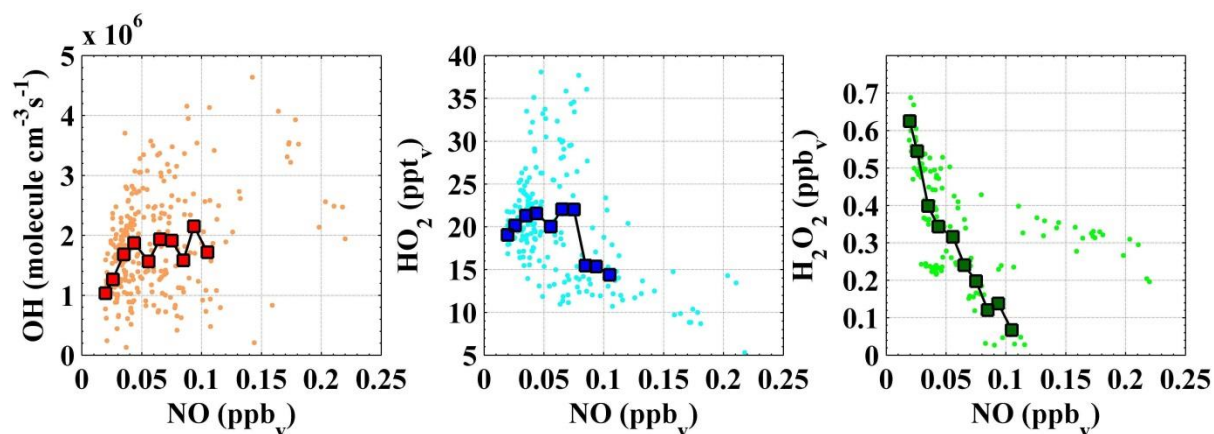


Figure: OH, HO₂ and H₂O₂ plotted as a function of NO. The square symbol are median values of 10ppt_v NO bin.

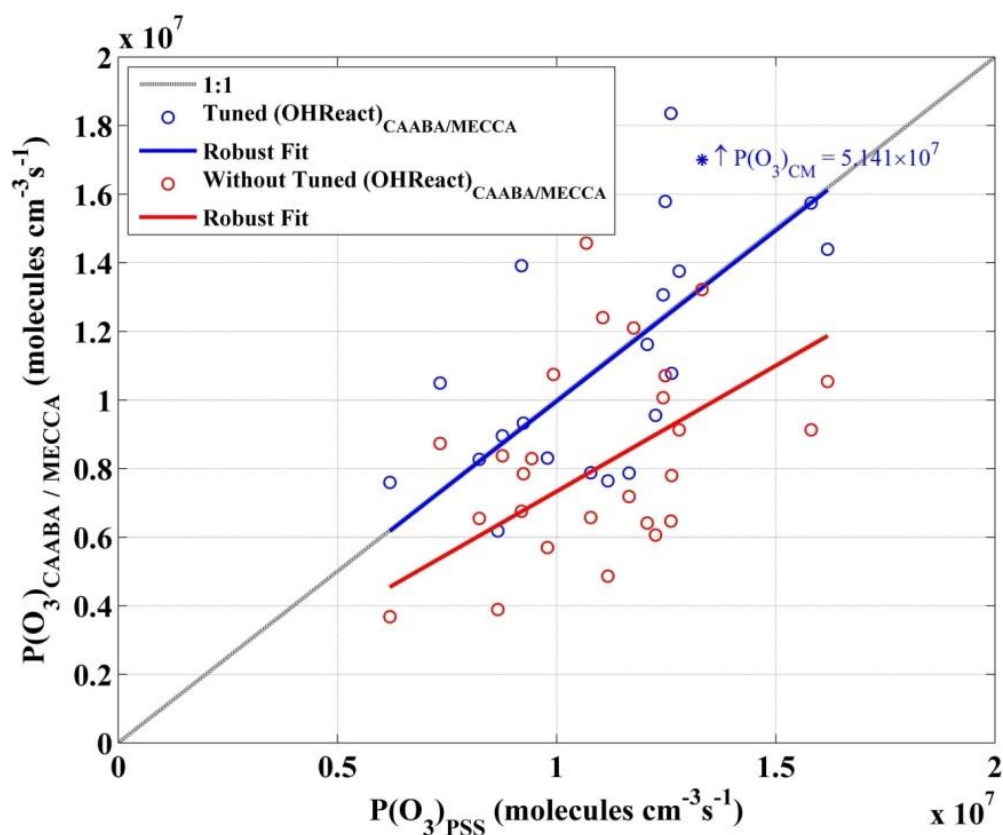
7.4.1.5 $P(O_3)_{PSS}$ and $P(O_3)_{CAABA/MECCA}$ 

Figure: $P(O_3)_{PSS}$ correlation with $(PO_3)_{CAABA/MECCA}$ from simulation. $P(O_3)_{PSS}$ is calculated based on Eq. 1.10. Blue data is based on simulations with tuned $(OHReact)_{CAABA/MECCA}$ while red data points are without tuning of $(OHReact)_{CAABA/MECCA}$. The slope is based on robust regression [it uses iteratively reweighted least squares ([Holland and Welsch, 1977](#))].

7.5 Mechanism Chemical Equations

The generic rate constants (KRO₂NO, KRO₂HO₂, KAPNO, KRO₂NO₃, KNO₃AL and KDEC) in the mechanism are based on MCM3.2 ([Jenkin et al., 1997](#); [Saunders et al., 2003](#)).

The Chemical Mechanism of MECCA

KPP version: 2.2.1_rs5

MECCA version: 3.3

Date: June 30, 2014.

Selected reactions:

“Tr && G && !S && !Cl && !Br && !I && !Hg”

Number of aerosol phases: 0

Number of species in selected mechanism:

Gas phase: 395

Aqueous phase: 0

All species: 395

Number of reactions in selected mechanism:

Gas phase (Gnnn): 979

Aqueous phase (Annn): 0

Henry (Hnnn): 0

Photolysis (Jnnn): 102

Heterogeneous (HETnnn): 0

Equilibria (EQnn): 0

Isotope exchange (DGnnn): 0

Dummy (Dnn): 0

All equations: 1081

7.5 Mechanism Chemical Equations

Table 1: Gas phase reactions

#	labels	reaction	rate coefficient	reference
G1000	SiTrG	$O_2 + O(^1D) \rightarrow O(^3P) + O_2$	$3.2E-11 \cdot \text{EXP}(70./\text{temp})$	Sander et al. (2003)
G1001	SiTrG	$O_2 + O(^3P) \rightarrow O_3$	$6.E-34 \cdot ((\text{temp}/300.)^{**(-2.4)}) \cdot \text{cair}$	Sander et al. (2003)
G2100	SiTrG	$H + O_2 \rightarrow HO_2$	$k_3rd(\text{temp}, \text{cair}, 5.7E-32, 1.6, 7.5E-11, 0., 0.6)$	Sander et al. (2003)
G2104	SiTrG	$OH + O_3 \rightarrow HO_2$	$1.7E-12 \cdot \text{EXP}(-940./\text{temp})$	Sander et al. (2003)
G2105	SiTrG	$OH + H_2 \rightarrow H_2O + H$	$2.8E-12 \cdot \text{EXP}(-1800./\text{temp})$	Sander et al. (2006)
G2107	SiTrG	$HO_2 + O_3 \rightarrow OH$	$1.E-14 \cdot \text{EXP}(-490./\text{temp})$	Sander et al. (2003)
G2109	SiTrG	$HO_2 + OH \rightarrow H_2O$	$4.8E-11 \cdot \text{EXP}(250./\text{temp})$	Sander et al. (2003)
G2110	SiTrG	$HO_2 + HO_2 \rightarrow H_2O_2$	k_HO2_HO2	Christensen et al. (2002), Kircher and Sander (1984)*
G2111	SiTrG	$H_2O + O(^1D) \rightarrow 2 OH$	$2.2E-10$	Sander et al. (2003)
G2112	SiTrG	$H_2O_2 + OH \rightarrow H_2O + HO_2$	$2.9E-12 \cdot \text{EXP}(-160./\text{temp})$	Sander et al. (2003)
G3101	SiTrG	$N_2 + O(^1D) \rightarrow O(^3P) + N_2$	$1.8E-11 \cdot \text{EXP}(110./\text{temp})$	Sander et al. (2003)
G3103	SiTrGN	$NO + O_3 \rightarrow NO_2 + O_2$	$3.E-12 \cdot \text{EXP}(-1500./\text{temp})$	Sander et al. (2003)
G3106	SiTrGN	$NO_2 + O_3 \rightarrow NO_3 + O_2$	$1.2E-13 \cdot \text{EXP}(-2450./\text{temp})$	Sander et al. (2003)
G3108	SiTrGN	$NO_3 + NO \rightarrow 2 NO_2$	$1.5E-11 \cdot \text{EXP}(170./\text{temp})$	Sander et al. (2003)
G3109	SiTrGN	$NO_3 + NO_2 \rightarrow N_2O_5$	k_NO3_NO2	Sander et al. (2003)*
G3110	SiTrGN	$N_2O_5 \rightarrow NO_2 + NO_3$	$k_NO3_NO2 / (3.E-27 \cdot \text{EXP}(10990./\text{temp}))$	Sander et al. (2003)*
G3200	TrG	$NO + OH \rightarrow HONO$	$k_3rd(\text{temp}, \text{cair}, 7.E-31, 2.6, 3.6E-11, 0.1, 0.6)$	Sander et al. (2003)
G3201	SiTrGN	$NO + HO_2 \rightarrow NO_2 + OH$	$3.6E-12 \cdot \text{EXP}(270/\text{temp})$	Atkinson et al. (2004)
G3202	SiTrGN	$NO_2 + OH \rightarrow HNO_3$	$k_3rd(\text{temp}, \text{cair}, 1.48E-30, 3., 2.58E-11, 0., 0.6)$	Möllner et al. (2010)
G3203	SiTrGN	$NO_2 + HO_2 \rightarrow HNO_4$	k_NO2_HO2	Sander et al. (2003)*
G3204	TrGN	$NO_3 + HO_2 \rightarrow NO_2 + OH + O_2$	$3.5E-12$	Sander et al. (2003)
G3205	TrG	$HONO + OH \rightarrow NO_2 + H_2O$	$1.8E-11 \cdot \text{EXP}(-390./\text{temp})$	Sander et al. (2003)
G3206	SiTrGN	$HNO_3 + OH \rightarrow H_2O + NO_3$	k_HNO3_OH	Sander et al. (2003)*
G3207	SiTrGN	$HNO_4 \rightarrow NO_2 + HO_2$	$k_NO2_HO2 / (2.1E-27 \cdot \text{EXP}(10900./\text{temp}))$	Sander et al. (2003)*
G3208	SiTrGN	$HNO_4 + OH \rightarrow NO_2 + H_2O$	$1.3E-12 \cdot \text{EXP}(380./\text{temp})$	Sander et al. (2003)
G4101	SiTrG	$CH_4 + OH \rightarrow CH_3O_2 + H_2O$	$1.85E-20 \cdot \text{EXP}(2.82 \cdot \log(\text{temp}) - 987./\text{temp})$	Atkinson (2003)
G4102	TrG	$CH_3OH + OH \rightarrow HCHO + HO_2$	$7.3E-12 \cdot \text{EXP}(-620./\text{temp})$	Sander et al. (2003)
G4103a	SiTrG	$CH_3O_2 + HO_2 \rightarrow CH_3OOH$	$4.1E-13 \cdot \text{EXP}(750./\text{temp}) / (1.+1./497.7 \cdot \text{EXP}(1160./\text{temp}))$	Sander et al. (2003)*

2

Table 1: Gas phase reactions (... continued)

#	labels	reaction	rate coefficient	reference
G4103b	SiTrG	$CH_3O_2 + HO_2 \rightarrow HCHO + H_2O + O_2$	$4.1E-13 \cdot \text{EXP}(750./\text{temp}) / (1.+497.7 \cdot \text{EXP}(-1160./\text{temp}))$	Sander et al. (2003)*
G4104	SiTrGN	$CH_3O_2 + NO \rightarrow HCHO + NO_2 + HO_2$	$2.8E-12 \cdot \text{EXP}(300./\text{temp})$	Sander et al. (2003)
G4105	TrGN	$CH_3O_2 + NO_3 \rightarrow HCHO + HO_2 + NO_2$	$1.3E-12$	Atkinson et al. (1999)
G4106a	SiTrG	$CH_3O_2 \rightarrow HCHO + HO_2$	$2.*R02+9.5E-14 \cdot \text{EXP}(390./\text{temp}) / (1.+1./26.2 \cdot \text{EXP}(1130./\text{temp}))$	Sander et al. (2003)
G4106b	SiTrG	$CH_3O_2 \rightarrow .5 HCHO + .5 CH_3OH$	$2.*R02+9.5E-14 \cdot \text{EXP}(390./\text{temp}) / (1.+26.2 \cdot \text{EXP}(-1130./\text{temp}))$	Sander et al. (2003)
G4107	SiTrG	$CH_3OOH + OH \rightarrow .6 CH_3O_2 + .4 HCHO + .4 OH + H_2O$	k_CH300H_OH	see note
G4108	SiTrG	$HCHO + OH \rightarrow CO + H_2O + HO_2$	$9.52E-18 \cdot \text{EXP}(2.03 \cdot \log(\text{temp}) + 636./\text{temp})$	Sivakumaran et al. (2003)
G4109	TrGN	$HCHO + NO_3 \rightarrow HNO_3 + CO + HO_2$	$3.4E-13 \cdot \text{EXP}(-1900./\text{temp})$	Sander et al. (2003)*
G4110	SiTrG	$CO + OH \rightarrow H + CO_2$	$1.57E-13 + \text{cair} \cdot 3.54E-33$	McCabe et al. (2001)
G4111	TrG	$HCOOH + OH \rightarrow CO_2 + HO_2 + H_2O$	$4.5E-13$	IUPAC (2013)
G4112e	TrGC	$HCHO + HO_2 \rightarrow HOCH_2O_2$	$7.7E-15 \cdot \text{EXP}(625./\text{temp})$	IUPAC (2013)
G4113e	TrGC	$HOCH_2O_2 \rightarrow HCHO + HO_2$	$2.E12 \cdot \text{EXP}(-7000./\text{temp})$	IUPAC (2013)
G4114e	TrGC	$HOCH_2O_2 + HO_2 \rightarrow .5 HOCH_2OOH + .5 HCOOH + .2 OH + .2 HO_2 + .3 H_2O$	$5.6E-15 \cdot \text{EXP}(2300./\text{temp})$	Jenkin et al. (2007)
G4115e	TrGC	$HOCH_2O_2 + NO \rightarrow NO_2 + HO_2 + HCOOH$	$2.8E-12 \cdot \text{EXP}(300./\text{temp})$	Sander et al. (2003)
G4116e	TrGC	$HOCH_2O_2 + NO_3 \rightarrow NO_2 + HO_2 + HCOOH$	$1.2E-12$	see note
G4117e	TrGC	$HOCH_2O_2 \rightarrow HCOOH + .62 HO_2$	$1.4E-12 \cdot R02$	see note
G4118e	TrGC	$HOCH_2OOH + OH \rightarrow HOCH_2O_2 + H_2O$	$0.6 \cdot k_CH300H_OH + \text{kroho}$	see note
G4119e	TrGC	$HOCH_2OOH + OH \rightarrow OH + HCOOH + H_2O$	$ks \cdot fsoh \cdot fsooh$	see note
G4200	TrGC	$C_2H_6 + OH \rightarrow C_2H_5O_2 + H_2O$	$1.49E-17 \cdot \text{temp} \cdot \text{temp} \cdot \text{EXP}(-499./\text{temp})$	Atkinson (2003)
G4201e	TrGC	$C_2H_4 + O_3 \rightarrow HCHO + .63 CO + .13 HO_2 + 0.37 HOCH_2OOH + .13 OH$	$1.2E-14 \cdot \text{EXP}(-2630./\text{temp})$	Sander et al. (2003)*
G4202	TrGC	$C_2H_4 + OH \rightarrow HOCH_2CH_2O_2 + H_2O$	$k_3rd(\text{temp}, \text{cair}, 1.E-28, 0.8, 8.8E-12, 0., 0.6)$	Sander et al. (2003)
G4203	TrGC	$C_2H_5O_2 + HO_2 \rightarrow C_2H_5OOH$	$7.5E-13 \cdot \text{EXP}(700./\text{temp})$	Sander et al. (2003)
G4204	TrGNC	$C_2H_5O_2 + NO \rightarrow CH_3CHO + HO_2 + NO_2$	$2.6E-12 \cdot \text{EXP}(365./\text{temp})$	Sander et al. (2003)
G4205	TrGNC	$C_2H_5O_2 + NO_3 \rightarrow CH_3CHO + HO_2 + NO_2$	$2.3E-12$	Atkinson et al. (1999)
G4206	TrGC	$C_2H_5O_2 \rightarrow .98 CH_3CHO + .38 HO_2 + .02 HOCH_2CH_2O_2$	$3.1E-13 \cdot R02$	Rickard and Pascoe (2009)*
G4207	TrGC	$C_2H_5OOH + OH \rightarrow .43 C_2H_5O_2 + .43 H_2O + .57 CH_3CHO + .57 OH$	$0.6 \cdot k_CH300H_OH + 8.01E-12$	see note
G4208ea	TrGC	$CH_3CHO + OH \rightarrow CH_3C(O)OO + H_2O$	$4.4E-12 \cdot \text{EXP}(365./\text{temp}) \cdot 0.95$	Atkinson et al. (2006)

3

Table 1: Gas phase reactions (... continued)

#	labels	reaction	rate coefficient	reference
G4208eb	TrGC	$\text{CH}_3\text{CHO} + \text{OH} \rightarrow .84 \text{HCOCH}_2\text{O}_2 + .1 \text{HCHO} + .1 \text{CO} + .06 \text{GLYOX} + .16 \text{OH} + \text{H}_2\text{O}$	$4.4\text{E}-12 \cdot \text{EXP}(365./\text{temp}) \cdot 0.05$	Atkinson et al. (2006)
G4209	TrGNC	$\text{CH}_3\text{CHO} + \text{NO}_3 \rightarrow \text{CH}_3\text{C}(\text{O})\text{OO} + \text{HNO}_3$	KN03AL	Sander et al. (2003)
G4210e	TrGC	$\text{CH}_3\text{COOH} + \text{OH} \rightarrow \text{CH}_3\text{O}_2 + \text{CO}_2 + \text{H}_2\text{O}$	$4.2\text{E}-14 \cdot \text{exp}(850./\text{temp})$	IUPAC (2013)
G4211et1	TrGC	$\text{CH}_3\text{C}(\text{O})\text{OO} + \text{HO}_2 \rightarrow \text{OH} + \text{CH}_3\text{O}_2 + \text{CO}_2$	KAPH02*0.70	Taraborrelli (2014)*
G4211et2	TrGC	$\text{CH}_3\text{C}(\text{O})\text{OO} + \text{HO}_2 \rightarrow \text{CH}_3\text{C}(\text{O})\text{OOH}$	KAPH02*0.12	Taraborrelli (2014)*
G4211et3	TrGC	$\text{CH}_3\text{C}(\text{O})\text{OO} + \text{HO}_2 \rightarrow \text{CH}_3\text{COOH} + \text{O}_3$	KAPH02*0.18	Taraborrelli (2014)*
G4212	TrGNC	$\text{CH}_3\text{C}(\text{O})\text{OO} + \text{NO} \rightarrow \text{CH}_3\text{O}_2 + \text{CO}_2 + \text{NO}_2$	$8.1\text{E}-12 \cdot \text{EXP}(270./\text{temp})$	Tyndall et al. (2001)
G4213	TrGNC	$\text{CH}_3\text{C}(\text{O})\text{OO} + \text{NO}_2 \rightarrow \text{PAN}$	k_CH3CO3_NO2	Tyndall et al. (2001)*
G4214	TrGNC	$\text{CH}_3\text{C}(\text{O})\text{OO} + \text{NO}_3 \rightarrow \text{CH}_3\text{O}_2 + \text{NO}_2 + \text{CO}_2$	4.E-12	Canosa-Mas et al. (1996)
G4217	TrGC	$\text{CH}_3\text{C}(\text{O})\text{OO} \rightarrow .7 \text{CH}_3\text{O}_2 + .7 \text{CO}_2 + .3 \text{CH}_3\text{COOH}$	$1.00\text{E}-11 \cdot \text{R02}$	Rickard and Pascoe (2009)
G4218	TrGC	$\text{CH}_3\text{C}(\text{O})\text{OOH} + \text{OH} \rightarrow \text{CH}_3\text{C}(\text{O})\text{OO} + \text{H}_2\text{O}$	0.6*k_CH300H_OH	Rickard and Pascoe (2009)*
G4220	TrGNC	$\text{PAN} + \text{OH} \rightarrow \text{HCHO} + \text{CO} + \text{NO}_2 + \text{H}_2\text{O}$	$9.50\text{E}-13 \cdot \text{EXP}(-650./\text{temp})$	Rickard and Pascoe (2009)
G4221	TrGNC	$\text{PAN} \rightarrow \text{CH}_3\text{C}(\text{O})\text{OO} + \text{NO}_2$	k_PAN_M	Sander et al. (2003)*
G4223e	TrGC	$\text{HOCH}_2\text{CHO} + \text{OH} \rightarrow .84 \text{HOCH}_2\text{CO} + .16 \text{HOCHCHO} + .2 \text{HO}_2 + \text{H}_2\text{O}$	8.00E-12	Rickard and Pascoe (2009)
G4224e	TrGNC	$\text{HOCH}_2\text{CHO} + \text{NO}_3 \rightarrow \text{HOCH}_2\text{CO} + \text{HNO}_3$	KN03AL	Rickard and Pascoe (2009)
G4255et2	TrGC	$\text{HOCH}_2\text{CO} \rightarrow \text{HOCH}_2\text{CO}_3$	KDEC*.97	Taraborrelli (2014)*
G4255et3	TrGC	$\text{HOCH}_2\text{CO} \rightarrow \text{OH} + \text{HCHO} + \text{CO}$	KDEC*.03	Taraborrelli (2014)*
G4256et2	TrGC	$\text{HOCH}_2\text{CHO} \rightarrow \text{GLYOX} + \text{HO}_2$	KDEC	Taraborrelli (2014)
G4225	TrGC	$\text{HOCH}_2\text{CO}_3 \rightarrow .7 \text{HCHO} + .7 \text{CO}_2 + .7 \text{HO}_2 + .3 \text{HOCH}_2\text{CO}_2\text{H}$	$1.00\text{E}-11 \cdot \text{R02}$	Rickard and Pascoe (2009)
G4226ea	TrGC	$\text{HOCH}_2\text{CO}_3 + \text{HO}_2 \rightarrow \text{HCHO} + \text{HO}_2 + \text{OH} + \text{CO}_2$	KAPH02*rc03_oh	Taraborrelli (2014)*
G4226eb	TrGC	$\text{HOCH}_2\text{CO}_3 + \text{HO}_2 \rightarrow \text{HOCH}_2\text{CO}_3\text{H}$	KAPH02*rc03_ooH	Taraborrelli (2014)*
G4226ec	TrGC	$\text{HOCH}_2\text{CO}_3 + \text{HO}_2 \rightarrow \text{HOCH}_2\text{CO}_3\text{H} + \text{O}_3$	KAPH02*rc03_o3	Taraborrelli (2014)*
G4227	TrGNC	$\text{HOCH}_2\text{CO}_3 + \text{NO} \rightarrow \text{NO}_2 + \text{HO}_2 + \text{HCHO} + \text{CO}_2$	KAPNO	Rickard and Pascoe (2009)
G4228	TrGNC	$\text{HOCH}_2\text{CO}_3 + \text{NO}_2 \rightarrow \text{PHAN}$	k_CH3CO3_NO2	Rickard and Pascoe (2009)
G4229	TrGNC	$\text{HOCH}_2\text{CO}_3 + \text{NO}_3 \rightarrow \text{NO}_2 + \text{HO}_2 + \text{HCHO} + \text{CO}_2$	KR02N03*1.60	Rickard and Pascoe (2009)
G4230e	TrGC	$\text{HOCH}_2\text{CO}_2\text{H} + \text{OH} \rightarrow .09 \text{HCHO} + .09 \text{CO}_2 + .91 \text{HCOCO}_2\text{H} + \text{HO}_2 + \text{H}_2\text{O}$	kco2h*ks*fs0h*fco2h	Taraborrelli (2014)
G4231ea	TrGC	$\text{HOCH}_2\text{CO}_3\text{H} + \text{OH} \rightarrow \text{HOCH}_2\text{CO}_3 + \text{H}_2\text{O}$	0.6*k_CH300H_OH	Taraborrelli (2014)
G4231eb	TrGC	$\text{HOCH}_2\text{CO}_3\text{H} + \text{OH} \rightarrow \text{HCOCO}_3\text{H} + \text{HO}_2$	ks*fs0h*fco2h	Taraborrelli (2014)
G4232	TrGNC	$\text{PHAN} \rightarrow \text{HOCH}_2\text{CO}_3 + \text{NO}_2$	k_PAN_M	Rickard and Pascoe (2009)
G4233	TrGNC	$\text{PHAN} + \text{OH} \rightarrow \text{HCHO} + \text{CO} + \text{NO}_2 + \text{H}_2\text{O}$	1.12E-12	Rickard and Pascoe (2009)

4

Table 1: Gas phase reactions (... continued)

#	labels	reaction	rate coefficient	reference
G4234e	TrGC	$\text{GLYOX} + \text{OH} \rightarrow 1.2 \text{CO} + .6 \text{HO}_2 + .4 \text{HCOCO}_3\text{A} + \text{H}_2\text{O}$	$3.1\text{E}-12 \cdot \text{EXP}(340./\text{temp})$	IUPAC (2013)
G4235e	TrGNC	$\text{GLYOX} + \text{NO}_3 \rightarrow 1.2 \text{CO} + .6 \text{HO}_2 + .4 \text{HCOCO}_3\text{A} + \text{HNO}_3$	KN03AL	Rickard and Pascoe (2009)
G4235et2	TrGNC	$\text{HCOCO}_3\text{A} \rightarrow 1.5 \text{CO} + .5 \text{HO}_2 + .5 \text{OH} + .5 \text{CO}_2$	KDEC	Taraborrelli (2014)
G4236	TrGC	$\text{HCOCO}_2 \rightarrow .7 \text{CO} + .7 \text{HO}_2 + .7 \text{CO}_2 + .3 \text{HCOCO}_2\text{H}$	$1.00\text{E}-11 \cdot \text{R02}$	Rickard and Pascoe (2009)
G4237e	TrGC	$\text{HCOCO}_3 + \text{HO}_2 \rightarrow \text{HO}_2 + \text{CO} + \text{CO}_2 + \text{OH}$	KAPH02	Feierabend et al. (2008), Taraborrelli (2014)
G4238	TrGNC	$\text{HCOCO}_3 + \text{NO} \rightarrow \text{HO}_2 + \text{CO} + \text{NO}_2 + \text{CO}_2$	KAPNO	Rickard and Pascoe (2009)
G4239	TrGNC	$\text{HCOCO}_3 + \text{NO}_3 \rightarrow \text{HO}_2 + \text{CO} + \text{NO}_2 + \text{CO}_2$	KR02N03*1.60	Rickard and Pascoe (2009)
G4239t2	TrGNC	$\text{HCOCO}_3 + \text{NO}_2 \rightarrow \text{HO}_2 + \text{CO} + \text{NO}_3 + \text{CO}_2$	k_CH3CO3_NO2	Orlando and Tyndall (2001), Taraborrelli (2014)*
G4240	TrGC	$\text{HCOCO}_2\text{H} + \text{OH} \rightarrow \text{CO} + \text{HO}_2 + \text{CO}_2 + \text{H}_2\text{O}$	kco2h*kt*fo*fco2h	Taraborrelli (2014)
G4241	TrGC	$\text{HCOCO}_3\text{H} + \text{OH} \rightarrow .2 \text{HCOCO}_3 + .8 \text{CO} + .8 \text{OH} + .8 \text{CO}_2 + \text{H}_2\text{O}$	$0.6 \cdot \text{k_CH300H_OH} + \text{kt} \cdot \text{fo} \cdot \text{fco2h}$	Taraborrelli (2014)
G4242	TrGC	$\text{HOCH}_2\text{CH}_2\text{O}_2 \rightarrow .6 \text{HOCH}_2\text{CH}_2\text{O} + .2 \text{HOCH}_2\text{CHO} + .2 \text{ETHGLY}$	$2.00\text{E}-12 \cdot \text{R02}$	Rickard and Pascoe (2009)
G4244	TrGC	$\text{HOCH}_2\text{CH}_2\text{O}_2 + \text{HO}_2 \rightarrow \text{HYETHO}_2\text{H}$	$2.00\text{E}-13 \cdot \text{EXP}(1250./\text{temp})$	Rickard and Pascoe (2009)
G4243	TrGNC	$\text{HOCH}_2\text{CH}_2\text{O}_2 + \text{NO} \rightarrow .24875 \text{HO}_2 + .4975 \text{HCHO} + .74625 \text{HOCH}_2\text{CH}_2\text{O} + .995 \text{NO}_2 + .005 \text{ETHOHN03}$	KR02N0	Orlando et al. (1998b)*
G4245	TrGNC	$\text{ETHOHN03} + \text{OH} \rightarrow .93 \text{NO}_3\text{CH}_2\text{CHO} + .93 \text{HO}_2 + .07 \text{HOCH}_2\text{CHO} + .07 \text{NO}_2 + \text{H}_2\text{O}$	ks*(fs0h*fch2ono2+f0no2*fpch2oh)+krohro	Taraborrelli (2014)
G4246a	TrGC	$\text{HYETHO}_2\text{H} + \text{OH} \rightarrow \text{HOCH}_2\text{CH}_2\text{O}_2 + \text{H}_2\text{O}$	0.6*k_CH300H_OH	Rickard and Pascoe (2009)
G4246b	TrGC	$\text{HYETHO}_2\text{H} + \text{OH} \rightarrow \text{HOCH}_2\text{CHO} + \text{OH} + \text{H}_2\text{O}$	ks*fs0oh*fpch2oh	Taraborrelli (2014)
G4246c	TrGC	$\text{HYETHO}_2\text{H} + \text{OH} \rightarrow \text{HOOCH}_2\text{CHO} + \text{HO}_2 + \text{H}_2\text{O}$	ks*fs0h*fpch2oh+krohro	Taraborrelli (2014)
G4247a	TrGC	$\text{HOCH}_2\text{CH}_2\text{O} \rightarrow \text{HO}_2 + \text{HOCH}_2\text{CHO}$	$6.00\text{E}-14 \cdot \text{EXP}(-550./\text{temp}) \cdot \text{C}(\text{ind}_02)$	Orlando et al. (1998b)
G4247b	TrGC	$\text{HOCH}_2\text{CH}_2\text{O} \rightarrow \text{HO}_2 + \text{HCHO} + \text{HCHO}$	$9.50\text{E}+13 \cdot \text{EXP}(-5988./\text{temp})$	Orlando et al. (1998b)
G4248	TrGC	$\text{ETHGLY} + \text{OH} \rightarrow \text{HOCH}_2\text{CHO} + \text{HO}_2 + \text{H}_2\text{O}$	2*ks*fs0h*fpch2oh+2*krohro	Taraborrelli (2014)
G4249e	TrGC	$\text{HCOCH}_2\text{O}_2 \rightarrow 0.6 \text{HCHO} + 0.6 \text{CO} + 0.6 \text{HO}_2 + 0.2 \text{GLYOX} + 0.2 \text{HOCH}_2\text{CHO}$	$2.00\text{E}-12 \cdot \text{R02}$	Taraborrelli (2014)
G4250e	TrGC	$\text{HCOCH}_2\text{O}_2 + \text{HO}_2 \rightarrow 0.85 \text{HOOCH}_2\text{CHO} + 0.15 \text{HCHO} + 0.15 \text{CO} + 0.15 \text{HO}_2 + 0.15 \text{OH}$	KR02H02*0.387	Taraborrelli (2014)
G4251e	TrGC	$\text{HCOCH}_2\text{O}_2 + \text{NO} \rightarrow \text{NO}_2 + \text{HCHO} + \text{CO} + \text{HO}_2$	KR02N0	Taraborrelli (2014)
G4252e	TrGC	$\text{HCOCH}_2\text{O}_2 + \text{NO}_3 \rightarrow \text{HCHO} + \text{CO} + \text{HO}_2 + \text{NO}_2$	KR02N03	Taraborrelli (2014)

5

Table 1: Gas phase reactions (... continued)

#	labels	reaction	rate coefficient	reference
G4253e	TrGC	$\text{HOCH}_2\text{CHO} + \text{OH} \rightarrow .71 \text{ OH} + .31 \text{ HCHO} + .31 \text{ CO} + .40 \text{ GLYOX} + .29 \text{ HCOCH}_2\text{O}_2$	$0.6 * k_{\text{CH300H_OH}} + k_{\text{sfsooh}} * f_{\text{cho}} * 8 * 10^{-12}$	Taraborrelli (2014)
G4254e	TrGNC	$\text{HOCH}_2\text{CHO} + \text{NO}_3 \rightarrow \text{OH} + \text{HCHO} + \text{CO} + \text{HNO}_3$	KN03AL	Rickard and Pascoe (2009)
G4257e	TrGC	$\text{NO}_3\text{CH}_2\text{CHO} + \text{OH} \rightarrow \text{HCHO} + \text{CO}_2 + \text{NO}_2 + \text{H}_2\text{O}$	1.E-11	Paulot et al. (2009a), Taraborrelli (2014)
G4258e	TrGNC	$\text{HOCH}_2\text{CO}_3 + \text{NO} \rightarrow \text{NO}_2 + \text{OH} + \text{HCHO} + \text{CO}_2$	KAPNO	Taraborrelli (2014)
G4259e	TrGNC	$\text{HOCH}_2\text{CO}_3 + \text{NO}_3 \rightarrow \text{NO}_2 + \text{OH} + \text{HCHO} + \text{CO}_2$	KRO2N03*1.60	Taraborrelli (2014)
G4260e	TrGC	$\text{HOCH}_2\text{CO}_3 + \text{HO}_2 \rightarrow 2 \text{ OH} + \text{HCHO} + \text{CO}_2$	KAPH02*rc03_oh	Taraborrelli (2014)
G4260et2	TrGC	$\text{HOCH}_2\text{CO}_3 + \text{HO}_2 \rightarrow \text{HOCH}_2\text{CO}_3\text{H}$	KAPH02*rc03_ooH	Taraborrelli (2014)*
G4260et3	TrGC	$\text{HOCH}_2\text{CO}_3 + \text{HO}_2 \rightarrow \text{HOCH}_2\text{CO}_2\text{H} + \text{O}_3$	KAPH02*rc03_03	Taraborrelli (2014)*
G4261e	TrGC	$\text{HOCH}_2\text{CO}_3 \rightarrow .7 \text{ OH} + .7 \text{ HCHO} + .7 \text{ CO}_2 + .3 \text{ HOCH}_2\text{CO}_2\text{H}$	1.00E-11*R02	Taraborrelli (2014)
G4262e	TrGC	$\text{HOCH}_2\text{CO}_3\text{H} + \text{OH} \rightarrow \text{HOCH}_2\text{CO}_3 + \text{H}_2\text{O}$	$2 * 0.6 * k_{\text{CH300H_OH}}$	Taraborrelli (2014)
G4263e	TrGC	$\text{HOCH}_2\text{CO}_3\text{H} + \text{OH} \rightarrow \text{HCOC}_2\text{O}_3\text{H} + \text{OH} + \text{H}_2\text{O}$	$k_{\text{sfsooh}} * f_{\text{co2h}}$	Taraborrelli (2014)
G4265e	TrGC	$\text{HOCH}_2\text{CO}_2\text{H} + \text{OH} \rightarrow \text{HCOC}_2\text{O}_2\text{H} + \text{OH} + \text{H}_2\text{O}$	$k_{\text{sfsooh}} * f_{\text{co2h}} + k_{\text{co2h}}$	Taraborrelli (2014)
G4266e	TrGC	$\text{CH}_2\text{CO} + \text{OH} \rightarrow .6 \text{ HCHO} + .6 \text{ HO}_2 + .6 \text{ CO} + .4 \text{ HOCH}_2\text{CO}_2\text{H}$	$2.8\text{E}-12 * \exp(510./\text{temp})$	Baulch et al. (2005), Taraborrelli (2014)*
G4267e	TrGC	$\text{CH}_3\text{CHOHOOH} + \text{OH} \rightarrow \text{CH}_3\text{COOH} + \text{OH}$	$k_{\text{tftooh}} * f_{\text{toh}} + k_{\text{rohro}}$	Taraborrelli (2014)
G4268e	TrGC	$\text{CH}_3\text{CHOHOH} + \text{OH} \rightarrow \text{CH}_3\text{CHOHO}_2$	$0.6 * k_{\text{CH300H_OH}}$	Taraborrelli (2014)
G4269e	TrGC	$\text{CH}_3\text{CHOHO}_2 \rightarrow \text{CH}_3\text{CHO} + \text{HO}_2$	$3.46\text{E}12 * \exp(-12500./ (1.98 * \text{temp}))$	Hermans et al. (2005), Taraborrelli (2014)
G4270e	TrGC	$\text{CH}_3\text{CHO} + \text{HO}_2 \rightarrow \text{CH}_3\text{CHOHO}_2$	$3.46\text{E}12 * \exp(-12500./ (1.98 * \text{temp})) / (6.34\text{E}26 * \exp(-14700./ (1.98 * \text{temp})))$	Hermans et al. (2005), Taraborrelli (2014)
G4271e	TrGC	$\text{CH}_3\text{CHOHO}_2 + \text{HO}_2 \rightarrow .5 \text{ CH}_3\text{CHOHOH} + .3 \text{ CH}_3\text{COOH} + 2 \text{ CH}_3\text{O}_2 + 2 \text{ HCOOH} + 2 \text{ OH}$	$5.6\text{E}-15 * \exp(2300./\text{temp})$	Taraborrelli (2014)
G4272e	TrGC	$\text{CH}_3\text{CHOHO}_2 \rightarrow \text{CH}_3\text{O}_2 + \text{HCOOH} + \text{OH}$	1.4E-12*R02	Taraborrelli (2014)
G4273e	TrGC	$\text{CH}_3\text{CHOHO}_2 + \text{NO} \rightarrow \text{CH}_3\text{O}_2 + \text{HCOOH} + \text{OH} + \text{NO}_2$	KRO2N0	Taraborrelli (2014)
G4300e	TrGC	$\text{C}_3\text{H}_8 + \text{OH} \rightarrow .736 \text{ iC}_3\text{H}_7\text{O}_2 + .264 \text{ C}_2\text{H}_5\text{O}_2 + .264 \text{ CO}_2 + .264 \text{ HO}_2 + \text{H}_2\text{O}$	$1.55\text{E}-17 * \text{temp} * \text{temp} * \exp(-61./\text{temp})$	Rickard and Pascoe (2009)*
G4301et2	TrGC	$\text{C}_3\text{H}_6 + \text{O}_3 \rightarrow .0855 \text{ CH}_3\text{CHOHOH} + .4389 \text{ CH}_3\text{CHO} + .4389 \text{ H}_2\text{O}_2 + .0456 \text{ CH}_3\text{COOH} + .285 \text{ HCOCH}_2\text{O}_2 + .0855 \text{ CH}_4 + .0855 \text{ CO}_2 + .0342 \text{ CH}_2\text{CO} + .0513 \text{ CH}_3\text{OH} + .0228 \text{ CH}_3\text{C(O)OO} + .57 \text{ HCHO} + .2709 \text{ CO} + .0688 \text{ HO}_2 + .1591 \text{ HOCH}_2\text{OOH} + .43 \text{ CH}_3\text{CHO} + .3766 \text{ OH}$	$6.5\text{E}-15 * \exp(-1900./\text{temp})$	Taraborrelli (2014)

6

Table 1: Gas phase reactions (... continued)

#	labels	reaction	rate coefficient	reference
G4302	TrGC	$\text{C}_3\text{H}_6 + \text{OH} \rightarrow \text{HYPROPO}_2$	$k_{\text{3rd}}(\text{temp}, \text{cair}, 8\text{E}-27, 3.5, 3\text{E}-11, 0., 0.5)$	Atkinson et al. (1999)
G4303	TrGNC	$\text{C}_3\text{H}_6 + \text{NO}_3 \rightarrow \text{PRONO}_3\text{BO}_2$	$4.6\text{E}-13 * \exp(-1155./\text{temp})$	Atkinson et al. (1999)
G4304	TrGC	$\text{iC}_3\text{H}_7\text{O}_2 + \text{HO}_2 \rightarrow \text{iC}_3\text{H}_7\text{OOH}$	$1.9\text{E}-13 * \exp(1300./\text{temp})$	Atkinson (1997)*
G4305	TrGNC	$\text{iC}_3\text{H}_7\text{O}_2 + \text{NO} \rightarrow .96 \text{ CH}_3\text{COCH}_3 + .96 \text{ HO}_2 + .96 \text{ NO}_2 + .04 \text{ iC}_3\text{H}_7\text{ONO}_2$	$2.7\text{E}-12 * \exp(360./\text{temp})$	Atkinson et al. (1999)
G4306	TrGC	$\text{iC}_3\text{H}_7\text{O}_2 \rightarrow \text{CH}_3\text{COCH}_3 + .8 \text{ HO}_2$	4.E-14*R02	Rickard and Pascoe (2009)*
G4307	TrGC	$\text{iC}_3\text{H}_7\text{OOH} + \text{OH} \rightarrow .27 \text{ iC}_3\text{H}_7\text{O}_2 + .73 \text{ CH}_3\text{COCH}_3 + .73 \text{ OH} + \text{H}_2\text{O}$	$1.66\text{E}-11 + 0.6 * k_{\text{CH300H_OH}}$	Rickard and Pascoe (2009)*
G4311	TrGC	$\text{CH}_3\text{COCH}_3 + \text{OH} \rightarrow \text{CH}_3\text{COCH}_2\text{O}_2 + \text{H}_2\text{O}$	$1.33\text{E}-13 + 3.82\text{E}-11 * \exp(-2000./\text{temp})$	Sander et al. (2003)
G4312e	TrGC	$\text{CH}_3\text{COCH}_2\text{O}_2 + \text{HO}_2 \rightarrow .15 \text{ OH} + .15 \text{ CH}_3\text{C(O)OO} + .15 \text{ HCHO} + .85 \text{ CH}_3\text{COCH}_2\text{O}_2\text{H}$	$8.6\text{E}-13 * \exp(700./\text{temp})$	Taraborrelli (2014)
G4313	TrGNC	$\text{CH}_3\text{COCH}_2\text{O}_2 + \text{NO} \rightarrow \text{CH}_3\text{C(O)OO} + \text{HCHO} + \text{NO}_2$	$2.9\text{E}-12 * \exp(300./\text{temp})$	Sander et al. (2003)
G4314	TrGC	$\text{CH}_3\text{COCH}_2\text{O}_2 \rightarrow .6 \text{ CH}_3\text{C(O)OO} + .6 \text{ HCHO} + .2 \text{ MGLYOX} + 2 \text{ CH}_3\text{COCH}_2\text{OH}$	$7.5\text{E}-13 * \exp(500./\text{temp}) * 2 * R02$	Tyndall et al. (2001)
G4321	TrGNC	$\text{CH}_3\text{COCH}_2\text{O}_2 + \text{NO}_3 \rightarrow \text{CH}_3\text{C(O)OO} + \text{HCHO} + \text{NO}_2$	KRO2N03	Rickard and Pascoe (2009)
G4315a	TrGC	$\text{CH}_3\text{COCH}_2\text{O}_2\text{H} + \text{OH} \rightarrow \text{CH}_3\text{COCH}_2\text{O}_2 + \text{H}_2\text{O}$	$0.6 * k_{\text{CH300H_OH}}$	Rickard and Pascoe (2009)*
G4315b	TrGC	$\text{CH}_3\text{COCH}_2\text{O}_2\text{H} + \text{OH} \rightarrow \text{MGLYOX} + \text{OH} + \text{H}_2\text{O}$	$k_{\text{sfsooh}} * f_{\text{co}}$	Taraborrelli (2014)
G4316e	TrGC	$\text{CH}_3\text{COCH}_2\text{OH} + \text{OH} \rightarrow \text{CH}_3\text{COCHOH} + \text{H}_2\text{O}$	$1.60\text{E}-12 * \exp(305./\text{temp})$	Taraborrelli (2014)
G4336ea	TrGC	$\text{CH}_3\text{COCHOH} \rightarrow \text{MGLYOX} + \text{HO}_2$	0.8485	Taraborrelli (2014)
G4317e	TrGC	$\text{MGLYOX} + \text{OH} \rightarrow .4 \text{ CH}_3\text{O}_2 + .6 \text{ CH}_3\text{C(O)OO} + 1.4 \text{ CO}$	$1.9\text{E}-12 * \exp(575./\text{temp})$	Baeza-Romero et al. (2007), IUPAC (2013)
G4331	TrGNC	$\text{MGLYOX} + \text{NO}_3 \rightarrow \text{CH}_3\text{C(O)OO} + \text{CO} + \text{HNO}_3$	KN03AL*2.4	Rickard and Pascoe (2009)
G4320	TrGNC	$\text{iC}_3\text{H}_7\text{ONO}_2 + \text{OH} \rightarrow \text{CH}_3\text{COCH}_3 + \text{NO}_2$	$6.2\text{E}-13 * \exp(-230./\text{temp})$	Atkinson et al. (1999)
G4322	TrGC	$\text{HYPROPO}_2 \rightarrow \text{CH}_3\text{CHO} + \text{HCHO} + \text{HO}_2$	8.80E-13*R02	Rickard and Pascoe (2009)
G4323	TrGC	$\text{HYPROPO}_2 + \text{HO}_2 \rightarrow \text{HYPROPO}_2\text{H}$	KRO2H02*0.520	Rickard and Pascoe (2009)
G4324	TrGNC	$\text{HYPROPO}_2 + \text{NO} \rightarrow \text{CH}_3\text{CHO} + \text{HCHO} + \text{HO}_2 + \text{NO}_2$	KRO2N0	Rickard and Pascoe (2009)
G4325	TrGNC	$\text{HYPROPO}_2 + \text{NO}_3 \rightarrow \text{CH}_3\text{CHO} + \text{HCHO} + \text{HO}_2 + \text{NO}_2$	KRO2N03	Rickard and Pascoe (2009)
G4326a	TrGC	$\text{HYPROPO}_2\text{H} + \text{OH} \rightarrow \text{HYPROPO}_2$	$0.6 * k_{\text{CH300H_OH}}$	Rickard and Pascoe (2009)
G4326b	TrGC	$\text{HYPROPO}_2\text{H} + \text{OH} \rightarrow \text{CH}_3\text{COCH}_2\text{OH} + \text{OH}$	$k_{\text{sfsoh}} * f_{\text{pch2oh}} + k_{\text{tftooh}} * f_{\text{pch2oh}}$	Taraborrelli (2014)
G4327	TrGNC	$\text{PRONO}_3\text{BO}_2 + \text{HO}_2 \rightarrow \text{PR}_2\text{O}_2\text{HNO}_3$	KRO2H02*0.520	Rickard and Pascoe (2009)
G4328	TrGNC	$\text{PRONO}_3\text{BO}_2 + \text{NO} \rightarrow \text{NOA} + \text{HO}_2 + \text{NO}_2$	KRO2N0	Rickard and Pascoe (2009)
G4329	TrGNC	$\text{PRONO}_3\text{BO}_2 + \text{NO}_3 \rightarrow \text{NOA} + \text{HO}_2 + \text{NO}_2$	KRO2N03	Rickard and Pascoe (2009)
G4330a	TrGNC	$\text{PR}_2\text{O}_2\text{HNO}_3 + \text{OH} \rightarrow \text{PRONO}_3\text{BO}_2$	$1.90\text{E}-12 * \exp(190./\text{temp})$	Rickard and Pascoe (2009)
G4330b	TrGNC	$\text{PR}_2\text{O}_2\text{HNO}_3 + \text{OH} \rightarrow \text{NOA} + \text{OH}$	$k_{\text{tftooh}} * f_{\text{ch2ono2}}$	Rickard and Pascoe (2009)

7

Table 1: Gas phase reactions (... continued)

#	labels	reaction	rate coefficient	reference
G4332	TrGNC	NOA + OH → MGLYOX + NO ₂	ks*fco*fono2+kp*fco	Taraborrelli (2014)
G4333e	TrGC	HOCH2COCHO + OH → .8609 HOCH2CO + .8609 CO + .1391 HCOCOCHO + .1391 HO ₂	1.9E-12*EXP(575./temp)+ks*fsoh*fco	Taraborrelli (2014)
G4334e	TrGNC	HOCH2COCHO + NO ₃ → HOCH2CO + CO + HNO ₃	KN03AL*2.4	Taraborrelli (2014)
G4337e	TrGC	CH3COCO2H + OH → CH ₃ C(O)OO + H ₂ O + CO ₂	4.9E-14*EXP(276./temp)	Mellouki and Mu (2003), Taraborrelli (2014)
G4338e	TrGC	HOCH2COCH2O2 → HCHO + HOCH2CO	R02*2.0E-12	Taraborrelli (2014)
G4339e	TrGC	HOCH2COCH2O2 + HO ₂ → .15 HCHO + .15 HOCH2CO + .15 OH + .85 HOCH2COCH2OOH	KR02H02*0.520	Taraborrelli (2014)
G4340e	TrGC	HOCH2COCH2O2 + NO → HCHO + HOCH2CO + NO ₂	KR02N0	Taraborrelli (2014)
G4341e	TrGC	HOCH2COCH2OOH + OH → HOCH2COCHO + OH	ks*fsooh*fco	Taraborrelli (2014)
G4342e	TrGC	HOCH2COCH2OOH + OH → HOCH2COCH2O2	.6*k_CH300H_OH	Taraborrelli (2014)
G4343e	TrGC	HOCH2COCH2OOH + OH → HCOCOCH2OOH + HO ₂	0.9295*1.60E-12*EXP(305./temp)	Taraborrelli (2014)*
G4344e	TrGC	HCOCOCH2O2 → 0.6 HCOCO3A + 0.6 HCHO + 0.2 HCOCOCHO + 0.2 HOCH2COCHO	2.00E-12*R02	Taraborrelli (2014)
G4345e	TrGC	HCOCOCH2O2 + NO → HCOCO3A + HCHO + NO ₂	KR02N0	Taraborrelli (2014)
G4346e	TrGC	HCOCOCH2O2 + HO ₂ → 0.85 HCOCOCH2OOH + 0.15 HCOCO3A + 0.15 HCHO + 0.15 OH	KR02H02*0.520	Taraborrelli (2014)
G4347e	TrGC	HCOCOCH2O2 + NO ₃ → HCOCO3A + HCHO + NO ₂	KR02N03	Taraborrelli (2014)
G4348e	TrGC	HCOCOCH2OOH + OH → HOOCH2CO3 + CO + H ₂ O	kt*fo*fco	Taraborrelli (2014)
G4349e	TrGC	HCOCOCH2OOH + OH → HCOCOCHO + OH + H ₂ O	ks*fsooh*fco	Taraborrelli (2014)
G4350e	TrGC	HCOCOCH2OOH + OH → HCOCOCH2O2 + H ₂ O	0.6*k_CH300H_OH	Taraborrelli (2014)
G4351e	TrGC	HCOCOCH2OOH + NO ₃ → HOOCH2CO3 + CO + HNO ₃	KN03AL*2.4	Taraborrelli (2014)
G4352e	TrGC	HCOCOCHO + OH → HCOCO3A + CO	2*kt*fco*fo	Taraborrelli (2014)
G4353e	TrGC	CH3CHCO + OH → .72 CO + .72 CH ₃ CHO + .72 HO ₂ + .21 CH3COCO2H + .07 CH ₃ CHO + .07 HO ₂ + .07 CO ₂	7.6E-11	Hatakeyama et al. (1985), Taraborrelli (2014)*
G4354e	TrGC	HCOCCH3CO + OH → CO + CH3COCHOH	1E-10*acho	Hatakeyama et al. (1985), Taraborrelli (2014)*
G4355e	TrGC	CH3COCHCO + OH → CO + CH3COCHOH	7.6E-11*acoch3	Hatakeyama et al. (1985), Taraborrelli (2014)*
G4400	TrGC	nC ₄ H ₁₀ + OH → LC ₄ H ₉ O ₂ + H ₂ O	1.81E-17*temp*temp*EXP(114./temp)	Atkinson (2003)*
G4401	TrGC	LC ₄ H ₉ O ₂ → 0.254 CO ₂ + 0.5552 MEK + 0.5552 HO ₂ + 0.3178 CH ₃ CHO + 0.4448 C ₂ H ₅ O ₂	2.5E-13*R02	Rickard and Pascoe (2009)*
G4402	TrGC	LC ₄ H ₉ O ₂ + HO ₂ → LC ₄ H ₉ OOH	KR02H02*0.625	Rickard and Pascoe (2009)

8

Table 1: Gas phase reactions (... continued)

#	labels	reaction	rate coefficient	reference
G4403	TrGNC	LC ₄ H ₉ O ₂ + NO → 0.9172 NO ₂ + 0.233 CO ₂ + 0.5092 MEK + 0.5092 HO ₂ + 0.2915 CH ₃ CHO + 0.408 C ₂ H ₅ O ₂ + 0.0828 LC4H9NO3	KR02N0	Rickard and Pascoe (2009)*
G4404	TrGC	LC ₄ H ₉ OOH + OH → 0.2285796 LC ₄ H ₉ O ₂ + 0.7117253 MEK + 0.1193902 CO ₂ + 0.0596951 C ₂ H ₅ O ₂ + 0.7714204 OH + H ₂ O	2.636E-11	Rickard and Pascoe (2009)*
G4405e	TrGC	MVK + O ₃ → .87 MGLYOX + 0.5481 CO + 0.1392 HO ₂ + 0.1392 OH + 0.3219 HOCH2OOH + .13 HCHO + 0.04680 OH + 0.04680 CO + 0.07280 CH ₃ C(O)OO + .026 CH ₃ CHO + .026 CO ₂ + .026 HCHO + .026 HO ₂ + 0.02402 MGLYOX + 0.02402 H ₂ O ₂ + 0.007176 CH3COCO2H	8.5E-16*EXP(-1520./temp)	Taraborrelli (2014)
G4406e	TrGC	MVK + OH → LHMKABO2	2.6E-12*EXP(610./temp)	Taraborrelli (2014)*
G4413	TrGC	MEK + OH → LMEKO2 + H ₂ O	3.24E-18*temp*temp*EXP(414./temp)	Rickard and Pascoe (2009)*
G4414ea	TrGC	LMEKO2 + HO ₂ → LMEKOOH	KR02H02*0.625*rcoch2o2_ooh	Taraborrelli (2014)
G4414eb	TrGC	LMEKO2 + HO ₂ → 0.538 HCHO + 0.538 CO ₂ + 0.459 HOCH ₂ CH ₂ O ₂ + 0.079 C ₂ H ₅ O ₂ + 0.462 CH ₃ C(O)OO + 0.462 CH ₃ CHO + OH	KR02H02*0.625*rcoch2o2_oh	Taraborrelli (2014)
G4415	TrGNC	LMEKO2 + NO → 0.538 HCHO + 0.538 CO ₂ + 0.459 HOCH ₂ CH ₂ O ₂ + 0.079 C ₂ H ₅ O ₂ + 0.462 CH ₃ C(O)OO + 0.462 CH ₃ CHO + NO ₂	KR02N0	Rickard and Pascoe (2009)*
G4416	TrGC	LMEKOOH + OH → 0.40851 CH ₃ COCH ₂ O ₂ + 0.350196 BIACET + 0.807212 OH + 0.048506 C ₂ H ₅ O ₂ + 0.505522 CO ₂ + 0.192788 LMEKO2 + H ₂ O	3.786E-11	Rickard and Pascoe (2009)*
G4417	TrGNC	LC4H9NO3 + OH → 0.91423 MEK + 0.08577 C ₂ H ₅ O ₂ + 0.17154 CO ₂ + NO ₂ + H ₂ O	9.598E-13	Rickard and Pascoe (2009)*
G4418	TrGNC	MPAN + OH → CH ₃ COCH ₂ OH + CO + NO ₂	3.2E-11	Orlando et al. (2002)
G4419	TrGNC	MPAN → MACO3 + NO ₂	k_PAN_M	see note
G4420	TrGC	LMEKO2 → 0.538 HCHO + 0.538 CO ₂ + 0.459 HOCH ₂ CH ₂ O ₂ + 0.079 C ₂ H ₅ O ₂ + 0.462 CH ₃ C(O)OO + 0.462 CH ₃ CHO	1.483E-12*R02	Rickard and Pascoe (2009)*
G4421e	TrGC	MACR + OH → .45 MACO3 + .55 MACRO2	8.E-12*EXP(380./temp)	Orlando et al. (1999b), Taraborrelli (2014)
G4422e	TrGC	MACR + O ₃ → 0.5481 CO + 0.1392 HO ₂ + 0.1392 OH + 0.3219 HOCH2OOH + .87 MGLYOX + .13 HCHO + .13 OH + .065 HCOCOCH2O2 + .065 CO + .065 CH ₃ C(O)OO	1.36E-15*EXP(-2112./temp)	Taraborrelli (2014)

9

Table 1: Gas phase reactions (... continued)

#	labels	reaction	rate coefficient	reference
G4423	TrGNC	MACR + NO ₃ → MACO3 + HNO ₃	KN03AL*2.0	Rickard and Pascoe (2009)
G4424e	TrGC	MACO3 → .7 MACO2 + .3 MACO2H	1.00E-11*R02	Taraborrelli (2014)
G4425e	TrGC	MACO3 + HO ₂ → MACO2 + OH	KAPH02*rc03_oh	Taraborrelli (2014)
G4425et2	TrGC	MACO3 + HO ₂ → MACO3H	KAPH02*rc03_ohh	Taraborrelli (2014)
G4425et3	TrGC	MACO3 + HO ₂ → MACO2H + O ₃	KAPH02*rc03_o3	Taraborrelli (2014)
G4426e	TrGNC	MACO3 + NO → MACO2 + NO ₂	8.70E-12*EXP(290./temp)	Taraborrelli (2014)
G4427	TrGNC	MACO3 + NO ₂ → MPAN	k_CH3CO3_NO2	Rickard and Pascoe (2009)
G4428e	TrGNC	MACO3 + NO ₃ → MACO2 + NO ₂	KR02N03*1.60	Taraborrelli (2014)
G4429e	TrGC	MACRO2 → .7 CH ₃ COCH ₂ OH + .7 HCHO + .7 HO ₂ + .3 MACROH	9.20E-14*R02	Taraborrelli (2014)
G4430e	TrGC	MACRO2 + HO ₂ → MACRO + OH	KR02H02*0.625*rc0ch2o2_oh	Taraborrelli (2014)
G4430et2	TrGC	MACRO2 + HO ₂ → MACROOH	KR02H02*0.625*rc0ch2o2_ohh	Taraborrelli (2014)
G4431e	TrGNC	MACRO2 + NO → .85 MACRO + .85 NO ₂ + .15 MACRN	KR02N0	Taraborrelli (2014)
G4432e	TrGNC	MACRO2 + NO ₃ → MACRO + NO ₂	KR02N03	Taraborrelli (2014)
G4433ea	TrGC	MACROOH + OH → MACRO2	0.6*k_CH300H_OH	Taraborrelli (2014)
G4433eb	TrGC	MACROOH + OH → CO + OH + CH ₃ COCH ₂ OH	kt*fo*ftch2oh*falk	Taraborrelli (2014)
G4433ec	TrGC	MACROOH + OH → CO + MGLYOX + HO ₂	ks*fs0h*fpch2oh + krohro	Taraborrelli (2014)
G4434e	TrGC	MACROH + OH → CH ₃ COCH ₂ OH + CO + HO ₂	kt*fo*ftch2oh*falk	Taraborrelli (2014)
G4434et2	TrGC	MACRO → .885 CH ₃ COCH ₂ OH + .885 CO + .115 MGLYOX + .115 HCHO + HO ₂	KDEC	Taraborrelli (2014)
G4435e	TrGC	MACO2H + OH → CH ₃ COCH ₂ OH + HO ₂ + CO ₂	(kadt+kadp)*aco2h+kco2h	Taraborrelli (2014)
G4436e	TrGC	MACO3H + OH → CH ₃ COCH ₂ OH + CO ₂ + OH	0.6*k_CH300H_OH+(kadt+kadp)*aco2h	Taraborrelli (2014)
G4437e	TrGC	LHMVKABO2 → .024 CO2H3CHO + .072 CH3COCHOH + .072 HCHO + .5280 CH ₃ C(O)OO + .5280 HOCH ₂ CHO + .176 BIACETOH + .2 HO12CO3C4	1.014E-12*R02	Taraborrelli (2014)*
G4438e	TrGC	LHMVKABO2 + HO ₂ → OH + HOCH ₂ CHO + CH ₃ C(O)OO	KR02H02*0.625*.88*rc0ch2o2_oh	Taraborrelli (2014)
G4438et2	TrGC	LHMVKABO2 + HO ₂ → LHMVKABOOH	KR02H02*0.625*(.12+.88*rc0ch2o2_ohh)	Taraborrelli (2014)
G4439ea	TrGNC	LHMVKABO2 + NO → .12 CH3COCHOH + .88 HOCH ₂ CHO + .88 CH ₃ C(O)OO + .12 HCHO + NO ₂	KR02N0*(1.-0.11)	Taraborrelli (2014)*
G4439eb	TrGNC	LHMVKABO2 + NO → HMVKNO3	KR02N0*0.11	Taraborrelli (2014)
G4440e	TrGNC	LHMVKABO2 + NO ₃ → .12 MGLYOX + .88 HOCH ₂ CHO + .88 CH ₃ C(O)OO + .12 HCHO + .12 HO ₂ + NO ₂	KR02N03	Taraborrelli (2014)*

10

Table 1: Gas phase reactions (... continued)

#	labels	reaction	rate coefficient	reference
G4441e	TrGC	LHMVKABOOH + OH → .12 CO2H3CHO + .88 BIACETOH + OH	0.6*k_CH300H_OH+.12*ks*fs0h*fpch2oh+.88*kt*ft0oh*fpch2oh*fco	Taraborrelli (2014)*
G4449e	TrGC	CO2H3CHO + OH → CO2H3CO3	kt*fo*falk	Taraborrelli (2014)
G4449et2	TrGC	CO2H3CHO + OH → CH3COCOCCHO + HO ₂ + H ₂ O	kt*fo*ftoh*fcho	Taraborrelli (2014)
G4450	TrGNC	CO2H3CHO + NO ₃ → CO2H3CO3 + HNO ₃	KN03AL*4.0	Rickard and Pascoe (2009)
G4451e	TrGC	CO2H3CO3 → CH3COCHOH + CO ₂	1.00E-11*R02	Taraborrelli (2014)
G4452e	TrGC	CO2H3CO3 + HO ₂ → OH + CH3COCHOH + CO ₂	KAPH02*rc03_oh	Taraborrelli (2014)
G4452et2	TrGC	CO2H3CO3 + HO ₂ → CO2H3CO2H + O ₃	KAPH02*rc03_o3	Taraborrelli (2014)
G4452et3	TrGC	CO2H3CO3 + HO ₂ → CO2H3CO3H	KAPH02*rc03_ohh	Taraborrelli (2014)
G4453e	TrGNC	CO2H3CO3 + NO → CH3COCHOH + NO ₂ + CO ₂	KAPNO	Taraborrelli (2014)
G4454e	TrGNC	CO2H3CO3 + NO ₃ → CH3COCHOH + NO ₂ + CO ₂	KR02N03*1.60	Taraborrelli (2014)
G4455	TrGC	CO2H3CO3H + OH → 0.5127 CO2H3CO3 + 0.4873 CH ₃ C(O)OO + 0.4873 CO + 0.4873 CO ₂ + 0.4873 OH	kt*fco2h*fco*ftoh+0.6*k_CH300H_OH	Taraborrelli (2014)*
G4455t2	TrGC	CO2H3CO2H + OH → CH3COCOC2H + HO ₂	kt*fco2h*fco*ftoh+kco2h	Taraborrelli (2014)
G4456a	TrGC	HO12CO3C4 + OH → BIACETOH + HO ₂	kt*ftoh*falk*fco	Taraborrelli (2014)
G4456b	TrGC	HO12CO3C4 + OH → CO2H3CHO + HO ₂	ks*fs0h*falk	Taraborrelli (2014)
G4457e	TrGC	MACO2 → .65 CH ₃ O ₂ + .65 CO + .65 HCHO + .35 OH + .35 CH ₃ COCH ₂ O ₂ + CO ₂	KDEC	Taraborrelli (2014)
G4458e	TrGC	LHMVKABO2 → .88 MGLYOX + .88 HCHO + .12 HOCH ₂ CHO + .12 CH ₃ C(O)OO + OH	KHSD	Taraborrelli (2014)
G4459e	TrGNC	MACRO2 → MGLYOX + HCHO + OH	KHSB	Taraborrelli (2014)
G4460e	TrGNC	HMVKNO3 + OH → .7 MGLYOX + .7 HCOOH + .7 NO ₃ + .3 CO2H3CHO + .3 NO ₂ + H ₂ O	5.6E-12	Taraborrelli (2014)
G4461e	TrGC	MACRN + OH → .08 CH ₃ COOH + .08 HCHO + .15 NO ₃ + .07 HCOOH + .07 MGLYOX + .85 CH ₃ COCH ₂ OH + .85 NO ₃ + .93 CO ₂ + H ₂ O	5.E-11	Taraborrelli (2014)
G4462e	TrGC	EZCH3CO2CHCHO → .9 CH3COCHCO + .1 CH ₃ C(O)OO + .01 GLYOX + .18 CO + .09 HO ₂ + OH	k16HS	Taraborrelli (2014)*
G4463e	TrGC	EZCHOCCH3CHO2 → HCOCCH3CO + OH	K16HS	Taraborrelli (2014)*
G4500e	TrGC	C ₂ H ₈ + O ₃ → .3508 MACR + 0.01518 MACO2H + .2440 MVK + .7085 HCHO + .11 HOCH ₂ OOH + .1275 C ₃ H ₆ + .1575 CH ₃ C(O)OO + .0510 CH ₃ O ₂ + 0.2625 HO ₂ + .27 OH + .09482 H ₂ O ₂ + .255 CO ₂ + .522 CO + 0.07182 HCHO + .03618 HCOCH ₂ O ₂ + .01782 CO	1.03E-14*EXP(-1995./temp)	Taraborrelli (2014)*

11

Table 1: Gas phase reactions (... continued)

#	labels	reaction	rate coefficient	reference
G4501e	TrGC	$C_2H_8 + OH \rightarrow .63 \text{ ISOPAB} + .30 \text{ ISOPCD} + .07 \text{ LISOPEFO2}$	$2.7E-11 \cdot \text{EXP}(390./\text{temp}) \cdot (1.-\text{iseq})$	Taraborrelli (2014)*
G4502	TrGNC	$C_2H_8 + NO_3 \rightarrow \text{NISOP2O}$	$3.15E-12 \cdot \text{EXP}(-450./\text{temp})$	Rickard and Pascoe (2009)
G4503e	TrGC	$\text{ISOPAB} + O_2 \rightarrow \text{LISOPACO2}$	5.530E-13	Taraborrelli (2014)*
G4504e	TrGC	$\text{ISOPAB} + O_2 \rightarrow \text{ISOPBO2}$	3.E-12	Taraborrelli (2014)*
G4505e	TrGC	$\text{ISOPCD} + O_2 \rightarrow \text{DLISOPACO2}$	6.780E-13	Taraborrelli (2014)*
G4506e	TrGC	$\text{ISOPCD} + O_2 \rightarrow \text{ISOPDO2}$	3.E-12	Taraborrelli (2014)*
G4507e	TrGC	$\text{LISOPACO2} \rightarrow \text{ISOPAB} + O_2$	$3.1E12 \cdot \text{exp}(-7900./\text{temp}) \cdot .6+$ $7.8E13 \cdot \text{exp}(-8600./\text{temp}) \cdot .4$	Taraborrelli (2014)*
G4508e	TrGC	$\text{ISOPBO2} \rightarrow \text{ISOPAB} + O_2$	$3.7E14 \cdot \text{exp}(-9570./\text{temp})$ $+4.2E14 \cdot \text{exp}(-9970./\text{temp})$	Taraborrelli (2014)*
G4509e	TrGC	$\text{DLISOPACO2} \rightarrow \text{ISOPCD} + O_2$	$5.65E12 \cdot \text{exp}(-8410./\text{temp}) \cdot .42+$ $1.4E14 \cdot \text{exp}(-9110./\text{temp}) \cdot .58$	Taraborrelli (2014)*
G4510e	TrGC	$\text{ISOPDO2} \rightarrow \text{ISOPCD} + O_2$	$5.0E14 \cdot \text{exp}(-10120./\text{temp})$ $+8.25E14 \cdot \text{exp}(-10220./\text{temp})$	Taraborrelli (2014)*
G4511e	TrGC	$\text{LISOPACO2} \rightarrow \text{ZCODOC23DBC00H} + HO_2$	K16HS	Taraborrelli (2014)*
G4512e	TrGC	$\text{DLISOPACO2} \rightarrow \text{ZCODOC23DBC00H} + HO_2$	K16HS	Taraborrelli (2014)*
G4513et3	TrGC	$\text{LISOPACO2} \rightarrow .9 \text{ LHC4ACCHO} + .8 HO_2 + .1 \text{ ISOPAOH}$	2.4E-12*R02	Rickard and Pascoe (2009)
G4514t2	TrGC	$\text{LISOPACO2} + HO_2 \rightarrow \text{LISOPACOOH}$.706*KR02H02	Rickard and Pascoe (2009)
G4515et2	TrGNC	$\text{LISOPACO2} + NO \rightarrow 0.95 \text{ LHC4ACCHO} + 0.95 HO_2 + 0.95 NO_2 + .05 \text{ LISOPACNO3}$	KR02N0	Lockwood et al. (2010), Taraborrelli (2014)
G4506et3	TrGNC	$\text{LISOPACO2} + NO_3 \rightarrow \text{LHC4ACCHO} + HO_2 + NO_2$	KR02N03	Rickard and Pascoe (2009)
G4507et3	TrGC	$\text{DLISOPACO2} \rightarrow .9 \text{ LHC4ACCHO} + .8 HO_2 + .1 \text{ ISOPAOH}$	2.4E-12*R02	Rickard and Pascoe (2009)
G4511et3	TrGC	$\text{DLISOPACO2} + HO_2 \rightarrow \text{LISOPACOOH}$.706*KR02H02	Rickard and Pascoe (2009)
G4512et3	TrGNC	$\text{DLISOPACO2} + NO \rightarrow 0.95 \text{ LHC4ACCHO} + 0.95 HO_2 + 0.95 NO_2 + .05 \text{ LISOPACNO3}$	KR02N0	Lockwood et al. (2010), Taraborrelli (2014)
G4513et4	TrGNC	$\text{DLISOPACO2} + NO_3 \rightarrow \text{LHC4ACCHO} + HO_2 + NO_2$	KR02N03	Rickard and Pascoe (2009)
G4514e	TrGC	$\text{LISOPACOOH} + OH \rightarrow \text{LISOPACO2}$	0.6*k_CH300H_OH	Taraborrelli (2014)
G4514et2	TrGC	$\text{LISOPACOOH} + OH \rightarrow \text{ZCODOC23DBC00H} + HO_2$	ks*fallyl1*fsoh	Taraborrelli (2014)
G4514et3	TrGC	$\text{LISOPACOOH} + OH \rightarrow \text{LHC4ACCHO} + OH$	ks*fs0oh*fallyl1+ krohro	Taraborrelli (2014)
G4514et4	TrGC	$\text{LISOPACOOH} + OH \rightarrow \text{IEPOX} + OH$	(kadt+kads)*ach2oh*ach2oh	Taraborrelli (2014)
G4515	TrGC	$\text{ISOPAOH} + OH \rightarrow \text{LHC4ACCHO} + HO_2$	(kadt+kads)*ach2oh*ach2oh+ ks*fs0h*fallyl1+krohro	Taraborrelli (2014)

12

Table 1: Gas phase reactions (... continued)

#	labels	reaction	rate coefficient	reference
G4516e	TrGNC	$\text{LISOPACNO3} + OH \rightarrow \text{LISOPACNO3O2}$	9.5E-11	Paulot et al. (2009a), Taraborrelli (2014)
G4517e	TrGC	$\text{ISOPBO2} \rightarrow .8 \text{ MVK} + .8 \text{ HCHO} + .8 HO_2 + .2 \text{ ISOPBOH}$	8.E-13*R02	Rickard and Pascoe (2009)
G4518	TrGC	$\text{ISOPBO2} + HO_2 \rightarrow \text{ISOPBOOH}$.706*KR02H02	Rickard and Pascoe (2009)
G4519e	TrGNC	$\text{ISOPBO2} + NO \rightarrow .947 \text{ MVK} + .947 \text{ HCHO} + .947 HO_2 + .947 NO_2 + .053 \text{ ISOPBNO3}$	KR02N0	Lockwood et al. (2010), Taraborrelli (2014)
G4520e	TrGNC	$\text{ISOPBO2} + NO_3 \rightarrow \text{MVK} + .75 \text{ HCHO} + .75 HO_2 + .25 CH_3O_2 + NO_2$	KR02N03	Rickard and Pascoe (2009)
G4521ea	TrGC	$\text{ISOPBOOH} + OH \rightarrow \text{IEPOX} + OH$	(kads+kadp)*ach2oh	Paulot et al. (2009b), Taraborrelli (2014)
G4521eb	TrGC	$\text{ISOPBOOH} + OH \rightarrow \text{ISOPBO2}$	0.6*k_CH300H_OH	Taraborrelli (2014)
G4521ec	TrGC	$\text{ISOPBOOH} + O_3 \rightarrow 0.1368 \text{ MACROOH} + 0.1368 H_2O_2 + 0.2280 HO_2 + 0.4332 CH_3COCH_2OH + 0.2280 CO_2 + 0.6384 OH + 0.2052 CO + .57 HCHO + .43 \text{ MACROOH} + 0.06880 HO_2 + 0.06880 OH + 0.2709 CO + 0.1591 HOCH_2OOH$	1.E-17	Taraborrelli (2014)*
G41911	TrGC	$\text{ISOPBOOH} + OH \rightarrow \text{MGLYOX} + HOCH_2CHO$	krohro+ks*falk*fs0h	Taraborrelli (2014)
G4522e	TrGC	$\text{ISOPBOH} + OH \rightarrow \text{MVK} + .75 \text{ HCHO} + .75 HO_2 + .25 CH_3O_2$	ks*falk*fs0h+(kadp+kads)*ach2oh	Taraborrelli (2014)
G4523e	TrGNC	$\text{ISOPBNO3} + OH \rightarrow \text{ISOPBDNO3O2}$	1.3E-11	Paulot et al. (2009a), Taraborrelli (2014)
G4524	TrGC	$\text{ISOPDO2} \rightarrow .8 \text{ MACR} + .8 HO_2 + .1 \text{ HCOC5} + .1 \text{ ISOPDOH}$	2.9E-12*R02	Rickard and Pascoe (2009)
G4525	TrGC	$\text{ISOPDO2} + HO_2 \rightarrow \text{ISOPDOOH}$.706*KR02H02	Rickard and Pascoe (2009)
G4526e	TrGNC	$\text{ISOPDO2} + NO \rightarrow .85 \text{ MACR} + .85 HO_2 + .85 NO_2 + .15 \text{ ISOPDNO3}$	KR02N0	Lockwood et al. (2010), Taraborrelli (2014)
G4527	TrGNC	$\text{ISOPDO2} + NO_3 \rightarrow \text{MACR} + \text{HCHO} + HO_2 + NO_2$	KR02N03	Rickard and Pascoe (2009)
G4528ea	TrGC	$\text{ISOPDOOH} + OH \rightarrow \text{IEPOX} + OH$	(kadt+kadp)*ach2oh	Paulot et al. (2009b), Taraborrelli (2014)
G4528eb	TrGC	$\text{ISOPDOOH} + OH \rightarrow \text{ISOPDO2}$	0.6*k_CH300H_OH	Taraborrelli (2014)
G4528ec	TrGC	$\text{ISOPDOOH} + OH \rightarrow \text{HCOC5} + OH$	kt*ft0oh*fallyl1*fpch2oh	Taraborrelli (2014)
G4528ed	TrGC	$\text{ISOPDOOH} + OH \rightarrow CH_3COCH_2OH + GLYOX + OH$	ks*fpch2oh*fs0h	Taraborrelli (2014)
G45222	TrGC	$\text{ISOPDOOH} + O_3 \rightarrow 1.393 OH + \text{BIACETOH} + .67 HCHO + 0.05280 HO_2 + 0.2079 CO + 0.1221 HOCH_2OOH$	1.E-17	Taraborrelli (2014)*

13

Table 1: Gas phase reactions (... continued)

#	labels	reaction	rate coefficient	reference
G4529e	TrGC	ISOPDOH + OH → HCOC5 + HO ₂	2.*krohro+(kt*ftoh*fallyl+ks*fsoh)*fpch2oh+(kadt+kadp)*ach2oh	Taraborrelli (2014)
G4530e	TrGNC	ISOPDNO3 + OH → ISOPBDNO3O2	1.3E-11	Paulot et al. (2009a), Taraborrelli (2014)
G4531	TrGNC	NISOP02 → .8 NC4CHO + .6 HO ₂ + .2 LISOPACNO3	1.3E-12*R02	Rickard and Pascoe (2009)
G4532	TrGNC	NISOP02 + HO ₂ → NISOP0OH	.706*KR02H02	Rickard and Pascoe (2009)
G4533	TrGNC	NISOP02 + NO → NC4CHO + HO ₂ + NO ₂	KR02N0	Rickard and Pascoe (2009)
G4534	TrGNC	NISOP02 + NO ₃ → NC4CHO + HO ₂ + NO ₂	KR02N03	Rickard and Pascoe (2009)
G4535	TrGNC	NISOP0OH + OH → NC4CHO + OH	1.03E-10	Rickard and Pascoe (2009)
G4536	TrGNC	NC4CHO + OH → LNISO3	4.16E-11	Rickard and Pascoe (2009)
G4537e	TrGNC	NC4CHO + O ₃ → .27 NOA + .027 HCOCO ₂ H + .0162 GLYOX + .0162 H ₂ O ₂ + .1458 HCOCO ₃ A + .0405 HCOOH + .0405 CO + .8758 OH + .365 MGLYOX + .73 NO ₂ + 0.7705 HCHO + .4055 CO ₂ + .73 GLYOX	2.40E-17	Taraborrelli (2014)*
G4538	TrGNC	NC4CHO + NO ₃ → LNISO3 + HNO ₃	KN03AL*4.25	Rickard and Pascoe (2009)
G4539	TrGNC	LNISO3 + HO ₂ → LNISO3OH	.5*.706*KR02H02 + .5*KAPH02	Rickard and Pascoe (2009)
G4540e	TrGNC	LNISO3 + NO → NOA + .5 HOCHCHO + .5 CO + .5 HO ₂ + NO ₂ + .5 CO ₂	.5*KAPNO + .5*KR02N0	Rickard and Pascoe (2009)
G4541e	TrGNC	LNISO3 + NO ₃ → NOA + .5 HOCHCHO + .5 CO + .5 HO ₂ + NO ₂ + .5 CO ₂	1.3*KR02N03	Rickard and Pascoe (2009)
G4542	TrGNC	LNISO3OH + OH → LNISO3	2.65E-11	Rickard and Pascoe (2009)
G4543e	TrGC	LHC4ACCHO + OH → LC578O2	(kadtertprim+kads)*acho*ach2oh	Taraborrelli (2014)
G4543et2	TrGC	LHC4ACCHO + OH → LHC4ACCO3	kcho	Taraborrelli (2014)
G4543et3	TrGC	LHC4ACCHO + OH → ZC0DC23DBC0D + HO ₂	ks*fsoh*fallyl	Taraborrelli (2014)
G4544	TrGC	LHC4ACCHO + O ₃ → .2225 CH ₃ C(O)OO + .89 CO + .0171875 HOCH ₂ CO ₂ H + .075625 H ₂ O ₂ + .0171875 HCOCO ₂ H + .2775 CH ₃ COCH ₂ OH + .6675 HO ₂ + .2603125 GLYOX + .2225 HCHO + .89 OH + .2603125 HOCH ₂ CHO + .5 MGLYOX	2.40E-17	Rickard and Pascoe (2009)
G4545	TrGNC	LHC4ACCHO + NO ₃ → LHC4ACCO3 + HNO ₃	KN03AL*4.25	Rickard and Pascoe (2009)
G4546e	TrGC	LC578O2 → .25 CH ₃ COCH ₂ OH + .75 MGLYOX + .25 HOCHCHO + .75 HOCH ₂ CHO + .75 HO ₂	9.20E-14*R02	Rickard and Pascoe (2009)
G4547e	TrGC	LC578O2 + HO ₂ → MGLYOX + HOCH ₂ CHO + OH	KR02H02*0.706*rcoch2o2_oh	Rickard and Pascoe (2009)
G4547et2	TrGC	LC578O2 + HO ₂ → LC578OOH	KR02H02*0.706*rcoch2o2_ooH	Rickard and Pascoe (2009)

14

Table 1: Gas phase reactions (... continued)

#	labels	reaction	rate coefficient	reference
G4548e	TrGNC	LC578O2 + NO → .25 CH ₃ COCH ₂ OH + .75 MGLYOX + .25 HOCHCHO + .75 HOCH ₂ CHO + .75 HO ₂ + NO ₂	KR02N0	Rickard and Pascoe (2009)
G4549e	TrGNC	LC578O2 + NO ₃ → .25 CH ₃ COCH ₂ OH + .75 MGLYOX + .25 HOCHCHO + .75 HOCH ₂ CHO + .75 HO ₂ + NO ₂	KR02N03	Rickard and Pascoe (2009)
G4586e	TrGC	LC578O2 → .25 CH ₃ COCH ₂ OH + .75 MGLYOX + .25 HOCH ₂ CHO + .75 HOCH ₂ CHO + HO ₂ + OH	KHSB	Taraborrelli (2014)
G4550e	TrGC	LC578OOH + OH → LC578O2	0.6*k_CH300H_OH	Taraborrelli (2014)*
G4550et2	TrGC	LC578OOH + OH → C10DC20OHC40D + HO ₂	kt*fo*ftch2oh*falk+ kt*ftoh*fpch2oh*fpch2oh+ ks*fsoh*fpch2oh	Taraborrelli (2014)*
G4551e	TrGC	LHC4ACCO3 → .3 LHC4ACCO2H + .7 OH + .35 MACRO2 + .35 LHMVKABO2 + .7 CO ₂	1.00E-11*R02	Taraborrelli (2014)*
G4552e	TrGC	LHC4ACCO3 + HO ₂ → 2 OH + .5 MACRO2 + .5 LHMVKABO2 + CO ₂	KAPH02*rco3_oh	Taraborrelli (2014)*
G4552et2	TrGC	LHC4ACCO3 + HO ₂ → LHC4ACCO3H	KAPH02*rco3_ooH	Taraborrelli (2014)
G4552et3	TrGC	LHC4ACCO3 + HO ₂ → LHC4ACCO2H + O ₃	KAPH02*rco3_o3	Taraborrelli (2014)
G4553e	TrGNC	LHC4ACCO3 + NO → .5 MACRO2 + .5 LHMVKABO2 + NO ₂ + CO ₂	KAPNO	Taraborrelli (2014)*
G4554	TrGNC	LHC4ACCO3 + NO ₂ → LC5PAN1719	k_CH3C03_N02	Rickard and Pascoe (2009)
G4555e	TrGNC	LHC4ACCO3 + NO ₃ → .5 MACRO2 + .5 LHMVKABO2 + NO ₂ + CO ₂	1.6*KR02N03	Taraborrelli (2014)*
G4556e	TrGC	LHC4ACCO2H + OH → OH + .5 MACRO2 + .5 LHMVKABO2 + CO ₂	2.52E-11	Taraborrelli (2014)
G4557	TrGC	LHC4ACCO3H + OH → LHC4ACCO3	2.88E-11	Rickard and Pascoe (2009)
G4558	TrGNC	LC5PAN1719 → LHC4ACCO3 + NO ₂	k_PAN_M	Rickard and Pascoe (2009)
G4559	TrGNC	LC5PAN1719 + OH → .5 MACROH + .5 HO12CO3C4 + CO + NO ₂	2.52E-11	Rickard and Pascoe (2009)
G4560a	TrGC	HCOC5 + OH → C59O2	3.81E-11	Rickard and Pascoe (2009)
G4560eb	TrGC	HCOC5 + O ₃ → BIACETOH + .335 H ₂ O ₂ + 0.67 HCHO + 0.2079 CO + 0.1221 HOCH2OOH + 0.05280 OH	7.51E-16*EXP(-1521./temp)	Taraborrelli (2014)
G4561	TrGC	C59O2 → CH ₃ COCH ₂ OH + HOCH2CO	9.20E-14*R02	Taraborrelli (2014)
G4562e	TrGC	C59O2 + HO ₂ → OH + CH ₃ COCH ₂ OH + HOCH2CO	KR02H02*0.706*rcoch2o2_oh	Taraborrelli (2014)
G4562et2	TrGC	C59O2 + HO ₂ → C59OOH	KR02H02*0.706*rcoch2o2_ooH	Taraborrelli (2014)
G4563	TrGNC	C59O2 + NO → CH ₃ COCH ₂ OH + HOCH2CO + NO ₂	KR02N0	Taraborrelli (2014)
G4564	TrGNC	C59O2 + NO ₃ → CH ₃ COCH ₂ OH + HOCH2CO + NO ₂	KR02N03	Taraborrelli (2014)

15

Table 1: Gas phase reactions (... continued)

#	labels	reaction	rate coefficient	reference
G4565	TrGC	C59OOH + OH → C59O2	9.7E-12	Taraborrelli (2014)
G4566e	TrGC	IEPOX + OH → LC578O2 + H2O	5.78E-11*EXP(-400/temp)	Paulot et al. (2009b), Taraborrelli (2014)
G4567e	TrGC	ISOPBO2 → MVK + HCHO + OH	KHSB	Taraborrelli (2014)
G4568e	TrGC	ISOPDO2 → MACR + HCHO + OH	KHSD	Taraborrelli (2014)
G4577ea	TrGC	ZCODC23DBC0OH + OH → .6 C1ODC2O2C4OOH + .4 C1OOHC2O2C4OD	kadt*acho*ach2ooh	Taraborrelli (2014)
G4577eb	TrGC	ZCODC23DBC0OH + OH → .6 C1ODC3O2C4OOH + .4 C1OOHC3O2C4OD	kads*acho*ach2ooh	Taraborrelli (2014)
G4577e	TrGC	ZCODC23DBC0OH + OH → ZCO3HC23DBCOD	kt*fo*falk+0.6*k_CH300H_OH	Taraborrelli (2014)
G4577et2	TrGC	ZCODC23DBC0OH + OH → OH + ZCODC23DBCOD	ks*fsooh*fallyl	Taraborrelli (2014)
G4577et3	TrGC	ZCODC23DBC0OH + O3 → .4672 OH + .2336 HCOCOC2O2 + .2336 CO + .2336 CH3C(O)OO + .4672 HOOCH2CHO + .1728 MGLYOX + .1901 OH + .0864 GLYOX + .02765 HOOCH2CHO + .02765 H2O2 + .02592 CH3OOH + .02592 CO2 + .01037 HCOCO3A + .01555 HOCH2OOH + .01555 CO + .006912 HOOCH2CO3 + .2628 OH + .1314 MGLYOX + .1314 OH + .1314 HCOCOC2O2OH + .02628 GLYOX + .0972 CH3COCH2O2H + .00972 HCOCOC2H + .005832 GLYOX + .005832 H2O2 + .05249 OH + .05249 HCOCO3A + .01458 HCHO + .01458 CO2 + .01458 HCOOH + .01458 CO	2.4E-17	Taraborrelli (2014)*
G4578e	TrGC	C1OOHC2O2C4OD → .78 CH3COCH2O2H + .78 HOCHCHO + .22 CO2H3CHO + .22 HCHO + .22 OH	8.00E-13*R02	Taraborrelli (2014)
G4579e	TrGC	C1OOHC2O2C4OD + NO → .78 CH3COCH2O2H + .78 HOCHCHO + .22 CO2H3CHO + .22 HCHO + .22 OH + NO2	KR02NO	Taraborrelli (2014)
G4580e	TrGC	C1OOHC2O2C4OD + HO2 → C1OOHC2OOHC4OD	KR02H02*0.706	Taraborrelli (2014)
G4580ea	TrGC	C1OOHC2O2C4OD → CH3COCH2O2H + GLYOX + OH	KHSB	Taraborrelli (2014)
G4581e	TrGC	C1ODC2O2C4OOH → OH + C1ODC2OOHC4OD	K15HSDHB	Taraborrelli (2014)
G4581et2	TrGC	C1OOHC2OOHC4OD + OH → C1ODC2OOHC4OD + OH	ks*fsooh*fpch2oh	Taraborrelli (2014)
G4581et3	TrGC	C1OOHC2OOHC4OD + OH → CH3COCH2O2H + OH + 2 CO + 2 HO2	kt*ftoh*fpch2oh*fpch2oh	Taraborrelli (2014)

16

Table 1: Gas phase reactions (... continued)

#	labels	reaction	rate coefficient	reference
G4581et4	TrGC	C1OOHC2OOHC4OD + OH → C1OOHC2O2C4OD	0.6*k_CH300H_OH	Taraborrelli (2014)
G4581et6	TrGC	C1ODC3O2C4OOH → MGLYOX + HOOCH2CHO + HO2	2.90E-12*R02	Taraborrelli (2014)
G4581et7	TrGC	C1ODC3O2C4OOH + NO → MGLYOX + HOOCH2CHO + HO2 + NO2	KR02NO	Taraborrelli (2014)
G4581et8	TrGC	C1ODC3O2C4OOH + HO2 → .5 CH3C(O)OO + .5 CO + .5 MGLYOX + .5 HO2 + HOOCH2CO3	KR02H02*0.706	Taraborrelli (2014)*
G4581et9	TrGC	C1ODC3O2C4OOH → MGLYOX + OH + HOOCH2CHO	KHSD	Taraborrelli (2014)
G4581et10	TrGC	C1OOHC3O2C4OD → .625 MGLYOX + 2 CO + 1.625 HO2 + .375 CH3C(O)OO + .375 CO2 + OH	K15HSDHB	Taraborrelli (2014)*
G4582e	TrGC	LHC4ACCO3 → ZCO3HC23DBCOD + HO2	K16HS	Taraborrelli (2014)*
G4583e	TrGC	ZCODC23DBCOD + OH → C1ODC2O2C4OD	2*kt*fo*falk+(kadt+kads)*acho*acho	Taraborrelli (2014)
G4584e	TrGC	C1ODC2O2C4OD + HO2 → OH + MGLYOX + HOCHCHO	KR02H02*0.706*rcoch2o2_oh	Taraborrelli (2014)
G4584et2	TrGC	C1ODC2O2C4OD + HO2 → C1ODC2OOHC4OD	KR02H02*0.706*rcoch2o2_oh	Taraborrelli (2014)
G4585e	TrGC	C1ODC2O2C4OD + NO → NO2 + MGLYOX + HOCHCHO	KR02NO	Taraborrelli (2014)
G4585et2	TrGC	C1ODC2O2C4OD → MGLYOX + HOCHCHO	8.00E-13*R02	Taraborrelli (2014)
G4585et3	TrGC	C1ODC2OOHC4OD + OH → MGLYOX + 2 CO + .5 OH	2*kt*fo*ftch2oh*falk+kt*ftoh*fcho*fpch2oh	Taraborrelli (2014)*
G4587e	TrGC	LISOPACNO3O2 + NO → .21 NOA + .21 HOCH2CHO + .21 HO2 + .49 HO12CO3C4 + .49 HCHO + .49 NO2 + .045 HMVKNO3 + .045 HCHO + .255 CH3COCH2OH + .255 NO3CH2CHO + .225 H2O2 + NO2	KR02NO	Taraborrelli (2014)
G4587et2	TrGC	LISOPACNO3O2 → .21 NOA + .21 HOCH2CHO + .21 HO2 + .49 HO12CO3C4 + .49 HCHO + .49 NO2 + .045 HMVKNO3 + .045 HCHO + .255 CH3COCH2OH + .255 NO3CH2CHO + .225 H2O2	8.00E-13*R02+KR02H02*0.706*c(ind_H02)	Taraborrelli (2014)
G4587et3	TrGC	ISOPBDNO3O2 + NO → .6 CH3COCH2OH + .6 HOCH2CHO + .26 MACRN + .14 HMVKNO3 + .4 HCHO + .4 HO2 + 1.6 NO2	KR02NO	Taraborrelli (2014)
G4587et4	TrGC	ISOPBDNO3O2 → .6 CH3COCH2OH + .6 HOCH2CHO + .26 MACRN + .14 HMVKNO3 + .4 HCHO + .4 HO2 + .6 NO2	2.9E-12*R02+KR02H02*0.706*c(ind_H02)	Taraborrelli (2014)

17

Table 1: Gas phase reactions (... continued)

#	labels	reaction	rate coefficient	reference
G4588e	TrGNC	LISOPACNO3 + O ₃ → .8704 OH + .365 HO ₂ + .73 MGLYOX + .4325 NO3CH2CHO + .135 CH3COCH2OH + .0675 GLYOX + .4325 NO ₂ + .0891 H ₂ O ₂ + .135 NOA + .0675 HOCHCHO + .3866 HOCH2CHO + .0405 CH3OH + .0405 CO + .0054 HOCH2CO	4.E-16	Taraborrelli (2014)
G4599e	TrGC	LISOPACOOH + O ₃ → 1.3272 OH + 0.36986 HO ₂ + .0432 H ₂ O ₂ + 0.23002 CO + .2025 CH ₃ OOH + .01215 HOCH2OOH + 0.3704 HCHO + .00405 CH ₃ OH + .0405 CO ₂ + .1825 HOCH2COCH2O ₂ + .365 MGLYOX + .3866 HOOCH2CHO + .135 CH ₃ COCH ₂ OH + .0675 GLYOX + .00324 HCOC3A + .3866 HOCH2CHO + .135 CH ₃ COCH ₂ O ₂ H + .0675 HOCHCHO + .0054 HOCH2CO	4.829E-16	Taraborrelli (2014)
G4598et3	TrGC	ZCO3HC23DBCOD + OH → .62 CO2H3CHO + .62 OH + .62 CO ₂ + .38 MGLYOX + .38 HCOC3H + .38 HO ₂	kadt*acho*aco2h	Taraborrelli (2014)*
G4598et4	TrGC	ZCO3HC23DBCOD + OH → .62 CH3COCO3H + 1.24 CO + 1.24 HO ₂ + .38 CH3COCHOH + .38 CO + .38 HO ₂ + .38 OH + .38 CO ₂	kads*acho*aco2h	Taraborrelli (2014)*
G41311	TrGC	LISOPEFO2 → .7143 MACR + .2857 MVK + HCHO + HO ₂	2.40E-12*R02	Taraborrelli (2014)
G41341	TrGC	LISOPEFO2 + NO → .7143 MACR + .2857 MVK + HCHO + HO ₂ + NO ₂	KR02N0	Taraborrelli (2014)
G41351t2	TrGC	LISOPEFO2 + HO ₂ → .7143 MACR + .2857 MVK + HCHO + HO ₂	KR02H02*0.706	Taraborrelli (2014)
G41361	TrGC	LISOPEFO2 + NO ₃ → .7143 MACR + .2857 MVK + HCHO + HO ₂ + NO ₂	KR02N03	Taraborrelli (2014)
G41378	TrGC	LISOPEFO2 → PEROXYRINGC2O2	9.39E9*EXP(-7322/temp)	Taraborrelli (2014)
G41341t2	TrGC	LISOPEFO2 → .7143 MACR + .2857 MVK + HCHO + OH	.7143*KHSD+.2857*KHSB	Taraborrelli (2014)
G413112	TrGC	PEROXYRINGC2O2 → CH3COCH2OOCH2CHO + HO ₂	8.00E-13*R02	Taraborrelli (2014)
G413416	TrGC	PEROXYRINGC2O2 + NO → CH3COCH2OOCH2CHO + HO ₂ + NO ₂	KR02N0	Taraborrelli (2014)*
G413519	TrGC	PEROXYRINGC2O2 + HO ₂ → PEROXYRINGC2OOH	KR02H02*0.706	Taraborrelli (2014)
G413618	TrGC	PEROXYRINGC2O2 + NO ₃ → CH3COCH2OOCH2CHO + HO ₂ + NO ₂	KR02N03	Taraborrelli (2014)
G413417	TrGC	PEROXYRINGC2O2 → CH3COCH2OOCH2CHO + OH	KHSB	Taraborrelli (2014)

18

Table 1: Gas phase reactions (... continued)

#	labels	reaction	rate coefficient	reference
G413619	TrGC	PEROXYRINGC2OOH + OH → PEROXYRINGC2O2	0.6*k_CH300H_DH	Taraborrelli (2014)
G413621	TrGC	PEROXYRINGC2OOH + OH → MGLYOX + 2 CO + 2 HO ₂	kt*ftoh*falk*fpch2oh	Taraborrelli (2014)*
G413622	TrGC	PEROXYRINGC2OOH + OH → .8405 HCHO + .8405 OH + .8405 CO2H3CHO + .1595 ClODC2OOHC4OD + .1595 HO ₂	ks*fsosh*falk*ks*fsosh*falk	Taraborrelli (2014)
G4136	TrGC	CH3COCH2OOCH2CHO + OH → CH ₃ C(O)OO + CO ₂ + 2 HCHO	kt*fo*ftch2oh	Taraborrelli (2014)*
G413610	TrGC	CH3COCH2OOCH2CHO + OH → GLYOX + CH ₃ C(O)OO + HCHO	ks*fcho*fsosh	Taraborrelli (2014)
G41361t2	TrGC	CH3COCH2OOCH2CHO + OH → MGLYOX + GLYOX + HO ₂	ks*fco*fsosh	Taraborrelli (2014)
G45mbo1	TrGC	MBO + OH → LMBOABO2	8.1E-12*EXP(610/TEMP)	Rickard and Pascoe (2009), Taraborrelli (2014)
G45mbo2	TrGC	MBO + O ₃ → HCHO + .16 CH ₃ COCH ₃ + .16 HO ₂ + .16 CO + .16 OH + .84 MBOOO	1.0E-17*0.57	Rickard and Pascoe (2009), Taraborrelli (2014)
G45mbo3	TrGC	MBO + O ₃ → IBUTALOH + .63 CO + .37 HOCH2OOH + .16 OH + .16 HO ₂	1.0E-17*0.43	Rickard and Pascoe (2009), Taraborrelli (2014)
G45mbo4	TrGC	MBO + NO ₃ → LNMBOABO2	4.6E-14*EXP(-400/TEMP)	Rickard and Pascoe (2009), Taraborrelli (2014)
G45mbo5	TrGC	LMBOABO2 + HO ₂ → LMBOABOOH	KR02H02*0.706	Rickard and Pascoe (2009), Taraborrelli (2014)
G45mbo6	TrGC	LMBOABO2 + NO → LMBOABNO3	KR02N0*(0.064+0.026)/2.	Rickard and Pascoe (2009), Taraborrelli (2014)
G45mbo7	TrGC	LMBOABO2 + NO → HOCH ₂ CHO + CH ₃ COCH ₃ + HO ₂ + NO ₂	KR02N0*(0.936+0.974)/2*.67	Rickard and Pascoe (2009), Taraborrelli (2014)
G45mbo8	TrGC	LMBOABO2 + NO → IBUTALOH + HCHO + HO ₂ + NO ₂	KR02N0*(0.936+0.974)/2*.33	Rickard and Pascoe (2009), Taraborrelli (2014)
G45mbo9	TrGC	LMBOABO2 → HOCH ₂ CHO + CH ₃ COCH ₃ + HO ₂	8.8E-13*R02*.67	Rickard and Pascoe (2009), Taraborrelli (2014)
G45mbo10	TrGC	LMBOABO2 → IBUTALOH + HCHO + HO ₂	8.8E-13*R02*.33	Rickard and Pascoe (2009), Taraborrelli (2014)
G45mbo11	TrGC	LMBOABOOH + OH → MBOACO + OH	.67*2.93E-11+.33*2.05E-12	Rickard and Pascoe (2009), Taraborrelli (2014)*

19

Table 1: Gas phase reactions (... continued)

#	labels	reaction	rate coefficient	reference
G45mbo12	TrGC	LMBOABOOH + OH → LMBOABO2	.6*k_CH300H_OH	Rickard and Pascoe (2009), Taraborrelli (2014)
G45mbo13	TrGC	LMBOABOOH + hν → HOCH ₂ CHO + CH ₃ COCH ₃ + HO ₂ + OH	1.14*jx(ip_CH300H)*.67	Rickard and Pascoe (2009), Taraborrelli (2014)
G45mbo14	TrGC	LMBOABOOH + hν → IBUTALOH + HCHO + HO ₂ + OH	1.14*jx(ip_CH300H)*.33	Rickard and Pascoe (2009), Taraborrelli (2014)
G45mbo15	TrGC	LMBOABNO3 + OH → MBOACO + NO ₂	.67*1.75E-12+.33*2.69E-12	Rickard and Pascoe (2009), Taraborrelli (2014)*
G45mbo16	TrGC	MBOACO + OH → MBOCOCO + HO ₂	3.79E-12	Rickard and Pascoe (2009)
G45mbo17	TrGC	MBOACO + hν → HCHO + HO ₂ + IPRHOCO3	J_ACETOL	Rickard and Pascoe (2009)
G45mbo18	TrGC	MBOCOCO + OH → CO + IPRHOCO3	1.38E-11	Rickard and Pascoe (2009)
G45mbo19	TrGC	MBOCOCO + hν → CO + HO ₂ + IPRHOCO3	jx(ip_MGLYOX)	Rickard and Pascoe (2009)
G45mbo20	TrGC	IBUTALOH + OH → IPRHOCO3	1.4E-11	Rickard and Pascoe (2009)
G45mbo21	TrGC	IBUTALOH + hν → CH ₃ COCH ₃ + HO ₂ + HO ₂ + CO	J_ACETOL	Rickard and Pascoe (2009)
G45mbo22	TrGC	IPRHOCO3 + HO ₂ → CH ₃ COCH ₃ + HO ₂ + OH	KAPH02*rco3_oh	Rickard and Pascoe (2009), Taraborrelli (2014)
G45mbo23	TrGC	IPRHOCO3 + HO ₂ → IPRHOCO2H + O ₃	KAPH02*rco3_o3	Rickard and Pascoe (2009), Taraborrelli (2014)
G45mbo24	TrGC	IPRHOCO3 + HO ₂ → IPRHOCO3H	KAPH02*rco3_ooh	Rickard and Pascoe (2009), Taraborrelli (2014)
G45mbo25	TrGC	IPRHOCO3 + NO → CH ₃ COCH ₃ + HO ₂ + NO ₂	KAPNO	Rickard and Pascoe (2009)
G45mbo26	TrGC	IPRHOCO3 + NO ₂ → C4PAN5	k_CH3CO3_NO2	Rickard and Pascoe (2009)
G45mbo27	TrGC	IPRHOCO3 + NO ₃ → CH ₃ COCH ₃ + HO ₂ + NO ₂	KRO2NO3*1.74	Rickard and Pascoe (2009)
G45mbo28	TrGC	IPRHOCO3 → CH ₃ COCH ₃ + HO ₂	1.00E-11*R02*0.7	Rickard and Pascoe (2009)
G45mbo29	TrGC	IPRHOCO3 → IPRHOCO2H	1.00E-11*R02*0.3	Rickard and Pascoe (2009)
G45mbo30	TrGC	IPRHOCO2H + OH → CH ₃ COCH ₃ + HO ₂	1.72E-12	Rickard and Pascoe (2009)
G45mbo31	TrGC	IPRHOCO3H + hν → CH ₃ COCH ₃ + HO ₂ + OH	1.14*jx(ip_CH300H)	Rickard and Pascoe (2009)
G45mbo32	TrGC	OH + IPRHOCO3H → IPRHOCO3	4.80E-12	Rickard and Pascoe (2009)
G45mbo33	TrGC	C4PAN5 → IPRHOCO3 + NO ₂	K_PAN_M	Rickard and Pascoe (2009)
G45mbo34	TrGC	C4PAN5 + OH → CH ₃ COCH ₃ + CO + NO ₂	4.75E-13	Rickard and Pascoe (2009)
G45mbo35	TrGC	LNMBOABO2 + HO ₂ → LNMBOABOOH	KRO2HO2*0.706	Rickard and Pascoe (2009), Taraborrelli (2014)
G45mbo36	TrGC	LNMBOABO2 + NO → .65 NO3CH2CHO + .65 CH ₃ COCH ₃ + .65 HO ₂ + .35 IBUTALOH + .35 HCHO + .35 NO ₂ + NO ₂	KRO2NO	Rickard and Pascoe (2009), Taraborrelli (2014)

20

Table 1: Gas phase reactions (... continued)

#	labels	reaction	rate coefficient	reference
G45mbo37	TrGC	LNMBOABO2 + NO ₃ → .65 NO3CH2CHO + .65 CH ₃ COCH ₃ + .65 HO ₂ + .35 IBUTALOH + .35 HCHO + .35 NO ₂ + NO ₂	KRO2NO3	Rickard and Pascoe (2009), Taraborrelli (2014)
G45mbo38	TrGC	LNMBOABO2 → .65 NO3CH2CHO + .65 CH ₃ COCH ₃ + .65 HO ₂ + .35 IBUTALOH + .35 HCHO + .35 NO ₂	8.8E-13*R02	Rickard and Pascoe (2009), Taraborrelli (2014)
G45mbo39	TrGC	LNMBOABOOH + OH → .65 C4MCONO3OH + .35 NMBOBCO + OH	.65*4.89E-12+.35*2.52E-12	Rickard and Pascoe (2009), Taraborrelli (2014)
G45mbo40	TrGC	LNMBOABOOH + OH → LNMBOABO2	.6*k_CH300H_OH	Rickard and Pascoe (2009), Taraborrelli (2014)
G45mbo41	TrGC	LNMBOABOOH + hν → NO3CH2CHO + CH ₃ COCH ₃ + HO ₂ + OH	1.14*jx(ip_CH300H)*.65	Rickard and Pascoe (2009), Taraborrelli (2014)
G45mbo42	TrGC	LNMBOABOOH + hν → IBUTALOH + HCHO + NO ₂ + OH	1.14*jx(ip_CH300H)*.35	Rickard and Pascoe (2009), Taraborrelli (2014)
G45mbo43	TrGC	C4MCONO3OH + OH → CH ₃ COCH ₃ + HCHO + CO ₂ + NO ₂	1.23E-12	Rickard and Pascoe (2009), Taraborrelli (2014)*
G45mbo44	TrGC	NMBOBCO + OH → NC4OHCO3	4.26E-12	Rickard and Pascoe (2009)
G45mbo45	TrGC	NC4OHCO3 + HO ₂ → IBUTALOH + NO ₂ + OH	KAPH02*rco3_oh	Rickard and Pascoe (2009), Taraborrelli (2014)
G45mbo46	TrGC	NC4OHCO3 + HO ₂ → NC4OHCO3H	KAPH02*(rco3_o3+rco3_ooh)	Rickard and Pascoe (2009), Taraborrelli (2014)
G45mbo47	TrGC	NC4OHCO3 + NO → IBUTALOH + NO ₂ + NO ₂	KAPNO	Rickard and Pascoe (2009)
G45mbo48	TrGC	NC4OHCO3 + NO ₂ → NC4OHCPAN	k_CH3CO3_NO2	Rickard and Pascoe (2009)
G45mbo49	TrGC	NC4OHCO3 + NO ₃ → IBUTALOH + NO ₂ + NO ₂	KRO2NO3*1.74	Rickard and Pascoe (2009)
G45mbo50	TrGC	NC4OHCO3 → IBUTALOH + NO ₂	1.00E-11*R02	Rickard and Pascoe (2009)
G45mbo51	TrGC	NC4OHCO3H + OH → NC4OHCO3	4.50E-12	Rickard and Pascoe (2009)
G45mbo52	TrGC	NC4OHCO3H → IBUTALOH + NO ₂ + OH	1.14*jx(ip_CH300H)	Rickard and Pascoe (2009)
G45mbo53	TrGC	NC4OHCPAN + OH → IBUTALOH + CO + NO ₂ + NO ₂	1.27E-12	Rickard and Pascoe (2009)
G45mbo54	TrGC	NC4OHCPAN → NC4OHCO3 + NO ₂	K_PAN_M	Rickard and Pascoe (2009)
G45mbo55	TrGC	MBOOO → IPRHOCO2H	1.60E-17*C(ind_H20)*(0.08+0.15)	Rickard and Pascoe (2009), Taraborrelli (2014)
G45mbo56	TrGC	MBOOO → IBUTALOH + H ₂ O ₂	1.60E-17*C(ind_H20)*0.77	Rickard and Pascoe (2009), Taraborrelli (2014)
G45mbo57	TrGC	MBOOO + CO → IBUTALOH	1.20E-15	Rickard and Pascoe (2009)
G45mbo58	TrGC	MBOOO + NO → IBUTALOH + NO ₂	1.00E-14	Rickard and Pascoe (2009)
G45mbo59	TrGC	MBOOO + NO ₂ → IBUTALOH + NO ₃	1.00E-15	Rickard and Pascoe (2009)

21

Table 1: Gas phase reactions (... continued)

#	labels	reaction	rate coefficient	reference
G45mbo60	TrGC	MBOOO + SO ₂ → IBUTALOH + H ₂ SO ₄	7.00E-14	Rickard and Pascoe (2009)
G410apin1	TrGC	APINENE + OH → LAPINABO2	1.47E-11*EXP(467/TEMP)*(.50+.25)	Vereecken et al. (2007), Taraborrelli (2014)*
G410apin2	TrGC	APINENE + OH → MENTHEN6ONE + HO ₂	1.47E-11*EXP(467/TEMP)*.25*.60	Vereecken et al. (2007), Taraborrelli (2014)*
G410apin3	TrGC	APINENE + OH → LVROO6R1O2	1.47E-11*EXP(467/TEMP)*.25*.40	Vereecken et al. (2007), Taraborrelli (2014)*
G410apin4	TrGC	LAPINABO2 + NO → PINAL + HO ₂ + NO ₂	KR02N0*0.770	Rickard and Pascoe (2009), Taraborrelli (2014)
G410apin5	TrGC	LAPINABO2 + NO → LAPINABNO3	KR02N0*0.230	Rickard and Pascoe (2009), Taraborrelli (2014)
G410apin6	TrGC	LAPINABO2 + HO ₂ → LAPINABOOH	KR02H02*0.914	Rickard and Pascoe (2009), Taraborrelli (2014)
G410apin7	TrGC	LAPINABO2 → PINAL + HO ₂	R02*(.33*9.20E-14+.67*8.80E-13)	Rickard and Pascoe (2009), Taraborrelli (2014)
G410apin9	TrGC	LAPINABOOH + OH → .33 LAPINABO2 + .67 C96CO3	.33*1.83E-11+.67*3.28E-11	Rickard and Pascoe (2009), Taraborrelli (2014)
G410apin10	TrGC	LAPINABOOH + hν → PINAL + HO ₂ + OH	1.14*jx(ip_CH300H)	Rickard and Pascoe (2009), Taraborrelli (2014)
G410apin11	TrGC	LAPINABNO3 + OH → .33 PINAL + .67 C96CO3 + NO ₂	.33*5.50E-12+.67*3.64E-12	Rickard and Pascoe (2009), Taraborrelli (2014)
G410apin12	TrGC	MENTHEN6ONE + OH → OHMENTHEN6ONEO2	(kads*kadt)*aco3ch3	Vereecken et al. (2007), Taraborrelli (2014)
G410apin13	TrGC	MENTHEN6ONE + hν → LVRO6R1O2 + OH	1.14*jx(ip_CH300H)	Vereecken et al. (2007), Taraborrelli (2014)
G410apin14	TrGC	OHMENTHEN6ONEO2 + NO → KR02N0		Vereecken et al. (2007), Taraborrelli (2014)
G410apin15	TrGC	LV2OHMENTHEN6ONE + HO ₂ + NO ₂ OHMENTHEN6ONEO2 + HO ₂ → KR02H02*0.914		Vereecken et al. (2007), Taraborrelli (2014)
G410apin16	TrGC	LV2OHMENTHEN6ONE OHMENTHEN6ONEO2 → LV2OHMENTHEN6ONE + HO ₂	R02*9.20E-14	Vereecken et al. (2007), Taraborrelli (2014)
G410apin17	TrGC	LV2OHMENTHEN6ONE + OH → LCARBON	1E-11	Vereecken et al. (2007), Taraborrelli (2014)
G410apin18	TrGC	LV2OHMENTHEN6ONE + hν → LCARBON + OH	1.14*jx(ip_CH300H)	Vereecken et al. (2007), Taraborrelli (2014)

22

Table 1: Gas phase reactions (... continued)

#	labels	reaction	rate coefficient	reference
G410apin18t2	TrGC	PINAL + OH → C96CO3	4.20E-11*0.772	Rickard and Pascoe (2009), Taraborrelli (2014)
G410apin19	TrGC	PINAL + OH → PINALO2	4.20E-11*0.228	Rickard and Pascoe (2009), Taraborrelli (2014)
G410apin20	TrGC	PINAL → C96O2 + CO + HO ₂	jx(ip_HOCH2CHO)	Rickard and Pascoe (2009), Taraborrelli (2014)
G410apin21	TrGC	PINAL + NO ₃ → C96CO3 + HNO ₃	3.80E-14	Rickard and Pascoe (2009), Taraborrelli (2014)
G410apin	TrGC	C96CO3 → 0.3 PINONIC + 0.7 C96O2	1.00E-11*R02	Rickard and Pascoe (2009), Taraborrelli (2014)
G410apint2	TrGC	C96CO3 + HO ₂ → PERPINONIC	KAPH02*rco3_ooh	Rickard and Pascoe (2009), Taraborrelli (2014)
G410apint3	TrGC	C96CO3 + HO ₂ → PINONIC + O ₃	KAPH02*rco3_o3	Rickard and Pascoe (2009), Taraborrelli (2014)
G410apint4	TrGC	C96CO3 + HO ₂ → C96O2 + OH	KAPH02*rco3_oh	Rickard and Pascoe (2009), Taraborrelli (2014)
G410apint5	TrGC	C96CO3 + NO ₂ → C10PAN2	k_CH3CO3_NO2	Rickard and Pascoe (2009), Taraborrelli (2014)
G410apint6	TrGC	C96CO3 + NO → C96O2 + NO ₂	KAPNO	Rickard and Pascoe (2009), Taraborrelli (2014)
G410apint7	TrGC	C96CO3 + NO ₃ → C96O2 + NO ₂	KR02N03*1.60	Rickard and Pascoe (2009), Taraborrelli (2014)
G410apint8	TrGC	C10PAN2 → C96CO3 + NO ₂	k_PAN_M	Rickard and Pascoe (2009), Taraborrelli (2014)
G410apint9	TrGC	C10PAN2 + OH → NORPINAL + CO + NO ₂	3.66E-12	Rickard and Pascoe (2009), Taraborrelli (2014)
G410apint10	TrGC	C96O2 → C97O2	1.30E-12*R02	Rickard and Pascoe (2009), Taraborrelli (2014)
G410apint11	TrGC	C96O2 + NO → C96NO3	KR02N0*0.157	Rickard and Pascoe (2009), Taraborrelli (2014)
G410apint12	TrGC	C96O2 + HO ₂ → C96OOH	KR02H02*0.890	Rickard and Pascoe (2009), Taraborrelli (2014)
G410apint13	TrGC	C96O2 + NO → C97O2 + NO ₂	KR02N0*0.843	Rickard and Pascoe (2009), Taraborrelli (2014)

23

Table 1: Gas phase reactions (... continued)

#	labels	reaction	rate coefficient	reference
G410apint14	TrGC	$C96NO3 + h\nu \rightarrow C97O2 + NO_2$	J_IC3H7NO3+J_ACETOL	Rickard and Pascoe (2009), Taraborrelli (2014)
G410apint15	TrGC	$C96NO3 + OH \rightarrow NORPINAL + NO_2$	2.88E-12	Rickard and Pascoe (2009), Taraborrelli (2014)
G410apint16	TrGC	$C96OOH + h\nu \rightarrow C97O2 + OH$	1.14*jx(ip_CH300H)+J_ACETOL	Rickard and Pascoe (2009), Taraborrelli (2014)
G410apint17	TrGC	$C96OOH + OH \rightarrow C96O2$	1.90E-12*EXP(190/TEMP)	Rickard and Pascoe (2009), Taraborrelli (2014)
G410apint18	TrGC	$C96OOH + OH \rightarrow NORPINAL + OH$	1.30E-11	Rickard and Pascoe (2009), Taraborrelli (2014)
G410apint19	TrGC	$C97O2 \rightarrow C98O2$	6.70E-15*R02	Rickard and Pascoe (2009), Taraborrelli (2014)
G410apint20	TrGC	$C97O2 + NO \rightarrow C98O2 + NO_2$	KR02N0	Rickard and Pascoe (2009), Taraborrelli (2014)
G410apint21	TrGC	$C97O2 + HO_2 \rightarrow C97OOH$	KR02H02*0.890	Rickard and Pascoe (2009), Taraborrelli (2014)
G410apint22	TrGC	$C97OOH + h\nu \rightarrow C98O2 + OH$	1.14*jx(ip_CH300H)+J_ACETOL	Rickard and Pascoe (2009), Taraborrelli (2014)
G410apint23	TrGC	$C97OOH + OH \rightarrow C97O2$	1.05E-11	Rickard and Pascoe (2009), Taraborrelli (2014)
G410apint24	TrGC	$C98O2 \rightarrow C614O2 + CH_3COCH_3$	6.70E-15*R02	Rickard and Pascoe (2009), Taraborrelli (2014)
G410apint25	TrGC	$C98O2 + NO \rightarrow C98NO3$	KR02N0*0.118	Rickard and Pascoe (2009), Taraborrelli (2014)
G410apint26	TrGC	$C98O2 + NO \rightarrow C614O2 + CH_3COCH_3 + NO_2$	KR02N0*0.882	Rickard and Pascoe (2009), Taraborrelli (2014)
G410apint27	TrGC	$C98O2 + HO_2 \rightarrow C98OOH$	KR02H02*0.890	Rickard and Pascoe (2009), Taraborrelli (2014)
G410apint28	TrGC	$C98OOH + h\nu \rightarrow C614O2 + CH_3COCH_3 + OH$	1.14*jx(ip_CH300H)+2.15*jx(ip_MGLYOX)	Rickard and Pascoe (2009), Taraborrelli (2014)
G410apint29	TrGC	$C98OOH + OH \rightarrow C98O2$	2.05E-11	Rickard and Pascoe (2009), Taraborrelli (2014)
G410apint30	TrGC	$PINONIC + OH \rightarrow C96O2$	6.65E-12	Rickard and Pascoe (2009), Taraborrelli (2014)

24

Table 1: Gas phase reactions (... continued)

#	labels	reaction	rate coefficient	reference
G410apint31	TrGC	$PINONIC + h\nu \rightarrow C96O2 + HO_2$	J_ACETOL	Rickard and Pascoe (2009), Taraborrelli (2014)
G410apint32	TrGC	$NORPINAL + OH \rightarrow C85CO3$	2.64E-11	Rickard and Pascoe (2009), Taraborrelli (2014)
G410apint33	TrGC	$NORPINAL + h\nu \rightarrow C85O2 + CO + HO_2$	jx(ip_HOCH2CHO)	Rickard and Pascoe (2009), Taraborrelli (2014)
G410apint34	TrGC	$NORPINAL + NO_3 \rightarrow C85CO3 + HNO_3$	KNG3AL*8.5	Rickard and Pascoe (2009), Taraborrelli (2014)
G410apint35	TrGC	$PERPINONIC + h\nu \rightarrow C96O2 + OH$	1.14*jx(ip_CH300H)+J_ACETOL	Rickard and Pascoe (2009), Taraborrelli (2014)
G410apint36	TrGC	$PERPINONIC + OH \rightarrow C96CO3$	9.73E-12	Rickard and Pascoe (2009), Taraborrelli (2014)
G410apint37	TrGC	$C85CO3 \rightarrow C85O2$	1.00E-11*R02	Rickard and Pascoe (2009), Taraborrelli (2014)
G410apint38	TrGC	$C85CO3 + NO \rightarrow C85O2 + NO_2$	KAPNO	Rickard and Pascoe (2009), Taraborrelli (2014)
G410apint39	TrGC	$C85CO3 + NO_2 \rightarrow C9PAN2$	k_CH3CO3_NO2	Rickard and Pascoe (2009), Taraborrelli (2014)
G410apint40	TrGC	$C85CO3 + HO_2 \rightarrow C85CO3H$	KAPH02*(rco3_ooh+rco3_o3)	Rickard and Pascoe (2009), Taraborrelli (2014)
G410apint41	TrGC	$C85CO3 + HO_2 \rightarrow C85O2 + OH$	KAPH02*rco3_oh	Rickard and Pascoe (2009), Taraborrelli (2014)
G410apint42	TrGC	$C85O2 \rightarrow C86O2$	6.70E-15*R02	Rickard and Pascoe (2009), Taraborrelli (2014)
G410apint43	TrGC	$C85O2 + HO_2 \rightarrow C85OOH$	KR02H02*0.859	Rickard and Pascoe (2009), Taraborrelli (2014)
G410apint44	TrGC	$C85O2 + NO \rightarrow C86O2 + NO_2$	KR02N0	Rickard and Pascoe (2009), Taraborrelli (2014)
G410apint45	TrGC	$C9PAN2 \rightarrow C85CO3 + NO_2$	k_PAN_M	Rickard and Pascoe (2009), Taraborrelli (2014)
G410apint46	TrGC	$C9PAN2 + OH \rightarrow C85OOH + CO + NO_2$	6.60E-12	Rickard and Pascoe (2009), Taraborrelli (2014)
G410apint47	TrGC	$C85CO3H \rightarrow C85O2 + OH$	1.14*jx(ip_CH300H)+J_ACETOL	Rickard and Pascoe (2009), Taraborrelli (2014)

25

Table 1: Gas phase reactions (... continued)

#	labels	reaction	rate coefficient	reference
G410apint48	TrGC	$C_8H_5CO_3H + OH \rightarrow C_8H_5CO_3$	1.02E-11	Rickard and Pascoe (2009), Taraborrelli (2014)
G410apint49	TrGC	$C_8H_5OOH + h\nu \rightarrow C_8H_5O_2 + OH$	1.14*jx(ip_CH300H)+J_ACETOL	Rickard and Pascoe (2009), Taraborrelli (2014)
G410apint50	TrGC	$C_8H_5OOH + OH \rightarrow C_8H_5O_2$	1.29E-11	Rickard and Pascoe (2009), Taraborrelli (2014)
G410apint51	TrGC	$C_8H_5O_2 \rightarrow C_5H_11O_2 + CH_3COCH_3$	6.70E-15*R02	Rickard and Pascoe (2009), Taraborrelli (2014)
G410apint52	TrGC	$C_8H_5O_2 + NO \rightarrow C_5H_11O_2 + CH_3COCH_3 + NO_2$	KR02N0	Rickard and Pascoe (2009), Taraborrelli (2014)
G410apint53	TrGC	$C_8H_5O_2 + HO_2 \rightarrow C_8H_5OOH$	KR02H02*0.859	Rickard and Pascoe (2009), Taraborrelli (2014)
G410apint54	TrGC	$C_8H_5OOH + h\nu \rightarrow C_5H_11O_2 + CH_3COCH_3 + OH$	1.14*jx(ip_CH300H)+ jx(ip_HOCH2CHO)	Rickard and Pascoe (2009), Taraborrelli (2014)
G410apint55	TrGC	$C_8H_5OOH + OH \rightarrow C_8H_5O_2$	3.45E-11	Rickard and Pascoe (2009), Taraborrelli (2014)
G410apint56	TrGC	$PINALO_2 + HO_2 \rightarrow PINALOOH$	KR02H02*0.914	Rickard and Pascoe (2009), Taraborrelli (2014)
G410apint57	TrGC	$PINALO_2 + NO \rightarrow PINALNO_3$	KR02N0*0.050	Rickard and Pascoe (2009), Taraborrelli (2014)
G410apint58	TrGC	$PINALO_2 + NO \rightarrow C106O_2 + NO_2$	KR02N0*0.950	Rickard and Pascoe (2009), Taraborrelli (2014)
G410apint59	TrGC	$PINALO_2 \rightarrow C106O_2$	6.70E-15*R02	Rickard and Pascoe (2009), Taraborrelli (2014)
G410apint60	TrGC	$PINALOOH + OH \rightarrow PINALO_2$	2.75E-11	Rickard and Pascoe (2009), Taraborrelli (2014)
G410apint61	TrGC	$PINALOOH + h\nu \rightarrow C106O_2 + OH$	1.14*jx(ip_CH300H)+jx(ip_HOCH2CHO)	Rickard and Pascoe (2009), Taraborrelli (2014)
G410apint62	TrGC	$PINALNO_3 + OH \rightarrow CO_235C_6CHO + CH_3COCH_3 + NO_2$	2.25E-11	Rickard and Pascoe (2009), Taraborrelli (2014)
G410apint63	TrGC	$PINALNO_3 + h\nu \rightarrow C106O_2 + NO_2$	J_IC3H7N03+jx(ip_HOCH2CHO)	Rickard and Pascoe (2009), Taraborrelli (2014)
G410apint64	TrGC	$C106O_2 + HO_2 \rightarrow C106OOH$	KR02H02*0.914	Rickard and Pascoe (2009), Taraborrelli (2014)

26

Table 1: Gas phase reactions (... continued)

#	labels	reaction	rate coefficient	reference
G410apint65	TrGC	$C106O_2 + NO \rightarrow C106NO_3$	KR02N0*0.125	Rickard and Pascoe (2009), Taraborrelli (2014)
G410apint66	TrGC	$C106O_2 + NO \rightarrow C716O_2 + CH_3COCH_3 + NO_2$	KR02N0*0.875	Rickard and Pascoe (2009), Taraborrelli (2014)
G410apint67	TrGC	$C106O_2 \rightarrow C716O_2 + CH_3COCH_3$	6.70E-15*R02	Rickard and Pascoe (2009), Taraborrelli (2014)
G410apint68	TrGC	$C106OOH + OH \rightarrow C106O_2$	8.01E-11	Rickard and Pascoe (2009), Taraborrelli (2014)
G410apint69	TrGC	$C106OOH + h\nu \rightarrow C716O_2 + CH_3COCH_3 + OH$	1.14*jx(ip_CH300H)+jx(ip_HOCH2CHO)	Rickard and Pascoe (2009), Taraborrelli (2014)
G410apint70	TrGC	$C106NO_3 + OH \rightarrow CO_235C_6CHO + CH_3COCH_3 + NO_2$	7.03E-11	Rickard and Pascoe (2009), Taraborrelli (2014)
G410apint71	TrGC	$C106NO_3 + h\nu \rightarrow C716O_2 + CH_3COCH_3 + NO_2$	J_IC3H7N03+ jx(ip_HOCH2CHO)	Rickard and Pascoe (2009), Taraborrelli (2014)
G410apint72	TrGC	$CO_235C_6CHO + NO_3 \rightarrow CO_235C_6CO_3 + HNO_3$	KN03AL*5.5	Rickard and Pascoe (2009), Taraborrelli (2014)
G410apint73	TrGC	$CO_235C_6CHO + OH \rightarrow CO_235C_6CO_3$	6.70E-11	Rickard and Pascoe (2009), Taraborrelli (2014)
G410apint74	TrGC	$CO_235C_6CHO + h\nu \rightarrow CHOC_3COCO_3 + CH_3C(O)OO$	2.15*jx(ip_MGLYOX)	Rickard and Pascoe (2009), Taraborrelli (2014)
G410apint75	TrGC	$CO_235C_6CO_3 + HO_2 \rightarrow C_235C_6CO_3H$	KAPH02*(rco3_ooH+rco3_o3)	Rickard and Pascoe (2009), Taraborrelli (2014)
G410apint76	TrGC	$CO_235C_6CO_3 + HO_2 \rightarrow CO_235C_6O_2 + OH$	KAPH02*rco3_oh	Rickard and Pascoe (2009), Taraborrelli (2014)
G410apint77	TrGC	$CO_235C_6CO_3 + NO \rightarrow CO_235C_6O_2 + NO_2$	KAPNO	Rickard and Pascoe (2009), Taraborrelli (2014)
G410apint78	TrGC	$CO_235C_6CO_3 + NO_2 \rightarrow C7PAN_3$	k_CH3CO_3_NO2	Rickard and Pascoe (2009), Taraborrelli (2014)
G410apint79	TrGC	$CO_235C_6CO_3 \rightarrow CO_235C_6O_2$	1.00E-11*R02	Rickard and Pascoe (2009), Taraborrelli (2014)
G410apint80	TrGC	$C_235C_6CO_3H + OH \rightarrow CO_235C_6CO_3$	4.75E-12	Rickard and Pascoe (2009), Taraborrelli (2014)
G410apint81	TrGC	$C_235C_6CO_3H + h\nu \rightarrow CO_235C_6O_2 + OH$	1.14*jx(ip_CH300H)+2.15*jx(ip_MGLYOX)	Rickard and Pascoe (2009), Taraborrelli (2014)

27

Table 1: Gas phase reactions (... continued)

#	labels	reaction	rate coefficient	reference
G410apint82	TrGC	$\text{CO235C6O2} + \text{HO}_2 \rightarrow \text{CO235C6OOH}$	KR02H02*0.770	Rickard and Pascoe (2009), Taraborrelli (2014)
G410apint83	TrGC	$\text{CO235C6O2} + \text{NO} \rightarrow \text{CO23C4CO3} + \text{HCHO} + \text{NO}_2$	KR02N0	Rickard and Pascoe (2009), Taraborrelli (2014)
G410apint84	TrGC	$\text{CO235C6O2} \rightarrow \text{CO23C4CO3} + \text{HCHO}$	2.00E-12*R02	Rickard and Pascoe (2009), Taraborrelli (2014)
G410apint85	TrGC	$\text{C7PAN3} + \text{OH} \rightarrow \text{CO235C5CHO} + \text{CO} + \text{NO}_2$	8.83E-13	Rickard and Pascoe (2009), Taraborrelli (2014)
G410apint86	TrGC	$\text{C7PAN3} \rightarrow \text{CO235C6CO3} + \text{NO}_2$	k_PAN_M	Rickard and Pascoe (2009), Taraborrelli (2014)
G410apint87	TrGC	$\text{CO235C6OOH} + \text{OH} \rightarrow \text{CO235C6O2}$	1.01E-11	Rickard and Pascoe (2009), Taraborrelli (2014)
G410apint88	TrGC	$\text{CO235C6OOH} + h\nu \rightarrow \text{CO23C4CO3} + \text{HCHO} + \text{OH}$	$1.14*\text{jx}(\text{ip_CH300H}) + 2.15*\text{jx}(\text{ip_MGLY0X})$	Rickard and Pascoe (2009), Taraborrelli (2014)
G410apint89	TrGC	$\text{C716O2} + \text{HO}_2 \rightarrow \text{C716OOH}$	KR02H02*0.820	Rickard and Pascoe (2009), Taraborrelli (2014)
G410apint90	TrGC	$\text{C716O2} + \text{NO} \rightarrow \text{CO13C4CHO} + \text{CH}_3\text{C}(\text{O})\text{OO} + \text{NO}_2$	KR02N0	Rickard and Pascoe (2009), Taraborrelli (2014)
G410apint91	TrGC	$\text{C716O2} \rightarrow \text{CO13C4CHO} + \text{CH}_3\text{C}(\text{O})\text{OO}$	8.80E-13*R02	Rickard and Pascoe (2009), Taraborrelli (2014)
G410apint92	TrGC	$\text{C716OOH} + \text{OH} \rightarrow \text{CO235C6CHO} + \text{OH}$	1.20E-10	Rickard and Pascoe (2009), Taraborrelli (2014)
G410apint93	TrGC	$\text{C716OOH} + h\nu \rightarrow \text{CO13C4CHO} + \text{CH}_3\text{C}(\text{O})\text{OO} + \text{OH}$	$1.14*\text{jx}(\text{ip_CH300H}) + \text{jx}(\text{ip_HOCH2CHO})$	Rickard and Pascoe (2009), Taraborrelli (2014)
G410apint94	TrGC	$\text{C511O2} \rightarrow \text{CH}_3\text{C}(\text{O})\text{OO} + \text{HCOCH2CHO}$	8.80E-13*R02	Rickard and Pascoe (2009), Taraborrelli (2014)
G410apint95	TrGC	$\text{C511O2} + \text{NO} \rightarrow \text{CH}_3\text{C}(\text{O})\text{OO} + \text{HCOCH2CHO} + \text{NO}_2$	KR02N0	Rickard and Pascoe (2009), Taraborrelli (2014)
G410apint96	TrGC	$\text{C511O2} + \text{HO}_2 \rightarrow \text{C511OOH}$	KR02H02*0.706	Rickard and Pascoe (2009), Taraborrelli (2014)
G410apint97	TrGC	$\text{C511OOH} + h\nu \rightarrow \text{CH}_3\text{C}(\text{O})\text{OO} + \text{HCOCH2CHO} + \text{OH}$	$1.14*\text{jx}(\text{ip_CH300H}) + \text{jx}(\text{ip_HOCH2CHO})$	Rickard and Pascoe (2009), Taraborrelli (2014)
G410apint98	TrGC	$\text{C511OOH} + \text{OH} \rightarrow \text{C511O2}$	7.49E-11	Rickard and Pascoe (2009), Taraborrelli (2014)

28

Table 1: Gas phase reactions (... continued)

#	labels	reaction	rate coefficient	reference
G410apint99	TrGC	$\text{HCOCH2CHO} + \text{OH} \rightarrow \text{HCOCH2CO3}$	4.29E-11	Rickard and Pascoe (2009), Taraborrelli (2014)
G410apint100	TrGC	$\text{HCOCH2CHO} + h\nu \rightarrow \text{HCOCH2O2} + \text{HO}_2 + \text{CO}$	$\text{jx}(\text{ip_HOCH2CHO})*2$	Rickard and Pascoe (2009), Taraborrelli (2014)
G410apint101	TrGC	$\text{HCOCH2CHO} + \text{NO}_3 \rightarrow \text{HCOCH2CO3} + \text{HNO}_3$	$2*\text{KN03AL*2.4}$	Rickard and Pascoe (2009), Taraborrelli (2014)
G410apint102	TrGC	$\text{C614O2} \rightarrow \text{CO23C4CHO} + \text{HCHO} + \text{HO}_2$	8.80E-13*R02	Rickard and Pascoe (2009), Taraborrelli (2014)
G410apint103	TrGC	$\text{C614O2} + \text{NO} \rightarrow \text{C614NO3}$	KR02N0*0.098	Rickard and Pascoe (2009), Taraborrelli (2014)
G410apint104	TrGC	$\text{C614O2} + \text{NO} \rightarrow \text{CO23C4CHO} + \text{HCHO} + \text{HO}_2 + \text{NO}_2$	KR02N0*0.902	Rickard and Pascoe (2009), Taraborrelli (2014)
G410apint105	TrGC	$\text{C614O2} + \text{HO}_2 \rightarrow \text{C614OOH}$	KR02H02*0.770	Rickard and Pascoe (2009), Taraborrelli (2014)
G410apint106	TrGC	$\text{C614NO3} + h\nu \rightarrow \text{CO23C4CHO} + \text{HCHO} + \text{HO}_2 + \text{NO}_2$	$2.15*\text{jx}(\text{ip_MGLY0X})$	Rickard and Pascoe (2009), Taraborrelli (2014)
G410apint107	TrGC	$\text{C614NO3} + \text{OH} \rightarrow \text{C614CO} + \text{NO}_2$	7.11E-12	Rickard and Pascoe (2009), Taraborrelli (2014)
G410apint108	TrGC	$\text{C614OOH} + h\nu \rightarrow \text{CO23C4CHO} + \text{HCHO} + \text{HO}_2 + \text{OH}$	$1.14*\text{jx}(\text{ip_CH300H}) + 2.15*\text{jx}(\text{ip_MGLY0X})$	Rickard and Pascoe (2009), Taraborrelli (2014)
G410apint109	TrGC	$\text{C614OOH} + \text{OH} \rightarrow \text{C614CO} + \text{OH}$	8.69E-11	Rickard and Pascoe (2009), Taraborrelli (2014)
G410apint110	TrGC	$\text{C614CO} + h\nu \rightarrow \text{CH3COCOCH2O2} + \text{HOCH}_2\text{CO}_3$	J_ACETOL	Rickard and Pascoe (2009), Taraborrelli (2014)
G410apint111	TrGC	$\text{C614CO} + \text{OH} \rightarrow \text{CO235C5CHO} + \text{HO}_2$	3.22E-12	Rickard and Pascoe (2009), Taraborrelli (2014)
G410apint112	TrGC	$\text{CH3COCOCH2O2} \rightarrow \text{CH}_3\text{C}(\text{O})\text{OO} + \text{HCHO} + \text{CO}$	2.00E-12*R02	Rickard and Pascoe (2009), Taraborrelli (2014)
G410apint113	TrGC	$\text{CH3COCOCH2O2} + \text{HO}_2 \rightarrow \text{CH3COCOCH2OOH}$	KR02H02*0.625	Rickard and Pascoe (2009), Taraborrelli (2014)
G410apint114	TrGC	$\text{CH3COCOCH2O2} + \text{NO} \rightarrow \text{CH}_3\text{C}(\text{O})\text{OO} + \text{HCHO} + \text{CO} + \text{NO}_2$	KR02N0	Rickard and Pascoe (2009), Taraborrelli (2014)
G410apint115	TrGC	$\text{CH3COCOCH2OOH} + \text{OH} \rightarrow \text{CH3COCOCHO} + \text{OH}$	ks*fc0*fs0oh	Rickard and Pascoe (2009), Taraborrelli (2014)

29

Table 1: Gas phase reactions (... continued)

#	labels	reaction	rate coefficient	reference
G410apint116	TrGC	$\text{CH}_3\text{COCOCCH}_2\text{OOH} + \text{OH} \rightarrow \text{CH}_3\text{COCOCCH}_2\text{O}$.6*k_CH300H_OH	Rickard and Pascoe (2009), Taraborrelli (2014)
G410apint117	TrGC	$\text{CH}_3\text{COCOCCH}_2\text{OOH} + h\nu \rightarrow \text{CH}_3\text{COCOCCHO} + \text{OH} + \text{HO}_2$	1.14*jx(ip_CH300H)	Rickard and Pascoe (2009), Taraborrelli (2014)
G410apint118	TrGC	$\text{CH}_3\text{COCOCCH}_2\text{OOH} + h\nu \rightarrow \text{CH}_3\text{C}(\text{O})\text{OO} + \text{CO} + \text{OH} + \text{HCHO}$	J_ACETOL	Rickard and Pascoe (2009), Taraborrelli (2014)
G410apint119	TrGC	$\text{CH}_3\text{COCOCCH}_2\text{OOH} + h\nu \rightarrow \text{CH}_3\text{C}(\text{O})\text{OO} + \text{HCOCO}_3$	2.15*jx(ip_MGLYOX)	Rickard and Pascoe (2009), Taraborrelli (2014)
G410apint120	TrGC	$\text{CO}_2\text{35C}_5\text{CHO} + \text{OH} \rightarrow \text{CO}_2\text{3C}_4\text{CO}_3 + \text{CO}$	1.33E-11	Rickard and Pascoe (2009), Taraborrelli (2014)
G410apint121	TrGC	$\text{CO}_2\text{35C}_5\text{CHO} + h\nu \rightarrow \text{CO}_2\text{3C}_4\text{CO}_3 + \text{CO} + \text{HO}_2$	jx(ip_MGLYOX)	Rickard and Pascoe (2009), Taraborrelli (2014)
G410apint122	TrGC	$\text{CO}_2\text{35C}_5\text{CHO} + \text{NO}_3 \rightarrow \text{CO}_2\text{3C}_4\text{CO}_3 + \text{CO} + \text{HNO}_3$	KN03AL*5.5	Rickard and Pascoe (2009), Taraborrelli (2014)
G410apint123	TrGC	$\text{CO}_2\text{3C}_4\text{CHO} + \text{OH} \rightarrow \text{CO}_2\text{3C}_4\text{CO}_3$	6.65E-11	Rickard and Pascoe (2009), Taraborrelli (2014)
G410apint124	TrGC	$\text{CO}_2\text{3C}_4\text{CHO} + h\nu \rightarrow \text{CH}_3\text{COCOCCH}_2\text{O}_2 + \text{HO}_2 + \text{CO}$	jx(ip_HOCH2CHO)	Rickard and Pascoe (2009), Taraborrelli (2014)
G410apint125	TrGC	$\text{CO}_2\text{3C}_4\text{CHO} + h\nu \rightarrow \text{CH}_3\text{C}(\text{O})\text{OO} + \text{HCOCH}_2\text{CO}_3$	2.15*jx(ip_MGLYOX)	Rickard and Pascoe (2009), Taraborrelli (2014)
G410apint126	TrGC	$\text{CO}_2\text{3C}_4\text{CHO} + \text{NO}_3 \rightarrow \text{CO}_2\text{3C}_4\text{CO}_3 + \text{HNO}_3$	KN03AL*5.5	Rickard and Pascoe (2009), Taraborrelli (2014)
G410apint127	TrGC	$\text{CO}_2\text{3C}_4\text{CO}_3 \rightarrow \text{CH}_3\text{COCOCCH}_2\text{O}_2$	1.00E-11*R02	Rickard and Pascoe (2009), Taraborrelli (2014)
G410apint128	TrGC	$\text{CO}_2\text{3C}_4\text{CO}_3 + \text{NO} \rightarrow \text{CH}_3\text{COCOCCH}_2\text{O}_2 + \text{NO}_2$	KAPNO	Rickard and Pascoe (2009), Taraborrelli (2014)
G410apint129	TrGC	$\text{CO}_2\text{3C}_4\text{CO}_3 + \text{NO}_2 \rightarrow \text{C}_5\text{PAN}_9$	k_CH3C03_NO2	Rickard and Pascoe (2009), Taraborrelli (2014)
G410apint130	TrGC	$\text{CO}_2\text{3C}_4\text{CO}_3 + \text{HO}_2 \rightarrow \text{CO}_2\text{3C}_4\text{CO}_3\text{H}$	KAPH02*(rco3_ooH+rco3_o3)	Rickard and Pascoe (2009), Taraborrelli (2014)
G410apint131	TrGC	$\text{CO}_2\text{3C}_4\text{CO}_3 + \text{HO}_2 \rightarrow \text{CH}_3\text{COCOCCH}_2\text{O}_2 + \text{OH}$	KAPH02*rco3_oh	Rickard and Pascoe (2009), Taraborrelli (2014)
G410apint132	TrGC	$\text{CO}_2\text{3C}_4\text{CO}_3\text{H} + h\nu \rightarrow \text{CH}_3\text{COCOCCH}_2\text{O}_2 + \text{OH}$	1.14*jx(ip_CH300H)+jx(ip_HOCH2CHO)	Rickard and Pascoe (2009), Taraborrelli (2014)

30

Table 1: Gas phase reactions (... continued)

#	labels	reaction	rate coefficient	reference
G410apint133	TrGC	$\text{CO}_2\text{3C}_4\text{CO}_3\text{H} + h\nu \rightarrow \text{CO}_2\text{3C}_4\text{CO}_3$	4.23E-12	Rickard and Pascoe (2009), Taraborrelli (2014)
G410apint134	TrGC	$\text{C}_5\text{PAN}_9 \rightarrow \text{CO}_2\text{3C}_4\text{CO}_3 + \text{NO}_2$	k_PAN_M	Rickard and Pascoe (2009), Taraborrelli (2014)
G410apint135	TrGC	$\text{C}_5\text{PAN}_9 + \text{OH} \rightarrow \text{CO}_2\text{3C}_3\text{CHO} + \text{CO} + \text{NO}_2$	3.12E-13	Rickard and Pascoe (2009), Taraborrelli (2014)
G410apint136	TrGC	$\text{HCOCH}_2\text{CO}_3 \rightarrow 0.7 \text{HCOCH}_2\text{O}_2 + 0.3 \text{HCOCH}_2\text{CO}_2\text{H}$	1.00E-11*R02	Rickard and Pascoe (2009), Taraborrelli (2014)
G410apint137	TrGC	$\text{HCOCH}_2\text{CO}_3 + \text{NO} \rightarrow \text{HCOCH}_2\text{O}_2 + \text{NO}_2$	KAPNO	Rickard and Pascoe (2009), Taraborrelli (2014)
G410apint138	TrGC	$\text{HCOCH}_2\text{CO}_3 + \text{NO}_2 \rightarrow \text{C}_3\text{PAN}_2$	k_CH3C03_NO2	Rickard and Pascoe (2009), Taraborrelli (2014)
G410apint139	TrGC	$\text{HCOCH}_2\text{CO}_3 + \text{HO}_2 \rightarrow \text{HCOCH}_2\text{CO}_3\text{H}$	KAPH02*rco3_ooH	Rickard and Pascoe (2009), Taraborrelli (2014)
G410apint140	TrGC	$\text{HCOCH}_2\text{CO}_3 + \text{HO}_2 \rightarrow \text{HCOCH}_2\text{CO}_2\text{H} + \text{O}_3$	KAPH02*rco3_o3	Rickard and Pascoe (2009), Taraborrelli (2014)
G410apint141	TrGC	$\text{HCOCH}_2\text{CO}_3 + \text{HO}_2 \rightarrow \text{HCOCH}_2\text{O}_2 + \text{CO}_2 + \text{OH}$	KAPH02*rco3_oh	Rickard and Pascoe (2009), Taraborrelli (2014)
G410apint142	TrGC	$\text{C}_3\text{PAN}_2 \rightarrow \text{HCOCH}_2\text{CO}_3 + \text{NO}_2$	k_PAN_M	Rickard and Pascoe (2009), Taraborrelli (2014)
G410apint143	TrGC	$\text{C}_3\text{PAN}_2 + \text{OH} \rightarrow \text{GLYOX} + \text{CO} + \text{NO}_2$	2.10E-11	Rickard and Pascoe (2009), Taraborrelli (2014)
G410apint144	TrGC	$\text{HCOCH}_2\text{CO}_2\text{H} + \text{OH} \rightarrow \text{HCOCH}_2\text{O}_2$	2.14E-11	Rickard and Pascoe (2009), Taraborrelli (2014)
G410apint145	TrGC	$\text{HCOCH}_2\text{CO}_2\text{H} + h\nu \rightarrow \text{HCOCH}_2\text{O}_2 + \text{HO}_2$	jx(ip_HOCH2CHO)	Rickard and Pascoe (2009), Taraborrelli (2014)
G410apint146	TrGC	$\text{APINENE} + \text{O}_3 \rightarrow \text{APINBOO}$	1.01E-15*EXP(-732/TEMP)*.50*.18	Capouet et al. (2008)
G410apint147	TrGC	$\text{APINENE} + \text{O}_3 \rightarrow \text{PINONIC}$	1.01E-15*EXP(-732/TEMP)*.50*.16	Capouet et al. (2008)
G410apint148	TrGC	$\text{APINENE} + \text{O}_3 \rightarrow \text{OH} + \text{NORPINAL} + \text{CO} + \text{HO}_2$	1.01E-15*EXP(-732/TEMP)*.50*.66	Capouet et al. (2008)
G410apint149	TrGC	$\text{APINENE} + \text{O}_3 \rightarrow \text{APINA00}$	1.01E-15*EXP(-732/TEMP)*.50*.12	Capouet et al. (2008)
G410apint150	TrGC	$\text{APINENE} + \text{O}_3 \rightarrow \text{OH} + \text{C109O}_2$	1.01E-15*EXP(-732/TEMP)*.50*(.22+.66)	Capouet et al. (2008)*
G410apint151	TrGC	$\text{APINA00} \rightarrow \text{PINAL} + \text{H}_2\text{O}_2$	1.00E-17*c(ind_H2O)	Rickard and Pascoe (2009), Taraborrelli (2014)
G410apint152	TrGC	$\text{APINA00} + \text{CO} \rightarrow \text{PINAL}$	1.20E-15	Rickard and Pascoe (2009), Taraborrelli (2014)

31

Table 1: Gas phase reactions (... continued)

#	labels	reaction	rate coefficient	reference
G410apint153	TrGC	APINAOO + NO → PINAL + NO ₂	1.00E-14	Rickard and Pascoe (2009), Taraborrelli (2014)
G410apint154	TrGC	APINAOO + NO ₂ → PINAL + NO ₃	1.00E-15	Rickard and Pascoe (2009), Taraborrelli (2014)
G410apint155	TrGC	APINAOO + SO ₂ → PINAL + H ₂ SO ₄	7.00E-14	Rickard and Pascoe (2009), Taraborrelli (2014)
G410apint156	TrGC	APINBOO → PINONIC	1.00E-17*c(ind_H2O)*(0.08+0.15)	Rickard and Pascoe (2009), Taraborrelli (2014)
G410apint157	TrGC	APINBOO → PINAL + H ₂ O ₂	1.00E-17*c(ind_H2O)*0.77	Rickard and Pascoe (2009), Taraborrelli (2014)
G410apint158	TrGC	APINBOO + CO → PINAL	1.20E-15	Rickard and Pascoe (2009), Taraborrelli (2014)
G410apint159	TrGC	APINBOO + NO → PINAL + NO ₂	1.00E-14	Rickard and Pascoe (2009), Taraborrelli (2014)
G410apint160	TrGC	APINBOO + NO ₂ → PINAL + NO ₃	1.00E-15	Rickard and Pascoe (2009), Taraborrelli (2014)
G410apint161	TrGC	APINBOO + SO ₂ → PINAL + H ₂ SO ₄	7.00E-14	Rickard and Pascoe (2009), Taraborrelli (2014)
G410apint162	TrGC	C109O2 → C89CO3 + HCHO	2.00E-12*R02	Rickard and Pascoe (2009), Taraborrelli (2014)*
G410apint163	TrGC	C109O2 + NO → C89CO3 + HCHO + NO ₂	KR02N0	Rickard and Pascoe (2009), Taraborrelli (2014)
G410apint164	TrGC	C109O2 + HO ₂ → C109OOH	KR02H02*0.914	Rickard and Pascoe (2009), Taraborrelli (2014)
G410apint165	TrGC	C109OOH → C89CO3 + HCHO + OH	1.14*jx(ip_CH300H)+jx(ip_HOCH2CHO)	Rickard and Pascoe (2009), Taraborrelli (2014)
G410apint166	TrGC	C109OOH + OH → C109CO + OH	5.47E-11	Rickard and Pascoe (2009), Taraborrelli (2014)
G410apint167	TrGC	C109OOH + hν → C89CO3 + HCHO + OH	J_ACETOL	Rickard and Pascoe (2009), Taraborrelli (2014)
G410apint168	TrGC	C109CO + OH → C89CO3 + CO	5.47E-11	Rickard and Pascoe (2009), Taraborrelli (2014)
G410apint169	TrGC	C109CO + hν → C89CO3 + CO + HO ₂	jx(ip_MGLYOX)+jx(ip_HOCH2CHO)	Rickard and Pascoe (2009), Taraborrelli (2014)

32

Table 1: Gas phase reactions (... continued)

#	labels	reaction	rate coefficient	reference
G410apint170	TrGC	C89CO3 → .56 C811CO3 + .14 C89O2 + 0.3 C89CO2H	1.00E-11*R02	Rickard and Pascoe (2009), Taraborrelli (2014)
G410apint171	TrGC	C89CO3 + HO ₂ → C89CO3H	KAPH02*rco3_ooH	Rickard and Pascoe (2009), Taraborrelli (2014)
G410apint172	TrGC	C89CO3 + HO ₂ → C89CO2H + O ₃	KAPH02*rco3_o3	Rickard and Pascoe (2009), Taraborrelli (2014)
G410apint173	TrGC	C89CO3 + HO ₂ → .80 C811CO3 + 0.20 C89O2 + OH	KAPH02*rco3_oh	Rickard and Pascoe (2009), Taraborrelli (2014)
G410apint174	TrGC	C89CO3 + NO ₂ → C89PAN	k_CH3CO3_NO2	Rickard and Pascoe (2009), Taraborrelli (2014)
G410apint175	TrGC	C89CO3 + NO → 0.80 C811CO3 + 0.20 C89O2 + NO ₂	KAPNO	Rickard and Pascoe (2009), Taraborrelli (2014)
G410apint176	TrGC	C89CO2H + OH → 0.80 C811CO3 + 0.20 C89O2	2.69E-11	Rickard and Pascoe (2009), Taraborrelli (2014)
G410apint177	TrGC	C89CO2H + hν → 0.80 C811CO3 + 0.20 C89O2 + HO ₂	jx(ip_HOCH2CHO)	Rickard and Pascoe (2009), Taraborrelli (2014)
G410apint178	TrGC	C89CO3H → 0.80 C811CO3 + 0.20 C89O2 + OH	1.14*jx(ip_CH300H)+jx(ip_HOCH2CHO)	Rickard and Pascoe (2009), Taraborrelli (2014)
G410apint179	TrGC	C89CO3H + OH → C89CO3	3.00E-11	Rickard and Pascoe (2009), Taraborrelli (2014)
G410apint180	TrGC	C89PAN → C89CO3 + NO ₂	k_PAN_M	Rickard and Pascoe (2009), Taraborrelli (2014)
G410apint181	TrGC	C89PAN + OH → CH ₃ COCH ₃ + CO13C4CHO + CO + NO ₂	2.52E-11	Rickard and Pascoe (2009), Taraborrelli (2014)
G410apint182	TrGC	C811CO3 → 0.7 C811O2 + 0.3 PINIC	1.00E-11*R02	Rickard and Pascoe (2009), Taraborrelli (2014)
G410apint183	TrGC	C811CO3 + HO ₂ → C811CO3H	KAPH02*rco3_ooH	Rickard and Pascoe (2009), Taraborrelli (2014)
G410apint184	TrGC	C811CO3 + HO ₂ → PINIC + O ₃	KAPH02*rco3_o3	Rickard and Pascoe (2009), Taraborrelli (2014)
G410apint185	TrGC	C811CO3 + HO ₂ → C811O2 + OH	KAPH02*rco3_oh	Rickard and Pascoe (2009), Taraborrelli (2014)
G410apint186	TrGC	C811CO3 + NO → C811O2 + NO ₂	KAPNO	Rickard and Pascoe (2009), Taraborrelli (2014)

33

Table 1: Gas phase reactions (... continued)

#	labels	reaction	rate coefficient	reference
G410apint187	TrGC	$C811CO3 + NO_2 \rightarrow C811PAN$	k_{CH3CO3_NO2}	Rickard and Pascoe (2009), Taraborrelli (2014)
G410apint188	TrGC	$PINIC + OH \rightarrow C811O2$	$7.29E-12$	Rickard and Pascoe (2009), Taraborrelli (2014)
G410ap188bf1	TrGC	$C89O2 + HO_2 \rightarrow C89OOH$	$KR02HO2*0.859$	Rickard and Pascoe (2009), Taraborrelli (2014)
G410ap188bf2	TrGC	$C89O2 + NO \rightarrow C89NO3$	$KR02NO*0.104$	Rickard and Pascoe (2009), Taraborrelli (2014)
G410ap188bf3	TrGNC	$C89O2 + NO \rightarrow C810O2 + NO_2$	$KR02NO*0.896$	Rickard and Pascoe (2009), Taraborrelli (2014)
G410ap188bf4	TrGNC	$C89O2 + NO_3 \rightarrow C810O2 + NO_2$	$KR02NO3$	Rickard and Pascoe (2009), Taraborrelli (2014)
G410ap188bf5	TrGC	$C89O2 \rightarrow C810O2$	$6.70E-15*R02$	Rickard and Pascoe (2009), Taraborrelli (2014)
G410ap188bf6	TrGC	$C89OOH + OH \rightarrow C89O2$	$3.61E-11$	Rickard and Pascoe (2009), Taraborrelli (2014)
G410ap188bf7	TrGJC	$C89OOH + h\nu \rightarrow C810O2 + OH$	$1.14*jx(ip_CH300H)+jx(ip_HOCH2CHO)$	Rickard and Pascoe (2009), Taraborrelli (2014)
G410ap188bf8	TrGC	$C89NO3 + OH \rightarrow CH_3COCH_3 + CO13C4CHO + NO_2$	$2.56E-11$	Rickard and Pascoe (2009), Taraborrelli (2014)
G410ap188bf9	TrGJNC	$C89NO3 + h\nu \rightarrow C810O2 + NO_2$	$J_IC3H7N03+jx(ip_HOCH2CHO)$	Rickard and Pascoe (2009), Taraborrelli (2014)
G410ap188bf10	TrGC	$C810O2 + HO_2 \rightarrow C810OOH$	$KR02HO2*0.914$	Rickard and Pascoe (2009), Taraborrelli (2014)
G410ap188bf11	TrGNC	$C810O2 + NO \rightarrow C810NO3$	$KR02NO*0.104$	Rickard and Pascoe (2009), Taraborrelli (2014)
G410ap188bf12	TrGNC	$C810O2 + NO \rightarrow CH_3COCH_3 + C514O2 + NO_2$	$KR02NO*0.896$	Rickard and Pascoe (2009), Taraborrelli (2014)
G410ap188bf13	TrGNC	$C810O2 + NO_3 \rightarrow CH_3COCH_3 + C514O2 + NO_2$	$KR02NO3$	Rickard and Pascoe (2009), Taraborrelli (2014)
G410ap188bf14	TrGC	$C810O2 \rightarrow CH_3COCH_3 + C514O2$	$6.70E-15*R02$	Rickard and Pascoe (2009), Taraborrelli (2014)
G410ap188bf15	TrGC	$C810OOH + OH \rightarrow C810O2$	$8.35E-11$	Rickard and Pascoe (2009), Taraborrelli (2014)

34

Table 1: Gas phase reactions (... continued)

#	labels	reaction	rate coefficient	reference
G410ap188bf16	TrGJC	$C810OOH + h\nu \rightarrow CH_3COCH_3 + C514O2 + OH$	$1.14*jx(ip_CH300H)+jx(ip_HOCH2CHO)$	Rickard and Pascoe (2009), Taraborrelli (2014)
G410ap188bf17	TrGNC	$C810NO3 + OH \rightarrow CH_3COCH_3 + CO13C4CHO + NO_2$	$4.96E-11$	Rickard and Pascoe (2009), Taraborrelli (2014)
G410ap188bf18	TrGJC	$C810NO3 + h\nu \rightarrow CH_3COCH_3 + C514O2 + NO_2$	$2.84*J_IC3H7N03+jx(ip_HOCH2CHO)$	Rickard and Pascoe (2009), Taraborrelli (2014)
G410ap188bf19	TrGC	$C514O2 + HO_2 \rightarrow C514OOH$	$KR02HO2*0.706$	Rickard and Pascoe (2009), Taraborrelli (2014)
G410ap188bf20	TrGNC	$C514O2 + NO \rightarrow C514NO3$	$KR02NO*0.129$	Rickard and Pascoe (2009), Taraborrelli (2014)
G410ap188bf21	TrGNC	$C514O2 + NO \rightarrow CO13C4CHO + HO_2 + NO_2$	$KR02NO*0.871$	Rickard and Pascoe (2009), Taraborrelli (2014)
G410ap188bf22	TrGNC	$C514O2 + NO_3 \rightarrow CO13C4CHO + HO_2 + NO_2$	$KR02NO3$	Rickard and Pascoe (2009), Taraborrelli (2014)
G410ap188bf23	TrGC	$C514O2 \rightarrow CO13C4CHO + HO_2$	$2.50E-13*R02$	Rickard and Pascoe (2009), Taraborrelli (2014)
G410ap188bf24	TrGC	$C514OOH + OH \rightarrow CO13C4CHO + OH$	$1.10E-10$	Rickard and Pascoe (2009), Taraborrelli (2014)
G410ap188bf25	TrGJC	$C514OOH + h\nu \rightarrow CO13C4CHO + HO_2 + OH$	$1.14*jx(ip_CH300H)+jx(ip_HOCH2CHO)$	Rickard and Pascoe (2009), Taraborrelli (2014)
G410ap188bf26	TrGC	$C514NO3 + OH \rightarrow CO13C4CHO + NO_2$	$4.33E-11$	Rickard and Pascoe (2009), Taraborrelli (2014)
G410ap188bf27	TrGJC	$C514NO3 + h\nu \rightarrow CO13C4CHO + HO_2 + NO_2$	$J_IC3H7N03+jx(ip_HOCH2CHO)*2.0$	Rickard and Pascoe (2009), Taraborrelli (2014)
G410apint189	TrGC	$C811O2 \rightarrow C812O2$	$1.30E-12*R02$	Rickard and Pascoe (2009), Taraborrelli (2014)
G410apint190	TrGC	$C811O2 + HO_2 \rightarrow C811OOH$	$KR02HO2*0.859$	Rickard and Pascoe (2009), Taraborrelli (2014)
G410apint191	TrGC	$C811O2 + NO \rightarrow C812O2 + NO_2$	$KR02NO$	Rickard and Pascoe (2009), Taraborrelli (2014)*
G410apint192	TrGC	$C811CO3H + h\nu \rightarrow C811O2 + OH$	$1.14*jx(ip_CH300H)$	Rickard and Pascoe (2009), Taraborrelli (2014)
G410apint193	TrGC	$C811CO3H + OH \rightarrow C811CO3$	$1.04E-11$	Rickard and Pascoe (2009), Taraborrelli (2014)

35

Table 1: Gas phase reactions (... continued)

#	labels	reaction	rate coefficient	reference
G410apint194	TrGC	$C811PAN \rightarrow C811CO3 + NO_2$	k_PAN_M	Rickard and Pascoe (2009), Taraborrelli (2014)
G410apint195	TrGC	$C811PAN + OH \rightarrow C721CHO + CO + NO_2$	6.77E-12	Rickard and Pascoe (2009), Taraborrelli (2014)
G410apint196	TrGC	$C812O2 \rightarrow C813O2$	9.20E-14*R02	Rickard and Pascoe (2009), Taraborrelli (2014)*
G410apint197	TrGC	$C812O2 + NO \rightarrow C813O2 + NO_2$	KR02N0	Rickard and Pascoe (2009), Taraborrelli (2014)
G410apint198	TrGC	$C812O2 + HO_2 \rightarrow C812OOH$	KR02H02*0.859	Rickard and Pascoe (2009), Taraborrelli (2014)
G410apint199	TrGC	$C812OOH + h\nu \rightarrow C813O2 + OH$	1.14*jx(ip_CH300H)	Rickard and Pascoe (2009), Taraborrelli (2014)
G410apint200	TrGC	$C812OOH + OH \rightarrow C812O2$	1.09E-11	Rickard and Pascoe (2009), Taraborrelli (2014)
G410apint201	TrGC	$C813O2 \rightarrow CH_3COCH_3 + C512O2$	6.70E-15*R02	Rickard and Pascoe (2009), Taraborrelli (2014)*
G410apint202	TrGC	$C813O2 + NO \rightarrow CH_3COCH_3 + C512O2 + NO_2$	KR02N0	Rickard and Pascoe (2009), Taraborrelli (2014)*
G410apint203	TrGC	$C813O2 + HO_2 \rightarrow C813OOH$	KR02H02*0.859	Rickard and Pascoe (2009), Taraborrelli (2014)
G410apint204	TrGC	$C813OOH + h\nu \rightarrow CH_3COCH_3 + C512O2 + OH$	1.14*jx(ip_CH300H)+jx(ip_MGLYOX)	Rickard and Pascoe (2009), Taraborrelli (2014)
G410apint205	TrGC	$C813OOH + OH \rightarrow C813O2$	1.86E-11	Rickard and Pascoe (2009), Taraborrelli (2014)
G410apint206	TrGC	$C721CHO + NO_3 \rightarrow C721CO3 + HNO_3$	KN03AL*8.5	Rickard and Pascoe (2009), Taraborrelli (2014)
G410apint207	TrGC	$C721CHO + OH \rightarrow C721CO3$	2.63E-11	Rickard and Pascoe (2009), Taraborrelli (2014)
G410apint208	TrGC	$C721CHO \rightarrow C721O2 + CO + HO_2$	jx(ip_H0CH2CHO)	Rickard and Pascoe (2009), Taraborrelli (2014)
G410apint209	TrGC	$C721CO3 + HO_2 \rightarrow C721CO3H$	KAPH02*rco3_ooh	Rickard and Pascoe (2009), Taraborrelli (2014)
G410apint210	TrGC	$C721CO3 + HO_2 \rightarrow C721O2 + OH$	KAPH02*rco3_oh	Rickard and Pascoe (2009), Taraborrelli (2014)

36

Table 1: Gas phase reactions (... continued)

#	labels	reaction	rate coefficient	reference
G410apint211	TrGC	$C721CO3 + HO_2 \rightarrow NORPINIC + O_3$	KAPH02*rco3_o3	Rickard and Pascoe (2009), Taraborrelli (2014)
G410apint212	TrGC	$C721CO3 + NO \rightarrow C721O2 + NO_2$	KAPNO	Rickard and Pascoe (2009), Taraborrelli (2014)
G410apint213	TrGC	$C721CO3 + NO_2 \rightarrow C721PAN$	k_CH3CO3_NO2	Rickard and Pascoe (2009), Taraborrelli (2014)
G410apint214	TrGC	$C721CO3 + NO_3 \rightarrow C721O2 + NO_2$	KR02N03*1.74	Rickard and Pascoe (2009), Taraborrelli (2014)
G410apint215	TrGC	$C721CO3 \rightarrow C721O2$	1.00E-11*R02*0.7	Rickard and Pascoe (2009), Taraborrelli (2014)
G410apint216	TrGC	$C721CO3 \rightarrow NORPINIC$	1.00E-11*R02*0.3	Rickard and Pascoe (2009), Taraborrelli (2014)
G410apint217	TrGC	$C721O2 + HO_2 \rightarrow C721OOH$	KR02H02*0.820	Rickard and Pascoe (2009), Taraborrelli (2014)
G410apint218	TrGC	$C721O2 + NO \rightarrow C722O2 + NO_2$	KR02N0	Rickard and Pascoe (2009), Taraborrelli (2014)
G410apint219	TrGC	$C721O2 \rightarrow C722O2$	1.30E-12*R02	Rickard and Pascoe (2009), Taraborrelli (2014)
G410apint220	TrGC	$C721CO3H + OH \rightarrow C721CO3$	9.65E-12	Rickard and Pascoe (2009), Taraborrelli (2014)
G410apint221	TrGC	$C721CO3H + h\nu \rightarrow C721O2 + OH$	1.14*jx(ip_CH300H)	Rickard and Pascoe (2009), Taraborrelli (2014)
G410apint222	TrGC	$NORPINIC + OH \rightarrow C721O2$	6.57E-12	Rickard and Pascoe (2009), Taraborrelli (2014)
G410apint223	TrGC	$C721PAN + OH \rightarrow C721OOH + CO + NO_2$	2.96E-12	Rickard and Pascoe (2009), Taraborrelli (2014)
G410apint224	TrGC	$C721PAN \rightarrow C721CO3 + NO_2$	k_PAN_M	Rickard and Pascoe (2009), Taraborrelli (2014)
G410apint225	TrGC	$C721OOH + OH \rightarrow C721O2$	1.27E-11	Rickard and Pascoe (2009), Taraborrelli (2014)
G410apint226	TrGC	$C721OOH + h\nu \rightarrow C722O2 + OH$	1.14*jx(ip_CH300H)	Rickard and Pascoe (2009), Taraborrelli (2014)
G410apint227	TrGC	$C722O2 + HO_2 \rightarrow C722OOH$	KR02H02*0.820	Rickard and Pascoe (2009), Taraborrelli (2014)

37

Table 1: Gas phase reactions (... continued)

#	labels	reaction	rate coefficient	reference
G410apint228	TrGC	$C722O2 + NO \rightarrow CH_3COCH_3 + C44O2 + NO_2$	KR02N0	Rickard and Pascoe (2009), Taraborrelli (2014)
G410apint229	TrGC	$C722O2 \rightarrow CH_3COCH_3 + C44O2$	6.70E-15*R02	Rickard and Pascoe (2009), Taraborrelli (2014)
G410apint230	TrGC	$C722OOH + OH \rightarrow C722O2$	3.31E-11	Rickard and Pascoe (2009), Taraborrelli (2014)
G410apint231	TrGC	$C722OOH + h\nu \rightarrow CH_3COCH_3 + C44O2 + OH$	1.14*jx(ip_CH300H)	Rickard and Pascoe (2009), Taraborrelli (2014)
G410apint232	TrGC	$C44O2 + HO_2 \rightarrow C44OOH$	KR02H02*0.625	Rickard and Pascoe (2009), Taraborrelli (2014)
G410apint233	TrGC	$C44O2 + NO \rightarrow HCOCH_2CHO + HO_2 + NO_2$	KR02N0	Rickard and Pascoe (2009), Taraborrelli (2014)
G410apint234	TrGC	$C44O2 \rightarrow HCOCH_2CHO + HO_2$	8.80E-13*R02	Rickard and Pascoe (2009), Taraborrelli (2014)
G410apint235	TrGC	$C44OOH + OH \rightarrow C44O2$	7.46E-11	Rickard and Pascoe (2009), Taraborrelli (2014)
G410apint236	TrGC	$C44OOH + h\nu \rightarrow HCOCH_2CHO + HO_2 + OH$	1.14*jx(ip_CH300H)	Rickard and Pascoe (2009), Taraborrelli (2014)
G410apint237	TrGC	$C512O2 \rightarrow C513O2$	1.30E-12*R02	Rickard and Pascoe (2009), Taraborrelli (2014)*
G410apint238	TrGC	$C512O2 + HO_2 \rightarrow C512OOH$	KR02H02*0.706	Rickard and Pascoe (2009), Taraborrelli (2014)
G410apint239	TrGC	$C512O2 + NO \rightarrow C513O2 + NO_2$	KR02N0	Rickard and Pascoe (2009), Taraborrelli (2014)*
G410apint240	TrGC	$C512OOH + h\nu \rightarrow C513O2 + OH$	1.14*jx(ip_CH300H)+jx(ip_HOCH2CHO)	Rickard and Pascoe (2009), Taraborrelli (2014)
G410apint241	TrGC	$C512OOH + OH \rightarrow CO13C4CHO + OH$	1.01E-10	Rickard and Pascoe (2009), Taraborrelli (2014)
G410apint242	TrGC	$C513O2 \rightarrow GLYOX + HOC2H4CO3$	8.80E-13*R02	Rickard and Pascoe (2009), Taraborrelli (2014)*
G410apint243	TrGC	$C513O2 + NO \rightarrow GLYOX + HOC2H4CO3 + NO_2$	KR02N0	Rickard and Pascoe (2009), Taraborrelli (2014)
G410apint244	TrGC	$C513O2 + HO_2 \rightarrow C513OOH$	KR02H02*0.706	Rickard and Pascoe (2009), Taraborrelli (2014)

38

Table 1: Gas phase reactions (... continued)

#	labels	reaction	rate coefficient	reference
G410apint245	TrGC	$CO13C4CHO + OH \rightarrow CHOC3COCO3$	1.33E-10	Rickard and Pascoe (2009), Taraborrelli (2014)
G410apint246	TrGC	$CO13C4CHO + h\nu \rightarrow CHOC3COO2 + CO + HO_2$	jx(ip_HOCH2CHO)*2	Rickard and Pascoe (2009), Taraborrelli (2014)
G410apint247	TrGC	$CO13C4CHO + NO_3 \rightarrow CHOC3COCO3 + HNO_3$	2*KNG3AL*5.5	Rickard and Pascoe (2009), Taraborrelli (2014)
G410apint248	TrGC	$C513OOH + h\nu \rightarrow GLYOX + HOC2H4CO3 + OH$	1.14*jx(ip_CH300H)+jx(ip_HOCH2CHO)	Rickard and Pascoe (2009), Taraborrelli (2014)
G410apint249	TrGC	$C513OOH + OH \rightarrow C513CO + OH$	9.23E-11	Rickard and Pascoe (2009), Taraborrelli (2014)
G410apint250	TrGC	$CHOC3COCO3 \rightarrow CHOC3COO2$	1.00E-11*R02	Rickard and Pascoe (2009), Taraborrelli (2014)
G410apint251	TrGC	$CHOC3COCO3 + HO_2 \rightarrow CHOC3COOOH$	KAPH02	Rickard and Pascoe (2009), Taraborrelli (2014)
G410apint252	TrGC	$CHOC3COCO3 + NO_2 \rightarrow CHOC3COPAN$	k_CH3C03_NO2	Rickard and Pascoe (2009), Taraborrelli (2014)
G410apint253	TrGC	$CHOC3COCO3 + NO \rightarrow CHOC3COO2 + NO_2$	KAPN0	Rickard and Pascoe (2009), Taraborrelli (2014)
G410apint254	TrGC	$CHOC3COO2 \rightarrow HCOCH_2CO_3 + HCHO$	2.00E-12*R02	Rickard and Pascoe (2009), Taraborrelli (2014)
G410apint255	TrGC	$CHOC3COO2 + HO_2 \rightarrow C413COOOH$	KR02H02*0.625	Rickard and Pascoe (2009), Taraborrelli (2014)
G410apint256	TrGC	$CHOC3COO2 + NO \rightarrow HCOCH_2CO_3 + HCHO + NO_2$	KR02N0	Rickard and Pascoe (2009), Taraborrelli (2014)
G410apint257	TrGC	$C513CO + OH \rightarrow HOC2H4CO_3 + CO + CO$	2.64E-11	Rickard and Pascoe (2009), Taraborrelli (2014)
G410apint258	TrGC	$C513CO + h\nu \rightarrow HOC2H4CO_3 + HO_2 + CO + CO$	jx(ip_MGLYOX)+2.15*jx(ip_MGLYOX)	Rickard and Pascoe (2009), Taraborrelli (2014)
G410apint259	TrGC	$C413COOOH + OH \rightarrow CHOC3COO2$	8.33E-11	Rickard and Pascoe (2009), Taraborrelli (2014)
G410apint260	TrGC	$C413COOOH + h\nu \rightarrow HCOCH_2CO_3 + HCHO + OH$	1.14*jx(ip_CH300H)+jx(ip_HOCH2CHO)+J_ACETOL	Rickard and Pascoe (2009), Taraborrelli (2014)
G410apint261	TrGC	$CHOC3COOOH + OH \rightarrow CHOC3COCO3$	7.55E-11	Rickard and Pascoe (2009), Taraborrelli (2014)

39

Table 1: Gas phase reactions (... continued)

#	labels	reaction	rate coefficient	reference
G410apint262	TrGC	$\text{CHOC3COOOH} + h\nu \rightarrow \text{CHOC3COO2} + \text{OH}$	$1.14 * \text{jx}(\text{ip_CH300H}) + \text{jx}(\text{ip_HOCH2CHO}) + \text{J_ACETOL}$	Rickard and Pascoe (2009), Taraborrelli (2014)
G410apint263	TrGC	$\text{CHOC3COPAN} \rightarrow \text{CHOC3COCO3} + \text{NO}_2$	$k_{\text{PAN_M}}$	Rickard and Pascoe (2009), Taraborrelli (2014)
G410apint264	TrGC	$\text{CHOC3COPAN} + \text{OH} \rightarrow \text{C4CODIAL} + \text{CO} + \text{NO}_2$	7.19E-11	Rickard and Pascoe (2009), Taraborrelli (2014)
G410apint265	TrGC	$\text{C4CODIAL} + \text{OH} \rightarrow \text{C312COCO3}$	3.39E-11	Rickard and Pascoe (2009), Taraborrelli (2014)
G410apint266	TrGC	$\text{C4CODIAL} + h\nu \rightarrow \text{HCOCOCH2O2} + \text{HO}_2 + \text{CO}$	$\text{jx}(\text{ip_HOCH2CHO})$	Rickard and Pascoe (2009), Taraborrelli (2014)
G410apint267	TrGC	$\text{C4CODIAL} + h\nu \rightarrow \text{HCOCH2CO3} + \text{HO}_2 + \text{CO}$	$\text{jx}(\text{ip_MGLYOX})$	Rickard and Pascoe (2009), Taraborrelli (2014)
G410apint268	TrGC	$\text{C4CODIAL} + \text{NO}_3 \rightarrow \text{C312COCO3} + \text{HNO}_3$	$2 * \text{RN03AL} * 4.0$	Rickard and Pascoe (2009), Taraborrelli (2014)
G410apint269	TrGC	$\text{C312COCO3} \rightarrow \text{HCOCOCH2O2}$	$1.00\text{E-}11 * \text{R02}$	Rickard and Pascoe (2009), Taraborrelli (2014)
G410apint270	TrGC	$\text{C312COCO3} + \text{HO}_2 \rightarrow \text{C312COCO3H}$	$\text{KAPH02} * \text{rco3_ooh}$	Rickard and Pascoe (2009), Taraborrelli (2014)
G410apint271	TrGC	$\text{C312COCO3} + \text{HO}_2 \rightarrow \text{HCOCOCH2O2} + \text{OH}$	$\text{KAPH02} * (1 - \text{rco3_ooh})$	Rickard and Pascoe (2009), Taraborrelli (2014)
G410apint272	TrGC	$\text{C312COCO3} + \text{NO}_2 \rightarrow \text{C312COPAN}$	$k_{\text{CH3CO3_NO2}}$	Rickard and Pascoe (2009), Taraborrelli (2014)
G410apint273	TrGC	$\text{C312COCO3} + \text{NO} \rightarrow \text{HCOCOCH2O2} + \text{NO}_2$	KAPNO	Rickard and Pascoe (2009), Taraborrelli (2014)
G410apint274	TrGC	$\text{C312COCO3H} + \text{OH} \rightarrow \text{C312COCO3}$	1.63E-11	Rickard and Pascoe (2009), Taraborrelli (2014)
G410apint275	TrGC	$\text{C312COCO3H} + h\nu \rightarrow \text{HCOCOCH2O2} + \text{OH}$	$1.14 * \text{jx}(\text{ip_CH300H}) + \text{jx}(\text{ip_MGLYOX})$	Rickard and Pascoe (2009), Taraborrelli (2014)
G410apint276	TrGC	$\text{C312COPAN} \rightarrow \text{C312COCO3} + \text{NO}_2$	$k_{\text{PAN_M}}$	Rickard and Pascoe (2009), Taraborrelli (2014)
G410apint277	TrGC	$\text{C312COPAN} + \text{OH} \rightarrow \text{HCOCOCHO} + \text{CO} + \text{NO}_2$	1.27E-11	Rickard and Pascoe (2009), Taraborrelli (2014)*
G410apint278	TrGC	$\text{HOC2H4CO3} \rightarrow 0.7 \text{HOCH}_2\text{CH}_2\text{O}_2 + 0.3 \text{HOC2H4CO2H}$	$1.00\text{E-}11 * \text{R02}$	Rickard and Pascoe (2009), Taraborrelli (2014)

40

Table 1: Gas phase reactions (... continued)

#	labels	reaction	rate coefficient	reference
G410apint279	TrGC	$\text{HOC2H4CO3} + \text{NO} \rightarrow \text{HOCH}_2\text{CH}_2\text{O}_2 + \text{NO}_2$	KAPNO	Rickard and Pascoe (2009), Taraborrelli (2014)
G410apint280	TrGC	$\text{HOC2H4CO3} + \text{HO}_2 \rightarrow \text{HOC2H4CO3H}$	$\text{KAPH02} * \text{rco3_ooh}$	Rickard and Pascoe (2009), Taraborrelli (2014)
G410apint281	TrGC	$\text{HOC2H4CO3} + \text{HO}_2 \rightarrow \text{HOCH}_2\text{CH}_2\text{O}_2 + \text{OH}$	$\text{KAPH02} * \text{rco3_oh}$	Rickard and Pascoe (2009), Taraborrelli (2014)
G410apint282	TrGC	$\text{HOC2H4CO3} + \text{HO}_2 \rightarrow \text{HOC2H4CO2H} + \text{O}_3$	$\text{KAPH02} * \text{rco3_o3}$	Rickard and Pascoe (2009), Taraborrelli (2014)
G410apint283	TrGC	$\text{HOC2H4CO3} + \text{NO}_2 \rightarrow \text{C3PAN1}$	$k_{\text{CH3CO3_NO2}}$	Rickard and Pascoe (2009), Taraborrelli (2014)
G410apint284	TrGC	$\text{HOC2H4CO2H} + \text{OH} \rightarrow \text{HOCH}_2\text{CH}_2\text{O}_2$	1.39E-11	Rickard and Pascoe (2009), Taraborrelli (2014)
G410apint285	TrGC	$\text{HOC2H4CO3H} + \text{OH} \rightarrow \text{HOC2H4CO3}$	1.73E-11	Rickard and Pascoe (2009), Taraborrelli (2014)
G410apint286	TrGC	$\text{HOC2H4CO3H} + h\nu \rightarrow \text{HOCH}_2\text{CH}_2\text{O}_2 + \text{OH}$	$1.14 * \text{jx}(\text{ip_CH300H})$	Rickard and Pascoe (2009), Taraborrelli (2014)
G410apint287	TrGC	$\text{C3PAN1} \rightarrow \text{HOC2H4CO3} + \text{NO}_2$	$k_{\text{PAN_M}}$	Rickard and Pascoe (2009), Taraborrelli (2014)
G410apint288	TrGC	$\text{C3PAN1} + \text{OH} \rightarrow \text{HOCH}_2\text{CHO} + \text{CO} + \text{NO}_2$	4.51E-12	Rickard and Pascoe (2009), Taraborrelli (2014)
G410apint289	TrGC	$\text{APINENE} + \text{NO}_3 \rightarrow \text{LNAPINABO2}$	$1.2\text{E-}12 * \text{EXP}(490./\text{temp})$	Rickard and Pascoe (2009), Taraborrelli (2014)
G410apint290	TrGC	$\text{LNAPINABO2} \rightarrow \text{PINAL} + \text{NO}_2$	$(.65 * 6.70\text{E-}15 + .35 * 2.50\text{E-}13) * \text{R02}$	Rickard and Pascoe (2009), Taraborrelli (2014)
G410apint291	TrGC	$\text{LNAPINABO2} + \text{NO} \rightarrow \text{PINAL} + \text{NO}_2 + \text{NO}_2$	KR02NO	Rickard and Pascoe (2009), Taraborrelli (2014)
G410apint292	TrGC	$\text{LNAPINABO2} + \text{HO}_2 \rightarrow \text{LNAPINABOOH}$	$\text{KR02HO2} * 0.914$	Rickard and Pascoe (2009), Taraborrelli (2014)
G410apint293	TrGC	$\text{LNAPINABO2} + \text{NO}_3 \rightarrow \text{PINAL} + \text{NO}_2 + \text{NO}_2$	KR02NO3	Rickard and Pascoe (2009), Taraborrelli (2014)
G410apint294	TrGC	$\text{LNAPINABOOH} + h\nu \rightarrow \text{PINAL} + \text{NO}_2 + \text{OH}$	$1.14 * \text{jx}(\text{ip_CH300H})$	Rickard and Pascoe (2009), Taraborrelli (2014)
G410apint295	TrGC	$\text{LNAPINABOOH} + \text{OH} \rightarrow \text{C96CO3}$	$.65 * 6.87\text{E-}12 + .35 * 1.23\text{E-}11$	Rickard and Pascoe (2009), Taraborrelli (2014)*

41

Table 1: Gas phase reactions (... continued)

#	labels	reaction	rate coefficient	reference
G410bpin	TrGC	BPINENE + OH → BPINAO2	$1.47E-11 * \text{EXP}(467/\text{TEMP}) * (0.8326 * 0.3 + 0.068) / (0.8326 + 0.068)$	Vereecken and Peeters (2012)*
G410bpint2	TrGC	BPINENE + OH → LVROO6R1O2	$1.47E-11 * \text{EXP}(467/\text{TEMP}) * 0.8326 * 0.7 / (0.8326 + 0.068)$	Vereecken and Peeters (2012)*
G410bpint3	TrGC	BPINAO2 + HO ₂ → BPINAOOH	KR02H02*0.914	Rickard and Pascoe (2009), Taraborrelli (2014)
G410bpint4	TrGC	BPINAO2 + NO → BPINANO3	KR02N0*0.240	Rickard and Pascoe (2009), Taraborrelli (2014)
G410bpint5	TrGC	BPINAO2 + NO → NOPINONE + HCHO + HO ₂ + NO ₂	KR02N0*0.760	Rickard and Pascoe (2009), Taraborrelli (2014)
G410bpint6	TrGC	BPINAO2 → NOPINONE + HCHO + HO ₂	9.20E-14*R02	Rickard and Pascoe (2009), Taraborrelli (2014)
G410bpint7	TrGC	BPINAOOH + OH → BPINAO2	1.33E-11	Rickard and Pascoe (2009), Taraborrelli (2014)
G410bpint8	TrGC	BPINAOOH + hν → NOPINONE + HCHO + HO ₂ + OH	1.14*jx(ip_CH300H)	Rickard and Pascoe (2009), Taraborrelli (2014)
G410bpint9	TrGC	BPINANO3 + OH → NOPINONE + HCHO + NO ₂	4.70E-12	Rickard and Pascoe (2009), Taraborrelli (2014)
G410bpint10	TrGC	LVROO6R1O2 + NO → LVROO6R3O2 + CH ₃ COCH ₃ + NO ₂	KR02N0*0.892	Vereecken and Peeters (2012), Taraborrelli (2014)
G410bpint11	TrGC	LVROO6R1O2 + NO → LVROO6R1NO3	KR02N0*0.108	Vereecken and Peeters (2012), Taraborrelli (2014)
G410bpint12	TrGC	LVROO6R1O2 + HO ₂ → LVROO6R1OOH	KR02H02*0.914	Vereecken and Peeters (2012), Taraborrelli (2014)
G410bpint13	TrGC	LVROO6R1O2 → LVROO6R3O2 + CH ₃ COCH ₃	1.60E-13*R02	Vereecken and Peeters (2012), Taraborrelli (2014)
G410bpint14	TrGC	LVROO6R3O2 → LVROO6R5O2	$5.68E10 * \text{exp}(-8745/\text{TEMP})$	Vereecken and Peeters (2012), Taraborrelli (2014)*
G410bpint15	TrGC	LVROO6R3O2 + NO → LVROO6R3O + NO ₂	KR02N0*0.890	Vereecken and Peeters (2012), Taraborrelli (2014)
G410bpint16	TrGC	LVROO6R3O2 + NO → LVROO6R3NO3	KR02N0*0.110	Vereecken and Peeters (2012), Taraborrelli (2014)
G410bpint17	TrGC	LVROO6R3O2 + HO ₂ → LVROO6R3OOH	KR02H02*0.820	Vereecken and Peeters (2012), Taraborrelli (2014)

42

Table 1: Gas phase reactions (... continued)

#	labels	reaction	rate coefficient	reference
G410bpint18	TrGC	LVROO6R3O2 → LVROO6R3O	2.50E-13*R02	Vereecken and Peeters (2012), Taraborrelli (2014)
G410bpint19	TrGC	LVROO6R3O → LVROO6R4P + HO ₂	$5.7E10 * \text{exp}(-2949/\text{TEMP})$	Vereecken and Peeters (2012), Taraborrelli (2014)*
G410bpint20	TrGC	LVROO6R5O2 → LVROO6R5P + OH	$9.17E10 * \text{exp}(-8706/\text{TEMP})$	Vereecken and Peeters (2012), Taraborrelli (2014)*
G410bpint21	TrGC	LVRO6R1O2 + NO → LVRO6R3O2 + NO ₂	KR02N0*0.747	Vereecken and Peeters (2012), Taraborrelli (2014)
G410bpint22	TrGC	LVRO6R1O2 + NO → LVRO6R1NO3	KR02N0*0.253	Vereecken and Peeters (2012), Taraborrelli (2014)
G410bpint23	TrGC	LVRO6R1O2 + HO ₂ → LVRO6R1OOH	KR02H02*0.914	Vereecken and Peeters (2012), Taraborrelli (2014)
G410bpint24	TrGC	LVRO6R1O2 → LVRO6R3O2	8.80E-13*R02	Vereecken and Peeters (2012), Taraborrelli (2014)
G410bpint25	TrGC	LVRO6R3O2 + NO → LVRO6R3P + NO ₂	KR02N0*0.893	Vereecken and Peeters (2012), Taraborrelli (2014)
G410bpint26	TrGC	LVRO6R3O2 + NO → LVRO6R3NO3	KR02N0*0.107	Vereecken and Peeters (2012), Taraborrelli (2014)
G410bpint27	TrGC	LVRO6R3O2 + HO ₂ → LVRO6R3OOH	KR02H02*0.914	Vereecken and Peeters (2012), Taraborrelli (2014)
G410bpint28	TrGC	LVRO6R3O2 → LVRO6R3P	5.00E-12*R02	Vereecken and Peeters (2012), Taraborrelli (2014)
G410bpint29	TrGC	NOPINONE + OH → NOPINDO2	1.55E-11	Lewis et al. (2005), Rickard and Pascoe (2009), Taraborrelli (2014)
G410bpint30	TrGC	NOPINDO2 + HO ₂ → NOPINDOOH	KR02H02*0.890	Rickard and Pascoe (2009), Taraborrelli (2014)
G410bpint31	TrGC	NOPINDO2 + NO → C89CO3 + NO ₂	KR02N0	Rickard and Pascoe (2009), Taraborrelli (2014)
G410bpint32	TrGC	NOPINDO2 → C89CO3	2.00E-12*R02	Rickard and Pascoe (2009), Taraborrelli (2014)
G410bpint33	TrGC	NOPINDOOH + OH → NOPINDCO + OH	2.63E-11	Rickard and Pascoe (2009), Taraborrelli (2014)
G410bpint34	TrGC	NOPINDOOH + hν → C89CO3 + OH	1.14*jx(ip_CH300H)	Rickard and Pascoe (2009), Taraborrelli (2014)

43

Table 1: Gas phase reactions (... continued)

#	labels	reaction	rate coefficient	reference
G410bpint35	TrGC	NOPINDCO + OH → C89CO3	3.07E-12	Rickard and Pascoe (2009), Taraborrelli (2014)
G410bpint36	TrGC	BPINENE + O ₃ → NOPINONE + .63 CO + .37 HOCH ₂ OOH + .16 OH + .16 HO ₂	1.5E-17*.051/(1-.027)	Nguyen et al. (2009), Taraborrelli (2014)
G410bpint37	TrGC	BPINENE + O ₃ → NOPINOO	1.5E-17*.368/(1-.027)	Nguyen et al. (2009), Taraborrelli (2014)
G410bpint38	TrGC	BPINENE + O ₃ → NOPINDO2 + OH	1.5E-17*.283/(1-.027)	Nguyen et al. (2009), Taraborrelli (2014)
G410bpint40	TrGC	BPINENE + O ₃ → C8BC + CO ₂	1.5E-17*(.104+.167)/(1-.027)	Nguyen et al. (2009), Taraborrelli (2014)*
G410bpint41	TrGC	C8BC + OH → C8BCO2	3.04E-12	Rickard and Pascoe (2009), Taraborrelli (2014)
G410bpint42	TrGC	C8BCO2 + HO ₂ → C8BCOOH	KR02H02*0.859	Rickard and Pascoe (2009), Taraborrelli (2014)
G410bpint43	TrGC	C8BCO2 + NO → C8BCNO3	KR02N0*0.138	Rickard and Pascoe (2009), Taraborrelli (2014)
G410bpint44	TrGC	C8BCO2 + NO → C89O2 + NO ₂	KR02N0*0.862	Rickard and Pascoe (2009), Taraborrelli (2014)
G410bpint45	TrGC	C8BCO2 → C89O2	2.50E-13*R02	Rickard and Pascoe (2009), Taraborrelli (2014)
G410bpint46	TrGC	C8BCOOH + OH → C8BCCO + OH	1.62E-11	Rickard and Pascoe (2009), Taraborrelli (2014)
G410bpint47	TrGC	C8BCOOH + hν → C89O2 + OH	1.14*jx(ip_CH300H)	Rickard and Pascoe (2009), Taraborrelli (2014)
G410bpint48	TrGC	C8BCNO3 + OH → C8BCCO + NO ₂	1.84E-12	Rickard and Pascoe (2009), Taraborrelli (2014)
G410bpint49	TrGC	C8BCNO3 → C89O2 + NO ₂	J_IC3H7N03	Rickard and Pascoe (2009), Taraborrelli (2014)
G410bpint50	TrGC	C8BCCO + OH → C89O2	3.94E-12	Rickard and Pascoe (2009), Taraborrelli (2014)
G410bpint51	TrGC	NOPINOO → NOPINONE + H ₂ O ₂	6.00E-18*c(ind_H2O)	Rickard and Pascoe (2009), Taraborrelli (2014)
G410bpint52	TrGC	NOPINOO + CO → NOPINONE	1.2E-15	Rickard and Pascoe (2009), Taraborrelli (2014)

44

Table 1: Gas phase reactions (... continued)

#	labels	reaction	rate coefficient	reference
G410bpint53	TrGC	NOPINOO + NO → NOPINONE + NO ₂	1.E-14	Rickard and Pascoe (2009), Taraborrelli (2014)
G410bpint54	TrGC	NOPINOO + NO ₂ → NOPINONE + NO ₃	1.E-15	Rickard and Pascoe (2009), Taraborrelli (2014)
G410bpint55	TrGC	NOPINOO + SO ₂ → NOPINONE + H ₂ SO ₄	7.E-14	Rickard and Pascoe (2009), Taraborrelli (2014)
G410bpint56	TrGC	BPINENE + NO ₃ → LNBPINABO2	2.51E-12	Rickard and Pascoe (2009), Taraborrelli (2014)
G410bpint57	TrGC	LNBPINABO2 + HO ₂ → LNBPINABOOH	KR02H02*0.914	Rickard and Pascoe (2009), Taraborrelli (2014)
G410bpint58	TrGC	LNBPINABO2 + NO → NOPINONE + HCHO + NO ₂ + NO ₂	KR02N0	Rickard and Pascoe (2009), Taraborrelli (2014)
G410bpint59	TrGC	LNBPINABO2 + NO ₃ → NOPINONE + HCHO + NO ₂ + NO ₂	KR02N03	Rickard and Pascoe (2009), Taraborrelli (2014)
G410bpint60	TrGC	LNBPINABO2 → NOPINONE + HCHO + NO ₂	9.20E-14*R02*0.7	Rickard and Pascoe (2009), Taraborrelli (2014)
G410bpint61	TrGC	LNBPINABO2 → BPINANO3	9.20E-14*R02*0.3	Rickard and Pascoe (2009), Taraborrelli (2014)*
G410bpint62	TrGC	LNBPINABOOH + OH → LNBPINABO2	9.58E-12	Rickard and Pascoe (2009), Taraborrelli (2014)
G410bpint63	TrGC	LNBPINABOOH + hν → NOPINONE + HCHO + NO ₂ + OH	1.14*jx(ip_CH300H)	Rickard and Pascoe (2009), Taraborrelli (2014)
G410apint296	TrGC	CARENE + OH → LAPINABO2	8.7E-11*(.50+.25)	Wolfe et al. (2011), Taraborrelli (2014)*
G410apint297	TrGC	CARENE + OH → MENTHEN6ONE + HO ₂	8.7E-11*.25*.60	Wolfe et al. (2011), Taraborrelli (2014)
G410apint298	TrGC	CARENE + OH → LVROO6R1O2	8.7E-11*.25*.40	Wolfe et al. (2011), Taraborrelli (2014)
G410apint299	TrGC	CARENE + O ₃ → APINBOO	2.E-16*.50*.18	Wolfe et al. (2011), Taraborrelli (2014)
G410apint300	TrGC	CARENE + O ₃ → PINONIC	2.E-16*.50*.16	Wolfe et al. (2011), Taraborrelli (2014)
G410apint301	TrGC	CARENE + O ₃ → OH + NORPINAL + CO + HO ₂	2.E-16*.50*.66	Wolfe et al. (2011), Taraborrelli (2014)

45

Table 1: Gas phase reactions (... continued)

#	labels	reaction	rate coefficient	reference
G410apint302	TrGC	CARENE + O ₃ → APINAO	2.E-16*.50*.12	Wolfe et al. (2011), Taraborrelli (2014)
G410apint303	TrGC	CARENE + O ₃ → OH + C109O2	2.E-16*.50*(.22+.66)	Wolfe et al. (2011), Taraborrelli (2014)*
G410apint304	TrGC	CARENE + NO ₃ → LNAPINABO2	9.5E-12	Wolfe et al. (2011), Taraborrelli (2014)
G410myrc	TrGC	BMYRCENE + OH → MYRCISOPO2	9.19E-12*exp(1071./temp)*0.64	Hites and Turner (2009), Orlando et al. (2000), Taraborrelli (2014)
G410myrct2	TrGC	BMYRCENE + OH → MYRCO2	9.19E-12*exp(1071./temp)*0.36	Hites and Turner (2009), Orlando et al. (2000), Taraborrelli (2014)
G410myrct3	TrGC	BMYRCENE + O ₃ → .25 CH ₃ COCH ₃ + .75 OH + .75 CH ₃ COCH ₂ O ₂ + MYRCCHO	4.7E-16	Atkinson and Arey (2003), Taraborrelli (2014)
G410myrct4	TrGNC	BMYRCENE + NO ₃ → MYRCNO3	1.1E-11	Atkinson and Arey (2003), Taraborrelli (2014)
G410myrct5	TrGC	MYRCO2 → CH ₃ COCH ₃ + HO ₂ + MYRCCHO	8.E-13*R02	Taraborrelli (2014)
G410myrct6	TrGC	MYRCO2 + HO ₂ → MYRCOOH	KR02H02	Taraborrelli (2014)
G410myrct7	TrGCN	MYRCO2 + NO → .80 CH ₃ COCH ₃ + .80 HO ₂ + .80 MYRCCHO + .80 NO ₂ + .20 MYRCNO3	KR02N0	Taraborrelli (2014)*
G410myrct8	TrGCJ	MYRCOOH + hν → CH ₃ COCH ₃ + OH + HO ₂ + MYRCCHO	1.14*jx(ip_CH300H)	Taraborrelli (2014)
G410myrct9	TrGC	MYRCOOH + OH → MYRCOOHISOPO2	1.55E-10	Baker et al. (2004), Taraborrelli (2014)
G410myrct10	TrGC	MYRCOOH + NO ₃ → CH ₃ COCH ₃ + SURCH3CHO + NISOPO2	4.7E-13	Baker et al. (2004), Taraborrelli (2014)
G410myrct11	TrGC	MYRCNO3 + OH → iC ₃ H ₇ ONO ₂ + MYRCCHOISOPO2	1.55E-10	see note
G410myrct12	TrGC	MYRCISOPO2 → MYRCISOPO	1.E-12*R02	Taraborrelli (2014)
G410myrct13	TrGC	MYRCISOPO2 + HO ₂ → MYRCISOPOOH	KR02H02	Taraborrelli (2014)
G410myrct14	TrGC	MYRCISOPO2 + NO → .8 MYRCISOPO + .8 NO ₂ + .2 MYRCISOPNO3	KR02N0	Taraborrelli (2014)
G410myrct15	TrGC	MYRCISOPO2 → MYRCHPALD + HO ₂	K16HS	Taraborrelli (2014)*
G410myrct16	TrGC	MYRCISOPO → CH ₃ COCH ₃ + SURCH3CHO + .43 MVK + .27 MACR + .7 HCHO + .29 LHC4ACCHO + HO ₂	KDEC	Taraborrelli (2014)

46

Table 1: Gas phase reactions (... continued)

#	labels	reaction	rate coefficient	reference
G410myrct17	TrGC	MYRCISOPNO3 + OH → CH ₃ COCH ₃ + HO ₂ + SURCH3CHO + ISOPBNO3	kadt*kads	Taraborrelli (2014)
G410myrct18	TrGC	MYRCISOPOOH + hν → MYRCISOPO + OH	1.14*jx(ip_CH300H)	Taraborrelli (2014)
G410myrct19	TrGC	MYRCISOPOOH + OH → SURCH3CHO + .43 ISOPBOOH + .27 ISOPDOOH + .29 LISOPACOOH + CH ₃ COCH ₃ + HO ₂	kadt*kads	Taraborrelli (2014)
G410myrct20	TrGCJ	MYRCHPALD + hν → OH + ZCODC23DBCOOH + HO ₂	J_HPALD	Taraborrelli (2014)
G410myrct21	TrGC	MYRCHPALD + OH → MYRCCHOHPALD + HO ₂ + CH ₃ COCH ₃	kadt*kads	Taraborrelli (2014)
G410myrct22	TrGC	MYRCHPALD + OH → SURCH3CO3 + SURCH3CHO + HCHO + GLYOX + HO ₂	(kadt*kads)*acho*ach2ooh	Taraborrelli (2014)
G410myrct23	TrGC	MYRCHPALD + O ₃ → MYRCCHOHPALD + .25 CH ₃ COCH ₃ + .75 OH + .75 CH ₃ COCH ₂ O ₂	4.7E-16	Taraborrelli (2014)
G410myrct24	TrGC	MYRCCHO + OH → SURCH3CHO + MYRCCHOISOPO2	1.55E-10	Baker et al. (2004), Taraborrelli (2014)
G410myrct25	TrGC	MYRCCHO + NO ₃ → SURCH3CHO + NISOPO2	4.7E-13	Baker et al. (2004), Taraborrelli (2014)
G410myrct26	TrGC	MYRCCHOISOPO2 → MYRCCHOISOPO	1.E-12*R02	Taraborrelli (2014)
G410myrct27	TrGC	MYRCCHOISOPO2 + HO ₂ → SURCH3CHO + .43 ISOPBOOH + .27 ISOPDOOH + .29 LISOPACOOH	KR02H02	Taraborrelli (2014)
G410myrct28	TrGC	MYRCCHOISOPO2 + NO → .8 MYRCCHOISOPO + .8 NO ₂ + .2 SURCH3CHO + .2 ISOPBNO3	KR02N0	Taraborrelli (2014)
G410myrct29	TrGC	MYRCCHOISOPO2 → MYRCCHOHPALD + HO ₂	K16HS	Taraborrelli (2014)*
G410myrct30	TrGC	MYRCCHOISOPO → SURCH3CHO + .43 MVK + .27 MACR + .7 HCHO + .29 LHC4ACCHO + HO ₂	KDEC	Taraborrelli (2014)
G410myrct31	TrGCJ	MYRCCHOHPALD + hν → SURCH3CHO + OH + ZCODC23DBCOOH + HO ₂	J_HPALD	Taraborrelli (2014)
G410myrct32	TrGC	MYRCCHOHPALD + OH → SURCH3CHO + .3 C1ODC2O2C4OOH + .2 C1OOHC2O2C4OD + .3 C1ODC3O2C4OOH + .2 C1OOHC3O2C4OD	(kadt*kads)*acho*ach2ooh	Taraborrelli (2014)
G410myrct33	TrGC	MYRCOOHISOPO2 → MYRCOOHISOPO	1.E-12*R02	Taraborrelli (2014)
G410myrct34	TrGC	MYRCOOHISOPO2 + HO ₂ → MYRCOOHISOPOOH	KR02H02	Taraborrelli (2014)
G410myrct35	TrGC	MYRCOOHISOPO2 + NO → .8 MYRCOOHISOPO + .8 NO ₂ + .2 CH ₃ COCH ₃ + .2 SURCH3CHO + .2 ISOPBNO3	KR02N0	Taraborrelli (2014)
G410myrct36	TrGC	MYRCOOHISOPO2 → MYRCOOHHPALD + HO ₂	K16HS	Taraborrelli (2014)*

47

Table 1: Gas phase reactions (... continued)

#	labels	reaction	rate coefficient	reference
G410myrct37	TrGC	MYRCCOOHISOPO \rightarrow CH ₃ COCH ₃ + SURCH3CHO + .43 MVK + .27 MACR + .7 HCHO + .29 LHC4ACCHO + HO ₂ + OH	KDEC	Taraborrelli (2014)
G410myrct38	TrGCJ	MYRCCOOHISOPOOH + h ν \rightarrow MYRCCOOHISOPO + OH	1.14*jx(ip_CH300H)	Taraborrelli (2014)
G410myrct39	TrGCJ	MYRCCOOHISOPOOH + h ν \rightarrow CH ₃ COCH ₃ + HO ₂ + SURCH3CHO + .43 ISOPBOOH + .27 ISOPDOOH + .29 LISOPACOOH + OH	1.14*jx(ip_CH300H)	Taraborrelli (2014)
G410myrct40	TrGCJ	MYRCCOOHHPALD + h ν \rightarrow CH ₃ COCH ₃ + OH + SURCH3CHO + OH + ZCODC23DBCOOH + HO ₂	J_HPALD	Taraborrelli (2014)
G410myrct41	TrGC	MYRCCOOHHPALD + OH \rightarrow CH ₃ COCH ₃ + OH + SURCH3CHO + .3 C1ODC2O2C4OOH + .2 C1OOHC2O2C4OD + .3 C1ODC3O2C4OOH + .2 C1OOHC3O2C4OD	(kadt+kads)*acho*ach2ooh	Taraborrelli (2014)
G410myrct42	TrGC	SURCH3CHO + OH \rightarrow SURCH3CO3 + H ₂ O	4.4E-12*EXP(365./temp)	Taraborrelli (2014)*
G410myrct43	TrGC	SURCH3CHO + h ν \rightarrow HCHO + HO ₂ + HO ₂ + CO	jx(ip_CH3CHO)	Taraborrelli (2014)
G410myrct44	TrGC	SURCH3CHO + NO ₃ \rightarrow HNO ₃ + SURCH3CO3	KNO3AL	Taraborrelli (2014)
G410myrct45	TrGC	SURCH3CO3 \rightarrow HCHO + HO ₂ + CO ₂	1.00E-11*0.7*R02	Taraborrelli (2014)
G410myrct46	TrGC	SURCH3CO3 \rightarrow SURCH3CO2H	1.00E-11*0.3*R02	Taraborrelli (2014)
G410myrct47	TrGC	SURCH3CO3 + HO ₂ \rightarrow OH + HCHO + HO ₂ + CO ₂	KAPH02*0.44	Taraborrelli (2014)
G410myrct48	TrGC	SURCH3CO3 + HO ₂ \rightarrow SURCH3CO3H	KAPH02*0.41	Taraborrelli (2014)
G410myrct49	TrGC	SURCH3CO3 + HO ₂ \rightarrow SURCH3CO2H + O ₃	KAPH02*0.15	Taraborrelli (2014)
G410myrct50	TrGC	SURCH3CO3 + NO ₂ \rightarrow SURPAN	k_CH3CO3_NO2	Taraborrelli (2014)
G410myrct51	TrGC	SURCH3CO3 + NO \rightarrow NO ₂ + HCHO + HO ₂ + CO ₂	KAPNO	Taraborrelli (2014)
G410myrct52	TrGC	SURCH3CO3 + NO ₃ \rightarrow NO ₂ + HCHO + HO ₂ + CO ₂	KRO2NO3*1.60	Taraborrelli (2014)
G410myrct53	TrGC	SURCH3CO2H + OH \rightarrow HCHO + HO ₂ + CO ₂	4.2E-14*exp(850./temp)	Taraborrelli (2014)*
G410myrct54	TrGC	SURCH3CO3H + h ν \rightarrow HCHO + HO ₂ + OH + CO ₂	1.14*jx(ip_CH300H)	Taraborrelli (2014)
G410myrct55	TrGC	SURCH3CO3H + OH \rightarrow SURCH3CO3 + H ₂ O	0.6*k_CH300H_OH	Taraborrelli (2014)
G410myrct56	TrGC	SURPAN \rightarrow SURCH3CO3 + NO ₂	k_PAN_M	Taraborrelli (2014)
G410myrct57	TrGC	SURPAN + OH \rightarrow HCHO + CO + NO ₂	9.50E-13*EXP(-650./temp)	Taraborrelli (2014)
G410afarnt	TrGC	FARNESENE + OH \rightarrow LFARNISOPO2	2.7E-11*EXP(390./temp)	Taraborrelli (2014)*
G410afarnt2	TrGC	FARNESENE + OH \rightarrow LFARNO2	2.*1.9E-11*exp(450./temp)	Taraborrelli (2014)*
G410afarnt3	TrGC	FARNESENE + O ₃ \rightarrow FARNCHO + .25 CH ₃ COCH ₂ O ₂ + .75 OH + .75 CH ₃ COCH ₂ O ₂	6.51E-15*exp(-829./temp)	Taraborrelli (2014)*
G410afarnt4	TrGC	FARNESENE + O ₃ \rightarrow MHO + MYRCCHO + .75 OH	6.51E-15*exp(-829./temp)	Taraborrelli (2014)*
G410afarnt5	TrGNC	FARNESENE + NO ₃ \rightarrow LFARNO2	2E-12*2*9.37E-12	Taraborrelli (2014)*

48

Table 1: Gas phase reactions (... continued)

#	labels	reaction	rate coefficient	reference
G410afarnt6	TrGC	LFARNO2 \rightarrow LFARNO	8.E-13*R02	Taraborrelli (2014)
G410afarnt7	TrGC	LFARNO2 + HO ₂ \rightarrow LFARNOOH	KRO2H02	Taraborrelli (2014)
G410afarnt8	TrGC	LFARNO2 + NO \rightarrow .75 LFARNO + .75 NO ₂ + .25 LFARNONO2	KRO2NO	Taraborrelli (2014)
G410afarnt9	TrGCJ	LFARNOOH + h ν \rightarrow LFARNO + OH	1.14*jx(ip_CH300H)	Taraborrelli (2014)
G410afarnt10	TrGC	LFARNOOH + OH \rightarrow MHO + MYRCCHOISOPO2	2.7E-11*EXP(390./temp)	Taraborrelli (2014)
G410afarnt11	TrGC	LFARNONO2 + OH \rightarrow .5 MHO + .5 FARNCHO + MYRCISOPNO3	2.*1.9E-11*exp(450./temp)	Taraborrelli (2014)
G410afarnt12	TrGC	LFARNO \rightarrow .5 MHO + .5 MYRCCHO + .5 FARNCHO + .5 CH ₃ COCH ₃ + HO ₂	KDEC	Taraborrelli (2014)
G410afarnt13	TrGC	LFARNISOPO2 \rightarrow LFARNISOPO	1.E-12*R02	Taraborrelli (2014)
G410afarnt14	TrGC	LFARNISOPO2 + HO ₂ \rightarrow LFARNISOPOOH	KRO2H02	Taraborrelli (2014)
G410afarnt15	TrGC	LFARNISOPO2 + NO \rightarrow .75 LFARNISOPO + .75 NO ₂ + .25 LFARNISOPNO3	KRO2NO	Taraborrelli (2014)
G410afarnt16	TrGC	LFARNISOPO2 \rightarrow MYRCCHOHPALD + HO ₂ + MHO	K16HS	Taraborrelli (2014)*
G410afarnt17	TrGC	LFARNISOPO \rightarrow MHO + MYRCCHOISOPO	KDEC	Taraborrelli (2014)
G410afarnt18	TrGC	LFARNISOPNO3 + OH \rightarrow MHO + HO ₂ + ISOPBNO3	kadt+kads	Taraborrelli (2014)
G410afarnt19	TrGC	LFARNISOPOOH + h ν \rightarrow LFARNISOPO + OH	1.14*jx(ip_CH300H)	Taraborrelli (2014)
G410afarnt20	TrGC	LFARNISOPOOH + OH \rightarrow MHO + MYRCCHOISOPO2	kadt+kads	Taraborrelli (2014)
G410afarnt21	TrGC	LFARNISOPOOH + O ₃ \rightarrow MHO + MYRCCHOISOPO2 + .75 OH	2.*6.51E-15*exp(-829./temp)	Taraborrelli (2014)*
G410afarnt22	TrGC	FARNCHO + OH \rightarrow FARNCHOO2	1.9E-11*exp(450./temp)	Taraborrelli (2014)*
G410afarnt23	TrGC	FARNCHO + OH \rightarrow FARNCHOISOPO2	2.7E-11*EXP(390./temp)	Taraborrelli (2014)*
G410afarnt24	TrGC	FARNCHO + O ₃ \rightarrow OPA + MYRCCHO + .75 OH	6.51E-15*exp(-829./temp)	Taraborrelli (2014)*
G410afarnt25	TrGNC	FARNCHO + NO ₃ \rightarrow FARNCHOISOPO2	2E-12	Taraborrelli (2014)*
G410afarnt26	TrGNC	FARNCHO + NO ₃ \rightarrow FARNCHOO2	9.37E-12	Taraborrelli (2014)*
G410afarnt27	TrGC	FARNCHOO2 \rightarrow FARNCHOO	8.E-13*R02	Taraborrelli (2014)
G410afarnt28	TrGC	FARNCHOO2 + HO ₂ \rightarrow FARNCHOOOH	KRO2H02	Taraborrelli (2014)
G410afarnt29	TrGC	FARNCHOO2 + NO \rightarrow .75 FARNCHOO + .75 NO ₂ + .25 FARNCHONO3	KRO2NO	Taraborrelli (2014)
G410afarnt30	TrGCJ	FARNCHOOOH + h ν \rightarrow FARNCHOO + OH	1.14*jx(ip_CH300H)	Taraborrelli (2014)
G410afarnt31	TrGC	FARNCHOOOH + OH \rightarrow OPA + HO ₂ + MYRCCHOISOPO2	2.7E-11*EXP(390./temp)	Taraborrelli (2014)*
G410afarnt32	TrGC	FARNCHONO3 + OH \rightarrow OPA + MYRCISOPNO3	1.9E-11*exp(450./temp)	Taraborrelli (2014)*
G410afarnt33	TrGC	FARNCHOO \rightarrow OPA + MYRCCHO + HO ₂	KDEC	Taraborrelli (2014)

49

Table 1: Gas phase reactions (... continued)

#	labels	reaction	rate coefficient	reference
G410afarnt34	TrGC	FARNCHOISOPO2 → FARNCHOISOPO	1.E-12*R02	Taraborrelli (2014)
G410afarnt35	TrGC	FARNCHOISOPO2 + HO2 → FARNCHOISOPOOH	KR02H02	Taraborrelli (2014)
G410afarnt36	TrGC	FARNCHOISOPO2 + NO → .75 FARNCHOISOPO + .75 NO2 + .25 FARNCHOISOPNO3	KR02N0	Taraborrelli (2014)
G410afarnt37	TrGC	FARNCHOISOPO2 → OPA + MYRCCHOHPALD + HO2 + MHO	K16HS	Taraborrelli (2014)*
G410afarnt38	TrGC	FARNCHOISOPO → OPA + MYRCCHOISOPO	KDEC	Taraborrelli (2014)
G410afarnt39	TrGC	FARNCHOISOPNO3 + OH → OPA + HO2 + ISOPBNO3	kadt+kads	Taraborrelli (2014)
G410afarnt40	TrGC	FARNCHOISOPPOOH + hν → FARNCHOISOPO + OH	1.14*jx(ip_CH300H)	Taraborrelli (2014)
G410afarnt41	TrGC	FARNCHOISOPPOOH + OH → OPA + MYRCCHOISOPO2	kadt+kads	Taraborrelli (2014)
G410afarnt42	TrGC	FARNCHOISOPPOOH + O3 → OPA + MYRCCHOISOPO2 + .75 OH	6.51E-15*exp(-829./temp)	Taraborrelli (2014)
G410afarnt43	TrGC	MHO + OH → MHO2	1.37E-10	Smith et al. (1996), Taraborrelli (2014)*
G410afarnt44	TrGC	MHO + O3 → .25 CH3COCH3 + .125 OPA + .25 GLYOX + .25 CH3COCH2O2 + .125 H2O2 + .75 OH + .75 CH3COCH2O2 + .75 OPA	3.9E-16	Grosjean et al. (1996), Taraborrelli (2014)*
G410afarnt45	TrGC	MHO + NO3 → MHO2	7E-12	Smith et al. (1996), Taraborrelli (2014)
G410afarnt46	TrGC	MHO2 → CH3COCH3 + OPA + HO2	8.E-13*R02	Taraborrelli (2014)
G410afarnt47	TrGC	MHO2 + HO2 → MHO2OH	KR02H02	Taraborrelli (2014)
G410afarnt48	TrGC	MHO2 + NO → .25 MHONO3 + .75 CH3COCH3 + .75 OPA + .75 HO2 + .75 NO2	KR02N0	Taraborrelli (2014)
G410afarnt49	TrGC	MHO2OH + OH → MHO2	0.6*k_CH300H_OH	Taraborrelli (2014)
G410afarnt50	TrGC	MHO2OH + OH → MHOCODOOH + HO2	kt*ftoh*falk*falk	Taraborrelli (2014)
G410afarnt51	TrGCJ	MHO2OH + hν → CH3COCH3 + OPA + OH	1.14*jx(ip_CH300H)	Taraborrelli (2014)
G410afarnt52	TrGCJ	MHOCODOOH + hν → CH3COCH3 + CH3COCH2O2 + SURCH3CO3 + OH	1.14*jx(ip_CH300H)+2.77*jx(ip_HOCH2CHO)	Taraborrelli (2014)*
G410afarnt53	TrGC	MHONO3 + OH → MHOCODNO3 + HO2	kt*ftoh*falk*fch2ono2	Taraborrelli (2014)
G410afarnt54	TrGC	MHOCODNO3 + hν → CH3COCH3 + NO2 + CH3COCH2O2 + SURCH3CO3	2.84*J_IC3H7N03	Taraborrelli (2014)
G410afarnt55	TrGC	OPA + OH → CH3COCH2O2 + SURCH3CO3	2.E-11	Fruekilde et al. (1997), Taraborrelli (2014)*

50

Table 1: Gas phase reactions (... continued)

#	labels	reaction	rate coefficient	reference
G410afarnt56	TrGCJ	OPA + hν → CH3COCH2O2 + SURCH3CO3 + HO2	jx(ip_CH3CHO)+jx(ip_CH3COCH3)	Taraborrelli (2014)

51

*Notes:

Rate coefficients for three-body reactions are defined via the function `k_3rd(T, M, k0300, n, kinf300, m, fc)`. In the code, the temperature T is called `temp` and the concentration of "air molecules" M is called `cair`. Using the auxiliary variables $k_0(T)$, $k_{inf}(T)$, and k_{ratio} , `k_3rd` is defined as:

$$k_0(T) = k_0^{300} \times \left(\frac{300\text{K}}{T}\right)^n \quad (1)$$

$$k_{inf}(T) = k_{inf}^{300} \times \left(\frac{300\text{K}}{T}\right)^m \quad (2)$$

$$k_{ratio} = \frac{k_0(T)M}{k_{inf}(T)} \quad (3)$$

$$\mathbf{k_3rd} = \frac{k_0(T)M}{1 + k_{ratio}} \times f_c \left(\frac{1}{1 + (0.0610(k_{ratio}/N))^2}\right) \quad (4)$$

A similar function, called `k_3rd_iupac` here, is used by Atkinson et al. (2005) for three-body reactions. It has the same function parameters as `k_3rd` and it is defined as:

$$k_0(T) = k_0^{300} \times \left(\frac{300\text{K}}{T}\right)^n \quad (5)$$

$$k_{inf}(T) = k_{inf}^{300} \times \left(\frac{300\text{K}}{T}\right)^m \quad (6)$$

$$k_{ratio} = \frac{k_0(T)M}{k_{inf}(T)} \quad (7)$$

$$N = 0.75 - 1.27 \times \log_{10}(f_c) \quad (8)$$

$$\mathbf{k_3rd_iupac} = \frac{k_0(T)M}{1 + k_{ratio}} \times f_c \left(\frac{1}{1 + (0.0610(k_{ratio}/N))^2}\right) \quad (9)$$

Structure Activity Relationship (SAR) for estimation of rate constants as developed by Taraborrelli (2010).

SAR for H-abstraction:

base rate constants

$$k_s = 8.42E-13 \quad (10)$$

$$k_t = 1.75E-12 \quad (11)$$

$$k_p = 1.24E-13 \quad (12)$$

$$k_{cho} = 5.55E-12 \times \text{EXP}(311/T) * .95 \quad (13)$$

$$k_{roho} = 1.6E-13 \quad (14)$$

$$k_{co2h} = .66 \times 4.2E-14 \times \text{exp}(850/T) \quad (15)$$

activation factors (parameter names starting with f)

$$f_{soh} = 3.44 \quad (16)$$

$$f_{toh} = 2.68 \quad (17)$$

$$f_{sooh} = 7. \quad (18)$$

$$f_{tooh} = 7. \quad (19)$$

$$f_{ono2} = 0.04 \quad (20)$$

$$f_{ch2ono2} = 0.2 \quad (21)$$

$$f_{cpn} = .25 \quad (22)$$

$$f_{allyl} = 3.6 \quad (23)$$

$$f_{alk} = 1.23 \quad (24)$$

$$f_{cho} = 0.55 \quad (25)$$

$$f_{co2h} = 1.67 \quad (26)$$

$$f_{co} = 0.73 \quad (27)$$

$$f_{o} = 8.15 \quad (28)$$

$$f_{pch2oh} = 1.29 \quad (29)$$

$$f_{tch2oh} = 0.53 \quad (30)$$

$$k_{adp} = 0.45E-11 \quad (31)$$

$$k_{ads} = 3.0E-11 \quad (32)$$

$$k_{adt} = 5.5E-11 \quad (33)$$

$$k_{adsecprim} = 3.0E-11 \quad (34)$$

$$k_{adtertprim} = 5.7E-11 \quad (35)$$

activation factors (parameter names starting with a)

$$a_{pan} = 0.56 \quad (36)$$

$$a_{cho} = 0.31 \quad (37)$$

$$a_{coch3} = 0.76 \quad (38)$$

$$a_{ch2ono2} = 0.47 \quad (39)$$

$$a_{ch2oh} = 1.7 \quad (40)$$

$$a_{ch2ooh} = 0.21 \quad (41)$$

$$a_{coh} = 2.2 \quad (42)$$

$$a_{cooh} = 2.2 \quad (43)$$

$$a_{co2h} = 0.25 \quad (44)$$

G2110: The rate coefficient is: `k_HO2_HO2 = (1.5E-12*EXP(19./temp)+1.7E-33*EXP(1000./temp)*cair)*(1.+1.4E-21*EXP(2200./temp)*C(ind_H2O))`. The value for the first (pressure-independent) part is from Christensen et al. (2002), the water term from Kircher and Sander (1984).

G3109: The rate coefficient is: `k_N03_N02 = k_3rd(temp,cair,2.E-30,4.4,1.4E-12,0.7,0.6)`.

G3110: The rate coefficient is defined as backward reaction divided by equilibrium constant.

G3203: The rate coefficient is: `k_N02_H02 = k_3rd(temp,cair,1.8E-31,3.2,4.7E-12,1.4,0.6)`.

G3206: The rate coefficient is: `k_HNO3_OH = 2.4E-14 * EXP(460./temp) + 1./ (1./`

SAR for H-addition do C-C double bonds:

base rate constants

52

(6.5E-34 * EXP(1335./temp)*cair) + 1./ (2.7E-17 * EXP(2199./temp)))

G3207: The rate coefficient is defined as backward reaction divided by equilibrium constant.

G4103a: Sander et al. (2006) recommend a zero product yield for HCHO. G4103b: Sander et al. (2006) recommend a zero product yield for HCHO.

G4107: The rate coefficient is: `k_CH3OOH_OH = 5.3E-12 * EXP(190./temp)`.

G4109: The same temperature dependence assumed as for CH₃CHO+NO₃.

G4201e: The product distribution is from Rickard and Pascoe (2009), after substitution of the Criegee intermediate by its decomposition products.

G4206: The product C₂H₅OH, which reacts only with OH, is substituted by its degradation products ≈ 0.1 HOCH₂CH₂O₂ + 0.9 CH₃CHO + 0.9 HO₂.

G4207: The rate constant 8.01E-12 is for the H abstraction in alpha to the -OOH group (Rickard and Pascoe, 2009) and 0.6*k_CH3OOH_OH is for the C₂H₅O₂ channel. The branching ratios are calculated from the terms of the rate coefficient at 298 K.

G4211et1: personal communication C. Gross (MPICH)

G4211et2: personal communication C. Gross (MPICH)

G4211et3: personal communication C. Gross (MPICH)

G4213: The rate coefficient is: `k_CH3CO3_N02 = k_3rd(temp,cair,8.5E-29,6.5,1.1E-11,1.,0.6)`.

G4218: The rate coefficient is the same as for the CH₃O₂ channel in G4107 (CH₃OOH+OH).

G4221: The rate coefficient `isk_PAN_M = k_CH3CO3_N02/9.E-29*EXP(-14000./temp)`, i.e. the rate coefficient is defined as backward reaction divided by equilibrium constant.

G4226ea: personal communication C. Gross (MPICH)

G4226eb: personal communication C. Gross (MPICH)

G4226ec: personal communication C. Gross (MPICH)

G4243: Orlando et al. (1998a) estimated that about 25% of the HOCH₂CH₂O in this reaction is produced with sufficient excess energy that it decomposes promptly. The decomposition products are 2 HCHO + HO₂.

G4255et2: personal communication C. Gross (MPICH)

G4255et3: personal communication C. Gross (MPICH)

G4260et2: personal communication C. Gross (MPICH)

G4260et3: personal communication C. Gross (MPICH)

G4266e: 0.4 CO₂HCH₂O₂ approximated to HOCH₂CO₂H

G4300: The product NC₃H₇O₂ is substituted with its degradation products C₂H₅O₂ + CO₂ + HO₂.

G4304: The value for the generic RO₂ + HO₂ reaction from Atkinson (1997) is used here.

G4306: The MCM (Rickard and Pascoe, 2009) products are 0.2 IPROPOL + 0.2 CH₃COCH₃ + 0.6 IC₃H₇O. IPROPOL and IC₃H₇O are substituted with their degradation products. We assume IPROPOL to be oxidized entirely to CH₃COCH₃ + HO₂ by OH. IC₃H₇O + O₂ produces the same products.

G4307: Analogous to G4207 for both rate coefficient and branching ratios.

G4315a: The same value as for G4107 (CH₃OOH + OH) is used, multiplied by the branching ratio of the CH₃O₂ channel.

G4343e: k for the major channel of ACETOL + OH

G4353e: .28 CH₃CHO₂CO₂H yield approximated by .14 CH₃COCO₂H + .14 CH₃CHO

G4354e: k for (CH₃)₂CCO adjusted

G4355e: k for (CH₃)₂CCO adjusted

G4400: LC₄H₉O₂ represents 0.127 NC₄H₉O₂ + 0.873 SC₄H₉O₂.

G4401: NC₄H₉O and SC₄H₉O are substituted with 2 CO₂ + C₂H₅O₂ and 0.636 MEK + HO₂ and 0.364 CH₃CHO + C₂H₅O₂, respectively. The stoichiometric coefficients on the right side are weighted averages.

G4403: The alkyl nitrate yield is the weighted average yield for the two isomers forming from NC₄H₉O₂ and SC₄H₉O₂.

G4404: The product distribution is the weighted average of the single isomer hydroperoxides. It is calculated from the rate constants of single channels and the ratio of the isomers NC₄H₉O₂ and SC₄H₉O₂. The overall rate constant for this reaction is calculated as weighted average of the channels rate constants. The relative weight of the products from NC₄H₉OOH and SC₄H₉OOH are then 0.0887 and 0.9113. The channels producing RO₂ are given the rate coefficient 0.6*k_CH3OOH_OH as for G4107. For NC₄H₉OOH the products are 0.327 NC₄H₉O₂ + 0.673 C₃H₇CHO + 0.673 OH. C₃H₇CHO is then substituted with 2 CO₂ + C₂H₅O₂. Hence, 0.327 NC₄H₉O₂ + 1.346 CO₂ + 0.673 C₂H₅O₂ + 0.673 OH. For SC₄H₉OOH the products are 0.219 SC₄H₉O₂ + 0.781 MEK + 0.781 OH.

G4406e: Lumped products from Taraborrelli et al. (2009).

G4413: LMEKO₂ represents 0.459 MEKAO₂ + 0.462 MEKB₂O + 0.079 MEKCO₂.

G4415: Alkyl nitrate formation is neglected. The products of MEKAO and MEKCO are substituted with HCHO + CO₂ + HOCH₂CH₂O₂ and HCHO + CO₂ + C₂H₅O₂.

G4416: LMEKOOH is assumed having the composition 0.459 MEKAOOH + 0.462 MEKBOOH + 0.079 MEKCOOH. MEKAOOH + OH gives 0.89 CO₂C₃CHO +

53

0.89 OH + 0.11 MEKAO2 + H₂O. CO₂C₃CHO is substituted with CH₃COCH₂O₂ + CO₂ and the products become 0.89 CH₃COCH₂O₂ + 0.89 CO₂ + 0.89 OH + 0.11 MEKAO₂ + H₂O. MEKBOOH + OH gives 0.758 BIACET + 0.758 OH + 0.242 MEKBO₂ + H₂O. MEKCOOH + OH gives 0.614 EGLYOX + 0.614 OH + 0.386 MEKCO₂ + H₂O. EGLYOX is substituted with C₂H₅O₂ + 2 CO₂ and the products become 0.614 C₂H₅O₂ + 1.228 CO₂ + 0.614 OH + 0.386 MEKCO₂ + H₂O.

G4417: The rate coefficient is the combination of the ones for the two isomers weighted by the relative abundances for NC4H9NO₃ and SC4H9NO₃, respectively. Product distribution is calculated accordingly. NC4H9NO₃ + OH gives C3H7CHO + NO₂ + H₂O with C3H7CHO being substituted with 2 CO₂ + C₂H₅O₂. After substitution is obtained 2 CO₂ + C₂H₅O₂ + NO₂ + H₂O. SC4H9NO₃ + OH gives MEK + NO₂ + H₂O. For the product distribution NC4H9NO₃ and SC4H9NO₃ account for 0.08577 and 0.91423, respectively.

G4419: The same value as for PAN is assumed.

G4420: Products are as in G4415. Only the main channels for each isomer are considered. Rate constant is the weighted average for the isomers.

G4437e: LHMVKABO₂ is a lumped species of virtual composition 0.3 HMVKAO₂ + 0.7 HMVKBO₂. The products are the weighted average for the permutation reactions of each single RO₂ in the MCM (Rickard and Pascoe, 2009).

G4439a: products are the weighted average for the decomposition of 0.3 HMVKAO + 0.7 HMVKBO.

G4440e: as for G4439a

G4441e: The rate coefficient and products are 30% for HMVKAOOH and 70% for HMVKBOOH.

G4455: CH₃COCOCO₃H assumed to photolyse quickly and give CH₃CO₃ + CO + CO₂ + OH

G4462e: EZCH₃CO₂CHCHO 90:10 mixture of the Z- and E-isomer, CH₃COCHO₂CHO → .1 CH₃CO₃ + .1 GLYOX + .9 CH₃COCHO₂CHO → .1 CH₃CO₃ + .1 GLYOX + .9 CH₃COCOCO₃ → CH₃CO₃ + .1 GLYOX + 1.8 CO + .9 HO₂; $k_{H-shift}^{1,6}$

G4463e: $k_{H-shift}^{1,6}$

G4500e: MVKO₂ substituted with HCHO + ACO₃ = 1.33 HCHO + .67 HCOCH₂O₂ + .33 CO

G4501e: coefficients from Paulot et al(2009)ACP

G4503e: $k = -3E-12^{*}.77 + 1.4E-12^{*}.23$

G4504e: $k = 1.5E-12^{*}2$.

G4505e: $k = -3E-12^{*}.46 + 1.1E-12^{*}.54$

G4506e: $k = 1.5E-12^{*}2$.

G4507e: eisopao₂ 60percent zisopao₂ 40percent, MIME species

G4508e: as for G4507e

G4509e: eisopao₂ 42percent and zisopao₂ 58percent

G4510e: as for G4509e

G4511e: $k_{H-shift}^{1,6}$

G4512e: $k_{H-shift}^{1,6}$

G4521ec: k parent alkene, branching from Rickard et al(1999)

G45222: HYBIACETOOA approximated to yield BIACETOH only, CH₃COCHO₂CHOH's main reaction with OH yields BIACETOH recycling OH → substitution with BIACETOH

G4537e: O₂NOCH₂COCH₂O₂ = NO₂ + 2 HCHO + CO₂

G4550e: LC578OOH = .6 C57OOH + .4 C58OOH

G4550et2: LC578OOH = .6 C57OOH + .4 C58OOH

G4551e: Peroxy vinyl radical chemistry neglected

G4552e: Peroxy vinyl radical chemistry neglected

G4553e: Peroxy vinyl radical chemistry neglected

G4555e: Peroxy vinyl radical chemistry neglected

G4577et3: from MIME ZC₃ODC₂3DBC₃OOH = 0.64 ZC₁ODC₂3DBC₄OOH + 0.36 ZC₁OOHC₂3DBC₄OOH, HOOCH₂COCH₂O₂ substituted with HCOCH₂OOH

G4581et8: C₁ODC₃OOHC₄OOH → C₁ODC₃ODC₄OOH → .5 CH₃CO₃ + .5 CO + .5 MGLYOX + .5 HO₂ + HOOCH₂CO₃

G4581et10: C₁ODC₃OOHC₄OOH + OH → .25 C₁ODC₃ODC₄OOH + .375 CO + .375 CH₃COCOCO₃ + .375 CO₂ + .375 HCOCOHCH₃CHO → .25(MGLYOX + 2 CO + 2 HO₂) + .375 CO + .375(CH₃CO₃ + 2 CO + HO₂) + .375 CO₂ + .375(MGLYOX + CO + 2 HO₂)

G4582e: $k_{H-shift}^{1,6}$

G4585et3: approximation H-abstraction only at C1

G4598et3: ZC₁O₃H₂C₂3DBC₄OOH 62percent G4598et4: HCOCOHCH₃CHO substituted with CH₃COCHOH + CO + HO₂

G4136: CH₃COCH₂O₂COCH₂CO₃ → CH₃CO₃ + CO₂ + 2 HCHO

G45mbo11: approximated to yield only MBOACO

G45mbo15: approx. not as in MCM!!!

G45mbo43: NO₃CH₂CO₃ = HCHO + CO₂ + NO₂ following to Paulot et al(2009)

G410apin1: H-abstraction channels neglected, branching ratios re-scaled. G410apin2: H-abstraction channels neglected, branching ratios re-scaled. G410apin3: H-abstraction channels neglected, branching ratios re-scaled.

G410apint150: endo-cyclic vinyl ROOH assumed not be formed

G410apint162: C₉20CO₃, C₁₀9CO, C₁₀9OH neglected

G410apint191: C₈11NO₃ neglected

G410apint196: C₈12OH neglected

G410apint201: C₈13OH neglected

G410apint202: C₈13NO₃ neglected

G410apint237: C₅12OH and CO₁₃C₄CHO neglected

G410apint239: C₅12NO₃ neglected

G410apint242: C₅13OH + C₅13CO neglected

G410apint277: C₃3CO is called HCOCOCO here

G410apint295: NC₁₀1CO substituted with C₉6CO₃

G410bpin: BPINBO₂ minor and similar to BPINAO₂, peroxy ring closure of BPINCO₂ is 0.6/s fast and traditional chemistry is neglected BPINCO₂=LVROO6R1O₂. G410bpint2: BPINBO₂ minor and similar to BPINAO₂, peroxy ring closure of BPINCO₂ is 0.6/s fast and traditional chemistry is neglected BPINCO₂=LVROO6R1O₂.

G410bpint14: 1,5-H-shift

G410bpint19: LVROO6R13OO formation neglected

G410bpint20: traditional reactions neglected because of complexity

G410bpint40: .167 is for the neglected lactone stemming from the dioxirane as C₈BC

G410bpint61: BPINBNO₃ produced but approximated by BPINANO₃

G410apint296: 2- and 3-CARENE together treated as the more emitted 3-CARENE, being similar to APINENE and assumed to yield the same products.

G410apint303: endo-cyclic vinyl ROOH assumed not be formed

G410myrct7: 20percent alkylnitrate yield like for APINENE

G410myrct15: $k_{H-shift}^{1,6}$

G410myrct29: $k_{H-shift}^{1,6}$

G410myrct36: $k_{H-shift}^{1,6}$

G410myrct53: k acetic acid + OH

G410myrct42: Surrogate acetaldehyde.

G410afarn: k for addition to the isoprene unit

G410afarn2: k for 2-methyl-2-butene

G410afarn3: O₃ + outer double bond k for 2-methyl-2-butene, OH-yield might be much lower

G410afarn4: O₃ + inner double bond, k for 2-methyl-2-butene, MYRCCHO approximation, OH-yield might be much lower

G410afarn5: k sum of 4-methylhexa-3,5-dienal (Baker et al., 2004) and twice 2-methyl-2-butene.

G410afarn16: $k_{H-shift}^{1,6}$

G410afarn21: k for 2-methyl-2-butene

G410afarn22: k for 2-methyl-2-butene

G410afarn23: k for addition to the isoprene unit

G410afarn24: k for 2-methyl-2-butene

G410afarn25: k of 4-methylhexa-3,5-dienal (Baker et al., 2004).

G410afarn26: k of 2-methyl-2-butene

G410afarn31: k for addition to the isoprene unit

G410afarn32: k of 2-methyl-2-butene

G410afarn37: $k_{H-shift}^{1,6}$

G410afarn43: 1.57E-10 for k was relative to k(trans-2-butene), with the new k=5.662E-11(IUPAC), k(MHO+OH) is 13percent lower

G410afarn44: .25 GLYOX + .25 CH₃COCH₂O₂ maor products of CH₃OCCH₂CHO₂CHO ox.

G410afarn52: CO₂H₃CO₃ approximation

G410afarn55: Approximation: OPACO₃ is CH₃COCH₂O₂ + SURCH₃CO₃.

Table 2: Photolysis reactions

#	labels	reaction	rate coefficient	reference
J1000	SuTrGJ	$O_2 + h\nu \rightarrow O(^3P) + O(^3P)$	jx(ip_02)	see note
J1001a	SuTrGJ	$O_3 + h\nu \rightarrow O(^1D)$	jx(ip_01D)	see note
J1001b	SuTrGJ	$O_3 + h\nu \rightarrow O(^3P)$	jx(ip_03P)	see note
J2101	SuTrGJ	$H_2O_2 + h\nu \rightarrow 2 OH$	JX(ip_H2O2)	see note
J3101	SuTrGNJ	$NO_2 + h\nu \rightarrow NO + O(^3P)$	jx(ip_N02)	see note
J3103a	SuTrGNJ	$NO_3 + h\nu \rightarrow NO_2 + O(^3P)$	jx(ip_N02O)	see note
J3103b	SuTrGNJ	$NO_3 + h\nu \rightarrow NO$	jx(ip_N002)	see note
J3104a	SuTrGNJ	$N_2O_5 + h\nu \rightarrow NO_2 + NO_3$	jx(ip_N205)	see note
J3200	TrGJ	$HONO + h\nu \rightarrow NO + OH$	JX(ip_HONO)	see note
J3201	SuTrGNJ	$HNO_3 + h\nu \rightarrow NO_2 + OH$	JX(ip_HNO3)	see note
J3202	SuTrGNJ	$HNO_4 + h\nu \rightarrow .667 NO_2 + .667 HO_2 + .333 NO_3 + .333 OH$	JX(ip_HNO4)	see note
J4100e	SuTrGJ	$CH_3OOH + h\nu \rightarrow HCHO + OH + HO_2$	1.14*jx(ip_CH300H)	see note
J4101a	SuTrGJ	$HCHO + h\nu \rightarrow H_2 + CO$	jx(ip_COH2)	see note
J4101b	SuTrGJ	$HCHO + h\nu \rightarrow H + CO + HO_2$	jx(ip_CHOH)	see note
J4104e	SuTrGJ	$HOCH_2OOH + h\nu \rightarrow OH + HO_2 + HCOOH$	1.14*jx(ip_CH300H)	see note
J4200e	TrGCJ	$C_2H_5OOH + h\nu \rightarrow CH_3CHO + HO_2 + OH$	1.14*jx(ip_CH300H)	see note
J4201	TrGCJ	$CH_3CHO + h\nu \rightarrow CH_3O_2 + HO_2 + CO$	jx(ip_CH3CHO)	see note
J4202e	TrGCJ	$CH_3C(O)OOH + h\nu \rightarrow CH_3O_2 + OH + CO_2$	1.14*jx(ip_CH3CO3H)	see note
J4204e	TrGNCJ	$PAN + h\nu \rightarrow .6 CH_3C(O)OO + .6 NO_2 + .4 CH_3O_2 + .4 CO_2 + .4 NO_3$	jx(ip_PAN)	see note
J4205ae	TrGCJ	$HOCH_2CHO + h\nu \rightarrow HCHO + 2 HO_2 + CO$	jx(ip_HOCH2CHO)*0.70	Taraborrelli (2014)
J4205be	TrGCJ	$HOCH_2CHO + h\nu \rightarrow 1.16 OH + .84 HCOCH_2O_2 + .1 HCHO + .1 CO + .06 GLYOX$	jx(ip_HOCH2CHO)*0.15	Taraborrelli (2014)
J4205ce	TrGCJ	$HOCH_2CHO + h\nu \rightarrow CH_3OH + CO$	jx(ip_HOCH2CHO)*0.15	Taraborrelli (2014)
J4206e	TrGCJ	$HOCH_2CHO + h\nu \rightarrow OH + HCHO + CO + HO_2$	1.14*jx(ip_CH300H)+jx(ip_HOCH2CHO)	Taraborrelli (2014)
J4206et2	TrGCJ	$HOCH_2CO_3H + h\nu \rightarrow HCHO + HO_2 + OH + CO_2$	1.14*jx(ip_CH300H)	Rickard and Pascoe (2009)*
J4207	TrGCJ	$PHAN + h\nu \rightarrow HOCH_2CO_3 + NO_2$	jx(ip_PAN)	see note
J4208	TrGCJ	$GLYOX + h\nu \rightarrow 2 CO + 2 HO_2$	jx(ip_GLYOX)	see note
J4209	TrGNCJ	$HCOCO_2H + h\nu \rightarrow 2 HO_2 + CO + CO_2$	jx(ip_MGLYOX)	Rickard and Pascoe (2009)*
J4210e	TrGNCJ	$HCOCO_3H + h\nu \rightarrow HO_2 + CO + OH + CO_2$	1.14*jx(ip_CH300H)+jx(ip_HOCH2CHO)	Rickard and Pascoe (2009)*

56

Table 2: Photolysis reactions (... continued)

#	labels	reaction	rate coefficient	reference
J4211e	TrGCJ	$HYETHO_2H + h\nu \rightarrow HOCH_2CH_2O + OH$	1.14*jx(ip_CH300H)	Rickard and Pascoe (2009)*
J4212	TrGCJ	$ETHOHNO_3 + h\nu \rightarrow HO_2 + 2 HCHO + NO_2$	J_IC3H7N03	see note
J4213e	TrGCJ	$HOCH_2CO_3H + h\nu \rightarrow OH + HCHO + CO_2 + OH$	2*1.14*jx(ip_CH300H)	Taraborrelli (2014)
J4214e	TrGC	$HOCH_2CO_2H + h\nu \rightarrow OH + HCHO + HO_2 + CO_2$	1.14*jx(ip_CH300H)	Taraborrelli (2014)
J4215e	TrGC	$CH_2CO + h\nu \rightarrow .4 CO_2 + .8 H + .34 CO + .34 OH + .34 HO_2 + .16 HCHO + .16 O(^3P) + .1 HCOOH + CO$	J_ketene* 0.36	Taraborrelli (2014)
J4216e	TrGC	$CH_3CHOHO_2H + h\nu \rightarrow CH_3O_2 + HCOOH + OH$	1.14*jx(ip_CH300H)	Taraborrelli (2014)
J4217e	TrGCJ	$NO_3CH_2CHO + h\nu \rightarrow HO_2 + CO + HCHO + NO_2$	1.59*J_IC3H7N03+jx(ip_CH3COCH3)	Taraborrelli (2014)
J4300e	TrGCJ	$iC_3H_7OOH + h\nu \rightarrow CH_3COCH_3 + HO_2 + OH$	1.14*jx(ip_CH300H)	von Kuhlmann (2001)*
J4301	TrGCJ	$CH_3COCH_3 + h\nu \rightarrow CH_3C(O)OO + CH_3O_2$	jx(ip_CH3COCH3)	see note
J4302	TrGCJ	$CH_3COCH_2OH + h\nu \rightarrow CH_3C(O)OO + HCHO + HO_2$	J_ACETOL	see note
J4303	TrGCJ	$MGLYOX + h\nu \rightarrow CH_3C(O)OO + CO + HO_2$	jx(ip_MGLYOX)	see note
J4304e	TrGCJ	$CH_3COCH_2O_2H + h\nu \rightarrow CH_3C(O)OO + HCHO + OH$	1.14*jx(ip_CH300H)+J_ACETOL	Taraborrelli (2014)
J4305e	TrGCJ	$HOCH_2COCH_2OOH + h\nu \rightarrow HOCH_2CO + HCHO + OH$	1.14*jx(ip_CH300H)+J_ACETOL	Taraborrelli (2014)
J4306	TrGNCJ	$iC_3H_7ONO_2 + h\nu \rightarrow CH_3COCH_3 + NO_2 + HO_2$	J_IC3H7N03	von Kuhlmann et al. (2003)*
J4307	TrGCJ	$NOA + h\nu \rightarrow CH_3C(O)OO + HCHO + NO_2$	J_IC3H7N03+jx(ip_CH3COCH3)	see note
J4309e	TrGCJ	$HYPPO_2H + h\nu \rightarrow CH_3CHO + HCHO + HO_2 + OH$	1.14*jx(ip_CH300H)	Taraborrelli (2014)
J4310e	TrGNCJ	$PR_2O_2HNO_3 + h\nu \rightarrow NOA + HO_2 + OH$	1.14*jx(ip_CH300H)	Taraborrelli (2014)
J4311e	TrGCJ	$HOCH_2COCHO + h\nu \rightarrow HOCH_2CO + CO + HO_2$	jx(ip_MGLYOX)	Taraborrelli (2014)
J4312e	TrGCJ	$CH_3COCO_2H + h\nu \rightarrow .5 CH_3CHO + .8 CO_2 + .4 CH_3C(O)OO + .3 HO_2 + .1 CH_3COOH + .1 OH + .2 CO$	JX(IP_MGLYOX)	Taraborrelli (2014)
J4313e	TrGCJ	$HCOCOCH_2OOH + h\nu \rightarrow HCOCO_3A + HCHO + OH$	1.14*jx(ip_CH300H)+J_ACETOL	Taraborrelli (2014)
J4314e	TrGCJ	$HCOCOCH_2OOH + h\nu \rightarrow HCOCH_2CO_3 + CO + HO_2$	JX(IP_MGLYOX)	Taraborrelli (2014)
J4315e	TrGCJ	$HCOCOCHO + h\nu \rightarrow HCOCO_3A + HO_2 + CO$	2*JX(IP_MGLYOX)	Taraborrelli (2014)
J4316e	TrGC	$CH_3COCO_3H + h\nu \rightarrow CH_3C(O)OO + OH + CO_2$	JX(IP_MGLYOX)+1.14*jx(ip_CH300H)	Taraborrelli (2014)
J4317e	TrGC	$CH_3CHCO + h\nu \rightarrow C_2H_4 + CO$	J_ketene*0.36*2.	Taraborrelli (2014)*
J4400e	TrGCJ	$LC_4H_9OOH + h\nu \rightarrow OH + 0.254 CO_2 + 0.5552 MEK + 0.5552 HO_2 + 0.3178 CH_3CHO + 0.4448 C_2H_5O_2$	1.14*jx(ip_CH300H)	Rickard and Pascoe (2009)*
J4401	TrGCJ	$MVK + h\nu \rightarrow C_3H_6 + CO$	jx(ip_MVK)	Taraborrelli (2014)*
J4403	TrGCJ	$MEK + h\nu \rightarrow CH_3C(O)OO + C_2H_5O_2$	0.42*jx(ip_CHOH)	von Kuhlmann et al. (2003)*

57

Table 2: Photolysis reactions (... continued)

#	labels	reaction	rate coefficient	reference
J4404e	TrGCJ	LMEKOOH + $h\nu$ → 0.538 HCHO + 0.538 CO ₂ + 0.459 HOCH ₂ CH ₂ O ₂ + 0.079 C ₂ H ₅ O ₂ + 0.462 CH ₃ C(O)OO + 0.462 CH ₃ CHO + OH	1.14*jx(ip_CH300H)+J_ACETOL	Rickard and Pascoe (2009)*
J4405	TrGCJ	BIACET + $h\nu$ → 2 CH ₃ C(O)OO	2.15*jx(ip_MGLYOX)	see note
J4406	TrGNCJ	LC4H9NO3 + $h\nu$ → NO ₂ + 0.254 CO ₂ + 0.5552 MEK + 0.5552 HO ₂ + 0.3178 CH ₃ CHO + 0.4448 C ₂ H ₅ O ₂	J_IC3H7N03	see note
J4407e	TrGNCJ	MPAN + $h\nu$ → .6 MACO3 + .6 NO ₂ + .4 MACO2 + .4 NO ₃	jx(ip_PAN)	Taraborrelli (2014)*
J4409e	TrGCJ	CO2H3CO3H + $h\nu$ → CH3COCHOH + OH + CO ₂	1.14*jx(ip_CH300H)	Taraborrelli (2014)
J4410	TrGCJ	CO2H3CO3H + $h\nu$ → CH ₃ C(O)OO + HO ₂ + HCOCO ₃ H	J_ACETOL	Rickard and Pascoe (2009)*
J4410t2	TrGCJ	CO2H3CO2H + $h\nu$ → CH ₃ C(O)OO + HCOCO ₂ H + HO ₂	J_ACETOL	Taraborrelli (2014)
J4411	TrGCJ	MACR + $h\nu$ → .5 MACO3 + .5 MACO2 + .5 CO + HO ₂	jx(ip_MACR)	see note
J4412e	TrGCJ	MACROOH + $h\nu$ → MACRO + OH	1.14*jx(ip_CH300H)+ 2.77*jx(ip_HOCH2CHO)	see note
J4414	TrGCJ	MACROH + $h\nu$ → CH ₃ COCH ₂ OH + CO + HO ₂ + HO ₂	2.77*jx(ip_HOCH2CHO)	see note
J4415e	TrGCJ	MACO3H + $h\nu$ → MACO2 + OH	1.14*jx(ip_CH300H)	Taraborrelli (2014)
J4416e	TrGCJ	LHMVKABOOH + $h\nu$ → .12 CH3COCHOH + .88 CH ₃ C(O)OO + .88 HOCH ₂ CHO + .12 HCHO + OH	1.14*jx(ip_CH300H)+J_ACETOL	Taraborrelli (2014)
J4418e	TrGCJ	CO2H3CHO + $h\nu$ → CH3COCHOH + CO + HO ₂	jx(ip_HOCH2CHO)+J_ACETOL	Taraborrelli (2014)
J4419	TrGCJ	HO12CO3C4 + $h\nu$ → CH ₃ C(O)OO + HOCH ₂ CHO + HO ₂	J_ACETOL	Rickard and Pascoe (2009)*
J4420e	TrGCJ	BIACETOH + $h\nu$ → CH ₃ C(O)OO + HOCH ₂ CO	2.15*jx(ip_MGLYOX)	Taraborrelli (2014)
J4421e	TrGC	HCOCCH3CO + $h\nu$ → .5 OH + .25 HCOCCH ₂ O ₂ + .25 CH ₃ C(O)OO + .5 CH ₃ CHO + .5 CO	J_KETENE	Taraborrelli (2014)
J4422e	TrGC	CH3COCHCO + $h\nu$ → .0192 CH3COCO2H + .1848 H ₂ O ₂ + .2208 MGLYOX + .36 OH + .36 CO + .56 CH ₃ C(O)OO + .2 CH ₃ CHO + .2 CO ₂ + .2 HCHO + .2 HO ₂	J_KETENE*0.5	Taraborrelli (2014)
J4422et2	TrGC	CH3COCHCO + $h\nu$ → CH ₃ CHO + CO	J_KETENE*0.5	Taraborrelli (2014)
J4423e	TrGCJ	CH3COCOCHO + $h\nu$ → CH ₃ C(O)OO + CO + CO + HO ₂	jx(ip_MGLYOX)	Taraborrelli (2014)
J4424e	TrGCJ	CH3COCOCHO + $h\nu$ → CH ₃ C(O)OO + HCOCO3A	2.15*jx(ip_MGLYOX)	Taraborrelli (2014)
J4424et2	TrGC	CH3COCOCO2H + $h\nu$ → CH ₃ C(O)OO + CO + CO ₂ + HO ₂	3.15*jx(ip_MGLYOX)	Taraborrelli (2014)
J4502et2	TrGCJ	LISOPACOOH + $h\nu$ → LHC4ACCHO + HO ₂ + OH	1.14*jx(ip_CH300H)	Rickard and Pascoe (2009)*
J4503et2	TrGNCJ	LISOPACNO3 + $h\nu$ → LHC4ACCHO + HO ₂ + NO ₂	0.59*J_IC3H7N03	see note

58

Table 2: Photolysis reactions (... continued)

#	labels	reaction	rate coefficient	reference
J4504e	TrGCJ	ISOPBOOH + $h\nu$ → MVK + HCHO + HO ₂ + OH	1.14*jx(ip_CH300H)	Rickard and Pascoe (2009)*
J4505e	TrGNCJ	ISOPBNO3 + $h\nu$ → MVK + HCHO + HO ₂ + NO ₂	2.84*J_IC3H7N03	see note
J4506e	TrGCJ	ISOPDOOH + $h\nu$ → MACR + HCHO + HO ₂ + OH	1.14*jx(ip_CH300H)	Rickard and Pascoe (2009)*
J4507	TrGNCJ	ISOPDNO3 + $h\nu$ → MACR + HCHO + HO ₂ + NO ₂	J_IC3H7N03	see note
J4508e	TrGNCJ	NISOPOOH + $h\nu$ → NC4CHO + HO ₂ + OH	1.14*jx(ip_CH300H)	Rickard and Pascoe (2009)*
J4509	TrGNCJ	NC4CHO + $h\nu$ → NOA + 2 CO + 2 HO ₂	jx(ip_MACR)	see note
J4510e	TrGNCJ	LNISOOH + $h\nu$ → NOA + OH + .5 HOCHCHO + .5 CO + .5 HO ₂ + .5 CO ₂	1.14*jx(ip_CH300H)	Taraborrelli et al. (2009)*
J4511e	TrGCJ	LHC4ACCHO + $h\nu$ → .5 LHC4ACCO3 + .5 HO ₂ + .5 OH + .25 MACRO2 + .25 LHMVKABO2	jx(ip_MACR)	Taraborrelli (2014)*
J4512e	TrGCJ	LC578OOH + $h\nu$ → .25 CH ₃ COCH ₂ OH + .75 MGLYOX + .25 HOCHCHO + .75 HOCH ₂ CHO + .75 HO ₂ + OH	1.14*jx(ip_CH300H)+ 2.77*jx(ip_HOCH2CHO)	Taraborrelli (2014)
J4513e	TrGCJ	LHC4ACCO3H + $h\nu$ → OH + .5 MACRO2 + .5 LHMVKABO2 + OH + CO ₂	J_HPALD	Taraborrelli (2014)*
J4514	TrGNCJ	LC5PAN1719 + $h\nu$ → .6 LHC4ACCO3 + .6 NO ₂ + .2 MACRO2 + .2 LHMVKABO2 + .4 CO ₂ + .4 NO ₃	jx(ip_PAN)	see note
J4515e	TrGCJ	HCOC5 + $h\nu$ → MACO2 + HOCH ₂ CO	0.5*jx(ip_MVK)	Taraborrelli (2014)
J4516e	TrGCJ	C59OOH + $h\nu$ → CH ₃ COCH ₂ OH + HOCH ₂ CO + OH	J_ACETOL+1.14*jx(ip_CH300H)	Taraborrelli (2014)
J4517e	TrGCJ	ZCODOC23DBCOOH + $h\nu$ → LHC4ACCO3 + OH	J_HPALD	Taraborrelli (2014)
J4518e	TrGCJ	ZCO3HC23DBCOD + $h\nu$ → .62 EZCH3CO2CHCHO + .38 EZCHOCCH3CHO2 + OH + CO ₂	J_HPALD	Taraborrelli (2014)
J4519e	TrGCJ	C10OHC20OHC4OD + $h\nu$ → CH ₃ COCH ₂ O ₂ H + OH + 2 CO + HO ₂	2.77*JX(IP_HOCH2CHO)	Taraborrelli (2014)
J4520e	TrGCJ	C10OHC20OHC4OD + $h\nu$ → .5 CH ₃ COCH ₂ O ₂ H + .5 HOCHCHO + .5 CO ₂ H ₃ CHO + .5 HCHO + 1.5 OH	2.*1.14*JX(IP_CH300H)	Taraborrelli (2014)
J4523e	TrGCJ	C10DC20OHC4OD + $h\nu$ → MGLYOX + HOCHCHO + OH	1.14*JX(IP_CH300H)	Taraborrelli (2014)
J4524e	TrGCJ	C10DC20OHC4OD + $h\nu$ → CO2H3CHO + CO + HO ₂ + OH	2.*2.77*JX(IP_HOCH2CHO)	Taraborrelli (2014)*
J4525	TrGCJ	PEROXYRINC2OOH + $h\nu$ → CH ₃ COCH ₂ OCH ₂ CHO + HO ₂ + OH	1.14*JX(IP_CH300H)	Taraborrelli (2014)
J4526	TrGCJ	PEROXYRINC2OOH + $h\nu$ → HCHO + OH + HO ₂ + CO ₂ H ₃ CHO	1.14*JX(IP_CH300H)	Taraborrelli (2014)*

59

Table 2: Photolysis reactions (... continued)

#	labels	reaction	rate coefficient	reference
J4525e	TrGCJ	ZCOCDC23DBCOD + hν → .5 CH3COCHCO + .5 HCOCCH3CO + CO + HO ₂ + OH	jx(ip_N02)*0.1*0.5	Taraborrelli (2014)
J4526e	TrGCJ	CH3COCH2OOCH2CHO + hν → CH3C(O)OO + HCHO + GLYOX + HO ₂	1.14*JX(IP_CH300H)+J_ACETOL	Taraborrelli (2014)
J4527e	TrGCJ	CH3COCH2OOCH2CHO + hν → CH3C(O)OO + HCHO + HCHO + CO + HO ₂	jx(ip_HOCH2CHO)	Taraborrelli (2014)

*Notes:

J-values are calculated with an external module and then supplied to the MECCA chemistry.

Values that originate from the Master Chemical Mechanism (MCM) by Rickard and Pascoe (2009) are translated according in the following way:

J(11) → jx(ip_CORH2)

J(12) → jx(ip_CHOH)

J(15) → jx(ip_HOCH2CHO)

J(18) → jx(ip_MACR)

J(22) → jx(ip_ACETOL)

J(23)+J(24) → jx(ip_MVK)

J(31)+J(32)+J(33) → jx(ip_GLYOX)

J(34) → jx(ip_MGLYOX)

J(41) → jx(ip_CH300H)

J(53) → J(iC₃H₇ONO₂)

J(54) → J(iC₃H₇ONO₂)

J(55) → J(iC₃H₇ONO₂)

J(56)+J(57) → jx(ip_N0A)

J4207: It is assumed that J(PHAN) is the same as J(PAN).

J4212: It is assumed that J(ETHOHNO₃) is the same as J(iC₃H₇ONO₂).

J4302: Following von Kuhlmann et al. (2003), we use J(CH₃COCH₂OH) = 0.11*jx(ip_CHOH). As an additional factor, the quantum yield of 0.65 is taken from Orlando et al. (1999a).

J4306: Following von Kuhlmann et al. (2003), we use J(iC₃H₇ONO₂) = 3.7*jx(ip_PAN).

J4307: NOA contains the chromophores of both CH₃COCH₃ and a nitrate group. It is assumed here that the J values are additive, i.e.: J(NO₃) = J(CH₃COCH₃) + J(iC₃H₇ONO₂).

J4317e: products Chong and Kistiakowsky 1964, 0.36 quantum yield at 334nm Kelley and Hase1975, factor 2 because of bigger structure and fit to C2H4.LBA

J4401: Romero et al(2005)

J4406: It is assumed that J(LC4H9NO₃) is the same as J(iC₃H₇ONO₂).

J4405: It is assumed that J(BIACET) is 2.15 times larger than J(MGLYOX), consistent with the photol-

ysis rate coefficients used in the MCM (Rickard and Pascoe, 2009).

J4414: It is assumed that J(MACROH) is 2.77 times larger than J(HOCH₂CHO), consistent with the photolysis rate coefficients used in the MCM (Rickard and Pascoe, 2009).

J4505: It is assumed that J(ISOPBNO₃) = 2.84 × J(iC₃H₇ONO₂), consistent with the photolysis rate coefficients used in the MCM (Rickard and Pascoe, 2009).

J4509: It is assumed that J(NC4CHO) is the same as J(MACR).

J4511e: Peroxy vinyl radical chemistry approximated

J4513e: Peroxy vinyl radical chemistry approximated

J4514: It is assumed that J(LC5PAN1719) is the same as J(PAN).

J4524e: the loss of C4OD is neglected

J4526: decomposition of a dialkoxy radical

References

- Atkinson, R.: Gas-phase tropospheric chemistry of volatile organic compounds: 1. Alkanes and alkenes, *J. Phys. Chem. Ref. Data*, 26, 215–290, 1997.
- Atkinson, R.: Kinetics of the gas-phase reactions of OH radicals with alkanes and cycloalkanes, *Atmos. Chem. Phys.*, 3, 2233–2307, 2003.
- Atkinson, R. and Arey, J.: Atmospheric Degradation of Volatile Organic Compounds, *Chemical Reviews*, 103(12), 4605–4638, 2003.
- Atkinson, R., Baulch, D. L., Cox, R. A., Hampson, Jr., R. F., Kerr, J. A., Rossi, M. J., and Troe, J.: Summary of evaluated kinetic and photochemical data for atmospheric chemistry: Web version August 1999, <http://www.iupac-kinetic.ch.cam.ac.uk>, 1999.
- Atkinson, R., Baulch, D. L., Cox, R. A., Crowley, J. N., Hampson, Jr., R. F., Hynes, R. G., Jenkin, M. E., Kerr, J. A., Rossi, M. J., and Troe, J.: Summary of evaluated kinetic and photochemical data for atmospheric chemistry: Web version March 2005, <http://www.iupac-kinetic.ch.cam.ac.uk>, 2005.
- Atkinson, R., Baulch, D. L., Cox, R. A., Crowley, J. N., Hampson, R. F., Hynes, R. G., Jenkin, M. E., Rossi, M. J., and Troe, J.: Evaluated kinetic and photochemical data for atmospheric chemistry: Volume II – gas phase reactions of organic species, *Atmos. Chem. Phys.*, 6, 3625–4055, 2006.
- Baeza-Romero, M. T., Glowacki, D. R., Blitz, M. A., Heard, D., Pilling, M. J., Rickard, A., and Seakins, P.: A combined experimental and theoretical study of the reaction between methylglyoxal and OH/OD radical: OH regeneration, *Phys. Chem. Chem. Phys.*, 9, 4114–4128, doi:10.1039/b702916k, 2007.
- Baker, J., Arey, J., and Atkinson, R.: Kinetics of the Gas-Phase Reactions of OH Radicals, NO₃ Radicals and O₃ with Three C₇-Carbonyls Formed From The Atmospheric Reactions of Myrcene, Ocimene and Terpinolene, *J. Atmos. Chem.*, pp. 241–260, 2004.
- Baulch, D. L., Bowman, C. T., Cobos, C., Cox, R. A., Just, T., Kerr, J. A., Pilling, M. J., Stocker, D., Troe, J., Tsang, W., Walker, R. W., and Warnatz, J.: Evaluated Kinetic Data for Combustion Modeling: Supplement II, *J. Phys. Chem. Ref. Data*, 34, 757–1397, 2005.
- Canosa-Mas, C. E., King, M. D., Lopez, R., Percival, C. J., Wayne, R. P., Shallcross, D. E., Pyle, J. A., and Daele, V.: Is the reaction between CH₃(O)O₂ and NO₃ important in the night-time troposphere?, *J. Chem. Soc. Faraday Trans.*, 92, 2211–2222, 1996.
- Capouet, M., Müller, J.-F., Ceulemans, K., Compernelle, S., Vereecken, L., and Peeters, J.: Modeling aerosol formation in alpha-pinene photo-oxidation experiments, *J. Geophys. Res.*, 8, doi:10.1029/2007JD008995, 2008.
- Christensen, L. E., Okumura, M., Sander, S. P., Salawitch, R. J., Toon, G. C., Sen, B., Blavier, J.-F., and Jucks, K. W.: Kinetics of HO₂ + HO₂ → H₂O₂ + O₂: Implications for stratospheric H₂O₂, *Geophys. Res. Lett.*, 29, doi:10.1029/2001GL014525, 2002.
- Feierabend, K. J., Zhu, L., Talukdar, R. K., and Burkholder, J. B.: Rate coefficients for the OH + HC(O)C(O)H (Glyoxal) reaction between 210 and 390 K, *J. Phys. Chem. A*, 112, 73–82, 2008.
- Fruekilde, P., Hjorth, J., Jensen, N., Kotzias, D., and Larsen, B.: Ozonolysis at vegetation surfaces: a source of acetone, 4-oxopentanal, 6-methyl-5-hepten-2-one, and geranyl acetone in the troposphere, *Atmos. Environ.*, doi:10.1016/S1352-2310(97)00485-8, 1997.
- Grosjean, E., Grosjean, D., and Seinfeld, J. H.: Gas-Phase Reaction of Ozone with Trans-2-Hexenal, Trans-2-Hexenyl Acetate, Ethylvinyl Ketone, and 6-Methyl-5-Hepten-2-One, *Int. J. Chem. Kinetics*, pp. 373–382, 1996.
- Hatakeyama, S., Honda, S., and Akimoto, H.: Rate constants and mechanism for reactions of ketenes with OH radicals in air at 299±2K, *Bull. Chem. Soc. Jpn.*, pp. 2157–2162, 1985.
- Hermans, I., Müller, J.-F., Nguyen, T. L., Jacobs, P. A., and Peeters, J.: Kinetics of α-Hydroxyalkylperoxy Radicals in Oxidation Processes. HO₂-Initiated Oxidation of Ketones/Aldehydes near the Tropopause, *J. Phys. Chem. A*, pp. 4303–4311, doi: 10.1021/jp044080v, 2005.
- Hites, R. A. and Turner, A. M.: Rate Constants for the Gas-Phase β-Myrcene+OH and Isoprene+OH Reactions as a Function of Temperature, *Int. J. Chem. Kinetics*, pp. 407–413, 2009.
- IUPAC: Evaluated Kinetic Data, <http://iupac.pole-ether.fr/>, 2013.
- Jenkin, M. E., Hurley, M. D., and Wallington, T. J.: Investigation of the radical product channel of the CH₃C(O)O₂ + HO₂ reaction in the gas phase, *Phys. Chem. Chem. Phys.*, 9, 3149–3162, doi:10.1039/b702757e, 2007.
- Kircher, C. C. and Sander, S. P.: Kinetics and mechanism of HO₂ and DO₂ disproportionations, *J. Phys. Chem.*, 88, 2082–2091, 1984.
- Lewis, P. J., Bennett, K. A., and Harvey, J. N.: A computational study of the atmospheric oxidation of

- nopinone, *Phys. Chem. Chem. Phys.*, pp. 1643–1649, doi:10.1039/b418909d, 2005.
- Lockwood, A. L., Shepson, P. B., Fiddler, M. N., and Alaghmand, M.: Isoprene nitrates: preparation, separation, identification, yields, and atmospheric chemistry, *Atmos. Chem. Phys.*, 10, 6169–6178, doi:10.5194/acp-10-6169-2010, 2010.
- McCabe, D. C., Gierczak, T., Talukdar, R. K., and Ravishankara, A. R.: Kinetics of the reaction OH + CO under atmospheric conditions, *Geophys. Res. Lett.*, 28, 3135–3138, 2001.
- Mellouki, A. and Mu, Y.: On the atmospheric degradation of pyruvic acid in the gas phase, *J. Photochem. Photobiol. A: Chem.*, doi:10.1016/S1010-6030(03)00070-4, 2003.
- Mollner, A. K., Valluvadasan, S., Feng, L., Sprague, M. K., Okumura, M., Milligan, D. B., Bloss, W. J., Sander, S. P., Martien, P. T., Harley, R. A., McCoy, A. B., and Carter, W. P. L.: Rate of Gas Phase Association of Hydroxyl Radical and Nitrogen Dioxide, *Science*, doi:10.1126/science.1193030, 2010.
- Nguyen, T. L., Peeters, J., and Vereecken, L.: Theoretical study of the gas-phase ozonolysis of β -pinene ($C_{10}H_{16}$), *Phys. Chem. Chem. Phys.*, doi:10.1039/b829284h, 2009.
- Orlando, J. J. and Tyndall, G. S.: The atmospheric chemistry of the HC(O)CO radical, *Int. J. Chem. Kinetics*, 33, 149–156, 2001.
- Orlando, J. J., Tyndall, G. S., Bilde, M., Ferronato, C., Wallington, T. J., Vereecken, L., and Peeters, J.: Laboratory and theoretical study of the oxy radicals in the OH- and Cl-initiated oxidation of ethene, *J. Phys. Chem. A*, 102, 8116–8123, 1998a.
- Orlando, J. J., Tyndall, G. S., Bilde, M., Ferronato, C., Wallington, T. J., Vereecken, L., and Peeters, J.: Laboratory and Theoretical Study of the Oxy Radicals in the OH- and Cl-Initiated Oxidation of Ethene, *J. Phys. Chem. A*, 102, 8116–8123, 1998b.
- Orlando, J. J., Tyndall, G. S., Fracheboud, J. M., Estupinan, E. G., Haberkorn, S., and Zimmer, A.: The rate and mechanism of the gas-phase oxidation of hydroxyacetone, *Atmos. Environ.*, 33, 1621–1629, 1999a.
- Orlando, J. J., Tyndall, G. S., and Paulson, S. E.: Mechanism of the OH-initiated oxidation of methacrolein, *Geophys. Res. Lett.*, 26, 1999b.
- Orlando, J. J., Noziere, B., Tyndall, G. S., Orzechowska, G. E., Paulson, S. E., and Rudich, Y.: Product studies of the OH- and ozone-initiated oxidation of some monoterpenes, *J. Geophys. Res.*, pp. 11 561–11 572, 2000.
- Orlando, J. J., Tyndall, G. S., Bertman, S. B., Chen, W., and Burkholder, J. B.: Rate coefficient for the reaction of OH with $CH_2=C(CH_3)C(O)OONO_2$ (MPAN), *Atmos. Environ.*, 36, 1895–1900, 2002.
- Paulot, F., Crouse, J. D., Kjaergaard, H. G., Kroll, J. H., Seinfeld, J. H., and Wennberg, P. O.: Isoprene photooxidation: new insights into the production of acids and organic nitrates, *Atmos. Chem. Phys.*, 9, 1479–1501, 2009a.
- Paulot, F., Crouse, J. D., Kjaergaard, H. G., Kürten, A., St. Clair, J. M., Seinfeld, J. H., and Wennberg, P. O.: Unexpected Epoxide Formation in the Gas-Phase Photooxidation of Isoprene, *Science*, 325, doi:10.1126/science.1172910, 2009b.
- Rickard, A. and Pascoe, S.: The Master Chemical Mechanism (MCM), <http://mcm.leeds.ac.uk>, 2009.
- Sander, S. P., Finlayson-Pitts, B. J., Friedl, R. R., Golden, D. M., Huie, R. E., Kolb, C. E., Kurylo, M. J., Molina, M. J., Moortgat, G. K., Orkin, V. L., and Ravishankara, A. R.: Chemical Kinetics and Photochemical Data for Use in Atmospheric Studies, Evaluation Number 14, JPL Publication 02-25, Jet Propulsion Laboratory, Pasadena, CA, 2003.
- Sander, S. P., Friedl, R. R., Golden, D. M., Kurylo, M. J., Moortgat, G. K., Keller-Rudek, H., Wine, P. H., Ravishankara, A. R., Kolb, C. E., Molina, M. J., Finlayson-Pitts, B. J., Huie, R. E., and Orkin, V. L.: Chemical Kinetics and Photochemical Data for Use in Atmospheric Studies, Evaluation Number 15, JPL Publication 06-2, Jet Propulsion Laboratory, Pasadena, CA, <http://jpldataeval.jpl.nasa.gov>, 2006.
- Sivakumaran, V., Hölscher, D., Dillon, T. J., and Crowley, J. N.: Reaction between OH and HCHO: temperature dependent rate coefficients (202–399 K) and product pathways (298 K), *Phys. Chem. Chem. Phys.*, 5, 4821–4827, 2003.
- Smith, A. M., Rigler, E., Kwok, E. S. C., and Atkinson, R.: Kinetics and Products of the Gas-Phase Reactions of 6-Methyl-5-hepten-2-one and trans-Cinnamaldehyde with OH and NO_3 Radicals and O_3 at 296(+2K), *Environ. Sci. Technol.*, pp. 1781–1785, 1996.
- Taraborrelli, D.: Isoprene Oxidation and its Impacts on the Atmospheric Composition, Ph.D. thesis, Johannes Gutenberg-Universität, Mainz, Germany, <http://d-nb.info/1003538770/34>, 2010.

- Taraborrelli, D.: Mainz Organics Mechanism, (in preparation), 2014.
- Taraborrelli, D., Lawrence, M. G., Butler, T. M., Sander, R., and Lelieveld, J.: Mainz Isoprene Mechanism 2 (MIM2): an isoprene oxidation mechanism for regional and global atmospheric modelling, *Atmos. Chem. Phys.*, 9, 2751–2777, <http://www.atmos-chem-phys.net/9/2751/2009>.
- Tyndall, G. S., Cox, R. A., Granier, C., Lesclaux, R., Moortgat, G. K., Pilling, M. J., Ravishankara, A. R., and Wallington, T. J.: The atmospheric chemistry of small organic peroxy radicals, *J. Geophys. Res.*, 106D, 12 157–12 182, 2001.
- Vereecken, L. and Peeters, J.: A theoretical study of the OH-initiated gas-phase oxidation mechanism of β -pinene ($C_{10}H_{16}$): first generation products, *Phys. Chem. Chem. Phys.*, pp. 3802–3815, doi:10.1039/c2cp23711c, 2012.
- Vereecken, L., Müller, J.-F., and Peeters, J.: Low-volatility poly-oxygenates in the OH-initiated atmospheric oxidation of α -pinene: impact of non-traditional peroxy radical chemistry, *Phys. Chem. Chem. Phys.*, 9, 5241–5248, doi:10.1039/b708023a, 2007.
- von Kuhlmann, R.: Tropospheric photochemistry of ozone, its precursors and the hydroxyl radical: A 3D-modeling study considering non-methane hydrocarbons, Ph.D. thesis, Johannes Gutenberg-Universität, Mainz, Germany, 2001.
- von Kuhlmann, R., Lawrence, M. G., Crutzen, P. J., and Rasch, P. J.: A model for studies of tropospheric ozone and nonmethane hydrocarbons: Model description and ozone results, *J. Geophys. Res.*, 108D, doi:10.1029/2002JD002893, 2003.
- Wolfe, G. M., Thornton, J. A., Bouvier-Brown, N. C., Goldstein, A. H., Park, J.-H., McKay, M., Matross, D. M., Mao, J., Brune, W. H., LaFranchi, B. W., Browne, E. C., Min, K.-E., Wooldridge, P. J., Cohen, R. C., Crouse, J. D., Faloona, I. C., Gilman, J. B., Kuster, W. C., de Gouw, J. A., Huisman, A., and Keutsch, F. N.: The Chemistry of Atmosphere-Forest Exchange (CAFE) Model Part 2: Application to BEARPEX-2007 observations, *Atmos. Chem. Phys.*, 11, 1269–1294, doi:10.5194/acp-11-1269-2011, 2011.

7.6 BIBLIOGRAPHY

Aldener, M., Brown, S. S., Stark, H., Williams, E. J., Lerner, B. M., Kuster, W. C., Goldan, P. D., Quinn, P. K., Bates, T. S., Fehsenfeld, F. C., and Ravishankara, A. R.: Reactivity and loss mechanisms of NO_3 and N_2O_5 in a polluted marine environment: Results from in situ measurements during New England Air Quality Study 2002, *J Geophys Res-Atmos*, 111, ArtID23s73
Doi 10.1029/2006jd007252, 2006.

Andrés-Hernández, M. D., Burkert, J., Reichert, L., Stöbener, D., Meyer-Arneke, J., Burrows, J. P., Dickerson, R. R., and Doddridge, B. G.: Marine boundary layer peroxy radical chemistry during the AEROSOLS99 campaign: Measurements and analysis, *Journal of Geophysical Research*, 106, 20833, 10.1029/2001jd900113, 2001.

Atkinson, R., Baulch, D. L., Cox, R. A., Crowley, J. N., Hampson, R. F., Hynes, R. G., Jenkin, M. E., Rossi, M. J., and Troe, J.: Evaluated kinetic and photochemical data for atmospheric chemistry: Volume I - gas phase reactions of O_x , HO_x , NO_x and SO_x species, *Atmos Chem Phys*, 4, 1461-1738, 2004.

Atkinson, R., Baulch, D. L., Cox, R. A., Crowley, J. N., Hampson, R. F., Hynes, R. G., Jenkin, M. E., Rossi, M. J., and Troe, J.: Evaluated kinetic and photochemical data for atmospheric chemistry: Volume II - gas phase reactions of organic species, *Atmos Chem Phys*, 6, 3625-4055, 2006.

Avnery, S., Mauzerall, D. L., Liu, J. F., and Horowitz, L. W.: Global crop yield reductions due to surface ozone exposure: 1. Year 2000 crop production losses and economic damage, *Atmos Environ*, 45, 2284-2296, DOI 10.1016/j.atmosenv.2010.11.045, 2011a.

Avnery, S., Mauzerall, D. L., Liu, J. F., and Horowitz, L. W.: Global crop yield reductions due to surface ozone exposure: 2. Year 2030 potential crop production losses and economic damage under two scenarios of O_3 pollution, *Atmos Environ*, 45, 2297-2309, DOI 10.1016/j.atmosenv.2011.01.002, 2011b.

Bakwin, P. S., Jacob, D. J., Wofsy, S. C., Munger, J. W., Daube, B. C., Bradshaw, J. D., Sandholm, S. T., Talbot, R. W., Singh, H. B., Gregory, G. L., and Blake, D. R.: Reactive Nitrogen-Oxides and Ozone above a Taiga Woodland, *J Geophys Res-Atmos*, 99, 1927-1936, Doi 10.1029/93jd02292, 1994.

Beaver, M. R., St Clair, J. M., Paulot, F., Spencer, K. M., Crouse, J. D., LaFranchi, B. W., Min, K. E., Pusede, S. E., Wooldridge, P. J., Schade, G. W., Park, C., Cohen, R. C., and Wennberg, P. O.: Importance of biogenic precursors to the budget of organic nitrates: observations of multifunctional organic nitrates by CIMS and TD-LIF during BEARPEX 2009, *Atmos Chem Phys*, 12, 5773-5785, DOI 10.5194/acp-12-5773-2012, 2012.

Bekooy, J. P., Meerts, W. L., and Dymanus, A.: High-Resolution Laser-rf Spectroscopy on the $A^2\Pi_{3/2}-X^2\Pi_{3/2}$ System of Iodine Oxide (IO), *J Mol Spectrosc*, 102, 320-343, Doi 10.1016/0022-2852(83)90044-9, 1983.

Bloss, W. J., Rowley, D. M., Cox, R. A., and Jones, R. L.: Kinetics and products of the IO self-reaction, *J Phys Chem A*, 105, 7840-7854, Doi 10.1021/Jp0044936, 2001.

Bohn, B., Corlett, G. K., Gillmann, M., Sanghavi, S., Stange, G., Tensing, E., Vrekoussis, M., Bloss, W. J., Clapp, L. J., Kortner, M., Dorn, H. P., Monks, P. S., Platt, U., Plass-Dülmer, C., Mihalopoulos, N., Heard, D. E., Clemitshaw, K. C., Meixner, F. X., Prevot, A. S. H., and Schmitt, R.: *Photolysis frequency measurement techniques: results of a comparison within the ACCENT project*, *Atmos. Chem. Phys.*, 8, 5373-5391, 10.5194/acp-8-5373-2008, 2008.

Bonn, B., Bourtsoukidis, E., Sun, T. S., Bingemer, H., Rondo, L., Javed, U., Li, J., Axinte, R., Li, X., Brauers, T., Sonderfeld, H., Koppmann, R., Sogachev, A., Jacobi, S., and Spracklen, D. V.: *The link between atmospheric radicals and newly formed particles at a spruce forest site in Germany*, *Atmos. Chem. Phys. Discuss.*, 13, 27501-27560, 10.5194/acpd-13-27501-2013, 2013.

Bourtsoukidis, E., Bonn, B., Dittmann, A., Hakola, H., Hellen, H., and Jacobi, S.: *Ozone stress as a driving force of sesquiterpene emissions: a suggested parameterisation*, *Biogeosciences*, 9, 4337-4352, DOI 10.5194/bg-9-4337-2012, 2012.

Bourtsoukidis, E., Williams, J., Kesselmeier, J., Jacobi, S., and Bonn, B.: *From emissions to ambient mixing ratios: online seasonal field measurements of volatile organic compounds over a Norway spruce-dominated forest in central Germany*, *Atmos. Chem. Phys.*, 14, 6495-6510, 10.5194/acp-14-6495-2014, 2014.

Bradshaw, J., Davis, D., Crawford, J., Chen, G., Shetter, R., Muller, M., Gregory, G., Sachse, G., Blake, D., Heikes, B., Singh, H., Mastromarino, J., and Sandholm, S.: *Photofragmentation two-photon laser-induced fluorescence detection of NO₂ and NO: Comparison of measurements with model results based on airborne observations during PEM-Tropics A*, *Geophys Res Lett*, 26, 471-474, Doi 10.1029/1999gl900015, 1999.

Brasseur, G., Orlando, J. J., Tyndall, G. S., and National Center for Atmospheric Research (U.S.): *Atmospheric chemistry and global change*, *Topics in environmental chemistry*, Oxford University Press, New York, xviii, 654 p. pp., 1999.

Brown, S. S., Stark, H., Ciciora, S. J., and Ravishankara, A. R.: *In-situ measurement of atmospheric NO₃ and N₂O₅ via cavity ring-down spectroscopy*, *Geophys Res Lett*, 28, 3227-3230, Doi 10.1029/2001gl013303, 2001.

Browne, E. C., and Cohen, R. C.: *Effects of biogenic nitrate chemistry on the NO_x lifetime in remote continental regions*, *Atmos Chem Phys*, 12, 11917-11932, DOI 10.5194/acp-12-11917-2012, 2012.

Burkert, J., Behmann, T., Andrés Hernández, M. D., Stöbener, D., Weißenmayer, M., Perner, D., and Burrows, J. P.: *Measurements of peroxy radicals in a forested area of Portugal*, *Chemosphere - Global Change Science*, 3, 327-338, [http://dx.doi.org/10.1016/S1465-9972\(01\)00014-9](http://dx.doi.org/10.1016/S1465-9972(01)00014-9), 2001.

Burkholder, J. B., Talukdar, R. K., Ravishankara, A. R., and Solomon, S.: *Temperature-Dependence of the HNO₃ UV Absorption Cross-Sections*, *J Geophys Res-Atmos*, 98, 22937-22948, Doi 10.1029/93jd02178, 1993.

Butkovskaya, N., Kukui, A., and Le Bras, G.: *Pressure and Temperature Dependence of Methyl Nitrate Formation in the CH₃O₂+NO Reaction*, *J Phys Chem A*, 116, 5972-5980, Doi 10.1021/Jp210710d, 2012.

Cadle, R. D., and Johnston, H. S.: *Chemical reactions in Los Angeles smog, 2nd Proceedings of the National Air Pollution Symposium, 1952.*

Calvert, J. G.: *Test of Theory of Ozone Generation in Los-Angeles Atmosphere, Environ Sci Technol, 10, 248-256, Doi 10.1021/Es60114a002, 1976.*

Calvert, J. G., and Stockwell, W. R.: *Deviations from the O₃-NO-NO₂ Photostationary State in Tropospheric Chemistry, Can J Chem, 61, 983-992, Doi 10.1139/V83-174, 1983.*

Cantrell, C. A., Shetter, R. E., Calvert, J. G., Parrish, D. D., Fehsenfeld, F. C., Goldan, P. D., Kuster, W., Williams, E. J., Westberg, H. H., Allwine, G., and Martin, R.: *Peroxy-Radicals as Measured in Rose and Estimated from Photostationary State Deviations, J Geophys Res-Atmos, 98, 18355-18366, Doi 10.1029/93jd01794, 1993.*

Cantrell, C. A., Shetter, R. E., Gilpin, T. M., and Calvert, J. G.: *Peroxy radicals measured during Mauna Loa observatory photochemistry experiment 2: The data and first analysis, J Geophys Res-Atmos, 101, 14643-14652, Doi 10.1029/95jd01698, 1996.*

Cantrell, C. A., Shetter, R. E., Calvert, J. G., Eisele, F. L., Williams, E., Baumann, K., Brune, W. H., Stevens, P. S., and Mather, J. H.: *Peroxy radicals from photostationary state deviations and steady state calculations during the Tropospheric OH Photochemistry Experiment at Idaho Hill, Colorado, 1993, J Geophys Res-Atmos, 102, 6369-6378, Doi 10.1029/96jd01703, 1997.*

Cantrell, C. A., Mauldin, L., Zondlo, M., Eisele, F., Kosciuch, E., Shetter, R., Lefer, B., Hall, S., Campos, T., Ridley, B., Walega, J., Fried, A., Wert, B., Flocke, F., Weinheimer, A., Hannigan, J., Coffey, M., Atlas, E., Stephens, S., Heikes, B., Snow, J., Blake, D., Blake, N., Katzenstein, A., Lopez, J., Browell, E. V., Dibb, J., Scheuer, E., Seid, G., and Talbot, R.: *Steady state free radical budgets and ozone photochemistry during TOPSE, J Geophys Res-Atmos, 108, Artn 8361 Doi 10.1029/2002jd002198, 2003.*

Cantrell, C. A.: *Technical Note: Review of methods for linear least-squares fitting of data and application to atmospheric chemistry problems, Atmos Chem Phys, 8, 5477-5487, 2008.*

Carpenter, L. J., Monks, P. S., Bandy, B. J., Penkett, S. A., Galbally, I. E., and Meyer, C. P.: *A study of peroxy radicals and ozone photochemistry at coastal sites in the northern and southern hemispheres, J Geophys Res-Atmos, 102, 25417-25427, Doi 10.1029/97jd02242, 1997.*

Carpenter, L. J., Clemitshaw, K. C., Burgess, R. A., Penkett, S. A., Cape, J. N., and McFadyen, G. C.: *Investigation and evaluation of the NO_x/O₃ photochemical steady state, Atmos Environ, 32, 3353-3365, Doi 10.1016/S1352-2310(97)00416-0, 1998.*

Chameides, W., and Walker, J. C. G.: *Photochemical Theory of Tropospheric Ozone, Journal of Geophysical Research, 78, 8751-8760, Doi 10.1029/Jc078i036p08751, 1973.*

Chameides, W. L., Davis, D. D., Bradshaw, J., Sandholm, S., Rodgers, M., Baum, B., Ridley, B., Madronich, S., Carroll, M. A., Gregory, G., Schiff, H. I., Hastie, D. R., Torres, A., and Condon, E.: *Observed and Model-Calculated No₂/No Ratios in Tropospheric Air Sampled during the Nasa Gte/Cite-2 Field-Study, J Geophys Res-Atmos, 95, 10235-10247, Doi 10.1029/Jd095id07p10235, 1990.*

- Chan, K. L., Pohler, D., Kuhlmann, G., Hartl, A., Platt, U., and Wenig, M. O.: *NO₂ measurements in Hong Kong using LED based long path differential optical absorption spectroscopy*, *Atmospheric Measurement Techniques*, 5, 901-912, DOI 10.5194/amt-5-901-2012, 2012.
- Chatfield, R. B., and Crutzen, P. J.: *Are There Interactions of Iodine and Sulfur Species in Marine Air Photochemistry*, *J Geophys Res-Atmos*, 95, 22319-22341, Doi 10.1029/Jd095id13p22319, 1990.
- Cicerone, R. J.: *Halogens in the Atmosphere*, *Rev Geophys*, 19, 123-139, Doi 10.1029/Rg019i001p00123, 1981.
- Clapp, L. J., and Jenkin, M. E.: *Analysis of the relationship between ambient levels Of O₃, NO₂ and NO as a function of NO chi in the UK*, *Atmos Environ*, 35, 6391-6405, Doi 10.1016/S1352-2310(01)00378-8, 2001.
- Cleary, P. A., Wooldridge, P. J., and Cohen, R. C.: *Laser-induced fluorescence detection of atmospheric NO₂ with a commercial diode laser and a supersonic expansion*, *Appl Optics*, 41, 6950-6956, Doi 10.1364/Ao.41.006950, 2002.
- Commane, R., Seitz, K., Bale, C. S. E., Bloss, W. J., Buxmann, J., Ingham, T., Platt, U., Pohler, D., and Heard, D. E.: *Iodine monoxide at a clean marine coastal site: observations of high frequency variations and inhomogeneous distributions*, *Atmos Chem Phys*, 11, 6721-6733, DOI 10.5194/acp-11-6721-2011, 2011.
- Crawford, J., Davis, D., Chen, G., Bradshaw, J., Sandholm, S., Gregory, G., Sachse, G., Anderson, B., Collins, J., Blake, D., Singh, H., Heikes, B., Talbot, R., and Rodriguez, J.: *Photostationary state analysis of the NO₂-NO system based on airborne observations from the western and central North Pacific*, *J Geophys Res-Atmos*, 101, 2053-2072, Doi 10.1029/95jd02201, 1996.
- Crowley, J. N., Schuster, G., Pouvesle, N., Parchatka, U., Fischer, H., Bonn, B., Bingemer, H., and Lelieveld, J.: *Nocturnal nitrogen oxides at a rural mountain-site in south-western Germany*, *Atmos Chem Phys*, 10, 2795-2812, 2010.
- Crutzen, P. J.: *Role of NO and NO₂ in the Chemistry of the Troposphere and Stratosphere*, *Annu Rev Earth Pl Sc*, 7, 443-472, DOI 10.1146/annurev.ea.07.050179.002303, 1979.
- Crutzen, P. J., Lawrence, M. G., and Poschl, U.: *On the background photochemistry of tropospheric ozone*, *Tellus A*, 51, 123-146, DOI 10.1034/j.1600-0889.1999.00010.x, 1999.
- Dari-Salisburgo, C., Di Carlo, P., Giammaria, F., Kajii, Y., and D'Altorio, A.: *Laser induced fluorescence instrument for NO₂ measurements: Observations at a central Italy background site*, *Atmos Environ*, 43, 970-977, 10.1016/j.atmosenv.2008.10.037, 2009.
- Davis, D. D., Chen, G., Chameides, W., Bradshaw, J., Sandholm, S., Rodgers, M., Schendal, J., Madronich, S., Sachse, G., Gregory, G., Anderson, B., Barrick, J., Shipham, M., Collins, J., Wade, L., and Blake, D.: *A Photostationary State Analysis of the NO₂-NO System Based on Airborne Observations from the Subtropical Tropical North and South-Atlantic*, *J Geophys Res-Atmos*, 98, 23501-23523, Doi 10.1029/93jd02412, 1993.

Day, D. A., Wooldridge, P. J., Dillon, M. B., Thornton, J. A., and Cohen, R. C.: A thermal dissociation laser-induced fluorescence instrument for in situ detection of NO₂, peroxy nitrates, alkyl nitrates, and HNO₃, *J Geophys Res-Atmos*, 107, Artn 4046
Doi 10.1029/2001jd000779, 2002.

Day, D. A., Farmer, D. K., Goldstein, A. H., Wooldridge, P. J., Minejima, C., and Cohen, R. C.: Observations of NO_x, Σ PNs, Σ ANs, and HNO₃ at a Rural Site in the California Sierra Nevada Mountains: summertime diurnal cycles, *Atmos Chem Phys*, 9, 4879-4896, 2009.

Dix, B., Baidara, S., Bresch, J. F., Hall, S. R., Schmidt, K. S., Wang, S. Y., and Volkamer, R.: Detection of iodine monoxide in the tropical free troposphere, *P Natl Acad Sci USA*, 110, 2035-2040, DOI 10.1073/pnas.1212386110, 2013.

Draxler, R. R., and Hess, G. D.: An overview of the HYSPLIT_4 modelling system for trajectories, dispersion and deposition, *Aust Meteorol Mag*, 47, 295-308, 1998.

Droppo, J. G.: Concurrent Measurements of Ozone Dry Deposition Using Eddy-Correlation and Profile Flux-Methods, *J Geophys Res-Atmos*, 90, 2111-2118, Doi 10.1029/Jd090id01p02111, 1985.

Duenas, C., Fernandez, M. C., Canete, S., Carretero, J., and Liger, E.: Assessment of ozone variations and meteorological effects in an urban area in the Mediterranean Coast, *Sci Total Environ*, 299, 97-113, Pii S0048-9697(02)00251-6
Doi 10.1016/S0048-9697(02)00251-6, 2002.

Durka, W., Schulze, E. D., Gebauer, G., and Voerkelius, S.: Effects of Forest Decline on Uptake and Leaching of Deposited Nitrate Determined from ¹⁵N and ¹⁸O Measurements, *Nature*, 372, 765-767, Doi 10.1038/372765a0, 1994.

Ehhalt, D. H., Rohrer, F., and Wahner, A.: Sources and distribution of NO_x in the upper troposphere at northern mid-latitudes *Journal of Geophysical Research: Atmospheres (1984-2012) Volume 97, Issue D4, Journal of Geophysical Research: Atmospheres (1984-2012)*, 97, 3725-3738, 1992.

Evans, M. J., Shallcross, D. E., Law, K. S., Wild, J. O. F., Simmonds, P. G., Spain, T. G., Berrisford, P., Methven, J., Lewis, A. C., McQuaid, J. B., Pilling, M. J., Bandy, B. J., Penkett, S. A., and Pyle, J. A.: Evaluation of a Lagrangian box model using field measurements from EASE (Eastern Atlantic Summer Experiment) 1996, *Atmos Environ*, 34, 3843-3863, Doi 10.1016/S1352-2310(00)00184-9, 2000.

FAO: *Global Forest Resources Assessment 2010*, FAO forestry paper, 163, Food and Agriculture Organization of the United Nations, Rome, xxxi, 340 p. pp., 2010.

Farmer, D. K., Perring, A. E., Wooldridge, P. J., Blake, D. R., Baker, A., Meinardi, S., Huey, L. G., Tanner, D., Vargas, O., and Cohen, R. C.: Impact of organic nitrates on urban ozone production, *Atmos Chem Phys*, 11, 4085-4094, 10.5194/acp-11-4085-2011, 2011.

Finlayson-Pitts, B. J., and Pitts, J. N.: *Chemistry of the upper and lower atmosphere : theory, experiments, and applications*, Academic Press, San Diego, xxii, 969 p. pp., 2000.

Fleming, Z. L., Monks, P. S., Rickard, A. R., Bandy, B. J., Brough, N., Green, T. J., Reeves, C. E., and Penkett, S. A.: *Seasonal dependence of peroxy radical concentrations at a Northern hemisphere marine boundary layer site during summer and winter: evidence for radical activity in winter*, *Atmos Chem Phys*, 6, 5415-5433, 2006.

Fong, C., and Brune, W. H.: *A laser induced fluorescence instrument for measuring tropospheric NO₂*, *Review of Scientific Instruments*, 68, 4253, 10.1063/1.1148384, 1997.

Fontijn, A., Sabadell, A. J., and Ronco, R. J.: *Homogeneous Chemiluminescent Measurement of Nitric Oxide with Ozone - Implications for Continuous Selective Monitoring of Gaseous Air Pollutants*, *Anal Chem*, 42, 575-579, Doi 10.1021/Ac60288a034, 1970.

Ge, B. Z., Sun, Y. L., Liu, Y., Dong, H. B., Ji, D. S., Jiang, Q., Li, J., and Wang, Z. F.: *Nitrogen dioxide measurement by cavity attenuated phase shift spectroscopy (CAPS) and implications in ozone production efficiency and nitrate formation in Beijing, China*, *J Geophys Res-Atmos*, 118, 9499-9509, Doi 10.1002/Jgrd.50757, 2013.

George, L. A., and O'Brien, R. J.: *Prototype Fage Determination of NO₂*, *Journal of Atmospheric Chemistry*, 12, 195-209, Doi 10.1007/Bf00048073, 1991.

Ghosh, B., Papanastasiou, D. K., Talukdar, R. K., Roberts, J. M., and Burkholder, J. B.: *Nitryl Chloride (ClNO₂): UV/Vis Absorption Spectrum between 210 and 296 K and O(P-3) Quantum Yield at 193 and 248 nm*, *J Phys Chem A*, 116, 5796-5805, Doi 10.1021/Jp207389y, 2012.

Griffin, R. J., Beckman, P. J., Talbot, R. W., Sive, B. C., and Varner, R. K.: *Deviations from ozone photostationary state during the International Consortium for Atmospheric Research on Transport and Transformation 2004 campaign: Use of measurements and photochemical modeling to assess potential causes*, *Journal of Geophysical Research*, 112, 10.1029/2006jd007604, 2007.

Gros, V., Poisson, N., Martin, D., Kanakidou, M., and Bonsang, B.: *Observations and modeling of the seasonal variation of surface ozone at Amsterdam Island: 1994-1996*, *J Geophys Res-Atmos*, 103, 28103-28109, Doi 10.1029/98jd02458, 1998.

Groß, C. B. M.: *Kinetische Studien zur OH-Bildung über die Reaktionen von HO₂ mit organischen Peroxyradikalen*, Johannes Gutenberg-Universität, Mainz, 2013.

Guenther, A., Hewitt, C. N., Erickson, D., Fall, R., Geron, C., Graedel, T., Harley, P., Klinger, L., Lerdau, M., McKay, W. A., Pierce, T., Scholes, B., Steinbrecher, R., Tallamraju, R., Taylor, J., and Zimmerman, P.: *A Global-Model of Natural Volatile Organic-Compound Emissions*, *J Geophys Res-Atmos*, 100, 8873-8892, Doi 10.1029/94jd02950, 1995.

Handisides, G. M.: *The Influence of Peroxy Radicals on Ozone Production*, Doktorgrades der Naturwissenschaften, Fachbereich Geowissenschaften Johann Wolfgang Goethe-Universität Frankfurt am Main 273 pp., 2001.

Harder, H.: *Messungen von Stickoxiden in der Bretange: Ein Beitrag zur Ozonbilanz*, Fakultät für Physik und Astronomie, Ruprecht-Karls-Universität Heidelberg, 77 pp., 1994.

Hargrove, J., Wang, L. M., Muyskens, K., Muyskens, M., Medina, D., Zaide, S., and Zhang, J. S.: Cavity ring-down spectroscopy of ambient NO_2 with quantification and elimination of interferences, *Environ Sci Technol*, 40, 7868-7873, Doi 10.1021/Es061287o, 2006.

Hari, P., and Kulmala, M.: Station for measuring ecosystem-atmosphere relations (SMEAR II), *Boreal Environ Res*, 10, 315-322, 2005.

Harrop, D. O.: *Air quality assessment and management : a practical guide*, Clay's library of health and the environment, Spon Press, London ; New York, xii, 384 p. pp., 2002.

Harwood, M. H., Jones, R. L., Cox, R. A., Lutman, E., and Rattigan, O. V.: Temperature-Dependent Absorption Cross-Sections of N_2O_5 , *J Photoch Photobio A*, 73, 167-175, Doi 10.1016/1010-6030(93)90001-2, 1993.

Harwood, M. H., Burkholder, J. B., Hunter, M., Fox, R. W., and Ravishankara, A. R.: Absorption cross sections and self-reaction kinetics of the IO radical, *J Phys Chem A*, 101, 853-863, Doi 10.1021/Jp962429b, 1997.

Hauglustaine, D. A., Madronich, S., Ridley, B. A., Walega, J. G., Cantrell, C. A., Shetter, R. E., and Hubler, G.: Observed and model-calculated photostationary state at Mauna Loa observatory during MLOPEX 2, *J Geophys Res-Atmos*, 101, 14681-14696, Doi 10.1029/95jd03612, 1996.

Hens, K., Novelli, A., Martinez, M., Auld, J., Axinte, R., Bohn, B., Fischer, H., Keronen, P., Kubistin, D., Nölscher, A. C., Oswald, R., Paasonen, P., Petäjä, T., Regelin, E., Sander, R., Sinha, V., Sipilä, M., Taraborrelli, D., Tatum Ernest, C., Williams, J., Lelieveld, J., and Harder, H.: Observation and modelling of HO_x radicals in a boreal forest, *Atmos. Chem. Phys. Discuss.*, 13, 28561-28629, 10.5194/acpd-13-28561-2013, 2013.

Herndon, S. C., Shorter, J. H., Zahniser, M. S., Nelson, D. D., Jayne, J., Brown, R. C., Miake-Lye, R. C., Waitz, I., Silva, P., Lanni, T., Demerjian, K., and Kolb, C. E.: NO and NO_2 emission ratios measured from in-use commercial aircraft during taxi and takeoff, *Environ Sci Technol*, 38, 6078-6084, Doi 10.1021/Es049701c, 2004.

Herriott, D., Kompfner, R., and Kogelnik, H.: Off-Axis Paths in Spherical Mirror Interferometers, *Appl Optics*, 3, 523-&, Doi 10.1364/Ao.3.000523, 1964.

Holland, P. W., and Welsch, R. E.: Robust Regression Using Iteratively Re-Weighted Least-Squares, *Commun Stat a-Theor*, 6, 813-827, Doi 10.1080/03610927708827533, 1977.

Hosaynali Beygi, Z.: *Oxidation photochemistry in the remote marine boundary layer*, Doktor der Naturwissenschaften, Max Planck Institute for Chemistry, Johannes Gutenberg-Universitaet in Mainz, Germany, International Max Planck Research School, 2010.

Hosaynali Beygi, Z., Fischer, H., Harder, H. D., Martinez, M., Sander, R., Williams, J., Brookes, D. M., Monks, P. S., and Lelieveld, J.: Oxidation photochemistry in the Southern Atlantic boundary layer: unexpected deviations of photochemical steady state, *Atmos. Chem. Phys.*, 11, 8497-8513, 10.5194/acp-11-8497-2011, 2011.

Jenkin, M. E., Saunders, S. M., and Pilling, M. J.: The tropospheric degradation of volatile organic compounds: A protocol for mechanism development, *Atmos Environ*, 31, 81-104, Doi

10.1016/S1352-2310(96)00105-7 (MCM v3.2, via website: <http://mcm.leeds.ac.uk/MCM>), 1997.

Jenkin, M. E., Andersen, M. P. S., Hurley, M. D., Wallington, T. J., Taketani, F., and Matsumi, Y.: A kinetics and mechanistic study of the OH and NO₂ initiated oxidation of cyclohexa-1,3-diene in the gas phase, *Physical Chemistry Chemical Physics*, 7, 1194-1204, Doi 10.1039/B417525c, 2005.

Johnston, H. S., Davis, H. F., and Lee, Y. T.: NO₃ photolysis product channels: Quantum yields from observed energy thresholds, *J Phys Chem-US*, 100, 4713-4723, Doi 10.1021/Jp952692x, 1996.

Keller-Rudek, H., Moortgat, G. K., Sander, R., and Sørensen, R.: The MPI-Mainz UV/VIS Spectral Atlas of Gaseous Molecules of Atmospheric Interest, *Earth Syst. Sci. Data*, 5, 365-373, 10.5194/essd-5-365-2013, 2013.

Kelly, T. J., Stedman, D. H., Ritter, J. A., and Harvey, R. B.: Measurements of Oxides of Nitrogen and Nitric-Acid in Clean-Air, *J Geophys Res-Oc Atm*, 85, 7417-7425, Doi 10.1029/Jc085ic12p07417, 1980.

Kleinman, L., Lee, Y. N., Springston, S. R., Lee, J. H., Nunnermacker, L., Weinsteinlloyd, J., Zhou, X. L., and Newman, L.: Peroxy Radical Concentration and Ozone Formation Rate at a Rural Site in the Southeastern United-States, *J Geophys Res-Atmos*, 100, 7263-7273, Doi 10.1029/95jd00215, 1995.

Kleinman, L. I.: The dependence of tropospheric ozone production rate on ozone precursors, *Atmos Environ*, 39, 575-586, DOI 10.1016/j.atmosenv.2004.08.047, 2005.

Kurtenbach, R., Kleffmann, J., Niedojadlo, A., and Wiesen, P.: Primary NO₂ emissions and their impact on air quality in traffic environments in Germany, *Environmental Sciences Europe*, 24, 21, 10.1186/2190-4715-24-21, 2012.

Land, D. V., Levick, A. P., and Hand, J. W.: The use of the Allan deviation for the measurement of the noise and drift performance of microwave radiometers, *Measurement Science and Technology*, 18, 1917-1928, 10.1088/0957-0233/18/7/018, 2007.

Leighton, P. A.: *Photochemistry of air pollution*, Physical chemistry,, 9, Academic Press, New York,, 300 p. pp., 1961.

Lelieveld, J., and Crutzen, P. J.: Influences of Cloud Photochemical Processes on Tropospheric Ozone, *Nature*, 343, 227-233, Doi 10.1038/343227a0, 1990.

Lelieveld, J., and Dentener, F. J.: What controls tropospheric ozone?, *J Geophys Res-Atmos*, 105, 3531-3551, Doi 10.1029/1999jd901011, 2000.

Lelieveld, J., van Aardenne, J., Fischer, H., de Reus, M., Williams, J., and Winkler, P.: Increasing ozone over the Atlantic Ocean, *Science*, 304, 1483-1487, DOI 10.1126/science.1096777, 2004.

Lelieveld, J.: ATMOSPHERIC CHEMISTRY A missing sink for radicals, *Nature*, 466, 925-926, Doi 10.1038/466925a, 2010.

Lelieveld, J., Barlas, C., Giannadaki, D., and Pozzer, A.: Model calculated global, regional and megacity premature mortality due to air pollution, *Atmos Chem Phys*, 13, 7023-7037, DOI 10.5194/acp-13-7023-2013, 2013.

Lenner, M.: Nitrogen-Dioxide in Exhaust Emissions from Motor-Vehicles, *Atmos Environ*, 21, 37-43, Doi 10.1016/0004-6981(87)90268-X, 1987.

Levy, H.: Normal Atmosphere - Large Radical and Formaldehyde Concentrations Predicted, *Science*, 173, 141-&, DOI 10.1126/science.173.3992.141, 1971.

Levy, H.: Photochemistry of Lower Troposphere, *Planet Space Sci*, 20, 919-&, Doi 10.1016/0032-0633(72)90177-8, 1972.

Li, J., Parchatka, U., Königstedt, R., and Fischer, H.: Real-time measurements of atmospheric CO using a continuous-wave room temperature quantum cascade laser based spectrometer, *Opt Express*, 20, 7590-7601, 10.1364/OE.20.007590, 2012.

Liu, S. C., Trainer, M., Fehsenfeld, F. C., Parrish, D. D., Williams, E. J., Fahey, D. W., Hubler, G., and Murphy, P. C.: Ozone Production in the Rural Troposphere and the Implications for Regional and Global Ozone Distributions, *J Geophys Res-Atmos*, 92, 4191-4207, Doi 10.1029/Jd092id04p04191, 1987.

Logan, J. A.: Nitrogen-Oxides in the Troposphere - Global and Regional Budgets, *J Geophys Res-Oc Atm*, 88, 785-807, Doi 10.1029/Jc088ic15p10785, 1983.

Logan, J. A.: Tropospheric Ozone - Seasonal Behavior, Trends, and Anthropogenic Influence, *J Geophys Res-Atmos*, 90, 10463-10482, Doi 10.1029/Jd090id06p10463, 1985.

Mannschreck, K., Gilge, S., Plass-Duelmer, C., Fricke, W., and Berresheim, H.: Assessment of the applicability of NO-NO₂-O₃ photostationary state to long-term measurements at the Hohenpeissenberg GAW Station, Germany, *Atmos Chem Phys*, 4, 1265-1277, 2004.

Martinez, M., Harder, H., Kovacs, T. A., Simpas, J. B., Bassis, J., Leshner, R., Brune, W. H., Frost, G. J., Williams, E. J., Stroud, C. A., Jobson, B. T., Roberts, J. M., Hall, S. R., Shetter, R. E., Wert, B., Fried, A., Alicke, B., Stutz, J., Young, V. L., White, A. B., and Zamora, R. J.: OH and HO₂ concentrations, sources, and loss rates during the Southern Oxidants Study in Nashville, Tennessee, summer 1999, *J Geophys Res-Atmos*, 108, Artn 4617 Doi 10.1029/2003jd003551, 2003.

Martinez, M., Harder, H., Kubistin, D., Rudolf, M., Bozem, H., Eerdeken, G., Fischer, H., Klupfel, T., Gurk, C., Königstedt, R., Parchatka, U., Schiller, C. L., Stickler, A., Williams, J., and Lelieveld, J.: Hydroxyl radicals in the tropical troposphere over the Suriname rainforest: airborne measurements, *Atmos Chem Phys*, 10, 3759-3773, 2010.

Matsumi, Y., Murakami, S., Kono, M., Takahashi, K., Koike, M., and Kondo, Y.: High-sensitivity instrument for measuring atmospheric NO₂, *Anal Chem*, 73, 5485-5493, Doi 10.1021/Ac010552f, 2001.

Matsumoto, J., Hirokawa, J., Akimoto, H., and Kajii, Y.: Direct measurement of NO₂ in the marine atmosphere by laser-induced fluorescence technique, *Atmos Environ*, 35, 2803-2814, Doi 10.1016/S1352-2310(01)00078-4, 2001.

- Matsumoto, J., and Kajii, Y.: Improved analyzer for nitrogen dioxide by laser-induced fluorescence technique, *Atmos Environ*, 37, 4847-4851, 10.1016/j.atmosenv.2003.08.023, 2003.
- Matsumoto, J., Kosugi, N., Nishiyama, A., Isozaki, R., Sadanaga, Y., Kato, S., Bandow, H., and Kajii, Y.: Examination on photostationary state of NO_x in the urban atmosphere in Japan, *Atmos Environ*, 40, 3230-3239, 10.1016/j.atmosenv.2006.02.002, 2006.
- Mcfarland, M., Ridley, B. A., Proffitt, M. H., Albritton, D. L., Thompson, T. L., Harrop, W. J., Winkler, R. H., and Schmeltekopf, A. L.: Simultaneous Insitu Measurements of Nitrogen-Dioxide, Nitric-Oxide, and Ozone between 20 and 31 Km, *J Geophys Res-Atmos*, 91, 5421-5437, Doi 10.1029/Jd091id05p05421, 1986.
- Molina, L. T., and Molina, M. J.: Ultraviolet-Absorption Spectrum of Chlorine Nitrite, *Clono, Geophys Res Lett*, 4, 83-86, Doi 10.1029/Gl004i002p00083, 1977.
- Molina, L. T., and Molina, M. J.: Chlorine Nitrate Ultraviolet-Absorption Spectrum at Stratospheric Temperatures, *J Photochem*, 11, 139-144, Doi 10.1016/0047-2670(79)80047-7, 1979.
- Monks, P. S.: Gas-phase radical chemistry in the troposphere, *Chemical Society reviews*, 34, 376-395, 10.1039/b307982c, 2005.
- Murphy, J. G., Day, A., Cleary, P. A., Wooldridge, P. J., and Cohen, R. C.: Observations of the diurnal and seasonal trends in nitrogen oxides in the western Sierra Nevada, *Atmos Chem Phys*, 6, 5321-5338, 2006.
- Newman, S. M., Howie, W. H., Lane, I. C., Upson, M. R., and Orr-Ewing, A. J.: Predissociation of the A²Π_{3/2} state of IO studied by cavity ring-down spectroscopy, *J Chem Soc Faraday T*, 94, 2681-2688, Doi 10.1039/A805103h, 1998.
- Nollet, L. M. L.: *Chromatographic analysis of the environment*, 3rd ed., *Chromatographic science series*, 93, CRC/Taylor & Franciss, Boca Raton, xx, 1297 p. pp., 2006.
- Nölscher, A. C., Williams, J., Sinha, V., Custer, T., Song, W., Johnson, A. M., Axinte, R., Bozem, H., Fischer, H., Pouvesle, N., Phillips, G., Crowley, J. N., Rantala, P., Rinne, J., Kulmala, M., Gonzales, D., Valverde-Canossa, J., Vogel, A., Hoffmann, T., Ouwersloot, H. G., Vilà-Guerau de Arellano, J., and Lelieveld, J.: Summertime total OH reactivity measurements from boreal forest during HUMPPA-COPEC 2010, *Atmos Chem Phys*, 12, 8257-8270, 10.5194/acp-12-8257-2012, 2012.
- Nölscher, A. C., Bourtsoukidis, E., Bonn, B., Kesselmeier, J., Lelieveld, J., and Williams, J.: Seasonal measurements of total OH reactivity emission rates from Norway spruce in 2011, *Biogeosciences*, 10, 4241-4257, 10.5194/bg-10-4241-2013, 2013.
- Novelli, A., Hens, K., Tatum Ernest, C., Kubistin, D., Regelin, E., Elste, T., Plass-Dülmer, C., Martinez, M., Lelieveld, J., and Harder, H.: Characterisation of an inlet pre-injector laser induced fluorescence instrument for the measurement of ambient hydroxyl radicals, *Atmos. Meas. Tech. Discuss.*, 7, 819-858, 10.5194/amtd-7-819-2014, 2014.

O'Brien, R. J.: *Photostationary State in Photochemical Smog Studies*, *Environ Sci Technol*, 8, 579-583, Doi 10.1021/Es60091a004, 1974.

Orlando, J. J., Tyndall, G. S., Moortgat, G. K., and Calvert, J. G.: *Quantum Yields for NO₃ Photolysis between 570 and 635nm* *J Phys Chem-Us*, 97, 10996-11000, Doi 10.1021/J100144a017, 1993.

Osthoff, H. D., Brown, S. S., Ryerson, T. B., Fortin, T. J., Lerner, B. M., Williams, E. J., Pettersson, A., Baynard, T., Dube, W. P., Ciciora, S. J., and Ravishankara, A. R.: *Measurement of atmospheric NO₂ by pulsed cavity ring-down spectroscopy*, *J Geophys Res-Atmos*, 111, Artn D12305 Doi 10.1029/2005jd006942, 2006.

Ouwensloot, H. G., de Arellano, J. V. G., Nolscher, A. C., Krol, M. C., Ganzeveld, L. N., Breitenberger, C., Mammarella, I., Williams, J., and Lelieveld, J.: *Characterization of a boreal convective boundary layer and its impact on atmospheric chemistry during HUMPPA-COPEC-2010*, *Atmos Chem Phys*, 12, 9335-9353, DOI 10.5194/acp-12-9335-2012, 2012.

Parra, J., and George, L. A.: *Development of an ambient pressure laser-induced fluorescence instrument for nitrogen dioxide*, *Appl Optics*, 48, 3355-3361, 2009.

Parrish, D. D., Trainer, M., Williams, E. J., Fahey, D. W., Hubler, G., Eubank, C. S., Liu, S. C., Murphy, P. C., Albritton, D. L., and Fehsenfeld, F. C.: *Measurements of the NO_x-O₃ Photostationary State at Niwot Ridge, Colorado*, *J Geophys Res-Atmos*, 91, 5361-5370, Doi 10.1029/Jd091id05p05361, 1986.

Paul, D., and Osthoff, H. D.: *Absolute Measurements of Total Peroxy Nitrate Mixing Ratios by Thermal Dissociation Blue Diode Laser Cavity Ring-Down Spectroscopy*, *Anal Chem*, 82, 6695-6703, Doi 10.1021/Ac101441z, 2010.

Perner, D., and Platt, U.: *Detection of Nitrous-Acid in the Atmosphere by Differential Optical-Absorption*, *Geophys Res Lett*, 6, 917-920, Doi 10.1029/Gl006i012p00917, 1979.

Perring, A. E., Bertram, T. H., Farmer, D. K., Wooldridge, P. J., Dibb, J., Blake, N. J., Blake, D. R., Singh, H. B., Fuelberg, H., Diskin, G., Sachse, G., and Cohen, R. C.: *The production and persistence of Sigma RONO₂ in the Mexico City plume*, *Atmos Chem Phys*, 10, 7215-7229, DOI 10.5194/acp-10-7215-2010, 2010.

Phillips, G. J., Tang, M. J., Thieser, J., Brickwedde, B., Schuster, G., Bohn, B., Lelieveld, J., and Crowley, J. N.: *Significant concentrations of nitryl chloride observed in rural continental Europe associated with the influence of sea salt chloride and anthropogenic emissions*, *Geophys Res Lett*, 39, Artm L10811 Doi 10.1029/2012gl051912, 2012.

Phillips, G. J., Pouvesle, N., Thieser, J., Schuster, G., Axinte, R., Fischer, H., Williams, J., Lelieveld, J., and Crowley, J. N.: *Peroxyacetyl nitrate (PAN) and peroxyacetic acid (PAA) measurements by iodide chemical ionisation mass spectrometry: first analysis of results in the boreal forest and implications for the measurement of PAN fluxes*, *Atmos Chem Phys*, 13, 1129-1139, DOI 10.5194/acp-13-1129-2013, 2013.

Platt, U., Perner, D., and Patz, H. W.: Simultaneous Measurement of Atmospheric CH₂O, O₃, and NO₂ by Differential Optical-Absorption, *J Geophys Res-Oc Atm*, 84, 6329-6335, Doi 10.1029/Jc084ic10p06329, 1979.

Platt, U., and Janssen, C.: Observation and role of the free radicals NO₃, ClO, BrO and IO in the troposphere, *Faraday Discuss*, 100, 175-198, Doi 10.1039/Fd9950000175, 1995.

Platt, U., and Stutz, J.: *Differential Optical Absorption Spectroscopy*, in, Springer-Verlag Berlin Heidelberg, 2008.

Platt, U., Meinen, J., Pöhler, D., and Leisner, T.: Broadband Cavity Enhanced Differential Optical Absorption Spectroscopy (CE-DOAS) - applicability and corrections, *Atmospheric Measurement Techniques*, 2, 713-723, 2009.

Poulida, O., Civerolo, K. L., and Dickerson, R. R.: Observations and Tropospheric Photochemistry in Central North-Carolina, *J Geophys Res-Atmos*, 99, 10553-10563, Doi 10.1029/94jd00404, 1994.

Rasmussen, D. J., Fiore, A. M., Naik, V., Horowitz, L. W., McGinnis, S. J., and Schultz, M. G.: Surface ozone-temperature relationships in the eastern US: A monthly climatology for evaluating chemistry-climate models, *Atmos Environ*, 47, 142-153, DOI 10.1016/j.atmosenv.2011.11.021, 2012.

Ridley, B. A., Madronich, S., Chatfield, R. B., Walega, J. G., Shetter, R. E., Carroll, M. A., and Montzka, D. D.: Measurements and Model Simulations of the Photostationary State during the Mauna-Loa-Observatory Photochemistry Experiment - Implications for Radical Concentrations and Ozone Production and Loss Rates, *J Geophys Res-Atmos*, 97, 10375-10388, 1992.

Riley, W. J.: A test suite for the calculation of time domain frequency stability, *Proceedings of the 1995 Ieee International Frequency Control Symposium*, 360-366, Doi 10.1109/Freq.1995.483922, 1995.

Riley, W. J.: *Handbook of Frequency Stability Analysis*, National Institute of Standards and Technology (NIST), U.S. Department of Commerce, 136 pp., 2008.

Roehl, C. M., Orlando, J. J., Tyndall, G. S., Shetter, R. E., Vazquez, G. J., Cantrell, C. A., and Calvert, J. G.: Temperature-Dependence of the Quantum Yields for the Photolysis of NO₂ near the Dissociation Limit, *J Phys Chem-US*, 98, 7837-7843, Doi 10.1021/J100083a015, 1994.

Roelofs, G. J., and Lelieveld, J.: Model study of the influence of cross-tropopause O₃ transports on tropospheric O₃ levels, *Tellus B*, 49, 38-55, DOI 10.1034/j.1600-0889.49.issue1.3.x, 1997.

Rohrer, F., Bruning, D., Grobler, E. S., Weber, M., Ehhalt, D. H., Neubert, R., Schussler, W., and Levin, I.: Mixing ratios and photostationary state of NO and NO₂ observed during the POPCORN field campaign at a rural site in Germany, *Journal of Atmospheric Chemistry*, 31, 119-137, Doi 10.1023/A:1006166116242, 1998.

Rohrer, F., and Berresheim, H.: Strong correlation between levels of tropospheric hydroxyl radicals and solar ultraviolet radiation, *Nature*, 442, 184-187, 10.1038/nature04924, 2006.

Rohrer, F., Lu, K. D., Hofzumahaus, A., Bohn, B., Brauers, T., Chang, C. C., Fuchs, H., Haseler, R., Holland, F., Hu, M., Kita, K., Kondo, Y., Li, X., Lou, S. R., Oebel, A., Shao, M., Zeng, L. M., Zhu, T., Zhang, Y. H., and Wahner, A.: Maximum efficiency in the hydroxyl-radical-based self-cleansing of the troposphere, *Nat Geosci*, 7, 559-563, Doi 10.1038/Ngeo2199, 2014.

Rosen, R. S., Wood, E. C., Wooldridge, P. J., Thornton, J. A., Day, D. A., Kuster, W., Williams, E. J., Jobson, B. T., and Cohen, R. C.: Observations of total alkyl nitrates during Texas Air Quality Study 2000: Implications for O₃ and alkyl nitrate photochemistry, *J Geophys Res-Atmos*, 109, Artn D07303 Doi 10.1029/2003jd004227, 2004.

Salisbury, G., Monks, P. S., Bauguitte, S., Bandy, B. J., and Penkett, S. A.: A seasonal comparison of the ozone photochemistry in clean and polluted air masses at Mace Head, Ireland, *Journal of Atmospheric Chemistry*, 41, 163-187, Doi 10.1023/A:1014202229304, 2002.

Sander, R., Baumgaertner, A., Gromov, S., Harder, H., Jockel, P., Kerkweg, A., Kubistin, D., Regelin, E., Riede, H., Sandu, A., Taraborrelli, D., Tost, H., and Xie, Z. Q.: The atmospheric chemistry box model CAABA/MECCA-3.0, *Geosci Model Dev*, 4, 373-380, DOI 10.5194/gmd-4-373-2011, 2011a.

Sander, S. P., Abbatt, J., Barker, J. R., Burkholder, J. B., Friedl, R. R., Golden, D. M., Huie, R. E., Kolb, C. E., Kurylo, M. J., Moortgat, G. K., Orkin, V. L., and Wine, P. H.: Chemical Kinetics and Photochemical Data for Use in Atmospheric Studies, in: *JPL Publication 10-6*, 2011b.

Saunders, S. M., Jenkin, M. E., Derwent, R. G., and Pilling, M. J.: Protocol for the development of the Master Chemical Mechanism, MCM v3 (Part A): tropospheric degradation of non-aromatic volatile organic compounds, *Atmos Chem Phys*, 3, 161-180, (MCM v3.2, via website: <http://mcm.leeds.ac.uk/MCM>), 2003.

Savitzky, A., and Golay, M. J. E.: Smoothing + Differentiation of Data by Simplified Least Squares Procedures, *Anal Chem*, 36, 1627-&, Doi 10.1021/Ac60214a047, 1964.

Schneider, M., Luxenhofer, O., Deissler, A., and Ballschmiter, K.: C-1-C-15 alkyl nitrates, benzyl nitrate, and bifunctional nitrates: Measurements in California and South Atlantic air and global comparison using C₂Cl₄ and CHBr₃ as marker molecules, *Environ Sci Technol*, 32, 3055-3062, Doi 10.1021/Es980132g, 1998.

Schneider, P., and R. van der A.: A global SCIAMACHY-based trend analysis of tropospheric NO₂ over megacities, *PRESCRIBE workshop*, Bremen, 2013.

Schönbein, C. F.: On the Odour Accompanying Electricity and on the Probability of its Dependence on the Presence of a New Substance, *Philosophical Magazine* 17, 293-294, 1840.

Schuster, G., Labazan, I., and Crowley, J. N.: A cavity ring down/cavity enhanced absorption device for measurement of ambient NO₃ and N₂O₅, *Atmospheric Measurement Techniques*, 2, 1-13, 2009.

Seinfeld, J. H., and Pandis, S. N.: *Atmospheric Chemistry and Physics - From Air Pollution to Climate Change* (2nd Edition), John Wiley & Sons, 2006.

Shetter, R. E., Stedman, D. H., and West, D. H.: *The NO/NO₂/O₃ Photostationary State in Claremont, California*, *Japca J Air Waste Ma*, 33, 212-214, 1983.

Shon, Z. H., Madronich, S., Song, S. K., Flocke, F. M., Knapp, D. J., Anderson, R. S., Shetter, R. E., Cantrell, C. A., Hall, S. R., and Tie, X.: *Characteristics of the NO-NO₂-O₃ system in different chemical regimes during the MIRAGE-Mex field campaign*, *Atmos Chem Phys*, 8, 7153-7164, 2008.

Sillman, S.: *The relation between ozone, NO_x and hydrocarbons in urban and polluted rural environments*, *Atmos Environ*, 33, 1821-1845, Doi 10.1016/S1352-2310(98)00345-8, 1999.

Simpson, I. J., Meinardi, S., Blake, D. R., Blake, N. J., Rowland, F. S., Atlas, E., and Flocke, F.: *A biomass burning source of C-1-C-4 alkyl nitrates*, *Geophys Res Lett*, 29, Artn 2168 Doi 10.1029/2002gl016290, 2002.

Simpson, I. J., Wang, T., Guo, H., Kwok, Y. H., Flocke, F., Atlas, E., Meinardi, S., Rowland, F. S., and Blake, D. R.: *Long-term atmospheric measurements of C-1-C-5 alkyl nitrates in the pearl river delta region of southeast China*, *Atmos Environ*, 40, 1619-1632, DOI 10.1016/j.atmosenv.2005.10.062, 2006.

Singer, R. J., Crowley, J. N., Burrows, J. P., Schneider, W., and Moortgat, G. K.: *Measurement of the Absorption Cross-Section of Peroxynitric Acid between 210 and 330 nm in the Range 253-298-K*, *J Photoch Photobio A*, 48, 17-32, Doi 10.1016/1010-6030(89)87086-8, 1989.

Singh, H. B., Ohara, D., Herlth, D., Bradshaw, J. D., Sandholm, S. T., Gregory, G. L., Sachse, G. W., Blake, D. R., Crutzen, P. J., and Kanakidou, M. A.: *Atmospheric Measurements of Peroxyacetyl Nitrate and Other Organic Nitrates at High-Latitudes - Possible Sources and Sinks*, *J Geophys Res-Atmos*, 97, 16511-16522, 1992.

Solomon, S., *Intergovernmental Panel on Climate Change.*, and *Intergovernmental Panel on Climate Change. Working Group I.: Climate change 2007 : the physical science basis : contribution of Working Group I to the Fourth Assessment Report of the Intergovernmental Panel on Climate Change*, Cambridge University Press, Cambridge ; New York, viii, 996 p. pp., 2007.

Song, W., Williams, J., Yassaa, N., Martinez, M., Carnero, J. A. A., Hidalgo, P. J., Bozem, H., and Lelieveld, J.: *Winter and summer characterization of biogenic enantiomeric monoterpenes and anthropogenic BTEX compounds at a Mediterranean Stone Pine forest site*, *Journal of Atmospheric Chemistry*, 68, 233-250, DOI 10.1007/s10874-012-9219-4, 2011.

Spirig, C., Neftel, A., Kleinman, L. I., and Hjorth, J.: *NO_x versus VOC limitation of O₃ production in the Po valley: Local and integrated view based on observations*, *J Geophys Res-Atmos*, 107, Artn 8191 Doi 10.1029/2001jd000561, 2002.

Stedman, D. H., and Jackson, J. O.: Photostationary State in Photochemical Smog, *Int J Chem Kinet*, 1, 493-501, 1975.

Stull, R. B.: *An Introduction to Boundary Layer Meteorology*, Kluwer Academic Publishers, Dordrecht, The Netherlands, 666 pp., 1988.

Taketani, F., Kawai, M., Takahashi, K., and Matsumi, Y.: Trace detection of atmospheric NO₂ by laser-induced fluorescence using a GaN diode laser and a diode-pumped YAG laser, *Appl Optics*, 46, 907-915, Doi 10.1364/Ao.46.000907, 2007.

Talukdar, R. K., Burkholder, J. B., Schmoltner, A. M., Roberts, J. M., Wilson, R. R., and Ravishankara, A. R.: Investigation of the Loss Processes for Peroxyacetyl Nitrate in the Atmosphere - UV Photolysis and Reaction with OH, *J Geophys Res-Atmos*, 100, 14163-14173, Doi 10.1029/95jd00545, 1995.

Talukdar, R. K., Herndon, S. C., Burkholder, J. B., Roberts, J. M., and Ravishankara, A. R.: Atmospheric fate of several alkyl nitrates .1. Rate coefficients of the reactions alkyl nitrates with isotopically labelled hydroxyl radicals, *J Chem Soc Faraday T*, 93, 2787-2796, 1997.

Taraborrelli, D., Lawrence, M. G., Butler, T. M., Sander, R., and Lelieveld, J.: Mainz Isoprene Mechanism 2 (MIM2): an isoprene oxidation mechanism for regional and global atmospheric modelling, *Atmos Chem Phys*, 9, 2751-2777, 2009.

Taraborrelli, D., Lawrence, M. G., Crowley, J. N., Dillon, T. J., Gromov, S., Gross, C. B. M., Vereecken, L., and Lelieveld, J.: Hydroxyl radical buffered by isoprene oxidation over tropical forests, *Nat Geosci*, 5, 190-193, Doi 10.1038/Ngeo1405, 2012.

Thieser, J.: *Atmospheric Reactive Nitrogen Chemistry via Cavity Ringdown Spectroscopy-From short-lived compounds to reservoir species*, Doctor of Natural Science, Max Planck Institute for Chemistry, University of Heidelberg, Germany, International Max Planck Research School for Atmospheric Chemistry and Physics 2013.

Thompson, A. M.: The Oxidizing Capacity of the Earths Atmosphere - Probable Past and Future Changes, *Science*, 256, 1157-1165, DOI 10.1126/science.256.5060.1157, 1992.

Thornton, J. A., Wooldridge, P. J., and Cohen, R. C.: Atmospheric NO₂: In situ laser-induced fluorescence detection at parts per trillion mixing ratios, *Anal Chem*, 72, 528-539, Doi 10.1021/Ac9908905, 2000.

Thornton, J. A., Wooldridge, P. J., Cohen, R. C., Martinez, M., Harder, H., Brune, W. H., Williams, E. J., Roberts, J. M., Fehsenfeld, F. C., Hall, S. R., Shetter, R. E., Wert, B. P., and Fried, A.: Ozone production rates as a function of NO_x abundances and HO_x production rates in the Nashville urban plume, *J Geophys Res-Atmos*, 107, Artn 4146 Doi 10.1029/2001jd000932, 2002.

Tiao, G. C., Reinsel, G. C., Pedrick, J. H., Allenby, G. M., Mateer, C. L., Miller, A. J., and Deluisi, J. J.: A Statistical Trend Analysis of Ozonesonde Data, *J Geophys Res-Atmos*, 91, 3121-3136, Doi 10.1029/Jd091id12p13121, 1986.

Trebs, I., Mayol-Bracero, O. L., Pauliquevis, T., Kuhn, U., Sander, R., Ganzeveld, L., Meixner, F. X., Kesselmeier, J., Artaxo, P., and Andreae, M. O.: Impact of the Manaus urban plume on trace gas mixing ratios near the surface in the Amazon Basin: Implications for the

NO-NO₂-O₃ photostationary state and peroxy radical levels, Journal of Geophysical Research, 117, 10.1029/2011jd016386, 2012.

Vandaele, A. C., Hermans, C., Simon, P. C., Carleer, M., Colin, R., Fally, S., Merienne, M. F., Jenouvrier, A., and Coquart, B.: Measurements of the NO₂ absorption cross-section from 42 000 cm⁻¹ to 10 000 cm⁻¹ (238-1000 nm) at 220 K and 294 K, J Quant Spectrosc Ra, 59, 171-184, Doi 10.1016/S0022-4073(97)00168-4, 1998.

*Vandaele, A. C., Hermans, C., Fally, S., Carleer, M., Colin, R., Merienne, M. F., Jenouvrier, A., and Coquart, B.: High-resolution Fourier transform measurement of the NO₂ visible and near-infrared absorption cross sections: Temperature and pressure effects, J Geophys Res-Atmos, 107, Artn 4348
Doi 10.1029/2001jd000971, 2002.*

Vaughan, S., Ingham, T., Whalley, L. K., Stone, D., Evans, M. J., Read, K. A., Lee, J. D., Moller, S. J., Carpenter, L. J., Lewis, A. C., Fleming, Z. L., and Heard, D. E.: Seasonal observations of OH and HO₂ in the remote tropical marine boundary layer, Atmos Chem Phys, 12, 2149-2172, 10.5194/acp-12-2149-2012, 2012.

Vogel, A. L., Auml;ijala, M., Corrigan, A. L., Junninen, H., Ehn, M., Petaja, T., Worsnop, D. R., Kulmala, M., Russell, L. M., Williams, J., and Hoffmann, T.: In situ submicron organic aerosol characterization at a boreal forest research station during HUMPPA-COPEC 2010 using soft and hard ionization mass spectrometry, Atmos Chem Phys, 13, 10933-10950, 2013.

*Volz-Thomas, A., Patz, H. W., Houben, N., Konrad, S., Mihelcic, D., Klupfel, T., and Perner, D.: Inorganic trace gases and peroxy radicals during BERLIOZ at Pabstthum: An investigation of the photostationary state of NO_x and O₃, J Geophys Res-Atmos, 108, Artn 8248
Doi 10.1029/2001jd001255, 2003.*

Wahid, A.: Influence of atmospheric pollutants on agriculture in developing countries: A case study with three new wheat varieties in Pakistan, Sci Total Environ, 371, 304-313, DOI 10.1016/j.scitotenv.2006.06.017, 2006.

Wayne, R. P., Barnes, I., Biggs, P., Burrows, J. P., Canosamas, C. E., Hjorth, J., Lebras, G., Moortgat, G. K., Perner, D., Poulet, G., Restelli, G., and Sidebottom, H.: The Nitrate Radical - Physics, Chemistry, and the Atmosphere, Atmos Environ a-Gen, 25, 1-203, Doi 10.1016/0960-1686(91)90192-A, 1991.

Whalley, L. K., Furneaux, K. L., Gravestock, T., Atkinson, H. M., Bale, C. S. E., Ingham, T., Bloss, W. J., and Heard, D. E.: Detection of iodine monoxide radicals in the marine boundary layer using laser induced fluorescence spectroscopy, Journal of Atmospheric Chemistry, 58, 19-39, 10.1007/s10874-007-9075-9, 2007.

Williams, J., Yassaa, N., Bartenbach, S., and Lelieveld, J.: Mirror image hydrocarbons from Tropical and Boreal forests, Atmos Chem Phys, 7, 973-980, 2007.

Williams, J., Crowley, J., Fischer, H., Harder, H., Martinez, M., Petaja, T., Rinne, J., Back, J., Boy, M., Dal Maso, M., Hakala, J., Kajos, M., Keronen, P., Rantala, P., Aalto, J., Aaltonen, H., Paatero, J., Vesala, T., Hakola, H., Levula, J., Pohja, T., Herrmann, F., Auld, J., Mesarchaki, E., Song, W., Yassaa, N., Nolscher, A., Johnson, A. M., Custer, T., Sinha, V.,

Thieser, J., Pouvesle, N., Taraborrelli, D., Tang, M. J., Bozem, H., Hosaynali-Beygi, Z., Axinte, R., Oswald, R., Novelli, A., Kubistin, D., Hens, K., Javed, U., Trawny, K., Breitenberger, C., Hidalgo, P. J., Ebben, C. J., Geiger, F. M., Corrigan, A. L., Russell, L. M., Ouwersloot, H. G., de Arellano, J. V. G., Ganzeveld, L., Vogel, A., Beck, M., Bayerle, A., Kampf, C. J., Bertelmann, M., Kollner, F., Hoffmann, T., Valverde, J., Gonzalez, D., Riekkola, M. L., Kulmala, M., and Lelieveld, J.: *The summertime Boreal forest field measurement intensive (HUMPPA-COPEC-2010): an overview of meteorological and chemical influences*, *Atmos Chem Phys*, 11, 10599-10618, DOI 10.5194/acp-11-10599-2011, 2011.

Wojtas, J., Stacewicz, T., Bielecki, Z., Czyzewski, A., and Nowakowski, M.: *NO₂ monitoring setup applying cavity enhanced absorption spectroscopy*, *Eurocon 2007: The International Conference on Computer as a Tool*, Vols 1-6, 2152-2154, 2007.

Wood, E. C., Wooldridge, P. J., Freese, J. H., Albrecht, T., and Cohen, R. C.: *Prototype for in situ detection of atmospheric NO₃ and N₂O₅ via laser-induced fluorescence*, *Environ Sci Technol*, 37, 5732-5738, Doi 10.1021/Es034507w, 2003.

Yang, J., Honrath, R. E., Peterson, M. C., Parrish, D. D., and Warshawsky, M.: *Photostationary state deviation-estimated peroxy radicals and their implications for HO_x and ozone photochemistry at a remote northern Atlantic coastal site*, *J Geophys Res-Atmos*, 109, Artn D02312
Doi 10.1029/2003jd003983, 2004.

Yassaa, N., Song, W., Lelieveld, J., Vanhatalo, A., Back, J., and Williams, J.: *Diel cycles of isoprenoids in the emissions of Norway spruce, four Scots pine chemotypes, and in Boreal forest ambient air during HUMPPA-COPEC-2010*, *Atmos Chem Phys*, 12, 7215-7229, DOI 10.5194/acp-12-7215-2012, 2012.

York, D., Evensen, N. M., Martinez, M. L., and Delgado, J. D.: *Unified equations for the slope, intercept, and standard errors of the best straight line*, *American Journal of Physics*, 72, 367-375, Doi 10.1119/1.1632486, 2004.

8 ACKNOWLEDGEMENTS

CURRICULUM VITAE

Erklärung

Ich versichere hiermit, dass ich die vorgelegte Arbeit selbständig verfasst und nur die angegebenen Quellen und Hilfsmittel verwendet habe.

M. U. Javed

Mainz, 2014